Adsorption of Cu(II) ions by means of foundry waste

Štrkalj, Anita; Glavaš, Zoran

University of Zenica
FACULTY OF METALLURGY AND TECHNOLOGY
Bosnia and Herzegovina

Univerzitet u Zenici
METALURŠKO-TEHNOLOŠKI FAKULTET
Bosna i Hercegovina

14th Scientific - Research Symposium
with International Participation

METALLIC AND NONMETALLIC MATERIALS
production – properties – application

XIV Naučno - stručni simpozijum
sa međunarodnim učešćem

METALNI I NEMETALNI MATERIJALI
proizvodnja – osobine – primjena

BOOK OF ABSTRACTS with electronic edition of Proceedings
KNJIGA ABSTRAKTA sa elektronskim izdanjem Zbornika radova

Zenica, Bosnia and Herzegovina, 27th-28th April 2023
Zenica, Bosna i Hercegovina, 27-28. april 2023.

EDITOR/UREDNIK
Dr Farzet Bikić

PUBLISHER/IZDAVAČ
Univerzitet u Zenici
Organizaciona jedinica Metalurško-tehnološki fakultet
Travnička cesta 1, 72000 Zenica
Tel: ++
387 401 831, 402 832, Fax: ++ 387 406 903

TECHNICAL ASSISTANCE AND DTP
KOMPJUTERSKA OBRADA TEKSTA
Amila Krnjić
Zahida Begović
Dejana Kasapović
Lamija Sušić

PRINTED BY/ŠTAMPA
ŠTAMPARIJA FOJNICA D.D.

ISSUE/TIRAŽ: 100 copies/primjeraka

ORGANIZING COMMITTEE/ORGANIZACIONI ODBOR

Dr Farzet Bikić, president
Dr Jusuf Duraković
Dr Ilhan Bušatlić
Dr Adnan Mujkanović
Dr Hasan Avdušinović
Mr Dejana Kasapović
Mr Amna Karić, secretary
Lamija Sušić, dipl. Ing.

INTERNATIONAL SCIENTIFIC/RESEARCH COMMITTEE/NAUČNI ODBOR

Dr Anžel Ivan, SI
Dr Avdušinović Hasan, BA
Dr Balanović Ljubiša, RS
Dr Begić-Hajdarević Đerzija, BA
Dr Berberović Edin, BA
Dr Bikić Farzet, BA
Dr Bizjak Milan, SI
Dr Bogdanović Grozdanka, RS
Dr Burzić Zijah, RS
Dr Bušatlić Ilhan, BA
Dr Bušatlić Nadira BA
Dr Chumbley Scott, US
Dr Ćubela Diana, BA
Dr Ćatić Sead, BA
Dr Dabić Pero, HR
Dr Delijić Kemal, CG
Dr Dolić Natalija, HR
Dr Dolinžek Slavko, SI
Dr Duraković Jusuf, BA
Dr Džubur Žana, BA
Dr Džonlagić Nusreta, BA
Dr Ekinović Sabahudin, BA
Dr Fidančevska Emilija, MK
Dr Gigović-Gekić Almaida, BA
Dr Gojić Mirko, HR
Dr Grubešić Ivana, BA
Dr Hadžikadunić Fuad, BA
Dr Halilović Azra, BA
Dr Hamedović Safet, BA
Dr Haračić Nedžad, BA
Dr Hessling Goetz, DE
Dr Herenda Safija, BA
Dr Holger Frenz, DE
Dr Imamović Aida, BA
Dr Imamović Nusret, BA
Dr Ivanković Hrvoje, HR
Dr Iličković Zoran, BA
Dr Janačković Đorđe, RS
Dr Jovanović Marina, BA
Dr Komatina Mirko, RS
Dr Kosec Borut, SI
Dr Korać Fehim, BA
Dr Krolo Petar, RH
Dr Lamut Jakob, SI
Dr Lazić Dragica, BA
Dr Lemeš Samir, BA
Dr Mamuzić Ilija, HR
Dr Medved Jožef, SI
Dr Merdić Nevzet, BA
Dr Mirjanić Dragoljub, BA
Dr Mujkanović Adnan, BA
Dr Nagode Aleš, SI
Dr Oruč Mirsada, BA
Dr Pašić Sead, BA
Dr Perušić Mitar, BA
Dr Ranogajec Jonjaua, RS
Dr Rustempašić Nerman, BA
Dr Salihović Senaid, BA
Dr Senk Dieter, DE
Dr Spužić Sead, AU
Dr Srbić Vladimir, RS
Dr Stanojlović Rodoljub, RS
Dr Stuhli Vedran, BA
Dr Suljagić Jasmin, BA
Dr Sunulahpašić Raza, BA
Dr Šetrajčić Jovan, BA
Dr Štrbac Nada, RS
Dr Volkov-Husović Tatjana, RS
Dr Vučenović Siniša, BA
Dr Vukojević Nedeljko, BA
Dr Vukojević-Medvidović Nediljka, HR
Dr Zelić Jelica, HR
Dr Zlokolica Miodrag, RS
Dr Zovko-Brodarac Zdenka, HR
Dr Žero Sabina, BA
Dr Živković Živan, RS

14(2023), No.14
ISSN2566-4344

14th Scientific – Research Symposium
with International Participation

METALLIC AND NONMETALLIC MATERIALS
production – properties – application

PROCEEDINGS

Zenica, B&H, April 27th 2023

CONTENTS

page

KEYNOTES PAPERS

METALLIC MATERIALS

PLENARY LECTURES

PYROPHYLLITE-MODIFIED CARBON PASTE ELECTRODE FOR CARBENDAZIM DETECTION IN WATER AND FOOD

Jasmina Grbović Novaković, Anđela Mitrović Rajić, Katarina Tošić, Sara Mijaković, Sanja Milošević Govedarević, Ana Vujačić Nikezić, Bojana Paskaš Mamula
Centre of Excellence for Hydrogen and Renewable Energy, "Vinča" Institute of Nuclear Sciences, National Institute of Republic of Serbia
Belgrade, Serbia

Jasmina Kustura, Enita Kurtanović, Belma Halilhodžić
Innovation Science Development Center (INRC), AD Harbi Ltd
Sarajevo, B&H

Keywords: pyrophyllite Parsovići, carbon paste electrode, electrochemical sensor

ABSTRACT
The work aims to design a pyrophyllite-modified carbon paste electrode for pesticide detection in aqueous solutions. The structural and morphological characterization of natural pyrophyllite clay for Parsovići mine, Bosnia and Herzegovina, and mechanically modified pyrophyllite was performed using X-ray diffraction analysis (XRD), scanning electron microscopy (SEM), Fourier transform infrared spectroscopy (FTIR) and particle size analysis (PSD). The electrochemical characteristics of the constructed electrode were investigated using cyclic voltammetry in 1 mM $K_4Fe(CN)_6$ in 0.1 M KCl and 0.5 M H_2SO_4 and differential pulse stripping voltammetry in Britton-Robinson buffer at pH 2-8. It was shown that the maximum at + 0.96 V versus Ag/AgCl originates from oxidation by carbendazim at pH 4 in the Britton-Robinson buffer. The electrode designed in this way showed numerous advantages such as good stability and sensitivity. The developed analytical method is linear over the range of 1 ppm to 10 ppm with r=0.999 and a detection limit of 0.3 ppm.

1. INTRODUCTION

The crystal lattice of 2:1 phyllosilicate mineral pyrophyllite consists of an octahedral sheet of $AlO_4(OH)_2$ located between two SiO_4 tetrahedral layers. The bonds between layers are weak van der Walls [1-8], so the layers can easily slide over each other. Pyrophyllite can be used in porcelain, building materials, fire-resistant material, insecticide, textiles, detergents, cosmetics, and as the filler for rubberizing, papermaking, painting, etc. [2,9-15]. Different applications of pyrophyllite starting from various types of ceramics including refractories, enamels, and ceramics membranes [9,10,1,17] to heavy metal and organic pollutant adsorbents [16-20] require different modifications methods [1-22]:

1. ion exchange with inorganic and organic cations and cationic complexes;
2. reaction with acids;
3. pillaring by different types of poly- (hydroxo metal) cation;
4. dehydroxylation and calcination, delamination and reaggregation of clay minerals;

One of the possible methods of modification is mechanochemical activation (MCA). MCA is an environmentally friendly green chemistry method that introduces structural disorder, reduces particle size, and increases of chemical reactivity of material [21-23]. It has been shown that in contrast to the high chemical stability of pyrophyllite, mechanochemically

activated pyrophyllite and its ores result in noteworthy structural distortion and reduction of particles and crystallite size [1-5,7,8,18,11,21,24-28]. Therefore in this work, we suggest the use of MCA as a modification technique for pyrophyllite as functionalized material for modified carbon paste electrode (CPE). CPEs are extensively used in the field of electrochemical sensors due to the low cost of materials, simple sample preparation, low background current, and wide potential window [29]. CPEs are a mixture of graphite (carbon) materials, a binder (paraffin oil, silicone oil, or tricresylphosphate), and some functionalization materials. Clay-based electrochemical sensors are used for qualitative and quantitative analysis of various gases and components in aqueous solutions [30-36]. Previous research has been done on clays such as sepiolite, serpentinite, kaolinite, haloysite, montmorillonite [31-36].

According to our best knowledge, there are no scientific studies related to the application of CPE based on mechanically modified pyrophyllite in electroanalytical practice. Therefore, we propose using pyrophyllite as the electrochemical active substance in CPEs as a working electrode for detecting the carbendazim pesticide. Determination of pesticide traces in food and water is of extreme interest since pesticides are highly toxic chemicals with pronounced carcinogenicity and endocrine-disrupting effects.

2. EXPERIMENTAL PART

X-ray diffraction has been used to determine the phase composition of samples using Rigaku Ultima IV, Japan). Crystallite size and lattice strain are calculated using XRD profile analysis using the Williamson-Hall plot according to Eq. (1) [37]:

$$\beta\cos(\theta) = 2\varepsilon\sin(\theta) + \frac{0.9\lambda}{D} \quad (1)$$

where k = 0.9 is the shape factor and β is the corrected peak full width at half maximum (FWHM) [33]

The $\beta\cos(\theta)$ is plotted as a function of $\sin(\theta)$, and a straight line is derived using the least squares method with an intercept at 0.9 λ/D and a slope of 2ε. Both crystallite size D and lattice strain ε are calculated from equation (1). The qualitative analysis of samples was performed on Thermo Scientific Nicolet iS10 Spectrometer using attenuated total reflectance (ATR) sampling technique. The surface modifications, the phase distribution of the MCA-activated clays, material homogeneity, and morphology of the powder particles were investigated by scanning electron microscopy (SEM) using model JOEL JSM6610LV, manufacturer JOEL, USA) equipped with EDS spectrometer model BLACK-Comet CXR-SR-50, manufacturer StellarNet Inc.). A Malvern 2000SM Mastersizer laser scattering particle size analysis system has been used to obtain quantitative clay particle size distributions. The Ag/AgCl electrode (saturated with KCl) was used as a reference electrode, the platinum wire was used as an auxiliary electrode, and different types of pyrophyllite-modified CPE with paraffin oil were used as the working electrodes. Voltametric analyses were done on Gamry potentiostat Interface 1010E.

3. RESULTS AND DISCUSSION

Figure 1 shows XRD patterns of pyrophyllite ore (P-0) from the Parsovići mine (Bosnia and Herzegovina). The ore contain pyrophyllite, quartz, kaolinite, calcite, and muscovite. Two major phases are pyrophyllite with characteristic reflections at 2θ 9.68 and 29.23 and quartz at 2θ 20.94 and 26.74 [11]. Mechanical modification causes a noticeable increase in the crystallite size of both quartz and pyrophyllite, thus indicating the presence of residual stress in the crystal lattice as shown in Figure 2. After 15 minutes of mechanical milling microstrain and crystallite size decreases.

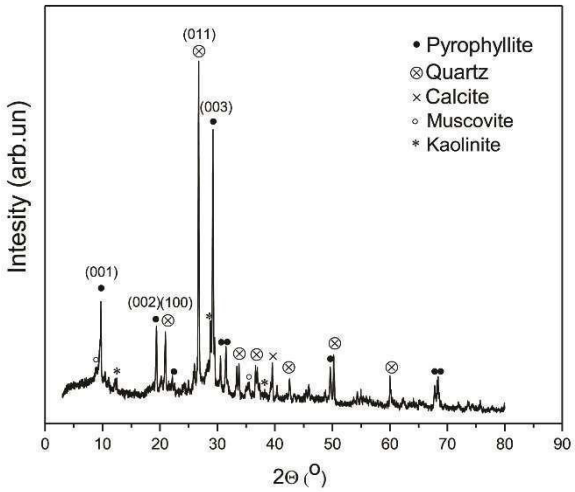

Figure 1. XRD patterns of pyrophyllite ore from the Parsovići mine, Bosnia and Herzegovina

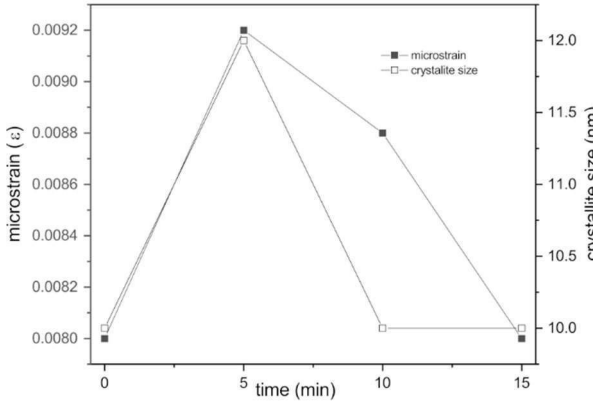

Figure 2. Microstrain and crystallite size of pyrophyllite samples milled from 0 to 15 minutes

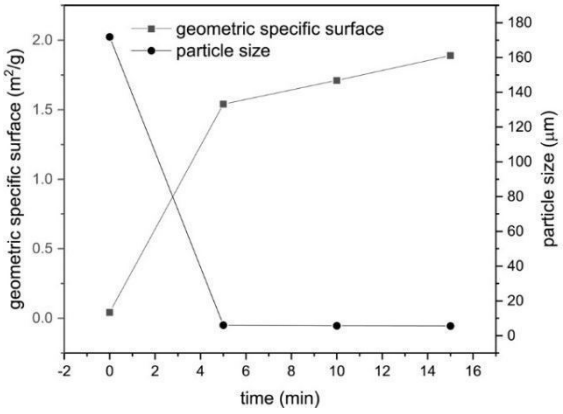

Figure 3. Changes in geometric-specific surface area and particle size during mechanical milling

FTIR spectra are shown in Figure 4. The unmilled sample (P-0) showed a strong band at 3672 cm^{-1} which can be assigned to OH vibration from Al-OH linkage [11]. At 1120 cm^{-1}, a strong band is observed that can be attributed to Si-O stretching vibration. The bands at 832 cm^{-1} and 943 cm^{-1} correspond to Al-OH bending vibration. The peak at 518 cm^{-1} can be assigned to Si-O-Si bending vibration. The vibration at 1616 cm^{-1} corresponds to bending the OH surface group [11]). The band at 802 cm^{-1} corresponds to the characteristic bands of silica [38]. The band at 754 cm^{-1} indicates the presence of Si–O–Al where Al is in tetrahedral coordination. It also indicates that there is a possible presence of sericite/muscovite minerals. The peak at 532 cm^{-1} can be assigned to octahedral AlO_6 sheet vibrations. The band at 1028 cm^{-1} can be assigned to the intense Si–O and Si–O–Al stretching vibrations, characteristic of aluminosilicates [9]. The band at 450 cm^{-1} corresponds to the bending of Si – O groups [39]. After 5 minutes of grinding, the bands at 779 cm^{-1} and 797 cm^{-1} appear indicating the presence of quartz [21] and thus confirming the results of XRD analysis. These vibrations are present even after 120 minutes of grinding, indicating that quartz has a more stable structure than pyrophyllite [7]. After 15 minutes of grinding, the vibration at 1120 cm^{-1} disappears indicating a breakdown of the Si-O band, which means that the tetrahedral sheets have been destroyed. Also, after 60 minutes of milling, the bands at 3673 cm^{-1}, 943 $cm^{-1,}$ and 832 cm^{-1} disappeared, as a result

of the release of OH groups from the Al-centered octahedrons. Therefore, the octahedral sheets are damaged [11]. The intensity of the band at 518 cm^{-1} decreases with increasing milling time as a consequence of the collapse of the Si-O-Al band, resulting in a broken link between the tetrahedral and octahedral sheets [11].
The differential pulse stripping voltammetry was used for the quantitative determination of carbendazim. Based on the previous results [40,41], an electrode with a composition of 50P:50C was chosen as the working electrode, where pyrophyllite was mechanochemically activated for a period of 15 minutes. Changes were monitored at pH 4 and 8.

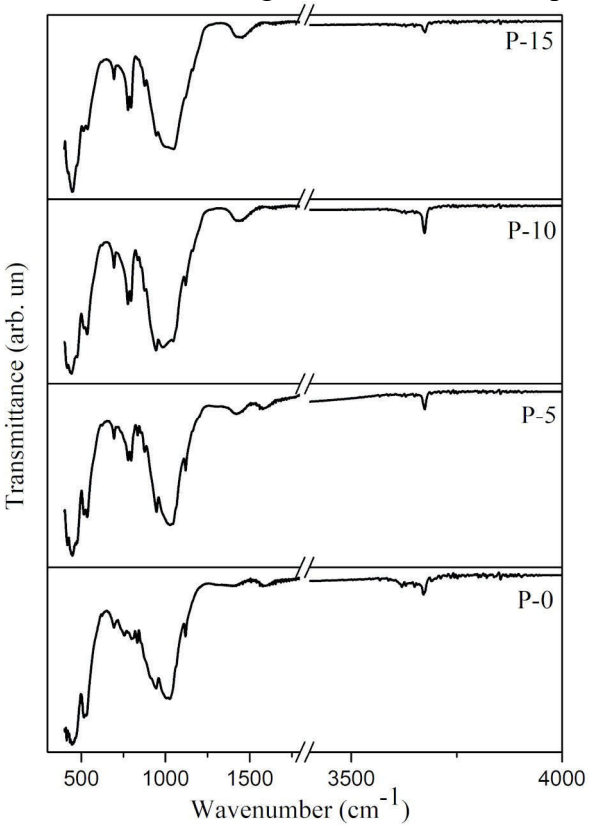

Figure 4. FTIR of pure and milled material from 0 to 15 minutes, P-O (O min), P-5 (5 min), P-10 (10 min), P-20 (20 min)

Figure 5 shows differential pulse voltammograms for the determination of carbendazim in Britton-Robinson buffer at pH 4. (lower) and pH 8 (higher). The maximum occurs at + 0.96 V and 0.73 respectively. The maximum intensity increases with increasing concentration of carbendazim [42]. The peak at around 0.5 V corresponds to the hydrogen evolution reaction.
From peak maxima, we have obtained the calibration curves for carbendazim detection with excellent linearity. The slope and intercept at pH 8 have the following values 0.40 and 8.85, while at pH 4 are 0.31 and 9.22.
The results show that the sensor constructed in this way, carbon paste modified with pyrophyllite where paraffin oil was used as the binding liquid, in Britton-Robinson buffer shows excellent sensitivity and a low detection limit in the range from 1 ppm to 10 pm. Kalijadis et al. used the method of differential pulse stripping voltammetry for qualitative and quantitative detection of carbendazim, where a carbon paste electrode obtained with nitrogen was used as the working electrode, while tricresyl phosphate was used as the binding liquid [43]. Ashrafi et al. investigated a carbon paste electrode with tricresyl phosphate as a binding fluid for the detection of carbendazim [44]. The influence of pH in

the Britton-Robinson buffer on pH in the range from 2 to 8 was also investigated. The maximum oxidation of carbendazim was most intense at pH 4.

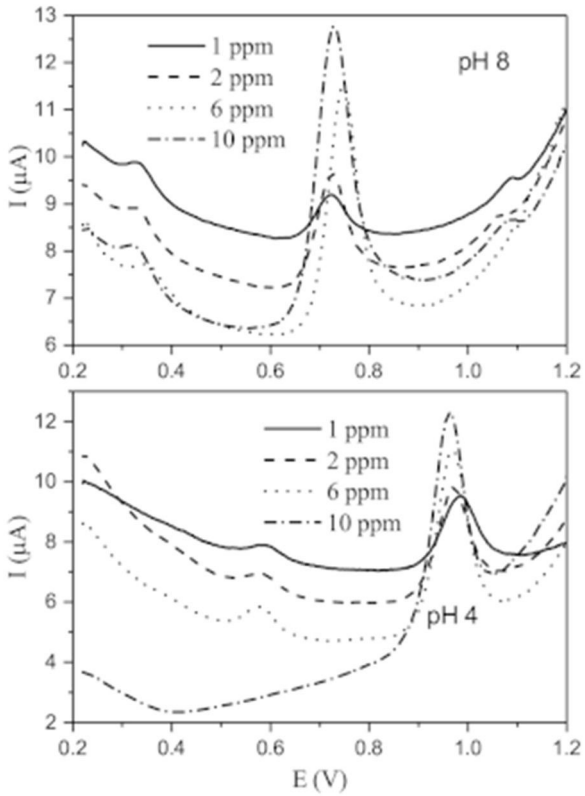

Figure 5. Differential pulse voltammograms for the determination of carbendazim in Britton-Robinson buffer at pH 4 (lower) and pH 8 (higher)

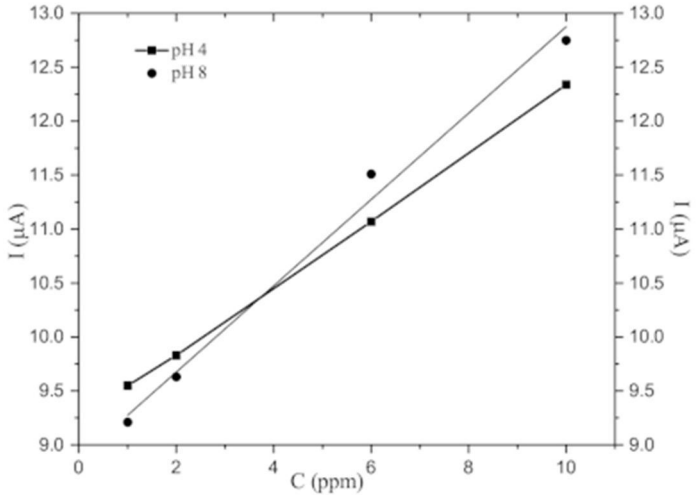

Figure 6. Calibration curve obtained for a pyrophyllite-modified carbon paste electrode with paraffin oil as a binding fluid for the detection of carbendazim in Britton-Robinson buffer at pH 4 and pH 8 in the concentration range from 1 ppm to 10 ppm

The influence of the presence of 2-hydroxypropyl-β-cyclodextrin on the electrochemical behavior of carbendazim was also investigated. The detection was followed by the method of differential pulse adsorptive "striping" voltammetry. It was found that the analytical performance of the tricresyl phosphate carbon paste electrode could be improved almost

two-fold by the addition of the 2-hydroxypropyl-β-cyclodextrin modifier. Guo and co-workers (Guo et al.) used cyclodextrin-graphene hybrid nanosheets as a material for the electrochemical detection of carbendazim [45]. The effect of pH was investigated in the range of 5 to 10 in 0.1 M phosphate buffer. At pH 7, the maximum oxidation by carbendazim was the most intense, so the measurements were performed at this pH value. Differential pulse voltammetry was used for carbendazim detection. The detection limit was 2.0·10−9 mol/L, and the relative standard deviation was 4.67%.

4. CONCLUSION

Mechanochemically activated pyrophyllite was used for the construction of electrochemical sensors. The microstructural and morphological characterization of the material was performed by X-ray structural analysis, scanning electron microscopy, and infrared spectroscopy with Fourier transform, and the particle size distribution was monitored by the laser diffraction method. The response of the sensor was obtained by differential pulse stripping voltammetry. Based on X-ray structural analysis, it was concluded that the mechanochemical modification leads to a change in the crystal structure of pyrophyllite. The particles change their morphology from lamellar to particles that do not have a characteristic shape already after 5 minutes of grinding while the specific surface area increases with the increase of milling time. Given that mechanical grinding causes the amorphization of soft phases of pyrophyllite ore, further insight into the structure of the material was provided by infrared spectroscopy with Fourier transform. It was shown that after 15 minutes of grinding the tetrahedral structure (SiO4 plate) collapses. Mechanochemically activated pyrophyllite was used to form a modified carbon paste electrode. This electrode is part of the pesticide detection sensor. The electrochemical properties of the obtained electrode were investigated by cyclic voltammetry and differential pulse stripping voltammetry. It was also shown that the reactions at the electrode are fast and reversible and that the electrode is stable. Differential pulse stripping voltammetry showed that this electrode can be used for qualitative and quantitative detection of carbendazim fungicides. The best results were obtained at pH 4, where the limit of detection was 0.3 ppm, the limit of quantification was 1.03 ppm, and the residual standard deviation was 2.3 %.

5. ACKNOWLEDGMENT

This work is supported by the Ministry of Science, Technology, and Innovation of The Republic of Serbia under Grant 451-03-68/2022/14/200017.
We thank AD Harbi Ltd for the assignment of mineral raw materials for research purposes.

6. REFERENCES

[1] H. Hayashi, K. Koshi, A. Hamada, H. Sakabe, Structural change of pyrophyllite by grinding, and its effect on the toxicity of the cell. *Clay Science 1*(5) (1962), 99-108

[2] S. Mohammadnejad, J. L. Provis, J. S. J. van Deventer, Effects of grinding on the preg-robbing behavior of pyrophyllite, *Hydrometallurgy*, 146 (2014), 154–163

[3] J. L. Pérez-Rodríguez, L. Madrid Sánchez del Villar, P. J. Sánchez-Soto, Effects of dry grinding on pyrophyllite, *Clay Minerals 23* (1988), 399–410

[4] P. J. Sánchez-Soto, A. Justo, J. L. Pérez-Rodríguez, Grinding effect on kaolinite-pyrophyllite-illite natural mixtures and its influence on mullite formation, *Journal of Materials Science 29(5)* (1994), 1276–1283

[5] J. M. Filio, K. Sugiyama, F. Saito, Y. Waseda, Effect of Dry milling on the Structures and Physical Properties of Pyrophyllite and Talc by a Planetary Ball Mill, *International Journal of the Society of Materials Engineering for Resources 1(1)* (1993), 140-147

[6] H. Sayılkan, S. Erdemoğlu, Ş. Şener, F. Sayılkan, M. Akarsu, M. Erdemoğlu, Surface modification of pyrophyllite with amino silane coupling agent for the removal of 4-nitrophenol from aqueous solutions, *Journal of Colloid and Interface Science 275(2)* (2004), 530–538

[7] J. Temuujin, K. Okada, T.S. Jadambaa, K.J.D. MacKenzie, J. Amarsanaa, Effect of grinding on the leaching behaviour of pyrophyllite, *Journal of the European Ceramic Society 23(8)* (2003), 1277–1282

[8] J. L. Pérez-Rodríguez, A. Wiewiora, V. Ramirez-Valle, A. Durán, L. A. Pérez-Maqueda, Preparation of nano-pyrophyllite: Comparative study of sonication and grinding, *Journal of Physics and Chemistry of Solids 68(5-6)* (2007), 1225–1229

[9] T. K. Mukhopadhyay, S. Ghatak, H. S. Maiti, Pyrophyllite as raw material for ceramic applications in the perspective of its pyro-chemical properties, *Ceramics International 36(3)* (2010), 909–916

[10] G. Li, J. Zeng, J. Luo, M. Liu, T. Jiang, G. Qiu, Thermal transformation of pyrophyllite and alkali dissolution behavior of silicon, *Applied Clay Science 99* (2014), 282–288

[11] J. Zhang, J. Yan, J. Sheng, Dry milling effect on pyrophyllite–quartz natural mixture and its influence on the structural alternation of pyrophyllite, *Micron 71 (2015)*, 1– 6

[12] H. Heller, R. Keren, Anionic polyacrylamide polymer adsorption by pyrophyllite and montmorillonite, *Clays and Clay Minerals 51(3)* (2003), 334–339

[13] A. Goswami, M. K. Purkait, Kinetic and Equilibrium Study for the Fluoride Adsorption using Pyrophyllite, *Separation Science and Technology 46(11)* (2011), 1797–1807

[14] S. Saxena, M. Prasad, S. S. Amritphale, N. Chandra, Adsorption of cyanide from aqueous solutions at pyrophyllite surface, *Separation and Purification Technology 24(1-2)* (2001), 263–270

[15] Gücek, S. Şener, S. Bilgen, M. A. Mazmancı, Adsorption and kinetic studies of cationic and anionic dyes on pyrophyllite from aqueous solutions, *Journal of Colloid and Interface Science 286(1)* (2005), 53–60

[16] Y. Jeong, S. Lee, S. Hong, C. Park, Preparation, characterization and application of low-cost pyrophyllite-alumina composite ceramic membranes for treating low-strength domestic wastewater, *Journal of Membrane Science 536* (2017), 108–115

[17] R. Ahmad, M. Aslam, E. Park, S. Chang, D. Kwon, J. Kim, Submerged low-cost pyrophyllite ceramic membrane filtration combined with GAC as fluidized particles for industrial wastewater treatment, *Chemosphere 206* (2018), 784–792

[18] J. B. Dixon, D. G. Schulze, L. W Zelazny, P. J Thomas, C. L. Lawrence, Chapter 13-Pyrophyllite-Talc Minerals, in: J. B. Dixon, D. G. Schulze (Ed.) Soil Mineralogy with Environmental Applications, Soil Science Society of America, (2002), 415-430

[19] X. Qin, J. Zhao, J. Wang, M. He, Atomic Structure, Electronic and Mechanical Properties of Pyrophyllite under Pressure: A First-Principles Study, *Minerals 10(9)* (2020), 778.

[20] R. Wardle, G. W. Brindley, The crystal structures of pyrophyllite, 1Tc, and of its dehydroxylate, *American Mineralogist 57* (1972), 732-750.

[21] I. Tole, K. Habermehl-Cwirzen, A. Cwirzen, Mechanochemical activation of natural clay minerals: an alternative to produce sustainable cementitious binders – review, *Mineralogy and Petrology 133* (2019), 449-462

[22] P. Baláž, M. Achimovičová, M. Baláž, P. Billik, Z. Cherkezova-Zheleva, J. M. Criado, F. J. Gotor, Hallmarks of mechanochemistry: from nanoparticles to technology, *Chemical Society Reviews* 42(18) (2013), 7571–7637

[23] T. K. Achar, A. Bose, P. Mal, Mechanochemical synthesis of small organic molecules, *Beilstein Journal of organic chemistry 13*(1) (2017), 1907-1931
[24] J. L. Pérez-Rodriguez, P. J. Sánchez-Soto, The influence of the dry grinding on the thermal behaviour of pyrophyllite, *Journal of Thermal Analysis 37(7)* (1991), 1401–1413
[25] K. Sugiyama, J. M. Filio, F. Saito, Y. Waseda, Structural change of kaolinite and pyrophyllite induced by dry grinding, *Mineralogical Journal 17(1)* (1994), 28–41
[26] P. J. Sánchez-Soto, J. L. Pérez-Rodríguez, I. Sobrados, J. Sanz, Influence of grinding in pyrophyllite-mullite thermal transformation assessed by ^{29}Si and ^{27}Al MAS NMR Spectroscopies, *Chemistry of Materials 9(3)* (1997), 677–684
[27] P. J. Sánchez-Soto, M. d. C. Jiménez de Haro, L. A. Pérez-Maqueda, I. Varona, J. L. Pérez Rodríguez, Effects of dry grinding on the structural changes of kaolinite powders, *Journal of American Ceramic Society 83(7)* (2000), 1649–1657
[28] A. Wiewióra, P. J. Sánchez-Soto, M. A. Avilés, A. Justo, J. L. Pérez-Rodríguez, Effect of dry milling and leaching on polytypic structure of pyrophyllite, *Applied Clay Science 8(4)* (1993), 261–282
[29] I. Švancara, K. Kalcher, A. Walcarius, K. Vytřas, Electroanalysis with Carbon Paste Electrodes, CRS Press: Boca Raton, FL, 2012
[30] U. Guth, S. Brosda, J. Schomburg, Applications of clay minerals in sensor techniques, *Applied Clay Science 11(2-4)* (1996), 229–236
[31] M. Pekin, D. E. Bayraktepe, Z. Yazan, Electrochemical sensor based on a sepiolite clay nanoparticle-based electrochemical sensor for ascorbic acid detection in real-life samples, *Ionics 23(12)* (2017), 3487–3495
[32] M. Z. Momčilović, M. S. Ranđelović, M. M. Purenović, J. S. Đorđević, A. Onjia, B. Matović, Morpho-structural, adsorption and electrochemical characteristics of serpentinite, *Separation and Purification Technology 163* (2016), 72–78
[33] S. P. Akanji, O. A. Arotiba, D. Nkosi, Voltammetric Determination of Pb(ii) Ions at a Modified Kaolinite-Carbon Paste Electrode, *Electrocatalysis 10(6)* (2019), 1–10
[34] E. S. Goda, M. A Gab-Allah, B. S. Singu, K. R. Yoon, Halloysite nanotubes based electrochemical sensors: A review, *Microchemical Journal 147* (2019), 1083-1096
[35] B. J. Sanghavi, G. Hirsch, S. P. Karna, A. K. Srivastava, Potentiometric Stripping Analysis of Methyl and Ethyl Parathion Employing Carbon Nanoparticles and Halloysite Nanoclay Modified Carbon Paste Electrode, *Analytica Chimica Acta 735* (2012), 37–45
[36] P. Kula, Z. Navrátilová, P. Kulová, M. Kotoucek, Sorption and determination of Hg(II) on clay modified carbon paste electrodes, *Analytica Chimica Acta 385(1-3)* (1999), 91-101
[37] G. K. Williamson, W. H. Hall, X-ray Line Broadening from Filed Aluminium and Wolfram, *Acta Metallurgica et Materialia 1(1)* (1953), 22-31
[38] S. S. Amritphale, S. Bhasin, N. Chandra, Energy efficient process for making pyrophyllite-based ceramic tiles using phosphoric acid and mineralizers, *Ceramics International 32(2)* (2006), 181–187
[39] M. Erdemoğlu, S. Erdemoğlu, F. Sayılkan, M. Akarsu, Ş. Şener, H.S Ayılkan, Organo-functional modified pyrophyllite: preparation, characterization and Pb(II) ion adsorption property, *Applied Clay Science 27(1-2)* (2004), 41–52
[40] A. Mitrović, T. Pantić, S. Dimitrijević, A. Ivanović, N. Novaković, S. Kurko, S. Milošević Govedarović, J. Grbović Novaković, Electrochemical sensors based on pyrophyllite – Parsovic, MCM2019, 14th Multinational Congress on Microscopy, September 15-20, 2019, Belgrade, Serbia, Program and the book of abstracts. 494-497.
[41] J. Milićević, S. Kurko, B. Paskaš Mamula,T. Trtić-Petrović, T. Pantić,S. Milošević Govedarević, A. Hodžić, J. Grbović Novaković, Electrochemical behaviour of pyrophyllite

carbon paste composite electrode, 3rd International Symposium on Materials for Energy Storage and Conversion, September 10-12th, 2018, Belgrade, Serbia, P 14, Program and the book of abstracts, 95

[42] A. I. Mitrović Rajić, J. S. Milićević, J. D. Grbović Novaković. Development of modified pyrophyllite carbon paste electrode for carbendazim detection, *Materials and Manufacturing Processes* (2022), 1-7

[43] A. Kalijadis, J. Djorđević, Z. Papp, B. Jokić, V. Spasojević, B. Babić, T. Trtić-Petrović, A novel carbon paste electrode based on nitrogen-doped hydrothermal carbon for electrochemical determination of carbendazim", Journal of Serbian. Chemical Society, 82 (11) (2017), 1259–1272

[44] A. M. Ashraf, J. Đorđević, V. Guzsvány, I. Švancara, T. Trtić-Petrović, M. Purenović, K. Vitřas, Trace determination of carbendazim fungicide using adsorptive stripping voltammetry with a carbon paste electrode containing tricresyl phosphate, *International Journal of Electrochemical Science 7(10)* (2012), 9717-9731

[45] Y. S. Guo, S. Guo, J. Li, E. Wang, S. Dong, Cyclodextrin–graphene hybrid nanosheets as enhanced sensing platform for ultrasensitive determination of carbendazim, *Talanta 84(1)* (2011), 60–64.

FERTILIZER BASED ON PYROPHYLLITE IN ACCORDANCE WITH THE REGULATION EU 2019/1009

Milan J. Adamović
Institute for Technology of Nuclear and Other Mineral Raw Materials
Belgrade, Serbia

Jasmina Kustura, Enita Kurtanović, Belma Halilhodžić, Atif Hodžić, Muhamed Harbinja
AD Harbi Ltd.
Sarajevo, B&H

Mirjana D. Stojanović
Engineering Academy of Serbia
Belgrade, Serbia

Keywords: pyrophyllite, multifunctional fertilizer, regulation (EU) 2019/1009, beets

ABSTRACT
We are currently witnessing the beginning of the global food crisis and disturbances in the fertilizer market. On the other hand, on July 16, 2022, Regulation (EU) 2019/1009 of the European Parliament and of the Council for laying down rules on the placing on the market of EU fertilizer products establishes strict rules on the safety and quality of fertilizers and repealing Regulation (EC) 2003/2003. The paper presents the modeling of process parameters of multifunctional fertilizer, as a compound inorganic macronutrient fertilizer/liming material/soil improver, based on pyrophyllite shale (pyrophyllite), deposits Parsovići, Konjic, BiH, enriched with dolomite, BiH to achieve the formulation of Product Function Categories (PFC) in terms of the content of secondary macronutrients (CaO and MgO) accordance with Regulation (EU) 2019/1009. The biological efficiency of the newly formulated fertilizer was tested through vegetation trials with beets (Beta vulgaris var. Conditiva).

1. INTRODUCTION

Today, the world is facing a potential food shortage and fertilizers for plant nutrition. Some projections suggest that fertilizer use may have to double to meet the demand for food until 2050. On the other hand, Regulation (EU) 2019/1009 of the European Parliament and of the Council for laying down rules for the placing on the market of EU fertilizer products and amending Regulation (EC) No. 1069/2009 and (EC) No. 1107/2009. The new (EU) Regulation 2019/1009 repeals Regulation (EC) No. 2003/2003, 16th July 2022, and establishes the wide quality, safety, and environmental criteria for “EU” fertilizers [1].
The new regulation provides strict rules on safety contaminants, pathogens, quality (the content of nutrients), and labeling requirements for all fertilizers to be traded freely across the EU. Producers will need to demonstrate that their products meet those requirements before affixing the CE mark. EU fertilizing products are divided into different Product Function Categories (PFC), which should each be subject to specific safety and quality requirements, adapted to their different intended uses. In terms of safety, the new ones are being introduced the limit values for contaminants in fertilizers (Cd, Pb, Ni, Cu, Zn, Hg, As) and other potentially toxic elements and pathogens) [2].

Facing the threatening deficiency of food and fertilizers and the strict requirements of Regulation (EU) 2019/1009, we need fast and comprehensive solutions at the world level. The aim of this paper is to define the parameters of obtaining a natural mineral multifunctional fertilizer based on pyrophyllite from deposits in Parsovići, Konjic, BiH, enriched with dolomite, BiH whose quality and safety are in line with the requirements of new regulations, which will contribute to reduced soil degradation, increasing biodiversity and improving soil quality as a priority for achieving sustainable agriculture. The biological efficiency of the newly formulated fertilizer was tested through vegetation trials with beets *(Beta vulgaris var. Conditiva).*

1.1. Pyrophyllite

Pyrophyllite is a type of phyllosilicate mineral, from the group of layered silicates, based on a combination of two tetrahedral (T) and one octahedral (O) plates, containing no isomorphic substitution and therefore no layer charge. The basic 2:1 structure (T-O-T), with silicon in the tetrahedral layer and aluminum in the octahedral layer, is pyrophyllite ($Al_2Si_4O_{10}(OH)_4$). The basal surfaces where the interlayer space is devoid of the hydrated counterions are hydrophobic, whereas edges resulting from the breaking of the sheets are hydrophilic in aqueous solutions, due to the occurrence of OH groups (essentially silanol). The sheets are held together only by weak van der Waals forces, which result in pyrophyllite's softness (Mohs hardness is between 1 and 1.5). Furthermore, the pyrophyllite has high density (2.7 and 2.9 gcm^{-3}), a relatively high cation exchange capacity (between 50 and 70 meq 100 g^{-1}), and a pH ranging from neutral to slightly alkaline, between 7.5-8.5. Pyrophyllite has a neutral electromagnetic charge [3,4,5,6].

The unique properties of pyrophyllite, such as its structure it its adsorption capacity, and ion exchange, have led to the use of pyrophyllite in agriculture as a soil regenerator and increased fertility. Pyrophyllite is used as a carrier of fertilizers in agriculture, where it improves the ability of the soil to retain nutrients and reduces leaching, and is an inert pesticide carrier. Improves the efficiency of mineral fertilizers, and has the ability to release tightly bound phosphates that already exist in the soil and make them available to plants. Pyrophyllite has high retention properties which make them very useful in decreasing the bioavailability of heavy metals in soils and preventing their inclusion in the food chain. Pyrophyllite naturally contains micro and macronutrients such as K, Mg, Ca, Si, Fe, Zn, Cu, P, and B essential for plant growth and development. This type of clay has a neutral pH and acts as a buffer in soil conditions and an acidity corrector. Due to the listed characteristics of pyrophyllite, the properties of the soil conditioner (regenerator) are attributed to it. It contributes to the improvement of the physical, chemical, and agrochemical properties of the soil. Improves soil structure, and permeability increases cation exchange capacity, increases soil's ability to retain nutrients and reduces rinsing and motility of heavy metals in the soil, improves the efficiency of mineral fertilizers, acts as a buffer, and regulates soil pH. All of the above justifies the growing global interest in its use to improve and maintain soil productivity in the function of sustainable agricultural production [7,8,9,10].

Also, pyrophyllite application in the amount of 25% of recommended fertilizer rate can reduce the use of mineral fertilizers in lettuce production without adverse effects on its yield and quality [11], pyrophyllite application of 2200 kg/ha in combination with mineral fertilizer NPK 15:15:5 in the amount of 0.8 t/ha confirmed a positive effect on cabbage yield [12]. Watering of onion with the suspension of water and pyrophyllite and suspension of water and enriched pyrophyllite with urea nitrogen compared to the control treatment (H_2O) contributed to the increase in biomass of onion heads by 18.31% and 24.09%, respectively ($p<0.01$) [9]. Pyrophyllite showed antibacterial properties against *Escherichia*

coli, *Staphylococcus aureus*, and *Enterococcus faecalis*, and antifungal properties against fungal pathogens (*Fusarium oxysporum, Phoma glomerata,* and *Rhizoctonia solani*). This mineral can also be used for biological control of *F. oxysporum* in the soil for growing potatoes [13]. Tribomechanically activated pyrophyllite converts a part of crystalline SiO_2 into amorphous, which in soil solutions converted to silica acid available to plants that are thought to contribute to plant biotic and abiotic stress tolerance [14].

2. EXPERIMENTAL

This phase included modeling of optimal process parameters required for obtaining a multifunctional fertilizer, PiroFert (working title), based on composite pyrophyllite enriched with dolomite, in order to comply with the requirements of EU regulation 2019/1009.

The starting raw materials are pyrophyllite shale (pyrophyllite) ($Al_2Si_4O_{10}(OH)_4$) from deposit Parsovići, Konjic, BiH and dolomite, BiH ($CaMg(CO_3)_2$).

The content of secondary macronutrients (CaO and MgO) and harmful elements, pH, and neutralization value in pyrophyllite and dolomite composite are shown in Tables 1 and 2, based on a laboratory report of the Faculty of Mining, Geology and Civil Engineering, University of Tuzla.

Table 1. Content of secondary macronutrients CaO and MgO, pH, neutralization value in the composite of pyrophyllite and dolomite

Parameter	MgO %	CaO %	ΣMgO+CaO %	pH (KCl)	NV*eq CaO
Composite	6.82	14.43	21.25	8.60	24.72

**neutralizing value*

Table 2. Content of hamful elements in composite of pyrophyllite and dolomite

Parameter	Cd mg/kg	Pb mg/kg	Cr^{6+} mg/kg	Cu mg/kg	Zn mg/kg	Ni mg/kg	Hg mg/kg	As mg/kg
Composite	<0.1	2.46	1.12	4.03	18.99	2.55	<1	<1

Investigation of the efficiency of composite PiroFert based on pyrophyllite and dolomite on the neutralization of acidic soil and its influence on the growth and development of beets *(Beta vulgaris var. Conditiva).*

The experiment was carried out at the location of the village of Banja, Aranđelovac, Serbia. The soil on which the beetroot was grown was in the type of oil. At 0-30 cm soil depth, the pH value (H_2O) was 5.1, and it was classified as acidic soil. After the calcification and fertilization of the soil, beetroot (*Beta vulgaris var. Conditiva*) was planted, which belongs to cultures with a weak tolerance to acidic soils (low pH). The experiment was carried out in a 1 m^2 cassette. Table 3 shows the variants of fertilization in the vegetation trial.

Table 3. Variants of fertilization in the vegetation trial

Variant of fertilizer	Control	Experiment with PiroFert
NPK (15:15:15), g/m^2	30 g	30 g
Compost from vegetable waste, g/m^2	5000 g	5000 g
PiroFert g/m^2	-	500 g

At the end of the vegetation trial, the length and mass of beet plant organs (roots and leaves) were measured on 5 selected plants (on the basis of pairs). The trial lasted five months.

3. RESULTS AND DISCUSSION

3.1. Formulation of multifunctional fertilizer based on pyrophyllite

Formulation of multifunctional fertilizer, based on quality and safety parameters for Product Function Categories PFC1, PFC2, and PFC3, defined in the Regulation EU 2019/1009:

1. **Category PFC1 (C, b):** Compound solid inorganic macronutrient fertilizer with more than one secondary macronutrient (calcium (Ca), magnesium (Mg), sodium (Na), sulphur (S)) and no primary macronutrients (nitrogen (N), phosphorus (P), potassium (K)) and must contain at least 1,5 % by mass of total magnesium oxide (MgO) and 1,5 % by mass of total calcium oxide. The sum of all declared macronutrient contents shall be at least 18 % by mass.
2. **Category PFC2:** Liming material: shall be an EU fertilizing product the function of which is to correct soil acidity and shall contain oxides, hydroxides, carbonates, or silicates of the nutrients calcium (Ca) or magnesium (Mg); minimum neutralizing value: 15 (equivalent CaO), minimum grain size: at least 70 % < 1 mm,
3. **Category PFC3 (B):** Inorganic soil improver, Soil improver is an EU fertilizer product whose function is to maintain, improve or protect the physical or chemical properties, structure, or biological activity of the soil to which it is added.

According to Directive EU 2019/1009, contaminants in fertilizer must not exceed the following limit values shown in Table 4.

Table 4. Content of harmful components in fertilizers according to the Directive EU 2019/1009) [2]

Category	Cd (mg/kg)	Cr(VI) (mg/kg)	Pb (mg/kg)	Cu (mg/kg)	Zn (mg/kg)	Ni (mg/kg)	Hg (mg/kg)	As (mg/kg)
PFC1	3	2	120	<600	<1500	100	1	40
PFC2	2	2	120	<300	<800	90	1	40
PFC3	1.5	2	120	<300	<800	100	1	40

Based on the content of secondary macronutrients CaO and MgO and the content of harmful components in the composite of pyrophyllite and dolomite, PiroFert, (Table 1 and 2), the product formulation was defined, mass fraction, based on pyrophyllite and a small part of dolomite where the sum of active components is above 18%, which is the minimum for registration (Σ CaO +MgO = 21.25%) which in terms of quality and safety meets the criteria of three categories PFC1, PFC2, and PFC3, EU directive 2019/1009, and can be registered as multifunctional fertilizers, as a compound inorganic macronutrient fertilizer/liming material/soil improver. The product must meet product-specific labeling requirements, obtaining the CE mark in order to be ready for the EU market. With dolomite content in the composite, the requirements of the regulation for regenerators (inorganic soil improver) and/or means for adjusting the pH value of the plastering material are met. It should be emphasized that pure pyrophyllite meets the requirements of registration as a conditioner (inorganic soil improver).

3.2. Results of the vegetation experiment with beetroot

The measurement of the length of the beet parts and the diameter of the root as well as the mass of the plant parts, at the end of the experiment (5 months after sowing), was carried out on 5 selected plants (on the principle of pairs) of each treatment. The results are shown in Table 5 and the appearance of the beets at the end of the experiment is shown in Figure 1.

Table 5. Average length and diameter of beet roots at the end of the experiment, cm

Parameters	Control	Experiment PiroFert	Index Control 100 %
Leaf	32.8	36.6	111.58
Root	14.2	18.2	128.17
Total	47.0	54.8	116.59
Root diameter, cm	4.0	5.3	132.50

The lengths of the main parts of the plant, leaves, and roots (Table 5) including the diameter of the roots indicate their more intensive development compared to the development of plants in the control treatment. Leaf length was greater by 11.58%, root by 28.17%, and root diameter by 32.50%.

Figure 1. The appearance of beets at the end of the experiment (whole plant, root, and section)

The average mass of the basic parts of the plant, leaves, and roots (Table 6), similar to the length of the same parts of the beet, was higher in the experimental treatment with PiroFert. The average mass of the leaf in this treatment was greater than the control treatment by 32.55%, the root by 48.97%, and the total mass of the plant by 40.07%.

Table 6. The average weight of the beet parts at the end of the experiment, g

Parameters	Control	Experiment PiroFert	Index Contol 100 %
Leaf	57.8	76.6	132.52
Root	49.0	73.0	148.97
Total	106.8	149.6	140.07

The results of the height and mass of beet plant organs are illustrated in Figure 2.

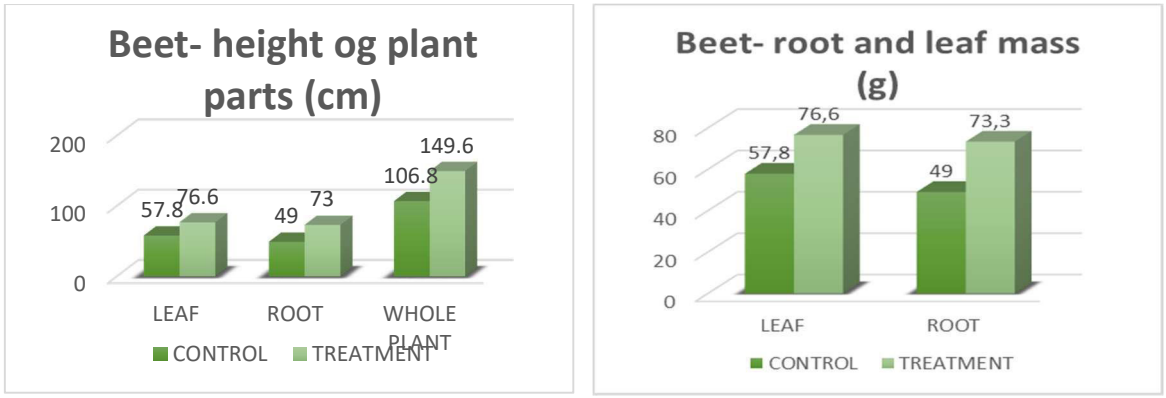

Figure 2. Experiment with beet, (composite – pyrophyllite/dolomite) and effects on height and mass of roots and leaves of the plant

Five months after the calcification and extraction of the beets, the pH value of the soil in the trial treatment (PiroFert) increased from 5.9 to 6.4, which indicates that the calcification with pyrophyllite and dolomite-based fertilizer, already in the first year, gave good and desired results.

As this is the first year of testing the PiroFert composite, it is necessary to repeat the test in order to determine the biological efficiency of the fertilizer.

4. CONCLUSION

The new Fertilizer Products Regulation (EU) 2019/1009 will apply from 16th July 2022 and establishes EU-wide quality, safety, and environmental criteria for fertilizers. In accordance with that, the paper promotes multifunctional fertilizer, as a compound inorganic macronutrient fertilizer/liming material/soil improver, based on pyrophyllite, deposits Parsovići, Konjic, BiH, enriched with dolomite to achieve the defined formulation of Product Function Categories (PFC), according to the new regulations. The new EU soil strategy for 2030 sets out a framework and concrete measures to protect and restore soils and ensure that they are used sustainably with the aim of reduced degradation and increased soil fertility, emphasizing the advantage of natural fertilizers over industrial ones. The aim of this paper is to promote the use of pyrophyllite as one of the most promising natural aluminosilicate materials, environmentally friendly and economically viable materials whose application meets the stringent requirements of sustainable agricultural production, the requirements of the new EU soil strategy for 2030 and new Fertilizer Products Regulation (EU) 2019/1009.

The use of pyrophyllite-based fertilizers with the addition of dolomite (PiroFert product AD Harbi Ltd. Sarajevo, Bosnia and Herzegovina) to neutralize acidic soil in beet growing conditions (*Beta vulgaris var. Conditiva*) had a positive effect on the correction-increase of soil pH as well as the formation of plant biomass (leaf and root length as well as root diameter). Analogously, in the treatment with the addition of PiroFert fertilizer to the soil, there was an increase in root yield, which was higher by 48.97% compared to the control treatment.

The same research should be continued in the second year with the aim of a more comprehensive overview of the effects of soil neutralization and its stabilization after calcification.

5. ACKNOWLEDGEMENTS

The authors are grateful to AD Harbi Ltd. Sarajevo, Bosnia and Herzegovina, for enabling the realization and publication of this paper.

6. REFERENCES

[1] https://eur-lex.europa.eu/legal-content/EN/TXT/PDF/?uri=CELEX:32019R1009&from=hr (1.3.2023)

[2] Mirjana Stojanović, Milan Adamović, Jasmina Kustura, Enita Kurtanović, Muhamed Harbinja: Multifunctional fertilizer based on pyrophyllite in accordance with the regulation EU 2019/1009. 53 rd International October Conference on Mining and Metallurgy. 2022,119-122

[3] S. Churakov, Ab Initio. Ab Initi Study of Sorption on Pyrophyllite: Structure and Acidity of the Edge Sites. J Phys Chem B 110 (9) (2006), 4135–4146

[4] S. Murtić, H. Čivić, E. Sijahović, I. Koleška, J. Jurković, M. Tvica. Use of pyrophyllite to reduce heavy metals mobility in a soil environment. Agronomy Research 18(1) (2020a), 194–205

[5] J. T. Kloprogge, Infrared and Raman spectroscopy of clay minerals. Edited by W. P. Gates, J. T. Kloprogge, J. Madejová, F. Bergaya. Elsevier, 8 (2017) p 150-199

[6] A. Essalhi, M. Essalhi, A. Toummite. Mineralogical and textural arguments for a metasomatic origin of the Ougnat pyrophyllite, Eastern Anti-Atlas, MoroccoJ Mat Env Sci 8(1) (2017), 22-32

[7] E. Hasanbegović, J. Huremović, S. Žero Adsorption capacity of nitrate from artificial fertilizers and soil on pyrophyllite Int J Environ. Sci Technol,18 (2021), 3731–3738

[8] M. Adamović, M. Stojanović, M. Harbinja, M. Maslovarić, A. Bočarov-Stančić, L. Pezo Ispitivanje efikasnosti korišćenja pirofilita u siliranju biljke kukuruza, Food Feed Res. 47 (2020), 109–118

[9] M. Adamović, M. Stojanović, A. Bočarov Stančić, M. Harbinja, J. Kustura, Influence of natural and enriched pyrophyllite on onion yield (Allium cepa L.) XI International Symposium on Agricultural Sciences AgroReS, (2022), 89-98

[10] A. Maaz, A. Ali Hussin, M. Ahmed, Haitham M. Ahmed, M. Hefni. Pyrophyllite: An Economic Mineral for Different Industrial Applications Appl. Sci. 11(23) (2021) 11357

[11] S. Murtić, Ć. Zahirović, L. Karić, J. Jurković, H. Čivić, E. Sijahović, Use of Pyrophyllite as Soil Conditioner in Lettuce Production. Nat Environ Pollut Technol,19 (1) (2020b) 355-359

[12] A. Govedarica-Lučić, S. Pašić, M. Jovović, A. Rahimić, effects of dose of pyrophyllite on yield and quality of the cabbageacta Sci. Pol. Hortorum Cultus, 20 (5) 2021, 25–32

[13] A. Bočarov-Stančić, J. Krulj, M. Maslovarić, A.Bodroža-Solaro, D. Rade, R. Jovanović, B. Beskorovajni,, M. Adamović, Antimicrobial activities of different agents including pyrophyllite against foodborne pathogens: a brief review Acta Periodica Technologica, 52 (2021) 189 -201

[14] S. Zargar, R. Mahajan, J. Bhat, M. Nazir, R. Deshmukh, Role of silicon in plant stress tolerance: opportunities to achieve a sustainable cropping system Biotech. 9(3) (2019) 73

REMOVAL OF POTENTIALLY TOXIC METAL IONS FROM AQUEOUS SOLUTION BY ADSORPTION ON MECHANOCHEMICALLY ACTIVATED PYROPHYLLITE

Tatjana M. Trtić-Petrović, Dajana Lazarević
University of Belgrade, Vinča Institute of Nuclear Sciences, National Institute of the Republic of Serbia,
Belgrade, Serbia

Irena Pušica
Primary Health Centre New Belgrade, Serbia Institution
Belgrade, Serbia

Jasmina Kustura, Belma Halilhodžić, Enita Kurtanović, Adnan Teletović, Atif Hodžić, Muhamed Harbinja
Innovative Scientific Development Center (INRC), AD HARBI Ltd.
Sarajevo, B&H

Keywords: adsorption, mechanochemical activation, potentially toxic metals, pyrophyllite.

ABSTRACT
Pollution of the environment with heavy metals is one of the greatest contemporary problems. Pyrophyllite is a hydrous aluminum silicate, with a wide variety of applications due to its high melting point and stable chemical properties. This study aims to examine the sorption properties of the mechanochemically activated pyrophyllite for the removal of divalent heavy metal ions (Zn, Cd, Pb, Cu, and Ni). The mechanochemical-activated pyrophyllite by milling was obtained from the Parsovići mine, Konjic site, AD Harbi Ltd., Sarajevo, Bosnia and Herzegovina. Heavy metal sorption experiments were performed by the "batch" method. Results clearly showed that the sorption of Me(II) is affected by granulation and amount of pyrophyllite, and sorption time. The following results were obtained: (1) the smaller pyrophyllite particle the removal of Me(II) is more efficient and the shorter contact time is required; (2) the sorption of Me(II) on pyrophyllite decreases in the following order Cu > Pb > Cd > Zn > Ni; (3) the increase of contact time increases the removal of Me(II) from the aqueous solution; (4) mutual competition of Me(II) for pyrophyllite binding sites – significantly more efficient sorption of Cd(II), Zn(II) and Ni(II) was achieved from individual solutions compared to the mixture. Our results show the high potential of pyrophyllite as a material for the removal of heavy metals from water solutions.

1. INTRODUCTION

Pollution of the environment with potentially toxic elements is one of the world's biggest problems, and most often originates from insufficiently or untreated industrial or municipal wastewater. Potentially toxic metals (PTMs) are considered hazardous environmental pollutants because of their high stability and toxicity even at low concentrations [1]. Removal of PTMs is essential in environmental remediation and cleanup. Adsorption is one of the conventional physicochemical processes sand has been used for the removal of heavy metals from various industrial effluents due to its simplicity and cost-effectiveness [2]. In addition, partitioning reactions (sorption) to clay mineral surfaces may control metal

mobility in soils [3]. The development of technology for the removal of PTMs from wastewater based on sorption on solid materials requires primarily sorbent materials of known kinetic parameters and sorption characteristics, which are non-toxic, available, chemically and mechanically stable, economically viable, and recyclable.
Pyrophyllite is a natural hydrous aluminum silicate clay mineral ($Al_2Si_4(OH)_{10}(OH)_2$) with a high melting point, stable chemical properties, and low cost. The elementary sheet of pyrophyllite is composed of an aluminium-oxygen/hydroxyl octahedral layer between two tetrahedral layers of silicon-oxygen. Pyrophyllite is hydrophobic due to the absence of hydroxyl groups on the basal surfaces of the elementary sheet [4]. The structure of pyrophyllite is similar to talc, but talc contains Mg^{2+} instead Al^{3+} in octahedral positions. The layered silicate structure of pyrophyllite crystals has natural adsorption activity [5]. Adsorption of metal cations is mainly occurred by cation exchange in the interlayers. Formation of inner-sphere metal complexes through $Si–O^-$ and $Al–O^-$ groups at both edge sites of clay particles is an additional adsorption mechanism [5]. Pyrophyllite edges are formed by the fracture of the ionic and covalent bonds and their numbers depend on the grinding procedure. Also, hydrophobic siloxane surfaces of pyrophyllite act as neutral adsorption sites and are accessible to nonpolar organic species [8]. The sorption characteristics of natural or modified pyrophyllite have been extensively studied [2,5,7,9-13].
Mechanochemical activation (MCA) is a simple method for the modification of solid materials that causes structural disorder, amorphization, and increased chemical reactivity [14]. MCA, usually performed by grinding, is an environmentally friendly process because of low energy consumption, processing temperatures, and cost.
This study aims to examine the properties of the mechanochemically activated pyrophyllite for the sorption of divalent heavy metal ions (Zn(II), Cd(II), Pb(II), Cu(II), and Ni(II)). The effect of contact time, initial metal-ion concentration, and amount of pyrophyllite on the removal of the targeted PTMs from the aqueous solution were studied.

2. EXPERIMENTAL

2.1. Chemicals

We used the following chemicals purchased from Sigma-Aldrich (St. Louis, MO, USA): zinc chloride ($ZnCl_2$), lead nitrate ($Pb(NO_3)_2$), cadmium nitrate ($Cd(NO_3)_2$) $4H_2O$), copper nitrate ($Cu(NO_3)_2$ $2.5H_2O$), nickel nitrate ($Ni(NO_3)_2$ $6H_2O$), potassium chloride (KCl), sodium hydroxide (NaOH), nitric acid (HNO_3), sodium acetate ($NaCH_3COO$). All chemicals are p.a. purity. Deionized water was obtained using a Milli-Q water purification system (Millipore, Bedford, MA, USA). Polyethylene laboratory bottles were used to prepare and store aqueous solutions of metal salts, as well as to perform experiments. These bottles were pre-washed in 10% HNO_3 to prevent heavy metal contamination.
Heavy metal stock solutions, containing 0.16 mol dm^{-3} of a single element (Zn(II), Pb(II), Cd(II), Cu(II) or Ni(II)), were prepared separately for each metal by dissolving an adequate amount of the salt in 0.1 dm^3 of deionized water. The stock solutions were stable for months at room temperature. Working heavy metal ions solutions, with a single metal concentration of 0.16 mM (10 ppm Cu (II), 10.5 ppm Zn(II), 9.4 ppm Ni(II); 17.98 Cd(II); and 33.1 ppm Pb(II)) and total metal ions concentration of 0.8 mM, were prepared shortly before each experiment by appropriate dilution of the stock solutions with deionized water.

2.2. Adsorbents

The row natural pyrophyllite was obtained from the deposits "Parsovići" - Konjic (AD HARBI Ltd., Sarajevo, Bosnia and Herzegovina). The samples were mechanochemical modified by milling and sieving crude pyrophyllite. The granulometric composition was determined by sieving the ground pyrophyllite through standard sieves with openings of

appropriate dimensions (0.1 mm and 0.045 mm). Three samples of pyrophyllite with granulation of < 0.1 mm (Pyr-0.1) and < 0.045 mm (Pyr-0.045) were used for PTMs adsorption studies.

2.3. Adsorption studies

PTMs adsorption experiments were performed by the "batch" method, i.e. direct contact of a certain amount of pyrophyllite and aqueous metal solution. Batch experiments of metal adsorption on pyrophyllite samples were carried out at room temperature by mixing mechanochemically modified pyrophyllite and working metal ions solution in closed polyethylene bottles. The samples were shaken on the laboratory shaker (Promax 2020, Heidolph, Schwabach, Germany) at the stirring speed of 200 rpm for better mass transport. After that, the liquid phases were separated by centrifugation at 1000 rpm followed by filtration through a 0.45 μmmicroporous membrane filter (Membrane Solutions LLC, TX, USA). The concentration of PTM ions in the aqueous phase was quantified by anodic stripping voltammetry with a 797 VA Computraceanalyser (Metrohm, Herisau, Switzerland) by using the Metrohm's procedure for the voltammetric determination of zinc, cadmium, lead, and copper in water samples No. 231/2.Ni(II) was determined by the addition of dimethylglyoxime as a complexing agent (Metrohm application note No. V-100).

The influence of different experimental parameters, such as the contact time (5 min - 24 h), the initial total metal ions concentration (25-600 mg dm^{-3}), the amount of adsorbent (0.5-10 g dm^{-3}), and granulation of pyrophyllite, on the removal efficiency of metal ions were investigated. The molar concentrations of Zn(II), Pb(II), Cd(II), and Cu(II) ions in a multi-metal solution were set to be equal. All experiments were carried out in duplicates and the data obtained were used for analysis.

The removal efficiency of particular metal ion (R) was evaluated using Eq. (1), respectively:

$$R(\%) = \left(\frac{C_{Me} - C_e}{C_{Me}}\right) 100 \quad (1)$$

where C_{Me} and C_e are the initial and equilibrium metal ion concentration (mg dm^{-3}).

The concentrations of alkali and alkali earth metal cations (Na(I), K(I), Ca(II), Mg(II)) were analyzed by the 861 Advanced Compact ion chromatography (IC) system (Metrohm, Herisau, Switzerland) with conductivity detector and analytical column Metrosep C2 (Metrohm, 150 mm x 4 mm). In the initial heavy metal ions solution the concentrations of Na(I), K(I), Ca(II) and Mg(II) ions were 0.1, 0.1, 0.2, and 0.5 mg dm^{-3}, respectively.

3. RESULTS AND DISCUSSION

The removal of potentially toxic divalent metal ions Me(II) from an aqueous solution is investigated in this work. The effects of contact time, MCA pyrophyllite particle size, and competitively of the targeted Me(II) for adsorption have been studied. Before the experiments of sorption of selected heavy metal ions, and considering the chemical composition of pyrophyllite, we examined whether pyrophyllite releases metal ions in equilibrium with the water. The experiments were performed by placing 200 mg of pyrophyllite in 100 cm^3 of deionized water, pH 5.0, and shaking on a laboratory shaker. The samples were taken at the following time intervals: 30 min, 1 h, 2 h, 3 h, 5 h, and 24 h and analyzed. No measurable amount of any tested metal ion was found in any of the samples, which indicates that these ions are not released (dissolved) from the pyrophyllite into deionized water.

3.1 The effect of adsorption time and particle size on Me(II) removal

Figure 1 shows the effect of contact time between pyrophyllite and the aqueous solution of the studied PTMs using two MCA pyrophyllites with different granulation: Pyr-0.1 and Pyr-0.045. The removal efficiency (R) of the studied Me(II) depends on adsorption time, the particle size of pyrophyllite, and the kind of metal ions.

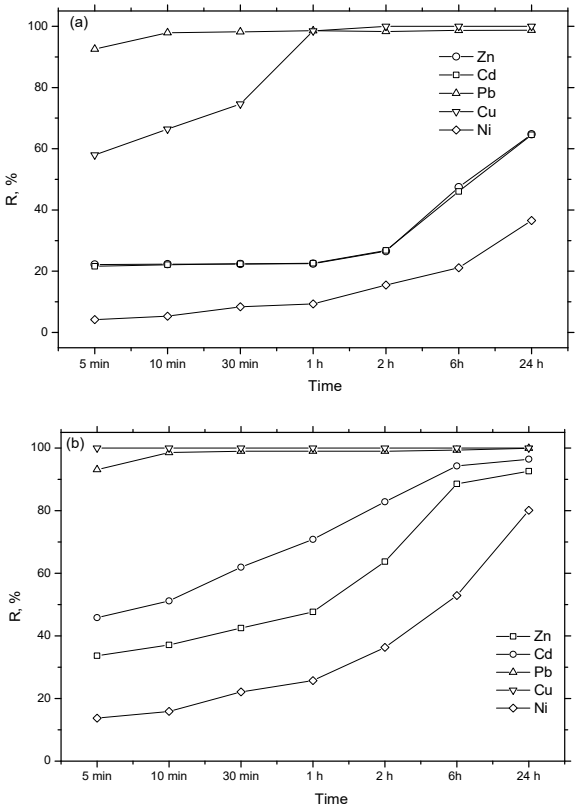

Figure 1. The effect of adsorption time on the removal of Me(II) using (a) Pyr-0.1; (b) Pyr-0.045. Experimental conditions: C_{Me} = 10 mg dm^{-3}, the volume of aqueous solution 25 cm^3, amount of pyrophyllite 1 g, shaking rate 200 rpm.

Removal efficiency increases with increasing adsorption time for all studied Me(II). It should be noted that pyrophyllite of smaller granulation (Pyr-0.045), due to the larger surface area, adsorbs more Me(II) for the same time compared to Pyr-0.1. The removal of Pb(II) and Cu(II) is notably higher and faster compared to Zn(II), Cd(II), and Ni(II). From Fig.1, it can be seen that Pyr-0.045 adsorbed > 98% Pb(II) and 100% Cu(II) from the aqueous solution after 10 min of contact, while it took 60 minutes to remove the same percentage of Pb(II) and Cu(II) with Pyr-0.1. The higher and faster removal of Zn(II), Cd(II), and Ni(II) was obtained using Pyr-0.045, and Zn(II) and Cd(II) reached the maximum of 95% after 24 h. Significantly lower removal (65% for Cd(II) and Zn(II), and 38% for Ni(II)) was obtained after 24h of contact with Pyr-0.1 without reaching the maximum. The results clearly show that pyrophyllite of smaller granulation removed the tested Me(II) from the aqueous solution faster and in a higher percentage: Cu(II) was completely removed after 5 min and 99% Pb(II) was removed after 30 min. The removal trend of other metal ions was similar to that of Pyr-0.1, but the removal percentage was significantly higher: 96.4%, 92.6%, and 80.1% for Cd(II), Zn(II), and Ni(II), respectively. The initial adsorption of Cu(II) and Pb(II) at Pyr-0.045 is very fast. The adsorption is a surface phenomenon, at the beginning of the adsorption the active sites at the surface of the

pyrophyllite filled up rapidly with the metal anions with high affinity towards pyrophyllite. Since Pyr-0.045 has a larger surface area, adsorption is both larger and faster compared to Pyr-0.1. Additionally, from Fig. 1 can be seen that the removal efficiency of Cd(II), Zn(II), and Ni(II) began to increase after the time when Pb(II) and Cd(II) reached the maximum removal. Adsorption of these Me(II) is much slower compared to Pb(II) and Cu(II) because Me(II) has to diffuse to the pores of pyrophyllite and inner binding sites. This also indicates competition for metal bonding sites on the pyrophyllite as well as a lower affinity for the binding sites.

From the obtained results shown in Fig. 1, it is clear that the removal of Me(II) from the solution i.e. the sorption of Me(II) on pyrophyllite is affected by the contact time, the amount of pyrophyllite and the granulation of pyrophyllite.

The following experiments aimed to determine the optimal amount of pyrophyllite for the removal of the targeted Me(II). From the results in Fig. 2, it can be seen the influence of the amount of pyrophyllite on the removal of Me(II). When the amount of pyrophyllite increases, the removal efficiency of the studied Me(II) also increases. This effect is especially pronounced in pyrophyllite with smaller particles (Pir – 0.045 μm) (Fig.2b). For example 2 g L^{-1} of Pir–0.045 is sufficient to remove 100% Cu(II) and 90% Pb(II). While, 24 g L^{-1} of Pir–0.045 removed 100% Cu(II), Pb(II) and Zn(II); and 97.7% Cd(II) and 93.5% Ni(II).

Comparing Figures 2 (a) and (b**)**, it can be concluded that even with the application of the triple amount of pyrophyllite with granulation of 100 μm compared to a pyrophyllite of granulation <45 μm, it is not possible to achieve such a successful removal of metal ions.

3.2 The competition of binding of tested metal ions to pyrophyllite

From obtained results shown in Figures 1 and 2, it is evident that Cu(II) and Pb(II) bind the fastest and in the highest percentage to pyrophyllite i.e. their removal from aqueous solutions is the biggest. Additionally, it is clear that the sorption of other investigated PTMs ions begins to increase when Cu(II) and Pb(II) reach equilibrium, which indicates the mutual competition of these ions for binding sites on pyrophyllite. Therefore, in the following experiments, we examined the sorption of individual PTMs ions on pyrophyllite and compared them with the results from a mixture of metals (Figure 3). To be able to follow the mutual competition Me(II), we chose the concentration pyrophyllite 8 mg dm^{-3}, because at this concentration Cu(II) achieves the maximum binding, and all the others Me(II) are less bound to pyrophyllite.

It can be concluded from Figure 3, that the sorption of Cu(II) is the same from the mixture of Me(II) and from the individual solution, which means that its binding is not affected by other metal ions, ie. Cu(II) is the most strongly bound to pyrophyllite. From a single solution of Pb(II) the sorption is 100%, while from the mixture it is 87%, and in this case, the competition of Pb(II) and Cu(II) can already be seen.

In the case of Cd(II), Zn(II), and Ni(II) of Me(II) which bind to pyrophyllite to a lower degree in the presence of Cu(II) and Pb(II), the improvement of binding from a single solution was highly pronounced. The sorption of Zn(II) was increased from 8% to 98%; from 21% to 85% for Ni(II), and slightly less for Cd(II) from 8% to 62%.

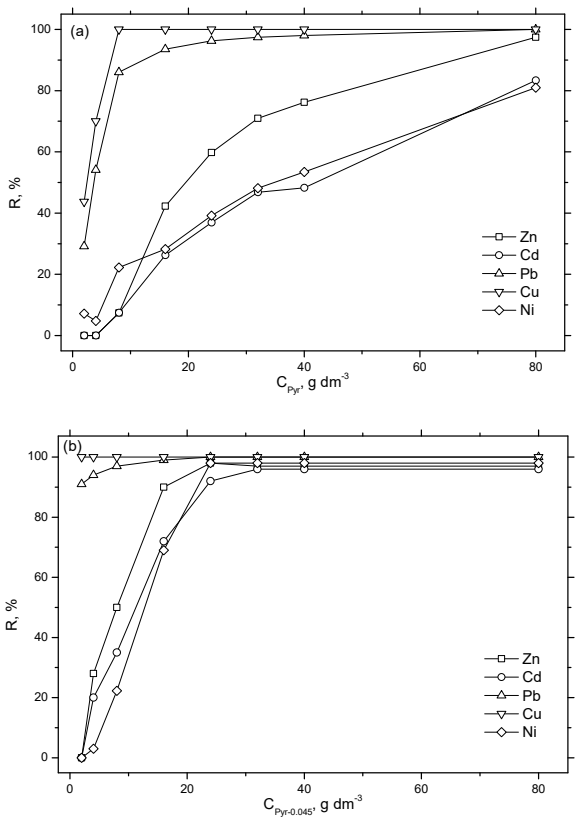

Figure 2. The effect of the amount of (a) Pyr – 0.1 and (b) Pyr – 0.045 on the removal of Me(II). Experimental conditions: C = 0.16 mM single metal, C_{tot} = 0.8 mM, the volume of aqueous solution 25 cm^3, amount of pyrophyllite 1 g, shaking rate 200 rpm, adsorption time 24h.

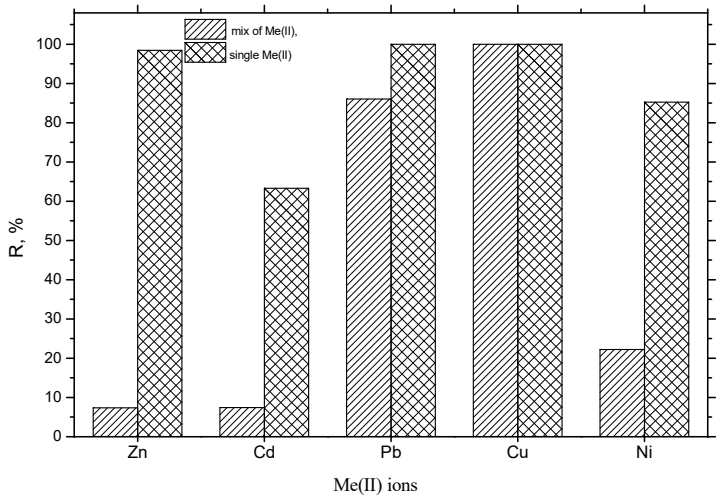

Figure 3. The removal efficiency of divalent metals from the mixture of solutions (concentration of each metal in the mixture C = 0.16 mM, total concentration of metal C_{tot} = 0.8 mM) and from single solutions (concentration of metal C = 0.16 mM)on Pyr-100.Experimental conditions: volume of aqueous solution 25 cm^3, amount of pyrophyllite 0.2 g, shaking rate 200 rpm, adsorption time 24h.

In all solutions obtained after the adsorption of metal ions on mechanically modified pyrophyllite, the concentrations of alkali and alkaline earth metals were determined (Table

2). During the adsorption of selected divalent metals from mechanically modified pyrophyllite, the release of alkali and alkaline earth metals decreased in the following sequence: Ca^{2+}> Mg^{2+}> K^{+}> Na^{+}. This indicates that divalent ions play the main role in ion exchange, primarily Ca^{2+}. The obtained results show that a smaller amount of alkali and alkaline metal ions were released by using pyrophyllites of larger granulation.

Table 1. Concentrations of alkali and alkaline earth metals released from pyrophyllite during the adsorption of heavy metals to pyrophyllite

Adsorbent	C, mM			
	Na	K	Ca	Mg
Pir -2mm	0.096	0.428	0.455	0.175
Pir - 100 μm	0.137	0.181	0.899	0.194

4. CONCLUSIONS

Contamination of water by potentially toxic metals from industrial and municipal wastewater is an acute environmental problem worldwide. This study focused on the mechanochemical activation of geopolymer - pyrophyllite and its adsorption characteristics towards heavy metals such as Cu(II), Pb(II), Ni(II), Zn(II) and Cd(II). The mechanochemical activation can be considered an ecologically friendly technique, which can contribute to reducing CO_2 emissions by replacing some thermally intensive processes. The mechanochemically modified pyrophyllite was found to be a high-potential adsorbent of metal ions fromwater through batch adsorption studies. The adsorption of the targeted metalions was evaluated as a function of experimental parameters such as pyrophyllite amount, the particle size of pyrophyllite, and contact time. The maximum removal efficiencies to the extent of 98 and 100 % for Pb(II) and Cu(II), respectively, were achieved using fine grinned pyrophyllite with particle size less than 45 μm for only 10 minutes. Additionally, the mutual competition of the studied ions for binding sites on pyrophyllite was found. The overall studies indicatet hat the mechanochemical-activated pyrophyllite could be used as an inexpensive and promising adsorbent for the removal of potentially toxic metals.

5. COPYRIGHT

6. REFERENCES

[1] Lakherwal D.: Adsorption of heavy metals: a review. *Int J Environ Res Dev.* 2014; 4: 41-48

[2] Erdemoğlu M, Erdemoğlu S, Sayılkan F, Akarsu M, Şener Ş, Sayılkan H.: Organo-functional modified pyrophyllite: preparation, characterisation and Pb(II) ion adsorption property. *Applied Clay Science* 2004; 27: 41-52

[3] Ford RG, Sparks DL.: The nature of Zn precipitates formed in the presence of Pyrophyllite. *Environ Sci Technol.* 2000; 34: 2479-83

[4] Drits, V. A., Guggenheim, S., Zviagina, B.B. and Kogure, T. 2012. Structures of the 2:1 layers of pyrophyllite and talc. *Clays Clay Miner.* 60(6): 574-587

[5] Panda L, Rath S. S, Rao D. S, Nayak B. B., Das B., Misra P. K. Thorough understanding of the kinetics and mechanism of heavy metal adsorption onto a pyrophyllite mine waste based geopolymer. *J Mol Liquids*. 2018; 263:428–441
[6] Gupta N, Prasad M, Singhal N, Kumar V. Modelling the Adsorption Kinetics of Divalent Metal Ions onto Pyrophyllite Using the Integral Method. *Ind Eng Chem Res.* 2009; 48: 2125-2133
[7] Prasad M, Saxena S. Attenuation of divalent toxic metal ions using natural sericitic pyrophyllite. *J Environ Manage.* 2008; 88: 1273-1282
[8] Sayilkan H, Erdemoğlu S, Sener S, Sayilkan F, Akarsu M, Erdemoğlu M. Surface modification of pyrophyllite with amino silane coupling agent for the removal of 4-nitrophenol from aqueous solutions. *J Colloid Interface Sci.* 2004; 275: 530-538
[9] Gücek A, Sener S, Bilgen S, Mazmanci M. A. Adsorption and kinetic studies of cationic and anionic dyes on pyrophyllite from aqueous solutions. *J Colloid Interface Sci.* 2005; 286: 53-60.
[10] Saxena S, Prasad M, Ampritphale S, Chandra N. Adsorption of cyanide from aqueous solutions at pyrophyllite surface. *Sep Pur Techn.* 2001; 24: 263–270
[11] Rai K., Maheshwari A. Removal of pollutants from industrial effluents using plastic clay and pyrophyllite. *Asian Journal of Chemistry,* 2002; 14: 739–745
[12] Sheng J, Xie Y, Zhou Y, Applied Clay Science Adsorption of methylene blue from aqueous solution on pyrophyllite, *Appl Clay Sci.* 2009; 46: 422–24
[13] Singh S, Jena SK, Das B. Application of pyrophyllite mine waste for the removal of cadmium and lead ions from aqueous solutions, Desalination and Water Treatment 2016; 57(19): 8952-66
[14] Tole I., Habermehl-Cwirzen K., Cwirzen A.: Mechanochemical activation of natural clay minerals: an alternative to produce sustainable cementitious binders – review, *Mineralogy and Petrology*113;2019:449–462

CHALLENGES IN THE APPLICATION OF THE LAW ON SAFETY AT WORK IN FBiH

Miliša Todorović
Tim Protekt doo
Stara Pazova, Republic of Serbia

Asmir Helvida
ArceloMittal
Zenica, B&H

Snežana Živković
University of Niš, Faculty of Occupational Safety
Niš, Republic of Serbia

Keywords: safety at work, prevention, safety culture

ABSTRACT
Occupational safety is a very important factor in the process of creating a safe work environment. The benefits employers, employees and even the state as a whole can reap greatly depend on the way occupational safety is organized and implemented. This paper aims to make a general analysis of the condition of safety at work in Bosnia and Herzegovina, with a special emphasis on the Federation of Bosnia and Herzegovina. The starting point of this paper is the fact that the current law on occupational safety was passed less than two years ago and certain doubts are sprouting up regarding its implementation. This is why there is a need for a deeper and more comprehensive analysis of existing legal situations, problems in implementation, and proposals that could improve or otherwise prove helpful in gaining a clearer understanding of the rights, obligations, and responsibilities of all parties involved, those being the state, employers, and employees. The initial hypothesis of the paper is that the current law on occupational safety, with all its vagueness, represents a good basis for improving the position and rights of employees. The descriptive method was used in the paper, along with a study of available literature, both domestic and foreign.

1. INTRODUCTION

Occupational safety is a very important area of social life. Man has always aspired to perform his activities in a way that will enable him to be safe. Injuries at work are determined by the imbalance between unfavourable work conditions and an insufficient understanding of occupational safety and health, by both employers and workers. Unfavourable working conditions include a wide range of biological, mechanical, and physical exposures to the environment, psychological demands related to specific tasks, the overall working environment, issues related to the handling and use of materials, tools, and machines, organizational factors, as well as pressure from the management to achieve the outlined plans and production targets [1]. Occupational safety can be defined as a set of technical, legal, psychological, pedagogical, health-related, and other activities and measures that identify hazards and harms and define steps that should prevent or reduce the possibility of injury at work. As we can see, the emphasis is placed on creating working conditions in which work-related injuries are completely prevented, or at least the possibility of them occurring is greatly reduced. The Statistical Office of European

Communities (Eurostat) states that in the EU, close to 3% of employed persons experienced an injury at work that caused an absence longer than three days, adding up to around 83 million calendar days of sick leave [2]. During the evolution of human society, safety at work went through different phases. In its initial phase, it did not have any special significance due to the social organization, the role of the state, and the development of the workforce. Over time, with the increasingly active involvement of the state in the relationship between the employee and the employer, the role and importance of occupational safety are gradually changing.

The very realization that injuries at work create huge expenses that have a negative impact on all aforementioned parties is reason enough for a more significant role of occupational safety. In that sense, drafting and harmonizing normative acts in the field of occupational safety is a necessary condition [3]. The economy of every country faces numerous changes every day. We are witnesses to countless accidents these days (from wars to earthquakes) which greatly complicate the functioning of business organizations. Changes are an integral part of the daily activities of all organizations and it is not an unknown fact that nowadays organizations have to work hard to stay afloat [4]. In such an environment, serious organizations are increasingly devoting themselves to getting a clearer understanding of costs as an opportunity to increase comparative advantages in the global market competition. During the determination of the types and overall scope of the costs, an increasing number of employers come to know that the share of costs that arise as an integral part of injuries at work represents a significant amount of money. A large number of studies indicate that the costs incurred as a result of injuries at work are at the level of 4% of the GDP of every national economy [5]. This information speaks for itself. What is problematic about this data is the fact that only 1% of that cost is visible and refers to the direct costs of an injury at work. What about the other costs, those which are not visible to that extent? How aware are the employers of their existence and their size? The very realization that a problem exists is good because it opens up opportunities to define activities that should help us reach an appropriate solution. The basis for looking at problems and coming up with solutions is the need to adopt certain legal acts and by-laws, change the safety culture, promote the role of safety at work in the process of creating benefits for all members of society, determine these benefits through a responsible policy and implementation of appropriate measures for safety at work. These are some of the questions we plan to deal with in our paper, with the intent to make a kind of cross-section that could serve as the starting point for further activities in the process of creating safe working conditions. In the first part of the paper, we will emphasize occupational safety itself, how it was created, what it used to be, what it is now, and what it should be in the future. Is the adoption of the Law on Occupational Safety the solution to all problems or should it only be a starting point for further activities? As much as the Law itself is the solution to all the problems, if there are no by-laws that should enable the implementation, the Law itself won't change anything. Who educates our occupational safety and fire protection engineers and do we have enough engineers from those fields who, through their activities, should contribute to the creation of a safer work environment?

What is our safety culture like and how do we think it can be changed? What is the role of every occupational safety and fire protection engineer in the process of changing the awareness of each individual about their role and importance in the process of creating a safe work environment? These are some of the questions we will try to answer in this paper. It is fact that there are no simple solutions and that every reader of this paper can observe these questions and dilemmas from a different angle. Different points of view and constructive thinking are always welcome in the process of acquiring valid views and conclusions which should change our perception of the role of each one of us in the process

of creating a better tomorrow. Finally, it is important to state that safety at work is not an ad hoc activity. To achieve appropriate conditions, constant improvement and development of the occupational safety organization are necessary. The organization of occupational safety refers to the entire system of measures undertaken with the aim of preventing and eliminating potential hazards that threaten the lives and health of employees. There are subjective and objective factors that cause hazards and injuries at work. Subjective factors are non-compliance with occupational safety regulations, deliberate use of protective equipment, insufficient expertise to perform work, psychological state of the worker, etc. Objective factors are means of production, which, through improvement, acquire technical and functional properties so that they become lesser threats to a worker's physical personality [6].

2. LEGAL BASIS

If we go back many years and centuries, numerous documents and objects show that the field of safety and health at work has always been present in social life. In some periods, its importance was greater than in others. Regardless of what period we are talking about, the position of workers improved over time. In the first phase, it was through the gradual organization of work in such a way that human power is consumed less and less and replaced wherever possible. The next phase is characterized by the production of tools for work, which, with their constructive characteristics, reduce the possibility of injuries at work. The third period refers to the gradual inclusion of all the elements of an organization in creating the safest possible working conditions. In this sense, certain normative activities have appeared throughout history, developed over time, and, through certain legal acts and by-laws, attempted to create working conditions in which there will be as few injuries at work as possible. Most of the countries around us have adopted new laws that regulate the field of occupational safety and health, and they are largely harmonized with normative acts of the European Union, which all countries of the region aspire to. The law defines this field, and numerous by-laws (rules, decrees et cet.) define all economic areas in a more precise way [7]. When we talk about the legal basis, it is important to mention at the very beginning that we truly need legal acts and by-laws that will clearly define the rights and obligations of employers and employees.

Generally speaking, most non-EU countries have already adopted Occupational Safety Laws that are harmonized with the norms of the European Union (Bosna and Hercegovina, Montenegro, Republic of Serbia). Observing the development of social relations through history, we can conclude that at a certain level of development, there is a need to define certain legal regulations that will regulate these relations [8]. Because of all this, it is necessary to work much more on the organizational culture of the workers as the process which creates the assumptions of appropriate safety culture as a road to avoiding injuries at work. The Federation of Bosnia and Herzegovina, as a part of Bosnia and Herzegovina, finally adopted the Occupational Safety and Health Act at the end of 2020, which would deal with the issue of occupational safety and create better and safer working conditions for employees. Until the adoption of this law, we had an absurd situation where the fines for non-compliance with the provisions of the existing Law on Occupational Safety were in 'Yugoslav dinars'.

A little earlier in the Brčko District and the Republic of Srpska, laws that deal with the issue of occupational safety and health were passed. In the Republic of Srpska, there is a Law on Occupational Safety and Health from 2008 (Official Gazette of the Republic of Srpska No. 01/2008 and 13/10), and in the Brčko District, the Law on Occupational Safety and Health from 2013. Both of these legal acts are harmonized with the European directive 89/391 which represents the foundation for regulating the field of safety at work.

Over the course of the paper, we will shift the focus of our analysis to the existing legal solution in the Federation of Bosnia and Herzegovina. However, before that, we have to give a general overview of existing legal acts that regulate the field of safety at work in the whole of Bosnia and Herzegovina as well as its immediate surroundings. The general impression is that the adopted Laws on Occupational Safety are harmonized with the EU directive dealing with these issues. What is an important prerequisite for the implementation of existing legal solutions? By-laws. What is our situation when we talk about by-laws? The very insight into the by-laws that regulate certain economic activities unequivocally raises the question of their compatibility with the times in which we live. A large number of by-laws are from the last century and the question is to what extent they can be adjusted to today's degree of economic growth and development. ((for example, in the FBiH we have General rulebook on hygienic and technical protective measures at work ("Official Gazette of FNRJ", no. 16/47, 18/47 and 36/50) and Rulebook on occupational safety when loading cargo into motor vehicles and unloading cargo from such vehicles ("Official Gazette of the SFRY", number 17/66)). The current issue is not only related to Bosnia and Herzegovina, because for example, in the Republic of Serbia, which passed the Law on Safety and Health at Work in 2005, the Rulebook on Occupational Safety in Agriculture is also still in force ("Official Gazette of the SFRY, no. 34/68). What means of plant protection were used then, and what is used now? We are not sure that the solutions from 60 years ago are appropriate. The problem with the Federal part of Bosnia and Herzegovina is only more pronounced because, until recently, there was no Law on Occupational Safety that could be applied in the right way, so it is clear that the by-laws are also not appropriate.

An integral part of the activities that await us is the continuous harmonization of legal regulations with the norms of the European Union. The development of techniques and technology, new knowledge, and experiences, lead to the creation of new regulations in the field of occupational safety. The problem arises at the moment when we start harmonizing, and our economic and social development is not at the appropriate level. For example, in the Republic of Serbia, the Rulebook on preventive measures for safe and healthy work when using equipment for working with a screen ("Official Gazette of RS", no. 106/09 and 93/13, 86/19) in the article 3 and 6 is defined that every worker who works for more than 4 hours in front of a computer has the right and obligation to perform an ophthalmological examination every 3 years. Many dilemmas arise in the implementation of this Rulebook. One of them refers to the clarification of the concept of working with a screen (view focused on the monitor) or working in front of the screen where the worker's view is not focused on the monitor all the time. Another, perhaps bigger problem in our opinion, concerns the purpose of this medical examination and the essence of protection at work. A simplified interpretation says that the worker undergoes a medical examination and during that examination, the dioptre in both eyes is determined to be -1. After three years, the dioptre increases to -3 and after 6 years, the dioptre is -5. What does an ophthalmological examination mean to us in that state? Is the essence of occupational health and safety to deal with prevention, or to manage the worker's new state through observing the declining results? Is the medical examination the main aspect of occupational safety or is it tackling the causes of visual impairment in workers? Are the workers properly trained to operate with the screen? Have the adjustments of the resolution and the importance of the refraction of natural and artificial light on the monitor been explained to the workers? Are there regular examinations of the lighting in the room (and not just once every 3 years per applicable regulations)? The main goal of occupational safety is dealing with the causes and not the consequences. We now face an important question: Is the law a necessary and

sufficient condition to create an environment in which the number of injuries at work would be reduced and working conditions would be improved.
Considering the novelty of the current Occupational Safety and Health Act in the Federation of Bosnia and Herzegovina, it is difficult for us to extract any relevant facts. On the other hand, the superficial analysis of the trend of injuries at work in the countries in the immediate vicinity of Bosnia and Herzegovina shows that there is no clear trend of reducing the numbers and severity of injuries at work (example, If we look at the annual reports of the labour inspector in the Republic of Serbia, we cannot see a trend of decreasing the number and severity of injuries at work). Why? It is difficult to give a simple answer to this question because a simple observation of some statistical data can lead us astray. What we can state with certainty is the fact that the development of techniques and technology leads toward the creation of safer tools and on that side one SHOULD see the trend of reducing the number of injuries at work. If we do not see it already, it is clear that we need to turn our attention to the worker who controls these tools for work. What is the worker's role in the process of creating a safe work environment and is their position about who should take care of safety at work actually the answer to all dilemmas?
The question of safety culture is very important, and until we deal with the problem of safety at work through the prism of values that determine that workers behave a certain way during the performance of defined work operations, we can hardly expect better statistics when we talk about the number and severity of injuries at work. Individual analyses of numerous cases of major accidents have established that safety culture has a very large impact on the creation of a safe work environment. It is a known fact that culture is very difficult and slow to change. That is why we must recognize it as a very important factor that affects the increase of business competencies of every organization and actively manage its growth and development. An appropriate safety culture creates the basic prerequisites for the long-term productivity of both employers and workers, as well as the state itself. On the other hand, it creates conditions for a safer environment for workers [9].
Since we are already talking about normative frameworks for improving working conditions, it is important to mention that we should think about starting the procedure for mandatory occupational injury insurance as soon as possible. In developed countries, this law is very often the main motivator for the employer to organize occupational safety affairs in such a way that no injuries occur at work. Every year, the insurance company agent, depending on the number of injuries and paid compensation claims, increases or decreases the value of the policy for each worker. This fact is very often a decisive motive for employers when we talk about taking care of workers' health.

3. CHALLENGES IN THE APPLICATION OF THE CURRENT LAW ON OCCUPATIONAL SAFETY IN THE FEDERATION OF BOSNIA AND HERZEGOVINA

Before we look back on the good, as well as solutions that could be improved upon, we have to state one important fact. The Law on Occupational Safety which was in force before this law was inapplicable for many reasons. The very fact that the fines were expressed in Yugoslav dinars speaks to the extent to which punitive measures could be the stimulus for the implementation of this law. We know very well that in the regions where we live, punitive measures are still the main incentive and that unless some sanctions are defined, a large number of employers will not deal with this problem. Because of all of this, we must praise the relevant ministries and other institutions that, within the framework of their activities, contributed to the adoption of the Occupational Safety and Health Act and that it represents the basis that should help us create safer working conditions for all workers. In all countries in the immediate vicinity, there have been several changes to the basic laws of

occupational safety that were adopted based on the EU directive 89/391, and this is nothing new. Practice is very often a control measure, and during the life of the law, good things and the things that need to be changed are seen in practice.
In Article 12 in paragraph 1 and 2 of the Occupational Safety and Health Act, the legislator predicted that each employer must prepare an Elaborate on the arrangement of the workplace for the activities defined in the act itself. In Article 12 in paragraph 2 of the Occupational Safety and Health Act If the work is carried out for more than seven days, the employer is obliged to report to the competent inspection body. What is the problem with the practice? What about reporting works that last less than seven days? In the case when the employer performs work activities at a certain location for a long time, they organize the construction site following all requirements. When work activities are carried out in one or two days, many improvisations are made in practice because it is "not worth it" to spend time preparing for a construction site. In such conditions, injuries at work often occur. We think that wherever there is an opportunity, employers who annually perform some activities that last less than 7 days (various activities for the maintenance of certain systems) should report through the general notification of works that in that year, in a certain area, they perform for the users of their service specific maintenance work. In addition, the law does not recognize the institution of continuity of work maintenance.
Someone can show up at the construction site and, due to the dynamics of the work, complete the work intermittently in shorter or longer time periods. (a company that performs the rough distribution of electrical installations and then comes to the final connection of the equipment) How do we then interpret that time limit "that if one performs work for longer than seven days", one must report the work? The law itself does not provide the possibility that the Application of Works and the Elaborate on the arrangement of the work site can be submitted to the competent state authorities in writing. Then the competent inspectors, in the office preparation of the examination of the work site, can familiarize themselves with the location, specific dangers and damages, the equipment used to perform the works, and the like. In Article 13 of the Occupational Safety and Health Act defines that the main contractor or investor should provide a unitary report on the organization of the work site. What do we do in a situation where an investor is a natural person who hires a construction company to construct a building? As a natural person, the investor does not know how to prepare such a document. On the other hand, if the investor hires a construction company, it can handle such preparations. However, in practice, construction companies often specialize in some types of work and hire subcontractors for others. How can someone, who deals with the execution of rough construction works, define the measures of safety at work, e.g., during the execution of sub-laying works? The usual solution is for each company to make its own Elaborate, which refers to their works and safety measures. Through the Agreement on mutual regulation of safety measures at work, the execution of the works is organized in such a way as to prevent mutual injuries of workers.
Article 26.3 of the Law defines that the employer may use hazardous substances only if they can't achieve the same work results by using harmless substances. The sequence of measures that every employer who uses hazardous substances should follow is defined in the rest of the articles. Some of these measures can be applied in the technological work process. However, a big problem occurs in situations where there is no permanent activity with dangerous substances and when neither the employer nor the employees, and often not even persons responsible for occupational health and safety, are aware of the potential consequences. In that sense, there are excellent normative solutions that foresee a system of permits for dangerous jobs, whether working at height, depth, or with dangerous substances. The person responsible for occupational health and safety is obliged to go to

the site, inspect the location, and only if all the conditions are met, give consent for that type of work. It is still a matter of good practice and not a legal obligation

In the continuation of the Low, the rights, obligations, and responsibilities of the person in charge of occupational safety and health are clearly defined. In addition, the employer's obligation to organize and train a certain number of workers to provide first aid and fire protection is also clearly defined. We would especially single out the clearly defined obligation of employers that every worker can and must receive work instructions in a language they can understand.

It is also interesting how the employer's obligation to appoint a trustee for occupational safety and health is defined (In Article 44 and 45 Law of the Occupational Safety and Health). In a large number of legal solutions, this obligation is left as an opportunity for the employee, but not as an obligation of the employer. In the continuation of the study of the law, we can clearly see the rights, obligations, and responsibilities of the workers as well as the rights concerning health supervision. An interesting solution exists in a part of the law that concerns the rights of workers in a situation where they work at a workplace with an increased risk, and after some time, it is determined they are no longer capable of working at that workplace.

The employer is obliged to transfer the worker to another workplace that matches his health capabilities if such a workplace exists. If such a place doesn't exist, the relevant provisions of the Occupational Safety and Health Act apply. Someone who had worked for 30 years at a workplace with an increased risk (e.g., working at great heights) can no longer pass a medical examination due to the inability to work at those heights. What kind of a job can they expect on the labor market? When we are talking about reporting injuries at work, is it clearly defined that every serious or fatal injury should be immediately reported to the Labor Inspectorate? Are we able to determine for each work injury whether it is serious or minor? What happens when we are wrong and the injury we characterized as minor turns into a serious injury? Does the person responsible for occupational safety and health bear any consequences?

In the continuation of the paper, we focused on the study of certain by-laws without which there is no application of the law itself. The Rules of risk assessment (Official Gazette of the Federation of Bosnia and Herzegovina 23/2021) represent a very important document without which there is no application of the law itself. Unfortunately, the Occupational Safety and Health Act was passed in November 2020 and it clearly defined the deadline by which employers should harmonize their operations with the law. This was impossible until the adoption of these Rules on risk assessment and a few other by-laws.

The next document that we will briefly analyze is the Rulebook on methods, procedures, and deadlines for periodic inspections and tests in the field of safety at work (Official Gazette of Federation of Bosnia and Herzegovina no. 23-21). The mentioned document gives clear guidelines on the deadlines and in what way the employer must inspect the installations, equipment, and the conditions of the working environment. What could be potentially problematic concerns the obligation of employers to test the conditions of the working environment, in summer and winter, every three years. In doing so, it is emphasized that summer tests should be organized in the period between April and September, and that winter tests can be done in the period between October and March. In the time of climate change, we have witnessed that in the last few years temperatures measured in November and December were above all usual values. By fulfilling the employer's obligations for testing the conditions of the working environment in October, when the outside temperature is over 15 ºC, the employer came to the information that the measured temperatures are within the limits the law defines as allowed. However, would those values be like that if the outside temperature was -5 ºC? Some of the solutions in the

neighboring countries (e.g., the Republic of Serbia, article 11 paragraph 3, Rulebook on the procedure for inspecting and checking work equipment and testing working environment conditions ("Official Gazette of RS", No. 15/2023) define that winter tests are organized when the outside temperature is below 5 ºC, and the summer tests are to be done when the outside temperature is above 15 ºC. In addition, through legal acts and by-laws, it is clearly defined that certified organizations are required to examine working conditions: lighting, microclimate, noise, and chemical and biological hazards while preparing the risk assessment act. That is all logical if the technological work process indicates the existence of all the mentioned hazards. However, the testing of chemical, physical and biological hazards in the company engaged in software development or any other administrative activity is problematic. The employer is obliged to pay a certain amount for tests of harmfulness that are certainly not present in the work process. In that way, the price of the service of creating a risk assessment report increases. Taking into account the time we live in and the serious difficulties in the economy, we think that with this attitude we are creating a certain amount of revolt and dissatisfaction among employers when it comes to the Occupational Safety and Health Act itself. At the end of this discussion, we would like to give a brief overview of another by-law, the Rulebook on the conditions of performing business (Official Gazette of Federation of Bosnia and Herzegovina No. 23-21). For the implementation of the obligations stipulated by the law, this is an important by-law.

To begin with, this Rulebook defines the professional qualification, work experience, and the number of workers one requires in other to be authorized to carry out defined activities with employers. The rulebook defines that the tasks referred to in Article 8 Rulebook on the conditions of performing business can be performed by an authorized organization that has at least three employees with a higher professional qualification- VII degree or higher education of the first cycle of the Bologna system of study (which is evaluated with at least 180, i. e. 240 ETCS points), namely: a) one graduate chemical engineer or graduate engineer of chemical technology or graduate technologist or a bachelor of chemistry or bachelor engineer of chemical engineering and technology, b) one graduate biologist or graduate engineer of medical-laboratory diagnostics or a bachelor of biology (major: biochemistry and physiology, microbiology, teaching), c) one graduate of chemical engineering or graduate engineer of chemical technology or graduate technologist or graduate biologist or graduate occupational safety engineer or graduate physics engineer or bachelor of chemistry or bachelor engineer of chemical engineering and technology or bachelor of biology (major: biochemistry and physiology, microbiology, teaching) or bachelor engineer of occupational safety or bachelor of physics. Do we have a sufficient number of trained staff for these jobs who have three years of work experience in the profession in the Federation of Bosnia and Herzegovina? I think we all know the answer to this question. In addition, each authorized organization must have all the equipment and a suitable laboratory for testing the conditions of the working environment. Authorized organizations have to hire significant resources at the very beginning to start dealing with the work for which they have been authorized. Due to such large expenses, the price of services is significantly higher. Of course, the employer is the one who ultimately pays the bill. Should we make the process of compliance with the legal solutions easier or harder for the employer? In our opinion, we only make it more difficult like this. A special issue is the number of authorized organizations and their ability to complete documentation for each legal entity in the Federation of Bosnia and Herzegovina. By looking at the occupational health and safety register on the website of the Federal Ministry of Labor and Social Policy Federation Bosnia and Herzegovina, it can be seen that only 34 organizations have authorization for these jobs. In some neighbouring countries (Republic of Serbia), in the initial years of application of the law, there were no such string conditions for the

registration of authorized organizations. Each company did not have to be registered for testing the conditions of the working environment, but hired special organizations which were licensed for those jobs. The next legal solution, ten years after the first version of the law, started to be a little stricter regarding the number of employees at those companies and their professional qualifications. However, each company had 10 years to find an authorized company to produce the necessary documentation. The Rulebook on the conditions of performing business (Official Gazette of Federation of Bosnia and Herzegovina No. 23-21) in article 11 define that authorized organization must have an occupational health specialist as part of the risk assessment team Insisting that each authorized company has a contract with an occupational medicine specialist is also a separate issue. How many doctors in that specialty do we have in the Federation of Bosnia and Herzegovina? Does this path create an environment in which a relatively small number of organizations receive authorizations, which as a consequence has a certain increase in the price of services? What we would also like to mention concerns the need to create a register of work injuries at the level of the Federation of Bosnia and Herzegovina. In the time of the development of informational technologies, it is necessary to think about the information of a software database in which the data on injuries at work would be automatically entered. Through the analysis of such a database, we could have insight into more detailed information about injuries at work, jobs in which they most often occur, who gets injured- younger or older workers, at what time of the day, what are the causes and what are sources of injuries at work and similarly. The new version of the Law on Safety and Health at Work, which is being prepared in the Republic of Serbia, defines the obligation to create such a register. After the formation of the database, we should deal with determining the causes of injuries at work. In order to solve any problem, it is important to clearly define the problem itself. But how can we define a problem if we do not have relevant data that could allow us to take a clear stand? An effective solution to the problem is a specific measure or a set of measures that eliminate or reduce the influence of one or more causes found on the cause-and-effect graph (for this reason, the cause becomes the “main/root” cause). The approach for creating effective measures includes the following: generating possible solutions, evaluating solutions, and selecting the best solutions [10].

4. CONCLUSION

To conclude, just a brief statement that the aforementioned legal solutions represent a good basis for creating conditions for safer work. We have to start with the fact that the mentioned legal solutions represent a significant step forward compared to the previous which weren’t applicable. Does this mean that the listed solutions are ideal? Of course not. Occupational safety is a job that happens continuously and many developed countries change their laws due to the changes in technology and work technology itself. The Faculty of Metallurgy in Zenica, as a higher educational institution that organizes and implements the study program of occupational safety and fire protection, has a great role and responsibility in the process of training professional staff who, through their activities, will in the coming time be an active participant in the process of improving working conditions.

5. REFERENCES

[1] Chau, N., Gauchard, G., Dehaene, D., Benamghar, L., Touron, C., Perrin, P., & Mur, J. Contributions of occupational hazards and human factors in occupational injuries and their associations with job, age, and type of injuries in railway workers. International Archives of Occupational and Environmental Health, Vol. 80, No.6, pp. 517-525, 2007

[2] Eurostat (Health and safety at work in Europe (1999-2007) - A statistical portrait. Available: http://ec.europa.eu/eurostat/documents/3217494/5718905/ KS-31-09-290-EN.PDF/88eef9f7-c229-40de-b1cd-43126bc4a946 (Accessed on 4 March 2018), 2010

[3] Todorović, M., Živković, S., Haznadarević, L.,: Managing projects in the field of environment and life quality, XIII. Znanstveno-stručna konferencija s međunarodnim sudjelovanjem „Manadžment i sigurnost“, Čakovec, Hrvatska, Zbornik radova, str. 295-308. ISBN 978-953-55241-6-8 UDK 005:331.4(063) UDK/UDC, 005.73:331.45, 2018.
[4] Živković, S., Todorović, M., Markič, M.: Komparativna analiza uticaja organizacione kulture na sistem bezbednosti i zdravlja na radu u poslovnim organizacijama u Sloveniji i u privrednim društvima u Srbiji, VI. Znanstveno-stručna konferencija s međunarodnim sudjelovanjem „Manadžment i sigurnost“, Čakovec, Hrvatska, Zbornik radova, str. 120-128. ISBN 978-953-55241-6-8 UDK 005:331.4(063) UDK/UDC 005.73:331.45(497.11) (497.4), 2011.
[5] Živković, S., Todorović, M., Markič, M.: Komparativna analiza uticaja organizacione kulture na sistem bezbednosti i zdravlja na radu u poslovnim organizacijama u Sloveniji i u privrednim društvima u Srbiji, VI. Znanstveno-stručna konferencija s međunarodnim sudjelovanjem „Manadžment i sigurnost“, Čakovec, Hrvatska, Zbornik radova, str. 120-128. ISBN 978-953-55241-6-8 UDK 005:331.4(063) UDK/UDC 005.73:331.45(497.11) (497.4), 2011.
[6] Todorović, M.. Značaj organizacije rada u cilju smanjenja broja i težine povreda na radu, Zbornik radova Nacionalne konferencije sa međunarodnim učešćem 50 godina organizovane zaštite na radu u Srbiji, Niš, str.313-320, 2010.
[7] Todorović, M., Živković, S. Organizational culture in the function of occupational health care at work, International conference - Life cycle engineering and management ICDQM - 2010, Proceedings, 155-161, 2010.
[8] Todorović, M., Živković, S., Spremo, G.: Uloga države u procesu stvaranja bezbednih uslova za rad, 17. Međunarodna konferencija „Upravljanje kvalitetom i pouzdanošću“ICDQM-2014, Beograd, Zbornik radova, str. 416-421. ISBN 978-86-86355-16-4 COBISS.SR-ID 207635724 CIP 005.6(082) 005.6:658.58(082) 62(082), 2014.
[9] Todorović, M., Živković, S.: Analysis of occupational injuries in the Republic, JEL classification: J28, UDC 613.6(497.11); ISBN: 978-86-6139-138-5, Faculty of Economics Nis, 2017
[10] Helvida, A., Hadžić, S., Todorović, M.: Uviđaj incidenata i utvrđivanje korjenitih uzroka, XVI. Međunarodna konferencija za bezbednost i zdravlje na radu, Makedonija, Zbornik radova, str. 151-159. ISBN 978-608-244-658-5, COBISS.MK-ID 111274762, cip 331-45/.48(082), 2019.

METALLIC MATERIALS

ANALYSIS OF PRODUCTION METHOD AND STABILIZING AGENT ON STRUCTURE OF ALUMINUM METAL FOAMS

Karla Grgić, Igor Ćulum, Branimir Lela, Jure Krolo, Sonja Jozić
University of Split,Faculty of Electrical Engineering, Mechanical Engineering, and Naval Architecture
Split, Republic of Croatia

Keywords: metalfoam, chip waste, recycling, relative density, stabilizer

ABSTRACT
Aluminium alloy foams are a form of porous metal whose structure resembles the shape of natural materials such as coral, bone, sponge, etc. Due to their structure, these materials retain good mechanical properties of the base material while being significantly lighter than non-porous metal. Metal foams can be used as energy and vibration absorbers, heat exchangers, insulators, and filters. The main disadvantage of this type of material is its high production cost. To reduce production costs, aluminium alloy chips are used as base material. Foams are made of A360 and AA 7075 aluminium alloys. To produce a porous structure, $CaCO_3$ is used as a foaming agent while Zn and CaOwere added as stabilizing agents. The main goal of the paper was to investigate the difference in the shape of pores and relative density after foaming with different stabilizing agents.

1. INTRODUCTION

Metal foams imitate the structure of coral, sponge, and bone [1]. They can be made from materials such as aluminium, titanium, nickel, and polymers [2]. They are characterized as low-density materials with high energy and sound absorption. Foams are divided into two groups, with open and closed cells. Open cell foams are made by compacting base material and space holder. After that material is heated and the space holder leaks [3]. They are used as filters, heat exchangers, and electrodes [4]. Closed-cell foams are made by compacting alloy powder and foaming agents such as TiH_2, $CaCO_3$, and others [5]. They can be made with hot compaction or extrusion. After that process, samples are heated depending on the foaming agent. Titanium hydride's decomposition temperature is close to the melting point of aluminium alloy thus making it an optimal foaming agent. Calcium carbonate, however, is much cheaper and, due to higher decomposition temperature, requires no pre-treatment which leads to lower production costs [6,7, 8].

Movahedi et. al. proved that foaming with calcium carbonate gives smaller pores, even though temperature, foaming time, and $CaCO_3$ concentration were higher. Foams produced with $CaCO_3$ have greater compression strength and energy absorption, but lower density [9]. Sudharsan et. al. proved that adding Mg and Cu, increased the wettability and stability of the foams. It is important to avoid premature gas release[10]. Wang et al. used the pre-oxidation process by heating TiH_2 to postpone gas release at lower temperatures[11]. Carbon dioxide gas stabilizes the foam and prevents coagulation. The difference between $TiH_2$and$CaCO_3$foaming agents is that $CaCO_3$ has a greater decomposition temperature which is needed for the foaming process[12,13].

The most common starting material for aluminium foam production is aluminium powder. The costs associated with this base material lead to a drastic increase in the overall productioncost[14]. Using chips that are a by-product of the different machining processes

could significantly decrease the production cost of these types of materials. The main challenge in producing foams from aluminium chips is the mixing of larger alloy chip waste and small powder grains of foaming agents. Tsudaet al. analyzed the influence of different base materialson pore sizes. Their researchconcluded that foams produced with powder alloy havea more homogeneousstructure than foams produced using alloy chip waste [15]. The goal of this paper is to analyze the expansion and shape of aluminium foam pores produced using different weight percentages of $CaCO_3$foaming agent. This paper is an extension of the previous article in which differences between foaming with TiH_2 and $CaCO_3$ were given [16].

2. EXPERIMENTAL WORK

Materials used for foam productionwere aluminium alloy chips A360 and AA 7075. Chips were produced on vertical machining center Spinner VC 560.The cutting tool and cutting parameters used for chip production of both alloys were the same to keep the chip dimensions comparable. The samples were split into groups: first to be compacted and second to be extruded. A certain percentage of foaming agent ($CaCO_3$) and stabilizing agents (CaO or Zn) was mixed with the aluminium alloy chips. The correct weight percentages of the foaming and stabilizing agents are shown in Table 1. Firstly, the mixture of both groups was cold compacted with a force of 400kN.Compression force was measured with the HBM load cell C6A 1MN sensor.

Table 1. Production parameters

Sample number	Process	Alloy	Foaming and stabilizing agent	Foaming temperature (°C)	Foaming time (min)
1	Extrusion	A360	5%$CaCO_3$ + 2% Zn	800	15
2	Extrusion	AA 7075	5%$CaCO_3$ + 2% Zn	800	15
3	Extrusion	A360	5%$CaCO_3$ + 2% CaO	800	15
4	Extrusion	AA 7075	5%$CaCO_3$ + 2% CaO	820	15
5	Extrusion	A360	5%$CaCO_3$ + 2% Zn	820	15
6	Extrusion	AA 7075	5%$CaCO_3$ + 2% Zn	820	15
7	Compaction	A360	3% $CaCO_3$ + 2% Zn	800	20
8	Compaction	AA 7075	3% $CaCO_3$ + 2% Zn	800	20

After cold compacting, the samples from the first group were hot compacted. The process started with heating in the furnace for 20 minutes at a temperature of 420 °C. The furnace used to heat the sample was Demiterm Easy 9. After the heating process, the sample was put in the hydraulic press. The mould used for the compression was heated to 400 °C. After that, the sample was hot pressed with a force of 400 kN. Omron temperature regulator E5CC and a relay G3PE-225B DC12-24 were used for measuring the temperature. Finally, the

samples were placed in a mould with a diameter of 40 mm and heated to foaming temperatures.
The second group of samples was hot extruded with previous heating in the furnace at the same temperature as the first group. They were also foamed at similar temperatures which are visible in Table 1. The mould used for the foaming of the second group was 22 mm in diameter.
Relative density can be calculated as a ratio of foams density (ρ_f) and the density of aluminium alloy (ρ_s)[17].

$$\rho = \frac{\rho_f}{\rho_s} \quad (1)$$

3. RESULTS

Table 2. shows the results of the calculated relative density. It can be seen that the density of compacted samples is higher in comparison with extruded samples. The main reason is the higher percentage of $CaCO_3$ in the extruded samples. In comparison with the previous research [16], relative densities are as low as 0,26. The important difference between these two analyses is the addition of Zn as a stabilizing agent.
It can be concluded that Zn promotes higher expansion, even though the amount of foaming agent is very low at just 3%. There is a small difference in relative density comparing two alloys A360 and AA 7075 with the same temperature and time of foaming. Because of the higher decomposition temperature of $CaCO_3$, different liquidus temperatures of aluminium alloys are not an influencing factor in the process.
From Table 2 be concluded that foams with the addition of CaO have the highest density of extruded samples. Because of that, this stabilizing agent was not used in the process of compaction. High relative densities with CaO can be attributed to the high oxide level in the material during foaming that prevents foam expansion. Oxides help to stabilize the foams, but in this process, they are already present after the decomposition of calcium carbonateinto CO_2.

Table 2. Relative density

Sample number	Process	Alloy	Foaming and stabilizing agent	Relative density
1	Extrusion	A360	5%$CaCO_3$ + 2% Zn	0,26
2	Extrusion	AA 7075	5%$CaCO_3$ + 2% Zn	0,286
3	Extrusion	A360	5%$CaCO_3$ + 2% CaO	0,41
4	Extrusion	AA 7075	5%$CaCO_3$ + 2% CaO	0,39
5	Extrusion	A360	5%$CaCO_3$ + 2% Zn	0,337
6	Extrusion	AA 7075	5%$CaCO_3$ + 2% Zn	0,289
7	Compaction	A360	3% $CaCO_3$ + 2% Zn	0,442
8	Compaction	AA 7075	3% $CaCO_3$ + 2% Zn	0,53

Comparing samples 1 and 5which are made of A360, it can be concluded that higher density is achieved when using a higher temperature of 820 °C. The reason for this can be the coagulation of foams at higher temperatures and the same foaming times, Figure 1.
Similar results are found in samples 2 and 6 even though this difference is far lower. At lower temperatures, sample 2 with AA 7075 has a higher relative density than sample 1. When comparing samples foamed at a higher temperature, the opposite was observed. This can be due to the end of the expansion of A360 at a lower temperature. After that, foam coagulates and leaks, and the density rises.

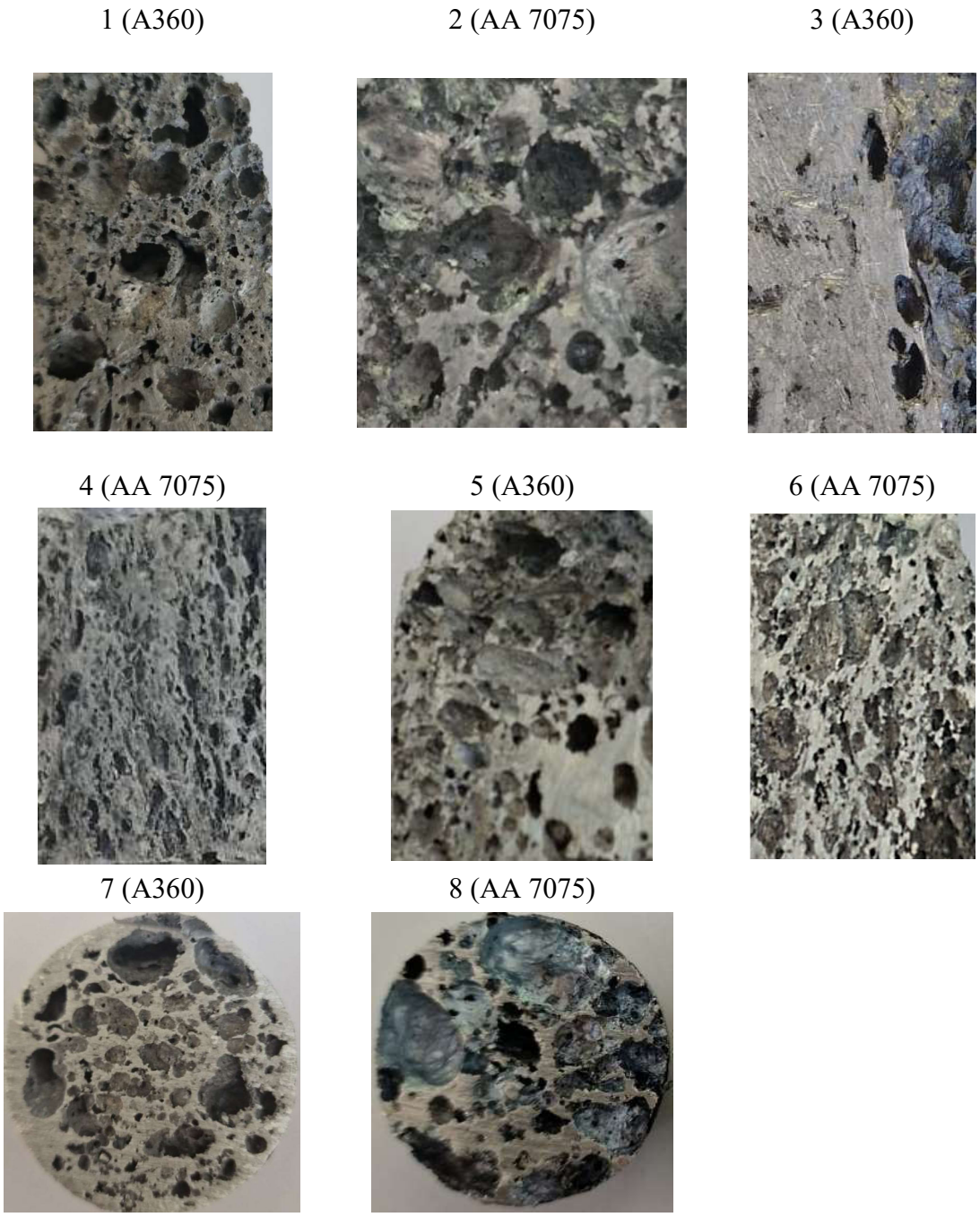

Figure 1 Microstructure of samples

Sample 4, made with CaO, has a structure that is horizontal with the foaming direction. This foam has no rounded and homogenous pores, Figure 1. It is also similar to sample 3 which has only a few larger pores directed in the same way as sample 4. Because of this inhomogeneous structure of foams, CaO was not used as a stabilizer for the compacted samples. As it was mentioned previously, calcium carbonate decomposes to CO_2 and the addition of CaO raises the viscosity of samples. Generally, oxides to one limit act as stabilizing agents, however, the viscosity in this sample is too high and prevents grow of foams.

Samples with zinc as a stabilizing agent have more rounded pores and structure that is not directed in one way. The first sample has the most homogenous structure out of the extruded samples. It can be concluded that A360 is more convenient for foaming with this stabilizing and foaming agent than AA 7075. That is confirmed by Figure 1, where samples 1, 5, and 7 have a more rounded structure. Samples 7 and 8 have rounded pores that are not directed. A more uniform structure was obtained due to a lower concentration of $CaCO_3$. Several larger pores can be related to powder accumulation at the beginning of the process.

4. CONCLUSION

In this paper production of aluminium foams using various production processes and stabilizing agents were analyzed. Aluminium A360 and AA 7075 chip waste were used in the foaming process together with $CaCO_3$ as a foaming agent. Additionally, Zn and CaO were used as stabilizing agents. Analyzing the pores and relative densities of the produced foams, the following was concluded:

- Samples with CaOhad an inhomogeneous structure that is related to higher oxide levels in the foam. Oxides act as stabilizers, but with a higher percentage, they raise the viscosity and prevent expansion.
- Zinc helps to stabilize the foams, and using this agent pores are more rounded than in samples 3 and 4 with CaO.
- Foams 7 and 8 had the highest density because of the lower $CaCO_3$ percentage. Rounded pores were also observed.
- The higher temperature of foaming leads to higher relative density. That can relate to an increase in pore diameter which can cause coagulation and leakage.
- At lower temperatures, sample 1 with A360 has a lower density than sample 2 with AA 7075, and at higher temperatures, there is a higher density with A360 foam.

5. ACKNOWLEDGMENT

This research has been supported by The Croatian Science Foundation through the project ALURECSS (IP-2020-02-8284).

6. REFERENCES

[1] Ashby M. F., Evans A., Fleck N. A., Gibson L. J., Hutchinson J. W., Wadley H. N.: Metal foams: a design guide, vol. 23, no. 1. 2002.

[2] Prados MartínE.: Microstructural parameters affecting the compressive response of closed-cell aluminum foams, Mech. Adv. Mater. Struct., vol. 0, no. 0, pp. 1–20, 2021, doi: 10.1080/15376494.2021.1872747.

[3] Ali H., Gábora A., Naeem M. A., Kalácska G., Mankovits T.: Effect of the manufacturing parameters on the pore size and porosity of closed-cell hybrid aluminum foams, Int. Rev. Appl. Sci. Eng., vol. 12, no. 3, p. 230, 2021, doi: 10.1556/1848.2021.00262.

[4] Bisht A., Gangil B.: Structural and physicomechanical characterization of closed-cell aluminum foams with different zinc additions, Sci. Eng. Compos. Mater., vol. 25, no. 4, pp. 789–795, 2018, doi: 10.1515/secm-2016-0307.

[5] Karuppasamy R., Barik D.: Production methods of aluminium foam: A brief review,Mater.

Today Proc., vol. 37, no. Part 2, pp. 1584–1587, 2020, doi: 10.1016/j.matpr.2020.07.161.
[6] Papadopoulos D. P., Omar H., Stergioudi F., Tsipas S. A., Michailidis N.: The use of dolomite as foaming agent and its effect on the microstructure of aluminium metal foams-Comparison to titanium hydride, Colloids Surfaces A Physicochem. Eng. Asp., vol. 382, no. 1–3, pp. 118–123, 2011, doi: 10.1016/j.colsurfa.2010.12.005.
[7] An J., Chen C., Zhang M.: Effect of CaCO3 content change on the production of closed-cell aluminum foam by selective laser melting, Opt. Laser Technol., vol. 141, no. November 2020, p. 107097, 2021, doi: 10.1016/j.optlastec.2021.107097.
[8] Kevorkijan V., Skapin S. D., Paulin I., Sustarsic B., Jenko M.: Synthesis and Characterisation of Closed Cells Aluminium Foams Containing Dolomite Powder As Foaming Agent, Mater. Tehnol., vol. 44, no. 6, pp. 363–371, 2010.
[9] Movahedi N., Mirbagheri S. M. H.: Comparison of the Energy Absorption of Closed-Cell Aluminum Foam Produced by Various Foaming Agents, Strength Mater., vol. 48, no. 3, pp. 444–449, 2016, doi: 10.1007/s11223-016-9783-y.
[10] N. Sudharsan, T. Rajasekaran, and G. S. Vinod-Kumar, "Optimizing the hot compaction parameters of Al-Mg-Cu foams processed through elemental powder route," *IOP Conf. Ser. Mater. Sci. Eng.*, vol. 402, no. 1, 2018, doi: 10.1088/1757-899X/402/1/012202.
[11] Wang H., Zhu D. F., Hou S., Yang D. H., Nieh T. G., Lu Z. P.: Cellular structure and energy absorption of Al–Cu alloy foams fabricated via a two-step foaming method, Mater. Des., vol. 196, 2020, doi: 10.1016/j.matdes.2020.109090.
[12] Jaafar A. H., Al-Ethari H., Farhan K.: Modelling and optimization of manufacturing calcium carbonate-based aluminum foam, Mater. Res. Express, vol. 6, no. 8, 2019, doi: 10.1088/2053-1591/ab2602.
[13] Praveen Kumar T.N., Venkateswaran S., Seetharamu S.: Effect of Grain Size of Calcium Carbonate Foaming Agent on Physical Properties of Eutectic Al–Si Alloy Closed Cell Foam, Trans. Indian Inst. Met., vol. 68, no. 1, pp. 109–112, 2015, doi: 10.1007/s12666-015-0631-8.
[14] Kumar G. S. V., García-Moreno F., Banhart J., Kennedy A.: The stabilising effect of oxides in foamed aluminium alloy scrap, Int. J. Mater. Res., vol. 106, no. 9, pp. 978–987, 2015, doi: 10.3139/146.111255.
[15] Tsuda S., Kobashi M., Kanetake N.: Producing technology of aluminum foam from machined chip waste, Mater. Trans., vol. 47, no. 9, pp. 2125–2130, 2006, doi: 10.2320/matertrans.47.2125.
[16] Grgić K., Lela B., Jozić S., Krolo J.: Aluminium foams made of various aluminium alloys scrap and various foaming agents, Mechanical Technology and Structural Materials. pp. 37–42, 2022.
[17] Farahani M. R., Rezaei Ashtiani H. R., Elahi S. H.: Effect of Zinc Content on the Mechanical Properties of Closed-Cell Aluminum Foams,Int. J. Met., 2021, doi: 10.1007/s40962-021-00635-2.

MANUFACTURING AND CHARACTERIZATION OF Ti6Al4V ALLOY BY SELECTIVE LASER MELTING

Matija Zorc, Aleš Nagode, Maja Pogačar, Blaž Karpe, Borut Kosec, Milan Bizjak
University of Ljubljana, Faculty of Natural Sciences and Engineering
Ljubljana, Slovenia

Keywords: additive manufacturing, selective laser melting, Ti6Al4V alloy, mechanical properties, microstructure

ABSTRACT
Titanium and its alloys, particularly Ti6Al4V, are widely used, especially in aerospace and medicine due to their relatively low density, high strength, and good corrosion resistance. However, there are formidable challenges in casting, forming, and machining titanium alloys, which result in final products that are considerably more expensive. Additive manufacturing is considered one of the most promising technologies for metallic materials due to its ability to produce complex geometries with high density and accuracy in a short amount of time. It allows the manufacturing of products with complex geometries that cannot be made with traditional metallurgical processes. One of the most widely used technologies for alloys is selective laser melting (SLM).
The most favourable conditions to be used during SLM process for Ti6Al4V alloy powder have been determined in this research. This was done by using process maps and the effect of different process parameters on the mechanical properties and microstructure of SLM samples from Ti6Al4V alloy powder. Three different laser powers and four different scanning speeds were used and the process maps of hardness and porosity were created. With these results, the optimal parameters with the highest hardness and the lowest fraction of porosity in the SLM Ti6Al4V samples were determined.

1. INTRODUCTION

Ti6Al4V is the most useful (α+β) titanium alloy, owing to its high strength, fracture toughness, low density, and excellent corrosion resistance. Traditional metallurgical processes used in the making of this alloy are expensive and difficult. Additive manufacturing allows the creation of complex shapes, which cannot be made in the traditional way. Selective laser melting (SLM) is one of the most commonly used additive manufacturing techniques (Figure 1). It is used for the production of metallic, ceramic, and composite components. This method often creates defects in the material such as porosity and cracks, but can also create high residual stresses. It is known that the shape and orientation of pores strongly influence the ductility of the material and that they act as nucleation sites for microcracks [1,2,3,4]. Microstructures of SLM-produced parts are different from those in parts made with traditional techniques. This is due to differences in solidification and cooling rates and is evident in different crystal grain sizes.

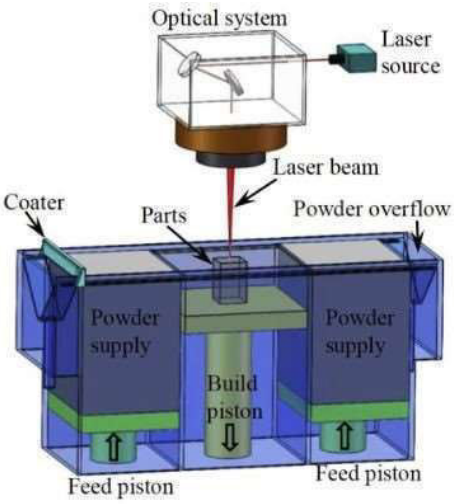

Figure 1. SLM method. Copyright 2019 by Elsevier [5]

There are many parameters at play during the SLM process, which need to be balanced for the best properties of the manufactured part: type of laser, laser intensity/power, laser beam diameter, scanning speed, hatch spacing, layer thickness, scanning strategy (Figure 2a) [6,7,8,9]. Regarding the material, these parameters are important as well: chemical composition, fluidity of the powder, density of the powder, absorption capability, and the distribution, shape and size of powder particles [6,7,8]. Three types of building direction are presented in Figure 2b.

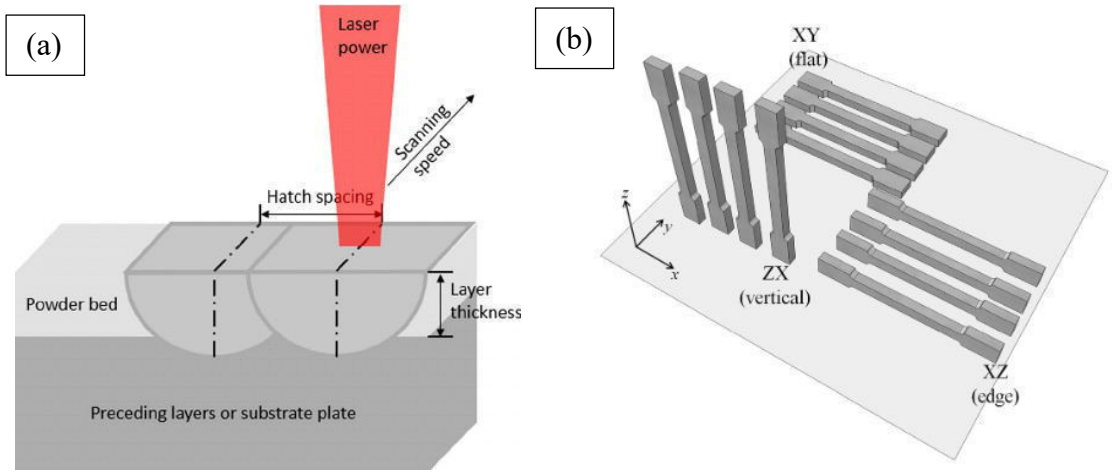

Figure 2. (a) Visualization of parameters during SLM process. Copyright 2015 by American Institute of Physics Publishing [10]; (b) Types of building direction. Copyright 2014 by Elsevier [11]

Microstructures of SLM manufactured samples from Ti6Al4V alloy are known to predominantly consist of acicular martensite α', which grows from columnar β grains (Figure 3). Its presence provides the part with high tensile strength, but at the same time makes it more brittle and less ductile. Especially the ductility is, compared to the samples created by traditional metallurgical techniques, drastically lower.

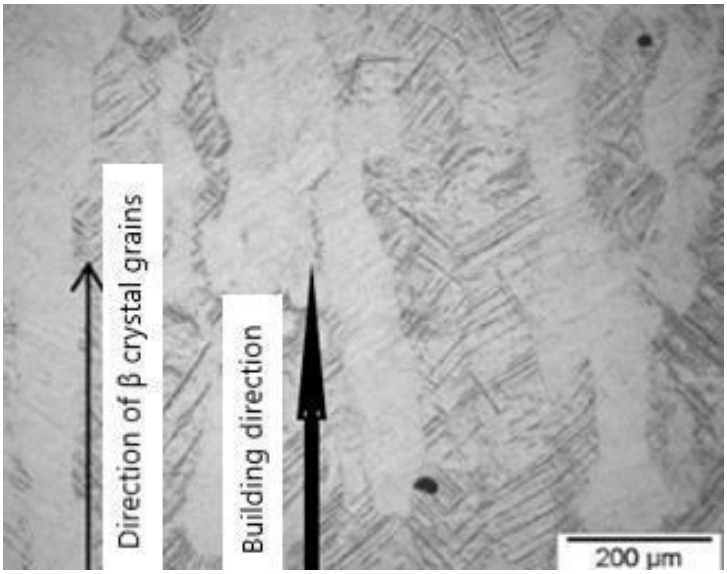

Figure 3. Typical microstructure in SLM manufactured Ti6Al4V sample [12]

2. EXPERIMENTAL WORK

The powder is commercially available and was bought on the market. Experimental work consisted of chemical analysis with ICP-OES, fluidity of the powder, which was measured according to the ASTM B213 standard, apparent density according to the ASTM B212 standard, angle of repose according to the ASTM C1444 standard, and tap density according to the ASTM B527 standard. The powder was spherical and had an average diameter of 24 µm (Figure 4).

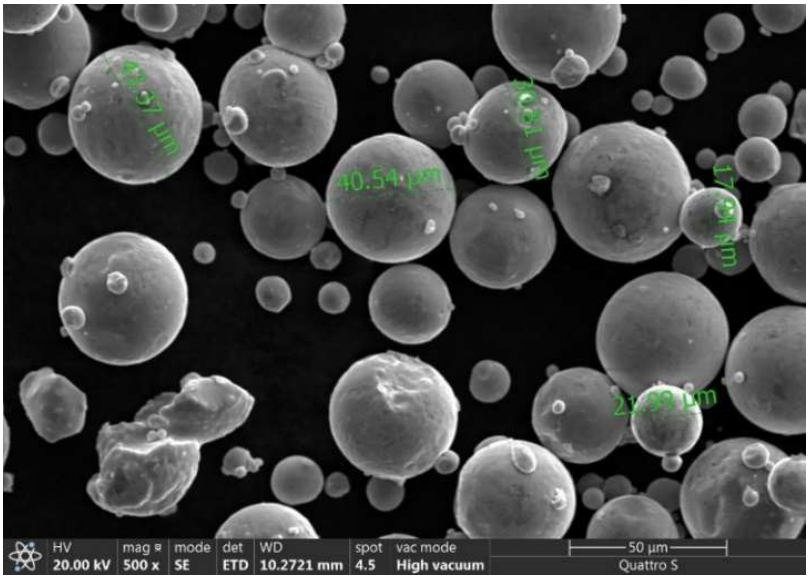

Figure 4: SEM photo of the used Ti6Al4V powder

Following the analyses, the samples were produced using the SLM method. Three different laser powers and four different scanning speeds were used. Other parameters remained constant. The parameters are shown in Table 1.

Table 1. Parameters used during experimental work

Sample	Laser power P [W]	Scanning speed v [mm/s]	Layer thickness t [µm]	Hatch spacing H [µm]	Laser beam diameter d [µm]
MP300/400	300	400	30	30	60
MP300/600	300	600	30	30	60
MP300/800	300	800	30	30	60
MP300/1000	300	1000	30	30	60
MP200/400	200	400	30	30	60
MP200/600	200	600	30	30	60
MP200/800	200	800	30	30	60
MP200/1000	200	1000	30	30	60
MP100/400	100	400	30	30	60
MP100/600	100	600	30	30	60
MP100/800	100	800	30	30	60
MP100/1000	100	1000	30	30	60

The samples were modeled in Solidworks and printed using Aconity 3D MINI printer located at the Institute for Materials and Technology in Ljubljana (Figure 5a). Samples were later metallographically prepared for microstructural analyses. These were done with ZEISS Imager Z2mlight microscope and Thermo Fisher Scientific FEGSEM Quattro scanning electron microscope, equipped with an EDS detector by Oxford Instruments located at the Department of Materials and Metallurgy at the Faculty of Natural Sciences and Engineering (University of Ljubljana) (Figure 5b). Hardness tests were performed using HV1 Vickers method. Tensile tests were performed according to the SIST EN ISO 6892-1 A224 standard. Samples were tested based on their building direction (XZ and XY (Figure 2b)).

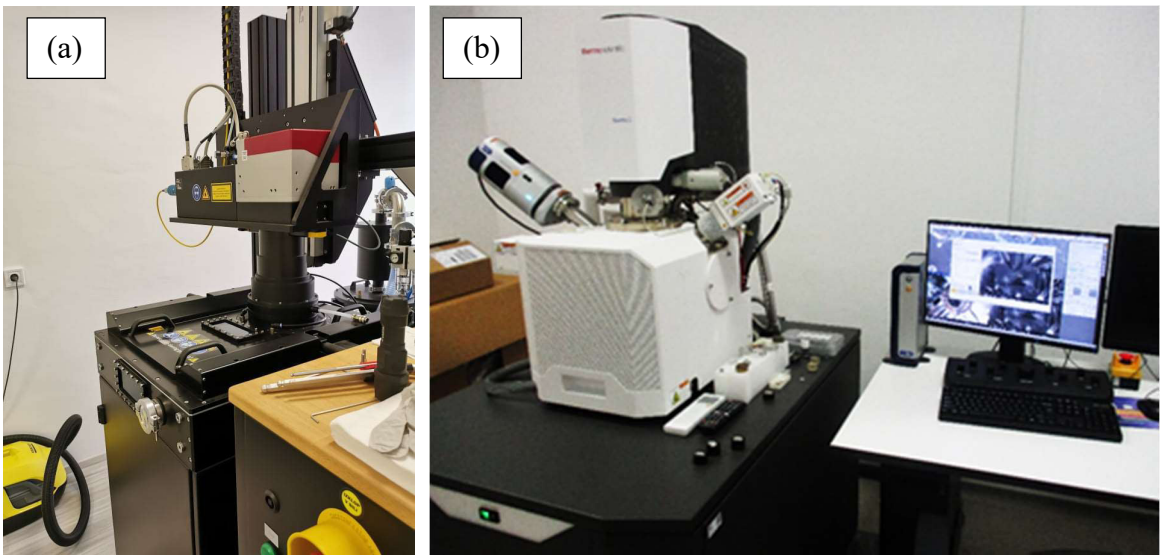

Figure 5. (a) Light microscope ZEISS Imager Z2m; (b) Electron microscope Thermo Fisher Scientific Quattro with an Oxford Instruments EDS detector

3. RESULTS

The chemical analysis has shown that the powder consists of 6,1wt% Al, 3,8 wt% V, and 0,22 wt% Fe with the remaining amount consisting of Ti. Other characteristics of the powder were also measured: fluidity was on average 2,05 g/s, tap density 2,56 g/cm^3, angle of repose 53,75°, and apparent density 2,43 g/cm^3.

The results show that the hardness achieves the largest value at 200 W and 1000 mm/s (Figure 6). Meanwhile, the proportion of porosity is by far the highest when 300 W of laser power and 800 mm/s scanning speed are used (Figure 7). This could be a consequence of reusing the powder. It is also worth noting that the porosity was not so severe across the whole sample. The region with the worst porosity was chosen to be presented as it could affect the properties of the manufactured part if ignored. Based on these results two combinations of parameters were chosen for further testing (200 W/400 mm/s and 200 W/1000 mm/s).

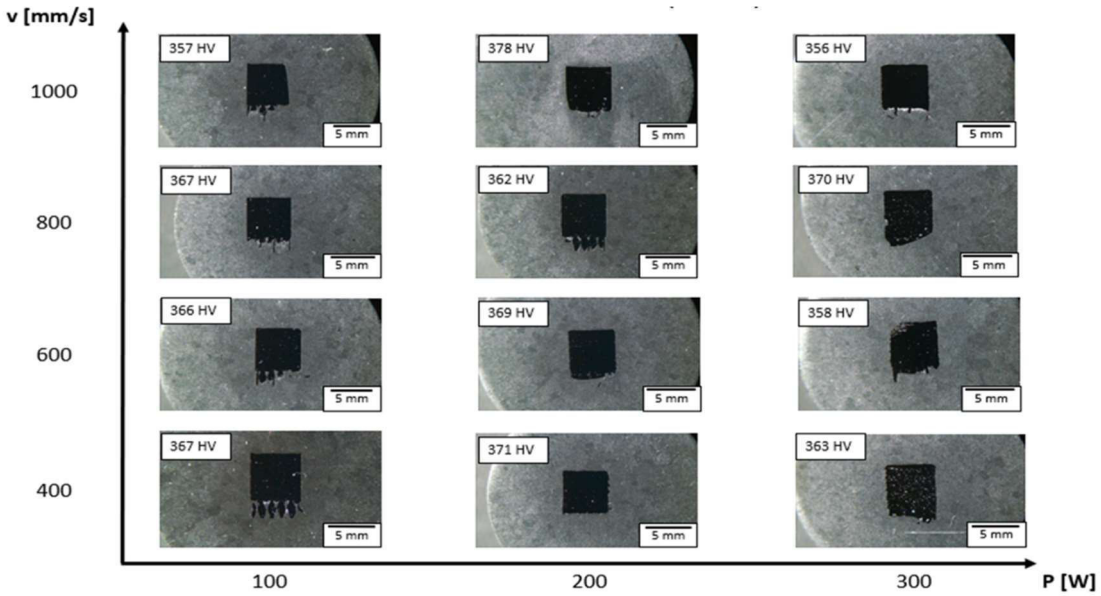

Figure 6. Hardness values at different parameters [HV1]

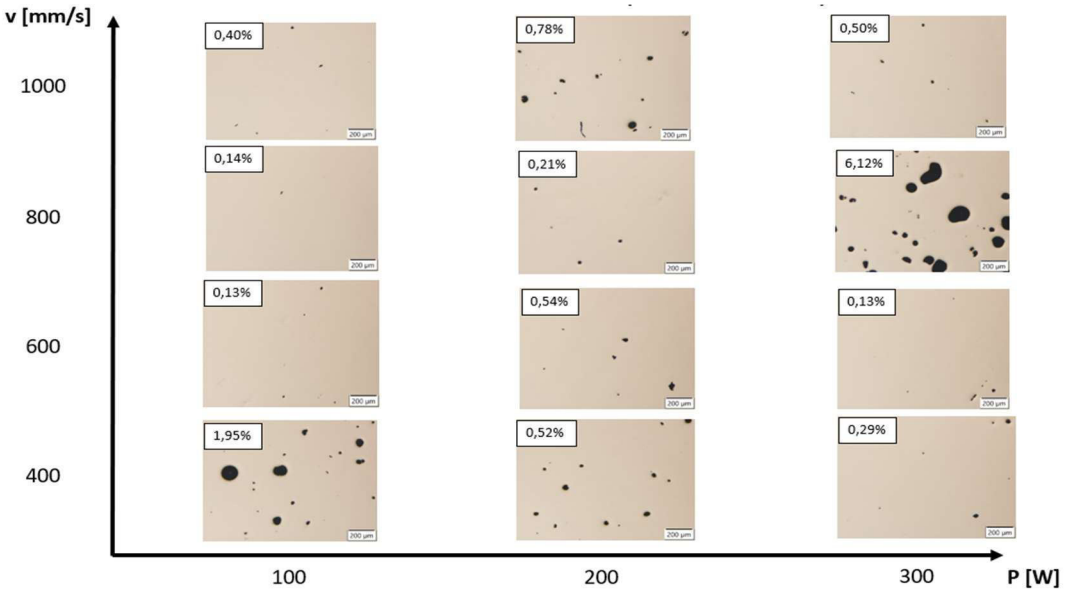

Figure 7. Porosity proportion at different parameters

The microstructures of both samples consist of martensite α', which has grown from the grain boundaries of elongated columnar β grains. These are oriented in the building direction. With higher scanning speeds, the columnar β grains become thinner (Figure 8).

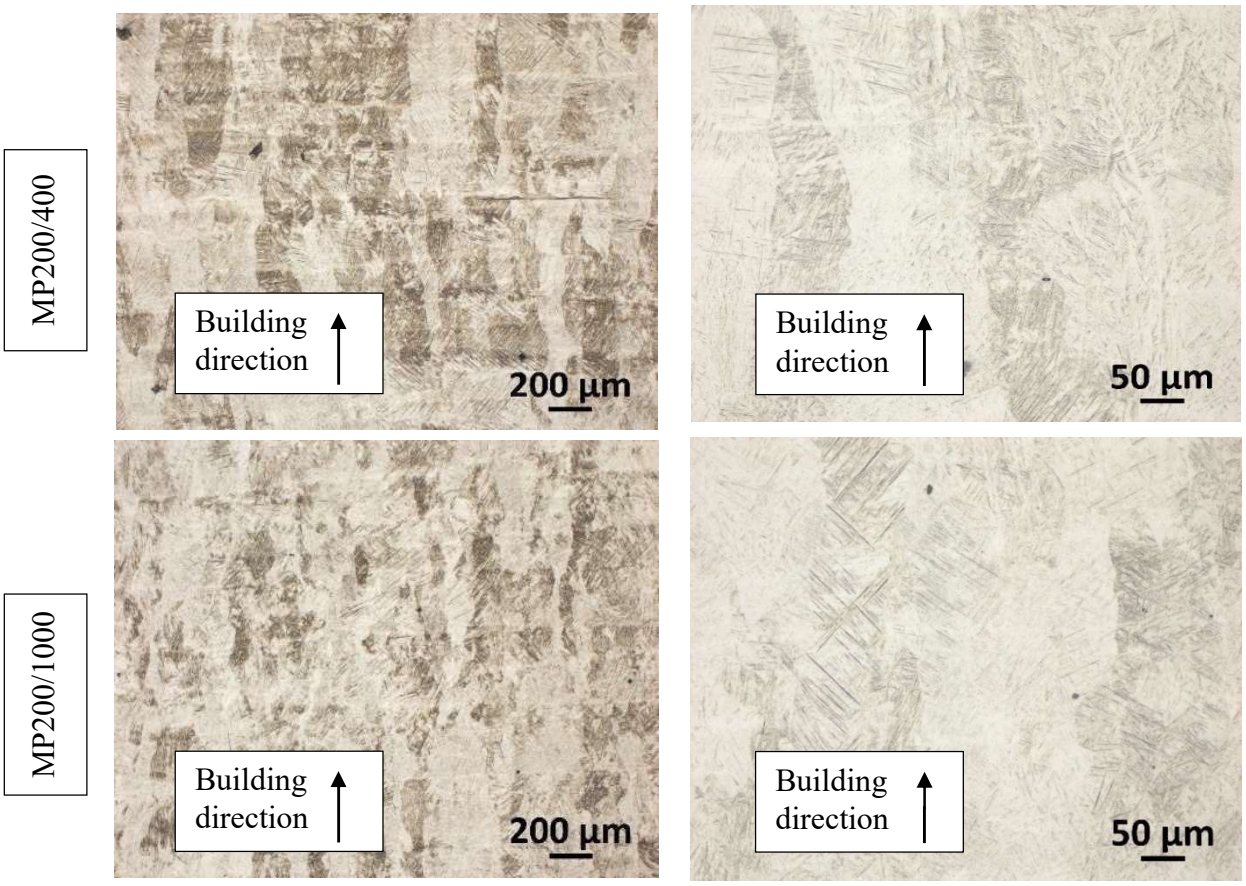

Figure 8. Microstructures in samples produced with chosen parameters - optical microscope

Microstructural analysis with SEM makes needles of acicular martensite α' more clearly visible. They have a "fishbone" shape, which is caused by the changes in the scanning direction. The martensite is much more pronounced at higher scanning speeds (Figure 9).

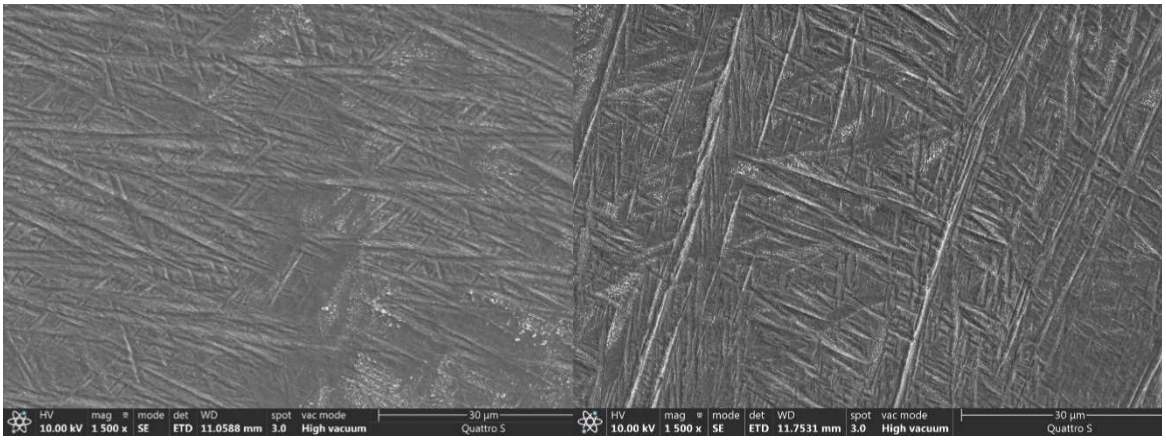

MP200/400 MP200/1000

Figure 9. Microstructures in samples produced with chosen parameters – SEM

The MP200/400 sample also had its tensile strength measured (Table 2). Three measurements were performed per building direction (XZ and XY). Samples built in XZ direction have an average tensile strength of 1185,67MPa, while those built in XY direction have an average of 1251,67 MPa. The average elongation was 5,7 % for XZ samples and 3,03 % for XY samples. The tensile strengths of similar samples found in the literature are between 1000 MPa and 1200 MPa [13,14,15].

Table 2. Tensile test results for MP200/400 sample

MP200/400	Length L_o[mm]	Final length L_u [mm]	Tensile strength R_m [MPa]	Elongation A [%]
XZ1	30	31,92	1170	6,4
XZ2	30	32,00	1176	6,7
XZ3	30	31,21	1211	4
Average			1185,67	5,7
XY1	30	30,69	1250	2,3
XY2	30	30,89	1270	3,0
XY3	30	31,14	1235	3,8
Average			**1251,67**	**3,03**

4. CONCLUSIONS

Samples from Ti6Al4V alloy in a powder form were produced using the SLM method. Different parameters were used and their effect on the properties analysed. Based on the experimental work the following conclusion can be made:

- Based on the hardness and level of porosity, the best parameters are 200 W of laser power and a scanning speed of 400 mm/s.
- Both of these parameters affect hardness more than they do porosity, except at 300 W of laser power and 800 mm/s scanning speed, which is an anomaly, that could be caused by reusing the powder.
- The Microstructure of Ti6Al4V samples consists of α' in the form of needles, which grow from the grain boundaries of prior columnar β grains. The width of β grains depends on the scanning speed.
- The tensile strength of Ti6Al4V samples is between 1000 MPa and 1300 MPa. Their ductility is low. This is caused by the acicular martensite and residual stresses.
- The building direction affects the mechanical properties. The tensile strength of the samples built in XY direction was 66 MPa higher than that of samples built in XZ direction.

5. REFERENCES

[1] A. Duran, Y. Castro, A. Conde, J. J. DeDamborenea. Sol-Gel Protective Coatings for Metals. Handbook of Sol-Gel Science and Technology. Edited by L. Klein. Madrid: Springer International Publishing AG, 2018

[2] T. Vilaro, C. Colin, J. D. Bartout. As-Fabricated and Heat-Treated Microstructures of the Ti-6Al-4V Alloy Processed by Selective Laser Melting. Metallurgical and Materials Transactions A, 2011, vol. 42, 3190–3199.

[3] S. Lui, Y. C Shin. Additive manufacturing of Ti6Al4V alloy: A review. Materials and Design, 2019, vol. 164, article no.: 107552.

[4] K. Zeng, D. Pal, B. Stucker. A review of thermal analysis methods in laser sintering and selective laser melting. Solid Freeform Fabrication Simposium, 2012, 796–814.

[5] J. Lui, Q. Sun, C. Zhou, X. Wang, H. Li, K. Guo, J. Sun. Achieving Ti6Al4V alloys with both high strength and ductility via selective laser melting. Materials Science & Engineering A, 2019, vol. 766, article no.: 138319.
[6] S. Kumar. Selective Laser Sintering/Melting. Comprehensive Materials Processing, 2014, vol 10, 93-134.
[7] I. J. Solomon, P. Sevvel, J. Gunasekaran. Metallic materials fabrication by selective laser melting: A review. Material's Today: Proceedings, 2021, vol. 37, 252-256
[8] C. Tan, K. Zhou, W. Ma, P. Zhang, M. Liu, T. Kuang. Microstructural evolution, nanoprecipitation behavior and mechanical properties of selective laser melted high-performance grade 300 maraging steel, Material & Design, 2017, vol. 134, 23–34.
[9] N. T. Aboulkhair, M. Simonelli, L. Parry, I. Ashcroft, C. Tuck, R. Hague. 3D printing of Aluminium alloys: Additive Manufacturing of Aluminium alloys using selective laser melting. Progress in Materials Science, 2019, vol. 106, article no.: 100578.
[10] C. Y. Yap, C. K. Chua, Z. L. Dong, Z. H. Liu, D. Q. Zhang, L. E. Loh, S. L. Sing. Review of selective laser melting: Materials and applications. Applied Physics Reviews 2, 2015, vol. 4, article No.: 041101
[11] M. Simonelli, Y. Y. Tse, C. Tuck, C. Effect of the build orientation on the mechanical properties and Fracture modes of SLM Ti6Al4V. Material Science & Engineering A, 2014, vol. 616, 1-11.
[12] M. Pogačar. Izdelava in karakterizacija zlitine Ti6Al4V s postopkom selektivnega laserskega taljenja (Manufacturing and characterization of Ti6Al4V alloy by selective laser melting). Master's thesis, University of Ljubljana, Faculty of Natural Sciences and Engineering, 2022.
[13] X. Z. Shi, S. Y. Ma, C. M. Lui, Q. R. Wu, J. P. Lu. Selective laser melting-wire arc additive manufacturing hybrid fabrication of Ti-6Al-4V alloy: microstructure and mechanical properties, Materials Science and Engineering: A, 2017, vol. 684, 196-204.
[14] P. Krakhmalev, G. Fredriksson, I. Yasroitsava, N. Kazantseva, A. Du Plessis, I. Yadroitsev. Deformation behavior and microstructure of Ti6Al4V manufactured by SLM. Physics Procedia, 2016, vol. 83, 778-788.
[15] D. Salikhyanov, V. Veselova, V. Volkov. Flow behavior and microstructure evolution of Ti-6Al-4V titanium alloy produced by selective laser melting compared to wrought. The International Journal of Advanced Manufacturing Technology, 2022, vol. 119, 953-967.

ADSORPTION OF Cu(II) IONS BY MEANS OF FOUNDRY WASTE

Anita Štrkalj, Zoran Glavaš
University of Zagreb, Faculty of Metallurgy
Sisak, Croatia

Keywords: adsorption, Cu(II) ions, waste after shot blasting of castings

ABSTRACT
This article deals with the analysis of the adsorptive properties of the waste produced during the shot blasting of castings in foundries. During this process, particles of moulding mixture and scale that remained on the surface of the casting after removal from the mould are removed. Since this waste contains particles of moulding mixture (SiO_2, carbon, ...) and scale (i.e. iron oxides), which as individual components are known as satisfactory adsorbents, its adsorption properties towards Cu(II) ions in aqueous solution were investigated. The obtained results show that the investigated waste has a significant adsorption capacity for binding Cu(II) ions.

1. INTRODUCTION

Casting is one of the oldest processes that man uses to shape metal. With this process, metal objects, i.e. castings of different shapes, dimensions and mass, chemical composition and mechanical properties are obtained relatively quickly according to customer requirements. Precisely because of these possibilities, the production of castings in the world is growing. In 2020, 105.5 million tons of castings were produced in the world [1]. However, the production of castings is not a completely ecological way of production. Due to the large number of materials used during production (sand, binder, etc.) and partial processing of castings (cleaning (shot blasting), grinding), as well as due to mass production, considerable amounts of various hazardous and non-hazardous waste are generated. Part of the non-hazardous waste is returned to production, while the rest cannot be reused and is disposed of in landfills. In order to reduce disposal, today non-hazardous waste from foundries is being researched a lot in terms of its further use. Very often, waste moulding mixture and slag are used in construction, but also in road construction [2,3]. In addition, tests of the adsorption properties of waste foundry materials are very widespread [4-7]. This type of research and the possibility of using it for the purpose of adsorption is certainly very significant since this type of waste usually consists of metal oxides, such as SiO_2, Al_2O_3, MgO, CaO, FeO, Fe_2O_3 (sand, slag, scale, waste after shot blasting), clay (binders) and carbon-based materials (various additives to improve the properties of the moulding mixture) which are known as good adsorbents.
In this article, using equilibrium adsorption models, waste after shot blasting was investigated as a potential adsorbent for the removal of Cu(II) ions from aqueous solutions.

2. MATERIALS AND METHODS

The waste produced during the shot blasting of castings was used as an adsorbent in this article. The shot blasting process consists of hitting shot pellets of appropriate dimensions on the surface of the casting, during which the scale, i.e. metal oxides and particles of the moulding mixture that remain on the casting after removing the casting from the sand

mould, are removed. Since the steel pellets hit the surface of the casting at high speed, some of them are damaged and due to the inappropriate granulometric composition, they can no longer be used for shot blasting. Damaged shot pellets, scale and sand that have fallen off the surface of the casting constitute waste. This type of waste and Cu(II) ions from the aqueous solution were used to form an adsorption system for the batch adsorption process.

For the experiment, 1 g of waste after shot blasting was used, which was placed in contact with 50 ml of a solution of Cu(II) ions of different concentrations (10, 30, 50, 70 and 100 mg/l). The research was carried out at a temperature of 22 °C and a pH of 5.69. After dynamic equilibrium was established (20 minutes), filtration was performed, and the concentration of Cu(II) ions in the obtained filtrates was determined by atomic absorption spectrometry.

From the data for the initial concentration of Cu(II) ions, the concentration of Cu(II) ions after adsorption (in the filtrate), the mass of the adsorbent and the volume of the adsorbate, the adsorption capacity q_e was determined according to the following equation [8]:

$$q_e = \frac{c_0 - c_e}{m} \cdot V \qquad (1)$$

where is:

c_0 - initial mass concentration of Cu(II) ions in the solution, mg/l,

c_e - equilibrium mass concentration of Cu(II) ions in the solution, mg/l,

m - the mass of waste after the shot blasting, g,

V – a volume of the solution of Cu(II) ions, l.

Several adsorption isotherms models were used for the equilibrium study, and their mathematical models are presented in Table 1.

Table 1. Mathematical representation of the isotherms used to describe the equilibrium data of the adsorption system waste after shot blasting/Cu(II) ions [9]

Isotherm model	Mathematical representation
Langmuir	$q_e = \frac{q_m K_L c_e}{1 + K_L c_e}$
Freundlich	$q_e = K_F c_e^{1/n}$
Dubin-Radushevich	$q_e = q_m \exp^{(-k \cdot \varepsilon^2)}$
Eadie-Hoffstee	$q_e = q_m - \frac{q_e}{K_c c_e}$
Temkin	$q_e = \frac{RT}{b_T} \ln K_T + \frac{RT}{b_T} \ln c_e$

3. RESULTS AND DISCUSSION

The study of adsorbent-adsorbate interactions is very important for the potential application of the investigated adsorbent. Most often, this interaction is studied through the adsorption capacity, and the experimental data are processed with different adsorption models, whereby a more detailed insight into the adsorption process is obtained.

Figure 1 shows the equilibrium state of the adsorption system waste after shot blasting/Cu(II) ions via the dependence $q_e = f(c_e)$.

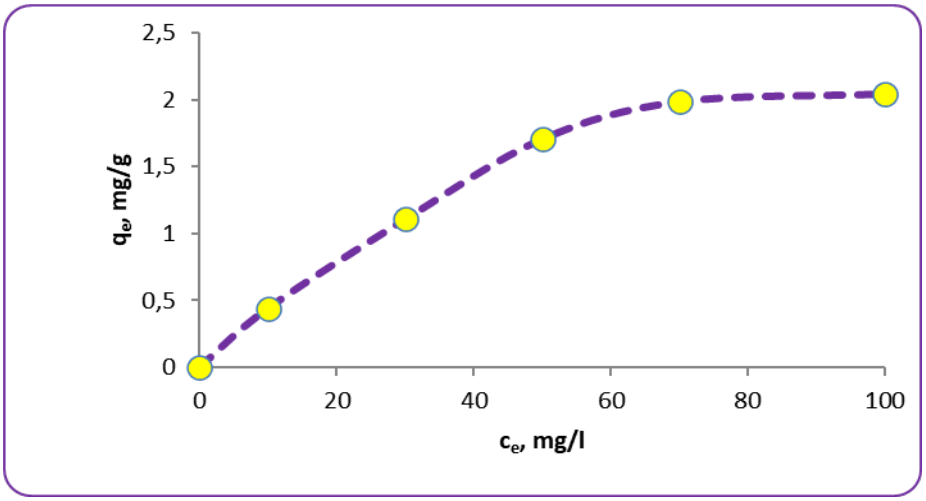

Figure 1. The equilibrium state of adsorption system waste after shot blasting/Cu(II) ions

It can be seen from Figure 1 that the waste after shot blasting shows the appropriate adsorption affinity towards Cu(II) ions. By increasing the concentration of ions in the solution, the adsorption capacity increases and at a concentration of 100 mg/l it reaches slightly more than 2 mg/g. An increase in the concentration of Cu(II) ions favours adsorption since more Cu(II) ions are available in the solution and, at the same time there are a lot of free places on the surface of the adsorbent, which is also an important factor in adsorption. This adsorbent-adsorbate behaviour is expected and is consistent with the behaviour of other waste materials that are being investigated as potential adsorbents [10 - 12].

However, from these data it is not possible to conclude about the type and method of adsorption (chemical or physical). For this reason, the equilibrium experimental data were processed using five isotherms models: Langmuir, Freundlich, Dubin-Radushevich, Eadie-Hoffsteev and Temkin according to the equations shown in Table 1.

Figures 2 - 6 graphically show the used adsorption isotherms models.

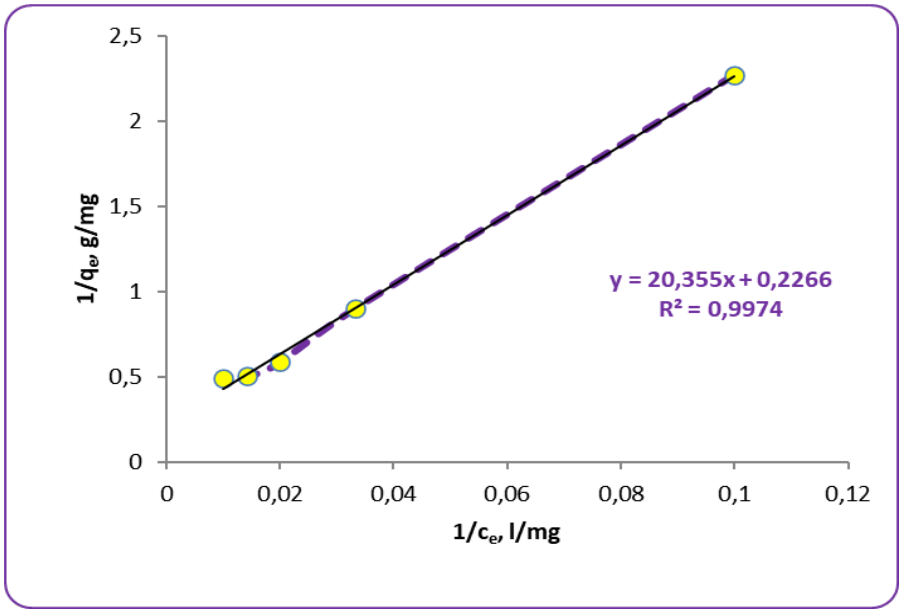

Figure 2. Langmuir adsorption isotherm model for the system waste after shot blasting/Cu(II) ions

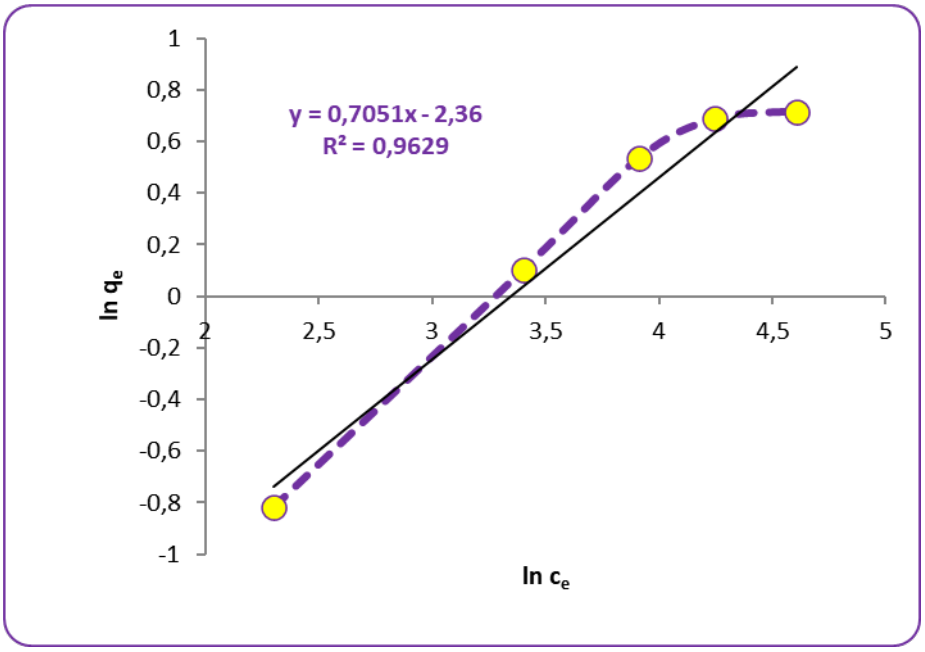

Figure 3. Freundlich adsorption isotherm model for the system waste after shot blasting/Cu(II) ions

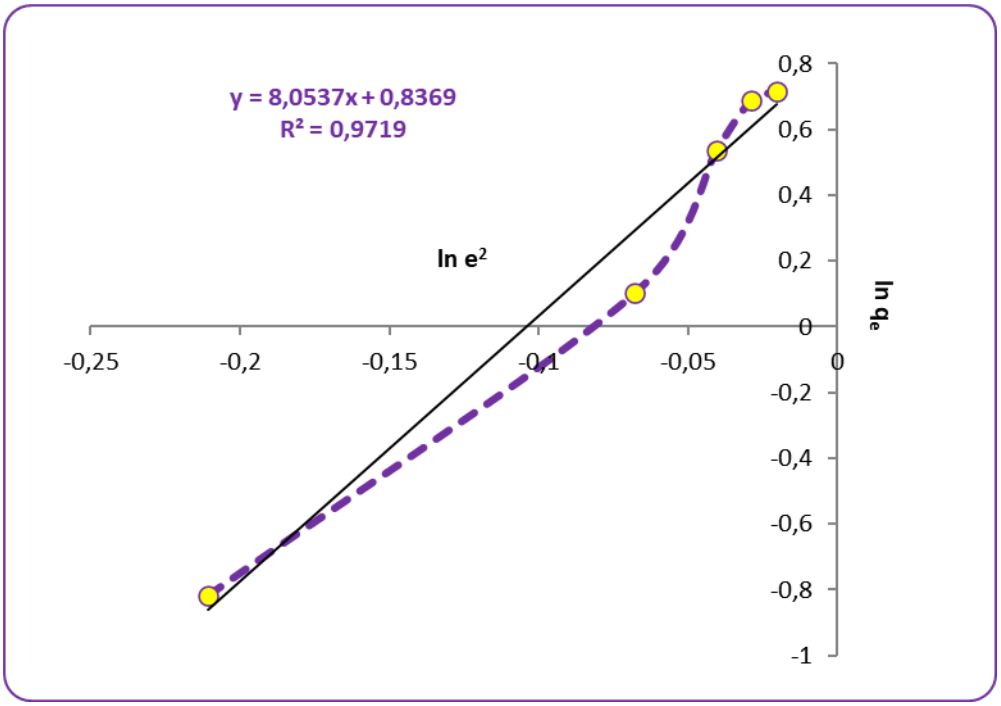

Figure 4. Dubin-Radushevich adsorption isotherm model for the system waste after shot blasting/Cu(II) ions

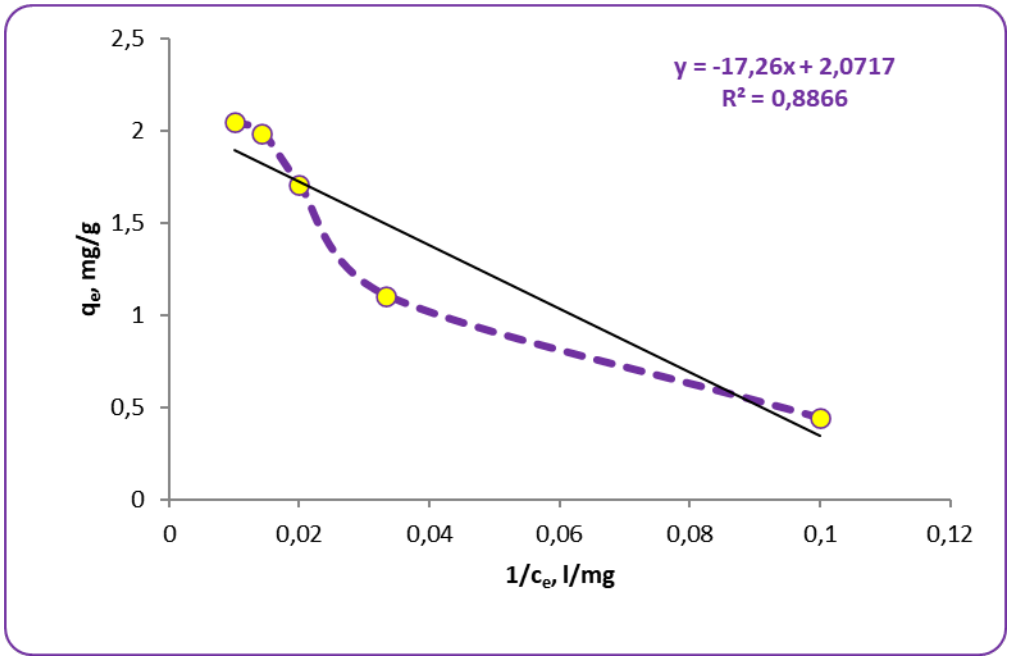

Figure 5. Eadie-Hoffstee adsorption isotherm model for the system waste after shot blasting/Cu(II) ions

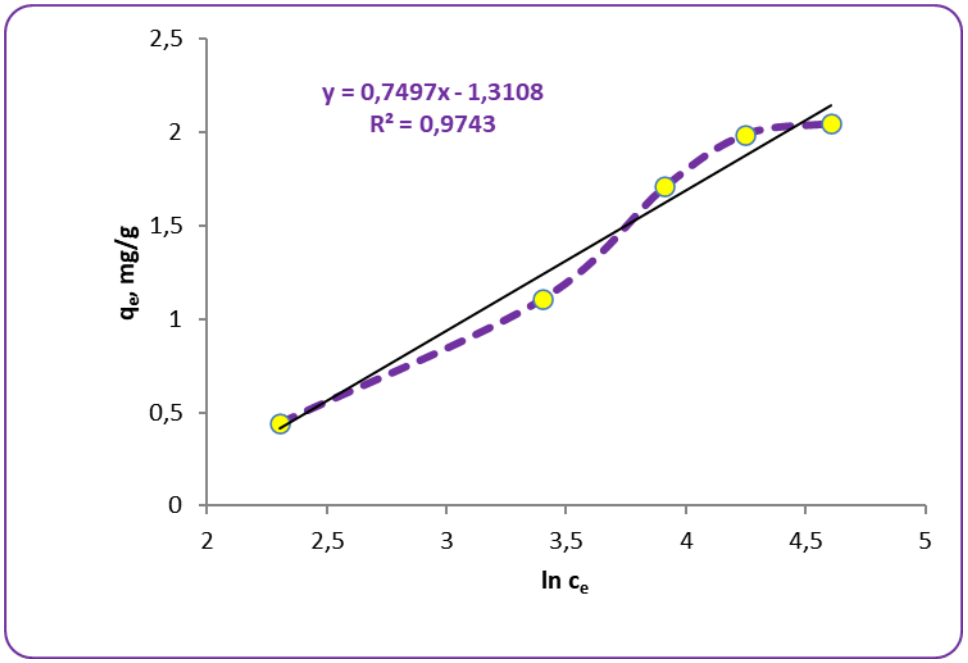

Figure 6. Temkin adsorption isotherm model for the system waste after shot blasting/Cu(II) ions

In order to choose the isotherm model that best describes the investigated system, the so-called fitting is usually used. There are numerous parameters that are used to assess the quality of fitted experimental data: coefficient of determination (R^2), mean absolute relative error (MARE), root mean squared relative error (RMRSE), Marquardt's per cent standard deviation (MPSD), hybrid fractional error function (HYBRID), average relative error (ARE), average relative standard error (ARS), sum squares errors (ERRSQ/SSE), the standard deviation of relative errors (SRE), Spearman's correlation coefficient (r_s), nonlinear chi-square test (χ^2).

In this article, the coefficient of determination was used to assess the quality of the fitted experimental data. Table 2 shows the coefficients of determination for all used isotherms models.

Table 2. Coefficients of determination for all used isotherms models (system waste after shot blasting /Cu(II) ions)

Isotherm model	Coefficients of determination, R^2
Langmuir	0,997
Freundlich	0,962
Dubin- Radushevich	0,971
Eadie-Hoffstee	0,886
Temkin	0,974

A comparison of the coefficients of determination (Table 2) shows that all coefficients are > 0.64, which means that all isotherms models can be used to describe the adsorption of the system waste after shot blasting/Cu(II) ions [13]. This conclusion coincides with literature definitions of certain isotherms, according to which the Langmuir adsorption isotherm indicates that adsorption is limited to the formation of only one adsorbate layer. It is also based on the assumption that all active sites have the same affinity for adsorbate molecules. In addition, if the Langmuir isotherm describes the investigated system well, it is assumed that adsorption takes place as chemisorption. Temkin model also indicates that adsorption is the result of the chemical bonding of adsorbate. According to the Freundlich and Dubin-Radushevich isotherms, adsorption takes place on a heterogeneous surface [9]. The data obtained in this research are in accordance with the literature claims mentioned above. Namely, the waste after shot blasting is very heterogeneous due to its composition, so the description of adsorption by the Freundlich and Dubin-Radushevich models is appropriate. It can be seen from Figure 1 that the adsorption capacity is constantly increasing, which indicates that desorption does not occur. Adsorption in which desorption does not occur is the result of chemical binding in one layer of adsorbent and adsorbate, which is in accordance with Langmuir and Temkin theory.

4. CONCLUSION

Based on the conducted research, the following can be concluded:

- adsorption of Cu(II) ions on the waste after shot blasting is possible under the tested conditions,
- as the concentration of Cu(II) ions increases, the adsorption capacity increases, since more Cu(II) ions are available in the solution, but there are also a lot of free places on the surface of the adsorbent,
- all investigated isotherms models (Langmuir, Freundlich, Dubin-Radushevich, Eadie-Hoffstee and Temkin) can be used to describe the adsorption system waste after shot blasting/Cu(II) ions. However, the Langmuir model best describes the examined system,
- since the Langmuir model best describes the examined system, it can be concluded that adsorption takes place as chemisorption, in one layer on a heterogeneous surface.

5. REFERENCES

[1] …, Census of World Casting Production, Modern Casting 111(2021) 12, 26-28.
[2] D. S. Leidel, M. Novakowski, D. Pohlman, Z. D. MacRunnels, M. H. MacKay, External Beneficial Reuse of Spent Foundry Sand, AFS Transactions 102(1994), 235-243.

[3] D. Križaić, V. Pavlic, Mogućnosti primjene korištenog ljevačkog pijeska kao industrijski proizvedenog agregata u građevinarstvu, Znanstveno-stručni ljevački skup: nove tehnologije i materijali u ljevaonicama, Sisak, 2011.
[4] A. Štrkalj, Z. Glavaš, Lj. Slokar, Microstructural and equilibrium adsorption study of the system of waste foundry molding sand/Cu(II) ions, Archives of metallurgy and materials 61(2016) 4, 1805-1812.
[5] A. Štrkalj, Z. Glavaš, I. Brnardić, Application of Foundry Waste for Adsorption of Hexavalent Chromium, Chemical and Biochemical Engineering Quarterly 27(2013) 1, 15-19.
[6] Z. Glavaš, A. Štrkalj, Kinetika adsorpcijskog procesa za sustav otpadna kalupna mješavina /Cu(II) ioni, Hrvatske vode 93(2015) 23, 185-190.
[7] S. Bello, I. A. Belloand, K. A. Adegoke, Adsorption of Dyes Using Different Types of Sand: A Review, South African Journal of Chemistry 66(2013), 117–129.
[8] B. Gezer, Adsorption capacity for the removal of organic dye pollutants from wastewater using carob powder, International Journal of Agriculture, Forestry and Life Science 2(2018), 1-14.
[9] K. Y. Foo, B. H. Hameed, In sights into the modeling of adsorption isotherm systems, Chemical Engineering Journal 156(2010) 1, 2-10.
[10] W. M. Ibrahim, A. F. Hassan, Y. A. Azab, Biosorption of toxic heavy metals from aqueous solution by *Ulvalactuca* activated carbon, Egyptian Journal of Basic and Applied Sciences 3(2016) 3, 241-249.
[11] M. Švábová, Z. Weishauptová, O. Pribyl, The effect of moisture on the sorption process of CO_2 on coal, Fuel 92(2012) 1, 187-196.
[12] J. B. Fernandes, S. G. Tilve, Adsorption behavior of methylene blue on glycerol based carbon materials, Journal of Environmental Chemical Engineering 6(2018) 2, 1714-1725.
[13] I. Šošić, V. Serdar, Uvod u statistiku, Školska knjiga, Zagreb, 2002.

HYDROGENATION PROCESS OF TITANIUM ALLOY FOR BIOMEDICAL PURPOSES

Aida Imamović, Mirsada Oruč
University of Zenica, Faculty of Metallurgy and Technology
Zenica, B&H

Šaban Žuna
Center for advanced technologies in Sarajevo
Sarajevo, B&H

Esad Hadžibulić
University of Sarajevo, Faculty of Mechanical Engineering
Sarajevo, B&H

Keywords: hydrogenation, powder metallurgy, TiAl6Nb7 alloy, recycling

ABSTRACT
The production of titanium is very expensive, so it is interesting to research technologies that require lower costs, such as the HDH hydrogenation-dehydrogenation process technology, which is used for cheaper powder production from the waste material of titanium alloys.
This paper presents the hydrogenation procedure of a recycled piece of the Ti6Al7Nb titanium alloy. Hydrogenation was carried out in a furnace for heat treatment at about 700°C in a hydrogen atmosphere. After hydrogenation, samples of the Ti-Al-Nb type alloy were mechanically crushed by the grinding process to a granulation below 120 μm.

1. INTRODUCTION
Titanium alloys are considered advanced and high-value materials due to their special properties and high production cost.
Titanium alloys are often used in the aerospace, automotive, and medical industries, due to their high strength/weight ratio, corrosion resistance, biocompatibility, and low thermal expansion characteristics. These alloys have a high strength/density ratio, and good mechanical properties at elevated temperatures up to 550 °C.
In addition to structural efficiency, Ti alloys are characterized by high corrosion resistance and do not cause chemical or immunological reactions in the human body. That is why they are successfully used for making implants and joint prostheses, but also for other purposes in surgery, dentistry, and other fields of medicine [1].
The disadvantage of using titanium alloys is the extremely high cost of raw materials, as well as the difficulties in machining this material into the final geometry. Thanks to techniques of "eliminating" machining, such as powder metallurgy, the loss of this relatively expensive material is reduced, and it is possible to obtain products with complicated shapes.

In this meaning, the HDH - hydrogenation-dehydrogenation process technology for obtaining titanium powder, which belongs to the range of recycling technologies, is of particular interest.

2. HDH TECHNOLOGY

The production of titanium powder is very expensive, so it is of interest to research technologies that require lower costs, such as recycling technologies. One such technology is the HDH process, which is used to produce powders from titanium alloy waste material that is not usable any more for medical purposes.

The HDH technology is based on hydrogenation and dehydrogenation processes based on a reversible reaction:

$$M + H_2 \leftrightarrow MH_2$$

The course of this reaction depends on the pressure of hydrogen gas. If the pressure is above the equilibrium pressure, hydrogen atoms enter the titanium materials and form a metallic hydrate, and if it is below this level, hydrogen atoms diffuse from the metal into the gas atmosphere [1,2].

Enrichment of materials based on titanium alloy with hydrogen by the hydrogenation process leads to an increase in the brittleness of the material, which can later be broken, that is, crushed to powder granulation under certain mechanical loads (usually with balls). The subsequent dehydrogenation process of the resulting powder aims to improve its properties, especially ductility.

The hydrogenation process is carried out by exposing titanium alloy waste to hydrogen gas at an elevated temperature. Hydrogenation is usually carried out in a furnace capable of operating with a protective atmosphere containing H_2. Titanium alloys can be hydrated at atmospheric pressure and temperatures lower than 800 ºC, forming titanium hydrides.

Titanium alloy waste is subjected to the hydrogenation process in a controlled hydrogen atmosphere in a chamber/furnace at a temperature between 550 ºC and 800 ºC from one to ten hours or longer, depending on the size of the pieces and the properties of the waste [1]. Operating conditions in the furnace should be adjusted to result in a hydrogen content in the waste between 1% and 2%. A higher hydrogen content than the above can be unfavorable. Also, the lower hydrogen content will not produce sufficient brittleness of the waste to enable easy and economical method by conventional milling processes. An example of an experiment for the production of powder by the HDH process is given in Figure 1.

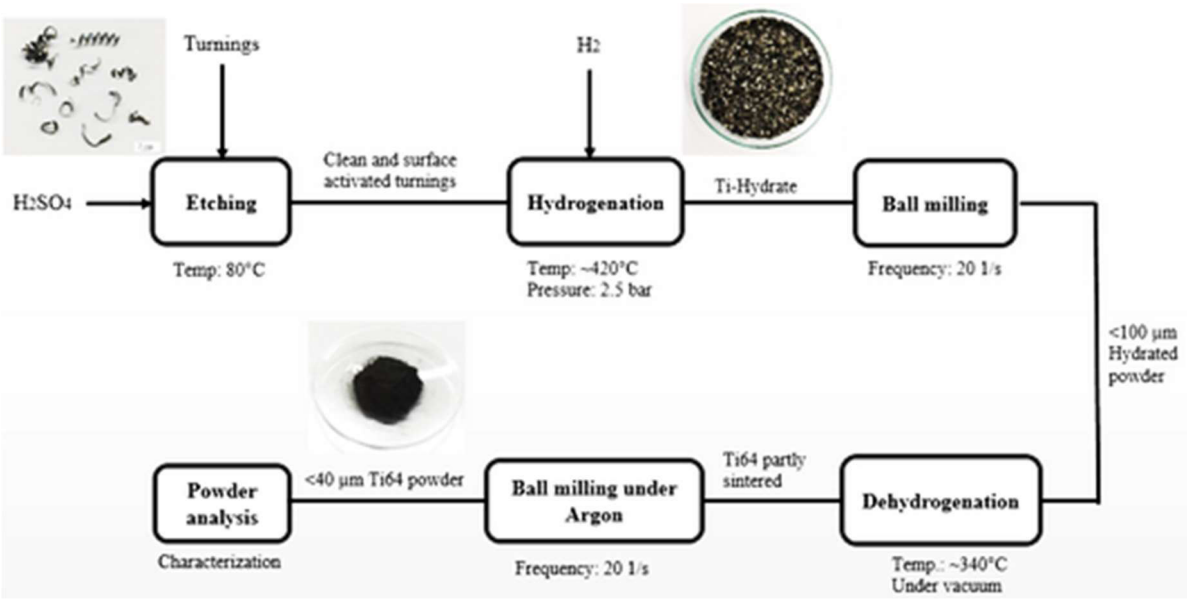

Figure 1. Example of an experiment for the production of titanium powder by the HDH process [2]

In the hydrogenation process, titanium alloy powder with unchanged chemical composition, with irregular particle shape, is obtained, Figure 2.

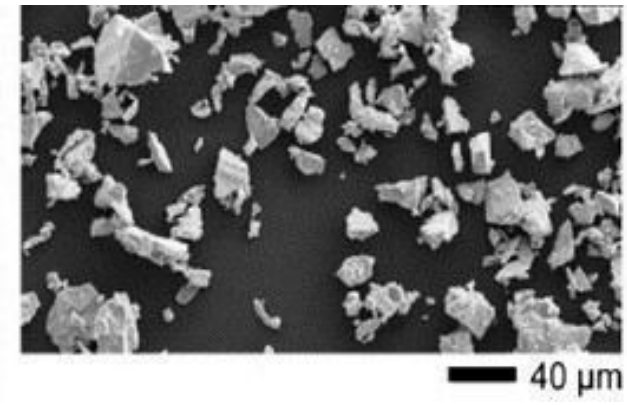

Figure 2.Titanium powder with irregular particle shape after the HDH process [2]

3. EXSPERIMENTAL PART

3.1. Titanium alloy type TiAl6Nb7

The Ti6Al7Nb type titanium alloy has the best corrosion resistance of all Ti-alloys. The alloying elements Al and Nb make the alloy more stable. This alloy in the presence of oxygen spontaneously forms a passive oxide film <1-2 nm thick of titanium oxide or mixed oxide TiO_2 (with Ti, Al, and Nb metal components). This protective layer is completely biocompatible and does not cause allergic reactions within the body or in contact with it.
The subject of the research is a titanium alloy of the designation EN, TiAl6Nb7/ASTM, F 1295, which was developed for medical use when the cytotoxic vanadium was replaced by niobium. This alloy has high strength, corrosion resistance, and exceptional biocompatibility. It does not cause chemical or immunological reactions in the human body

and is widely used in medicine for the production of implants, prostheses, and their parts, Figure 3.
A recycled piece of titanium alloy - screw-type consumable raw material, Figure 4, was hydrogenated in a specially modified heat treatment furnace with a protective atmosphere at the "Center for Advanced Materials" in Sarajevo.

Figure 3. Schematic representation of the application of titanium alloys for medical purposes [7]

Figure 4. Recycled piece of titanium alloy for hydrogenation [7]

3.2.Chemical and mechanical properties of the alloy TiAl6Nb7

The chemical composition of the TiAl6Nb7 alloy is presented in Table 1.

Table 1. Chemical composition of TiAl6Nb7 alloy, in mass. %

C	Al	Nb	Fe	Ta	O	N	H	Ti
max.0,08	5,5-6,5	6,6-7,5	maks. 0,25	maks. 0,50	maks. 0,05	maks. 0,009	maks. 0,5	ostalo

The mechanical properties of the TiAl6Nb7 alloy are presented in Table 2.

Table 2. Mechanical properties of TiAl6Nb7 alloy

Parameter	Tensile strength	Yield stress	Elongation
Value	≥ 900 MPa	≥ 795 MPa	≥ 10%

4. RESULTS OF THE HYDROGENATION PROCESS

Hydrogenation, that is, temporary alloying with hydrogen, was carried out at a temperature of about 700 °C in an electric resistance furnace. The sample was treated in an atmosphere of nitrogen and hydrogen. Figure 5 shows a heat treatment furnace with a protective atmosphere that was used to simulate the hydrogenation process at the "Center for Advanced Technologies" in Sarajevo.
After hydrogenation, samples of the TiAl6Nb7 type alloy were mechanically crushed by the milling process, Figure 6, to a granulation below 125 μm, that is, with a greater proportion of granulation below 60 μm, Figure 7.
In this process, the titanium alloy powder is obtained, with an irregular shape of particles, but extremely favorable granulations, with a significant share of

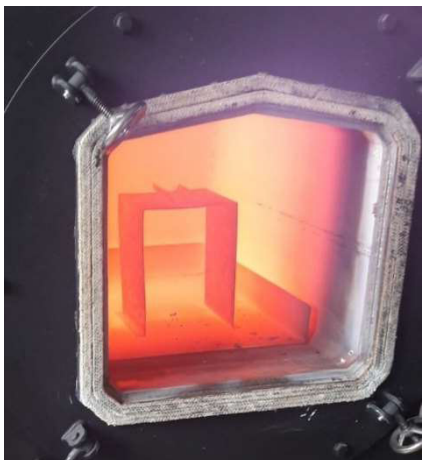

Figure 5. Hydrogenation process in a heat treatment furnace with a protective atmosphere [8]

Figure 6.Milling of hydrated TiAl6Nb7 titanium alloy

Figure 7. Titanium powder after hydrogenation and milling of TiAl6Nb7 titanium alloy

particle sizes below 60 µm, which means that a "low-cost" high-value powder based on titanium alloy can be obtained.

The hydrogenation process carried out was successful because the hydrated sample could relatively easily be mechanically crushed to the powder. and to use in the dehydrogenation process and obtain titanium powder with a satisfactory chemical composition.

.

5. CONCLUSION

- The process of hydrogenation of TiAl6Nb7 type titanium alloy formed intermetallic compounds of metal and hydrogen, so-called hydrides by absorbing a considerable amount of hydrogen. The formed compounds led to the brittleness of this alloy, as it was required.
- In this experiment, the necessary parameters for the hydrogenation process were established according to the size of the recycled product, related to thermal treatment.
- The developed hydrogenation process was successful and the result was a hydrated sample that could be crushed mechanically.
- Favorable particle sizes, mostly below 60 µm, were achieved by milling the hydrated sample.
- The results obtained in this research indicate the possibility of developing the HDH procedure as an economic procedure for the production of "low-cost" high-value powder based on titanium alloy.

6. REFERENCES

[1] Mohammadali Kadivar: Micro-grinding of titanium, Chalmers University of Technology, Gothenburg, Sweden 2018

[2] Zhigang Zak Fang, James D. Paramore, Pei Sun, K. S. Ravi Chandran, Ying Zhang, Yang Xia, Fei Cao, Mark Koopman, Michael Free: Powder metallurgy of titanium – past, present, and future, International Materials Reviews, Vol. 63, No. 7, 407–459, 2018

[3] Jonathan Phillips, Anthony Janssen, Troy Y. Ansell, Claudia C. Luhrs: Creating Strong Titanium/Titanium Hydride Brown Bodies at Ambient Pressure and Moderate Temperatures, Materials (Basel). 2020 Nov; 13(21): 5008

[4] Robert L. Powell, Luh C. Tao: Reclaiming Scrap Titanium, Official Gazette of the United States Patent Office, Volume 768, By United States. Patent Office 1961

[5] Mertol Gökelma, Dilara Celik, Onur Tazegul, Huseyin Cimenoglu, Bernd Friedrich: Characteristics of Ti6Al4V Powders Recycled from Turnings via the HDH Technique, Metals 2018, 8(5), 336; https://doi.org/10.3390/met8050336
[6] An Overview of Highly Porous Titanium Processed via Metal Injection Molding in Combination with the Space Holder Method Metals 2022, 12(5), 783; https://doi.org/10.3390/met12050783
[7] http://www.instrumentaria.hr/kategorija-proizvoda/osteosinteza/,
[8] Šaban Žuna: Osvajanje tehnologije dobijanja praha legura titana za medicinske i druge svrhe, Javna ustanova "Centar za napredne tehnologije u Sarajevu", 2022.

EFFECT OF PARTICLE SHAPE AND SIZE OF COPPER POWDERS ON THE PROPERTIES OF SINTERED PARTS

Ivana Marković, Dragan Manasijević, Ljubiša Balanović, Uroš Stamenković, Milijana Mitrović
University of Belgrade, Technical Faculty in Bor
Bor, Serbia

Stevan Trujić
HBIS Group Serbia Iron & Steel
Smederevo, Serbia

Keywords: electrolytic powders, water-atomized powders, sintering

ABSTRACT
The particle shape and size of the starting powders represent the most important physical properties, on which the quality of the compacts and final sintered products depends. Two types of powder were analyzed in the paper - electrolytic copper powder with a dendritic particle shape and water-atomized copper powder with an irregular particle shape. The starting powders were sieved through a sieve system with openings of 45 μm, 80 μm, and 120 μm. The characterization of the obtained fractions of both powders was performed by determining the shape and dimensions of the particles using SEM microscopy in combination with ImageJ software, and the apparent density and flow rate were determined using the Hall flowmeter funnel. Pressing of each powder fraction was done using a pressure of 600 MPa. The compacts were further sintered at 1000°C for 2 hours to obtain the final sintered parts. After sintering, their density, hardness, and electrical conductivity were determined and their microstructure was analyzed. The results indicate a great influence of the characteristics of the starting powders on the properties of the final parts obtained by the powder metallurgy route. The particle shape of the powders had a more pronounced influence compared to the particle size.

1. INTRODUCTION

The powder metallurgy (PM) route includes obtaining the final products through compact the starting powders and sintering them under controlled conditions. The main disadvantage of the classical PM process is the impossibility of achieving a full density of final products, due to their porosity, and that is why the mechanical properties of sintered parts are lower [1,2]. Properties of sintered parts depend on the parameters such as characteristics of the starting powders, compaction pressure, sintering temperature and time, etc. If the compaction pressure, sintering temperature, and time are higher, the density is superior, and the porosity is lower. Mechanical and electrical properties are also dependent on the density and porosity, therefore, they increase with an increase in compaction pressure, sintering temperature, and time, but all this increases the process cost [3].

In addition to the process parameters, the particle shape and size have a great influence on all operations during obtaining parts using the PM route and on the quality of the final sintered products. The particle shape has a large effect on the contacts between particles and therefore has a significant influence on their behavior during pressing and sintering. Generally, the compacts obtained from coarse powder particles have a higher density compared with the compacts from fine powders [4].

To obtain the required properties in the final sintered parts, a suitable combination of process parameters is required [5,6]. This paper presents the effects of particle shape and size of the starting copper powders, on the properties of powders, green compacts, and sintered samples. In the case of powders, the evaluated properties were apparent density and flow rate. In green compacts, density was evaluated, and in sintered samples hardness, electrical conductivity, and microstructure of PM parts were discussed. To obtain samples with different average particle sizes, water-atomized and electrolytic copper powders were sieved and separated with sieves with openings of 45 μm, 80 μm, and 120 μm.

2. EXPERIMENTAL PART

Water-atomized copper powder (supplied by Centrochem) with an irregular particle shape and electrolytic copper powder (supplied by Pometon) with a dendritic particle shape were used as starting materials. Commercial powders were sieved to obtain fractions with a narrow powder particle size distribution (in the range of about 40 μm). The powders were sieved on sieves with openings of 45 μm, 80 μm, and 120 μm. In this way, three fractions were obtained: - 45 μm, + 45 μm - 80 μm, and + 80 μm - 120 μm. The powder's designations are given in Table 1. The first letter in the designations indicates whether the powder was obtained by water-atomization (A) or by electrolytic method (E). Other letters indicate the range of particle sizes in that powder: very fine (VF) with particles below 45 μm, fine (F) with particles from 45 μm to 80 μm, and medium (M) with particles from 80 μm to 120 μm. This classification is based on the paper [7].

Table 1. The powder's/sample's designation

Fractions	Atomized powders	Electrolytic powders
- 45	A-VF (Atomized - Very Fine)	E-VF (Electrolytic - Very Fine)
+ 45-80	A-F (Atomized - Fine)	E-F (Electrolytic - Fine)
+ 80-120	A-M (Atomized - Medium)	E-M (Electrolytic - Medium)

The characterization of the powders included the determination of the shape and morphology of the particles, particle size distribution of powders, the apparent density, and the flow rate of the powders. The shape and morphology of the particles were determined using SEM "Tescan VEGA 3LMU" microscope. The average particle size and particle size distribution of each powder were obtained based on SEM microphotographs, using the image analysis software ImageJ. The particle size was measured along the longest axis. The apparent density and the flow rate of the powders were examined using the Hall flowmeter funnel. The apparent density was done according to the ISO 3923 standard, and the flow rate was according to the ISO 4490 standard [8,9].

The powders were further compacted on a hydraulic press "Mohr & Federhaff & Losenhausen" with a pressure of 600 MPa. The compacts were sintered in a furnace "Elektron ELP-08" in an atmosphere of argon at a temperature of 1000 °C for 2 h, to obtain sintered parts. Density, hardness, and electrical conductivity were measured and the microstructure was analyzed using optical microscopy. The hardness was measured using "VEB Leipzig" Vickers hardness tester with a load of 10 kg. The device "Institute dr. Forster Sigmatest 2.063" was used for measuring electrical conductivity. The optical microscope used to observe the microstructures was "Carl Zeiss Jena Epytip 2".

3. RESULTS AND DISCUSSION

3.1 Characterization of powders

Figure 1 presents SEM microphotographs of copper powders with different sizes and shapes depending on the obtaining method. The water-atomized powders (Figs. 1a-c) appear in an irregular shape while the electrolytic powders show a typical dendritic shape (Figs. 1d-f).

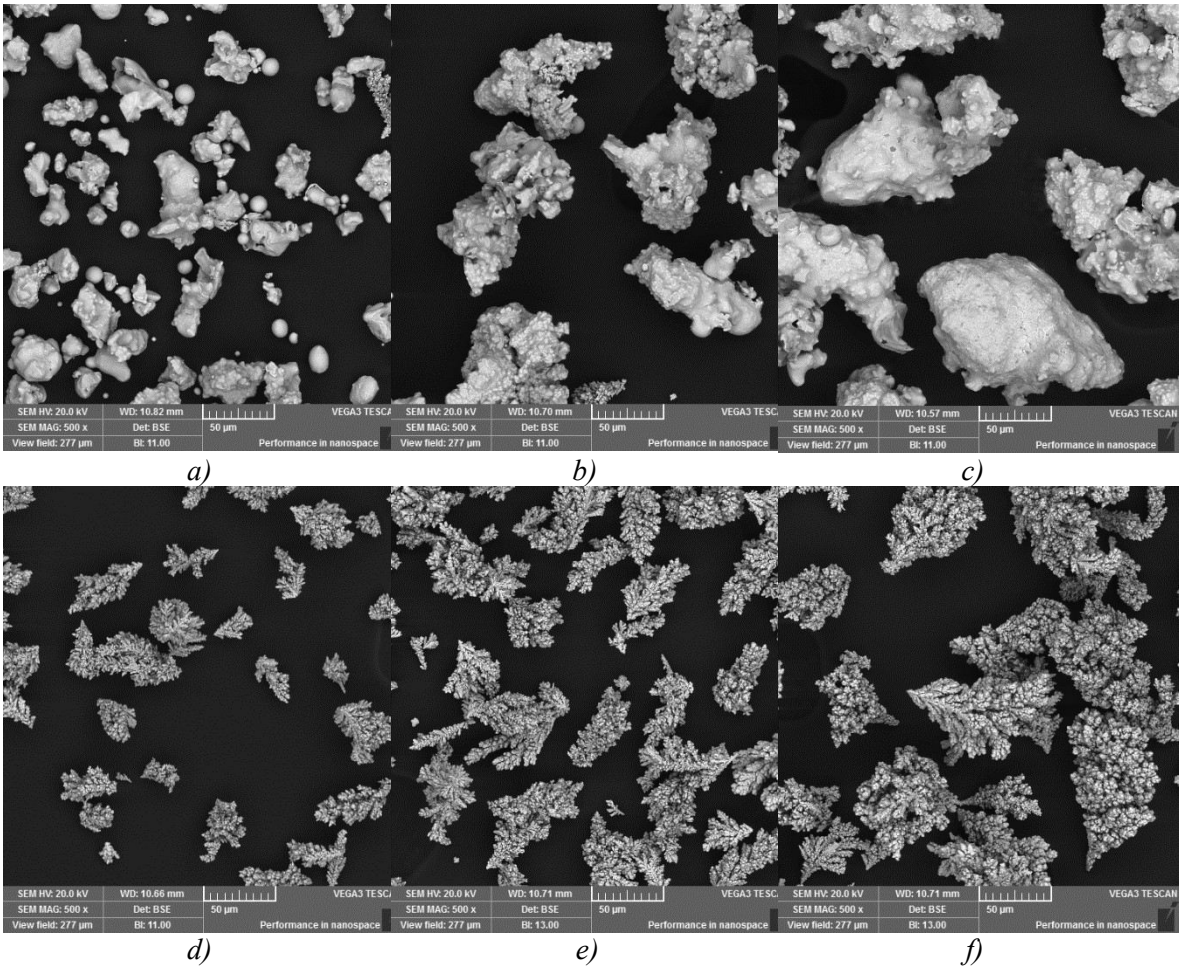

Figure 1. SEM microphotographs of copper powders (a) A-VF; (b) A-F; (c) A-M; (d) E-VF; (e) E-F; (f) E-M

Figure 2 shows the average particle size and particle size distribution of atomized copper powders A-VF, A-F, and A-M. The A-VF powder has the finest average particle size as compared to others, which is 25.2 µm. Powder A-F is coarser, with an average particle size of 64.7 µm. The powder A-M is the coarsest with an average particle size of 125.7 µm.

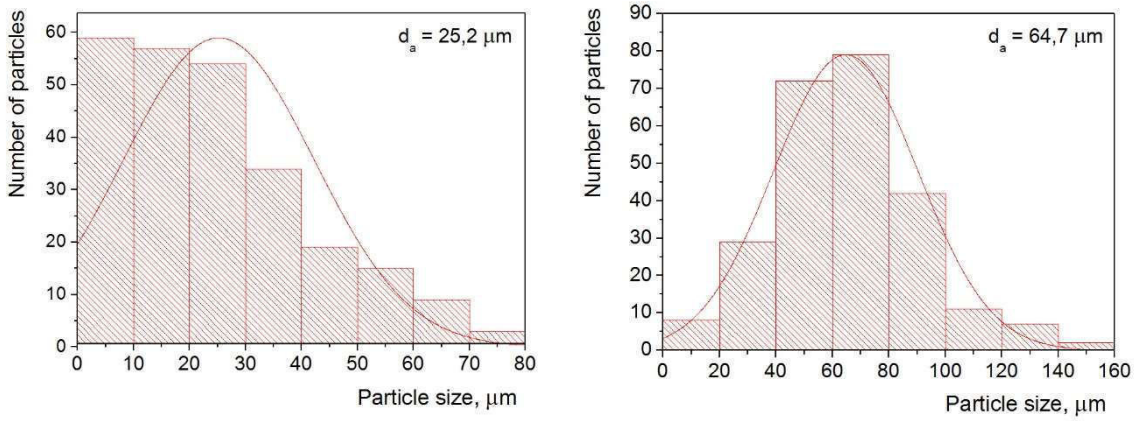

a) *b)*

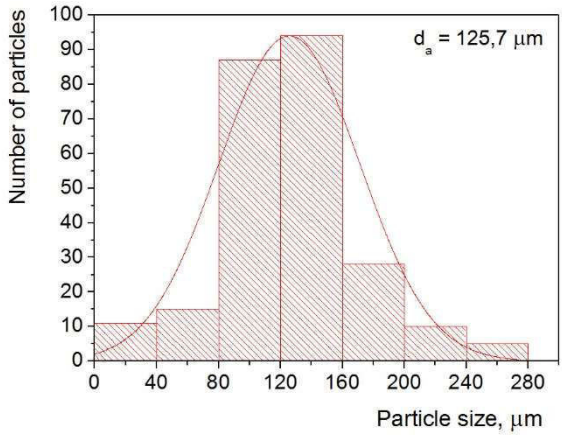

c)

Figure 2. The average particle size (d_a) and particle size distribution of atomized copper powders (a) A-VF; (b) A-F; (c) A-M

Figure 3 shows the average particle size and particle size distribution of electrolytic copper powders E-VF, E-F, and E-M. The E-VF powder has the finest average particle size, which is 36.4 μm. Powder E-F is coarser, with an average particle size of 51.7 μm. The coarsest electrolytic copper is E-M powder with an average particle size of 84.2 μm.
Comparing the same fractions of atomized and electrolytic powder, it can be noticed that VF atomized powder is finer than electrolytic one, while F and M atomized powders are coarser than F and M electrolytic copper powders, respectively.
Figure 4 shows the apparent density and the flow rate of loose powders. The apparent density of the metal powder is influenced by the theoretical density of the metal, the granulometric composition of the powder, particle shape, surface and roughness of the individual particles, particle packing, oxidation degree, and porosity. Generally, the apparent density increases with an increase in particle size (this behavior was not shown in this paper, but vice versa), if the particle shape becomes less spherical and more irregular and with an increase in surface roughness [10].

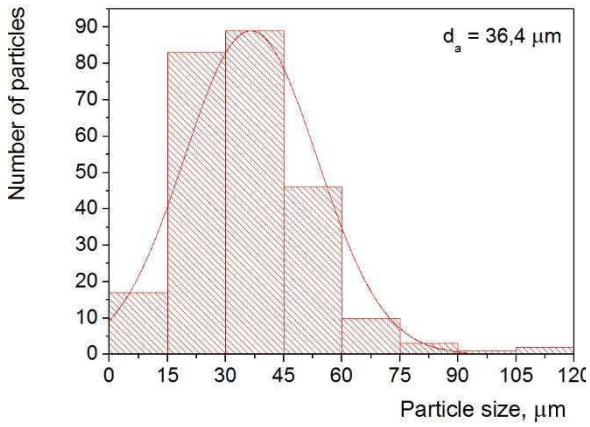

a)

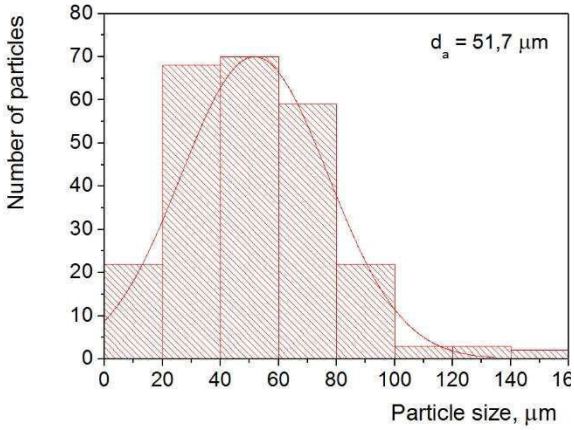

b)

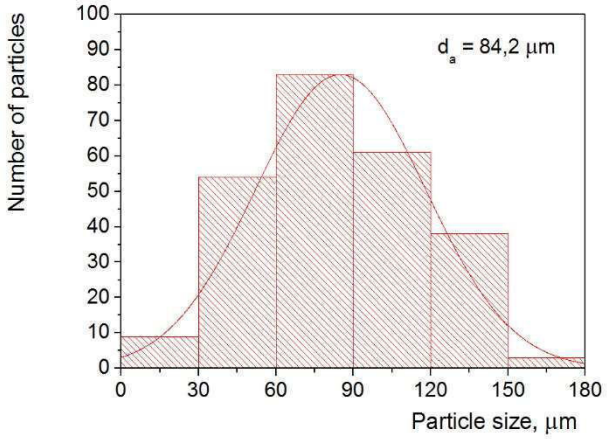

c)

Figure 3. The average particle size (d_a) and particle size distribution of electrolytic copper powders (a) E-VF; (b) E-F; (c) E-M

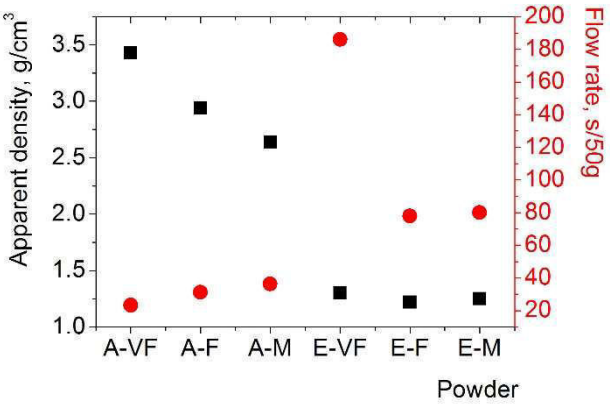

Figure 4. The apparent density and the flow rate of loose powders

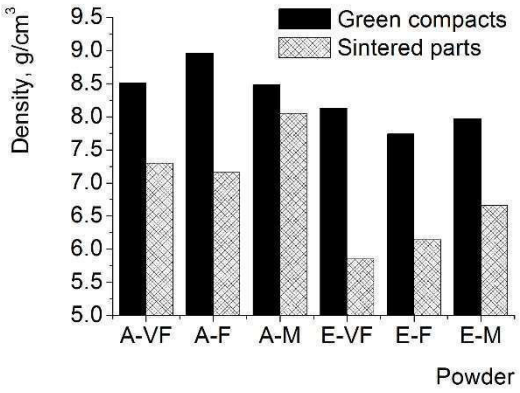

Figure 5. The densities of green compacts and sintered parts

It is generally observed that atomized copper powders have higher apparent densities and flow rates compared to electrolytic powders. This is related to the shape of the particles. In the case of dendritic electrolytic copper powder, the presence of bulges and dents in the particle surface, as well as the increase in the specific surface area of the particles increase the friction between particles, this makes it difficult to move the particles relative to each other and causes poor packing of the dendrite particles. Because of that, atomized powders have a higher apparent density and flow rate than dendritic powders [11,12].
The highest apparent density and flow rate are observed for A-VF powder (3.43 g/cm^3 and 23.32 s/50g, respectively). The lowest apparent density was achieved in E-F powder (only 1.22 g/cm^3), while E-VF powder showed the lowest flow rate (186 s/50g).

3.2 Characterization of sintered parts

Figure 5 shows the results of measuring the densities of green compacts and sintered parts from different types of powders. It can be concluded that the density of sintered parts decreased compared to the density of green compacts. This is unusual behavior. The expansion of the parts most likely occurred due to the reaction of residual gases in compacts with the atmosphere in the sintering furnace, i.e. with residual oxygen inside the furnace.

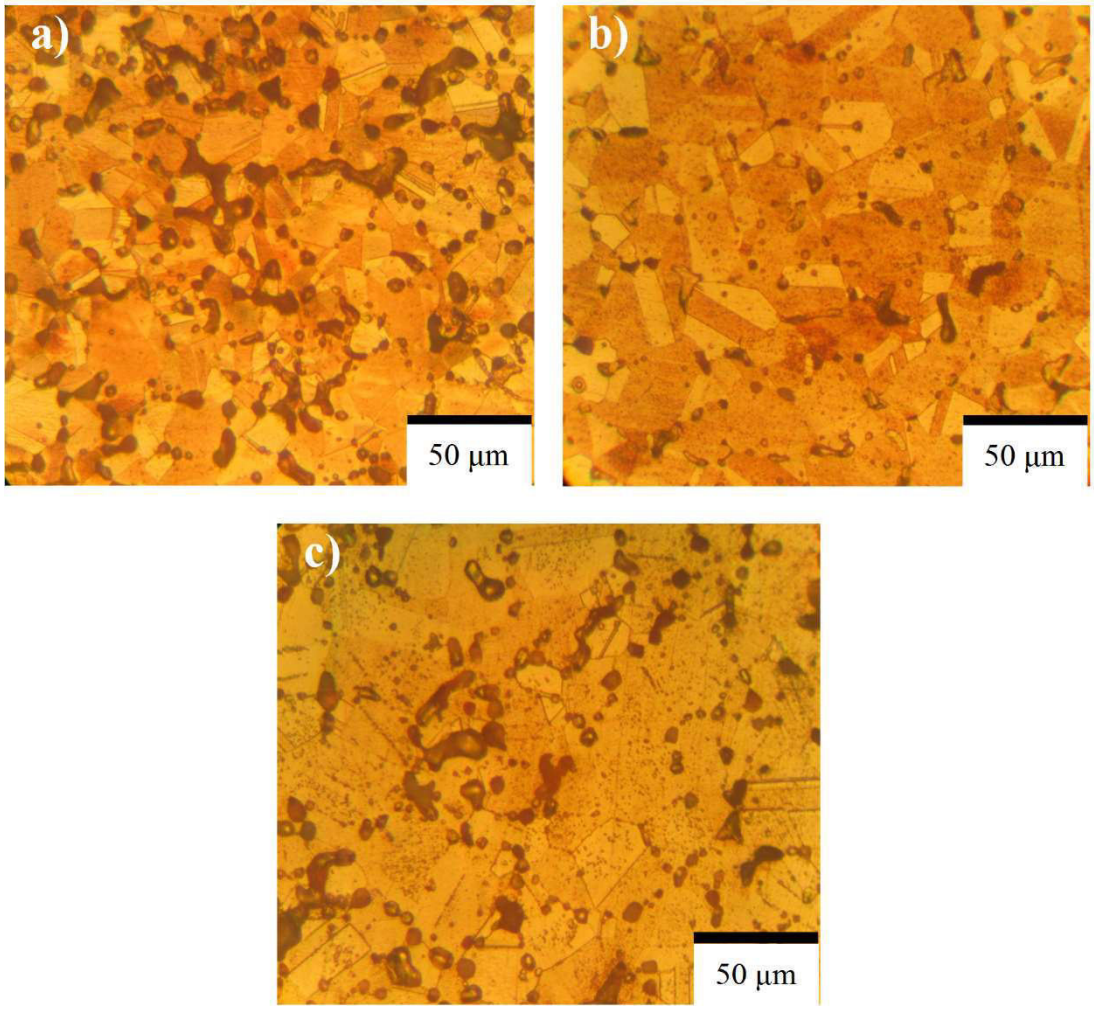

Figure 6. Optical micrographs of sintered copper obtained from atomized powder (a) A-VF; (b) A-F; (c) A-M

Sintered parts obtained from atomized copper powders have significantly higher density values compared to parts obtained from electrolytic copper powders. In the case of parts obtained from electrolytic copper powder, a clear tendency is observed that the density of the parts increases with an increase in the particle size of the starting powder. The same results were obtained by Chang and Wu [4]. This tendency is not expressed in parts obtained from atomized copper powder.

Figure 6 shows the microstructures of sintered parts obtained from atomized powders with different particle sizes. Polygonal grains with annealing twins are observed. The tendency of grains and microstructure consolidation is observed with an increase in the particle size of the starting powder from which the parts were obtained. Spherical pores are present at the grain boundaries and within the crystal grains themselves. The porosity is indicated, especially for the samples obtained from powders A-VF and A-M.

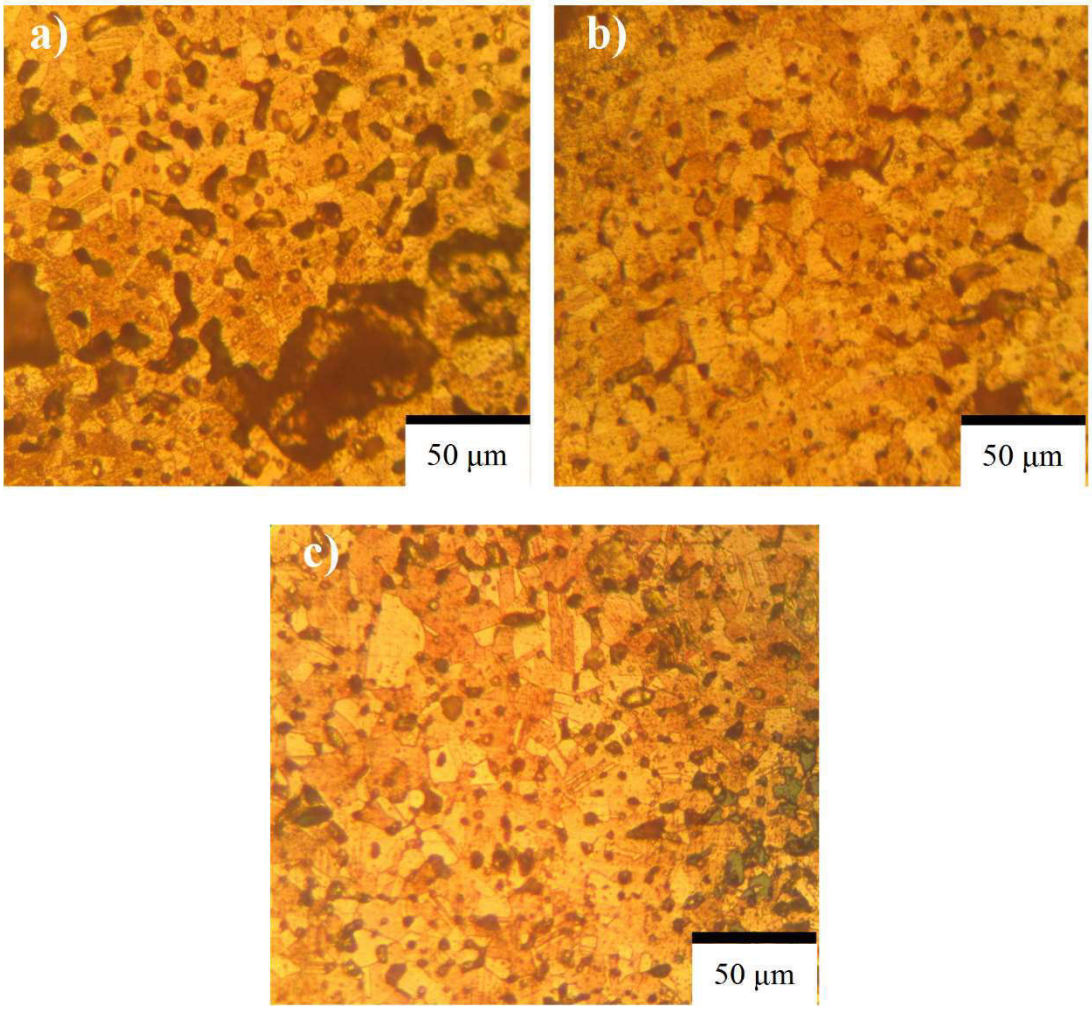

Figure 7. Optical micrographs of sintered copper obtained from electrolytic powder (a) A-VF; (b) A-F; (c) A-M

Figure 7 presents the microstructures of sintered samples obtained from electrolytic powders with different particle sizes. For the same starting powders (the same fractions), a finer-grained microstructure was observed in parts obtained from electrolytic powders compared to parts obtained from atomized powders. The microstructure is dominated by pores, which are large and different in shape. All sintered parts are more porous compared to samples obtained from atomized copper powders. The porosity is the most pronounced for the sample obtained from the electrolytic E-VF powder with the finest particle size, which was also confirmed by the results of the density measurement.

Figure 8 shows the hardness and electrical conductivity of sintered parts obtained from powders of different sizes and shapes. Sintered parts obtained from atomized powders have higher hardness and electrical conductivity values compared to parts obtained from electrolytic copper powders. This is understandable, considering the higher density values of the parts obtained from atomized copper. The sample from A-M powder has the highest hardness value, which is 34.57 HV10. The sample from A-F powder has the highest electrical conductivity, which is 38.15 MS/m. The lowest values of hardness and electrical conductivity were obtained for the parts obtained from the electrolytic copper powder E-VF with the finest particles, which also showed the lowest density value.

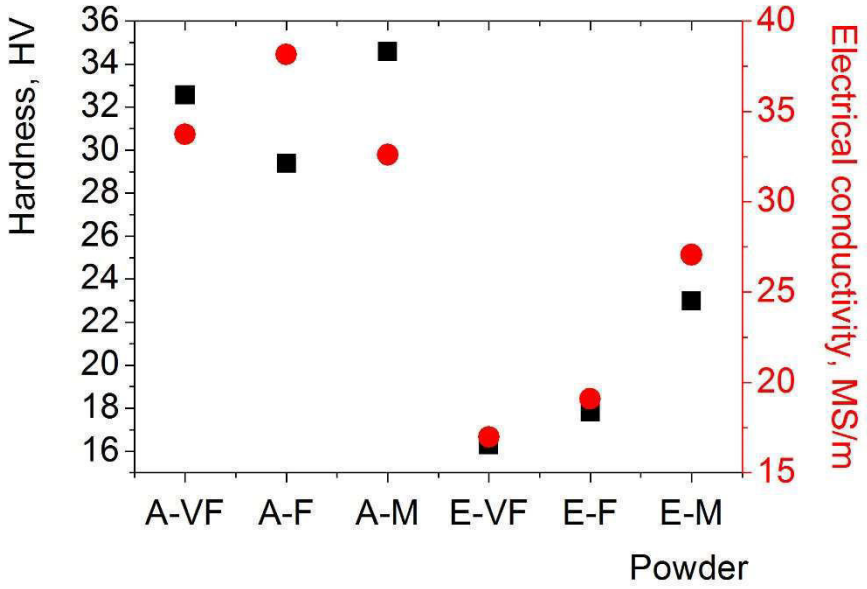

Figure 8. Hardness and electrical conductivity values of the sintered parts

4. CONCLUSIONS

The influence of the copper particle shape and size on some properties of powders, compacts, and PM parts was analyzed. The following conclusions can be drawn:

- Atomized powders showed higher values of apparent density and flow rate compared to electrolytic powders. Increasing the particle size of atomized powder showed a decrease in apparent density and flow rate (atypical behavior). However, increasing the particle size of electrolytic powder showed an increase in flow rate (typical behavior).
- The density of the sintered parts decreased compared to the density of the compacts. Sintered parts obtained from atomized powders have significantly higher density values compared to parts obtained from electrolytic powders.
- The finer microstructure was achieved in sintered parts obtained from electrolytic powders but with much more pronounced pores compared to the parts obtained from atomized powders.
- Sintered parts obtained from atomized powders have higher hardness and electrical conductivity values compared to parts obtained from electrolytic powders.

5. ACKNOWLEDGEMENT

The research presented in this paper was done with the financial support of the Ministry of Science, Technological Development and Innovations of the Republic of Serbia, with the funding of the scientific research work at the University of Belgrade, Technical Faculty in Bor, according to the contract with registration number 451-03-47/2023-01/200131.

6. REFERENCES

[1] Neikov O.D., Naboychenko S.S.: Handbook of Non-Ferrous Metal Powders: Technologies and Applications, Elsevier, Amsterdam, 2009

[2] Delavari M., Salarvand A., Rahi A., Shahri F.: The Effect of Powder Metallurgy Process Parameters on Mechanical Properties of Micro and Nano-Iron Powder, International Journal of Engineering, Science and Technology, 3(9) (2011) 86-94

[3] Kumar N., Bharti A., Dixit M., Nigam A.: Effect of Powder Metallurgy Process and its Parameters on the Mechanical and Electrical Properties of Copper-Based Materials: Literature Review, Powder Metallurgy and Metal Ceramics, 59(2020) 401-410

[4] Chang C.C., Wu M.R.: Effects of Particle Shape and Temperature on Compaction of Copper Powder at Micro Scale, MATEC Web of Conferences, 123 (2017) 00011
[5] Edosa O.O., Tekweme F.K., Gupta K.: A Review on the Influence of Process Parameters on Powder Metallurgy Parts, Engineering and Applied Science Research, 49(3) (2022) 433-443
[6] Sanchez F., Bolarin A.M., Molera P., Mendoza J.E., Ocampo M.: Relationship Between Particle Size and Manufacturing Processing and Sintered Characteristics of Iron Powders, Revista Latinoamericana de Metalurgia y Materiales, 23 (1) (2003) 6
[7] Vlachos N., Chang I.T.H.: Investigation of Flow Properties of Metal Powders from Narrow Particle Size Distribution to Polydisperse Mixtures Through an Improved Hall-Flowmeter, Powder Technology, 205 (2011) 71-80.,
[8] Standard ISO 3923-1:2008, Metallic Powders - Determination of Apparent Density - Part 1: Funnel Method, 2008
[9] Standard ISO 4490:2018, Metallic Powders - Determination of Flow Rate by Means of a Calibrated Funnel (Hall Flowmeter), 2018
[10] Yadroitsev I.: Selective Laser Melting: Direct Manufacturing of 3D-Objects by Selective Laser Melting of Metal Powders, Central University of Technology, 2009
[11] Thummler F., Oberacker R.: An Introduction to Powder Metallurgy, The Institute of Materials, London, 1993
[12] Uslan I., Usta Y., Saritas S.: The Effects of Powder Morphology on the Apparent Density and the Flow Rate of Metal Powders, Powder Metallurgy World Congress, 2006, PD01-W-03

THERMAL AND MICROSTRUCTURAL ANALYSIS OF THE LOW-MELTING Bi–In–Sn TERNARY ALLOYS

Ljubiša Balanović, Dragan Manasijević, Ivana Marković, Milan Gorgievski, Uroš Stamenković,
University of Belgrade, Technical Faculty in Bor
Bor, Serbia

Dajana Milkić
Measuring Transformers Factory Zaječar (FMT Zaječar)
Zaječar, Serbia

Keywords: Bi-In-Sn alloys, differential thermal analysis (DTA), microstructure, SEM-EDS

ABSTRACT
Low-melting alloys, based on bismuth, indium, and tin, have found commercial use in soldering, safety devices, coatings, and bonding applications, due to their low melting point temperature of eutectic compositions and small differences between their liquidus and solidus temperatures. Based on this, the accurate knowledge of their thermal properties such as melting and solidification temperatures, latent heat of melting, supercooling tendency, etc. is of immense importance. In the present research, low-melting alloy from three cross-sections Bi-Sn50In50, Sn-In50Bi50, and In-Bi50Sn50 (wt.%) was investigated using differential thermal analysis (DTA), and by scanning electron microscopy (SEM) with energy dispersive spectrometry (EDS). Temperatures of phase transformations, determined by DTA, and phase compositions of co-existing phases, determined by EDS analysis, were found to support the corresponding calculated phase compositions quite well. The experimentally obtained results were compared with the results of thermodynamic calculation according to the CALPHAD approach, and a close agreement was noticed.

1. INTRODUCTION

Solders known as fusible metal or material become an important element since it will ensure the continuity of the production of electrical and mechanical in the electronic packaging [1]. As is known to all, Tin-Lead (Sn-Pb) solders have been used for many years due to their good chemical, physical, thermal, and mechanical properties as traditional solders in the field of electronic packaging [2]. However, concerning the toxicity of Pb to human health and the environment, many countries have limited or banned the production and application of Sn-Pb solders in many fields by means of legislation [3,4]. For example, the implementation of WEEE directives [5] and RoHS [6-8] regulations in the national legislation of the European Union, the USA, and Japan lasted until January 2, 2013. Since consumer needs for electronic devices are increasing every day, the need for new lead-free alloys that are suitable for soldering is also increasing [9]. The Sn-Bi base lead-free solders are proposed as one of the most popular alloys due to the low melting temperature (eutectic point: 139^{O}C) and low cost. However, they are not widely used because of the lower wettability, fatigue resistance, and elongation compared to traditional Sn-Pb solders. So alloying is considered an effective way to improve the properties of Sn-Bi solders with the addition of elements Al, Cu, Zn, Ga, Ag, Sb, as well as indium [10]. The alloy from Bi-In-Sn system was investigated by

Noor et al. [9], as a potential candidate to replace Tin-Lead (Sn-Pb) solders. That alloy gives a low melting temperature in the range of 65-100 ℃, which is directly contributed by the addition of In. The lowest melting temperature ensures that the solder melts and forms a joint with the substrates, after which it solidifies again in the shortest period. The melting temperature of the alloy from the Bi-In-Sn system is about 60℃ because In and Bi have the ability to effectively reduce the melting temperature of the solder. Based on this study, it was concluded that according to the microstructure analysis, the presence of the intermetallic compound BiIn can be observed for the solder with the Bi-In-Sn system. Recently, Zhou et al [11] investigated the microstructure, phase morphology, temperature, and heat of the fusion of several alloys from the Bi-In-Sn system. The examination was carried out by scanning electron microscopy (SEM) with energy dispersive spectrometry (EDS), X-ray diffraction (XRD), differential scanning calorimetry (DSC), and a density analysis instrument. Based on the obtained results, it was concluded that the alloys have an extremely low melting point as well as a high density [11]. Yang et al. [12] performed a thermodynamic calculation using the CALPHAD method, as well as corresponding experiments to design low-temperature Bi-In-Sn solders. They concluded that when it comes to the mechanical characteristics of the solder, during air cooling, a large relaxation limit of the solder, high tensile strength, and much better elongation are obtained than the conventional solder. The Bi-Sn system has a low melting point. In order to improve the mechanical characteristics of the Bi-Sn solder, In was added and they obtained a better elongation of the solder, thus maintaining a low melting temperature. Shalaby et al. [13] found that the addition of In elements had a critical effect on the onset point of the Sn-58Bi solder which meant that adding 2 wt.% In could decrease the onset point of the solder from 139.06°C to 129.68°C and increase the tensile and shear strength. Chen et al. [14] studied the effects of In addition on the melting temperature and tensile properties of Sn-Bi solder. When the content of In addition was 5 wt.%, the onset point was decreased by about 20°C, and tensile properties were poor decreasing from 71.8 MPa to 68.3 MPa when the content of the, In addition, was at 3 wt.%. With increasing In content, the peak temperature of the composite solder was reduced by 10°C. The most important thermodynamic optimization of the Bi-In-Sn system, which is based on new experimental data, was carried out by Witusiewicz et al. [15]. A new thermodynamic description is presented for the ternary Bi-In-Sn system in the entire range of compositions. The parameters for the thermodynamic models of the constituent binary systems Bi-In, Bi-Sn, and In-Sn were adopted from earlier research, and those for the system Bi-In-Sn were optimized using experimental data on phase equilibria as well as data on melting enthalpy of different alloys available in the literature. In the present research, low-melting alloy from three cross-sections Bi-Sn50In50, Sn-In50Bi50, and In-Bi50Sn50 was investigated using differential thermal analysis (DTA), and by scanning electron microscopy (SEM) with energy dispersive spectrometry (EDS). Although there are numerous studies of the thermal and structural characteristics, the Bi-In-Sn ternary system is still in the research phase.

2. EXPERIMENTAL PROCEDURE

Sample preparation in the present study consisted in melting the raw metals Bi, In, and Sn with a purity of 99.999 mass%, in an induction furnace under a protective argon atmosphere. The melting procedure involved heating the samples together with the furnace for about 90 min, to the temperature of 100 °C above the liquidus line, keeping them at that temperature for 60 minutes to ensure the homogenization of the molten alloy, and slowly cooling inside the furnace. Then, the samples were annealed at 100 °C for three hours in order to eliminate internal stresses and additional homogenization. The

total mass of the prepared sample was about 4 g, while the total mass loss was less than 1 mass%. Phase transition temperatures and corresponding heat effects were determined by a simultaneous thermal analyzer (TA Instruments SDT Q600) [16]. The reference material was an empty alumina crucible. Prior to DTA measurements, temperature and enthalpy calibrations were performed using pure metal standards (In and Zn) under the measurement conditions. The sample's masses were about 30 mg and each sample was investigated by performing two heating cycles using the heating rate of 10 °C/min in the temperature interval from room temperature up to 300 °C, in a stream of inert gas (nitrogen) to prevent oxidation of the sample. Scanning electron microscope (SEM) (TESCAN VEGA3) [17], with an energy dispersive spectrometer (EDS) (Oxford Instruments X-act) [18], was used for microstructural investigation of the prepared alloys. The compositions of the coexisting phases as well as the total composition of the prepared alloys were determined using surface and spot EDS analysis. All SEM images of microstructures were recorded in the backscattered electron mode [17]. The analyzed samples were prepared by the classic metallographic process by polishing the samples with diamond pastes and etching them with an aqueous solution of ferric chloride.

3. RESULTS AND DISCUSSION

3.1. Thermodynamic calculation

Thermodynamic calculation of phase equilibria according to the CALPHAD (calculation of phase diagram) approach [19, 20] can provide valuable information about expected microstructure, phase transformation temperatures, and the thermal properties of the investigated material. In this work, thermodynamic calculations were performed using a thermodynamic dataset from Witusiewicz et al. [15]. Figure 1 presents a space phase diagram of the Bi-In-Sn system in combination with the constitutive In-Sn, Bi-Sn, and In-Bi binary systems.

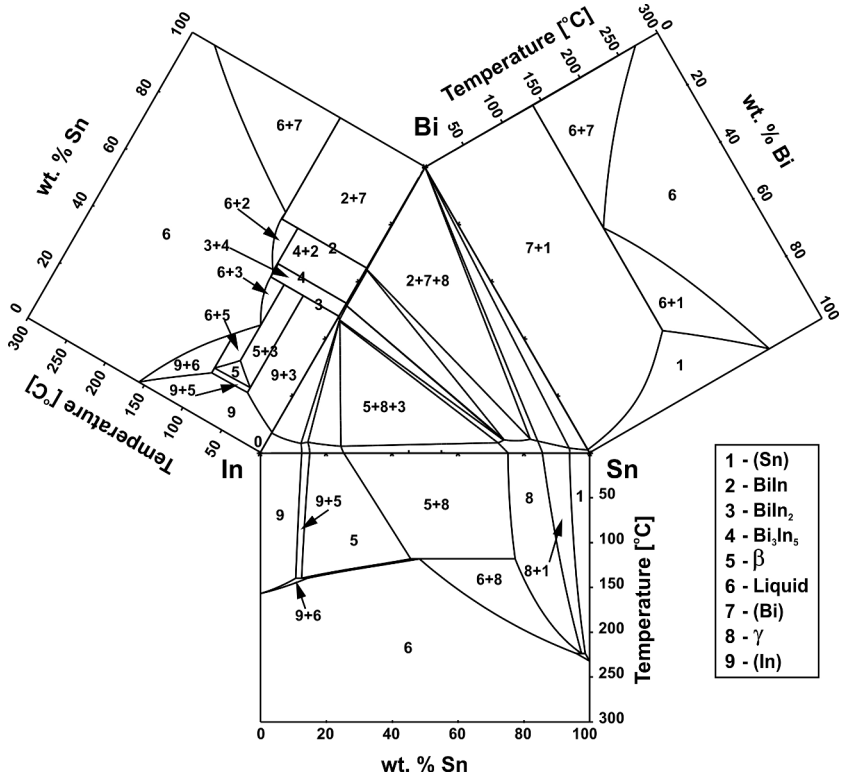

Figure 1. Space ternary phase diagram of Bi-In-Sn ternary system calculated using the thermodynamic parameters from Witusiewicz et al.[15]

Calculated isothermal section of the Bi-In-Sn system at room temperature, with marked phases and drawn compositions of the investigated alloys are shown in Figure 2.

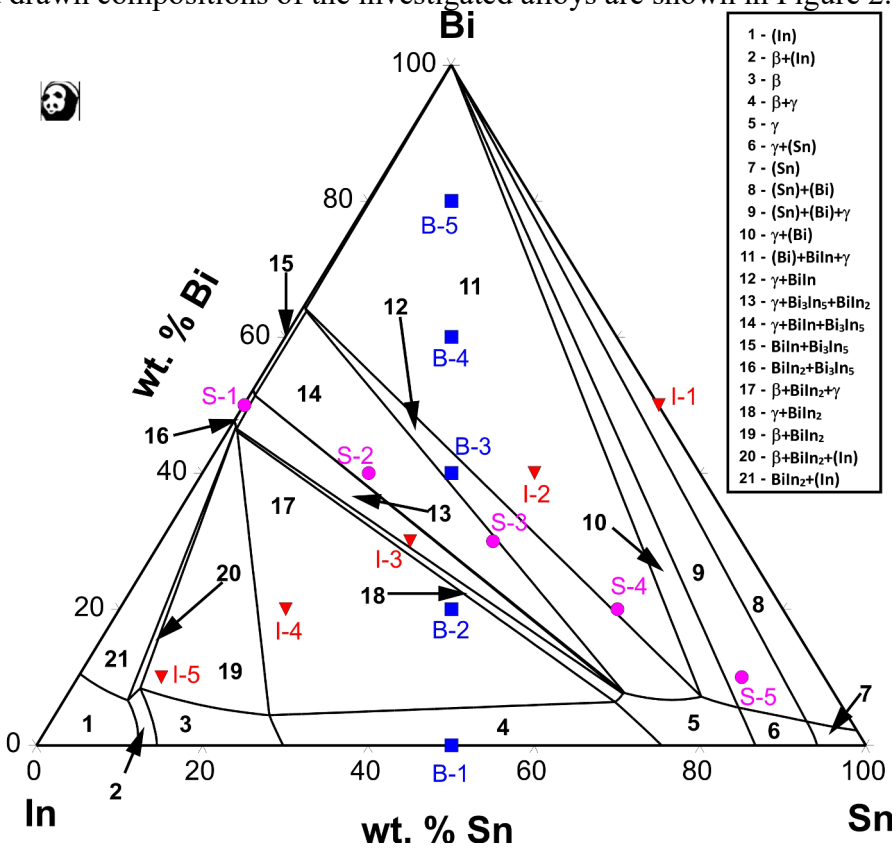

Figure 2. Calculated isothermal section of the Bi-In-Sn system at room temperature, based on thermodynamic parameters from Witusiewicz et al. [15] with marked phases and drawn compositions of the investigated alloys

3.2. Thermal analysis

Differential thermal analysis (DTA) was used to determine the melting temperature and temperature of phase transformations of the investigated alloys. Figure 3 shows examples of DTA heating curves for some of the tested alloys. It should be noted that the sample was heated twice to 300 °C in a nitrogen atmosphere with a heating rate of 10 °min^{-1}, and the results of the second heating are shown. The liquid temperature was determined from the temperature of the DTA peak while other phase transition temperatures were determined from the onset temperature of the DTA peak in the heating process.

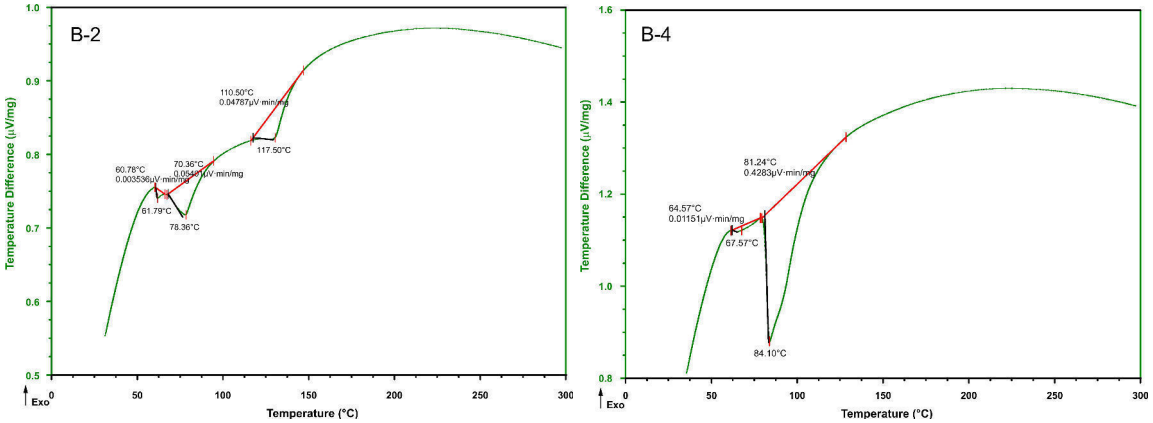

a) Investigated alloy B-2 and B-4 from Bi-Sn50In50 vertical section

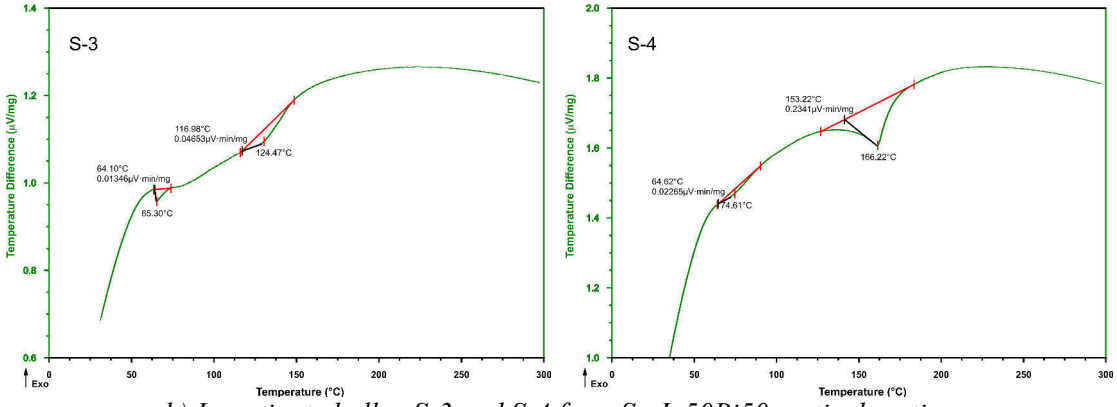

b) Investigated alloy S-3 and S-4 from Sn-In50Bi50 vertical section

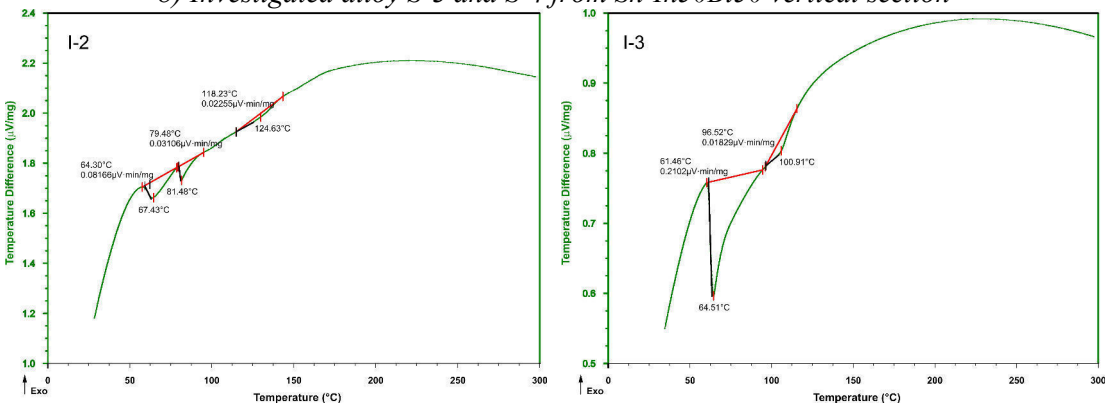

c) Investigated alloy I-2 and I-3 from In-Bi50Sn50 vertical section

Figure 3. DTA heating curve of investigated alloys from Bi-In-Sn ternary system

Experimentally determined temperatures of phase transformations in the investigated alloys of vertical sections Bi-Sn50In50, Sn-In50Bi50, and In-Bi50Sn50 are presented in Table 1. Figure 4 presents calculated vertical sections with mass fraction ratios In/Sn=1, Bi/Sn=1, and Bi/In=1 of the ternary Bi-In-Sn system compared with DTA experimental results: a) Bi-Sn50In50, b) Sn-In50Bi50 and c) In-Bi50Sn50. Experimentally determined temperatures of phase transformations of the investigated alloys were in good agreement with calculated values.

Table 1. Experimentally determined temperatures of phase transformations of the investigated alloys

Samples	Temperature, °C	
	Phase transformations	Liquidus
B-1	/	117,75
B-2	60,78; 70,36;	117,50
B-3	68,86	80,28
B-4	64,57	84,10
B-5	66,42; 85,32;	186,13
S-1	/	92,67
S-2	/	63,67
S-3	64,10	124,47
S-4	64,63	166,22
S-5	63,67	200,61
I-2	64,43; 79,48;	124,03
I-3	61,46	100,91
I-4	61,16	93,22
I-5	67,52	128,94

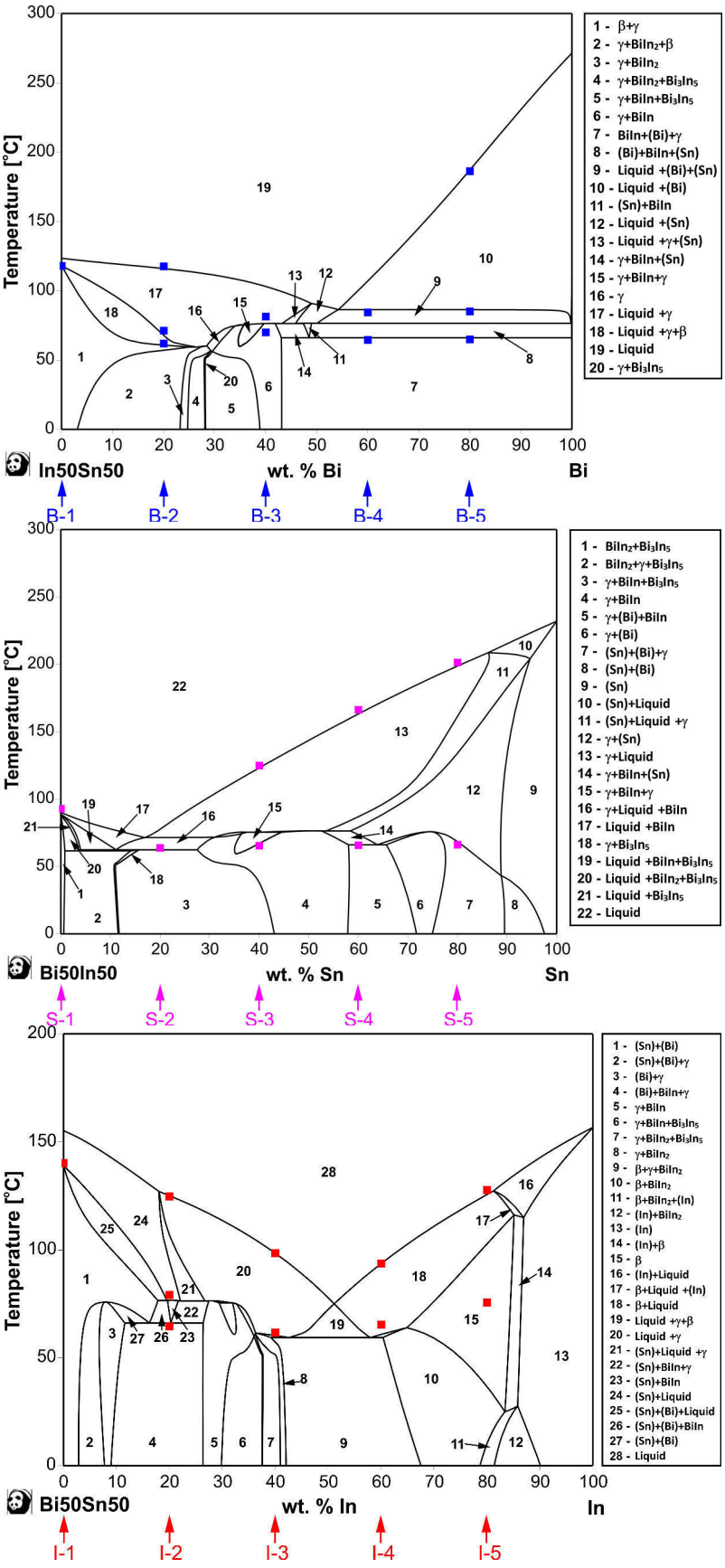

Figure 4. *Calculated vertical sections of the ternary Bi-In-Sn system, based on thermodynamic parameters from Witusiewicz et al. [15], compared with DTA experimental results: a) Bi-Sn50In50, b) Sn-In50Bi50 and c) In-Bi50Sn50*

3.3. Scanning Electron Microscopy (SEM-EDS)

The following images show SEM microphotographs of the investigated alloys B-2, B-3, and B-5 from Bi-Sn50In50 vertical section; S-2, S-3, and S-4 from Sn-In50Bi50 vertical section; I-3 and I-4 from In-Bi50Sn50 vertical section at different magnifications: a) 100x; b) 500x; c) 1000x; d) 2000x.

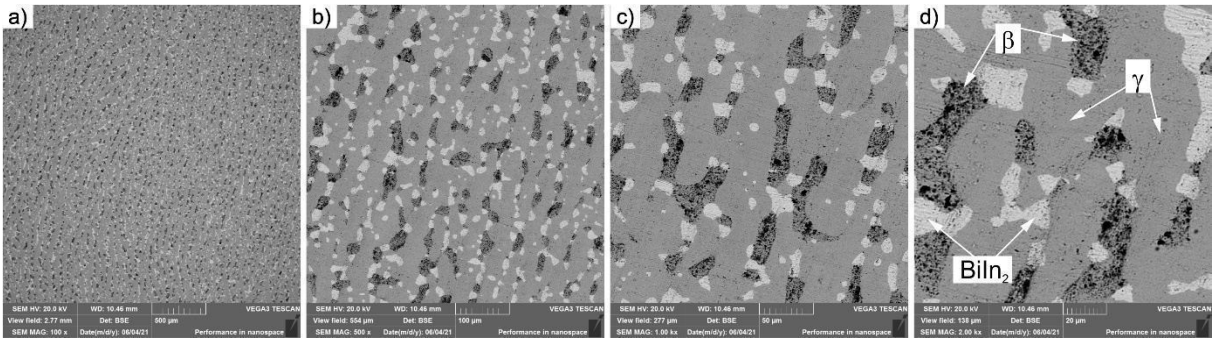

B-2

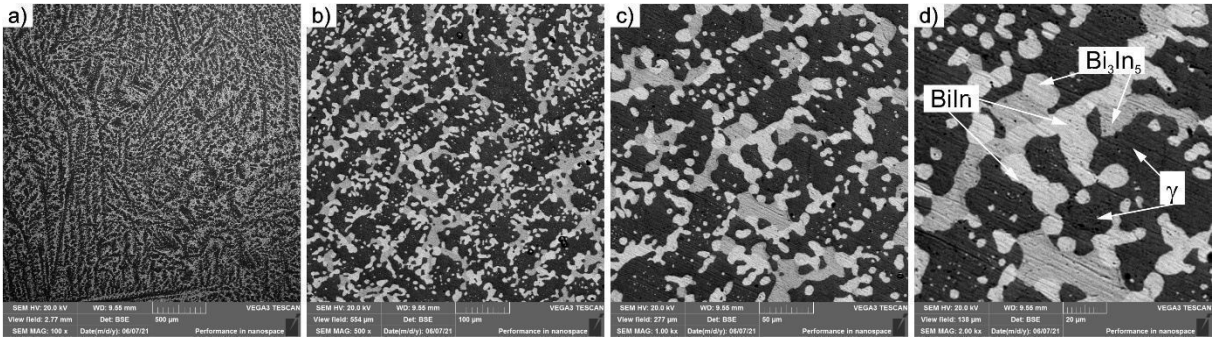

B-3

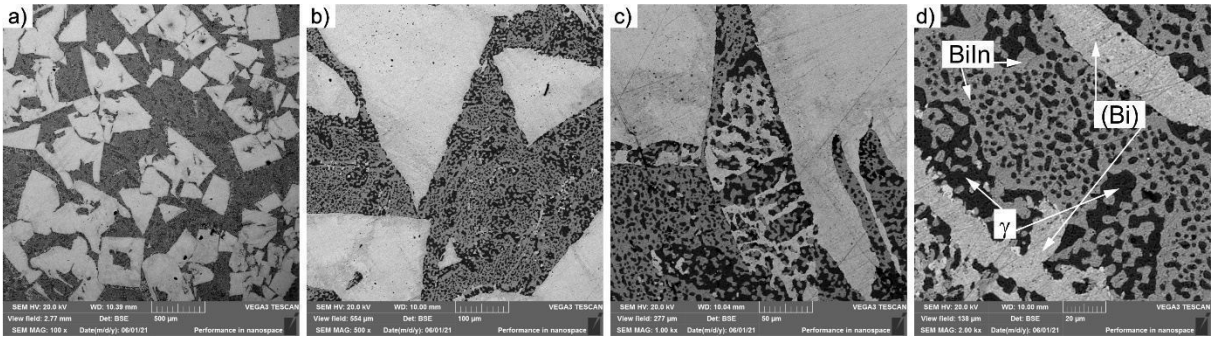

B-5

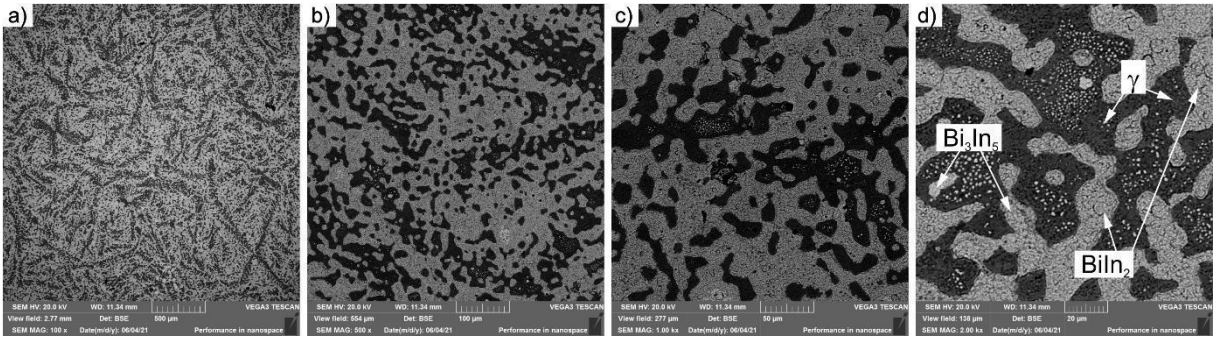

S-2

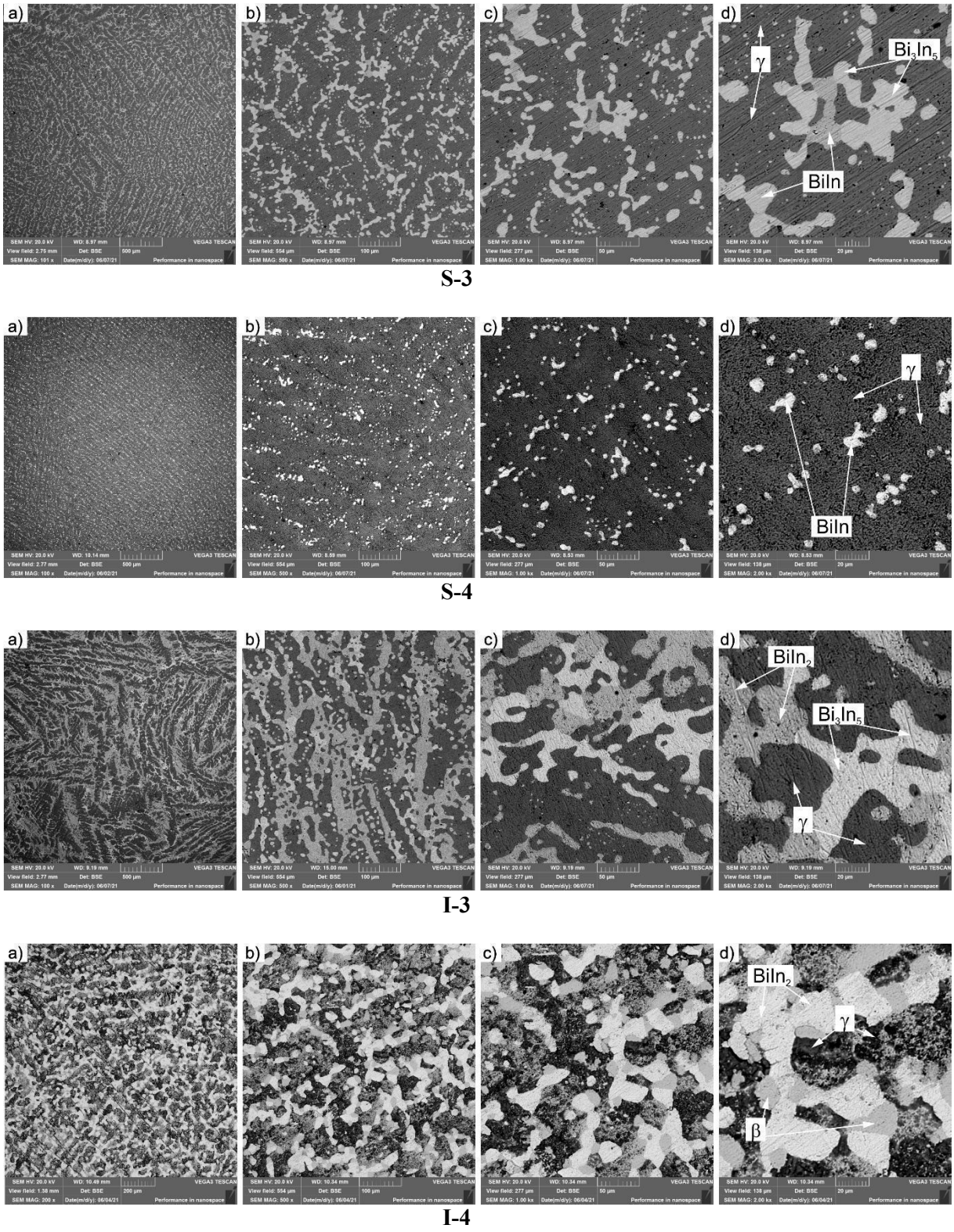

Figure 5. *SEM microphotographs of the investigated alloys B-2, B-3, and B-5 from Bi-Sn50In50 vertical section; S-2, S-3, and S-4 from Sn-In50Bi50 vertical section; I-3 and I-4 from In-Bi50Sn50 vertical section at different magnifications: a) 100x; b) 500x; c) 1000x; d) 2000x*

In SEM microphotographs of alloy B-2, it can be clearly seen that the microstructure consists of three phases: the largest dark gray phase is the γ phase, $BiIn_2$ is the light gray phase, and the black phase is the β phase. While in alloy B-3, the microstructure consists

of three phases: the largest black phase is the γ phase, the dark gray phase is BiIn, and the light gray phase is the Bi_3In_5 phase. The microstructure of alloy B-5 consists of three phases: the black phase is the γ phase, the light gray phase is a solid solution based on bismuth (Bi), and the dark gray phase is the BiIn phase. In the SEM microphotographs of the S-2 and S-3 alloys, the microstructure consists of three phases: the black phase is the γ phase, the light gray phase is Bi_3In_5 and the dark gray phase is $BiIn_2$ at the alloy S-2 and BiIn at the alloy S-3. The microstructure of S-4 alloys consists of only two phases: the black phase is the γ phase, and the light gray phase is BiIn, while the third phase, a solid solution based on bismuth (Bi), which should be present in this alloy, has not been identified. In the SEM microphotograph of the I-3 alloy, the base of the microstructure is the same black γ phase. Two more phases are present there. The light gray phase is the stoichiometric compound Bi_3In_5, and the dark gray phase is the same stoichiometric compound $BiIn_2$. In the case of I-4 alloys, the base of the microstructure is also the black γ phase. Two more phases are also present there. The light gray phase is the stoichiometric compound $BiIn_2$, and the dark gray phase is the β phase. Experimentally determined phase compositions of co-existing phases in the investigated alloys were found to support the corresponding calculated phase compositions based on thermodynamic parameters from Witusiewicz et al. [15], quite well.

4. CONCLUSIONS

In the present research, low-melting alloys from three cross-sections Bi-Sn50In50, Sn-In50Bi50, and In-Bi50Sn50 was investigated using differential thermal analysis (DTA), and by scanning electron microscopy (SEM) with energy dispersive spectrometry (EDS). Temperatures of phase transformations, determined by DTA, were compared with the calculated vertical sections (three vertical sections were investigated), and a close agreement was obtained. Phase compositions of co-existing phases, determined by EDS analysis, were found to support the corresponding calculated phase compositions quite well. The experimentally obtained results were compared with the results of thermodynamic calculation according to the CALPHAD (calculation of phase diagram) approach, based on thermodynamic parameters from Witusiewicz et al. [15], and a close agreement was noticed.

5. ACKNOWLEDGEMENT

This work has been financial supported by the Ministry of Science, Technological Development and Innovations of the Republic of Serbia, with the funding of the scientific research work at the University of Belgrade, Technical Faculty in Bor, according to the contract with registration number 451-03-47/2023-01/200131. The authors are grateful to V.T. Witusiewicz for kindly providing TDB file for thermodynamic calculations.

6. REFERENCES

[1] Said R.M., Salleh M.A.A.M., Saud N., Ramli M.I.I.: Superconducting Lead-free Solder Joint: A Short Review, IOP Conference Series: Materials Science and Engineering, Volume 957 (Issue 1), Pahang, Virtual; Malaysia, IOP Publishing Ltd, (2020)

[2] Cheng S., Huang C.-M., Pecht M.: A review of lead-free solders for electronics applications, Microelectronics Reliability, 75 (2017) 77-95

[3] Aksoy C., Mousavi T., Brittles G., Grovenor C.R.M., Speller S.C.: Lead-Free Solders for Superconducting Applications, IEEE Transactions on Applied Superconductivity, 26 (3) (2016)

[4] Kotadia H.R., Howes P.D., Mannan S.H.: A review: On the development of low melting temperature Pb-free solders, Microelectronics Reliability, 54 (6) (2014) 1253-1273

[5] Directive 2002/96/EC of the European parliament and of the council, on waste electrical and electronic equipment (WEEE), Official Journal of the European Union, L 37 (2003) 24-38
[6] Directive 2002/95/EC of the European parliament and of the council on the restriction of the use of certain hazardous substances in electrical and electronic equipment (RoHS), Official Journal of the European Union, L 37 (2003) 19-23
[7] Puttlitz K., Galyon G.: Impact of the ROHS directive on high-performance electronic systems Part I: need for lead utilization in exempt systems, Journal of Materials Science: Materials in Electronics, 18 (1) (2007) 331-346
[8] Puttlitz K., Galyon G.: Impact of the ROHS Directive on high-performance electronic systems Part II: key reliability issues preventing the implementation of lead-free solders, Journal of Materials Science: Materials in Electronics, 18 (1) (2007) 347-365
[9] Mhd. Noor E.E., Ismail A.B., Sharif N.M., Ariga T., Hussain Z.: Characteristic of low temperature of Bi-In-Sn solder alloy, Proceedings of the IEEE/CPMT International Electronics Manufacturing Technology (IEMT) Symposium, (2008)
[10] Yang F., Zhang L., Liu Z.Q., Zhong S.J., Ma J., Bao L.: Properties and Microstructures of Sn-Bi-X Lead-Free Solders, Advances in Materials Science and Engineering, 2016 (2016)
[11] Zhou K., Tang Z., Lu Y., Wang T., Wang H., Li T.: Composition, Microstructure, Phase Constitution and Fundamental Physicochemical Properties of Low-Melting-Point Multi-Component Eutectic Alloys, Journal of Materials Science & Technology, 33 (2) (2017) 131-154
[12] Yang C.H., Zhou S., Lin S.K., Nishikawa H.: Development of Sn-Bi-In-Ga quaternary low-Temperature solders, 2019 International Conference on Electronics Packaging, ICEP 2019, (2019)
[13] Shalaby R.M.: Effect of silver and indium addition on mechanical properties and indentation creep behavior of rapidly solidified Bi–Sn based lead-free solder alloys, Materials Science and Engineering: A, 560 (2013) 86-95
[14] Chen X., Xue F., Zhou J., Yao Y.: Effect of In on microstructure, thermodynamic characteristic and mechanical properties of Sn–Bi based lead-free solder, Journal of Alloys and Compounds, 633 (2015) 377-383
[15] Witusiewicz V.T., Hecht U., Böttger B., Rex S.: Thermodynamic re-optimisation of the Bi–In–Sn system based on new experimental data, Journal of Alloys and Compounds, 428 (1-2) (2007) 115-124
[16] Quezada-Castillo E., Aguilar-Castro W., Quezada-Alván B.: Ion release from non precious dental alloys in the oral cavity, Revista Materia, 27 (2) (2022)
[17] Mang S.R., Choi H., Lee H.J.: Investigation of Sn–Bi–In ternary solders with compositions varying from Sn–Bi eutectic point to 76 °C ternary eutectic, Journal of Materials Science: Materials in Electronics (2022)
[18] Peng Y., Li C., Xiao K., Yang J., Pu C., Gao P., Guo S., Zhang J., Yi J.: Effects of Ga alloying on microstructure and comprehensive performances of Sn–9Zn–2Bi alloys for the microelectronics industry, Microelectronics Reliability, 135 (2022)
[19] Saunders N., Miodownik A.P.: CALPHAD (CALculation of PHAse Diagrams): A comprehensive guide, New York, Pergamon, 1998
[20] Lukas H., Fries S.G., Sundman B.: Computational thermodynamics: the Calphad method, Cambridge university press, 2007

RELATIONSHIP OF MICROSTRUCTURAL TRANSFORMATIONS IN AUSTEMPERED NODULAR CAST WITH MICROHARDNESS VALUES

Adisa Burić, Belma Fakić, Edib Horoz
University of Zenica, Institute “Kemal Kapetanović”
Zenica, B&H

Hasan Avdušinović, Raza Sunulahpašić
University of Zenica, Faculty of Metallurgy and Technology
Zenica, B&H

Keywords: austempered ductile iron, isothermal improvement, ausferitic, microhardness, microstructure

ABSTRACT
Austempered ductile iron is the last addition to the group of ductile irons obtained by isothermal improvement of classic ductile iron. Austempered nodular cast iron has improved mechanical properties and a different matrix microstructure compared to known iron-based castings. This type of casting is obtained by isothermal improvement - austempering, whereby the resulting microstructure consists of a mixture of ausferitic (acicular) ferrite and residual, isothermally transformed, carbon-enriched, stable, austenite. Changing the austempering parameters (temperature and time of austenitization and isothermal transformation) affects the obtained ausferite microstructure, and thus the mechanical properties. The most influential parameter that affects the mechanical properties of austempered ductile iron is the isothermal transformation temperature. This paper will present the relationship between microhardness values and microstructural transformations in the material due to the effect of elevated temperatures.

1. INTRODUCTION

One of the materials whose production increases year by year is ductile iron. The properties of ductile iron can be further improved by isothermal transformation - austempering, whereby the newly produced material is called ADI material (Austempered Ductile Iron). The special properties of ADI material compared to classic ductile iron are a direct consequence of the microstructure created during austempering. The microstructure is conditioned primarily by austempering parameters (temperature and time of austenitization, and temperature and time of isothermal transformation), as well as by chemical composition.

Austempered ductile iron is the last addition to the group of ductile irons obtained by austempering classic ductile iron. Austempering of ductile iron belongs to the group of procedures that change the microstructure of the entire metallic matrix, and is carried out in order to improve the mechanical properties of the casting (strength, elongation, toughness, dynamic strength, etc.).

Austempered ductile iron has improved mechanical properties and a different matrix microstructure compared to known iron-based castings. The new microstructure of the matrix is called ausferite, Figure 1. Ausferite is obtained by heat treatment- austempering, whereby the resulting microstructure consists of a mixture of ausferitic (acicular) ferrite

and residual, isothermally transformed, carbon-enriched, stable, austenite [1]. The morphology and composition of the microstructure of ADI material directly depend on the parameters of austempering (austenitization and isothermal transformation). Depending on the obtained microstructure we will have different values of mechanical properties.

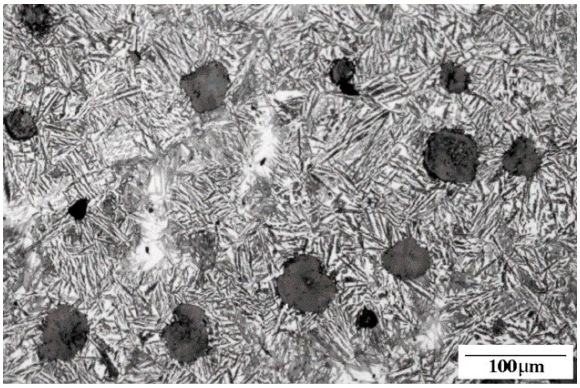

Figure 1. Microstructure of austempered ductile iron [2]

An extraordinary combination of mechanical properties primarily depends on the microstructure, i.e. on the type and amount of individual phases, as well as their morphology.
The microstructure, and thus the mechanical properties, are controlled by the correct choice of austempering parameters, chemical composition, and graphite morphology, figure 2. The most influential parameter that affects the mechanical properties of ADI material is the isothermal transformation temperature, [3]. Transformation at higher temperatures (approx. from 330 °C to 400 °C) results in high ductility and toughness, but lower strength and hardness. On the other hand, transformation at lower temperatures (approx. 250 °C to 330 °C) achieves high strength, hardness, and wear resistance, but lower toughness [4]

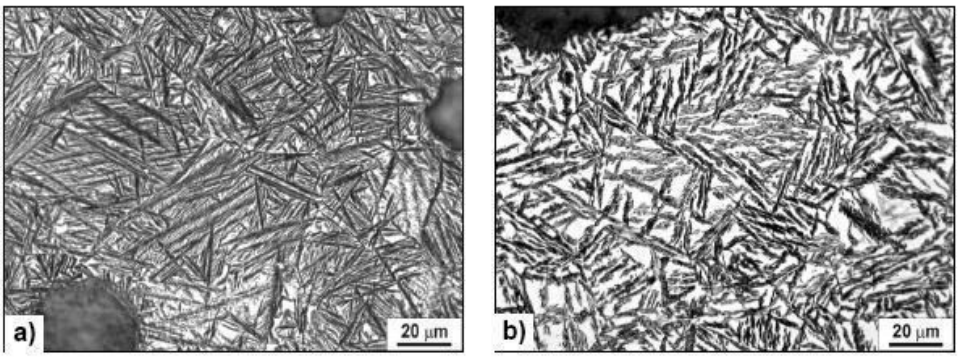

Figure 2. Ausferite microstructure of ADI material
a) the lower area of isothermal transformation; b) upper area of isothermal transformation [4]

Figure 3 shows the influence of isothermal transformation temperature on the mechanical properties of austempered ductile iron.

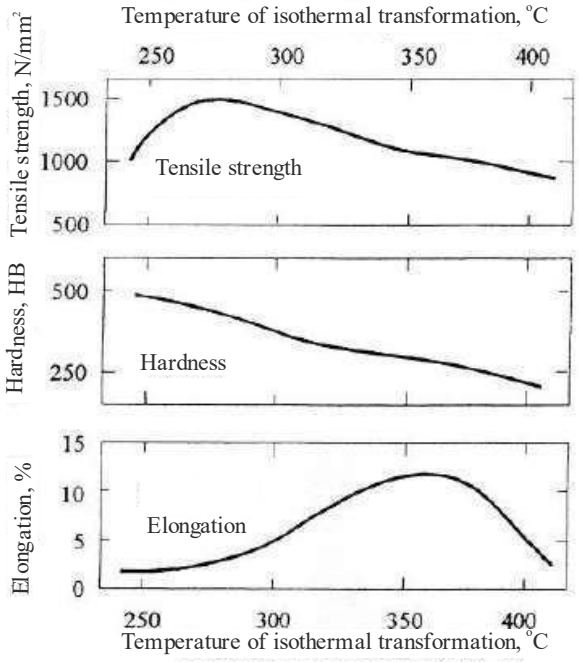

Figure 3. Influence of isothermal transformation temperature on the mechanical properties of austempered ductile iron [5]

2. PRODUCTION PROCESS OF THE AUSTEMPERED DUCTILE IRON

Within this work, ductile iron alloyed with Mo, Ni, and Cu was chosen as the starting material for the production of austempered ductile iron. This nodular casting was produced by a commercial casting process in a medium frequency induction furnace with a nominal power of 750 kW and a capacity of 1.5 t in the company "Pobjeda" Tešanj branch of the Turbe foundry.

Thermal treatments (austenitization and isothermal transformation) to obtain austempered ductile iron were carried out at the "Kemal Kapetanović" Institute in Zenica and at the Faculty of Metallurgy and Technology.

The heat treatment procedure is shown diagrammatically in Figure 4, and consists of the following steps:

- heating to austenitizing temperature 870°C,
- holding at the austenitization temperature,
- rapid cooling to the temperature of isothermal transformation 350°C,
- holding at the temperature of isothermal transformation,
- air cooling to room temperature.

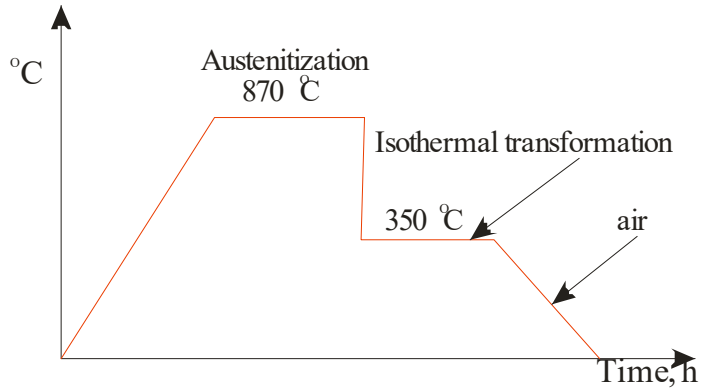

Figure 4. Thermal treatment to obtain austempered ductile iron

The initial phase of austempering is austenitization, where the initial base of ductile iron is transformed into austenite, as well as its enrichment with carbon.

The height of the austenitization temperature and holding time controls the amount of dissolved carbon in the austenite, which further affects the kinetics of transformations in the second phase of heat treatment. The austenitization temperature, which is used in the austempering of nodular cast iron castings, is in the range of 820 °C to 950 °C [6].

The second stage of the thermal treatment of the casting is the cooling of the initial austenite microstructure to the selected transformation temperature. Isothermal transformation implies a rapid transition from the austenitizing temperature to the temperature of isothermal transformation, holding at that temperature and cooling in air. The temperature interval in which transformations of the starting austenite microstructure take place is between 270°C and 400°C [7].

An ausferite microstructure of ADI material is formed by isothermal transformation. Ausferite is formed by the formation of ferrite bundles within previous austenite grains.

The medium used for the isothermal transformation of the samples was KNO_3, and the holding time in the medium was 90 minutes. In the process of formation of the final microstructure in austempered ductile iron, the temperature of isothermal transformation plays an important role. The size and shape of the ferrite phase and the amount of residual austenite largely depend on the value of the selected isothermal transformation temperature. If at the end of the technological process, one wants to obtain a casting that will have high values of tensile strength and hardness with lower values of ductile properties, it is necessary to choose lower temperatures of isothermal transformation (270 °C to 330 °C) [7].

After thermal treatment of the starting material, austempered ductile iron with the properties prescribed for this type of material was obtained.

Based on the results of dilatometric and differential thermal analysis (DTA) obtained in the framework of previous research [8], it was decided to subsequently thermally treat the ADI samples at 5 different temperatures as follows: 400 °C, 420 °C, 470 °C, 520 °C and 550 °C. The goal of the research is to show whether the change in microstructure at elevated temperatures affects the change in mechanical properties, which was monitored through the results of the microhardness test.

3. TESTING THE PROPERTIES OF THE INITIAL ADI MATERIAL AND SUBSEQUENTLY THERMALLY TREATED SAMPLES

After the final (subsequent) thermal treatments, in order to observe the behaviour of the material under conditions of elevated working temperatures, detailed tests were carried out, both on these samples and on the initial ADI material. Among other things, the tests

included detailed microstructural analysis using an light microscope and microhardness testing

3.1 Analysis of the microstructure on a light microscope

Microstructure analysis was carried out in the Metallographic Laboratory of the "Kemal Kapetanović" Institute in Zenica on an Olympus PMG3 light microscope with additional equipment for image storage. The microstructure tests were carried out with the aim of determining possible microstructural transformations in the material due to the effect of elevated temperatures. Figures 5 to 10 show the microstructures of the initial austempered ductile iron and samples additionally thermally treated at appropriate temperatures.

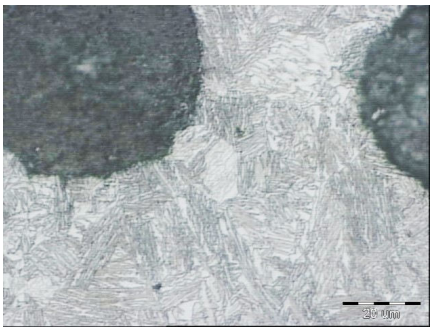

Nital *x750*

Figure 5. Microstructure of the starting material (Austempered ductile iron)
Ausferite microstructure composed of fine acicular ferrite and residual austenite with separated carbon in the form of nodules

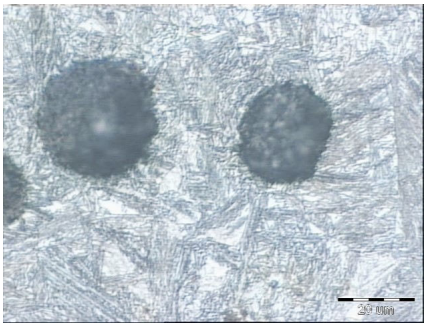

Nital *x750*

Figure 6. Microstructure of additionally treated material (400 °C/2h)
Ausferite microstructure is composed of acicular ferrite, residual austenite, and excreted graphite nodules. A noticeable process of degradation of the initial microstructure.

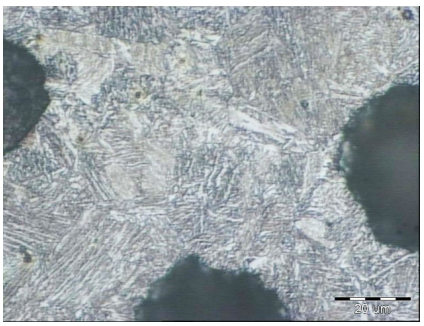

Nital *x750*

Figure 7. Microstructure of additionally treated material (420 °C/2h)
Ausferite microstructure is composed of acicular ferrite, residual austenite, and excreted graphite nodules, with noticeable degradation of the initial microstructure.

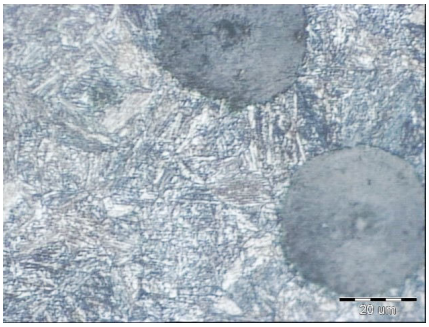

Nital x750

Figure 8. Microstructure of additionally treated material (470 °C/2h)
Ausferite microstructure is composed of acicular ferrite, residual austenite, and excreted graphite nodules, with noticeable degradation of the initial microstructure

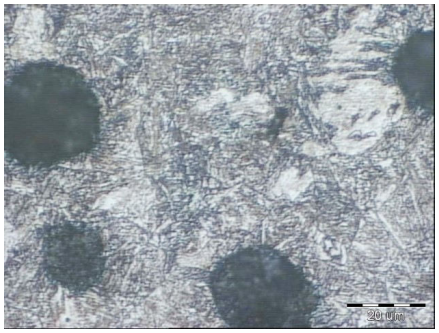

Nital x750

Figure 9. Microstructure of additionally treated material (520 °C/2h)
Ausferite microstructure in traces, acicular ferrite degraded, needles broken, initial microstructure almost completely degraded.

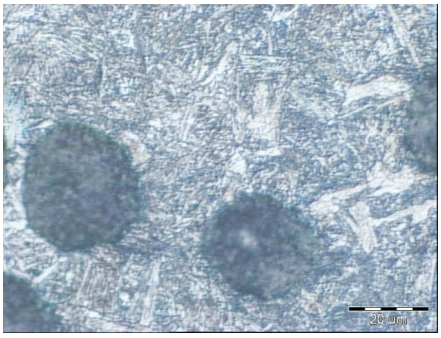

Nital x750

Figure 10. Microstructure of additionally treated material (550 °C/2h)
Ausferite microstructure in traces, acicular ferrite degraded, needles broken, initial microstructure almost completely degraded.

3.2 Microhardness test

The microhardness test HV0.03 per cross-section of the samples was carried out on a ZWICK hardness and microhardness test device. The goal of this test is to determine changes in microhardness values that are related to microstructural transformations in the material due to the effect of elevated temperatures. Figure 11 shows the locations of the microhardness test by the cross-section of the sample of the initial ADI material, while Table 1 gives the individual microhardness values for this sample. The other 5 samples treated at temperatures of 400 °C, 420 °C, 470 °C, 520 °C and 550 °C were tested on the

same principle. The average values of tested microhardness for all samples are given in Table 2 and Figure 12.

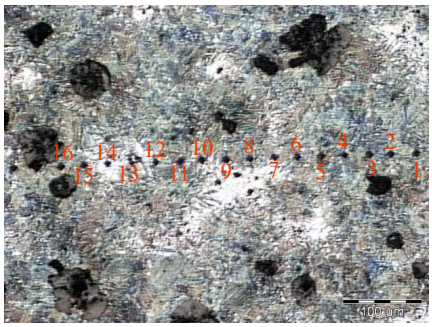

Nital *x150*

Figure 11. Locations of HV0.03 microhardness imprints on the cross-section of the sample

Table 1. Values of microhardness HV0.03 on the sample of the initial ADI material (Average 424HV0.03)

Location	Values of microhardness HV0,03	Location	Values of microhardness HV0,03
1	386	9	329
2	386	10	329
3	386	11	530
4	481	12	460
5	421	13	530
6	371	14	505
7	421	15	443
8	421	16	386

Table 2. Average microhardness values for the samples

Sample:	ADI material	400 °C/2h	420 °C/2h	470 °C/2h	520 °C/2h	570 °C/2h
Average microhardness values HV0,03	424	474	454	677	444	394

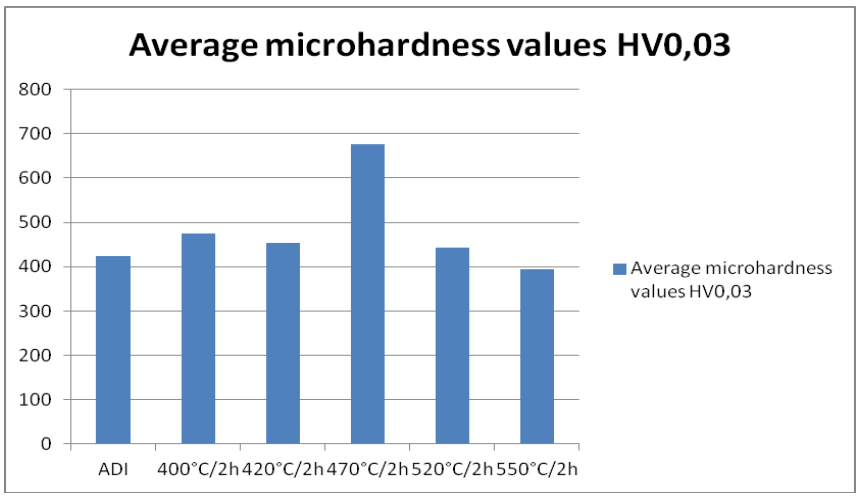

Figure 12. Graphic representation of the average values of microhardness HV0.03

4. CONCLUSION

Depending on the stability of the microstructure, i.e. the insight into the transformation of the initial ausferite microstructure when exposing the material to elevated working temperatures, one can talk about the properties of isothermal nodular cast iron at elevated temperatures.

Based on the results of earlier research, it was concluded that certain microstructural transformations occur due to the heating of isothermally improved nodular samples, which is most clearly noticeable in the temperature interval from 450 °C to 500 °C[8].

Based on this fact, an experiment was designed for these tests, and a subsequent heating regime was defined, which represents the simulation of the behaviour of austempered ductile iron at elevated temperatures.
Based on the microhardness values tested on the mentioned samples, it can be concluded that the microhardness value increased precisely in the temperature interval 450 °C to 500 °C, Figure 12. More precisely, the highest increase in the microhardness value was observed on the sample that was subsequently treated at 470 °C, which is a consequence of the microstructural transformation. So, the research confirmed that at higher temperatures the microstructure broke down into ferrite and carbide. Carbides are microconstituents that increase the value of microhardness.

5. REFERENCE

[1] Harding, R.A. The production, properties and automotive applications of austempered ductile iron, Kovove Mater., 45, (2007), 1-16
[2] www.phase-trans.msm.cam.ac.uk
[3] Zhang, J. W., Zhang, N., Zhang, M. T., Lu, L. T., Zeng, D. F., Song, Q. P.: Microstructure and mechanical properties of austempered ductile iron with different strength grades, Materials Letters, 119 (2014), 47-50
[4] Rainović D., „Uticaj mikrostrukture na prelaznu temperaturu ADI materijala“, Doktorska disertacija, Fakultet tehničkih nauka, Novi Sad, 2015.
[5] Vuković G.: Erozijsko trošenje izotermički poboljšanog te naknadno sačmarenog nodularnog lijeva, Završni rad, Fakultet strojarstva i brodogradnje, Zagreb, 2008.
[6] M. Gagne, The Sorelmetal handbook of Ductile Iron, Rio Tintop Iron&Titanium Inc., Montreal Canada 2004
[7] Avdušinović H.: Utvrđivanje optimalnih parametara proizvodnje odlivaka od austemperovanog nodularnog liva različite debljine stijenke, Doktorska disertacija, Fakultet za metalurgiju i materijale, Zenica, 2010.
[8] Dervišić Š.: Utvrđivanje optimalnih parametara proizvodnje odlivaka od austemperovanog nodularnog liva različite debljine stijenke, Doktorska disertacija, Fakultet za metalurgiju i materijale, Zenica, 2010.

EFFECT OF MIXING OF COOLING MEDIA ON MICROSTRUCTURE AND HARDNESS OF STEEL 23MnB4

Almaida Gigović-Gekić, Hasan Avdušinović, Amna Hodžić
University of Zenica, Faculty of Metallurgy and Technology
Zenica, B&H

Branka Muminović
University of Zenica, Institute “Kemal Kapetanović”
Zenica, B&H

Keywords: quenching, cooling intensity, microstructure, hardness

ABSTRACT
Steel cooling is an important technological operation because the final microstructure of the steel, and therefore its properties, depends on the cooling rate. The speed of steel cooling depends on numerous factors, one of which is the movement of the cooling media. This paper presents the results of testing the influence of mixing the cooling media on the microstructure and hardness of 23MnB4 steel. Two media that are usually used for quenching steel (water and oil) were used for the test. The samples were cooled in an unstirred media and in a stirred media with three different stirring speeds (500, 750, and 1000 rpm). The results showed that mixing the media has an influence on the microstructure and hardness of steel. Samples that were cooled in a mixed medium had a higher hardness. The mixing speed had a greater influence on the hardness in the case of cooling in water. The microstructure after cooling in the water and oil was martensite-bainite. With an increasing cooling rate, the ratio of martensite in microstructure increases.

1. INTRODUCTION

Steel cooling is an extremely important technological operation during the heat treatment of steel because the final microstructure of the steel, and therefore its properties, depends on the cooling rate. In practice, three methods of cooling are usually distinguished; slow, normal, and fast. Slow cooling is the cooling of samples in the furnace and is most often used in the annealing process. Normal cooling is carried out in the air, as in the case of normalization. Rapid cooling is applied during quenching and has the greatest impact on microstructure and properties. The cooling rate is affected by various factors such as:

- type of media used (initial temperature, boiling point, specific heat, thermal conductivity, viscosity, etc.),
- media movement,
- type of material being cooled (chemical composition, thermal conductivity, and specific heat),
- the mass of the samples, the ratio of surface area and volume,
- condition of the surface of the sample being treated, and
- sample design.

Of the mentioned factors that affect the cooling rate, in practice, only the medium used for cooling can be influenced, that is, the correct choice of the cooling media and its mixing [1-3].

The aim of the test is to show whether the mixing of media during quenching affects the microstructure and hardness of 23MnB4 steel.

2. EXPERIMENTAL PART

The material tested in this work was the steel 23MnB4 with a chemical composition given in Table 1. Because the tested samples are taken from the screw, the chemical composition is given according to the standard EN 10263-4: 2001 Steel rod, bars, and wire for cold heading and cold extrusion, Technical delivery conditions for steels for quenching and tempering.

Table 1. Chemical composition of 23MnB4 [4]

Chemical composition [wt.%]	C	Si_{max}	Mn	P_{max}	S_{max}	Cr_{max}	Cu_{max}	B
	0.20-0.25	0.30	0.90-1.20	0.025	0.025	0.30	0.25	0.0008-0.005

The analysis of a microstructure and hardness were done for the initial state and 8 quenched samples cooling with different rates (no mixing, 500, 750, and 1000 rpm) in two cooling media (water and oil). The samples were cylindrical in shape dimension Ø18x10 mm. The heating temperature was 880 ºC and the samples were heated together with a furnace at room temperature. The quantity of cooling media was a two-liter. Digital overhead Stirrer LLG-uni STIRRER OH2 used for stirring, Figure 1. The speed range of the stirrer is from 50 to 2200 rpm.

Before analysis of microstructure, the samples were prepared by grinding, polishing, and etching by nital (HNO_3 + ethanol). The microstructural analysis was carried out by the Olympus optical microscope with a maximum magnification of x1000. The microstructure of the initial state is shown in Figure 2. The microstructure is the ferrite-pearlite. From the figures, it could be noticed that the microstructure on the surface is more directed than in the center.

Figure 1. Digital overhead Stirrer LLG-uni STIRRER OH2

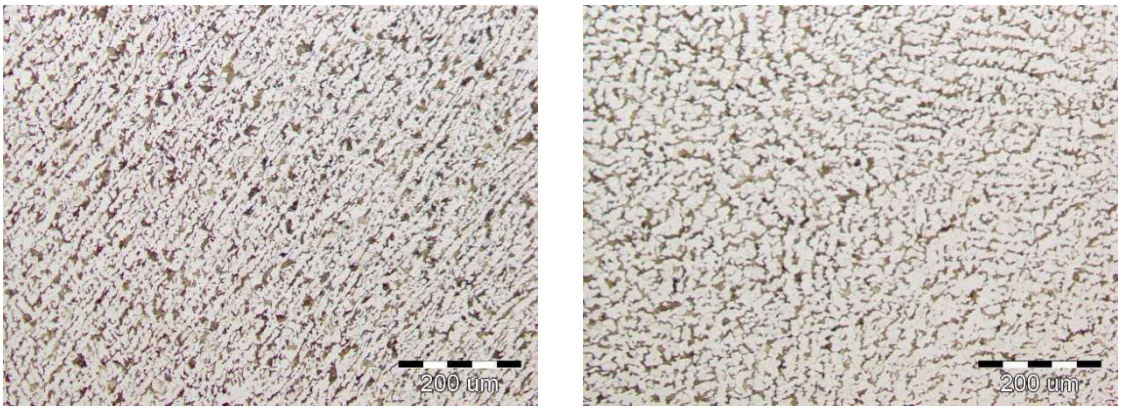

a) *b)*

Figure 2. The microstructure of the initial state: a) surface and b) center, x100

Hardness tests, according to standard BAS EN ISO 6506-1:2015 and BAS EN ISO 6508-1:2017were performed on specimens prepared for microstructure analysis.

3. RESULTS AND DISCUSSION

3.1. Analysis of microstructure

The microstructure of the quenched samples in the different media with different cooling rates is shown in Figures 3 to 10. All samples showed fine-grained microstructure.

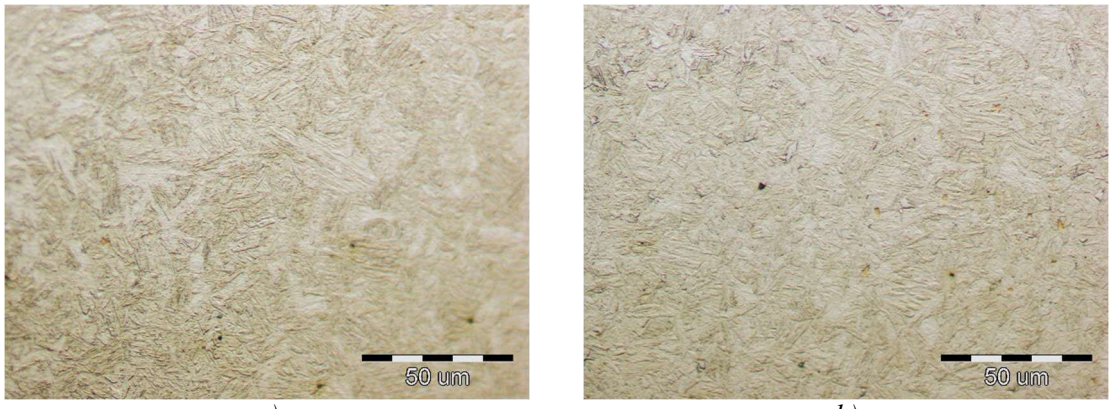

a) *b)*

Figure 3. The microstructure of the sample cooled in the water without mixing: a) surface and b) center, x500

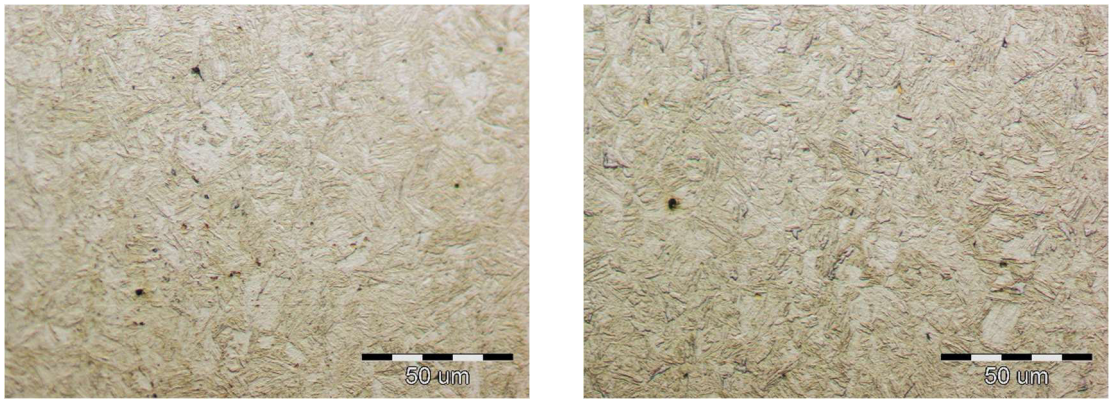

a) *b)*

Figure 4. The microstructure of the sample cooled in the water with mixing of 500 rpm: a) surface and b) center, x500

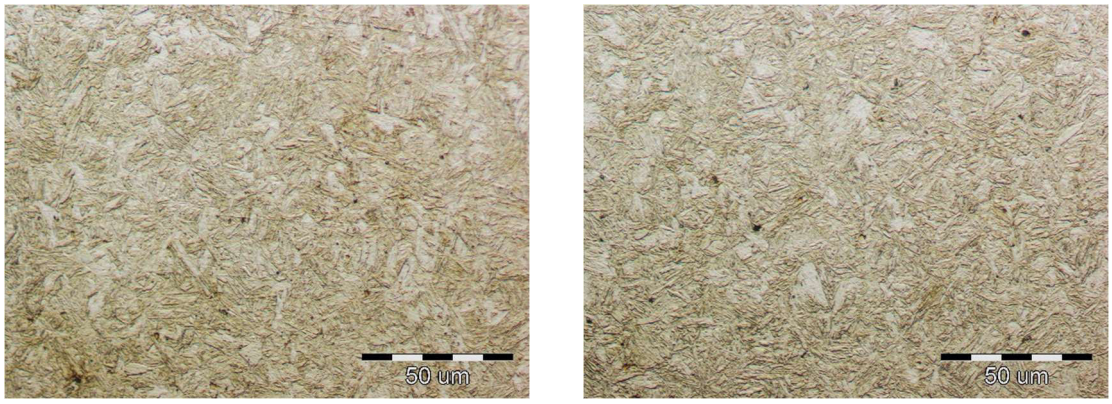

a) *b)*

Figure 5. The microstructure of the sample cooled in the water with a mixing of 750 rpm: a) surface and b) center, x500

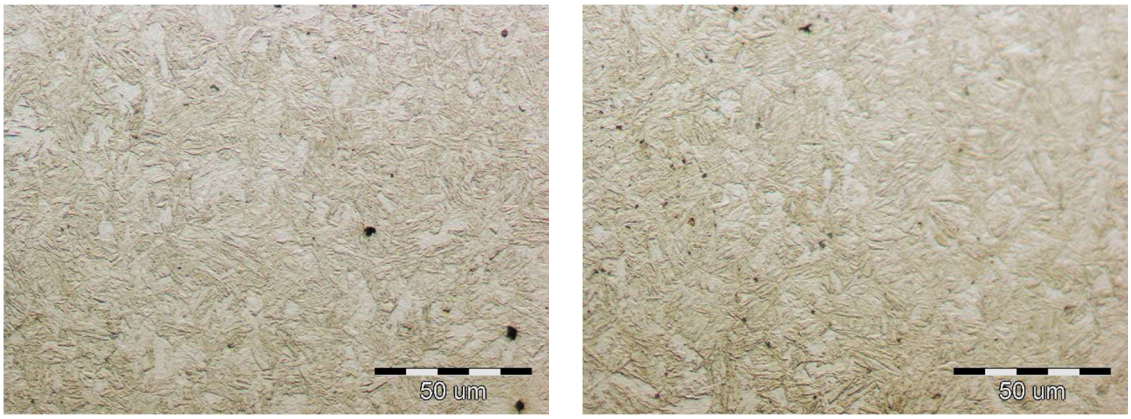

a) *b)*

Figure 6. The microstructure of the sample cooled in the water with a mixing of 1000 rpm: a) surface and b) center, x500

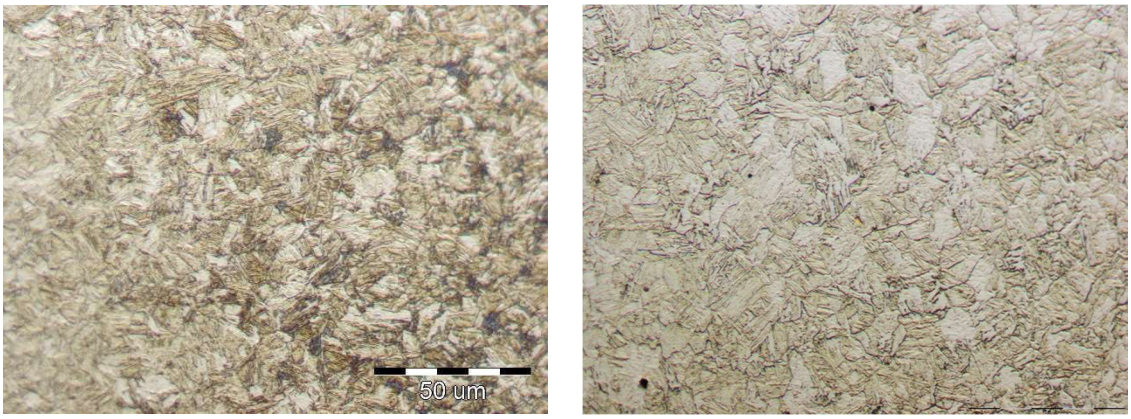

a) *b)*

Figure 7. The microstructure of the sample cooled in the oil without mixing: a) surface and b) center, x500

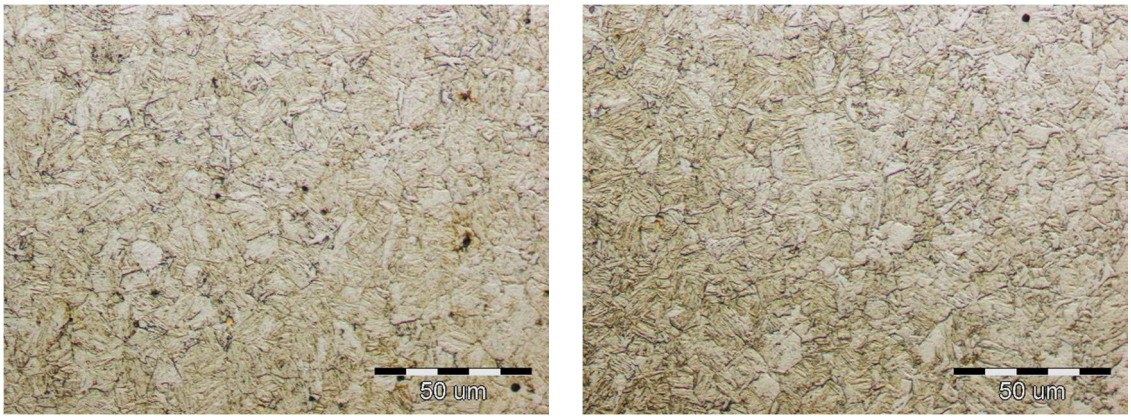

a) *b)*

Figure 8. The microstructure of the sample cooled in the oil with a mixing of 500 rpm: a) surface and b) center, x500

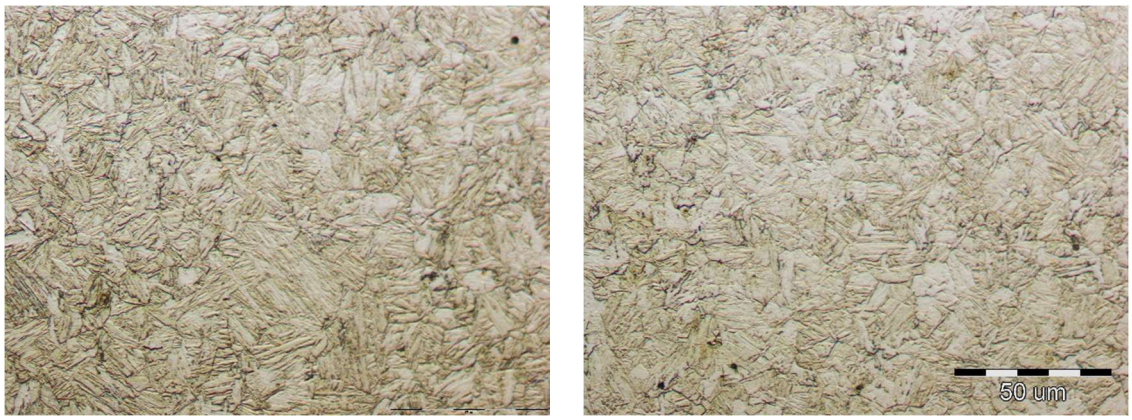

a) b)

Figure 9. The microstructure of the sample cooled in the oil with a mixing of 750 rpm: a) surface and b) center, x500

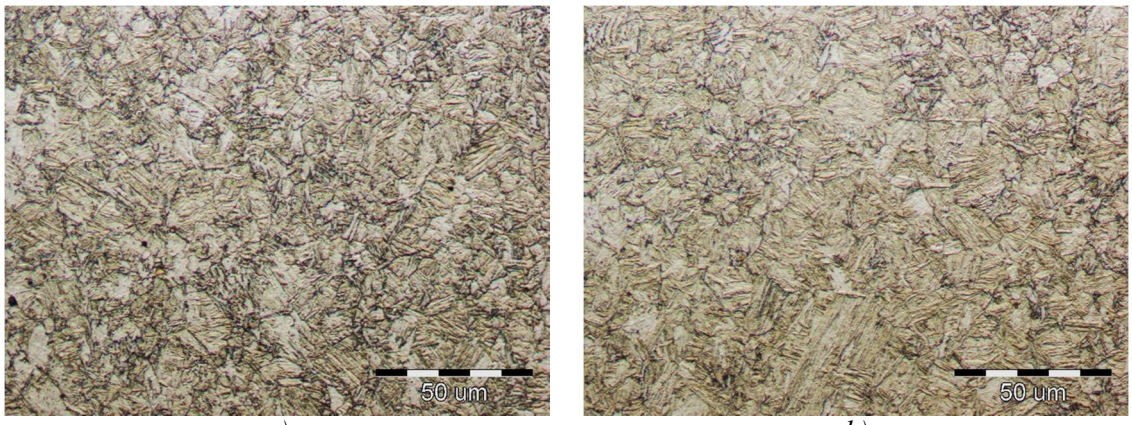

a) b)

Figure 10. The microstructure of the sample cooled in the oil with a mixing of 1000 rpm: a) surface and b) center, x500

Analysis of the microstructure after cooling in the water and oil showed the martensite-bainite microstructure. After quenching in oil the microstructure was more bainite (Figure 7-10) while the microstructure after cooling in water was martensite with bainite (Figure 3-6) because the cooling rate was faster. The microstructure is the same on the surface and center of the sample. For these dimensions, the steel has good hardenability.

3.2 Analysis of hardness

The results of the hardness analysis are presented in Table 2.

Table 2. Analysis of hardness

Sample	Cooling mode	Hardness (HBW 2,5/187,5)						Hardness [HV]*
		Single values					Average	
Sample 1 (initial state)	-	184	187	187	184	187	**186**	**184**
		Hardness (HRC)						
		Single values					Average	
Sample 2 (quenching in water)	No mixing	41	42	42	42	43	**42**	**406**

Sample	Cooling mode	Hardness (HBW 2,5/187,5)						Hardness [HV]*
		Single values					Average	
Sample 1 (initial state)	-	184	187	187	184	187	**186**	**184**
		Hardness (HRC)						
		Single values					Average	
Sample 3 (quenching in water)	500 rpm	44	46	42	46	44	**44**	**438**
Sample 4 (quenching in water)	750 rpm	47	47	46	47	48	**47**	**474**
Sample 5 (quenching in water)	1000 rpm	49	49	49	47	48	**48**	**490**
Sample 6 (quenching in oil)	No mixing	38	38	38	39	39	**38**	**361**
Sample 7 (quenching in oil)	500 rpm	41	42	42	41	41	**41**	**393**
Sample 9 (quenching in oil)	1000 rpm	41	41	42	42	43	**42**	**406**
Sample 8 (quenching in oil)	750 rpm	41	41	42	42	42	**42**	**406**

*https://www.steelexpress.co.uk/steel-hardness-conversion.html

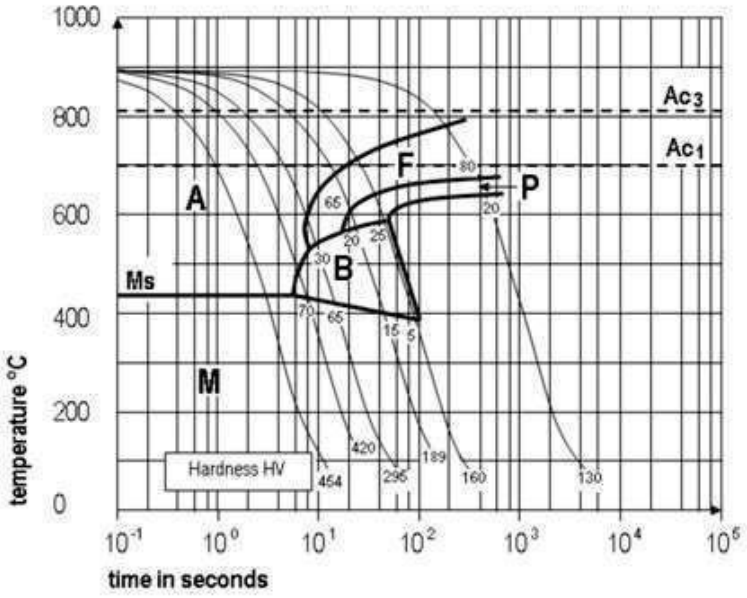

Figure 11. CCT diagram for steel 23MnB4 [4]

The hardness analysis showed that the samples cooled in water have a higher hardness compared to the samples cooled in oil. The rate of oil mixing did not significantly affect the cooling rate of the samples, except in the case that the oil mixing resulted in a hardness that could be achieved by cooling in water without mixing. The rate of water mixing

affected the rate of cooling. As the mixing speed increases, the hardness of the samples increases.
According to the literature [4] from the analysis of the CCT diagram (Figure 11) it can be seen that the hardness values obtained for cooling in oil correspond to the area of transformation of austenite into martensite and bainite. The hardness obtained for higher cooling rates, i.e. water mixing, corresponds to the transformation of austenite into martensite. With an increase in the cooling rate, the proportion of martensite in the martensite-bainite microstructure also increases. For mixing speeds of 500, 750, and 1000 revolutions, 100% martensite is obtained.

4. CONCLUSIONS

The aim of the test is to show whether the mixing of media during quenching affects the microstructure and hardness of 23MnB4 steel. The initial microstructure of steel was ferrite-pearlite. Analysis of the microstructure after cooling in the water and oil showed the martensite-bainite microstructure. Samples that were cooled in a mixed medium had a higher hardness. The mixing speed had a greater influence on the hardness in the case of cooling in water. With an increasing cooling rate, the ratio of martensite in microstructure increases. The rate of oil mixing did not significantly affect the cooling rate of the samples, except in the case that the oil mixing resulted in a hardness that could be achieved by cooling in water without mixing. After quenching, the microstructure is the same on the surface and center of the sample. For these dimensions, the steel has good hardenability.
In the end from the results, it could be concluded that the mixing process has an influence on the cooling rate of the steel 23MnB4. With mixing, it is possible to get the same hardness for steel quenched in the oil as the cooling in water without mixing. The mixing rate has more influence on the cooling in water than in the oil.

5. ACKNOWLEDGMENT

The authors would like to thank the Institute "Kemal Kapetanović" for participating in the study.

6. REFERENCES

[1] Steel Heat Treatment Handbook: Steel Heat Treatment Metallurgy and Technologies, Edited by G.E. Totten, Taylor & Francis Group, 2006.
[2] K. E. Thelning: Steel and its heat treatment, Butterworth-Heinemann, Oxford, Second edition 1984, Reprinted 2000.
[3] A. Gigović-Gekić, H. Avdušinović: Termička obrada metala, Praktikum s teorijom, Univerzitet u Zenici, Metalurško-tehnološki fakultet, Zenica, 2019.
[4] https://www.lucefin.com/wp-content/files_mf/152336964123MnB4.pdf [13.02.2023.]

THE INFLUENCE OF ALLOYING ELEMENTS TO CAST IRON MICROSTRUCTURE

Anida Henjaković
Pobjeda dd Tešanj, Podružnica "Livnica"
Turbe, B&H

Hasan Avdušinović, Amir Muslić
University of Zenica, Faculty of Metallurgy and Technology
Zenica, B&H

Keywords: alloying, cast irons, microstructure, molybdenum, chromium, copper

ABSTRACT

Gray cast iron belongs to the group of iron casts that contain graphite particles in the microstructure. Graphite particles in gray cast iron have the shape of lamellae and are connected to each other. The specific combination of properties of gray cast iron, which is satisfactory for many applications, and simple and cheap production are the main reasons for its very wide application. For many years, gray cast iron has been the most used material for making metal castings. In this paper, there are microstructure tests for different variations of alloying gray cast iron with chromium, molybdenum, and copper. The assumption is that these elements influence the formation of pearlite in the microstructure, in different combinations.

1. INTRODUCTION

The quality and properties of gray cast iron depend on the shape, distribution, and size of the separated graphite lamellas and the microstructure of the metal matrix. The chemical composition is an important factor that affects the shape of the graphite and the microstructure of the metal matrix [1].

Cast iron with lamellar graphite (gray cast iron) includes a class of iron-based materials characterized by a microstructure with the presence of graphite separated in the form of lamellae in the metal matrix. In order to fully understand the issues of production and properties of this group of castings, the influence of the chemical composition is easiest to observe if the influence of individual elements is discussed according to the groups as follows:

1. Basic elements
2. Accompanying elements
3. Alloying elements and trace elements

Alloying elements and elements present in traces are elements that affect the properties of cast iron. Sometimes these elements are deliberately added with the aim of increasing their influence on the desired properties of the casting (addition of copper or tin with the aim of obtaining a pearlite microstructure of the metal matrix), and they can also be found in the melt as unwanted elements that have a negative effect on the properties of the casting (lead, bismuth, nitrogen, etc.) [2,3].

2. INFLUENCE OF CHEMICAL COMPOSITION ON MICROSTRUCTURE OF GRAY IRON CASTINGS

Copper is a graphitizer and promotes the formation of pearlite, and also increases the strength of the formed pearlite. It is expected that in ferrite or ferrite and pearlite cast iron base, copper has a stronger effect [4]. During hardening, graphite/austenite separates at the boundary and thus represents a diffusion barrier for carbon in the casting cooling process. Taking into account this fact, it is clear that in the process of transformation in the solid state, the formation of pearlite is promoted, while it is not a carbide promoter. Unlike manganese, there is no danger of carbide formation, and copper is a stronger promoter of pearlite. Amounts recommended as alloying additions range up to 1,55% copper. Research has shown that the addition of 0,82% copper has the same effect on achieving a pearlite microstructure as 1,74% manganese. The difference in the microstructures is that in the case of alloying with copper, a microstructure was obtained without the presence of carbides, in contrast to alloying with manganese, where a larger amount of separated carbides was observed. The combination of the addition of copper and silicon in the casting increases the security of the formation of microstructure without the presence of whitening, that is, the sensitivity of the casting to different wall thicknesses per cross-section is reduced and the possibility of metastable hardening in thinner sections is reduced. Silicon reduces the solubility of carbon in the solid and liquid phase, increases the diffusion of carbon at all temperatures, and acts as a graphitizer, reducing the tendency to form carbides. As other graphitizes, it separates into a solid phase during solidification and raises the solidification temperatures of the stable eutectic (Fe-C), and lowers the solidification temperatures of the metastable eutectic (Fe-Fe_3C). Carbide-forming elements (chromium, vanadium, etc.) do the opposite. The negative effect of copper comes to the fore in the case of efforts to obtain a ferrite microstructure, where a casting with a maximum of 0.03% copper must be provided to avoid the appearance of pearlite in the microstructure of the casting. It should be emphasized that only the addition of a highly pure copper alloy from a well-known manufacturer in foundries gives the desired effect [2,3]. Copper promotes the formation of graphite and it is a pearlite stabilizing element. It can have a grain refining effect [5].

Molybdenum is an alloying element that has mild carbide-forming properties. In the case of alloying with molybdenum over 0.3%, separated carbides rich in molybdenum are noticeable at the grain boundaries, where the effect is much more pronounced in thicker sections of the casting due to the occurrence of segregation. The important role of molybdenum is that it improves the hardenability of the casting during the heat treatment process, especially in combination with copper and nickel. In addition to improving hardenability, molybdenum affects the fragmentation of the graphite phase, affecting the increase in the number of eutectic cells, while reducing the effect of the variation of properties across the cross-section of the casting in the case of different wall thicknesses in the casting. The negative side of the presence of molybdenum as an alloying element is if you want to get a pearlite microstructure, and therefore it is mostly recommended to add molybdenum together with some of the elements that will prevent the formation of certain amounts of ferrite in the microstructure. Most often, these are combinations of molybdenum + chromium, molybdenum + copper, molybdenum + tin, or combinations with several alloying elements, such as molybdenum + copper + nickel and similar combinations. Taking into account the above facts, it can be said that molybdenum is one of the most versatile alloying elements used in iron-based castings [2]. Molybdenum hardens ferrite and strongly increases the hardenability of austenite. It is a carbide stabilizer (not as strong as chromium) and when in high enough concentrations, it can form carbides [6].

Chromium prevents graphitization and stabilizes primary, eutectic, and eutectoid carbides [7]. Chromium is one of the alloying elements that has the strongest potential for carbide formation. In the hardening process, like other carbide formers, it lowers the temperature of the stable eutectic and raises the temperature of the metastable eutectic. Since it lowers the hardening interval, it increases the tendency toward the formation of spalling in the microstructure of the casting. The maximum amount of chromium that is allowed (to achieve a cast structure without the presence of carbides) is 0.05%, although, in the case of a larger amount of manganese, this value is even lower due to the effect of manganese on the formation of carbides. Chromium carbides are highly resistant to heat treatment even after several hours of annealing. The tendency of chromium to form carbides affects the increase in the mechanical properties of the casting. The negative side is that these carbides mostly segregate along the grain boundaries [2].

3. EXPERIMENTAL PART

In the practical part of the work, the results of testing gray cast iron samples are presented in order to explain the influence of alloying elements on the microstructure of the tested samples. Four melts of gray cast iron were prepared, one melt from regular production and one with each of the alloying elements: copper, molybdenum, and chromium.

3.1 Chemical composition of the melts

Table 1 shows the chemical composition of sample 1, a sample from regular production.

Table 1.Chemical compositions for sample 1, sample from regular production

/	Chemical composition, wt. %							
	C	Si	Mn	Cr	Mo	Cu	P	S
Sample 1	3,585	1,945	0,717	0,104	0,012	0,195	0,057	0,077

Table 2 shows the chemical composition of sample 2, alloyed with copper.

Table 2. Chemical compositions for sample 2, alloyed with copper

/	Chemical composition, wt. %							
	C	Si	Mn	Cr	Mo	Cu	P	S
Sample 2	3,545	2,049	0,641	0,103	0,016	1,046	0,042	0,051

Table 3 shows the chemical composition of sample 3, alloyed with molybdenum.

Table 3. Chemical compositions for sample 3, alloyed with molybdenum

/	Chemical composition, wt. %							
	C	Si	Mn	Cr	Mo	Cu	P	S
Sample 3	3,623	1,926	0,689	0,115	0,830	0,200	0,046	0,089

Table 4 shows the chemical composition of sample 4, alloyed with chromium.

Table 4. Chemical compositions for sample 4, alloyed with chromium

/	Chemical composition, wt. %							
	C	Si	Mn	Cr	Mo	Cu	P	S
Sample 4	3,499	1,862	0,759	0,587	0,015	0,200	0,035	0,076

4. RESULTS

Metallographic samples were prepared for the microstructure analysis (optical microscopy) for three types of cast iron and one for samples from regular production. According to the photographs of the microstructure shown in the etched state, it was shown that the mentioned alloying elements are pearlitizers, that is, we confirmed the pearlite microstructure on each sample (figures of all samples etched by nital 2%, magnification 100x, and 200x).

Figure 1 shows the microstructure of sample 1, gray cast iron from regular production.

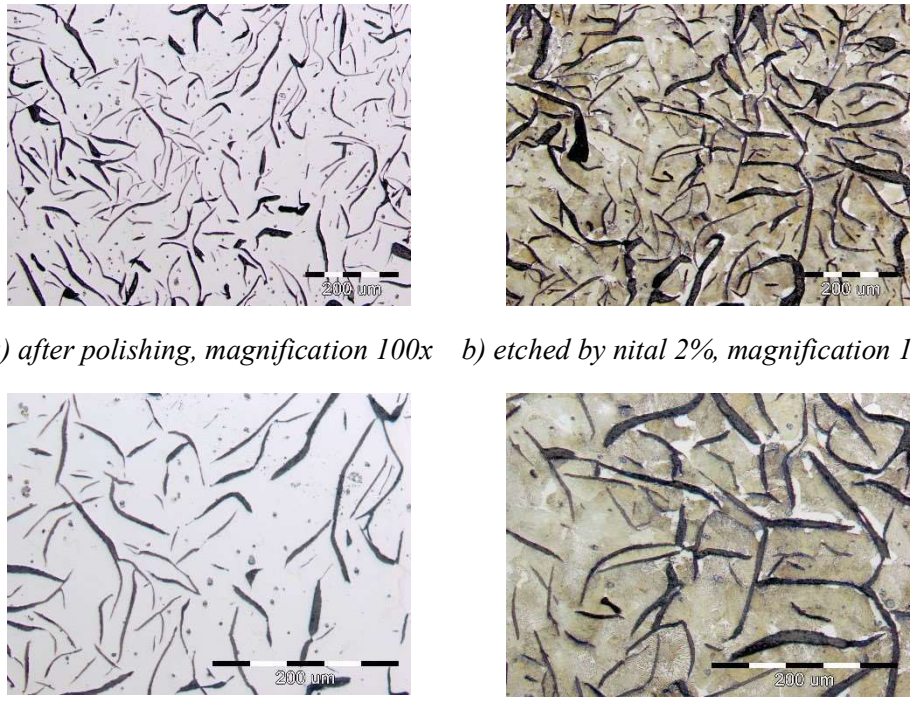

a) after polishing, magnification 100x *b) etched by nital 2%, magnification 100x*

c) *after polishing, magnification 200x* *d) etched by nital 2%, magnification 200x*

Figure 1. Microstructure of sample 1, gray cast iron from regular production

Figure 2 shows the microstructure of sample 2, gray cast iron alloyed with copper (1,046 wt %).

a) after polishing, magnification 100x *b) etched by nital 2%, magnification 100x*

c) *after polishing, magnification 200x* *d) etched by nital 2%, magnification 200x*

Figure 2. Microstructure of sample 2,gray cast iron alloyed with copper (1,046 wt, %)

Figure 3 shows the microstructure of sample 3, gray cast iron alloyed with molybdenum, (0,83 wt, %).

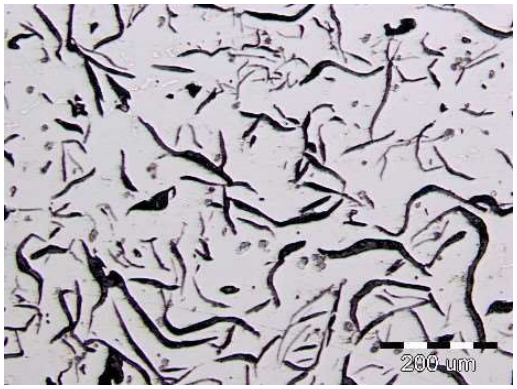

a) after polishing, magnification 100x *b) etched by nital 2%, magnification 100x*

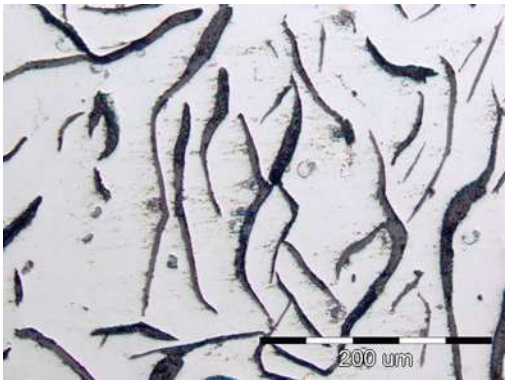

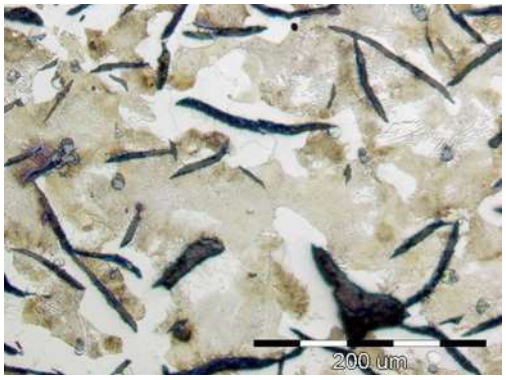

c) *after polishing, magnification 200x* *d) etched by nital 2%, magnification 200x*

Figure 3. Microstructure of sample 3,gray cast iron alloyed with molybdenum (0,830 wt %)

Figure 4 shows the microstructure of the sample 4, gray cast iron alloyed with chromium (0,587 wt, %).

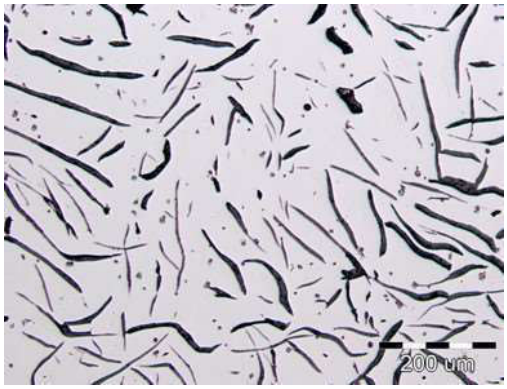

a) after polishing, magnification 100x

b) etched by nital 2%, magnification 100x

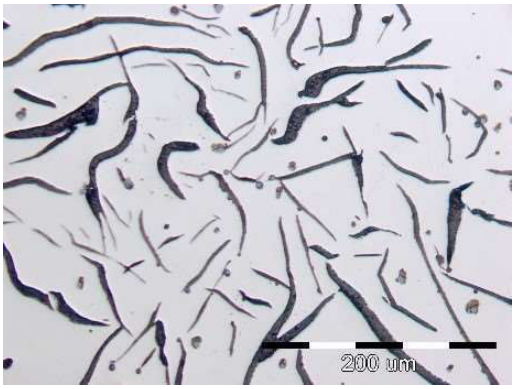

c) *after polishing, magnification 200x*

d) etched by nital 2%, magnification 200x

Figure 4. Microstructure of the sample 4, gray cast iron alloyed with chromium (0,587 wt, %)

5. CONCLUSIONS

Based on the microstructure, we can confirm that these alloying elements copper, molybdenum, and chromium are pearlitizers.

Chromium is also a carbide former, carbides mostly segregate along the grain boundaries (shown on the microstructure of sample 4, etched by nital 2%, magnification 200x).

In this case, copper is the biggest pearlitizer in combination with manganese(shown on the microstructure of sample 2, etched by nital 2%, magnification 100 x and 200x), where the least amount of ferrite is present.

Molybdenum is the mildest pearlitizer, which is why we have the most ferrite. Molybdenum creates fields (islands) of ferrite in the microstructure, creating a greater proportion of smaller graphite lamellae in the microstructure(shown on the microstructure of sample 3, etched by nital 2%, magnification 100 x and 200x). This is one of the reasons for the higher proportion of ferrite in the matrix.

6. REFERENCES

[1] Z. Glavaš, F. Unkić: Lijevanje željeznih metala, Metalurški fakultet, Sisak, Hrvatska, 2008
[2] Hasan Avdušinović: ŽELJEZNI LIV – knjiga I, Zenica, 2015
[3] J. Campbell: Complete casting handbook, University of Birgham, UK, 2011
[4] Effect on the Mechanical Properties of Gray Cast Iron with Variation of Copper and Molybdenum as Alloying Elements; International Journal of Engineering Research & Technology (IJERT) ISSN: 2278-0181 Vol. 3 Issue 5, May – 2014
[5] Overview of Alloying Elements and their Effects in Grey Iron

[6] https://old.foundrygate.com/upload/artigos/7ZmcrE9zgVGm6iKwHxeNNjbEdqt1.pdf, 6.3.2023
[7] Matthew Hasbrouck: The effects of molybdenum, chromium, and niobium on gray iron for brake rotor applications, Michigan Technological University, 2021
[8] Savez ljevača Hrvatske: Ljevački priručnik, Zagreb, 1985.

CHARACTERISTICS OF THE MICROSTRUCTURE AND GRAIN SIZE OF S690QL STEEL IN THE HARDENED AND TEMPERED STATE

Mirsada Oruč, Aida Imamović, Almaida Gigović-Gekić
University of Zenica, Faculty of Metallurgy and Technology
Zenica, B&H

Milenko Rimac
Maneco Kakanj
Kakanj, B&H

Keywords: steel S690 QL, grain size, microstructure

ABSTRACT
Steel S690 QL is a high-strength quenched and tempered, fine-grained structural steel with a minimum yield strength of R_{eH} of 690 MPa and with guaranteed toughness (Charpy) for rolled plates with a thickness of 3 to 50 mm. This paper presents the examination and analysis of the microstructure and grain size results after quenching and tempering. Also, the aim of the examination is to consider the segments of the technological process and its influence on the physical and metallurgical characteristics, primarily on the microstructure and grain size, which affect the tensile characteristics and toughness at low temperatures.

1. INTRODUCTION

The high-strength steels are developed mainly to achieve the highest possible yield stress and tensile strength by reducing the load-bearing sections and the total cost of materials [1]. The steel S690 QL is a high-strength structural steel produced in accordance with the EN 10025-6 standard. It is heat treated by quenching and tempering and has good bending and welding properties. According to the mark, this is structural steel, (S) with a minimum yield strength of 690 MPa, quenched and tempered (Q), and toughness tested at low temperature (L) [2]. This steel belongs to the group of quality structural steels, so it is recommended that they have a certain content of elements for refining the microstructure as aluminium for example, especially the grain size. Standard EN 10025-6:2004+A1:2009 prescribes that the minimum soluble aluminium content should be 0.010% if the total aluminium content is 0,013%. According to the EN 10025-1 standard, if the content of niobium is 0,02%, titanium 0,02%, and vanadium 0,003%, the carbon content is limited to 0,18% for plates with a thickness of 30 mm [3].

2. STEEL S690QL

Hot-rolled plates made of HSLA steel (S690 QL) in the hardened and tempered state are used for testing. According to the standard EN 10025-6, the technical requirements for delivery prescribe the chemical composition, tensile characteristics, and 30J toughness at the temperature of -40°C in the longitudinal section, and 27 J in the cross-section. Only the toughness in cross-section in the values of 27 J is prescribed in the document „Technical data sheet Acroni“. The values of the mechanical properties for S690 QL steel plate are given in Table 1 for thicknesses greater than 3 mm and less than 50 mm. The values for the

yield stress and tensile strength depend on the thickness of the plates. Because the thickness of the tested samples was 10 and 40 mm, Table 1 presented only values for this thickness.

Table 1. Mechanical properties of the steel S690 QL according to standard EN 10025-6

Yield stress R_{eH}, MPa	Tensile strength R_m, MPa	Elongation %	Toughness -40°C, J
Min. 690	770 - 940	14	30

The chemical composition, processing technology, and final heat treatment favour the formation of a fine-grained microstructure, i.e. the microstructure typical for the hardened and tempered state. The EN 10025-6:2004+A1:2009 standard does not prescribe the appearance of the microstructure, nor the grain size, for these plate thicknesses. However, a complete evaluation of the quality of the produced plates, and the examination of the microstructure and grain size are of great importance. Testing and analysis of the toughness were carried out at a temperature of - 40°C, from 10 plates of different thicknesses.

3. EXSPERIMENTAL PART

3.1 Chemical analysis

The chemical analysis of the produced melts is given in Table 2, together with the standard (according to the standard EN 10025-6) prescribed maximum content of elements.

Table 2. Chemical analysis of melts

Melt	The chemical composition, %													
	C	Si	Mn	P	S	Cr	Cu	Ni	Al	Mo	Ti	Nb	N	B
Standard Max	0.22	0.86	1.80	0.025	0.012	1.60	0.55	2.10	*	0.74	0.07	0.07	0.016	0.006
T-1	0.144	0.27	1.20	0.007	0.0005	0.34	0.24	0.208	0.074	0.19	0.017	0.024	0.0050	0.0032
T-2	0.148	0.34	1.40	0.008	0.0010	0.54	0.22	0.255	0.052	0.30	0.021	0.025	0.0061	0.0032
T-3	0.149	0.30	1.14	0.005	0.0001	0.32	0.20	0.207	0.055	0.16	0.017	0.023	0.0055	0.0032
T-4	0.148	0.27	1.13	0.005	0.0005	0.36	0.24	0.210	0.048	0.17	0.015	0.022	0.0052	0.0032
T-5	0.144	0.28	1.11	0.007	0.0005	0.31	0.25	0.197	0.080	0.18	0.015	0.023	0.0068	0.0032

**According to the standard, the aluminum content is not specified because it interacts with the presence of nitrogen*

The chemical composition of all melts is in accordance with EN 10025-6 and DIN EN 10025-1, for steel S690 QL and for the main elements, as well as for additional requirements regarding the regulation of nitrogen content and elements that translate it into stable microconstituents.

3.2 Hot rolling and heat treatment

Hot rolling was performed according to standard rolling technology. In the technological process of hot rolling, the slabs are placed in a furnace that is heated to a temperature of approx. 1300°C for one hour. In certain cases due to occasional disturbances in the technological process, that time is extended, which can certainly affect the structure and mechanical properties, especially the grain size. Also, the temperature at the end of rolling, which can vary, can have an influence on the microstructure and grain size. All the mentioned can produce certain inhomogeneities in the microstructure, especially in the properties in the longitudinal and cross-section. The heat treatment by hardening and tempering is carried out according to a standard technological procedure in accordance with the procedures carried out for HSLA structural steels, and they are aligned with the

parameters that ensure the formation of a fine improved structure, which allows the prescribed tensile characteristics and toughness to be achieved at low temperatures.
Figure 1 shows ten heat-treated samples for microstructure and grain size testing. The samples are 100x200mm in size and 10mm to 40mm thick. The samples were cut from the plates produced from 5 different melts. The direction of rolling is marked with an arrow on the plates and the sample mark is written too. It is connected to the plate mark and the number of the melt from which it was produced. The aim of the examination is to consider the segments of the technological process and its influence on the physical and metallurgical characteristics, primarily on the microstructure and grain size, which affect the tensile characteristics and toughness at low temperatures.

Figure 1. Samples for testing microstructure and grain size taken from melts from T-1 to T-5

3.3. Testing
3.3.1 Microstructure
Analysis of the microstructure was performed in the metallographic laboratory of the Institute „Kemal Kapetanović“ (IKK), on a longitudinal section after etching in 2% HNO_3, on an Olympus PMG 3 optical microscope according to the ASTM E 407-07 standard. The microstructure of all samples is tempered fine grain microstructure, Figure 2. The microstructure on the longitudinal section is in the form of strips, which is enhanced by the presence of elements that are prone to the formation of segregations, and the technological process of rolling itself, and certain thermal processes in the production technology, also have an influence. Reducing anisotropy in hot-rolled plates is an important metallurgical task and during production, it is attempted to make plates with as much uniformity of microstructure as possible on the longitudinal and cross-section, which is especially important for toughness at low temperatures.

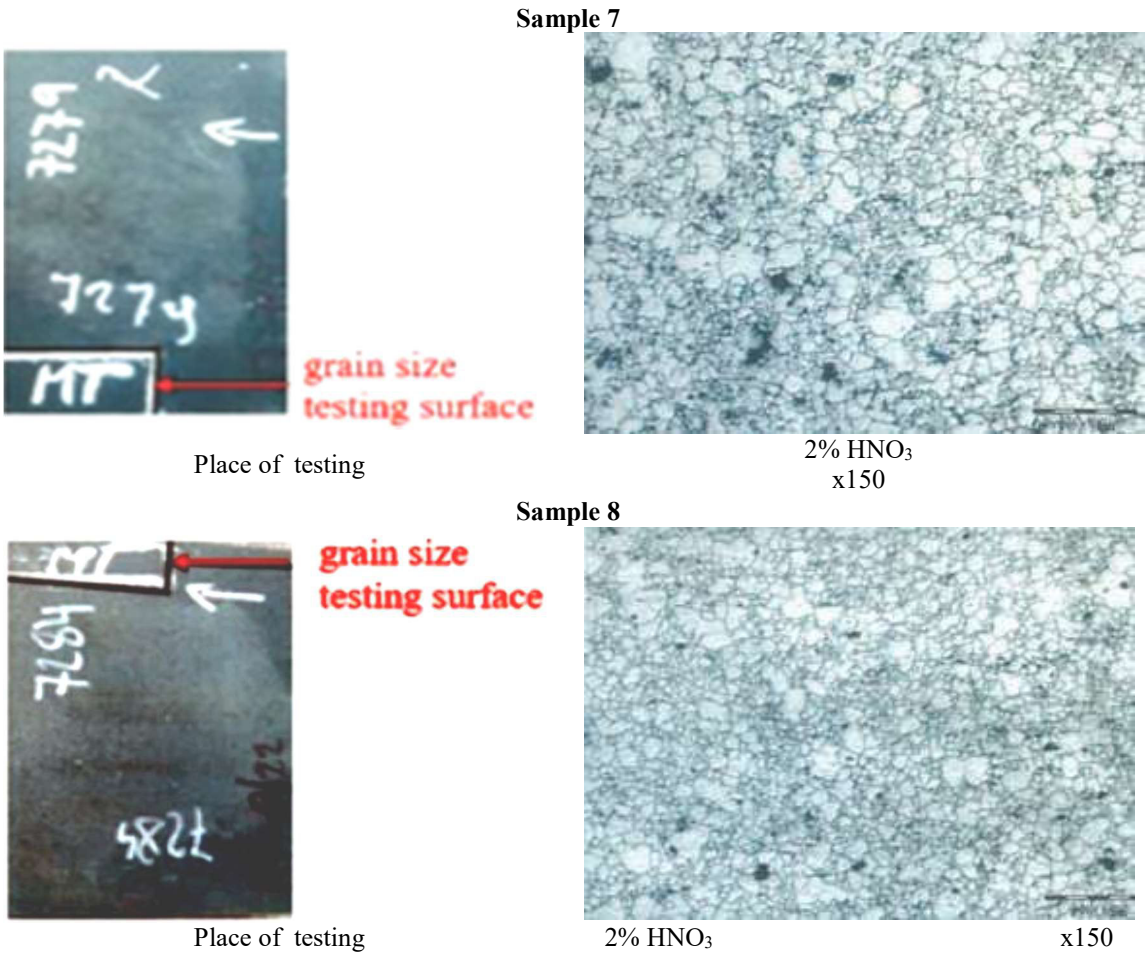

Figure 2. The appearance of grain size for individual melt samples

3.3.2 Grain size

The grain size was tested on the IKK according to the ASTM E 412-Plate13 standard. The results of testing the grain size and thickness of the test plates are given in Table 3 and in the diagram in Figure 3. The maximum, minimum, and average sizes are shown. Because the grain borders were not visible, the samples (before testing) were heated to the austenitization temperature of 860 °C, keep for 60 min, and cooled in water.

Table 3. The grain size of samples for steel S690 QL

Sample	Thickness D, mm	Grain size		
		Average grain size, P	Maximum grain size, D_{max}	Minimum grain size, D_{min}
1	25	7.5	6.0	10.5
2	30	7.0	5.5	9.5
3	25	7.5	5.5	10.5
4	20	7.0	5.5	10.0
5	20	7.5	5.5	9.5
6	15	7.0	5.5	10.0
7	25	7.0	5.5	9.5
8	25	7.5	5.5	9.5
9	25	7.0	5.5	9.5
10	25	7.5	5.5	10.0

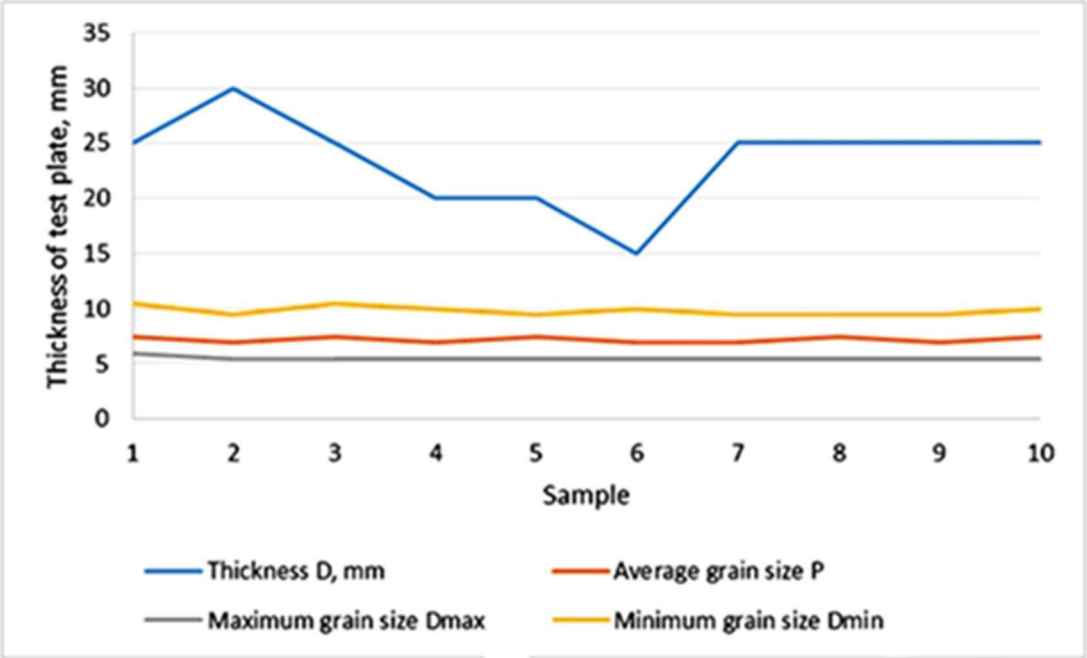

Figure 3. Grain size in accordance with plate thickness

Considering that standards EN 10025-6 [4,5] and DIN EN 10025-1 [3] for plates of these thicknesses, made of steel S690 QL, do not provide prescribed values for grain size and microstructure, the assessment was made based on comparing the results between individual plates. The analysis of the grain size for all samples showed that the results were uneven, ranging from a minimum size of 10.5 to a maximum size of 5.5. The Microstructure of samples after the heat treatment was generally fine-grained but an inhomogeneous structure with maximum or minimum grain size was noticed in the same places. It should be analysed in some future experiments. Some minor differences in grain size that exist between individual plate samples cannot be considered as a rule, which can be seen in the photomicrographs of characteristic samples 7 and 8 in Figure 2.

In general, it could be said that all the tested plates have a fine-grained tempered microstructure with an average grain size of 7 and 7.5. In all slab samples, minor inhomogeneities are visible due to the presence of individual or small groups of larger grains up to 5 in size, but no difference in grain size was observed in slabs of different thicknesses.

4. CONCLUSIONS

By analysing the chemical composition of steel S690QL for all 5 melts, it was confirmed that the chemical composition in accordance with standard EN 10025-6 and DIN EN 10025-1 both according to the conditions for the main elements, as well as for additional requirements regarding the regulation of the nitrogen content and the elements that translate it into a stable microconstituent. All produced melts are made with a high degree of purity in terms of sulphur and phosphorus content. The grain size was measured for all plates to determine the degree of homogeneity. All tested plates have a fine-grained structure with an average grain size of 7 to 7.5. The minimum measured grain size was 10.5 and the maximum size of 5.5. The minimum and maximum sizes refer to individuals or groups of grains. This means that there is inhomogeneity in microstructure i.e. the presence of an individual or smaller groups of larger (5.5) and finer grains (10.5). It can be assumed that such grains are associated with an uneven distribution of certain elements, i.e. insufficient

concentration in micro surfaces (especially those that affect the grain size through the precipitation of their compounds). The heat treatment by quenching and tempering on the test samples indicates the presence of a fine-tempered microstructure.

5. REFERENCES

[1] Svojstva i primjena visokočvrstih čelika – NSK
[2] https://zir.nsk.hr › object › unin:1986 › preview [december 2022],
[3] Oruč M., Begovac F., Vitez, I., Sunulahpašić R.: Čelik i čelični liv, Podjela i označavanje, Fakultet za metalurgiju i materijale, Univerzitet u Zenici, Zenica, 2008.,
[4] DIN EN 10025-1:2005,
[5] EN 10025-6 (EN 10025-6:2019),
[6] EN 10025-6 S690QL celik 1 - Steel Material Supplier,
[7] https://gangsteel.com › en-10025-6-s690ql-celik-1, [december 2022].

PROPERTIES OF AUSTENITE STAINLESS STEEL X8CrNiS18-9 MICROALLOYED WITH TELLURIUM

Derviš Mujagić, Aida Imamović
University of Zenica, Faculty of Metallurgy and Technology
Zenica, B&H

Mustafa Hadžalić
University of Zenica, Institute ″Kemal Kapetanović″
Zenica, B&H

Keywords: tellurium, machinability, corrosion resistance, mechanical properties

ABSTRACT
More recently modified stainless steels have been used to produce various structural elements that work in complex operating conditions. Stainless steel X8CrNiS18-9 (standard EN 10088-3: 2005) is the most commonly used austenitic stainless steel due to its good machinability. This steel has high mechanical and working properties thanks to complex alloying, primarily with the elements such as chromium and nickel. The content of sulphur present in the steel from 0.15 to 0.35% improves machinability. However, sulphur at the same time decreases the mechanical properties, particularly toughness. The addition of sulphur, which is the cheapest available additive for free machining, will impair not only the transverse strength and toughness but also the corrosion resistance.
The aim of this work is to determine the influence of tellurium on the machinability, corrosion resistance and mechanical properties of the mentioned steel.

1. INTRODUCTION

Tellurium in the periodic table of elements belongs to the group consisting of oxygen and sulphur [1].
It appears in the form of telluride in steel. Due to the extremely low melting point of iron telluride, Figure 1, (1187 K – 914 °C), which is precipitated in the form of a film at the boundaries of the primary grains, tellurium must be bound to manganese [2, 3].
The presence of tellurium in steel leads to the formation of globular sulphide inclusions, which at the same time favorably affect the machinability of steel since its presence in steel reduces the energy required to separate the material in the shear zone during cutting. This is due to the low melting point of manganese telluride (1428 K – 1155 °C) [3], which is lower than the melting point of manganese sulphide in Figure 2 [2], and the very high chemical surface activity of tellurium.
The addition of tellurium to improve the cut surface is due to the lubrication ability of manganese telluride. In sulphur alloy steels, tellurium always occurs as telluride because it is minimally soluble in manganese sulphide (0.01%). Tellurium occurs in steels in inclusions in the form of manganese (sulpho) telluride ($MnTe_xS_{(1-x)}$), as a white envelope of manganese sulphide (Figure 3), or in the form of globular inclusions, which are at the base of manganese sulphide or manganese silicate. The formation pattern depends on the tellurium content of the steel. It is necessary to consider the ratio Mn:S = 4 and Mn:Te = 20. Otherwise, during hot processing, characteristic cracks occur along the edges of the intermediate products [1].

Tellurium forms manganese telluride (MnTe) inclusions and is apparently more effective than sulphur for machinability of austenitic stainless steels. As well as selenium, it also promotes globularization and expansion of sulphide inclusions. However, tellurium causes problems with hot processing of austenitic stainless steels and has not been used for commercial purposes [4].

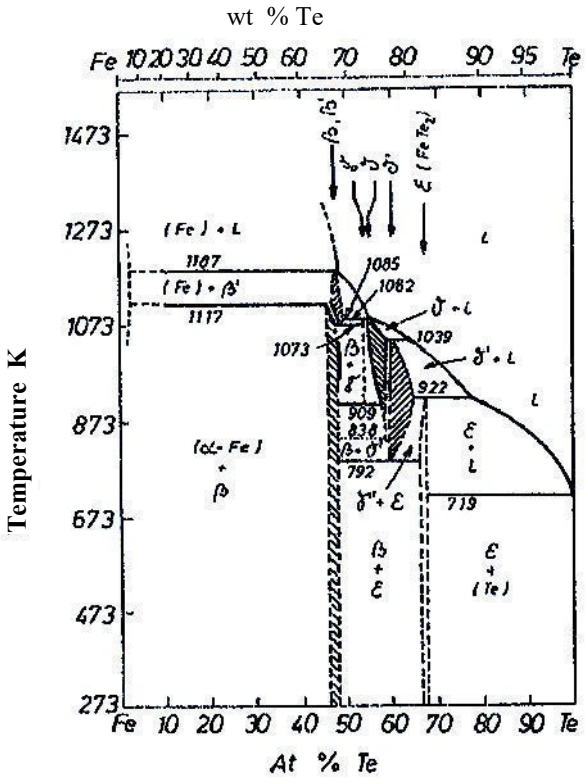

Figure 1. Fe – Te binary phase diagram [2,3]

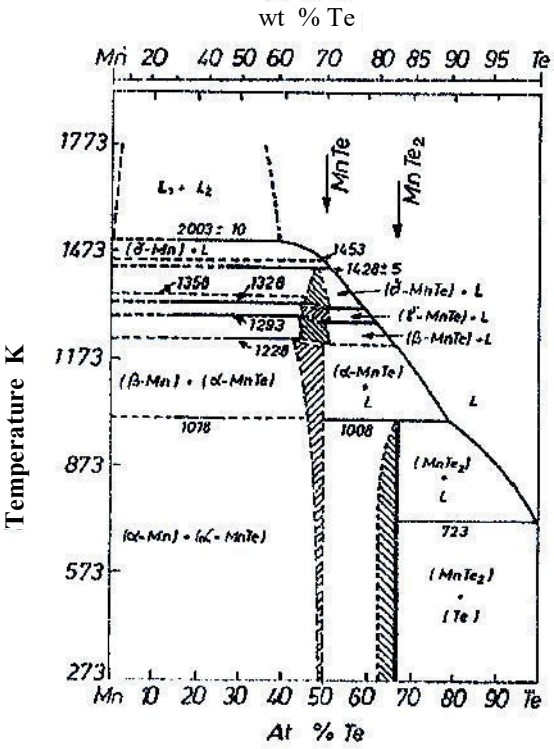

Figure 2. Mn – Te binary phase diagram [2,3]

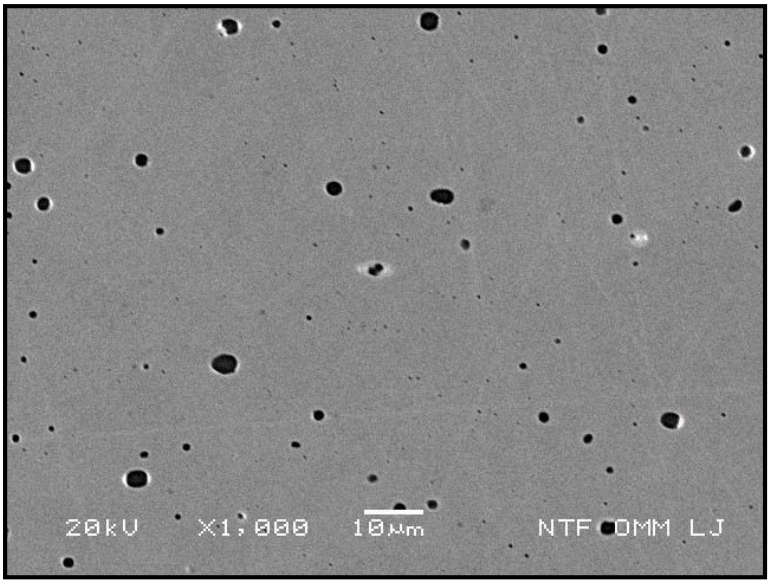

Figure 3. Tellurium, as a white envelope around manganese sulphide inclusions [5]

2. EXPERIMENTAL RESEARCH AND TEST RESULTS

The aim of the research was to examine the influence of the tellurium on machinability, corrosion resistance and mechanical properties of austenitic stainless steel X8CrNiS18-9

with and without alloying with tellurium. Production of austenitic stainless steel X8CrNiS18-9 was performed in a vacuum induction furnace at the Institute "Kemal Kapetanović" in Zenica. The ingots (Figure 4), were processed by forging, hot rolling and heat treatment.

Figure 4. Ingot after the solidification process [5]

The chemical analysis of the two melt variants is given in Table 1.

Table 1. Chemical analysis of melt variants [5]

Melt variants	Chemical composition (%)							
	C	Si	Mn	P	S	Cr	Ni	Te
Without alloying elements	0,03	0,42	0,61	0,021	0,18	18,3	9,4	–
Alloyed with Te	0,05	0,40	0,80	0,010	0,16	18,9	9,3	0,033

In preliminary research is planned that after primary processing (approx ϕ 50 mm) samples will be tested by cutting forces, in order to determine to what extent the modification of the chemical composition affects the machinability of this material, and corrosion resistance. Of particular importance is to determine the behavior of nonmetallic inclusions in the process of developing structural parts and in a later exploitation. For this reason it is planned to simulation processing of austenitic stainless steel by plastic processing and by forging and rolling with two different degrees of processing. After that, the samples will be taken and laboratory testing of mechanical properties will be performed on them.

2.1. Machinability

In the Laboratory for metal cutting and machine tools of the Faculty of Mechanical Engineering in Zenica, the machinability test of the ingots was done, based on the estimation of parameters of the cutting force. Testing on both samples was performed under the same treatment regime. The results of the cutting force tests (individual forces F_x, F_y, and F_z as well as the resultant force F_R) are given in Table 2.

Table 2. The results of the cutting force tests [5]

Melt variants	Cutting force (N)			The resultant force F_R (N)
	Component F_x	Component F_y	Component F_z	
Without alloying elements	180	218	361	458,52
Alloyed with Te	154	200	317	405,22

The melt micro-alloyed with tellurium has significantly lower resultant cutting force and accordingly significantly better machinability compared to melt without alloying elements.

2.2. Corrosion resistance

General corrosion tests for X8CrNiS18-9 stainless steel samples were performed on a potentiostat/galvanostat PAR 263A-2 device in an electrochemical cell prescribed by ASTM G5-94. The samples were tested in a solution of 1% HCl at room temperature. The solution was previously deaerated with argon for 30 minutes as provided by ASTM G5-94. To test the general corrosion of the X8CrNiS18-9 stainless steel samples, the Tafel Directional Extrapolation Method described by ASTM G3-89 was used.
The results of testing the general corrosion rate of these samples are given in Table 3.

Table 3. Test results for general corrosion rate [5]

Melt variants	Corrosion current, I_{Corr} (μA)	Corrosion rate, v_{Corr} (mm/godinu)	Open Circuit Potential, $E_{(I=0)}$ (mV)
Without alloying elements	4,266	4,955	-475,320
Alloyed with Te	8,949	10,390	-504,517

The melt micro-alloyed with tellurium has a significantly worse corrosion rate compared to melt without alloying elements.

2.3. Mechanical properties

After the rolling process was completed, specimens were prepared for mechanical testing (tensile properties and impact toughness testing). The tests were performed at the Mechanical Laboratory of the Institute "Kemal Kapetanović" in Zenica.
The results of the tensile properties and impact toughness testing are given in Table 4.

Table 4. Test results of tensile properties and impact toughness in rolled condition [5]

Melt variants	Conventional yield strength $R_{p0,2}$ (N/mm^2)	Tensile strength R_m (N/mm^2)	Elongation A (%)	Reduction Z (%)	Impact toughness (J) KV 300 J	
					Individually (J)	Average (J)
Without alloying elements	349	670	50,0	70	60	57
					56	
					56	
Alloyed with Te	314	635	46,5	59	58	62
					69	
					60	

The melt micro-alloyed with tellurium has slightly worse tensile strength, but also slightly better impact toughness value compared to melt without alloying elements.

3. CONCLUSIONS

The aim of the research was to determine the effects of tellurium in austenitic stainless steel with the addition of sulphur X8CrNiS18-9 on the machinability, corrosion resistance and mechanical properties of the mentioned steel.

After all the tests performed, it is possible to draw the following conclusions:

- Nonmetallic inclusions of manganese sulphide types, in combination with tellurium, can be translated into a suitable form, whose shape is more spherical. These inclusions are more effective than pure sulphide in free-machining austenitic stainless steels, while effectively acting as shaving breakers and thus they improve machinability.
- With regard to the effect of tellurium microalloying on the corrosion rate of austenitic stainless steel X8CrNiS18-9, it can be concluded that melt alloyed with tellurium shows a marked increase in corrosion rate compared to the melt without alloying additives.
- But, on the other hand, all values of tensile properties (tensile strength, conventional yield strength, elongation and reduction), as well as impact toughness, are within the limits prescribed by the relevant standard for the material specified.

4. REFERENCES

[1] K. Hribar: ″Vpliv kovinskih in nekovinskih dodatkov na obliko vključkov in tehnološke lastnosti jekel″, Magistrsko delo, Jesenice, 1981

[2] W. G. Moffat.: ″The Handbook of Binary Phase Diagrams″, Copright © 1978, by the General Electric Company;

[3] D. Bhattacharya, D. T. Quinto: Metallurgical Transactions, vol. 11 A, june 1980, pp. 919 – 934

[4] http://www.cartech.com/techarticles.aspx?id=1604 (april 2020)

[5] D. Mujagić – "Doprinos istraživanju uticaja mikrolegiranja sa borom, cirkonijem i telurom na osobine austeninog nehrđajućeg čelika sa dodatkom sumpora X8CrNiS18-9", doktorska disertacija, Univerzitet u Zenici, Metalurško – tehnološki fakultet, Zenica, 2017

MICROSTRUCTURAL DEGRADATION OF BOILER HEADERS STEELS UNDER LONG TERM EXPOSURE TO HIGH TEMPERATURE

Armin Husika
Termoelektrana „Kakanj“
Kakanj, B&H

Belma Fakić
University of Zenica, Institute “Kemal Kapetanović”
Zenica, B&H

Milenko Rimac
Maneco Kakanj
Kakanj, B&H

Keywords: headers, testing, structure, hardness, condition rating

ABSTRACT
This paper describes the process of degradation of the structure of the inlet header of the intermediate reheater (MPr) 2 input header at the boiler of Unit 7 of the Thermal Power Plant Kakanj, determined on the basis of tests of replicas and hardness at characteristic places of the header. Headers, with minor delays, have been in continuous operation since 1988. Hardness was tested at replica pickup sites, on the basis of which the correlation between structure degradation and hardness drop resulting from exploitation during the long-term high-temperature operation was estimated.
The change in hardness is certainly one of the most reliable indicators of the structure degradation degree, which is directly related to the service life of the installed components. The subject of the test was the inlet header of the intermediate heater made of low alloy steel 15Mo3, consisting of ferrite-pearlite microstructure, and having calculated values for the allowed hardness in the range from 133 to 176 HB. The structure degradation assessment was performed according to VGB-S-517 by comparing the microstructure of the replicates with the corresponding standards, and the hardness was tested according to ASTM A 956/1996-method A.
The examination has shown that in the exploitation life achieved so far, there has been a partial or complete degradation of the structure, which is reflected in the initial and delayed coagulation of the perlite lamellae (Grades 2a and 3a). The hardness at the test sites is at or below the lower than the prescribed 133HB. The tests confirmed that there is a good correlation between the degree of degradation of the structure and the hardness, which can be used in assessing the condition and planning the extent of testing on critical components.

1. INTRODUCTION

As part of the regular tests of critical components of the headers and steam lines on boiler unit 7, limited NDT tests were carried out. The headers have been in continuous operation from 1988 to 30th April 2019 [1] with minor downtime and partial reconstructions in operation for a total of 136.930 hours, which exceeds the projected service life of approx. 100.000 hours.

Assessments of the condition of the materials were made based on the results of tests performed on the condition of the materials in accordance with applicable standards and regulations and primarily based on the assessment of the material structure degradation of the headers and the decrease in hardness in the period from commissioning to the tests carried out as part of this work. Processes of structural degradation and changes in hardness are certainly the most reliable indicators, which are directly related to the service life of the installed components. A schematic view of the section of the boiler of block 7, with sections of the superheater and reheated is given in Figure 1 [1].

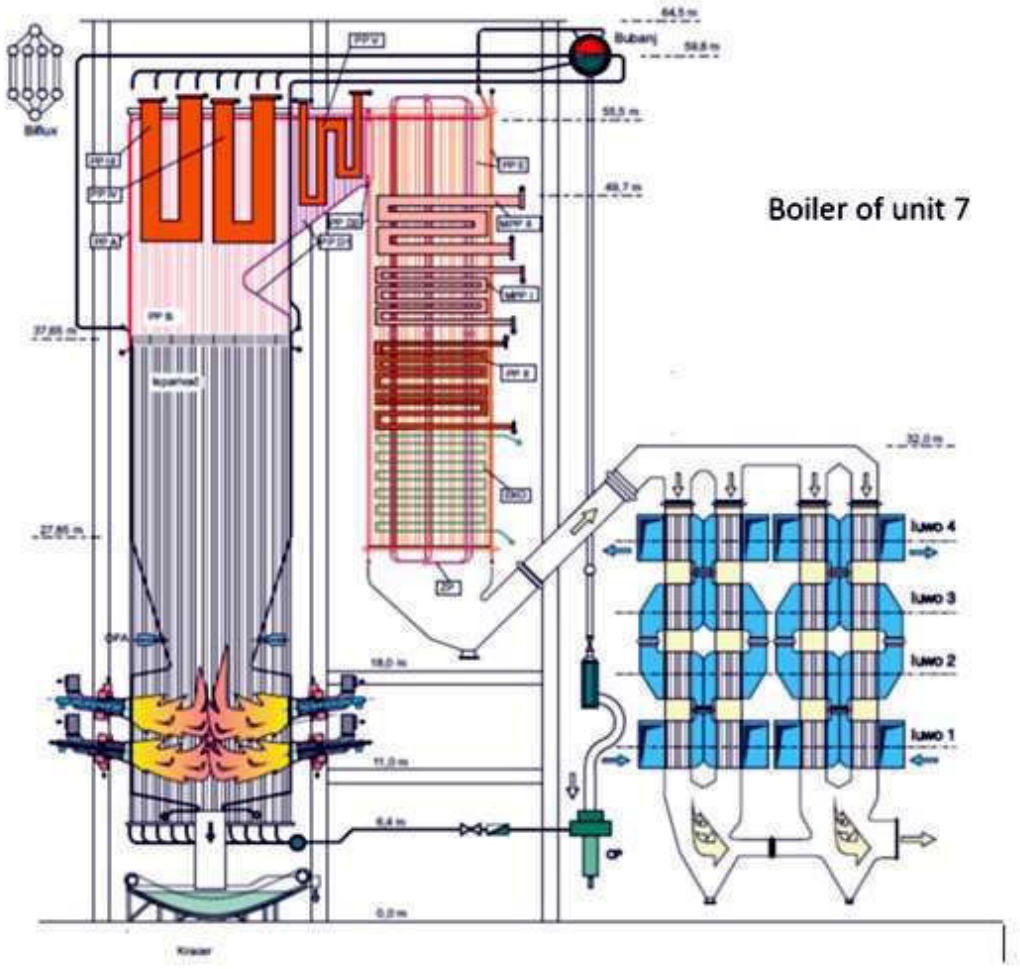

Figure 1. Schematic representation of the section of the boiler of unit 7[1]

2. MATERIALS AND METHODS

2.1. Materials

The inlet headers of the reheated MPr 2 of boiler unit 7, dimensions Ø508x25 mm (hereafter MPr 2 header), are made of low-alloy steel with the addition of molybdenum, marking 15Mo3 according to the standard DIN 17175 [2]. The prescribed chemical composition and mechanical properties are given in Table 1.

Table1. Chemical composition and mechanical properties of 15Mo3 steel according to the DIN 17175 standard

Steel	Standard	Chemical composition, mass %						R_m	Hardness
		C	Si	Mn	P, max	S, max.	Mo	MPa	HB
15Mo3	DIN17175	0,12 - 0,20	0,10 - 0,35	0,40 - 0,80	0,035	0,035	0,25 - 0,35	450 - 690	133-176*

**The hardness is calculated from the tensile strength according to the DIN 50150 standard because No hardness is prescribed [3]*

The initial microstructure of steel 15Mo3 in the normalized state consists of ferrite and a smaller proportion of pearlite and during exploitation, it changes due to long-term work at elevated temperatures. In 15Mo3 steel, structural degradation begins with the breakdown of pearlite lamellae and gradual coagulation of the initial pearlite lamellar structure, followed by gradual carbide coarsening. These processes mainly consist of changes in the carbide structure of the steel. The addition of molybdenum affects the stabilization of the carbide phase, and very stable molybdenum carbides have a favorable effect on slowing down the creep process. During exploitation, coagulation and solidification of carbides occur, which separate along the grain boundaries, which leads to structural degradation and a decrease in mechanical properties. These processes take place in the stationary creep region and are noticed by observation of the microstructure from replicas on a light microscope (further LM). Degradation processes in the stationary region dominantly affect the creeping flow in the tertiary phase, in which the formation of microcracks and fracture occurs.

In the main, in low-alloyed ferritic-pearlite steels, under conditions of elevated temperatures, the most obvious process is the degradation of cementite Fe_3C, which in the initial degradation process changes the morphology, but not the composition. The composition of the initial mixture of cementite and M_2C-type carbides in the matrix develop into a more complex carbide conglomeration that includes M_7C_3, $M_{23}C_6$, and finally M_6C carbides. In addition to changes in carbide geometry, other structural changes occur at high temperatures, depending on the temperature, such as recrystallization, grain growth, the evolution of the dislocation structure, and oxidation and decarburization.

In the research of Salonen and Auerkari [4], experimental tests on and scanning electron microscope (SEM), the mechanism of degradation of the structure of 15Mo3 steel after treatment at high temperatures in simulated exploitation conditions was determined. From these investigations, microstructures LM are shown in Figures 2a, b, c, d, and in Figure 3a, b with SEM, which indicate the degree of degradation of 15Mo3 steel according to the modified VGB-S-517 scale [4,5].

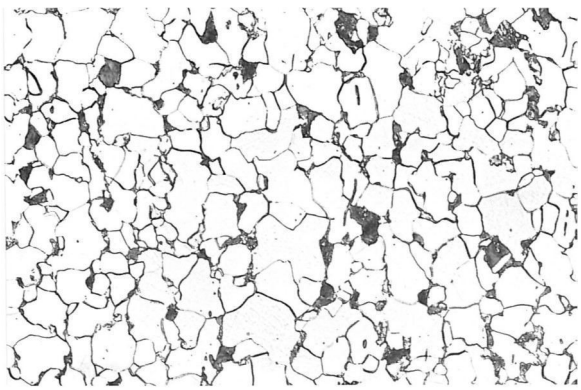

a) Initial ferrite-pearlite structure

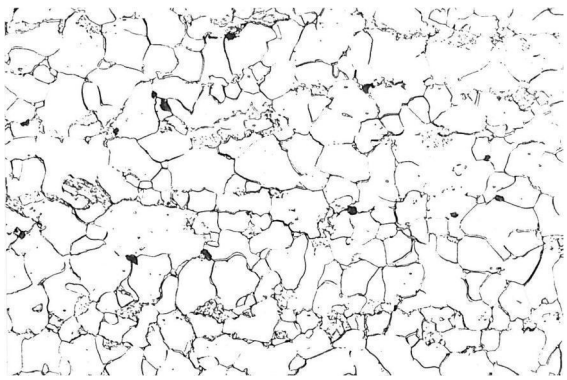

b) Coagulated carbides in pearlite

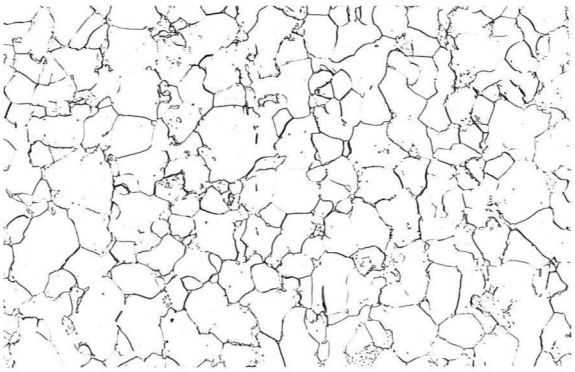

c) Coarse coagulated carbides dispersed in the matrix and degraded pearlite grains

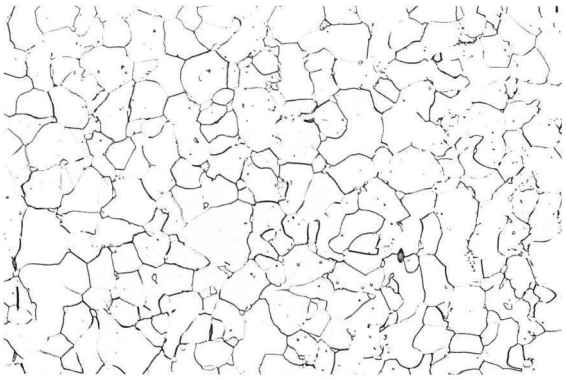

d) Coarse coagulated carbides and completely degraded pearlite grains

Figure 2. Degradation process microstructure of 15Mo3 steel

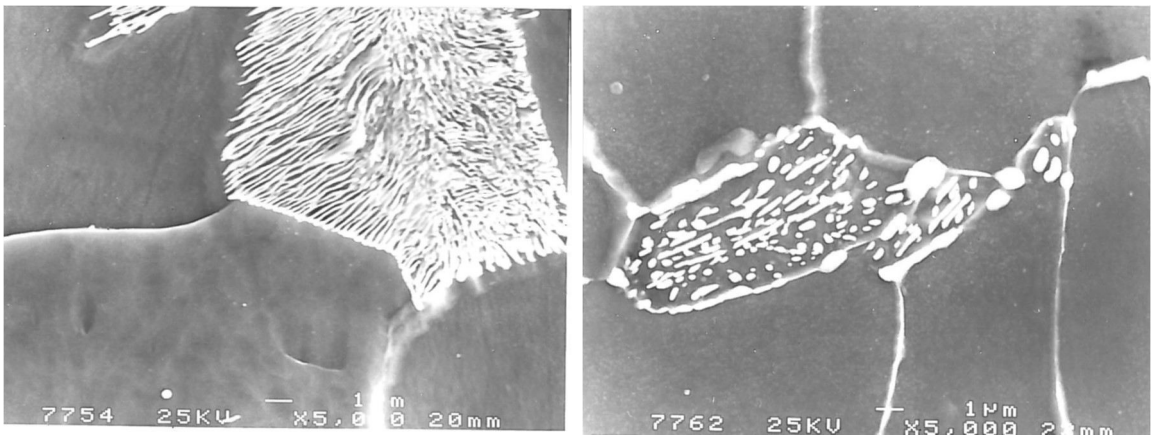

a) b)

Figure 3. Initial ferrite-pearlite structure (a) and coagulated carbides in degraded pearlite grains (b)

2.2. Methods

At critical points of the reheater MPr 2, non-destructive testing (NDT) was performed. In particular, the structure was examined using the method of taking replicas (R) at identified critical points of headers and welded joints (FW). For a more exact assessment of the state of the material, the hardness was also tested in the same places, so it was possible to compare the degradation of the structure and the corresponding decrease in hardness. The test results were compared with the ratings and results of earlier tests (tests performed at the same places in previous tests) and the measured hardness values according to DIN 50150 [2].

3. EXAMINATION

3.1 Microstructure

The degradation degree of 15Mo3 steel microstructure in the MPr 2 header was tested according to the ASTM E 407-07 [6] and BAS ISO 3057:1998 standards [7]. The position of the replicas is marked on the scheme of the MPr 2 header in Figure 4 where the tested parts of the header are shown and photographed. The assessment of the degradation degree of the microstructure was carried out according to the regulations of VGB-S-517, by comparing it with standards valid for similar steel 14MoV6. Figures 5a, b, c, d, e, and f show the microstructures of the tested replicas with magnifications of x150 and x750. The replicas marked R1 and R2 have an initial degradation degree of microstructure, with

partially coagulated carbides in the boundaries of the pearlite grains (Figures 5a, b, and 5e, f), and were graded according to the VGB-S-517 scale with grade 2a. The structure of replica R3 was rated 3a, and in the microstructure, increased degradation of pearlite lamellae and coarsening of carbides were noted in comparison to replicas R1 and R2 (Figures 5d, and c).

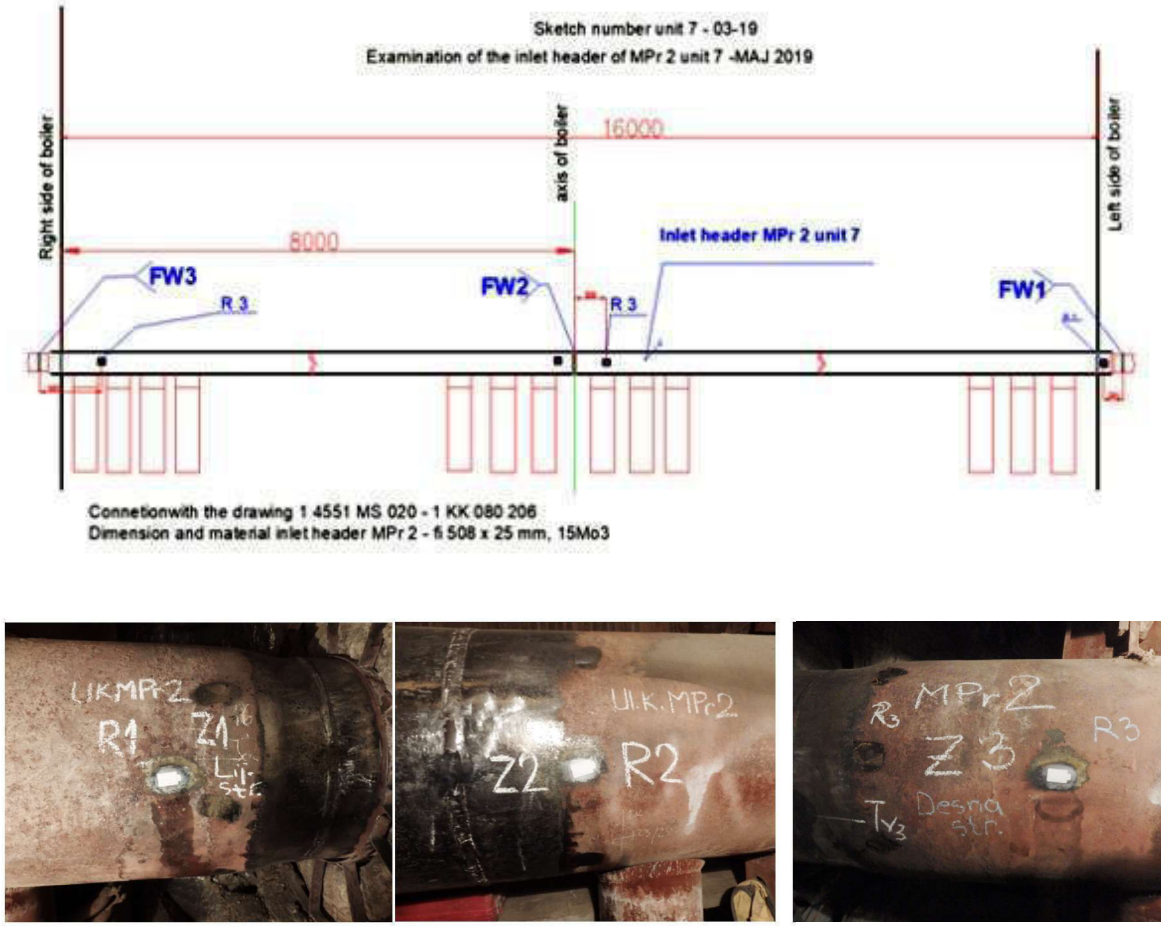

Figure 4. The position of the replicas on the header MPr 2 and photos taken from the investigated places

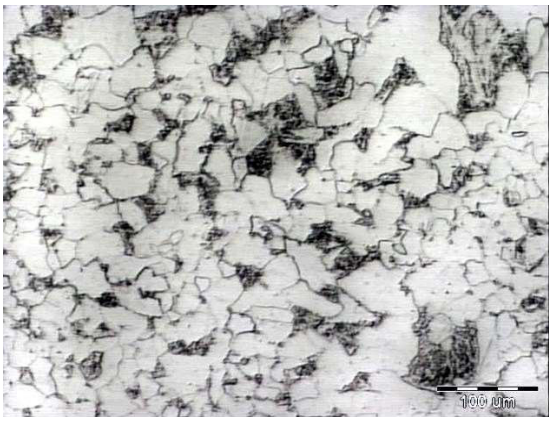

a) Microstructure of the replica R1 (2b)x150

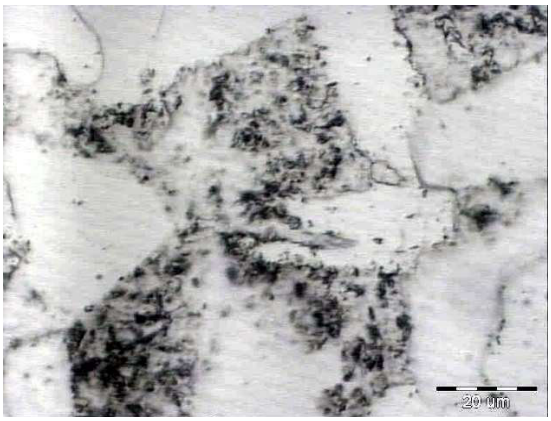

b) Microstructure of the replica R1 (2b)x750

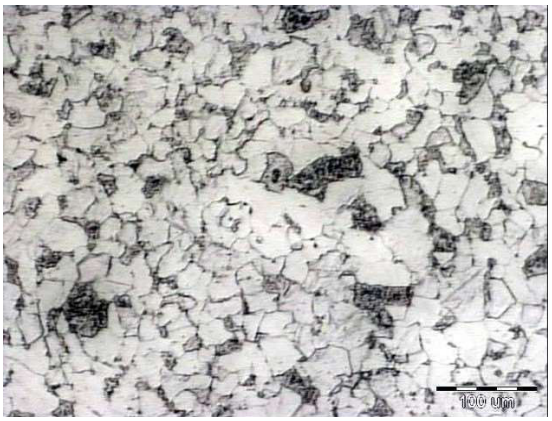

c) Microstructure of the replica R2 (2b)x150

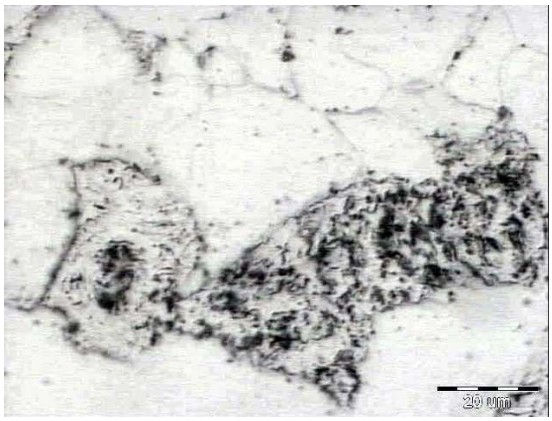

d) Microstructure of the replica R2 (2b)x750

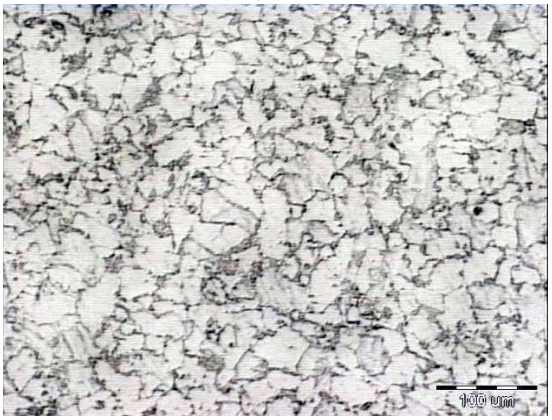

e) Microstructure of the replica R2 (3a)x150

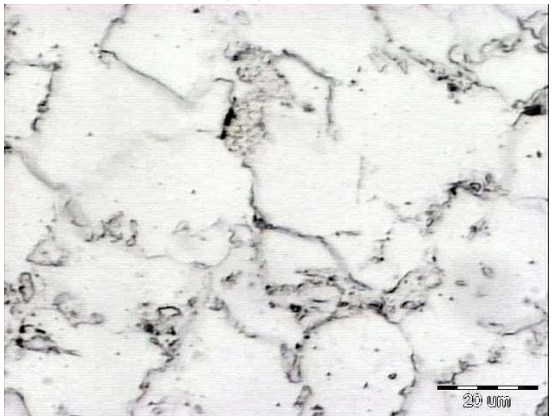

f) Microstructure of the replica R2 (3a)x750

Figure 5. Ferritic and degraded pearlite microstructure with spheroidized coarse carbides inside pearlite grains, with advanced weathering and individual micropores without orientation (a, b, c, d), and more advanced weathering with numerous micropores with orientation (e,f)

3.2. The hardness of the MPr 2 header at the points of taking replicas

The test of the hardness of the steel of the header MPr 2 was carried out according to the standard ASTM A 956/1996- method A by the Brinell method [8]. The test was carried out at the points where the replicas were taken (scheme in Figure 3). The test results are given in Table 2, where the individual and average measured hardness values are listed. The results of the hardness test are graphically presented in Figure 6. The average value of the measured hardness values, which ranged from 125 to 136 HB, is 133 HB.

Table 2. Test results of the hardness of the inlet header of the reheater MPr 2

Replica (VGB)	Hardness at the point of taking replicas [HB]					
	Individual					Average
R1 (2b)	128	134	136	133	132	133
R2 (2b)	130	128	131	131	128	130
R3 (3a)	126	127	127	126	125	126

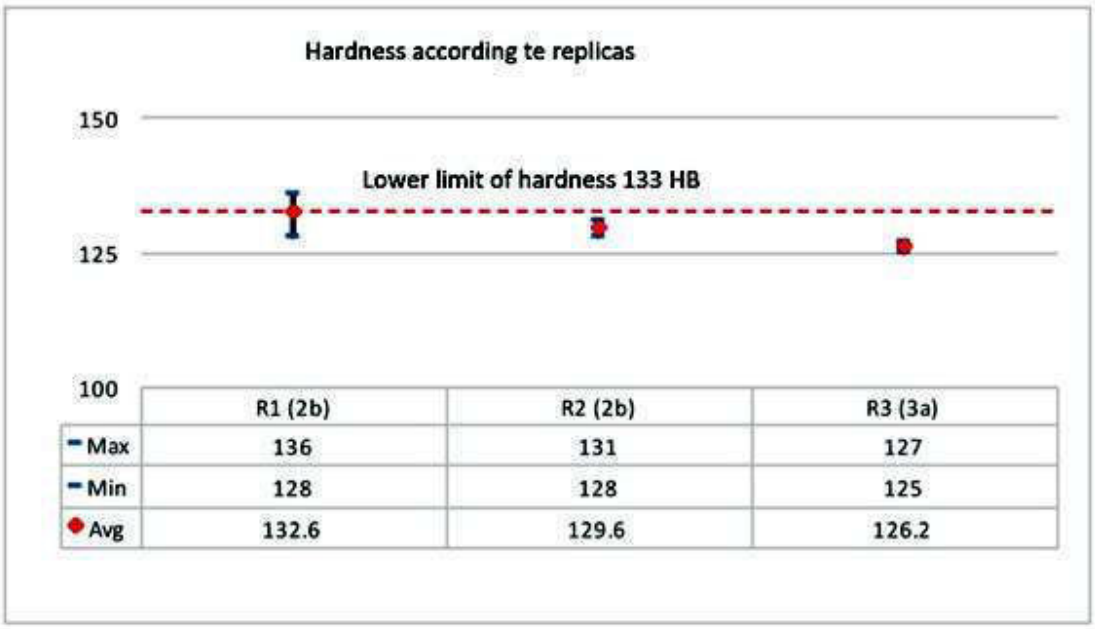

Figure 6. Scattering of MPr 2 header hardness results measured at replicate locations

Based on the results from Table 2 and from the diagram of the hardness range in Figure 6, it can be seen that all the mean values of the measured hardnesses are below the lower prescribed limit of 133 HB. A particularly low hardness was measured in replica R3, where the degree of degradation is 3a.

3.3. Hardness of welded joints

The hardness test on the welded joints of the MPr 2 header was carried out at the places marked on the diagram of the MPr 2 header in Figure 4. The hardness was measured on both sides of the welded joint, on the base material (BM), the heat-affected zone (HAZ), and the weld metal (WM). The results of the test, for the mean values of the measured hardness in all zones of the welded joint, are given in Table 3, and the range of the measured values is shown in the histograms in Figure 7. From Table 3, and from Figure 7, it can be seen that all welded joints FW1, FW2, and FW3 have in the zones of the base material low hardness, which are at the lower prescribed limit, or below that limit, and corresponding to the hardness measured at the points of taking the replicas.

Table 3. The hardness of the welded joints on the inlet header of the reheater MPr 2

Place	Hardness [HB]				
	BM	HAZ	WM	ZUT	OM
FW1	134	176	183	189	132
FW2	130	172	165	159	138
FW3	126	191	183	184	133

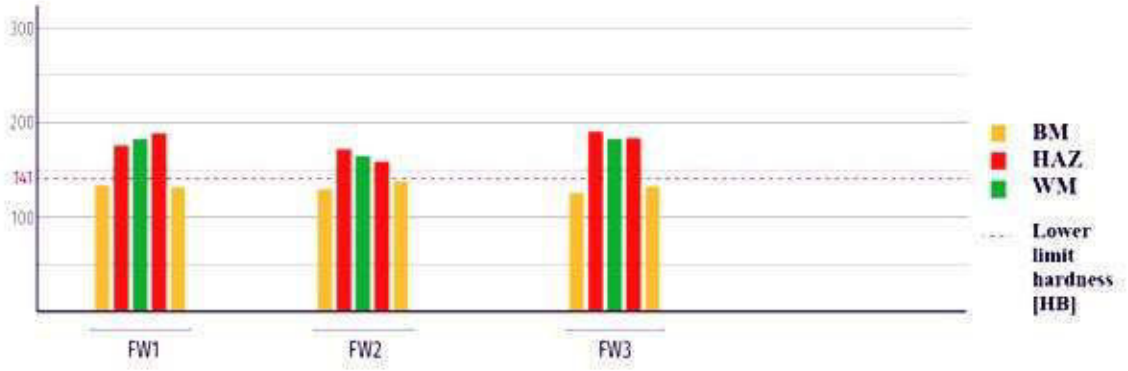

Figure 6. Scattering of hardness on the welded joints of the inlet header of the reheater MPr2

4. CONCLUSION

The conducted tests provided very useful data, which are important for assessing the material condition of critical components after long-term exploitation, which exceeds the designed life span. These data are very important because they can significantly contribute to a safer and more efficient assessment for the next period of exploitation. This does not exclude the application of other NDT methods, which in combination with the conducted tests can contribute to more reliable conclusions, especially when it comes to fractional errors on the tested components.

Examination of the microstructure revealed that there was a degradation of the structure, which was more pronounced in replica R3, compared to replicas R1 and R2. The microstructure mainly consists of ferrite and degraded pearlite, in which there are spheriodized coarse carbides formed by the decomposition of pearlite lamellae, with locally present disoriented micropores (replicas R1 and R2), and numerous oriented micropores in replica R3. Hardness testing of the replicas and welds showed low hardness values at or below the lower prescribed limit of 133 HB for 15Mo3 steel.

In this way, it was confirmed that there is a harmonious relationship between the degradation of the microstructure and the decrease in hardness. It can be stated with certainty that the assessment of the degree of microstructure degradation and the decrease in hardness are reliable methods for assessing the condition of the tested components, in non-destructive testing. This can be important if in this way the scope of the tests can be reduced in some cases, and thus reduce the time required for the tests.

5. REFERENCES

[1] Milenko Rimac, TTDU Maneco Kakanj, Abdulah Koro, Energoinvest Institut za materijale i kvalitet IMQ Sarajevo, Belma Fakić Institut „Kemal Kapetanović“ Zenica, Elaborat 02-19 – Utvrđivanje stanja kritičnih komponenti kotla bloka 7 u Termoelektrani „Kakanj“ Kakanj, juni 2019.

[2] Standard DIN 50150 - Testing of metallic materials - conversion of hardness values, 2000.

[3] Standard ASTM A 956 - method A - Standard Test Method for Leeb Hardness Testing of Steel Products, 1996.

[4] Standard DIN 17175 – Seamless Tubes of Heat – resistant Steels – Technical Conditions of Delivery, May 1979.

[5] VTT Publications 280 – Microstructural degradation of boiler tube steels under long-term exposure to high temperature, Jorma Salonen&Pertti Auerkari, Technical research center of Finland ESPOO 1996.

[6] Standard VGB-S-517- 00-2014. - Guidelines for rating the microstructural composition and creep rupture damage of creep-resistance steel for high-pressure pipelines and boiler components and their weld connections.
[7] Standard ASTM E 407-07 - Standard Practice for Microetching Metals and Alloys, May 1, 2007.
[8] Standard BAS ISO 3057 - Non-destructive testing - Metallographic replica techniques of surface examination, 1998.

THE INFLUENCE OF HEAT TREATMENT ON MICROSTRUCTURE AND THERMAL PROPERTIES OF C45 TOOL STEEL

Uroš Stamenković, Ivana Marković, Srba Mladenović, Dragan Manasijević, Ljubiša Balanović, Avram Kovačević, Milan Nedeljković, Jovana Božinović
University of Belgrade, Technical Faculty in Bor
Bor, Serbia

Keywords: C45 steel, Microstructure, Martensite, Thermal properties, Tempering

ABSTRACT
In this paper, C45 medium carbon tool steel was investigated after various heat treatments. The thermal properties, specifically thermal diffusivity and thermal conductivity, were measured and also the microstructure analysis was done on a light microscope. Heat treatment of the samples included: 1) the normalization heat treatment at 900°C for one hour and cooling in the air; 2) quenching the samples in water and in oil separately after reheating them at 880°C for one hour and; 3) tempering the quenched samples at 200°C-350°C for 2 hours. The results show the highest values of thermal properties for the normalized sample. Also, the lowest values were recorded for the quenched samples, and the values of thermal properties for the tempered samples are between the values of the quenched and normalized samples. Microstructure analysis shows a typical ferrite-pearlite structure after normalization. Martensite appeared in the water-quenched sample. However, the microstructure of the oil-hardened sample predominately consists of ferrite and pearlite because the critical cooling rate was not reached. Tempered samples quenched in the water had the microstructure of tempered martensite.

1. INTRODUCTION

Steels with a carbon content between 0.3-0.5% are often called medium carbon steels. These steels are used in many applications. Because of their mechanical, physical, and other properties, many of them are essentials for building parts in many industries. Those industries are automotive, naval, civil, military, electrical, etc. [1]. Medium carbon steels can exhibit different properties when subjected to various heat treatments [2]. The most common heat treatment for these steels includes quenching and tempering at high temperatures in order to achieve highly tempered martensitic microstructure which would provide the highest values of toughness and high wear resistivity [3]. In addition, medium carbon steels are considered to be a type of tool steel. For tool steels, besides good mechanical properties, several thermophysical properties are very relevant for tool design [4]. Two of those thermophysical properties are thermal diffusivity and thermal conductivity. These properties sometimes dictate the lifespan of the tool. For example, higher thermal conductivities in steels can reduce temperature gradients that appear in tools during their application [5,6]. Thermophysical properties are greatly influenced by different heat treatments, especially given the fact that a large number of these tools are used in applications at elevated temperatures. Medium carbon steel research is usually based on investigating the mechanical properties after various heat treatments. Some heat treatments have already been investigated by other researchers. In most cases, the authors dealt with how quenching in water, aqueous polymer solutions, or aqueous salt solutions as well as subsequent tempering affects the mechanical properties of C45 steel [3,7].

Groom et al. monitored the change in mechanical properties after oil quenching and tempering [8]. A. Laouissi et al. colleagues made their contribution by optimizing the heat treatment process, investigating the influence of annealing temperature as well as the influence of different types of quenching (in air, in water, and in hydrochloric acid solution) on mechanical properties [1]. Some authors examined the thermal properties of different steels after various heat treatments, including C45 steel. Wilzer et al. investigated the influence of heat treatment on the thermophysical properties of martensitic steels. They showed that tempering increases the values of thermal conductivity and thermal diffusivity, but with a decrease in hardness values [4,9].
The primary aim of this paper is the investigation of thermal properties of C45 medium carbon tool steel after normalization, and subsequently after quenching and low to medium temperature tempering (200°C-350°C). The secondary aim is to investigate the microstructures that appear after various heat treatments and see if those structures are in agreement with the obtained results for thermal properties.

2. EXPERIMENTAL PROCEDURE

Experiments were performed on C45 medium carbon tool steel with the defined chemical composition given in Table 1. Steel was received in the form of hot extruded bars with a diameter of 20 mm. The samples were firstly normalized at 900°C for one hour in an electric resistance furnace in order to normalize and eliminate the structure after the manufacturing process, and then cooled in still air. Normalized samples were then annealed at 880°C, for one hour and quenched separately in oil and in cold water. Quenched samples were tempered at different temperatures (200°C-350°C) for 2 hours. Samples were separated for further analysis after normalization, quenching, and tempering. Characterization of the samples included measuring the thermal properties and microstructural analysis on an light microscope. The Xenon flash method was applied to determine the thermal diffusivity of the investigated samples after different heat treatments by irradiating the disc-shaped specimens with a diameter of 12.7 mm with the xenon lamp in a nitrogen atmosphere. The thermal conductivity as a function of temperature was calculated according to the equation:

$$\lambda(T) = \rho(T) \times c_p(T) \times \alpha(T) \quad (1)$$

where, λ - thermal conductivity; (W/m*K), ρ – density; (kg/m^3), c_p – specific heat capacity; (J/kg*K), α - thermal diffusivity; (cm^2/s), T – temperature; (°C).

Light microscopy was used for the investigation of the microstructure. Preparation of the samples included wet grinding on a series of SiC papers, and polishing with alumina suspension with two different granulations of Al_2O_3: particle sizes of 0.3 μm and 0.05 μm. 4% Nital solution was used for the etching of the samples by immersion to reveal the microstructure. The microstructures were examined on two light microscopes CarlZeiss Jena Epytip 2 and Reichert MeF2. Also, the equipment used and various steps in the heat treatment process can be seen in Figure 1a-d.

Table 1. Chemical composition of investigated steel (mass. %)

C45 medium carbon steel				
Fe	C	Mn	S	P
98.51-98.98	0.42-0.5	0.6-0.9	≤0.05	≤0.04

Figure 1. Equipment and different steps in the heat treatment process: a) electric resistance furnace; b) sample heating; c) and d) samples after tempering for 2 hours at different temperatures

3. RESULTS AND DISCUSSION

3.1. The properties of investigated samples after normalizing

After normalization heat treatment, the fabricated structure was removed and the structure of investigated samples was normalized. Obtained results show relatively high values of thermal diffusivity and thermal conductivity, 16.97 mm^2/s, and 60.9 W/m*K, respectively. The relatively high values for thermal properties were obtained due to the normalization heat treatment which involved high-temperature heating and slow cooling leading to an equilibrium state at room temperature. The equilibrium state caused by slow cooling has a low density of dislocation and vacancies, so the movement of electrons (as thermal energy carriers) is facilitated. In this state, samples had a microstructure that consisted of a fine mixture of ferrite and pearlite, shown in Figure 2a-b. Duka et al. stated that the microstructure of C45 steel is composed of 66% pearlite and 34% ferrite [10].

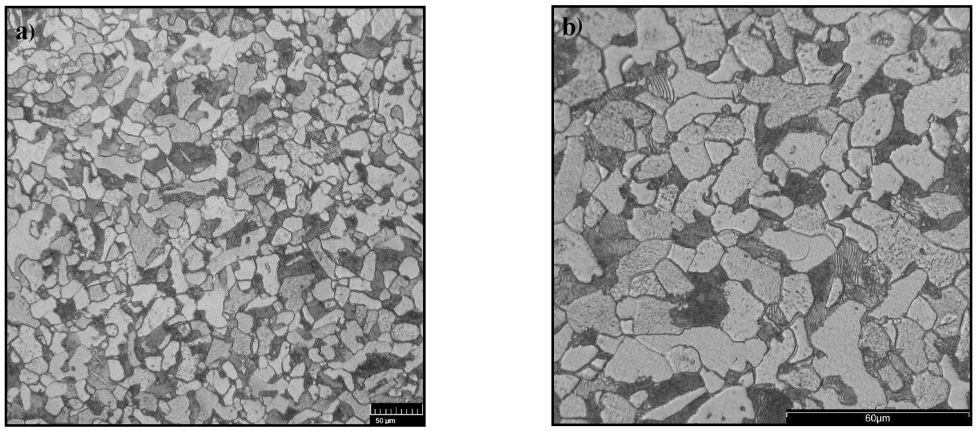

Figure 2. Microstructure of the investigated C45 steel after the normalization heat treatment; a) magnification is x500; b) magnification is x1000

3.2. The properties of investigated samples after quenching

After the normalizing heat treatment, samples were austenitized and quenched to room temperature using two different quenchants. Table 2 shows the results after quenching separately in oil and in water.

Table 2. Thermal properties of the investigated steel after quenching

Type of quenchant	Thermal diffusivity (mm^2/s)	Thermal conductivity (W/m*K)
Water	11.41	43.76
Oil	11.88	46.49

The values of thermal diffusivity and thermal conductivity decreased after quenching in water and oil when compared to the values obtained after normalization. The absolute decrease in thermal diffusivity and thermal conductivity after quenching in water is 5.56 mm^2/s and 17.14 W/m*K, respectively. After quenching in oil, the results are somewhat different and an absolute decrease of 5.09 mm^2/s and 14.41 W/m*K was recorded for thermal diffusivity and thermal conductivity, respectively. After quenching in water, the formation of martensite led to the formation of a supersaturated solid solution of carbon in the iron matrix. According to Wilzner, all other elements that enter into the composition of steel are trapped in addition to carbon during tempering. In this regard, martensite is characterized by high supersaturation as well as a high density of dislocations and vacancies. This type of structure hinders the movement of electrons, as carriers of thermal energy, lowering the values of thermal properties [4,9].

These characterizations are less pronounced in the samples that were quenched in oil, because, due to the insufficient cooling rate, a mixed microstructure is expected. This can be concluded by comparing the results obtained after quenching in water with those obtained after quenching in oil. The comparison of those results shows that higher values of thermal properties are obtained after quenching in oil.

The microstructural analysis confirmed the statements above to some extent. After quenching in water, finely distributed martensite needles can be observed in the microstructure. For the oil-quenched sample, the critical cooling rate was not reached, therefore no martensite was formed. The microstructure of the oil-hardened sample is of a mixed type, which predominately consists of ferrite and pearlite. Microstructures can be seen in Figure 3a-d.

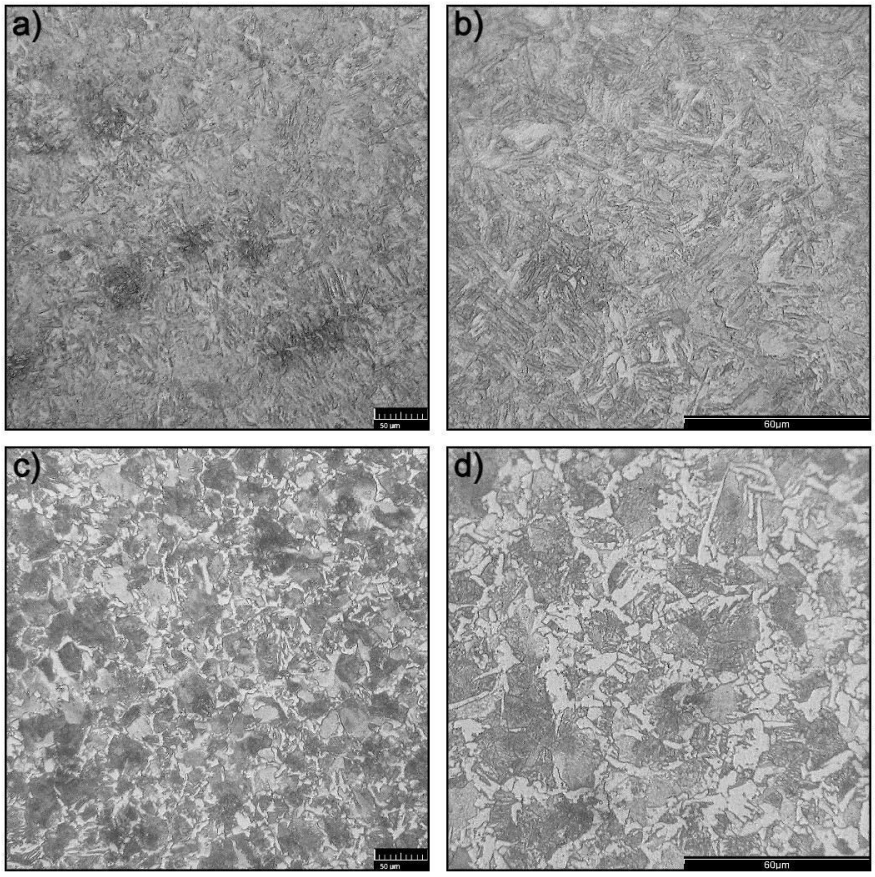

Figure 3. Microstructure of the investigated C45 steel after quenching;
a) in water, magnification is x500; b) in water, magnification is x1000; c) in oil, magnification is x500; d) in oil, magnification is x1000

3.3. The properties of investigated samples after tempering

After quenching in water and oil separately, samples were subjected to tempering at different temperatures for 2 hours. During tempering, changes in the thermal properties were observed and investigated. Figure 4 shows the obtained values for thermal diffusivity and thermal conductivity after tempering at 200°C-350°C for 2 hours. Analysis of the obtained results shows that the values of thermal diffusivity and thermal conductivity gradually increase with the increase of tempering temperature.

The reason for the increase in values of thermal properties lies in the tempering of hardened samples. Winczek et al. stated that steels with a carbon content > 0.2 wt.% starts tempering even at room temperature [11]. During tempering, there is a reduction in stress and the transformation of martensite that was formed by quenching into tempered martensite. After tempering in this temperature range there are a couple of processes that occur simultaneously: the diffusion of carbon atoms; the loss of tetragonality of martensite; the formation of cubic ferrite; the formation of cementite; the decomposition of residual austenite; whereby lower hardness values are recorded [4,7,8,11].

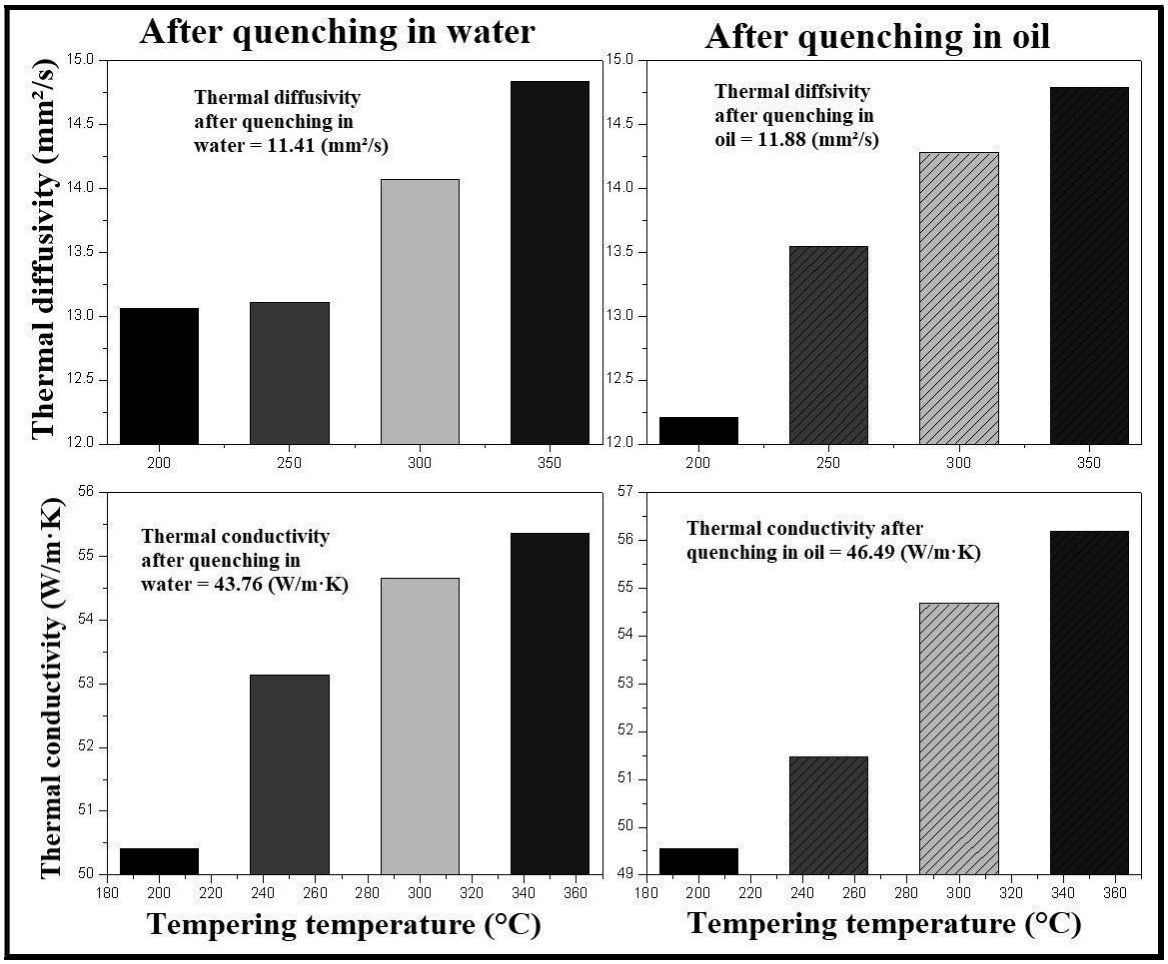

Figure 4. Change in thermal properties after tempering quenched samples at different temperatures for 2 hours

During tempering, with the increase in tempering temperature, a slight rearrangement in the structure occurs. Change in thermal properties depends on two mutual processes, namely: 1) thermal vibrations in the lattice caused by the increase in temperature and 2) precipitation of carbon atoms from the supersaturated martensitic lattice. Consequently, these two processes are at odds. So essentially, one process (1) hinders the movement of

electrons and causes the values of thermal properties to decrease and one process (2) facilitated the movement of electrons and causes the increase of values for investigated thermal properties. Depending on which of the processes is more active at a given moment, values of thermal properties will be defined accordingly. Given that, the measurements of the thermal properties in this part of the experiment were made at room temperature, the thermal vibrations were significantly reduced, so in this case, the process of precipitation from the supersaturated martensite prevailed [4,9,12].
As for the samples that were tempered after quenching in oil, obtained values for those samples show a similar trend to the water-quenched samples, which is interesting considering that no martensitic microstructure was obtained in these samples. It can be assumed that due to the heating of those samples, the acceleration of diffusion and the removal of possible residual stresses occurred causing the values of thermal properties to increase in comparison to the quenched sample.

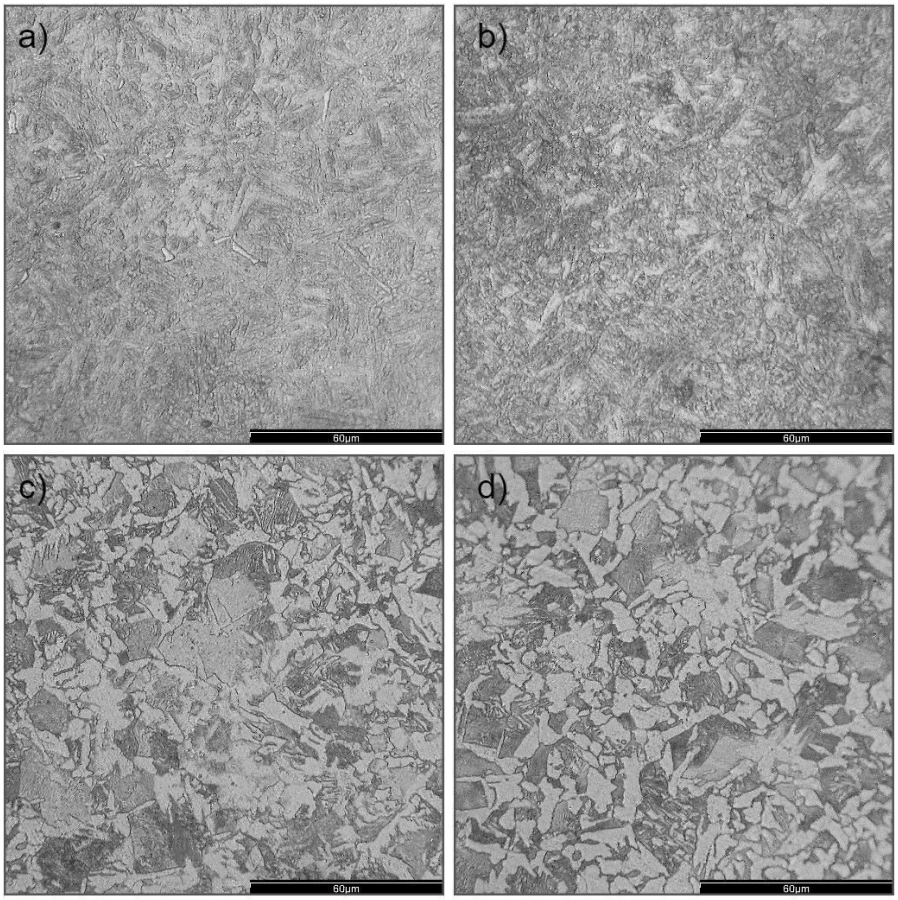

Figure 5. Microstructures after: a) quenching in water and tempering at 200°C, 2h; b) quenching in water and tempering at 350°C, 2h; c) quenching in oil and tempering at 200°C, 2h; d) quenching in oil and tempering at 350°C, 2h;

Analysis of the microstructures after tempering is in agreement with the given statements about the influence of tempering on thermal properties. Figure 5a-d shows the microstructures after quenching and tempering at 200°C and 350°C for 2 hours. After quenching in water and tempering, microstructures are well homogenized and they consist of tempered martensite where martensitic needles are less pronounced. Due to the low tempering temperatures, microstructures do not differ as much as those obtained after quenching. As for the microstructures obtained after quenching in oil and tempering, considering that the critical cooling rate was not achieved by quenching in oil, and that

martensite was not formed, concrete changes in the microstructure cannot be expected. The grains are somewhat larger due to exposure to slightly higher temperatures.

4. CONCLUSIONS

The influence of different heat treatments on the microstructure and thermal properties of C45 medium carbon tool steel was investigated. Some conclusions can be outlined:

- After normalization heat treatment, values of thermal properties are the highest of all investigated states. Microstructure consists of a fine mixture of ferrite and pearlite.
- Quenching in water caused the formation of martensite in the structure. The values of thermal diffusivity and thermal conductivity decreased in comparison to the values obtained for the normalized sample. The relative decrease in values of thermal diffusivity and thermal conductivity were, 33% and 28%, respectively.
- The critical cooling rate was not achieved by quenching in oil, so martensite was not present in the microstructure. Nevertheless, the values of thermal diffusivity and thermal conductivity decreased in comparison to the values obtained for the normalized sample. The relative decrease in values of thermal diffusivity and thermal conductivity were, 30% and 24%, respectively.
- After tempering the quenched samples, the values of the thermal properties gradually increase with the increase of the tempering temperature. The values of thermal diffusivity and thermal conductivity had the lowest increase at the tempering temperature of 200°C and the highest increase at the tempering temperature of 350°C. The relative increase in values of thermal properties was in the range of 20-30%.
- Microstructural analysis after quenching in water and tempering showed typical microstructure of tempered martensite.

5. ACKNOWLEDGEMENT

The research presented in this paper was done with the financial support of the Ministry of Science, Technological Development and Innovation of the Republic of Serbia, with the funding of the scientific research work at the University of Belgrade, Technical Faculty in Bor, according to the contract with registration number 451-03-47/2023-01/ 200131.

6. REFERENCES

[1] Laouissi A., Blaoui M.M., Abderazek H., Nouioua M., Bouchoucha A.: Heat Treatment Process Study and ANN-GA Based Multi-Response Optimization of C45 Steel Mechanical Properties, Metals and Materials International, 28 3087-3105, 2022

[2] Davanageri M.B., Narendranath S., Kadoli R.: Influence of Heat Treatment on Microstructure, Hardness and Wear Behavior of Super Duplex Stainless Steel AISI 2507, American Journal of Materials Science, 5(3C) 48-52, 2015

[3] Wozniak W., Sasiadek M., Jachowicz T., Edl M., Zajac P.: Studies on the Mechanical Properties of C45 Steel with Martensitic Structure after a High Tempering Process, Advances in Science and Technology Research Journal, 16(3) 306-315, 2022

[4] Wilzer J., Ludtke F., Weber S., Theisen W.: The influence of heat treatment and resulting microstructures on the thermophysical properties of martensitic steels, Journal of Material Science, 48 8483-8492, 2013

[5] Valls I., Casas B., Rodriguez N.: Importance of tool material thermal conductivity in the die longevity and product quality in HPDC, Tool steels—deciding factor in worldwide production, 8th international tooling conference, Mainz, Aachen, Germany, 2009

[6] Hamasaiid, A., Valls, I., Heid, R., Eibisch, H.: A comparative experimental study on the use of two hot work tool steels for high pressure die casting of aluminum alloys: high thermal

conductivity HTCS® and conventional 1.2343 (AISI H11), 9th international tooling conference: developing the world of tooling, Leoben, Austria, 2012
[7] Haiko O., Kaijalainen A., Pallaspuro S., Hannula J., Porter D., Liimatainen T., Komi J.: The Effect of Tempering on the Microstructure and Mechanical Properties of a Novel 0.4C Press-Hardening Steel, Applied Science, 9 4231, 2019
[8] Grum J., Žerovnik P.: Statistical Processing Of A Voltage Signal Of The Magnetic Barkhausen-Noise Emitted By Quenched And Tempered Specimens of C45 Steel, 16th World Conference on NDT, Montreal, Canada, 2004
[9] Wilzer J., Kupferle J., Weber S., Theisen W.: Temperature-dependent thermal conductivities of nonalloyed and high-alloyed heat-treatable steels in the temperature range between 20 and 500 °C, Journal of Material Science, 49 4833-4843, 2014
[10] Duka E., Oettel H., Dilo T.: Connection between micro and macro hardness pearlitic-ferritic steel, 2nd International Advances in Applied Physics and Materials Science Congress, Antalya, Turkey, 2012
[11] Winczek J., Kulawik A.: Dilatometric and hardness analysis of C45 steel tempering with different heating-up rates, Metalurgija, 51(1) 9-12, 2012
[12] Tritt T.M.: Thermal Conductivity: Theory, Properties and Applications, Kluwer Academic/Plenum Publisher, New York, 2004

THERMAL PROPERTIES OF COPPER BASE SHAPE MEMORY ALLOY

Borut Kosec, Blaž Karpe, Aleš Nagode, Milan Bizjak
University of Ljubljana, Faculty of Natural Sciences and Engineering
Ljubljana, Slovenia

Ladislav Vrsalović
University of Split, Faculty of Chemistry and Technology
Split, Croatia

Diana Ćubela
University of Zenica, Faculty of Metallurgy and Technology
Zenica, B&H

Mirko Gojić, Ivana Ivanić, Stjepan Kožuh
University of Zagreb, Faculty of Metallurgy
Sisak, Croatia

Keywords: Thermal properties, Measurement, Copper base shape memory alloy, Rapid solidification

ABSTRACT
The mechanical properties and microstructure of copper base shape memory alloys are relatively well known, while data on thermal properties (thermal conductivity, specific heat, and temperature conductivity) are not available. In the frame of our investigation work thermal properties of rapidly solidified Cu-Al-Ni-Mn alloy were determined.
As the first part of the work, a study and evaluation of the operation of the device for determining the thermal properties of Hot Disk TPS 2200, today one of the more modern and high-quality instruments for determining thermal properties has been carried out.
In the second part of the work, the measurements and analysis of thermal properties of rapidly solidified Cu-Al-Ni-Mn shape memory alloy in accordance with the standard ISO 22007-2 at ambient and elevated temperatures have been done.

1. INTRODUCTION

Shape memory alloys (SMA) are relatively a new class of advanced functional materials that are able to memorize and recover their original shape after being significantly deformed from heating over the phase transformation temperature [1].
The main advantage of Cu-based SMA is their low price compared to other SMA. The properties of Cu-Al-Ni alloys are superior to those of Cu-Zn-Al alloys due to their wide range of useful transformation temperatures and small hysteresis. Although Cu-Al-Ni alloys have better thermal and electrical stability and higher operating temperatures, their practical applications are sometimes restricted by very small shape changes due to their poor workability and susceptibility to brittle intergranular cracks [2]. Their very high elastic anisotropy and large grain size cause brittle and poor mechanical properties owing to the high degree of order in the parent phase. Typically composition of Cu-Al-Ni SMA is in the range Cu-(13-15 m. %)Al-(3-4.5 m. %)Ni [3]. Adding some alloying elements

such as Mn, Fe, Ti, Zr, B, etc. to the alloys can significantly improve their ductility and other properties which modify their operating temperatures [4,5].
In the frame of our investigation, we have investigated the thermal properties of rapidly solidified Cu-Al-Ni-Mn shape memory alloy [6] produced by the melt-spinning procedure (Figure 1). The chemical composition of the testing Cu-Al-Ni-Mn alloy is in Table 1.

Table 1. Chemical composition of the testing Cu-Al-Ni-Mn alloy (in m.%)

Al	Ni	Mn	Cu
12.7	4.2	2.4	rest

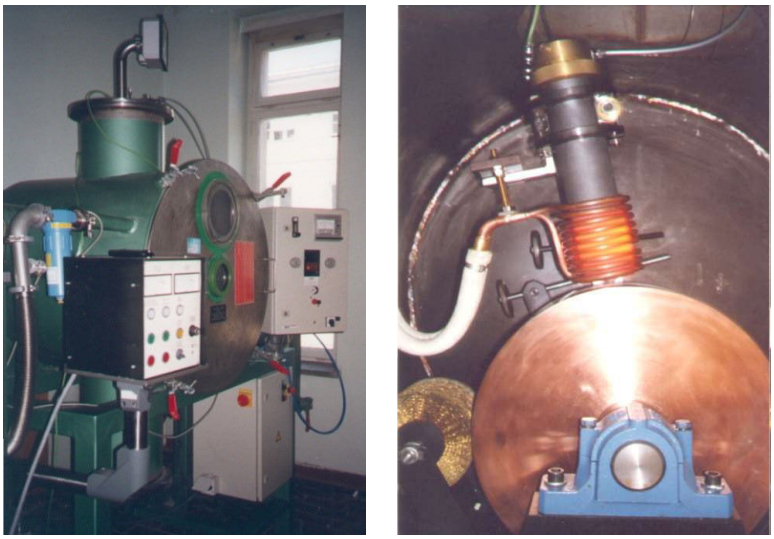

Figure 1. Melt spinner at the Faculty of Natural Sciences and the Engineering University of Ljubljana [7]

Single Roll Melt Spinning is the most commonly used process for the production of rapidly solidified thin metal foils or ribbons with amorphous, microcrystalline, or even combined microstructure. In this type of process, a molten material is introduced onto the surface of the spinning wheel, where a melted puddle is formed, and as a final result metal ribbons are formed (Figure 2).

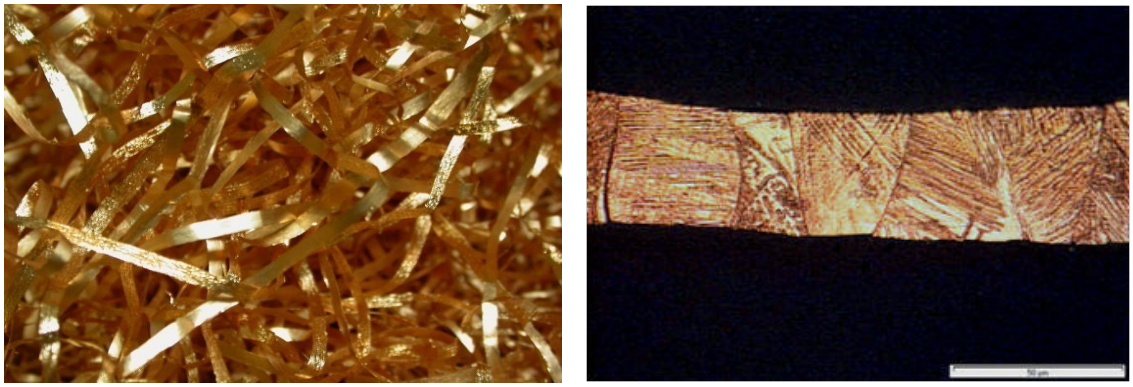

a) b)

Figure 2. Rapidly solidified Cu-Al-Ni-Mn shape memory alloy thin ribbons (a), microstructure (b)

Figure 3. Disks from the ground and molded rapidly solidified Cu-Al-Ni-Mn shape memory alloy

The final products are in the form of thin and narrow ribbons, which could be in further production steps subjected to milling and molded into useful shapes by different methods of powder metallurgy. In our case, we have made disks from the ground and molded alloys (Figure 3). From them, testing samples to perform measurements of thermal properties of dimensions Ø40 x 13 mm have been done.

2. THERMAL PROPERTIES MEASUREMENT

In our research, we used one of the most advanced instruments for determining the thermal properties, Hot Disk TPS 2200, a product of Hot Disk AB Company, Gothenburg, Sweden (Figure 4) [8].

.

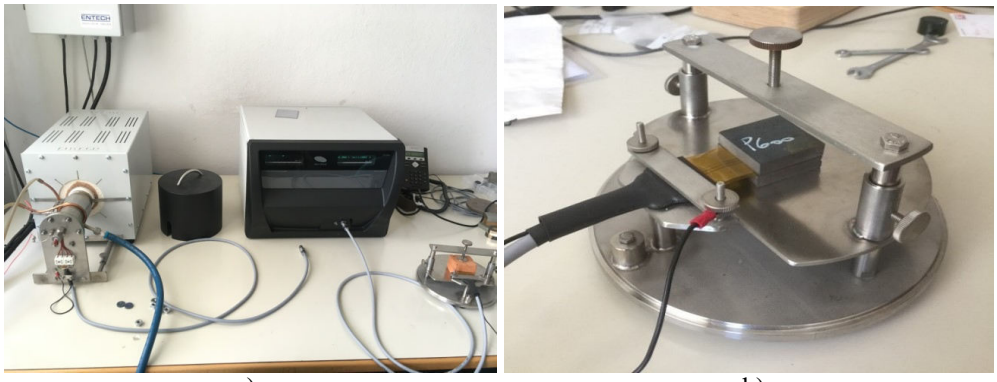

a) b)

Figure 4. Instrument Hot Disk TPS 2200 (a). Measuring sensor sandwiched between two halves of a sample during measurement (b)

The instrument can be used for determining the thermal properties of various materials including pure metals, alloys, minerals, ceramics, plastics, glasses, powders, and viscous liquids with thermal conductivity in the range from 0.01 to 500 W/mK, thermal diffusivity from 0.01 to 300 mm^2/s and heat capacity up to 5 MJ/m^3K. Measurements can be performed in a temperature interval between -50°C to 750 °C [9].

The hot disk measuring method is a transient plane source technique (TPS). Based on the theory of TPS, the instrument utilizes a sensor element in the shape of a 10 μm thick double spiral, made by etching from pure nickel foil. Spiral is mechanically strengthened and electrically insulated on both sides by thin polyimide foil (Kapton ®Du Pont) for measurements up to 300 °C or mica foil for measurements up to 750 °C.

Sensor acts both as a precise heat source and resistance thermometer for recording the time-dependent temperature increase. During the measurement of solids, encapsulated Ni-sensor is sandwiched between two halves of the sample and constant precise pre-set

heating power is released by the sensor, followed by 200 resistance recording in a pre-set measuring time, from which the relation between time and temperature change is established. Based on the time-dependent temperature increase of the sensor, the thermal properties of the tested material are calculated.

3. EXPERIMENTAL WORK

Measurements and analysis of thermal properties of testing samples from the testing rapidly solidified copper base shape memory alloy were performed in accordance with ISO 22007-2 standard [10] in the Laboratory for Thermotechnical Measurements, Faculty of Natural Sciences and Engineering, University of Ljubljana. In Figure 5 complete data of thermal properties measurements are presented.

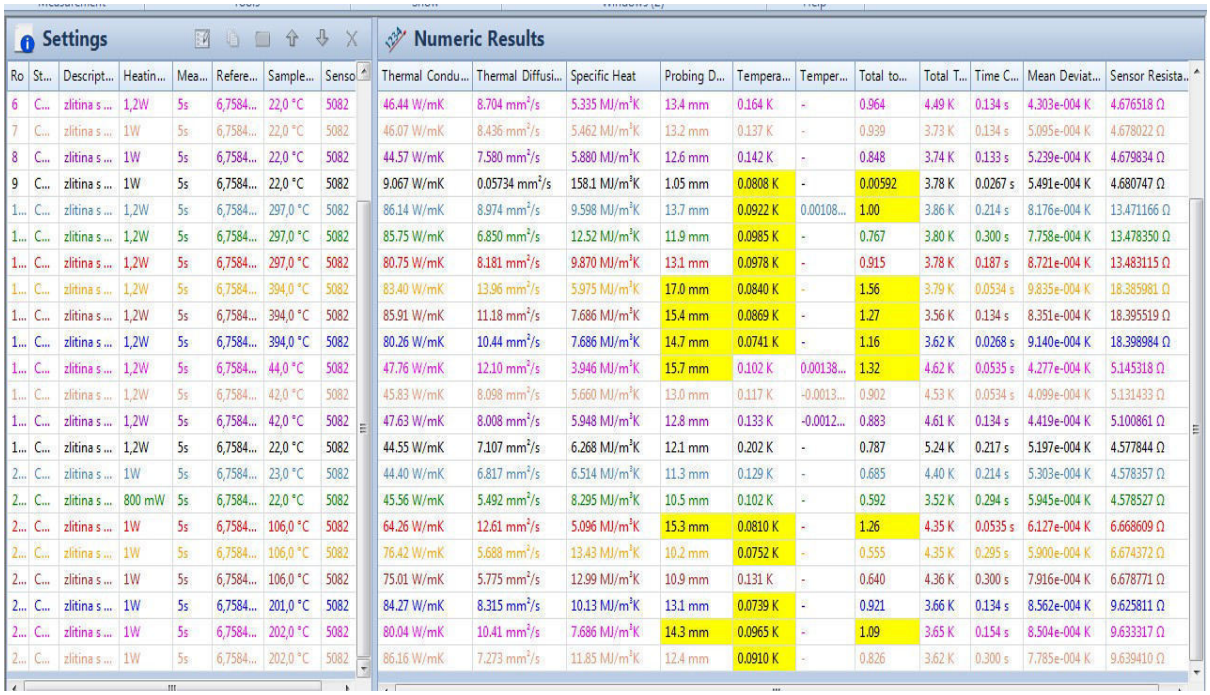

Figure 5. Data of TPS measurements

In Table 2 thermal properties (thermal conductivity, specific heat, and temperature conductivity) of analysed rapidly solidified Cu-Al-Ni-Mn shape memory alloy at ambient temperature (approx. 22 ^{o}C) are presented.

Table 2. Thermal properties of analysed Cu-Al-Ni -Mn shape memory alloy at ambient temperature

	Cu-Al-Ni-Mn
Thermal conductivity	45.30 W/mK
Specific heat	6.29 MJ/m^{3}K
Temperature conductivity	7.36 mm^2/s

Thermal conductivity of analysed Cu-Al-Ni-Mn shape memory alloy on the temperature interval between ambient temperature (approx. 22 ^{o}C) and temperature 400 ^{o}C growing up from 45.30 W/mK to 86.45 W/mK (Figure 6).

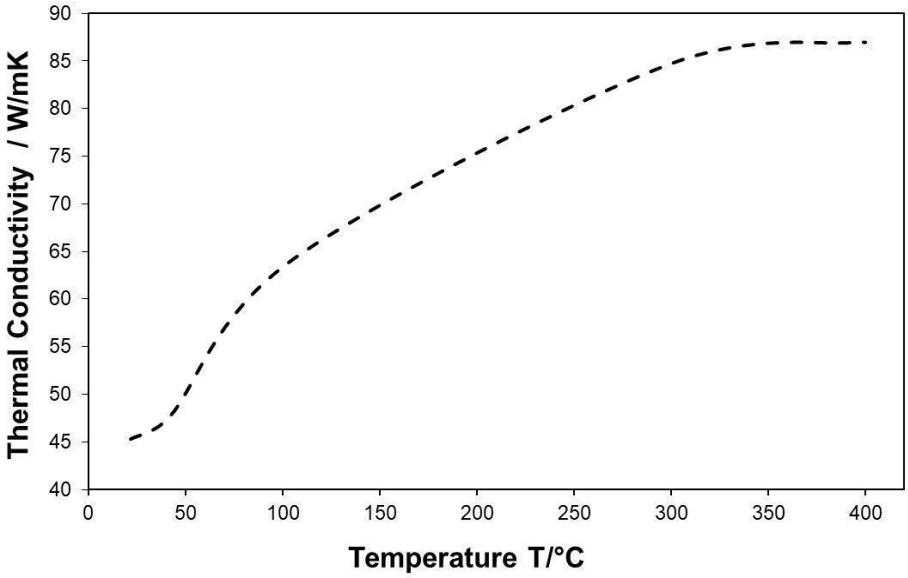

Figure 6. Thermal conductivity at elevated temperatures

4. CONCLUSIONS

In the frame of investigation thermal properties of rapidly solidified Cu-Al-Ni-Mn shape memory alloy were determined. The measurements and analysis of thermal properties of rapidly solidified Cu-Al-Ni-Mn shape memory alloy have been done in accordance with the standard ISO 22007-2 at ambient and elevated temperatures.

The values of thermal properties of Cu-Al-Ni-Mn alloy at ambient temperature (approximately 22 °C) are:

thermal conductivity 45.30 W/mK,

specific heat 6.29 MJ/m^{3}K, and

temperature conductivity 7.36 mm^2/s.

We found that investigated rapidly solidified Cu-Al-Ni-Mn shape memory alloy at ambient temperature has almost 100 % lower heat conductivity at a temperature of 400 ^{o}C.

5. REFERENCES

[1] H. H. Libermann, Rapidly solidified alloys, Marcel Dekker, London, 1993.

[2] L. A. Dobrzanski, Technical and Economical Issues of Materials Selection, Silesian Technical University, Gliwice, 1997

[3] M. Gojić, L. Vrsalović, S. Kožuh, A. C. Kneissl, I. Anžel, S. Gudić, B. Kosec, M. Kliškić, Electrochemical and microstructural study of Cu-Al-Ni shape memory alloy, Journal of Alloys and Compounds, 509 (2011) 41, 9782-9790

[4] I. Ivanić, S. Kožuh, F. Kosel, B. Kosec, I. Anžel, M. Bizjak, M. Gojić. The influence of heat treatment on fracture surface morphology of the CuAlNi shape memory alloy. Engineering failure analysis.77 (2017), 85-92

[5] G. Lojen, I. Anžel, A. C. Kneissl, E. Unterweger, B. Kosec, M. Bizjak, Microstructure of rapidly solidified Cu-Al-Ni shape memory alloy ribbons, Journal of Materials Processing Technology, 162/163 (2005), 220-229

[6] I. Ivanić, M. Gojić, S. Kožuh, B. Kosec. Microstructural analysis of CuAlNiMn shape-memory alloy before and after the tensile testing. Materiali in tehnologije.. 48 (2014) 5, 713-718

[7] B. Kosec, Device for rapid solidifying of metal alloys, Euroteh, 3 (2004), 32-33.

[8] B. Kosec, B. Karpe**,** Instrument for the thermal properties analysis Hot Disk TPS 2200, IRT3000, 1 (2017), 67

[9] B. Karpe, M. Vodlan, I. Kopač, I. Budak, A. Nagode, A. Pavlič, T. Puškar, B. Kosec. Thermal properties of materials used in dental medicine. Advanced technologies and materials. 43 (2018) 1, 7-10
[10] International standard ISO 22007 (2009). Plastics – Determination of thermal conductivity and thermal diffusivity – Part 1: General principles. Reference: ISO 22007:2009(E)

EFFECT GRAIN SIZE OF S690QL STEEL ON IMPACT FRACTURE AT LOW TEMPERATURE

Mirsada Oruč, Aida Imamović, Raza Sunulahpašić
University of Zenica, Faculty of Metallurgy and Technology
Zenica, B&H

Gorazd Kosec
SIJ Acroni d.o.o. Jesenice
Jesenice, Slovenia

Keywords: high-strength structural steel, grain size, toughness, low temperature

ABSTRACT
Toughness testing is one of the most important and most applied dynamic tests of materials. Many materials are subjected to this test in order to ensure the safety of work in adverse conditions. Thus, for steel S690QL, which is a high-strength fine-grained structural steel in the quenched and tempered state, the minimum conventional yield stress R_{eH} of 690 MPa with guaranteed toughness (Charpy impact energy) at a temperature of -40°C of 30 J is prescribed, for rolled plates with a thickness of 3 to 50 mm. In this work, testing and analysis of the results of impact energy at a temperature of - 40°C was carried out for 10 samples of plates of different thicknesses, produced from steel S690 QL. With these tests, the aim is to consider the segments of the technological process, which have an impact on the physical-metallurgical characteristics, primarily on the formed microstructure and grain size, which affect the toughness values at low temperatures.

1. INTRODUCTION

Testing the toughness of a notched specimen according to Charpy is one of the oldest mechanical tests of materials under operational conditions, and serves to determine its resistance to brittle fracture. The microstructure has a great influence on the toughness of the material. Reducing the grain size for most metallic materials has a particularly favourable effect on toughness. Thus, reducing the grain size by one grade on the ASTM scale lowers the transition temperature to 15°C. Deformed material also has higher toughness, i.e. lower transition temperature due to its anisotropic structure, especially in the longitudinal direction [1].

The impact resistance of solid materials represents the ability of materials to deform under the influence of an impact load in such a way that cracks do not appear on the sample or its fracture. Based on this test, an insight into the toughness of the material is obtained. Namely, it came to the conclusion that based on the determination of bending strength, it is not possible to predict the way the material will fracture; for example, under certain circumstances, metals that normally behave ductile suddenly fracture with a very small degree of plastic deformation.

It should be noted that there is no unequivocal relationship between toughness and other mechanical properties of materials, but it is certain that usually, a material with high toughness has low values for strength and high values for elongation and contraction [2].

Testing of the impact energy of fracture (toughness) for most materials is standardized, and values are specified for many materials, especially steel products, which must have

exactly defined minimum values of the impact energy of fracture at a certain temperature, before use, especially for responsible machine parts.

1.2. Steel S690QL

Hot-rolled plates are made of high-strength fine-grained structural steel grade S690 QL, which is mainly supplied in hardened and tempered conditions. The technical requirements for the delivery of plates made of this steel according to the standard prescribe the chemical composition and impact energy at a temperature of -40 °C on a longitudinal section in the amount of 30 J. In the document Technical data sheet Acroni, the values for impact energy only in the value of 27 J in cross-section. Table 1 shows the chemical composition of the produced hot-rolled plates made of steel S690 QL. All melts are produced with the prescribed content of elements according to the standards EN 10025-6:2004+A1:2009 and DIN EN 10025-1, and a high degree of purity, i.e. the content of phosphorus and sulphur.

Table 1. Chemical composition of the produced melts

Melt	Content of elements , %												
	C	Si	Mn	P	S	Cr	Cu	Ni	Mo	Ti	Nb	N	B
Standard (Max.)	0,22	0,86	1,80	0,025	0,012	1,60	0,55	2,10	0,74	0,07	0,07	0,016	0,006
S-1	0,144	0,27	1,20	0,007	0,0005	0,340	0,24	0,208	0,19	0,017	0,024	0,005	0,0032
S-2	0,148	0,34	1,40	0,008	0,0010	0,540	0,22	0,255	0,30	0,021	0,025	0,0061	0,0032
S-3	0,149	0,30	1,14	0,005	0,0001	0,320	0,20	0,207	0,16	0,017	0,023	0,0055	0,0032
S-4	0,148	0,27	1,13	0,005	0,0005	0,360	0,24	0,210	0,17	0,015	0,022	0,0052	0,0032
S-5	0,144	0,28	1,11	0,007	0,0005	0,310	0,25	0,197	0,18	0,015	0,023	0,0068	0,0032

Hot rolling and heat treatment by quenching and tempering of hot-rolled plates made of S690QL steel was carried out according to standard technologies used in production. The temperature of heating and the end of rolling, which can vary, can have an effect on the microstructure and grain size. The material is heat-treated by the hardening and tempering process and has good bending and welding properties.

2. EXPERIMENTAL WORK

To check and evaluate the quality of the manufactured plates made of S690 QL steel, ten samples (test plates) were submitted for testing and analysis of the test results. According to the standard EN 10025-6:2004+A1:2009 and the standard DIN EN 10025-1, which complies with this standard, tests of toughness were performed on the longitudinal section of the test tubes at a temperature of – 40 °C. According to the same test method from these standards, the toughness of the cross-section of the test tubes was additionally tested. The grain size was determined on the cross-section of the samples according to the ASTM E 112 - 13 standard.

The supplied samples are test plates with dimensions of 100 mm x 200 mm, cut from ten hot-rolled plates of different thicknesses, produced from 5 melts, from which three longitudinal and cross-sectional test tubes were cut and made, on which the toughness test was performed at a temperature from – 40 °C.

These tests, in addition to the chemical composition and tensile characteristics, are a basic indicator of the quality of the manufactured panels. The test was carried out to determine the mutual dependence between toughness and grain size at low temperatures [3].

The analysis of the test results also aims to consider the segments of the technological process, which have an effect on the physical and metallurgical characteristics, primarily on the formed microstructure and grain size, which significantly affect the values of impact energy at low temperatures.

3. EXAMINATIONS

Tests and evaluation of results were performed according to standards EN 10025-6 and DIN EN 10025-1, according to standard procedures applied in the accredited testing Mechanical and Metallographic Laboratory of the Institute "Kemal Kapetanović" of the University of Zenica. The delivery standard EN 10025-6 prescribes the testing of tensile characteristics and toughness on the longitudinal section at a temperature of – 40 °C. The toughness is determined by the standard on the test tubes taken in the direction of rolling, designated as longitudinal test tubes. When determining Charpy impact energy according to the EN DIN 10025-1 standard, the average of the results of three tested test tubes is taken, and the mean value must correspond to the prescribed value of 30 J. Only one individual value can be below this value if it is not less than 70% of the prescribed values. Likewise, if the mean value has a nominal value and two individual values are below, in both of these cases three additional test tubes are taken and tested [1].

The grain size was tested according to the standard ASTM E 412 - Plate 13. The standards EN 10025-6:2004+A1:2009 and DIN EN 10025-1 for the tested plate thicknesses do not prescribe grain size testing, but the conducted tests can contribute to the relationship between grain sizes and toughness at low temperatures.

Figure 1 shows the test plate schematically, with the position of the specimen for testing the toughness on the longitudinal and cross sections, as well as the position of the samples for determining the grain size. In Figure 1, the arrow indicates the direction of rolling on the plate.

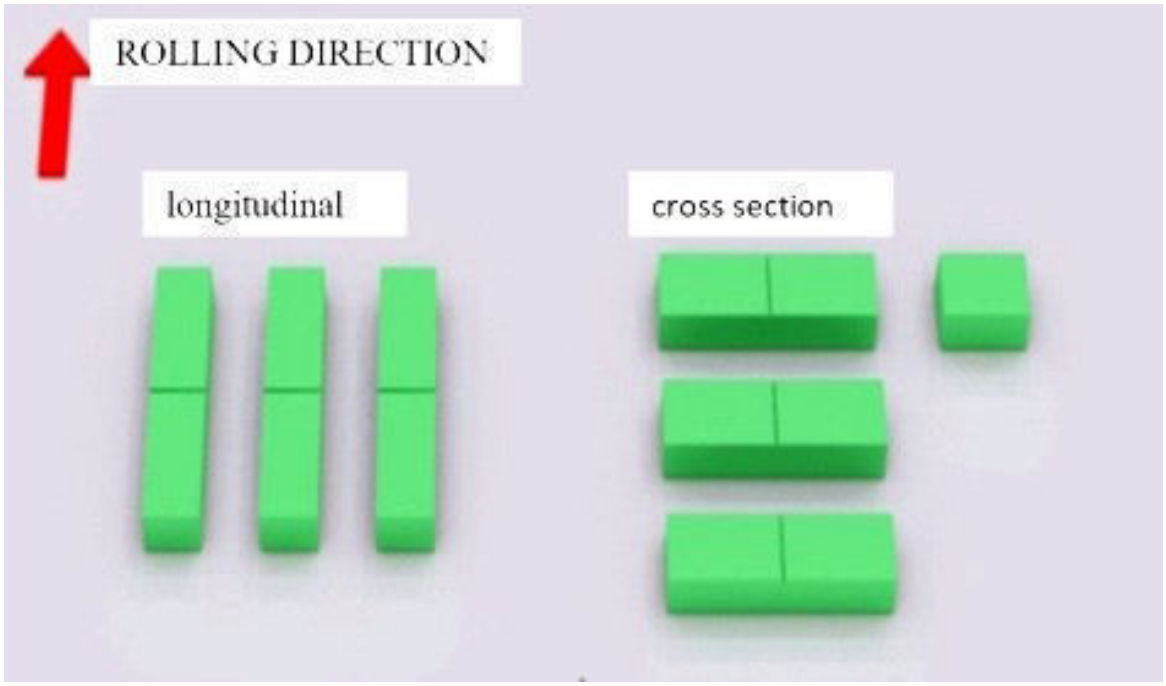

Figure 1. Position of specimen for testing toughness and samples for grain size

3.1 Toughness test at a temperature of -40 ^{o}C

The test of toughness at a temperature of -40 °C was performed on all ten samples of test panels on the longitudinal and transverse sections using the Charpy method with a notch-V, in the accredited Mechanical Laboratory of the Institute „Kemal Kapetanović", according to the standard BAS EN ISO 184-1:2017 [4]. Table 2 shows the test results, and Figure 2 shows histograms.

Table 2. Test values of impact energy and grain size of test plate samples made of S690 QL steel at a temperature of – 40 °C.

Test plate Mark	D	Impact energy, J								Size grain, ASTM
		Longitudinal				Cross-section				
		1	2	3	Average	1	2	3	Average	P
1	25	65	63	73	**67**	92	80	61	**78**	**7,5**
2	30	51	51	36	**46**	52	34	43	**43**	**7,0**
3	25	184	177	161	**174**	153	126	127	**135**	**7,5**
4	20	108	114	122	**115**	82	88	72	**81**	**7,0**
5	20	121	96	113	**110**	84	65	96	**82**	**7,5**
6	15	161	132	155	**151**	102	98	96	**99**	**7,0**
7	25	147	142	145	**145**	116	116	114	**115**	**7,0**
8	25	176	161	181	**173**	124	161	128	**138**	**7,5**
9	25	187	133	140	**137**	100	104	107	**104**	**7,0**
10	25	147	164	166	**159**	128	118	137	**128**	**7,5**
D - Plate thickness, mm; P - Average grain size										

Standard DIN EN 10025-6 [5] for steel S690 QL prescribes for impact energy a minimum average value of three tests of 30 J at a temperature of – 40 °C, only on the longitudinal section of the plate. The minimum lower limit, on the histogram in Figure 2, is marked with a horizontal line.

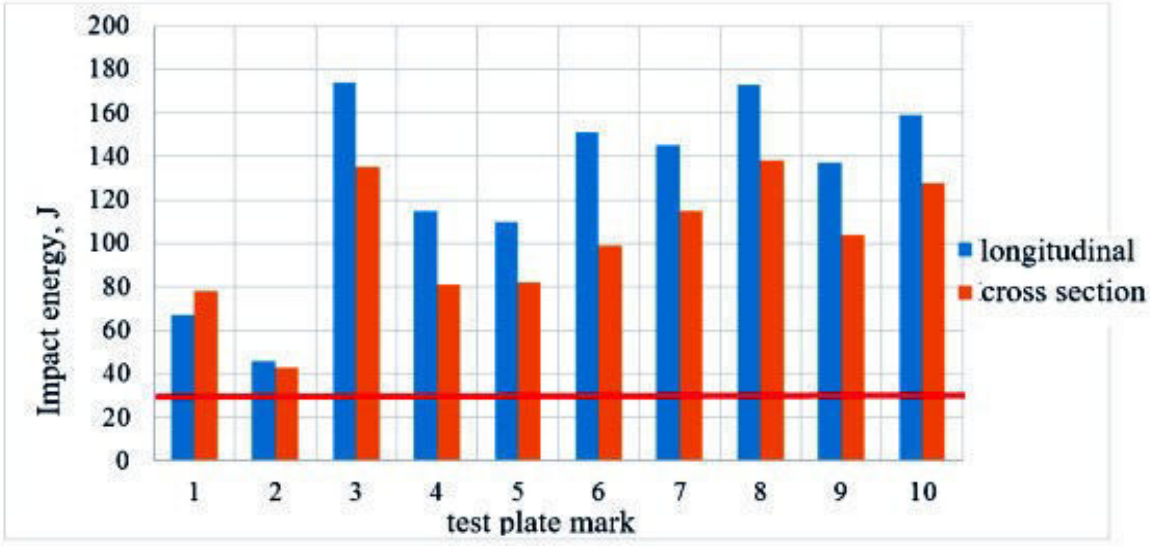

Figure 2. Average values of impact energy on longitudinal and cross-sections

The obtained results for mean impact energy values are within the prescribed limits for all tested samples. In most of the plate samples, the values of impact energy in both the longitudinal section and the cross-section have high values. From the diagram, it is also noticeable that the values on the longitudinal section are higher, compared to the cross-section, but smaller differences indicate a positive degree of achieved anisotropy of the produced panels.

3.2 Examination of the grain size

The grain size test on the cross-section of the samples was performed on all ten submitted samples in the accredited Metallographic Testing Laboratory of the Institute „Kemal Kapetanović“ according to the ASTM E 412-13 standard. The test results for the mean

values of the three tests are given in Table 2 and in Figure 2 together with the results of the impact energy test. Tests have established that all samples of test panels have a uniform fine-grained grain size and that individual larger grains have no effect on toughness.
Figure 3 shows the relationship between toughness in the longitudinal and transverse directions and the average grain size.

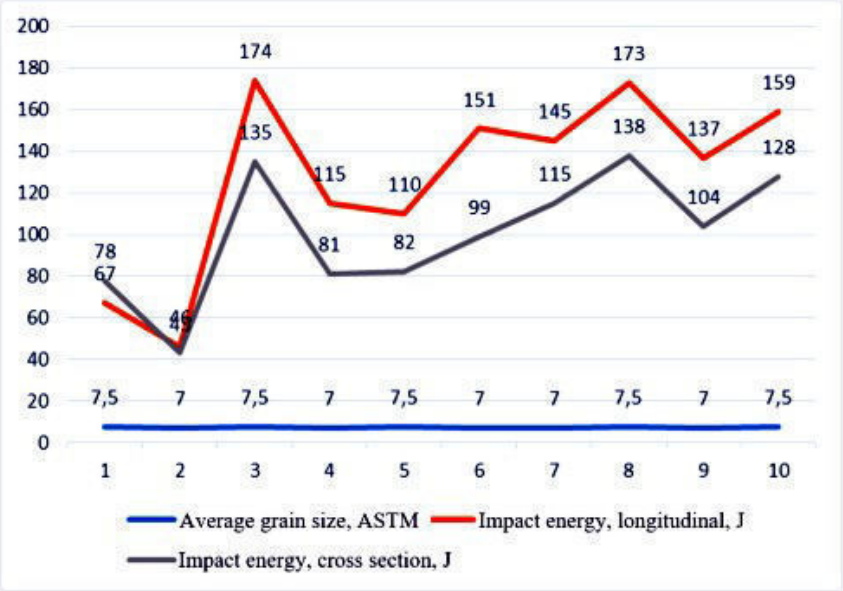

Figure 3. Dependence of impact energy in the longitudinal and transverse direction and average grain size

Figure 3 shows that grain size has the same effect on toughness in both longitudinal and cross sections, and that impact energy lines in both directions equally follow grain size. The evaluated grain sizes cannot be fully related to the achieved impact energy results, because as already stated, the test samples have on average uniform grain size values with locally larger grains, which did not affect the result.
The analysis of the microstructure revealed that a fine-improved microstructure was present in all the tested panels on the samples.

4. CONCLUSIONS

After hardening and tempering, the test samples have an improved microstructure characteristic of plates made by hot rolling with subsequent heat treatment.
The testing and analysis of the results of the impact energy test at – 40 °C on the longitudinal section of ten samples of plates, produced from 5 different melts, was carried out according to the standards EN 10025-6 and DIN EN 10025-1. In order to determine the degree of homogeneity in the longitudinal and cross-section, the toughness was tested according to the same standards and in the cross-section, and the grain size was also measured on all plates. The values of toughness in the longitudinal and transverse directions differ to a lesser degree, but this difference did not affect the anisotropy to a greater degree because all values are within the limits required by the standard.
So, by testing the impact energy at a temperature of – 40 °C, it was determined that all the average and individual values of the impact energy of fracture are significantly above the permitted values. Plates made of two melts have significantly lower values compared to all other tested plates, but this cannot be related to the achieved quality in these batches

because the values are within the limits prescribed by the standard. These plates have uniform values when tested on the longitudinal section, and a slightly smaller difference in the values tested on both sections. In the case of the other eight panels, this difference is pronounced and the values in the longitudinal test are higher than the results in the cross-section, which is expected for rolled products.
The obtained results for toughness indicate that it is grain sizes that have a favorable effect on high values of toughness. Some minor differences in grain size that exist between individual plates cannot be seen as a definite rule, and this can be seen through the toughness values, which are within the required values for all samples. It means that the toughness is mainly influenced by the average grain size, and not by individual groups of larger grains if the other grains are smaller on average. It can be assumed that such grains are connected with the uneven distribution of certain chemical elements, i.e. insufficient concentration in microsurfaces (especially those that influence the grain size through the precipitation of their compounds).

5. REFERENCES

[1] I. Vitez, M. Oruč, R. Sunulahpašić: Ispitivanje metalnih materijala, mehanička i tehnološka ispitivanja, Fakultet za metalurgiju i materijale, Univerzitet u Zenici, Zenica, 2006.
[2] M. Oruč, R. Sunulahpašić: Materijali u građevinarstvu I, Politehnički fakultet, Univerzitet u Zenici, 2014.
[3] EN 10025-6 S690QL celik 1 - Steel Material Supplier
[4] https://gangsteel.com › en-10025-6-s690ql-celik-1
[5] BAS EN ISO 184-1:2017
[6] EN 10025-6 (EN 10025-6:2019)

APPLICATION OF THE BAS EN ISO 1463:2022 STANDARD IN THE CHARACTERIZATION OF PIPE MATERIALS FOR THERMAL ENERGY PLANTS

Belma Fakić, Adisa Burić, Edib Horoz
University of Zenica, Institute "Kemal Kapetanović"
Zenica, B&H

Keywords: steel pipe, oxide layer, standard,measurement, uncertainty

ABSTRACT
Long-term exposure of superheater and steam intermediate superheater pipe materials to high temperatures in the operating conditions that prevail in thermal power plants leads to the appearance of the oxide layer.Oxide layer forms on the inner wall of the pipe, which acts as a heat insulator and reduces heat transfer through the pipe wall.The action of the oxide layer as an insulator and limiting the transfer of heat to water vapor inside the pipe leads to overheating of the pipe wall.This paper presents the measurement of the thickness of the oxide layer on the outer and inner side of the pipeusing the standard method BAS EN ISO 1463:2022 with a presentation of the measurement results with pronounced measurement uncertainty.

1. INTRODUCTION

The high temperatures and pressures that exist in the components of thermal power plants - pipes of superheaters and steam reheaters, lead to changes in the structure of the material as well as the appearance of an oxide layer.The appearance of overheating of the material due to the formation of an oxide layer on the inside of the pipe wall can have a significant impact on the service life of the component.

2. OXIDE LAYER

The oxide layer that appears on the pipe walls of superheaters and steam reheaters in thermal power plants acts as an insulator and leads to overheating of the pipe wall. The presence of deposits of oxide layers on the pipe walls increases the temperature of the metal, which accelerates the creep mechanism and thus reduces the service life of the material [1]. On the inner surface of a pipe made of low-alloy steel (up to 3% Cr), which is exposed to steam generated in boilers, an oxide layer is formed at different levels.When the temperature of the metal is below 560°C and there is a high partial pressure of oxygen, a layer of magnetite (Fe_3O_4) and hematite (Fe_2O_3) appears.At higher temperatures, an additional layer of wustite (FeO) may appear.If the steel has more alloying elements, spinel oxide $(Fe, Cr, Mo)_3O_4$, can form as the oxide layer grows in the direction of the pipe wall.These oxides are formed according to the following reactions [1,2]:

Wustite:

$$Fe + \frac{1}{2}O_2 = FeO;$$

Magnetite:

$$3FeO + \frac{1}{2}O_2 = Fe_3O_4$$

Hematite:

$$2Fe_3O_4 + \frac{1}{2}O_2 = 3Fe_2O_3$$

Wustite is the lowest valence iron oxide that exists over a wide compositional range that does not quite include the stoichiometric composition of FeO.
Magnetite is an iron oxide of intermediate valence that has a composition close to the stoichiometric composition of Fe_3O_4.Magnetite is the most abundant oxide on the inner wall of superheater and steam reheater tubes operating in conventional chemical cycles.
Hematite is the highest valence iron oxide with a composition close to the stoichiometric composition of Fe_2O_3 [3,4].

2.1 Consequences of the appearance of the oxide layer

In exploitation conditions that exist in thermal power plants, the appearance of the oxide layer can result in:

a) reduction of the cross-sectional area of the pipe material - which leads to an increase in stress;
b) thermal insulation of the pipe - the oxide layer has a significant effect on the heat transfer of the pipe, while an increase in the temperature of the pipe material leads to accelerated material;
c) peeling of oxide scales - peeling of thick oxide would be useful in terms of reducing the effect of thermal insulation.However, the scaled oxide can lead to pipe overheating if trapped in the system, thereby reducing the steam flow rate within the pipe [1].

3. MATERIAL AND METHOD OF MEASUREMENT

For the purposes of this work, the sample of steam reheater pipe ϕ 45x6 mm, made of material 13CrMo4-4was prepared. After years of exposure to the high temperature and pressure that exist in thermal power plants, a significant presence of oxide layers on the inner and outer walls of the pipes was observed. The chemical composition of pipes according to the standard DIN 17175 [5] and chemical analysis are given in Table 1.

Table 1. Chemical composition

	Mass (%)						
	C	Si	Mn	P	S	Cr	Mo
Standard DIN 17175	0,10-0,18	0,10-0,35	0,40-0,70	max 0,035	max 0,035	0,70-1,10	0,45-0,65
Pipe ϕ 45x6 13CrMo4-4	0,14	0,25	0,57	0,011	0,019	0,70	0,35

The cross-section of the pipe sample was prepared in accordance with standard ASTM E 3-Standard Guide for Preparation of Metallographic Specimens [6]. The cutting was carried out on a CUT machine with a diamond cutting plate with the addition of an emulsion for cooling the cutting surface. Rough preparation - wet grinding on sandpaper grades 240, 400, 600, and 1000 SiC, and fine preparation - polishing with diamond suspension grades 9 and 3 microns was carried out on a machine for automatic sample preparation.
The prepared test surface was observed on a calibrated light microscope at magnifications of 50 and 100 times.
Standard BAS EN ISO 1463:2022 [7] describes, among other things, the method of measuring the thickness of oxide layers. Sample preparation - grinding, polishing and, if necessary, etching is carried out in order to obtain clearly defined layers.

3.1 Measurement of thickness of the oxide layer

The thickness of the oxide layer is measured using the software Analysis 5.1 with a light microscope OLYMPUS PMG3.The input to the software is calibrated using a calibrated object micrometer. The choice of magnification at which the measured oxide layer is observed is between one and a half and three times the thickness of the oxide layer. The appearance of the pipe from which the sample was taken is given in Figure 1. Representative micrographs of the oxide layer are given in Figure 2.

Figure 1. Pipe of steam reheater, after exploitation [8]

Uneatched x150

Figure 2. The oxide layer, inside the wall of the pipe [8]

The results of measuring the thickness of the oxide layer and the uncertainty of measurement of the thickness of the oxide layer are given in Table 2. The calculation of measurement uncertainty is done in accordance withthe instruction of Determination of measurement uncertainty when measuring the thickness of the metal or oxide layer UMT7-06-01 [9].

PIPE ϕ45x6 mm, material 13CrMo4-4;
Overlap factor for t-distribution (Student's distribution):
Number of degrees of freedom: f = n-1 = 5-1 = 4 and the confidence level P = 68, 27 is: t = 1,11
Measurement of the uncertainty of micrometer from calibration certificate: 2,38
Coverage factor: 2

Table 2. Measuring the thickness of the oxide layer and uncertainty of measurement

No.of ofmeasur. n	Thickness layer D_i (μm)	Mean value D_{sr}	Standard deviation S_D	Measur. uncertainty μ_D	Measur. of micrometer μ_C	Combined uncertainty $\mu_C(D)$	Extended measure. uncertainty $\mu(D)$
1.	163,2						
2.	166,0						
3.	166,9	165,18	1,883	1,045	1,19	1,584	3,2
4.	166,7						
5.	163,1						

The result of measuring the thickness of the oxide layer was: 165,2±3,2 microns.

4. CONCLUSION

The measured value of the thickness of the oxide layer on the inner wall of the pipe ϕ45x6 mm, made of material 13CrMo4-4 in the value of 165.2±3.2 μ indicates that attention should be paid to the remaining life of the pipe.Namely, the application of an oxide layer on the inner wall of the pipe for operational conditions in thermal power plants (temperatures over 450°C) can lead to degradation of the microstructure [1], because the oxide layer will act as a thermal insulator, causing local overheating of the pipe.
The BAS EN ISO 1463:2022 standard provides a good basis for measuring the thickness of the oxide layer and seeing the general picture in the characterization of pipe materials used in thermal power plants, as well as estimating the remaining life of the pipe material.

5. REFERENCES

[1] B. Cardoso and others: Microstructural Degradation of Boiler Tubes Due to the Presence of Internal Oxide Layer, Journal of Materials Research and Technology, 2012
[2] Brian S. Mitchell: An introduction to materials engineering, New Jersey, 2004
[3] Leonard E. Samuels: Light Microscopy of Carbon Steels, Ohio, USA, 2010
[4] D. Ćubela (translate) Bruce L. Brafitt: Metallographer's guide, Practices and procedures for irons and steels, Zenica, 2016.
[5] Standard DIN 17175: Seamless Tubes of Heat-Resistant Steels, technical conditions of delivery, 1979
[6] Standard ASTM E 3 - Standard Guide for Preparation of Metallographic Specimens, 2017
[7] Standard BAS EN ISO 1463-, 2022
[8] Branko R. and others: Examination and determination of the condition of the boiler material of Unit 6 at the Kakanj Thermal Power Station, Zagreb, 1997
[9] Fakić B. and others: Determination of measurement uncertainty when measuring the thickness of the metal or oxide layer UMT7-06-01, Zenica, 2021

CONTRIBUTION TO MECHANICAL PROPERTIES ASSESSMENT OF SPHERICAL CYLINDRICAL HEAD SHELLS MADE BY THE INCREMENTAL SHEET FORMING

Mustafa Hadžalić
University of Zenica, Institute "Kemal Kapetanović"
Zenica, B&H

Raza Sunulahpašić
University of Zenica, Faculty of Metallurgy and Technology
Zenica, B&H

Zlatan Ištvanić
Metacomm Jajce
Jajce, B&H

Keywords: Incremental sheet forming (ISF), pressure vessel floors, mechanical properties

ABSTRACT
The paper describes the determination of the mechanical properties of the spherical floors of pressure vessels, obtained by the welding process and shaped by the process of gradual local deformation in the cold state, i.e. by the process of Incremental sheet forming (ISF). Spherical cylindrical bottoms are an integral part of most closed-pressure vessels. Cylindrical pressure vessel floors are made from one part, but the standards also allow for welded construction when the dimensions of the floors are larger than the standard dimensions of the sheet metal for production. Pressure vessel floors obtained by the welding process and shaped by the process of gradual local deformation in the cold state, i.e. by the process of incremental deformation, have a multiaxial initial stress state, which differs significantly from the initial stress state of the cylindrical part of the vessel.
Checking the behavior of such floors before completing the vessel itself, i.e. before putting it into operation, is necessary, on the one hand, due to a large number of influencing factors, and on the other hand, due to the high cost of testing the real construction itself.
The aim of the test is to determine the influence of the parameter: type of material, thickness, and diameter on the following quantities: mechanical properties, R_{eH}, R_m, A_5, and total energy used for impact, KV.

1. INTRODUCTION

The floors of pressure vessels are exposed to a complex stress state (the appearance of tensile and bending stresses), which differs from the stress states of the cylindrical part of the pressure vessel, and therefore the considerations related to the cylindrical part of the vessels cannot be explicitly mapped to the behavior and integrity of the floors. On the other hand, in the case of large pressure vessels, the floors are very often made from large starting pieces (sheets) whose dimensions exceed the standard commercial dimensions, and it is necessary to form the starting pieces by welding procedures, which further impairs the integrity of the starting material.
The welded joint as a complex and heterogeneous structure represents a critical place in the welded construction. Therefore, in most cases, the safety of a welded structure is evaluated

based on the properties of the welded joint as a whole, and the properties of all its constituent parts. In many cases, the behavior of the welded joint as a whole differs from the behavior of the weld metal, the heat-affected zone (HAZ), and the base metal. The European directive for pressure equipment 97/23/EC [1] should ensure the operational safety of pressure equipment with specifics in design, construction, and testing. An alternative is the testing of samples taken from the structure itself before installation, i.e. simulating the behavior of the floors during exploitation using plate test tubes. The procedure of metal processing by gradual deformation using the mechanical action of an indenter is relatively insufficiently researched, especially in the field of integrity assessment as a multidisciplinary approach.

A good part of the previous research was focused on the optimization of technology and the development of machines for this purpose because there are a large number of applications of the products obtained by this method, especially parts made of steel sheets. Individual parts are installed in responsible machine structures and must meet the strict requirements that treat such products, which certainly include pressure vessels. The process of making the wedges by incremental deformation together with rolling around the circumference, to pull out the cylindrical part of the wedge, additionally complicates the state of stress due to the presence of high local pressure.

This approach to analysis enables obtaining the data necessary for a reliable assessment of the head properties, defining the parameters of choices and decisions, and determining the cause of bad behavior aimed at the correction and improvement of the manufacturing technology.

This paper contributes to the evaluation of the mechanical properties of cylindrical floors made by the ISF forming process.

2. TECHNOLOGY OF MANUFACTURING SPHERICAL FLOORS BY INCREMENTAL DEFORMATION

The process of forming by incremental deformation is the process of forming metal by progressive local deformation - incremental sheet forming (ISF). In the ISF procedure, the tool is moved along the contour of the workpiece, creating small deformations in the material, which gradually shape it into the desired shape. This method of manufacturing requires low production costs, and low tool costs and represents a potentially attractive solution for flexible production.

The construction technology must be designed based on all relevant influences to ensure that the floors are safe during working life. Allowable stresses for pressure equipment must be limited by possible errors in operating conditions, to eliminate the uncertainty arising from manufacturing, calculation models, actual operating conditions, and material characteristics and behavior. The incremental deformation of the roundel is performed on a hydraulic press with an exchangeable tool and pressure force. The final shaping of the torus was done on a press type P2MF 200x4 – Sertom, Milan, Figure 1 [2].

Figure 1. Production of floors by incremental deformation process [2]

Floors for experimental research are made by gradual pressing from initial preparations, the so-called rounds, obtained from welded sheets. During such a process of making floors, pressure zones are observed along the radius as a consequence of the manufacturing technology with a combination of welding and plastic deformation. Floors made for experimental research have a large number of segments that are radially welded. Welded joints are stiffer and thicker than the base material, thus preventing the material from stretching and causing the appearance of waviness at the edges.
Earlier research and experience in application [3] showed that the most commonly used material for making floors is hot-rolled carbon steel sheet in the range of 200 to 800 N/mm^2. These steels have good plasticity properties and the production speed depends on the thickness of the material and the magnitude of the tensile strength for the same shape and size. Also, it was observed that with these materials, the waviness at the edges is smaller with thicker materials.

3. EXPERIMENTAL RESEARCH

The mechanical tests presented in this paper are aimed at obtaining a more complete picture of the state of the material of spherical pressure vessel floors, made by welding from several segments. The floors are made of two different materials, S235JR and P460NL1, in two thicknesses (6 mm and 15 mm) for a specific diameter (1500 mm).
Chemical composition from quality S235JR and P460NL1 according to the standard EN 10028-3:2017, is given in Table 1 [2].

Table 1. Chemical composition from quality S235JR and P460NL1 [2]

Chemical composition of the base material, %											
steel grade	C	Si	Mn	P	S	Al	Cr	Ni	Mo	Cu	C_{EV}
S235JR, #6 mm	0,13	0,22	0,41	0,012	0,009	0,037	0,016	0,10	0,001	0,32	0,25
S235JR, #15 mm	0,13	0,22	0,40	0,012	0,006	0,036	0,016	0,12	0,001	0,35	0,26
P460NL1, #6 mm	0,17	0,40	1,55	0,010	0,003	0,028	0,04	0,04	0,004	0,02	0,47
P460NL1, #15 mm	0,18	0,56	1,67	0,016	0,003	0,032	0,04	0,52	0,003	0,04	0,52

In addition to the known influential parameters on the production of pressure vessel floors by the incremental deformation process, the behavior of floors with a welded joint remains unknown.

The welding technology in accordance with EN ISO 4063 is 121 (EPP/LP). Welding was performed with protective powder, preheating temperature 180 ^{0}C, weld width 15-17 KJ/cm for 6 mm thick sheets and 27-44 KJ/cm for 15 mm thick sheets.
The aim of the investigation is to determine the influence of the parameters: type of material, thickness, and diameter on the following mechanical properties, R_{eH}, R_m, A_5, and total energy used for impact, KV. The mechanical properties of the base material are given in Table 2.

Table 2. The mechanical properties of the base material [2]

Base material	Mechanical properties of the base material									
	R_{eH}, MPa		$R_{p0,2}$, MPa		R_m, MPa		A_5		KV, J	
	min.	max.	min.	max.	min.	max.	min.	max.	min.	max.
S234JR+N 6 mm	345	366	-	-	456	488	32,9	33,3	-	-
S234JR+N 15 mm	330	350	-	-	455	485	32,1	32,1	-	-
P 460 NL1 NT 6 mm	469	493	-	-	515	595	28	34	-	-
P 460 NL1 NT 15 mm	466	474	371	380	608	620	24,2	29,2	-	-

Regard to the defined problem of this specific structure (pressure vessel), primarily refers to the process of making the bottom of the vessel (processing by plastic deformation) as well as the procedure of preliminary welding to achieve the desired diameter, the experimental part of the research is carried out on series of test tubes taken from the floor of the vessel. The samples were taken from the initial welded sheets before any applied technology (series I), then from the finished floors produced by plastic deformation (series II).
The samples for the conducted tests are standard test tubes that in some cases are modified (adjusted) to obtain the most accurate results. The focus of the test is the heat-affected zone as potentially the most critical place from the aspect of safety as well as quality control possibilities. Destructive tests refer to the definition of material properties by destructive tests on test tubes according to current standards, that is, the determination of parameters used in the assessment of the safety and integrity of the analyzed material.

3.1 Scheme of sample extraction

Floors for experimental research were made using the plastic incremental deformation process. The initial preparation for making the floor is a circular sheet of tin, the so-called. roundels. For the experiment, two roundels of different dimensions were made: ϕ1500x6 mm and ϕ1500x15 mm. Samples were made in two sets (series):

- Ist set samples from the starting sheet,
- IInd set is sheet metal samples after plastic deformation.

To assess the impact of the weakest place, i.e. heat-affected zone, after plastic deformation, the test tubes were taken from the direction transverse to the longitudinal axis of the welded joint, Figure 3, Figure 4, and Figure 5.

Figure 3. Taking samples from the manufactured floor

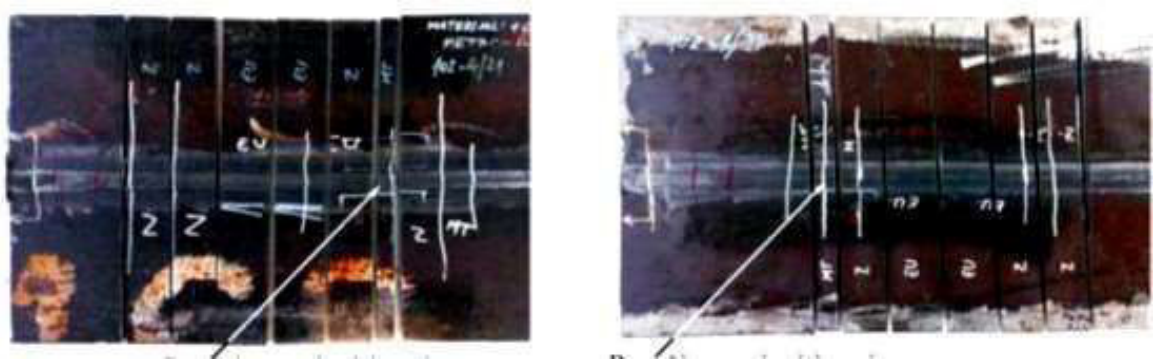

test surface, the thickness of 6 mm test surface, the thickness of 15 mm

Figure 4. Location of taking samples of sheet P460NL1 NT

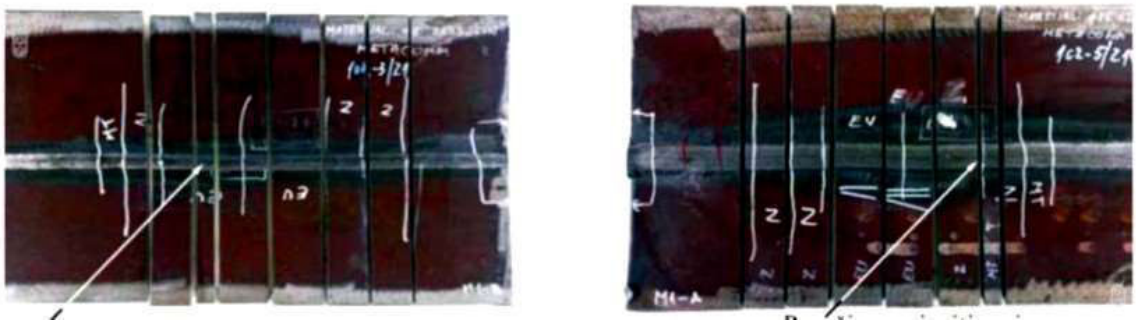

test surface, the thickness of 6 mm test surface, the thickness of 15 mm

Figure 5. Location of taking samples of sheet S235JR+N

3.2 Determination of tensile properties

Tensile tests of test tubes removed from the bottom of the pressure vessel were performed at room temperature +18 °C. The test was performed on a universal hydraulic machine for static tests AMSLER, ser. No. 599/625.

The test procedure itself is defined by the standard BAS EN ISO 6892-1:2017 B [4], on test tubes for tensile tests whose geometry is given by the standard BAS EN ISO 4136:2014 [5]. The test tubes were modified with an incised transverse groove in the heat-affected zone, which is the subject of the study, Figure 6.

The tests were carried out for two series of samples and materials of the M1 and M2 designations.

Figure 6. Test tubes for the determination of tensile properties - series II

A typical layout of the tensile test diagram for the test tube of series I (sheet 15 mm, material M1) is given in Figure 7, and for series II (sheet 15 mm, material M2) in Figure 8. The results of tensile tests of the test tubes for the two series are given in Table 3 and Table 4.

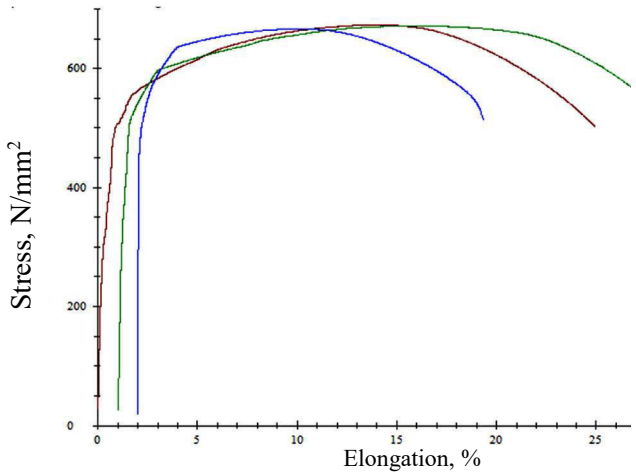

Figure 7. Stress-elongation diagram of series I test tubes

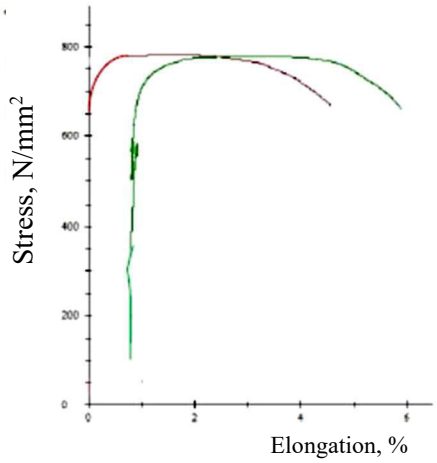

Figure 8. Stress-elongation diagram of series II test tubes

Table 3. Tensile test results of test tubes from series I for two materials

Material	S235JR+N (M1) ϕ1500 mm		P460 NL1 (M2) ϕ1500 mm	
Thickness	6 mm (M1-B)	15 mm (M1-A)	6 mm (M2-D)	15 mm (M2-C)
R_{eH}, MPa	344	340	407	531
R_m, MPa	465	475	593	670
A_5 (%)	27,33	34,0	20,83	31,6

Table 4. Tensile test results of test tubes from series II for two materials

Material	S235JR+N (M1) ϕ1500 mm		P460 NL1 (M2) ϕ1500 mm	
Thickness	6 mm (M1-B)	15 mm (M1-A)	6 mm (M2-D)	15mm (M2-C)
R_{eH}, MPa	534	612	614	763
R_m, MPa	597	637	682	780
A_5 (%)	9,75	10,75	9,5	11,75

Analyzing the results of the tensile test given in Table 3 and Table 4, it can be stated that the results are within the limits of the values for the analyzed materials after welding – series I and after plastic deformation – series II. The characteristic of the curve corresponds to a ductile material.
The values of the mechanical properties on the samples from series II (samples from the floors after plastic deformation) are above the values in the base material, Table 4, except for the ductile properties. Plastic deformation led to the strengthening of the material and an increase in the values of yield stress and tensile strength. At the same time, a decrease in ductile properties, i.e. a decrease in material elongation, was observed. Fracture took place in a controlled manner in the heat-affected zone. This indicates that it is about "overmatching", that is, that the mechanical properties of the strength are better in the heat-affected zone than in the base material.

3.3 Determining the impact energy of fracture

Determining the work required for fracture under established test conditions is most often used for ongoing control of the quality and homogeneity of the material, as well as its processing. This test procedure can determine the tendency to brittle fracture, that is, the tendency to increase brittleness during the exploitation (aging).
Impact tests of the samples were performed on a 300 J Charpie pendulum at a room temperature of +20 °C. The test procedure itself was carried out according to ISO 148-1:2017 [6] on standard test tubes (BAS EN ISO 9016:2012, [7]) whose layout is given in Figure 9.

Figure 9. Shape and dimensions of a standard test tube with a V notch for testing by the Charpie method

The test obtained the results of the total energy expended on impact. The test results of the impact properties of test tubes are given in Table 5 and Table 6.

Table 5. Test results of test tubes from series I for two materials (notch in the HAZ)

Material	S235JR+N (M1) ϕ1500 mm		P460 NL1 (M2) ϕ1500 mm	
Thickness	6 mm (M1-B)	15 mm (M1-A)	6 mm (M2-D)	15 mm (M2-C)
KV, J	52- welded joint	56- welded joint	47- welded joint	75- welded joint
	53-HAZ	87-HAZ	35-HAZ	48-HAZ

Table 6. Test results of test tubes from series II for two materials (notch in the HAZ)

Material	S235JR+N (M1) ϕ1500 mm		P460 NL1 (M2) ϕ1500 mm	
Thickness	6 mm (M1-B)	15 mm (M1-A)	6 mm (M2-D)	15 mm (M2-C)
KV, J	45	103	15	41

The total energy spent on impact in the heat-affected zone of series II is reduced compared to series I. The effect of strengthening due to plastic deformation is the cause of the reduction in toughness.

4. CONCLUSIONS

Pressure vessels belong to one of the most complex and responsible machine constructions. The modern standard for pressure vessels EN 13445:2002 and the corresponding regulations for pressure equipment (PED) show all the seriousness with which the problem of vessels and other pressure equipment is approached in the developed world. Modern standards are constantly supplemented with new knowledge that is regularly checked and implemented in new versions of the standard. However, these regulations do not adequately cover floors made by incremental deformation, and the level to guarantee the complete safety of the construction is also questionable.

In the paper, various influencing parameters (materials S235JR and P460NL1, thickness 6 mm and 15 mm, for a specific diameter of 1500 mm) on the mechanical properties, R_{eH}, R_m, A_5, and the total energy used for the impact, KV, were analyzed. For these influential parameters, it is empirically assumed that they are the key technological parameters for the production of spherical pressure vessel floors, made by welding from several segments. The effect of the welded joint was observed without any geometric irregularity, that is, with the assumption that there are no unacceptable defects.

Analyzing the results of the tensile test given in Table 3 and Table 4, it can be stated that the results are within the limits of the values for the analyzed materials after welding – series I and after plastic deformation – series II. The characteristic of the curve corresponds to a ductile material.

The values of the mechanical properties of the samples from series II (samples from the floors after plastic deformation) are above the values in the base material. The plastic deformation led to the strengthening of the material and an increase in the values of the yield stress and tensile strength. At the same time, a decrease in ductile properties, i.e. a decrease in material elongation, was observed. The fracture occurred in a controlled manner in the heat-affected zone. This indicates that the mechanical properties of strength are better in the heat-affected zone than in the base material.

By examining the total energy spent on impact, it can be concluded that the total energy spent on impact in the heat-affected zone of series II is reduced compared to series I. The strengthening effect due to plastic deformation is the cause of the reduction in toughness.

Floors made by the process of incremental deformation of welded starting pieces as an integral part of closed pressure vessels have met the requirements of the standards defining pressure vessels and guaranteeing the safety of these responsible constructions.

5. REFERENCES

[1] Pressure Equipment Directive – PED 97/23/EC, EU, 1997.

[2] Zlatan Ištvanić: Prilog utvrđivanju integriteta cilindričnih danaca izrađenih postupkom inkrementalne deformacije, doktorska disertacija, Mašinski fakultet, Univerzitet u Zenici, Zenica, 2022.

[3] Michael B. Prime: Residual stress measurement by successive extension of a slot: The crack compliance method, Applied Mechanics Reviews, Vol. 52, No. 2, pp. 75-96, 1999.

[4] BAS EN ISO 6892-1:2017 B: Metallic materials — Tensile testing — Part 1: Method of test at room temperature
[5] BAS EN ISO 4136:2014: Destructive tests on welds in metallic materials — Transverse tensile test
[6] ISO 148-1:2017: Metallic materials — Charpy pendulum impact test — Part 1: Test method
[7] BAS EN ISO 9016:2012: Destructive tests on welds in metallic materials — Impact tests — Test specimen location, notch orientation and examination

NDT TESTING AND DETERMINATION OF THE STATE OF THE MATERIALS OF THE HEADERS OF THE BOILER UNIT 5 IN THE THERMAL POWER PLANT KAKANJ

Armin Husika
Termoelektrana “Kakanj“
Kakanj, B&H

Belma Fakić,
University of Zenica, Institute “Kemal Kapetanović”
Zenica, B&H

Milenko Rimac,
Maneco Kakanj
Kakanj, B&H

Keywords: headers, NDT testing, welded joint, structure, hardness,

ABSTRACT
In order to examine the state of critical components of the boiler of Unit 5 of Kakanj Thermal Prema wer Plant, headers were tested in order to undertake appropriate technological measures and activities on the basis of insight into the current state of affairs, and to make recommendations for further exploitation. From first commissioning in 1969 to 30 April 2019 the Unit 5 boiler had 271.403 operating hours in operation and was designed for 100.000 hours. During the exploitation so far, several modifications and revitalizations have been carried out on the block, although some components from the installation period are still in operation (superheater headers Pr 5 and Pr 6). The testing program was made on the basis of analysis and evaluation of the results from previous tests and records of performed repairs on the tested components (repair of individual cracks on welded joints, created during exploitation in the previous period). The paper presents the most important data on past exploitation, the results of the NDT tests, as well as the hardness and structure tests on the replicas.
Material condition assessments of critical components of Pr 5 and Pr 6 superheaters, unit 5 boiler, and recommendations for further exploitation were made based on NDT tests, as well as hardness and structure tests, in accordance with prescribed, norms and applicable standards, and structural degradation assessment and the hardness drop from the commissioning of the block to the tests carried out in the course of this work on the same or similar components.

1. INTRODUCTION

In order to assess the condition of the critical components, which have been in operation for the longest time on boiler block 5 in the Thermal Power Plant Kakanj, tests were carried out on the following headers during regular overhaul:

a) Mixing header of superheater Pr 5 (KP 13),
b) Outlet headers of superheater Pr 5 – left (KP 14L) and right (KP 14D),
c) Exit header Pr 6 (KP 16).

According to the test program, the following non-destructive tests are planned according to valid standards, regulations, and methods:

a) Visual and dimensional control of headers,

b) Ultrasonic measurement of the thickness of the header walls,
c) Examining the microstructure of the material by taking replicas and the hardness at the place where the replicas were taken,
d) Examination of welded joints by magnetic and ultrasonic methods and measurement of hardness.

2. BASIC DATA ON THE BOILER OF BLOCK 5

Unit 5 is a 110 MW steep tube condensing unit with natural water circulation in the evaporator, liquid slag removal, and a triple bypass, delivered from the former Czechoslovak Republic. From the first commissioning in 1969. until the overhaul on April 30, 2019. 271.403 h in exploitation working hours were achieved. In the course of exploitation so far, several modifications and revitalizations have been carried out on the unit, and there are some parts of the boiler that are still in use, and have not been changed since the unit was put into operation [1].

3. MATERIALS

3.1 Basic data on the materials of the tested boiler headers of block 5

Basic data on the material of the tested headers from the block 5 boiler superheater are given in Table 1.

Table 1. Basic data on the materials of the tested boiler headers of block 5

Ordinal number	The name of the component	Material	Dimension [mm]	Installation time
1.	Pr5-KP13	15128.5	Ø 273 x 25	1987
2.	Pr 5 - KP 14L i KP 14D	15128.5	Ø 324 x 36	1987
3.	Pr 6 - KP 16	15128.5	Ø 273 x 46	1981

3.2 Properties of the steel from which the tested headers are made

The tested headers of the boiler of block 5 are made of low-alloy chromium-molybdenum-vanadium steel of the designation 15128.5 according to the standard ČSN 41 5128 [2] in a normalized state. Steel 15128.5 is designed to withstand long-term loads at an elevated temperature of 545 ˚C, and the designed service life is approx. 100.000 hours. The microstructure of steel 15128.5 consists mainly of ferrite with a smaller proportion of softened bainite and pearlite in the amount of 4 to 15 %. Alloying elements influence the course of material degradation and the primarily formed coherent carbides under the long-term influence of temperature change into another non-coherent form, as a result of which the process of forming new carbides from elements dissolved in the ferrite solid solution begins. In the further process, coagulation and solidification of carbides occur, which leads to the degradation of the structure and a decrease in mechanical properties. The described processes take place in the stationary region of creep and are observed by observing the microstructure on a microscope. Degradation processes in the stationary area dominantly affect the creep flow in the tertiary phase, in which the formation of microcracks and fractures occurs [3].

Table 2 shows the chemical composition and mechanical properties of steel 15128.5 according to the standard ČSN 415128 [2] and steel 14MoV63 according to the standard DIN 17175 [4], because the regulation for the evaluation of structure degradation VGB-S-517 [5] applies only to steel 14MoV63, which according to its chemical composition and mechanical properties is almost identical to steel 15128.5, so this regulation can also be used for steel 15128.5.

Table 2. Chemical composition, tensile strength, and hardness of steel 15 128.5 and 14MoV63

Steel	Content of elements, %								R_m	Hardness
	C	Si	Mn	P	S	Cr	Mo	V	MPa	HB
15 128.5*	0,10 - 0,18	0,15 - 0,40	0,45 - 0,70	Max 0,04	Max 0,04	0,50 - 0,75	0,40 - 0,60	0,22 - 0,35	490- 690	140 - 197
14MoV63	0,10 - 0,18	0,10 - 0,35	0,40 - 0,70	Max 0,035	Max 0,035	0,22 -0,32	0,25 - 0,35	0,22 - 0,32	450 - 690	135 - 181**

** Steel 15128.5 in a normalized state (normally cooled and quenched) according to ČSN 41 5128 [2]*
***Hardness is derived from tensile strength according to standard DIN 50150 [7]*

4. PROGRAM AND EXAMINATION SCOPE

The following tests were performed on the boiler superheater headers of block 5, KP 13, KP 14L, KP 14D, and KP 16:

4.1. Visual inspection of header ovality, corrosion damage, and cracks,
4.2. Ultrasonic measurement of wall thickness on each header,
4.3. Microstructure with replicas on each header,
4.4. Assessment of the degree of degradation of the microstructure according to VGB-S-517,
4.5. Measurement of hardness at all points of taking replicas,
4.6. Examination of the welded joints of the headers with magnetic particles and ultrasound,
4.7. Measurement of the hardness of welded joints.

5. OBJECTIVE OF THE TEST AND ANALYSIS OF PREVIOUSLY PERFORMED TESTS

The analysis was done with the aim of comparing the obtained results with previous tests, especially with the previous results performed on the same components as with the tests conducted in 2019. The assessment of the condition of the tested components was carried out based on the characteristics of the materials taken from the standard, treated as the initial state of the material, and the results obtained by testing in 1997, 2002, and 2019.

6. EXAMINATION

As part of this work, a visual inspection, measurement of the ovality and thickness of the header walls, and testing of welded joints were performed, as these are the methods used to detect imperfections according to the requirements of standards and acceptance criteria. Testing the degree of degradation of the microstructure using replicas, testing the hardness at the place of taking the replicas, and measuring the hardness of welded joints are methods that, based on the results and analysis of previous tests, indicate the degradation of the material of the tested components. The following tests were conducted on the superheater headers of boiler 5: KP 13, KP 14L and KP 14D, and KP 16 during the overhaul period of block 5 in 2019, and the obtained test results are listed in Table 3.

Table 3. Header test results

Ordinal number	Test method	Test result
6.1.	Visual inspection	Visual inspections determined that all tested headers, welded joints, suspensions, supports and other elements meet the acceptance criteria.
6.2	Measuring ovality (dimensional control)	Measurements confirmed that the ovality of chambers KP 13, KP 14L, and KP 14D, KP 16 meet the requirements of the EN 10216-2 standard.
6.3	Measurement of wall thickness using ultrasound	Measurements of the thickness of the header walls KP 13, KP 14L and KP 14D, and KP 16 with tolerances according to standards showed that there is no significant deviation from the nominal thickness of the header walls.
6.4	Examination of welded joints with magnetic particles	The tested butt-welded joints on the headers and fillet welded joints of headers KP 13, KP 14L and KP 14D, and KP 16 with headers meet the acceptance criteria.
6.5	Examination of welded joints using ultrasound	The tested butt welds on headers KP 13, KP 14L and KP 14D, and KP 16 meet EN ISO 17640/EN ISO 5817 - B, with the level of acceptance according to EN ISO 11666 Level 2. – On the header, KP 16 at the welded joint FW 1-1, a defect of length 12 mm at a depth of 8 mm was detected, with an excess of the registration curve of 1 Db, and as such it meets the acceptance criteria. – On the welded joint FW 1-5, a 25 mm long defect was detected at a depth of 48 mm, exceeding the registration curve by 2 Db, and as such it meets the acceptance criteria.

6.1 Examinationof the degree of degradation of the microstructure using the method of taking replicas

The results of testing the degree of degradation of the steel microstructure on the header KP 13, KP 14 L, KP 14 D, and KP 16 are similar, and therefore we show the microstructure and images on the header KP 13 as an example of the degree of degradation of the imputed chambers.

All tested microstructures of the replica headers KP 13, KP 14L and KP 14D, and KP 16 of the block 5 boiler superheater were evaluated according to VGB-S-517 regulations with degradation level 3a, which indicates the beginning of complete degradation of the structure due to long-term loading. The tested microstructures on the replicas are completely degraded and consist of ferrites with coarse carbides segregated along the grain boundaries and locally connected in arrays. The presence of bainite and pearlite, which are common microconstituents in the delivery state of this type of steel, was not observed in the microstructures.

Figure 1 shows the place where the replica was taken, and Figure 2 shows the microstructure of replicas R1 and R2 of the chamber of KP 13.

Figure 1.Place of taking the replica at the header of KP 13

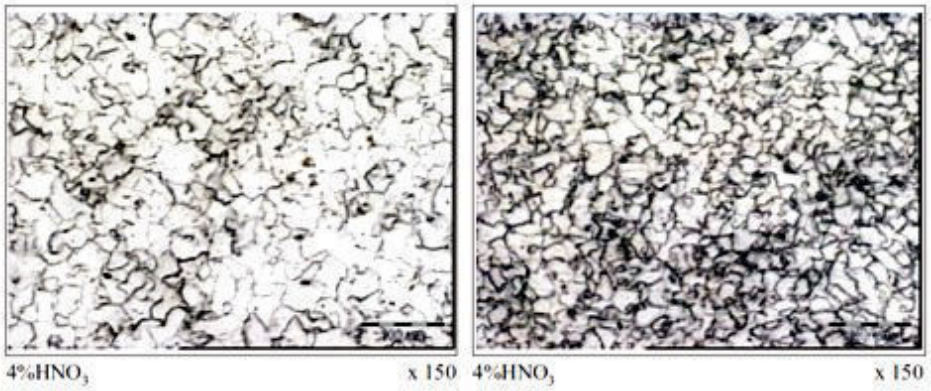

Figure 2.Microstructure of replicas R1 and R2 of header KP 13

6.2 Hardness test at the point of taking replicas

The prescribed values for the hardness of steel 15 128.5 in the normalized state according to the standard ČSN 41 5128 are in the range of 140 to 197 HB. The results of the hardness test at the place of taking the replica headers KP 13, KP 14L and KP 14D, and KP 16 are given in Tables 4, 5, and 6.

Table 4. Hardness at the place of taking replicas of chamber KP 13

Label replicas	Position pipes	Hardness, HB Individual values					Middle HB	VGB-S-517
R1	Left	148	151	149	153	142	149	3a
R2	Middle	151	154	151	148	145	150	3a
R3	Right	142	141	142	146	140	142	3a

Table 5. Hardness at the point of collection of header replicas KP 14L and KP 14D

Label replicas	Position pipes	Hardness, HB Individual values					Middle HB	VGB-S-517
R1	Left	154	161	158	160	164	159	3a
R2	Left	169	170	170	162	172	169	3a
R3	Left	141	142	140	140	140	141	3a
R1	Right	134	139	137	136	136	136	3a
R2	Right	150	150	155	147	152	151	3a
R3	Right	146	151	154	156	156	156	3a

Table 6. Hardness at the place of taking replicas of chamber KP 16

Label replicas	Position pipes	Hardness, HB Individual values					Middle HB	VGB-S-517
R1	Left	142	145	140	138	142	141	3a
R2	Middle	135	139	135	135	132	135	3a
R3	Right	136	138	142	140	142	140	3a

Based on the results from Tables 4, 5, and 6, the following can be observed:

- All measured hardness values on the KP 13 header are close to the lower prescribed limit of 140 HB.
- The measured hardnesses on the KP 14D header with the R1 replica have values below the prescribed lower limit (average value 136 HB), and with the R3 replica on the left side on the KP 14L headers they are at the very lower limit (average value 141 HB). The measured hardnesses at the places where the replicas were taken, along with the other replicas, are above the prescribed lower limit.
- Measured hardnesses at the measurement points in the header of KP 16 at the replicas R1 and R3 are at the lower prescribed limit of 140 HB, and at the place at the replica R2 they are with an average value of 135 HB below the prescribed limit.
- The measured hardnesses are fully in line with the ratings of the high degree of structural degradation of 3a.

6.3 Measurement of the hardness of the welded joints of the headers

The hardness test was performed on the welded joints of chambers KP 13, KP 14L and KP 14D, and KP 16 of the boiler superheater of block 5. The hardness was measured on both sides of the welded joint on the base material (BM), heat-affected zones (HAZ), and weld metal (WM). The test results for the mean values of the measured hardness in all zones of the welded joint are given in Tables 7, 8, and 9.

Tables 7. The hardness of welded joints on header KP 13

Place of examination	The hardness of the welded joints, HB						
	FW1-1	FW1- 2	FW 1-3	FW 1-4	FW 1-5	FW1-6	FW1-7
BM	143	145	149	150	155	154	135
HAZ	173	231	222	302	222	230	216
WM	223	229	225	329	304	219	213
HAZ	227	219	231	305	253	212	201
BM	157	151	144	152	138	138	140

Tables 8. The hardness of welded joints on headers KP 14L, and KP 14D

Place of examination	The hardness of the welded joints, HB					
	FW1-1	FW1-2	FW 1-3	FW 1-1	FW 1-2	FW1-3
	Left side			Right side		
BM	144	146	170	159	153	142
HAT	257	272	241	236	277	216
WM	239	254	225	225	262	214
HAZ	240	286	232	239	277	228
BM	146	170	138	147	148	142

Tables 9. The hardness of welded joints on header KP 16

Place of examination	The hardness of the welded joints, HB							
	FW1-1	FW1-2	FW1-3	FW1-4	FW1-5	FW2-1	FW2-2	FW2-4
BM*	196	140	149	139	140	152	164	165
HAZ	270	191	206	184	234	***	***	***
WM	251	189	194	180	222	205	191	201
HAZ	246	192	213	200	238	***	***	***
BM**	141	150	137	150	195	146	138	140

Basic material of the vestibule, ** Exit chamber, * Not measured because the weld, the angle between the pipes is 90⁰*

Analysis of the results of measuring the hardness of welded joints on the superheater headers is given in Table 10.

Tabela 10. Analysis of the results of measuring the hardness of the welded joints of the headers

Tested header	Results of hardness testing of welded joints
KP 13	Based on the test results from Table 7, it can be concluded that in all welded joints and zones, the hardness is above the lower prescribed limit, except for welded joint FW 1-7, which in the base material has one value at the lower limit, and the other below the lower prescribed limit. values.
KP14L and KP14D	Based on the test results from Table 7, it can be concluded that the hardness of the welded joints in all zones is above the lower prescribed limit, with the conclusion that the hardness in the base material of the welded joints is FW 1-1, FW 1-2, on the left side and of the welded joint FW 1-3 on the right side near the lower border.
KP 16	Based on the results from Table 9, it can be concluded that the hardness of the welded joints in the base material is close to or below the prescribed values, although differences in the measured values from different sides of the welded joint in the base material were also observed. Welded joint FW 1-3 has the worst results.

7. CONCLUSIONS AND RECOMMENDATIONS

a) In all tested components, an increased level of microstructure degradation and a significant decrease in hardness was found.
b) Through the conducted tests and comparison with the results from previous tests, it can be concluded that there was progress in the initial degradation of the microstructure and a significant drop in hardness.
c) The results of testing the hardness and degree of degradation of the structure are given in Table 11.

Table 11. Hardness and structure of the examined components during the period of exploitation

Year	KP 13		KP 14L		KP 14D		KP 16	
	Hardness	Structure	Hardness	Structure	Hardness	Structure	Hardness	Structure
1997	187	2a	161/174	1	149/161	1	174	1
	182	2a	*	*	*	*	174	1
2002	*	*	139	2a	145	2a	*	*
2019	149	3a	136	3a	159	3a	141	3a
	150	3a	151	3a	169	3a	135	3a
	142	3a	153	3a	141	3a	140	3a

d) Changes in hardness values are given in Figure 3 for chamber KP 13 with a diagram of hardness changes.

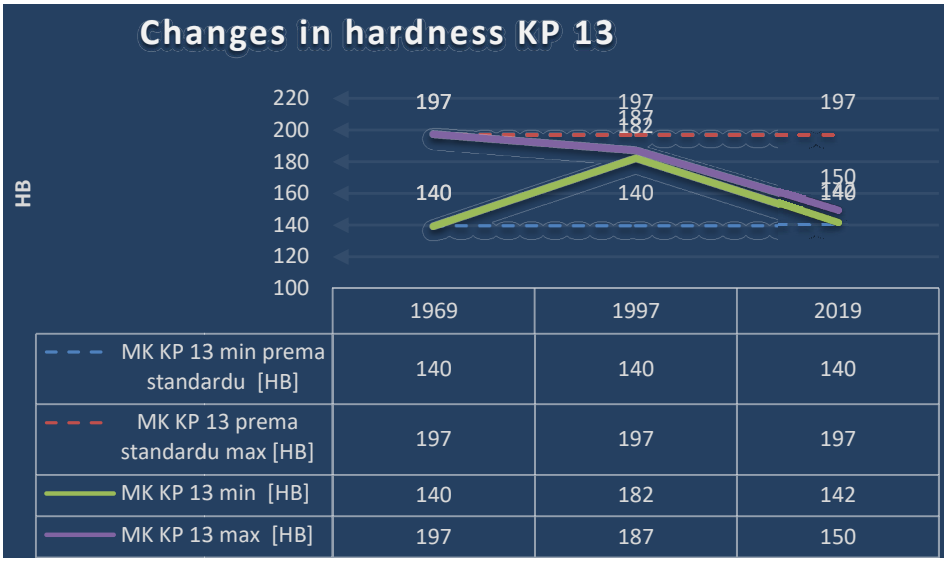

Figure 3. Change in the header of the KP 13 during the period of exploitation

e) Based on the data from Figure 2 and Table 10, it can be concluded that there has been a significant degradation of the microstructure, since the initial test in 1997, with a grade of 1 for headers KP 14L and KP 14D, and header KP 16, and grade 2a for header KP 13, up to a grade of 3a for all headers examined in 2019.
f) In the entire exploitation life, the largest drop in hardness since 1997 was recorded in the KP 13 header, in the amount of approx. 55 HB, compared to the KP 14D and KP 14L headers, and the KP 16 header, where this drop amounted to approx. 20 HB.
g) The summary analysis of test results is briefly described for all tested components in Table 12.

Table 12. A descriptive evaluation of test results for the chambers KP 13, KP 14L, KP 14D, and KP 16

Header	Visual and dimen.	Wall thickness	Hardness HB	Structure	Magnetic tests	UT	The hardness of welds HB
KP 13	Acceptable	No deviation	Acceptable (142-150)	Degradation Grade 3a	Defect repair on FW3	Acceptable	Acceptable (143-152)
KP 14L	Acceptable	No deviation	Partially acceptable (136-159)	Degradation Grade 3a	Acceptable	Acceptable	Partially acceptable (142-150)
KP 14D	Acceptable	No deviation	Acceptable (141-159)	Degradation Grade 3a	Acceptable	Acceptable	Acceptable (142-159)
KP 16	Acceptable	No deviation	Not acceptable (135-141)	Degradation Grade 3a	Acceptable	Defect repair on FW1	Partially acceptable (137-196)

Table 13 lists the recommendations for the times for which the tested components can be safely used under normal operating conditions.

Table 13. Recommendations for further exploitation

Unit 5 boiler component	Recommendation for exploitation, h	Remark
Header KP 13	15.000	Monitor the development of defects on FW 3
Header KP 14L	10.000	Tighter control
Header KP 14D	15.000	
Header KP 16	10.000	Monitor the development of defects on FW 1.Tighter control.

8. REFERENCES

[1] M. Rimac, TTDU Maneco Kakanj, A. Koro, Energoinvest Institut za materijale i kvalitet IMQ Sarajevo, Belma Fakić Institut „Kemal Kapetanović“ Zenica, Elaborat 03-19 – Utvrđivanje stanja kritičnih komponenti kotla bloka 5 u Termoelektrani „Kakanj“ Kakanj, juni 2019.

[2] Standard ČSN 41 5128 - ČESKOSLOVENSKÁ STÁTNÍ NORMA, OCEL 15 128, Cr-Mo-V, JK 125 325, 1984

[3] E.Kratina, B.Fakić, A.Husika Proces degradacije mikrostrukture materijala i uticaj na osobine u termoenergetskim postrojenjima u toku dugotrajne eksploatacije na povišenim temperaturama, VII Naučno/stručni simpozij sa međunarodnim učešćem „Metalni i nemetalni materijali“ Zenica, BiH, 15-16. maj 2008.

[4] Standard DIN 17175 – Seamless Tubes of Heat – resistant Steels – Technical Conditions of Delivery, May 1979

[5] Standard VGB-S-517-00-2014.-Guidelines for rating the microstructural composition and creep rupture damage of creep-resistance steel for high-pressure pipelines and boiler components and their weld connections

[6] Standard ASTM A 956-*method A*-Standard Test Method for Leeb Hardness Testing of Steel Products, 1996

[7] Standard DIN 50150- Testing of metallic materials - conversion of hardness values, 2000

[8] Standard ASTM E 407-07-Standard Practice for Microetching Metals and Alloys, May 1, 2007

[9] Standard BAS ISO 3057-Non-destructive testing - Metallographic replica techniques of surface examination, 1998

THE EFFECT OF CYSTEINE ON THE CORROSION CHARACTERISTICS OF BIOALLOY

Safija Herenda, Merima Begović, Edhem Hasković
University of Sarajevo, Faculty of Science
Sarajevo, B&H

Vanja Asanović
University of Montenegro, Faculty of Metallurgy and Technology
Podgorica, Montenegro

Keywords: Shape Memory Alloys, corrosion, cysteine.

ABSTRACT
Many alloys exhibit the shape memory effect, but only the Cu-Al-Zn, Cu-AI-Ni, and Ni-Ti alloys are presentand of commercial importance. The greatest use of these alloys is in biomedicine (filters, orthodontic implants, guide wires for catheters, etc.). Shape-memory alloys may be found in sensors in automobiles, consumer products, and generally in smart materials.
The electrochemical behavior of Cu-Al-Zn alloy in phosphate buffer without and in the presence of cysteine was investigated.
Electrochemical researchwas performed in a traditional three-electrode system by means of the Tafel extrapolation method. The results showed that the presence of cysteine leads to a decrease in the corrosion rate and the density (values) of the corrosion current, which indicates that the tested inhibitor is efficient. In other words, it provides alloys with protection against corrosion.

1. INTRODUCTION

Shape memory alloys (SMA) are materials that have the ability to return to a former shape when subjected to an appropriate thermomechanical procedure. Pseudoelastic and shape memory effects are some of the behaviors presented by these alloys [1].
The key transformation responsible for the behavior of shape-memory alloys is martensitic transformation. Martensitic transformation is a reversible crystallographic reorientation process between two stable phases. The transformation takes place when the Gibbs energy of martensite becomes lower than the Gibbs energy of austenite at a temperature below the critical temperature t0, which represents the temperature of thermodynamic equilibrium at which the Gibbs energies of both phases are equal [2,3].
The chemical composition of the alloy, the heat treatment procedure, the cooling rate, the grain size, and the number of transformation cycles are the main factors that influence the transformation temperature of shape-memory alloys [3].
During the phase transformation, several physical properties of the material change.
The transformation of austenite into martensite is associated with the release of heat (exothermic phase transformation). The reverse transformation of martensite into austenite is associated with supplying energy for the reaction (endothermic phase transformation).When a shape memory alloy undergoes a phase transformation, it transforms from a highly ordered phase (austenitic phase) to a low-ordered phase (martensitic phase).
NiTi alloys possess good properties of shape memory effect, pseudoelasticity, and biocompatibility. However, these alloys are significantly more expensive than copper-

based shape memory alloys. Right after NiTi, the second commercially applied shape-memory alloy is the Cu-Al-Zn alloy, which is cheaper and simpler to manufacture, and has better electrical and thermal conductivity. The disadvantage compared to the NiTi alloy is that the Cu-Al-Zn alloy has worse shape memory properties.
However, shape memory Cu-Al-Zn alloys show a significant shape memory effect in a certain range of chemical compositions.
Metal biomaterials have by far been used in biomedicine for the longest time.Numerous biomaterials and medical devices are commonly used today as prosthetic devices in dental, orthopedic, cardiovascular, ophthalmological, and reconstructive surgery. They are also successfully used in interventions, such as angioplasty (stents) and hemodialysis (membranes), for surgical sutures or bioadhesives, but also as devices for the controlled release of drugs. E.g. they are used for fixing and replacing hard tissue (artificial hip, artificial knee, plates for fixing broken bones, various applications in dentistry, etc.) and for making surgical instruments.
The reactions of living organisms to biomaterials are different; under certain circumstances, some material is well accepted by the organism, while, under other circumstances, the same material is not accepted by the organism [4,5].Corrosion is defined as the destructive and unintentional degradation of a material caused by its environment.Today, corrosion is one of the important causes of the global material and energy crisis and is the cause of significant losses in the economy of every country [6]. The harmful effects of corrosion can cause numerous negative consequences, such as to lead to a decrease in the utility value of materials, more expensive maintenance and shortened durability of structures, production stoppages, accidents, etc.
Corrosion control of metal is of technical, economical, environmental, and aesthetical importance. The use of inhibitors is the best way to prevent metal and alloys from corrosion [7].
A corrosion inhibitor is a substance applied to an environment that significantly reduces the corrosion rate of materials (especially metals) exposed to that environment.
Organic compounds, predominantly, those with O, N, S, P, and/or π electrons in their molecular structure have received considerable attention as metal corrosion inhibitors. It is believed that organic compounds get adsorb onto a metal surface through their active center (heteroatom or π-bond) and form a protective layer that prevents the corrosive agents in the aggressive environment from gaining access to the metal surface.
Compared to the inorganic metal corrosion inhibitors, the organic inhibitors are less toxic to both humans and the environment making discontinuation not to be the best option. [8,9].
Cysteine has the ability to control the corrosion of various metals. Generally, cysteine is a very interesting amino acid that contains the amino group [–NH_2], carboxyl group [–COOH], and thiol group [–SH]. It can coordinate with metals through the nitrogen atom, the oxygen atom of the carboxyl group, and Sulphur atom of the thiol group [10].
Phosphate buffers are widely used because they help maintain a constant pH level in a particular environment. Generally speaking, most researchers using phosphate buffers try to maintain a pH of 7.4 because the properties closely match those of the human body.
Compounds that contain polar functional groups that allow them to be efficiently adsorbed have found application in corrosion inhibition because of their effectiveness. Amino acids are also included in such compounds [11].
Amino acids are considered green inhibitors, and they are characterized by non-toxicity, biodegradability, cheap production and a high degree of purity of the produced compound, and solubility in aqueous media [12].

The presence of heteroaromatics in the structure of amino acids (they contain at least one carboxylic acid and an amino group, usually attached to the same carbon) increases their ability to be used as corrosion inhibitors. Previous tests have shown that the effectiveness of inhibition primarily depends on the molecular structure of the amino acid being tested, the size of the molecule, and the type of interaction with the metal surface [13,14]. The highest efficiency of inhibition in the presence of cysteine was attributed to the fact that the amino acid containing S can be adsorbed as a bidentate ligand, whereby coordination takes place both through the amino group (or carboxyl) and through the –SH group [15].

2. EXPERIMENTAL

The aim of this study is to focus on the effect of cysteine concentration (2 mM, 4 mM, 8 mM) on the corrosion behavior of Cu-18,05Zn-5,35Al bioalloys in phosphate buffer, pH = 7.
This tested bioalloy was prepared using solution annealing at a temperature of 850 ^{0}C for 10 min., then quenched into water at 15 ^{0}C.
Phosphate buffer was prepared by dissolving 3,405 g of potassium dihydrogen phosphate (KH_2PO_4) in distilled water in a 500 mL volumetric flask and 4,450 g disodium hydrogen phosphate (Na_2HPO_4) in distilled water in a volumetric flask. A pH value of 7,00 was adjusted by adding 100 mL KH_2PO_4 and 150 mL Na_2HPO_4 to a 250 mL volumetric flask.
A 0,5mol/L cysteine solution was prepared by dissolving 1,5145 g of cysteine in distilled water in a 25 mL volumetric flask.
The sample was prepared for electrochemical research after polishing with grinding paper, degreasing in ethanol, and washing with distilled water. The work surface of the tested bioalloy was 25 cm^2.
Electrochemical researchwas performed in a traditional three-electrode system by means of the Tafel extrapolation method. Tafel extrapolation is a mathematical technique used to estimate either the corrosion current (I_{corr}) or the corrosion potential (E_{corr}) in an electrochemical cell, and by extension, the corrosion rate [16].The three-electrode system consists of a working electrode, a counter electrode, and a reference electrode. The most common lab reference electrodes are the Saturated Calomel Electrode and the Ag/AgCl electrode.
Potentiostat/galvanostat Vertex one, Ivium Technologiesis being used for electrochemical testing of corrosion rate.

3. RESULTS AND DISCUSSION

The corrosion current density (I_{corr}) and corrosion potential (E_{corr}) were obtained by employing the Tafel extrapolation method.The Tafel extrapolation line is based on the polarization curve obtained when the overpotential is between -0,300 V do 0,05 V. The scan rate was 20 mV /s.
The efficiency of the inhibitor, Ei (%), was calculated based on following equation:

$$Ei = \frac{\pi - \pi'}{\pi} \quad (1)$$

where: π - corrosion rate in solution without corrosion inhibitor (mm year^{-1})
π'- corrosion rate in solution with corrosion inhibitor (mm year^{-1}).

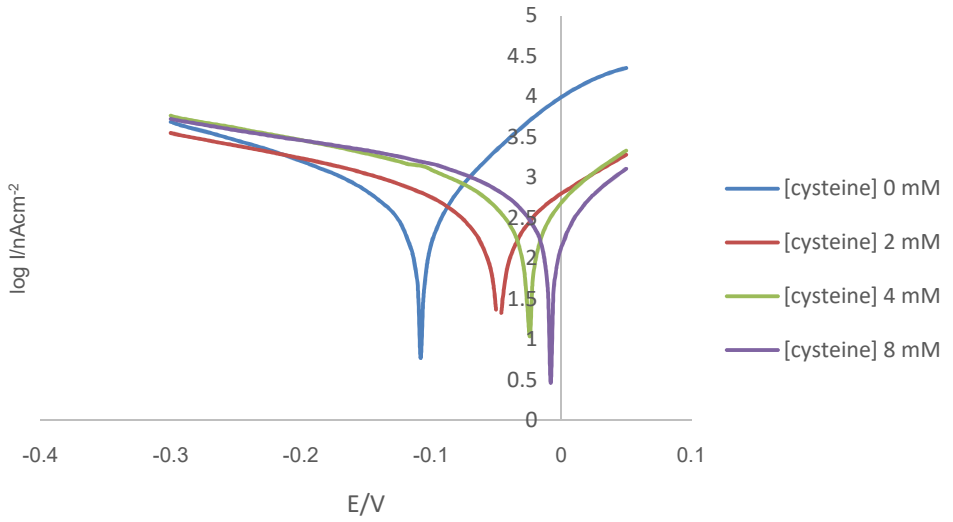

Figure 1. Tafel extrapolation graph of the effect of cysteine concentration on the corrosion behavior of Cu-18,05Zn-5,35Al bioalloy

Table 1. The corrosion parameters determined by Tafel extrapolations method

Inhibitor	$c_{inh.}$ (mM)	$E_{corr.}$ (V)	I (A)	I (A/cm^2)	R_p (Ω)	β_a (V/dec)	β_k (V/dec)	$v_{corr.}$(mm/yr.)
-	0	-0,1034	$4{,}65\times10^{-7}$	$4{,}65\times10^{-6}$	$5{,}09\times10^{4}$	0,078	0,182	0,05405
Cysteine	2	-0,0209	$3{,}75\times10^{-7}$	$3{,}75\times10^{-6}$	$8{,}15\times10^{4}$	0,095	0,272	0,04364
Cysteine	4	-0,0048	$5{,}96\times10^{-7}$	$5{,}96\times10^{-6}$	$4{,}15\times10^{4}$	0,070	0,298	0,06928
Cysteine	8	0,0290	$7{,}07\times10^{-7}$	$7{,}07\times10^{-6}$	$3{,}06\times10^{4}$	0,058	0,374	0,08221

Based on the values of corrosion parameters determined by Tafel extrapolation (Table 1) it was confirmed that cysteine can be applied in order to reduce the corrosion rate. In the investigated concentration range of the cysteine in phosphate buffer, the lowest rate of corrosion is at the concentration of inhibitor(cysteine) of 2 mmol/L and which amounts to 0.04364 mm/year and its effectiveness amounts to 19,10%.

By further increasing of the concentration of cysteine, the inhibitory effect decrease, because the corrosion rate is greater than the rate of corrosion of the examined bioalloy without the presence of the inhibitor. In other words, at a concentration of 4 mmol/L and 8 mmol/L inhibitor functions as an activator because the corrosion rate is higher than the rate of corrosion without an inhibitor.

4. CONCLUSION

As the obtained results have shown, the presence of cysteine in concentration 2 mmol/L leads to a decrease in the corrosion rate and the density (values) of the corrosion current, as well as to an increase in polarization resistance values, which indicates that the corrosion inhibitor is efficient in appropriate concentration.

5. REFERENCES

[1] Machado LG, Savi MA.: Medical applications of shape memory alloys. Braz J Med Biol Res. 2003 Jun;36(6):683-91. doi: 10.1590/s0100-879x2003000600001. Epub 2003 Jun 3. PMID: 12792695., 2003

[2] I. Ivanić, M. Gojić, S. Kožuh. Slitine s prisjetljivosti oblika (I. dio): najznačajnija svojstva, *Kemija u industriji* 63. 2014. 9-10; 323-329

[3] K. Otsuka, C. M. Wayman. Shape memory materials. University of Cambridge, Cambridge. 1998
[4] Tanikić, D. I., Manić, M. T., Ranđelović, S. S., Brodić, D. T. Legure koje pamte oblik i njihova upotreba u medicini. *Vojno tehničk iglasnik*. 2014 62(4), 59-71
[5] L. G. Machado, M. A. Savi. Medical applications of shape memory alloys. *Braz. J. Med. Biol. Res.* 2003 36, str. 683–691
[6] Juraga, I., Alar, V., Šimunović, V., Stojanović, I. *Korozija i metode zaštite od korozije*. Zagreb: Fakultet strojarstva i brodogradnje. 2012
[7] Manoj Acharya, Jinendra Singh Chouhan, Anita Dixit, D. K. Gupta*:* Green Inhibitors for Prevention of Metal and Alloys Corrosion: An Overview, 2013
[8] S. A. Umoren, M. M.Solomon: Synergistic corrosion inhibition effect of metal cations and mixtures of organic compounds: A Review, Journal of Environmental Chemical Engineering, 5(1), 246- 273., 2017
[9] Malinović B., Djuričić T., Zorić D.: Corrosion behaviour of stainless steel EN 1.4301 in acid media in presence of PBTCA inhibitor, University of Banja Luka, Faculty of Technology, Banja Luka, 2020
[10] A. Sahaya Raja, R. Venkatesan, R. Sonisheeba, J. Thomas Paul raj S. Sivakumar, P. Angel, J. Sathiyabama: Corrosion Inhibition by Cysteine - An Over View, Corrosion Research Centre, PG and Research Department of Chemistry G.T.N Arts College, Dindigul, TN, India, 2014
[11] Antonijević M. M., Petrović M. B. Inhibitori korozije bakra*. Zaštita materijala*. 2007.,48
[12] B. El Ibrahimi, Jmiai A., Bazzi L., El Issami S. Amino acids and their derivatives as corrosion inhibitors for metals and alloys*. Arabian Journal of Chemistry*. 2017, str. 1878-5352
[13] Radovanović, B. M*. Uticaj organskih inhibitora na koroziono ponašanje mesinga u rastvoru natrijum – sulfata*. Doktorska disertacija. Univerzitet u Beogradu. Tehničkifakultet u Boru. 2012
[14] D. Q. Zhang, Q. R. Cai, X. M. He, L. X. Gao and G. D. Zhou. *Mater. Chem. Phys*. 2008 *112*, str. 353
[15] Ivanov, S., Rajčić – Vujasinović M., Stević, Z. Uticaj hloridnih jona na koroziono ponašanje hladno deformisane bakarne žice u alkalnoj sredini, *Zaštita materijala,* 2006., *Vol.47,* str. 33-38
[16] Neeraj K Namboodiri, Tafel extrapolation method, 2020

ELECTRICAL PROPERTIES OF GRANULAR METALS

Maja Đekić, Ajla Karić, Amra Salčinović Fetić, Melisa Baždar, Belma Husković
University of Sarajevo, Faculty of Science
Sarajevo, B&H

Dijana Dujak
Universitty of Sarajevo, Faculty of Electrical Engineering
Sarajevo, B&H

Diana Ćubela
University of Zenica, Faculty of Metallurgy and Technology
Zenica, B&H

Keywords: granular metals, electrical resistance, weak contacts

ABSTRACT
Metallic materials in granular packings show different electrical properties from their bulk counterparts. In this paper, we investigate the temporal evolution of the electrical conductivity of granular metals. We use metallic beads arranged in different one-, two- and three-dimensional ensembles through which different constant currents are injected. The conductivity behavior in all three types of systems is qualitatively similar. The results show the rise of conductivity which is more pronounced in the earlier stages of the time evolution. We investigate the influence of the dimensionality, the number of beads, and the values of the injected currents on the conductivity behavior.

1. INTRODUCTION

Granular metals display quite unique electrical resistance behavior when compared to their bulk counterparts. For any conducting wire, the resistance is proportional to its length and inversely proportional to its cross-section area while it remains constant in time. In granular metals, the resistance is caused by both the individual resistance of the grains as well as by the contacts between them [1]. A few authors have recorded the decrease in resistance with time in granular metals [2,3,4] which is more pronounced in the earlier stages of the time evolution. The origin of this phenomenon can be found in the theory of contact resistance. Because of the fact that every surface has some roughness either on a micro or even nanoscale, the electrical contact between the granules is established through discrete spots, known as a-spots or asperities which determine the actual size of the contact area. It is usually much smaller than the nominal contact area [5]. This affects the electromechanical properties of the materials due to the large pressure exerted on these spots. Contact resistance can also originate from the tunneling, especially in metallic powders covered with thin oxide layers [2]. Over the years, many theoretical models have been developed in order to model contact resistance. However, most of them include major simplifications ignoring correlations between asperities, the roughness of the surface, or the existence of the oxide layer [6,7].

Various authors suggest that the number of beads, temperature, vibrations, packing, and applied force [8,9] can also influence the electrical properties of these materials. According to

[10], the properties of the granular materials seem to be universal i.e. independent of the type and size of the grains but are rather attributed to the granular structure of the system itself.
In this paper, we measure a flow of different fixed currents through 1D, 2D, and 3D compact packings of steel cylinders in order to examine the effect of dimensionality, the number of cylinders, and the current value on the resistance behavior.

2. EXPERIMENTAL PROCEDURE

The schematic of the experimental setup is shown in Figure 1.

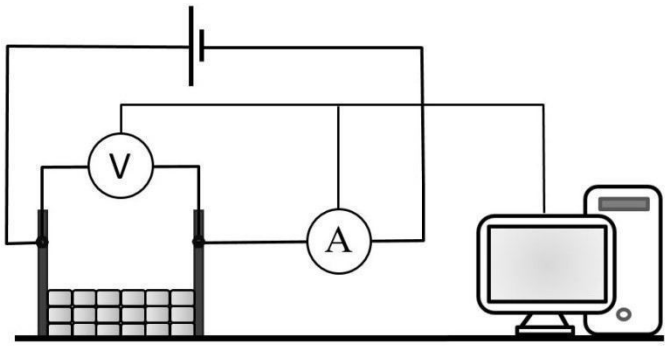

Figure 1. Sketch of the experimental setup. The current is injected into the cylinder packing. The voltage and the current are registered and the resistance is calculated

The steel cylinders with a diameter of 5 mm are placed in an isolating box with plate electrodes on the side walls. The box is placed under a small inclination angle of 15° onto an anti-vibration table. A fixed current is injected into a cylinder packing from a current source Kiethley 228, while the current and voltage are measured with Multimetars GDM 8621A (GW – Instek). The data is acquired by a computer program that calculates resistance using Ohm's law. The temperature is measured using PeakTech Digital-Thermometer. Small variations between 1-2°C are recorded and do not seem to alter the behavior of resistance.
The cylinders were first arranged in a 1D linear chain containing 18 beads (Figure 2 a) and a fixed current between 10 mA and 80 mA was imposed onto the chain for 600 s with 10 s step. For every current value, a set of five measurements has been conducted. After each measurement, new contacts between the cylinders were established by reducing the current to zero, removing the cylinders from the box, and after a couple of minutes placing them back in the same place as before.
2D packings of cylinders were formed by placing them in rows, starting from two rows up to ten rows (Figure 2 b), thus containing 36 to 180 beads respectively. The current injected into 2D packings was 50 mA and one measurement was conducted for each number of rows. The current and voltage were measured and recorded every 10 s for 300 s.
3D packings were formed by placing the cylinders into rows and columns 3 by 3 (162 beads), 5 by 3 (270 beads), and 7 by 3 (378 beads) with 50 mA current injected into them (Figure 2c). The current and voltage were measured every 10 s for 300 s. Note that for 2D and 3D arrangements of cylinders, new contacts were established after each measurement.

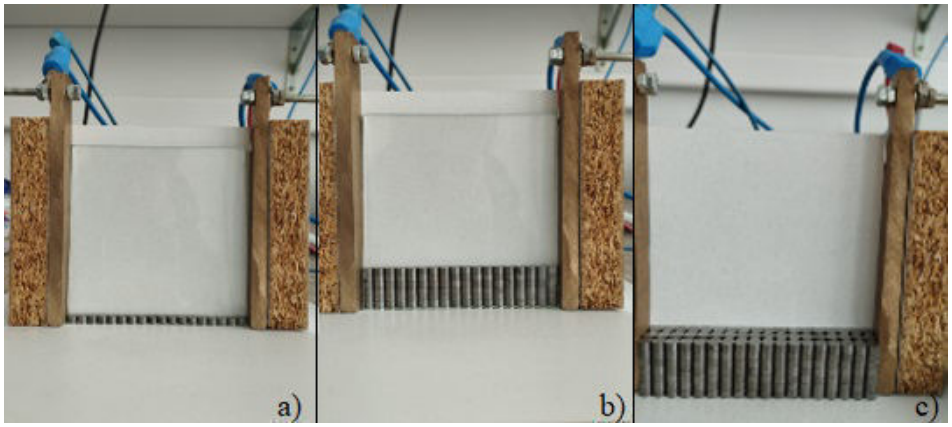

Figure 2. a) 1D packing b) 2D packing containing 6 rows and c) 3D packing containing five rows and three columns of the cylinders.

Scanning electron microscopy (SEM) was performed using JEOL JSM IT 200LA while atomic force microscopy (AFM) imaging was performed using Nanosurf CoreAFM. AFM imaging was acquired in dynamic mode using NanosurfDynAl-900 tips (nom. freq. 190 kHz, nom. force const. 48 N/m) with a linear scanning time of 1 s and scan resolution of 256 points per line. The measurements were performed in air ambient temperature and humidity. Analysis of the images was carried out using WsXM software [11].

3. RESULTS AND DISCUSSION

The typical behavior of the electrical conductivity σ in a 1D linear chain is presented in Figure 3.

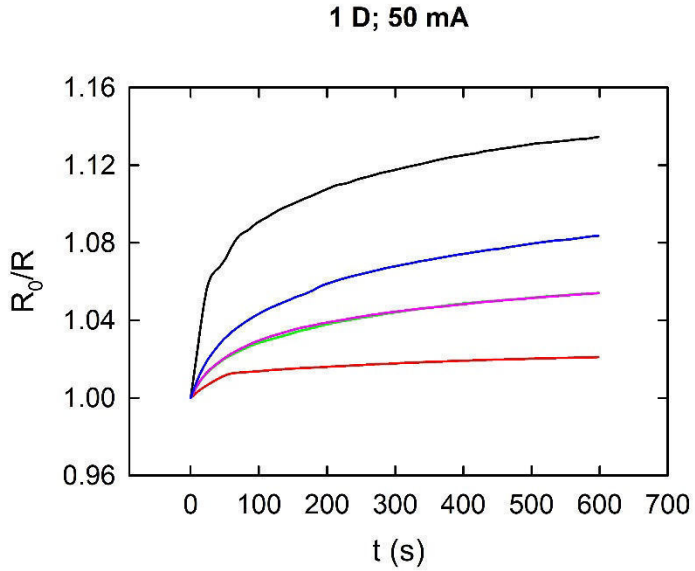

Figure 3. Five measurements of the normalized conductivity ($\sigma=R_0/R$, where R_0 is the initial resistance and R is the measured resistance) for 50 mA current injected into the 1D chain

The electrical conductivity rises with time which is more pronounced in the earlier stages of the experiment. For each new packing the initial value of the resistance is different as well as the rate of the resistance change, which had been previously established [4]. Qualitatively, the electrical conductivity in 2D arrangements of cylinders (Figure 4) is similar to the one in 1D linear chains.

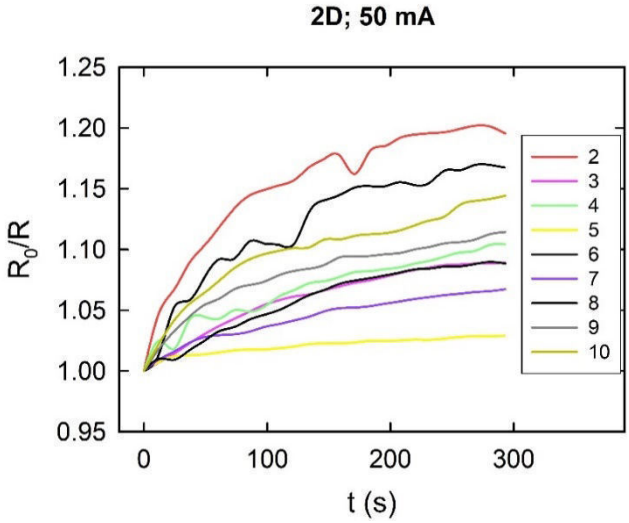

Figure 4. Normalized conductivity ($\sigma=R_0/R$, where R_0 is the initial resistance and R is the measured resistance) for 50 mA current injected into the 2D packings containing from 2 to 10 rows

This unusual result can be understood when analyzing the current paths in 2D systems. According to [12] the current in 2D systems seems to be localized in desecrate linear paths regardless of the strength of the injected current.
3D packings display similar conductivity behavior as 1D and 2D system, as illustrated in Figure 5.

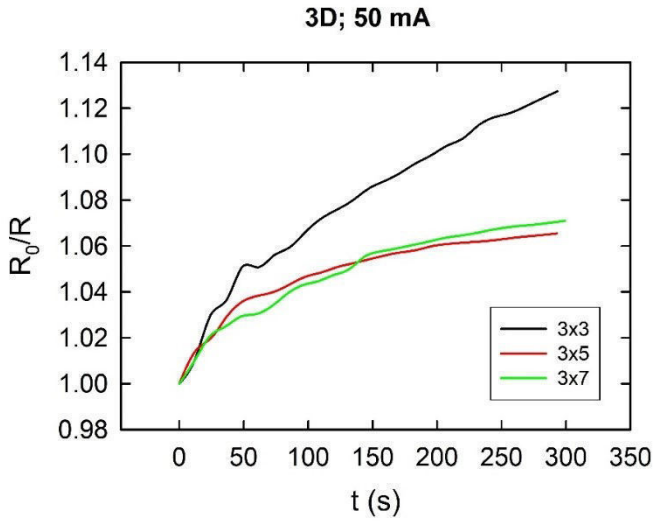

Figure 5. Normalized conductivity ($\sigma=R_0/R$, where R_0 is the initial resistance and R is the measured resistance) for 50 mA current injected into the 3D packings of cylinders

According to our results, dimensionality does not seem to influence the behavior of the time evolution of conductivity in granular metals because the current seems to stay localized in linear paths.
Next, we examine the current strength of the conductivity behavior. Since all the packings regardless of the dimensionality display similar behavior, we examined only 1D packings of cylinders for the current values between 10 mA and 80 mA, as presented in Figure 6.

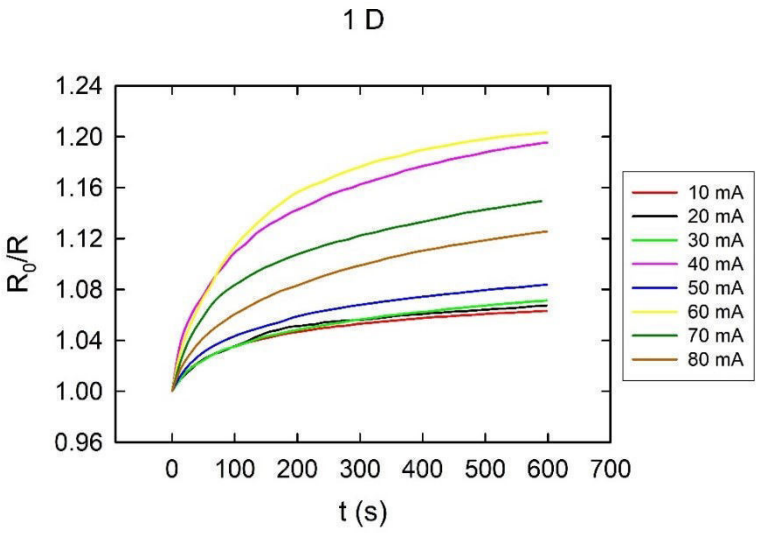

Figure 6. Normalized conductivity ($\sigma=R_0/R$, where R_0 is the initial resistance and R is the measured resistance) for currents between 10 mA and 80 mA injected into the linear chain of cylinders

Qualitatively, the conductivity behaves in the same manner for all the current values. The initial values of conductivity and the rates of conductivity rise do not seem to correlate with the current strength. Namely, for each stronger current imposed on the system, the initial conductivity can either be smaller or larger than for the previously imposed weaker current. According to our measurements, the most significant influence on conductivity seems to be originating from the contact resistance which is greatly affected by the cylinders' surfaces. In order to examine the cylinder surfaces, SEM imaging, presented in Figure 7 was performed. The surface showed visible scratches due to the cutting.

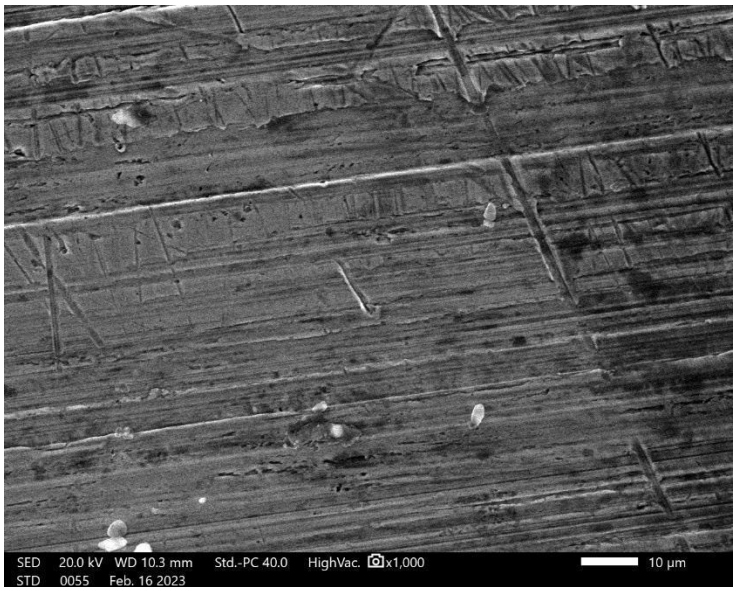

Figure 7. SEM image of the cylinder surface

In order to examine the topography of the cylinders, AFM imaging was conducted. Figure 8 represents a 3D image of a flat surface of one cylinder. The image revealed needle-like

asperities and also some deep furrows. Surface roughness is 93 nm rms, but the differences in height are rather pronounced and go up to 592 nm in some places.

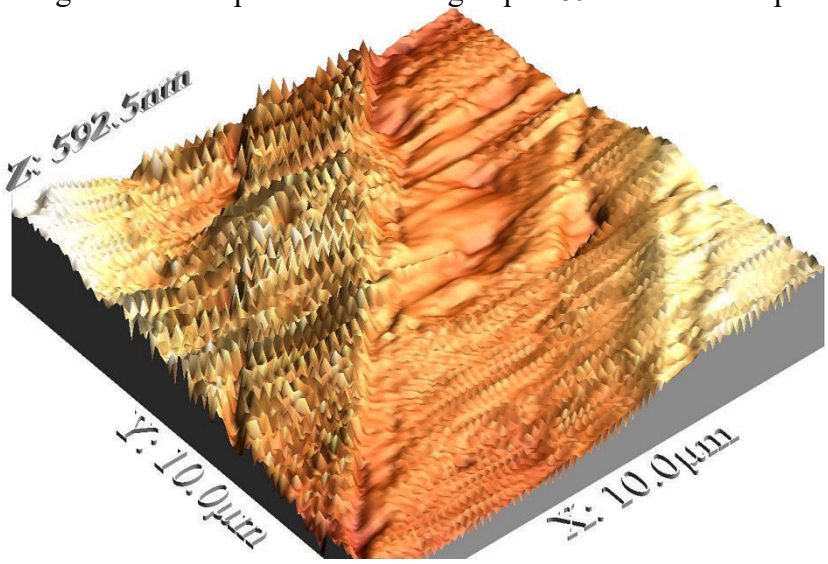

Figure 8. 3D image of the cylinder surface

4. CONCLUSION

Our results show that in granular ensembles of steel metallic cylinders, the conductivity rises with time regardless of the dimensionality of the current strength injected into them. A similar trend was observed in other granular systems of different metals. This may be attributed to the granular nature of the material itself, which seems to not depend on the dimensionality, number of grains, shape, size, or even grain material. A predominant factor in this behavior originates from the contact resistance which is associated with the number and height of asperities as well as with the oxide layers on the metallic surface. AFM measurements of our samples revealed very rough samples with a lot of needle-shaped asperities. The highest of them contribute to conductivity, while the shorter ones, especially if they are in the furrows, probably do not influence conductivity. In order to investigate whether it is possible to influence the conductivity behavior with mechanical treatment of the surface of the cylinders, in our next experiments we are planning to measure conductivity after polishing.

5. REFERENCES

[1] R. Holm.: Electric contacts: Theory and Application, Springer-Verlag Berlin Heidelberg New York, 1967

[2] Z. M. Jakšić et al.: The Electrical Conductance Growth of a Metallic Granular Packing, Eur. Phys. J. B 90:108, 2017

[3] S. Dorbolo et al.: Aging Process of Electrical Contacts in Granular Matter, Journal of Applied Physics Vol 94, Number 12, 2003

[4] D. Dujak et al.: Temporal Evolution of Electrical Resistance through Granular Packing of Ni Beads, Bulliten of Chemists and Technologists of Bosnia and Herzegovina, 58, 33-38, 2022.

[5] Hirpa L. Gergele et al.: Study of Contact Area and Resistance in Contact Desing of Tubing Connections, 13th International Research/Expert Conference "Trends in the Development of Machinery and Associated Technology", TMT, Hammamet, Tunisia, 2009

[6] K. Bourbatache et al.: Discrete Modeling of Electrical Transfer in Multi-Contact Systems, Granular Matter, 14:1-10, 2012

[7] Benjamin F. Toler et al.: A Review of Micro-Contact Physics for Microelectromechanical Systems (MEMS) Metal Contact Switches, J.Micromech. Microeng. 23, 2013

[8] S. S. Yoon et al.: Pattern Formations in Granular Systems and Their Implications to Dynamics of Ferroelectrics, J. Korean Phys. Soc. 35 S1326, 1999
[9] E. Falcon et al.: Nonlinear Electrical Conductivity in a 1D Granular Medium, Eur. Phys. J. B 38, 475-483, 2004
[10] M. Massalska-Arodź et al., Experimental Observations of Structural Relaxation in Granular Matter, Physical Review E, Vol 55, No. 1, 1997
[11] I. Horcas et al.: WSXM: A software for scanning probe microscopy and a tool for nanotechnology, Review of Scientific Instruments 78, 013705, 2007
[12] M. Creyssels et al.: Some Aspects of Electrical Conduction in Granular Systems of Various Dimensions, Eur. Phys. J. E 23, 255-264, 2007

INVESTIGATION OF CUTTING CONDITIONS INFLUENCE ON SURFACE ROUGHNESS DURING MQL MACHINING OF STEEL

Tarik Gazić, Sabahudin Ekinović, Edin Begović, Ibrahim Plančić
University of Zenica, Faculty of Mechanical Engineering
Zenica, B&H

Keywords: design of experiment, regression analysis, experimental setup, linear regression model, cutting conditions, surface roughness

ABSTRACT
In the paper, the influence of the cutting conditions (cutting speed, feed, and depth of cut) during the machining of the cylindrical steel part on the surface roughness (average surface roughness-Ra) is analysed using experimental investigation. The material used in the full factorial experimental investigation was C45 steel, a diameter of 50 mm, machined on a conventional lathe POTISJE ADA 501M. Cooling and lubrication were realised by means of JOOM MQL system model J-T2X-012-2K-T, from Daido Metal, which supplies a cutting zone with oil-on-water droplets average size of 100 microns and with an oil film thickness of 1000 Å. Carbide inserts SNMG 120408-MA Grade US735 MITSUBISHI were used as cutting tools. The results of the experiment show that cutting speed is the most influential factor in surface roughness. Increasing cutting speed, the surface roughness decreases. This factor seems to be the only one that is statistically significant. Feed is the second strongest factor followed by the depth of cut. Both are statistically insignificant for 0.05 level of significance (95% reliability). The linear regression model is, by appropriate mathematical operation, transformed, coded, and decoded into the exponential model. The model is represented by diagrams given at the end of the work.

1. INTRODUCTION

Design of Experiment (DoE) is a powerful tool for achieving significant improvements in product quality and process efficiency. The methodology is not used only in engineering problems but also in various spheres of science and sociological studies. The basic parts of experiment planning, known as key steps of DoE, are [1]:

- **Setting objectives** - define the task of the experiment, scope, and materials, setting goals of the experiment, etc.
- **Selecting process variables** - process variables include both inputs and outputs - i.e., influential factors and responses.
- **Selecting an experimental design** - the choice of an experimental design depends on the objectives of the experiment and the number of influential factors investigated.
- **Association of treatments** - it is necessary to determine how to associate treatments with units (coded or uncoded), whereby only one of the treatments can be applied to each unit,
- **Conducting an experiment** - the experiment is performed according to the previously defined plan matrix,

Analysis and conclusions - obtained results are analyzed and conclusions are drawn.

In a statistical experiment, the influence of one or more factors on a certain phenomenon is observed. These factors are called controlled factors.

The observed phenomenon can also be influenced by random factors called uncontrolled or experimental errors [2]. To draw concrete conclusions from an experiment, it is

necessary to plan the performance of the experiment in a certain way and at the same time examine the conditions under which it is possible to reduce the experimental error. A well-planned experiment allows us to obtain clear interpretations and avoid complicated analyses, and a poorly planned experiment gives us wrong conclusions about a process.
In this case, Regression Analysis will be used as an investigation methodology to find out the functional relationship between input and output data. Regression analysis helps to quantitatively express the dependence between variables [3].

2. EXPERIMENTAL SETUP

In this study, the influence of cutting condition parameters, cutting speed expressed through the number of revolutions per minute n (rpm), feed rate f (mm/rev), and depth of cut d (mm), on average surface roughness Ra (microns) will be considered. The test was made on one cylindrical C45 steel rod, in which is incised 10 groves that enable easier distinction between experimental runs (Fig 1.).

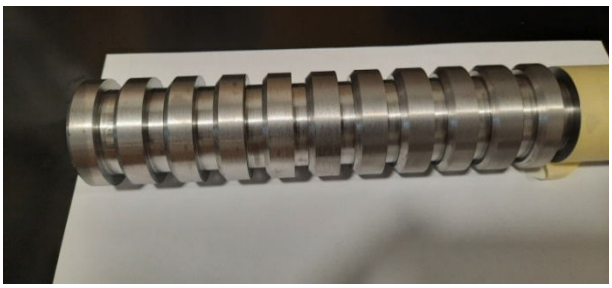

Figure 1. Cylindrical steel rod with 11 ribs

Every rib is used for one experiment with different cutting conditions. Machining is performed on the conventional lathe POTISJE type ADA PA 501M, in the laboratory LORAM, Faculty of Mechanical Engineering in Zenica.

Figure 2. Conventional lathe POTISJE type ADA PA 501M

For the purposes of the experiment, a medium-level of MQL lubrication system (Water 17.5 ml/min, Oil 30 cc/hour) was used (Fig. 3). MQL is the process of applying small amounts of high-quality lubricant directly to the cutting tool/work piece interface instead of using traditional flood coolants. MQL minimizes environmental impact by significantly reducing fluid usage and eliminating the need for coolant treatment and disposal. A flow rate in the range of 50–500 ml/hour is commonly applied for most industrial applications [4]. Due to the low consumption of cutting fluids, MQL is considered an environmentally friendly cooling technique.

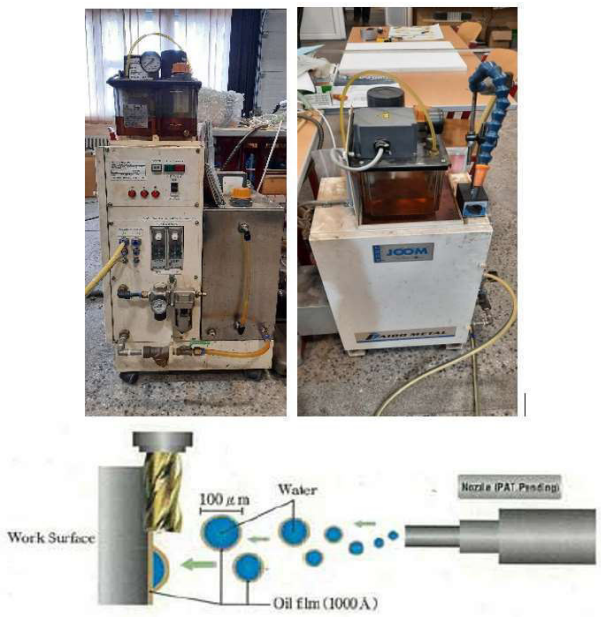

Figure 3. JOOM MQL system

Water and oil levels were kept constant throughout all experiments. Machining is performed with a replaceable cutting insert (carbide grade) type SNMG 120408-MAUS735, manufactured by MITSUBISHI. Cutting conditions were set up according to the cutting insert's producer recommendations.

Figure 4. Replaceable cutting insert type SNMG 120408-MAUS735

A full factorial design with k = 3 factors on 2 levels was applied. The number of runs is:

$$N = 2^k + n_0 = 2^3 + 3 = 11 \quad (1)$$

where n_0 is the number of replicates in the central point.
The primary goal has been to define cutting conditions that produce the best results of Ra factor – values of surface roughness. The specified experimental limits are given in Table 1.:

Table 1. The values of factor levels and cutting conditions

Factors	Factor levels	Cutting speed *n (rpm)*	Feed, *s (mm/rev)*	Depth of cut *d(mm)*
		X_1	X_2	X_3
Upper level	+1	910	0,196	1,5
Central point	0	600	0,124	1
Lower level	-1	265	0,049	0,5

Experimental runs have been randomized and are presented in Table 2. Roughness measuring was performed on a 3D Measuring system MicroCadMahr device for contactless measuring. The measurement was performed at 3 different points on rib circumference, rotated for 120 deg. Results were processed by *MarSurf XR20 V1-21.1* software.

Table 2. Plan of experiment with measuring results for parameter Ra

Exp. point N	Plan matrix				Measurement results Ra (μm)				
	X_0	Number of revolutions	Feed	Cutting depth	Measurements			Raaverage	
		X_1	X_2	X_3	I	II	III	y	ln(y)
1.	1	1	1	1	3,8	4,8	4,7	4,4	1,49
2.	1	-1	1	1	4,4	4,6	4,8	4,6	1,53
3.	1	1	-1	1	3,6	3,3	2,7	3,2	1,16
4.	1	-1	-1	1	4,7	4,3	4	4,3	1,47
5.	1	1	1	-1	3,6	4,3	4,6	4,2	1,43
6.	1	-1	1	-1	5	5,3	5,5	5,3	1,66
7.	1	1	-1	-1	3,9	4,2	4,2	4,1	1,41
8.	1	-1	-1	-1	5,5	4,4	4,9	4,9	1,60
9.	1	0	0	0	3,9	4,1	3,4	3,8	1,34
10.	1	0	0	0	4,1	4,4	4,6	4,4	1,47
11.	1	0	0	0	4,6	4,5	3,7	4,3	1,45

3. ANALYSIS OF RESULTS

Analysis of results was performed by Data Analysis Tool Pack from the Microsoft Excel software package [6]. It has been shown the analysis for the case given in Table 2. It has been assumed that the exponential function is a possible description of relations between parameters and cutting conditions:

$$Ra = C \cdot n^x \cdot f^y \cdot d^z \ \ldots \tag{2}$$

where:

- *C* is constant and x, y, and z, are the exponents.
- n is the number of revolutions, [rpm];
- f is feed rate, [mm/rev];
- d is the depth of cut, [mm].

As mentioned, appropriate statistical processing of data will be performed using *MS Excel* [5,7]. In the case of data shown in Table 2, data processing generates the following output:

Table 3. Regression analysis from MS Excel

Regression Statistics	
Multiple R	0,8529
R Square	0,7275
Adjusted R Square	0,6108
Standard Error	0,0816
Observations	11

Table 3.1 ANOVA table

ANOVA	df	SS	MS	F	Significance F
Regression	3	0,12	0,04	6,232	0,0217
Residual	7	0,04	0,00		
Total	10	0,17			

Table 3.2 Coefficients values and its significance

	Coefficients	Standard Error	t-Stat	P-value
Intercept	1,4545	0,024	59,05	1,05E-10
X1	-0,0949	0,028	-3,28	0,013
X2	0,0584	0,028	2,022	0,082
X3	-0,0563	0,028	-1,95	0,0920

On the basis of these results, the linear regression model was obtained as follows:

$$y = 1{,}45455 - 0{,}09493 \cdot X_1 + 0{,}0584 \cdot X_2 - 0{,}05635 \cdot X_3 \quad \ldots (3)$$

From the ANOVA table (Table 3), the given model adequately describes the analysed process. Also, only the number of revolutions, X_1, significantly influences the model (P-value less than 0.05, for 95% reliability). Transforming this model into natural coordinates gives:

$$Ra = 12{,}94 \cdot n^{-0{,}154} \cdot f^{0{,}0864} \cdot d^{-0{,}102} \quad (4)$$

Figure 5 shows the graphical interpretation of obtained correlation in the case of the Ra surface roughness parameter. The first 2D Figure (5.1.) shows the function when statistically significant factors are included, in this case only n. In Figures 5.2 and 5.3 insignificant factors are also included to obtain 3D visualisation of its effect.
This 2D and 3D interpretation is obtained in the software MathCAD.

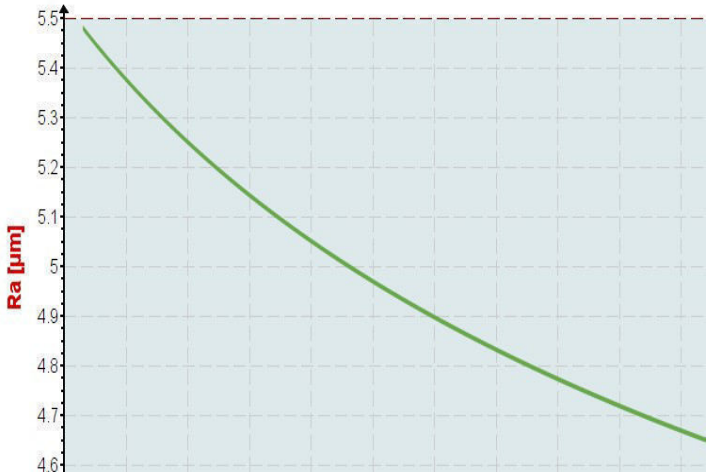

1) Ra = f (n)

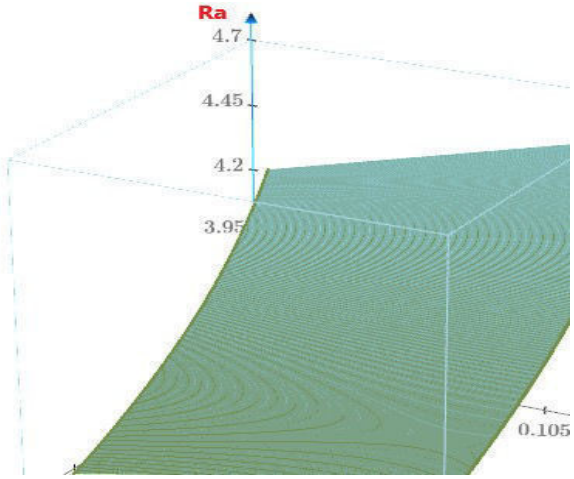

2) Ra = f (n, f), d = const.

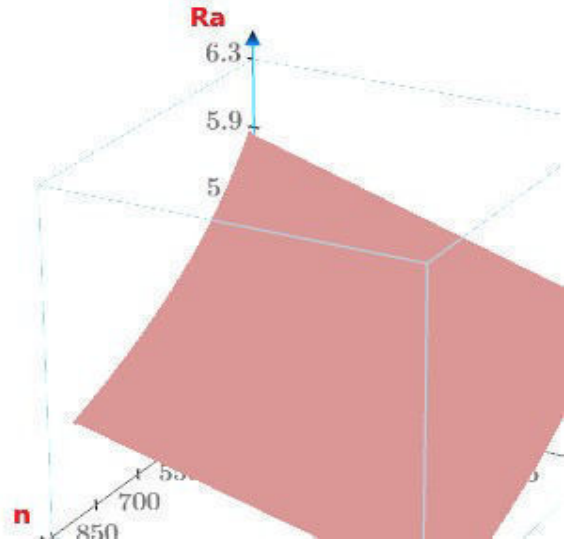

3) Ra = f (n, d), f = const.

Figure 5.Cutting conditions influence on average roughness Ra

4. CONCLUSION

Functional relationship between the input data *n*, *f*, *d,* and *Ra* factor as output is obtained by regression analysis.

This relationship is expressed through the mathematical model in the form of the equation (eq.4) that connects a dependent variable with independent variables quantity respecting appropriate assumptions and constraints.

As previously shown, the exponential model adequately describes the functional relationship between input and output data, as shown in the *ANOVA* table ($F>F_{tab}$ $F_{0.05,3,6}$ = 4.7571, for $\alpha = 0{,}05$, $k = 3$, and $N-k-1 = 6$).

By analyzing individual factor significance, it can be stated that in this model, only cutting speed is a statistically significant factor. Increasing cutting speed (the number of revolutions), surface roughness is decreasing. The other two influential factors, feed, and depth of cut, are statistically insignificant under analysed experimental conditions and probability of 95%.

5. REFERENCES

[1] NIST/SEMATECH e-Handbook of Statistical Methods, 17.02.2022., http://www.itl.nist.gov/div898/handbook

[2] S. Datta. Design of experiments, pp. 1-4, 2018

[3] J. Stanić. Metod inženjerskog merenja, (The method of engineering measurement), pp. 5-32, 60-80, 1981.

[4] M. S. Najiha, M. M. Rahman, K. Kadirgama, M. M. Noor and D. Ramasamy. Multi-objective optimization of minimum quantity lubrication in end milling of aluminium alloy AA6061T6, International Journal of Automotive and Mechanical Engineering, 2015;12.: http://dx.doi.org/10.15282/ijame.12.2015.15.0250

[5] N. Bradley. Applied mathematics and computer science, pp. 4-35, 2007

[6] S. Ekinović. Metode statističke analize u MS Excel-u", (Statistical methods in MS Excel), 2, pp. 27-50, 188-210, 2008.

[7] O. M. Baksalary, G. Trenkler. An alternative look at the linear regression model, 2021, https://doi.org/10.1007/s00362-021-01280-x

SOME ASPECTS OF A METALLURGY CONSULTING IN THE INDUSTRIAL TRANSITION OF B&H

Faik Uzunović
University of Zenica, Faculty of Metallurgy and Technology
Zenica, B&H

Keywords: plastic deformation v.s. mechanical maintenance in the industrial transition, metallurgy consulting

ABSTRACT
Some specific aspects of metallurgy consulting in the industrial transition of Bosnia and Herzegovina are presented in this paper. The theoretical part of the paper is mostly concerned with a short overview of ZELJEZARA ZENICA cum ARCELORMITTAL-ZENICA (AMZ) product-mix and the facilities transition, as an example of the a.m. transition, although these parameters are realistic in the practice. In the practical part, some judicial cases-pictures related to the plastic deformation of the structures-facilities are presented, along with general proposals-solutions how to overcome the problems related to an occurrence of plastic deformation of the a.m. structures-facilities, through proper mechanical maintenance, management, and consulting with renown institutions. The figures supplied in the practical part express the significant extent of the plastic deformations and are taken from the court expert judicial cases in different B&H companies. It may be an incentive for the technical faculties and institutes in B&H to visit metal sector production plants and offer their consulting services, in order to prevent the (dangerous) occurrence of plastic deformation of the structures-facilities, which can lead to worker injuries, structure-machinery breaks and to the un-planed stopping of normal production.

1. INTRODUCTION

U and I-beams are commonly used structural steel shapes in building industrial facilities and fixing the different types of machinery for the metal sector production [1].
Besides the recuperation of the infrastructure, as a war-ravaged country, B&H is still in the process of an industrial transition from unprofitable to profitable industry production [2].
A sort of very clear and metallurgy-oriented example of that industrial transition is ZELJEZARA ZENICA cum ARCELORMITTAL-ZENICA (AMZ) product mix and the facilities transition, along with mechanical maintenance of these facilities.
A simple comparison related to the final product mix, the facilities, and along with the characteristics of mechanical maintenance regarding the a.m. example is presented in the theoretical part of this paper comprising the content of the Table1.
In the practical part, some pictures of plastically deformed structures-facilities are presented. These pictures were taken from judicial cases related to different companies in B&H. They reflect the consequences of plastic deformation occurrences. Such overloading (could be produced by many reasons) which is a reason for plastic deformation occurrences can be produced by many technical reasons and unexpected events (like earthquakes and/or similar events), but can be also the consequence of a sort of poor mechanical maintenance, or negligence of the initial signs of the plastic deformation occurrences, or of an attempt to minimize mechanical maintenance expenses.
Whatever the reason is, there is a need to prevent the (dangerous) occurrence of plastic deformation of the structures-facilities, which can lead to worker injuries, machinery

breaks, and unplanned stopping of normal production [3]. That is why it is advisable that a related staff from the technical faculties and institutes in B&H go to visit metal sector production plants, advise their management and offer their own consulting services.

2. THEORETICAL/PRACTICAL APPROACH TO THE INDUSTRIAL TRANSITION REGARDING ŽELJEZARA ZENICA cum ARCELORMITTAL-ZENICA (AMZ)

As an example of a theoretical and at the same time practical approach in industrial transition, there is the case of ZELJEZARA ZENICA cum ARCELORMITTAL-ZENICA (AMZ) product-mix and the facilities transition, along with the characteristics of mechanical maintenance of these facilities.

Table 1. ŽELJEZARA ZENICA cum ARCELORMITTAL-ZENICA (AMZ) product mix and facilities

No.	ŽELJEZARA ZENICA - Final product facilities/products	AMZ- Final product facilities
1	Blooming/blooms	-
2	Continuous billet mill (after Blooming)/billets	-
3	Continuous billet mill (after CC machine)/billets	-
4	Heavy section mill/heavy sections	-
5	Medium section mill/medium sections	-
6	Light section mill – continuous/light sections	Yes (improved one-working)
7	Light section mill - line train mechanized/light sections	-
8	Light section mill - line train 320 mm – manual/light sections	
9	Light section mill - line train 280 mm – manual/light sections	
10	Wire rod mill - continuous/wire rod	Yes (the same one-working)
11	Wire rod mill - semi-continuous/wire rod	-
12	Single pass mill/ultra light sections	-
13	Forging shop/free forged & rolled pieces	Yes (the same one-off)

It is easy to notice from Table 1 that only two continuous rolling mills from former ZELJEZARA ZENICA operate nowadays in ARCELORMITTAL-ZENICA, and even one of them needed a high investment to be improved for meeting the requirements of profitability in a modern market economy.

The only excess or new final product facility in ARCELORMITTAL-ZENICA v.s. ZELJEZARA ZENICA is a Cold rolling-drawing mill, supplied with meshes & girders welding facilities.

Comprising all workforce including the one from preparatory and molten metal facilities (Coke oven, Sinter plants, Blast furnaces, Steel shops), Quality control, Transportation, Gas-Energy & Control-Measurement units, along with Maintenance units, and Food & Catering service units, there were about 22 000 workers in ZELJEZARA ZENICA in 1990-ies (production was about 1,8 million t/y), and nowadays, there are about 2 000 workers in ARCELORMITTAL-ZENICA (production was-is about 0,8 million t/y).

From the theoretical point of view, it is advisable to optimize production in a process of an industrial transition, to work on the best performance facilities, and to reduce labour force as well as maintenance expenses, as ARCELORMITTAL-ZENICA does in practice, but at a same time, it increases the risk of collapsed or damaged facilities, due to a lack of a proper pre-emptive oriented maintenance.

3. PRACTICAL APPROACH TO THE METALLURGY CONSULTING ORIENTED ACTIVITIES IN B&H METALLIC AND NON-METALLIC SECTOR

Besides that enormous a.m. mentioned ARCELORMITTAL-ZENICA reduction in labour force and accordingly higher profitability, there is also higher profitability-oriented practice to reduce proper maintenance, which is nowadays more full-wearing oriented, instead of more pre-emptive oriented maintenance.

There are also similar a.m. problems in the other metallic and non-metallic materials sector companies in B&H.

Figures 1 to 7 supplied in the practical part of this paper, express a significant extent of the plastic deformations, which lead to the break of a structure in a metallic material production plant, and similar figures 8 to 11 express also a significant extent of the plastic deformations, which did not (yet) lead to the break of a structure in a non-metallic material production plant. They are both taken from the court expert judicial cases in different B&H companies.

Figure 1. A broken sort of portal crane

Figure 2. Western layout view from a broken portal crane

Figure 3. Eastern layout view from a broken portal crane

Figure 4. Detailed position of a heavy bended section of a broken portal crane

Figure 5. Detailed position of a deeply corroded section of a broken portal crane

Figure 6. Detailed position of a welded and deeply corroded section of a broken portal crane

Figure 7. Detailed position of the small ductile breaks of a broken portal crane section

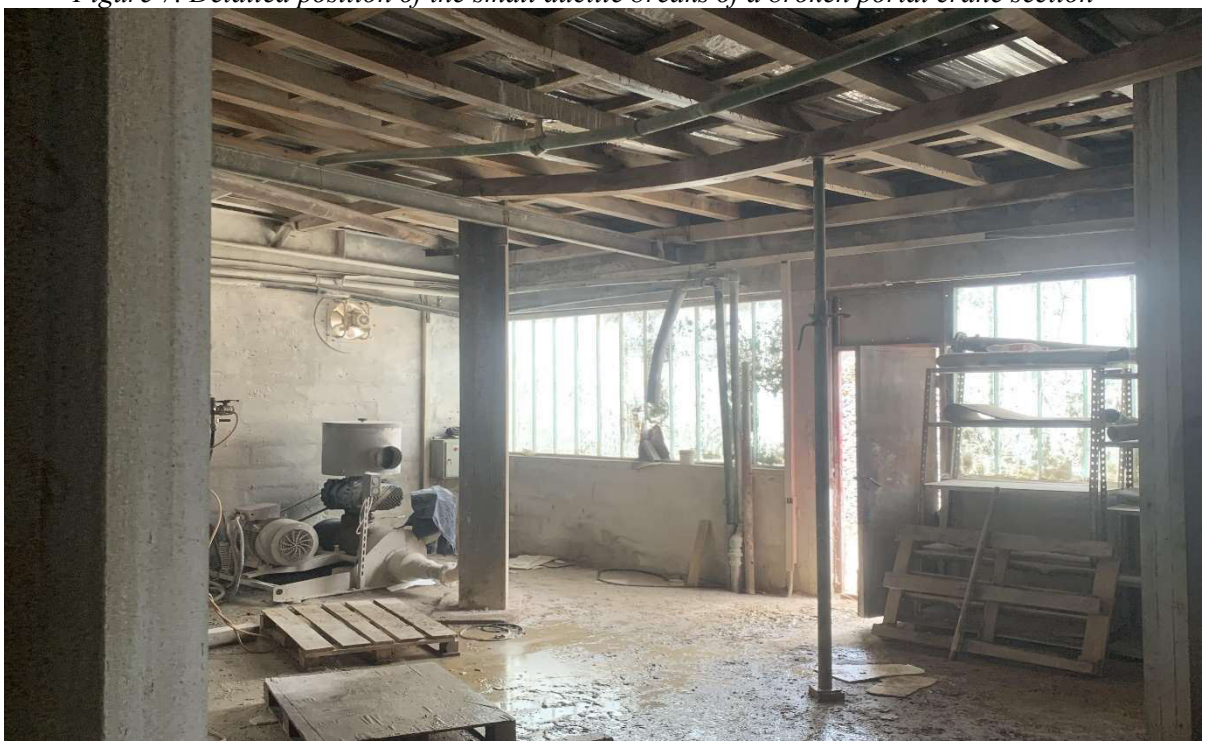

Figure 8. Detailed position of the wooden and steel section supports to plastically deformed sections

Figure 9. Another position of the wooden and steel section supports plastically deformed sections

Figure 10. Detailed position of the wooden section supports to plastically deformed sections & roof

Figure 11. Detailed position of plastically deformed sections & roof

All figures are very illustrative and easy to understand for the teaching staff from metallurgy and materials engineering faculties or institutes, as well as for the mechanical engineering ones. Such combined teams might organize visits to metallic and non-metallic product factories around B&H to convey some advice and messages about the dangerous consequences of any extent of plastic deformation occurrence on the structures and machinery.

Special attention during these proposed visits should be paid to the potential reasons for the occurrence of any (dangerous) extent of plastic deformation such as:

A- insufficient safety coefficient in designing
B- overloading
C- welding spots treatment
D- insufficient or non-regular corrosion protection
E- chemically aggressive environment
F- heating and freezing conditions (especially at welding spots)
G- vibrations and shocks
H- other reasons

It is not the aim of this article to treat from a metallurgy or material science point of view the a.m. problems from A to H, that can cause an occurrence of any (dangerous) extent of plastic deformation on different steel structures, than to give an incentive for more frequent visits of the teaching staff to the industrial facilities presenting at a spot short review of the a.m. topics, namely from A - H.

On the other hand, it is also advisable to make the Faculty of Metallurgy and Technology, Zenica, more visible among the companies-institutions in B&H and in the region, because it is illustrative in figures 1 to 11 that there could be a lot of potential "patients" having a

sort of similar problems (since the companies these photo-figures are taken from, are well known and respected companies in B&H, so one could imagine what is a situation in less known companies).
One more useful action to enhance an offer of "metallurgical" consulting activities is to make the application be recognized and registered in the Federal Ministry of Justice, as the institution for consulting activities in the area of metallic and non-metallic materials along with related technologies (as well as in all area corresponding to the study programs of Faculty of Metallurgy and Technology, Zenica).
Another area to enhance an offer of technical-technological consulting activities could be organized along with any Faculty of Mechanical Engineering, since from my experience, the majority of the transition companies in B&H are keen to reduce labour force as well as maintenance expenses, but that practice at a same time increases the risk of collapsed or damaged facilities, due to a lack of a proper pre-emptive oriented maintenance. Daily, weekly, and monthly maintenance periods are advisable to be a part of a production diagram, especially if the facilities are dated from the last century.

3. CONCLUSIONS

1. An overloading (or bad welding spots treatment, insufficient or non-regular corrosion protection, chemically aggressive environment, heating and freezing conditions /especially at welding spots/, vibrations, shocks, and some other unexpected reasons) can lead to an occurrence of plastic deformation, and all that can be a consequence of a sort of poor mechanical maintenance, or of the negligence of the initial signs of the plastic deformation occurrences.
2. It is advisable to optimize production in a process of an industrial transition, to manage production on the best-performance facilities, and to reduce labour force as well as maintenance expenses, but at the same time, it increases the risk of collapsed or damaged facilities, due to a lack of a proper pre-emptive oriented maintenance.
3. Regular visits of the teaching staff or experts to the industrial facilities presenting at a spot short review of the a.m. topics presented in the first conclusion are advisable.
4. It is also advisable to make the Faculty of Metallurgy and Technology, Zenica, more visible among the companies in B&H and in the region because it is illustrated in Figures 1 to 11 that there could be a lot of potential "patients" having a sort of similar problems.
5. For enhancing an offer for "metallurgical-technical" consulting activities it is needed to make the application to be recognized and registered in B&H Federal Ministry of Justice, as the institution for consulting activities in the area of metallic and non-metallic materials along with related technologies, as well as in all area corresponding to the study programs of Faculty of Metallurgy and Technology.
6. Another area to enhance an offer of technical-technological consulting activities could be organized along with the Faculty of Mechanical Engineering, since from my experience, the majority of the transition companies in B&H are keen to reduce labour force as well as maintenance expenses, but that practice at a same time increases the risk of collapsed or damaged facilities, due to a lack of a proper pre-emptive oriented maintenance. Daily, weekly, and monthly maintenance periods are advisable to be a part of a production diagram, especially if the facilities are dated from the last century.

4. REFERENCES

[1] F. Uzunović and the others, Survey of the selected sector, published by USAID – BBAC, USAID, Sarajevo, December 1997

[2] S. Tomašević and F. Uzunović: Restructuring of the steel industry in 1990, with a special view to the rolling technology in developing countries, especially in I-beam production, The first metallurgical symposium of Iran, Teheran 1991
[3] F. Uzunović, O. Beganović, and L. Sušić L.: The latest improvements in I-beams production and its application in building and maintenance, 7th International Conference MAINTENANCE 2022

NONMETALLIC MATERIALS

PARTIAL REPLACEMENT OF CEMENT WITH CALCINED CLAYS FROM CENTRAL BOSNIA

Marina Jovanović, Adnan Mujkanović, Nadira Bušatlić, Nedžad Haračić, Amina Čaušević
University of Zenica, Faculty of Metallurgy and Technology
Zenica, B&H

Keywords: calcined clay, kaolin, replacement cementitious materials, pozzolanic clay activity

ABSTRACT
Two clays from deposits located in the region of Central Bosnia, and kaolin obtained from a local spark plug and technical ceramics factory were calcined at 800, 900, and 1000 ºC. The pozzolanic activity of calcined raw materials was determined using the P test. Calcined clay from the deposit Bilalovac showed slightly better reactivity compared to calcined clay from the deposit Klokoti, and in both clays, the reactivity increased with increasing calcination temperature. Calcined kaolin was more reactive than clays and the highest reactivity was achieved when calcined at 800 °C. The strengths of mortars in which 20 % of cement was replaced with calcined raw materials showed the same trend of behavior as in the P test. Partial replacement of cement with calcined clays lead to a slight decrease in the strength of cement mortar, and the best results were obtained with clays calcined at 1000 °C.

1. INTRODUCTION

Each tonne of cement releases a little under a tonne of carbon dioxide, approximately half of that produced by the calcination of limestone. The remainder results from fuel used for the production of electrical energy needed for the grinding process and for fuel used in firing the materials [1]. The potential for atmospheric carbon reduction in the cement industry is through the resource-efficient use of pozzolanic materials. The possibilities of using new materials that can replace part of the clinker in Portland cement or part of the cement in concrete mixes are being intensively researched [2-9]. New materials should reduce energy consumption and gas emissions, and improve the characteristics of cement, mortar, and concrete to which they are added. The replacement materials have in common that they, in finely divided form, can react with $Ca(OH)_2$ in the presence of water to form a variety of excess cement phases.

Traditionally, the market for industrial pozzolans has been dominated by pulverised fuel ash (PFA) and blast furnace slag (BFS). In the long term, these resources are in decline; most of the world's production of suitable blast furnace slag and fly ash are already destined for use in the cement industry and it would seem timely to consider other options for blended cement production. Calcined clays, even those of somewhat lower quality (with a lower kaolinite content), are regarded as an appropriate alternative to the existing replacement materials [10-16].

This paper presents the results of research into the possibility of using domestic raw materials as substitute cement materials. For this purpose, two readily available local clays from central Bosnia were examined. Kaolin obtained from the "Enker" Factory in Tešanj was tested as a material for comparison.

2. EXPERIMENTAL WORK

2.1 Raw materials

The used raw materials were:

- clay from the exploitation field of the former factory of refractory materials from Busovača from the locality Klokoti - designated as clay A,
- clay from the area of the municipality of Kiseljak from the locality of Bilalovac - designated as clay B,
- kaolin from the "Enker" factory in Tešanj - designated as kaolin K.

Particle size distribution analysis of raw materials was carried out using the laser method on a Malvern Mastersizer 2000 particle size analyzer.

Loss on ignition was determined gravimetrically after heating up samples at 900 °C. The content of SiO_2 was also determined gravimetrically, while the content of Al_2O_3, Fe_2O_3, TiO_2, CaO, MgO, K_2O, Na_2O, and MnO after dissolving with acids was determined on a Perkin Elmer atomic absorption spectrometer.

The mineralogical composition of clays and kaolin was determined using simultaneous DTA and TGA on the instrument Netzsch STA 409 CD and XRD analysis. During DTA and TGA tests, samples were heated in a nitrogen atmosphere from room temperature to 1000 ˚C at a heating rate of 10 ˚C/min. X-ray diffraction analysis was performed on a Brucker D8 ENDEAVOR XRD diffractometer.

2.2. Preparation of samples

Dried raw clays A and B and kaolin K and water were used to prepare the samples for calcination. The dried raw clays were first sieved on a 1 mm sieve. 300 g of each of the clays and kaolin were weighed on an analytical balance. 65 ml of water was added to clay A, 75 ml to clay B, and 99 ml to kaolin K. The pastes were mixed by hand and shaped into cylinders with a height of 40 mm and a diameter of 33 mm. The prepared cylinders were air-dried for one day and then placed into the furnace for calcination according to the firing regime shown in Figure 1. After calcination, the samples were marked with a letter corresponding to the raw material (A, B, and K) and a number corresponding to the calcination temperature (800, 900, and 1000 ºC).

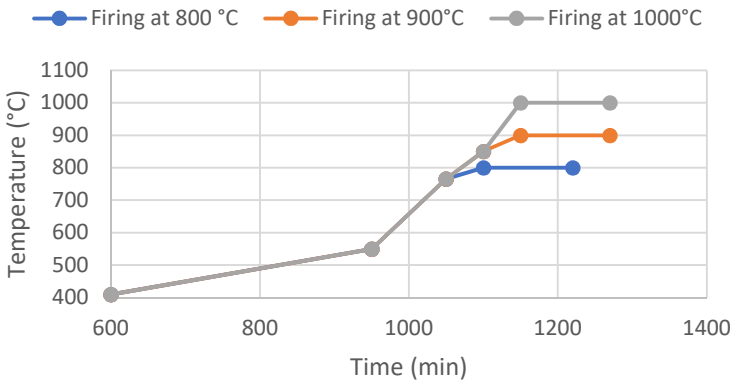

Figure 1. The regime for the firing of samples

The calcined samples were ground in a mill manufactured by "Herzog", power 400 W, dimensions 1.0 x 0.60 x 0.70 m, weight 80 kg, capacity 200 g. The grinding bodies were eccentric rings, and the grinding time was 30 seconds. Mineralogical analysis of ground calcined samples was performed using X-ray diffraction analysis on an XRD diffractometer Brucker D8 ENDEAVOR.

2.3 Determination of the pozzolanic reactivity of clays and kaolin

In this work, two methods were used for assessing the pozzolanic reactivity of clay and kaolin:

- portlandite ($Ca(OH)_2$) consumption test - marked as P test
- test of changes in cement mortar strength with 20 % replacement of cement with calcined clays and kaolin.

A pozzolanic reaction takes place between the cementitious replacement material and $Ca(OH)_2$ in the presence of free water to form C-S-H, C-A-H, or C-A-S-H phases. Since it is complicated and difficult to directly measure the amount of replacement cementitious material consumed in the pozzolanic reaction, an alternative method that is usually accepted to study the progress of the reaction is to determine the consumption of $Ca(OH)_2$. For a sample containing unreacted $Ca(OH)_2$, the mass loss due to dehydration of $Ca(OH)_2$ within a certain temperature range can be measured by TG analysis. The most common temperature range in which the decomposition of portlandite ($Ca(OH)_2$) occurs in the literature is around 350 to 550°C [10].

In this work, the temperature range 450 – 560 °C was used to determine mass loss via TGA under conditions of heating in a nitrogen atmosphere at a heating rate of 10 °C/min. This temperature range was chosen because the curves obtained on the device on which the test was carried out showed that within this range a reaction takes place accompanied by mass loss. In order to measure the properties of cementitious materials at a very early age, it is necessary to remove free water to stop cement hydration. Free water is replaced in the first step with an organic solvent that can be mixed with water, and in the second step, the solvent is removed by evaporation. Isopropanol was chosen as an inert solvent replacing water due to its minimal effect on the microstructure [10,17-19].

The preparation of the mixtures consisted of weighing 10 g of calcined raw materials for each separately in a plastic container and then adding 10 g of pure $Ca(OH)_2$, manual mixing for 1 minute. After mixing, 20 ml of distilled water was added, and the whole mixture was stirred for another 2 minutes. After that, the plastic container was closed, labeled, and placed in a laboratory oven at 40 ºC. After 7, 14, and 28 days, the containers were taken out of the oven, and a part (approximately 1/4) was taken from each sample, and placed in another plastic container into which isopropanol was poured in an amount that is approximately ten times greater than the amount of the separated sample as hydration would stop. The rest of the paste was closed again and returned to the oven until the next sampling. The samples prepared in this way were left in isopropanol for three days. After three days, isopropanol was separated by filtration, and the samples were dried in a laboratory oven with a digital thermoregulator at 60 ºC to a constant mass. The samples were then subjected to DTG/TG analyses to determine the amount of unreacted portlandite. Analyses were performed on a Netzsch STA 409 instrument from room temperature to 1000 °C, with a heating rate of 10 °C/min. Samples with an initial mass of approximately 50 mg were placed in an alumina crucible. During the measurement, the furnace was purged with nitrogen flow at a rate of 40 ml/min. The analysis results were processed using Netzsch Proteus Thermal Analysis software.

Cement mortars with 20 % replacement of cement with calcined clays and kaolin were prepared and tested on compressive and flexural strength after 7, 28, and 90 days according to the standard EN 196-1.

3. RESULTS AND DISCUSSION

3.1 Characteristics of raw materials

The particle size distribution of the starting raw materials is shown in Table 1. Kaolin K consists of smaller particles compared to clays, while clay B has the largest particles and

the differences in granulation between clays A and B are smaller compared to the differences between kaolin and clays. This confirms the assumption that kaolin K has the most clay minerals and the least impurities.

Table 1. Particle size of clays A and B and kaolin K

Sample	Particle diameter [μm]		
	d(0.1)	d(0.5)	d(0.9)
Clay A	3.481	12.261	33.479
Clay B	4.225	15.678	44.076
Kaolin K	2.468	8.870	21.528

Table 2. Chemical composition of raw materials

Component	Chemical composition (wt. %)		
	Clay A	Clay B	Kaolin K
SiO_2	70.7	63.60	48.90
Al_2O_3	17.8	22.3	37.81
Fe_2O_3	1.40	2.04	1.20
CaO	1.27	0.95	/
TiO_2	0.003	0.006	0.00
MgO	0.48	0.76	0.00
MnO	0.008	0.008	/
K_2O	3.65	4.66	2.20
Na_2O	0.30	0.50	/
ZnO	0.019	0.016	/
LOI	4.11	4.98	12.17

Table 2 shows results related to the chemical analysis of raw materials. Chemical analysis shows that all three tested raw materials have the most SiO_2 and Al_2O_3, which is typical for clays and indicates the presence of clay minerals and quartz and possibly feldspar. Kaolin K has the most Al_2O_3, which is assumed to have the most kaolinite, and clay A the least. On the other hand, clay A has the most SiO_2, so it is assumed that this clay has the most quartz compared to the other two raw materials. Potassium is in third place in terms of representation in raw materials, and it comes from illite and muscovite or from potassium feldspar, and it is most abundant in clay B. In fourth place is iron, which most likely comes from illite. The amount of CaO in the clays is insignificant, which indicates that the clays do not contain calcium compounds, primarily carbonate. Kaolin K has the highest loss on annealing, which again indicates a large amount of kaolinite, while in the case of clays A and B this loss is much smaller and does not differ much, indicating a smaller amount of clay minerals compared to kaolin K.
Figure 2 shows differential thermal analyses and thermogravimetric analyses of raw materials. Thermal tests on a DTA/TG device confirmed the presence of kaolinite (endothermic peaks at 585, 586 and 608 °C on DTA curves, as well as a significant mass loss on the TG curves in that temperature regions), illite and/or muscovite (mass loss at around 900 °C) in all three raw materials. Again, it was confirmed that the most kaolinite has kaolin K, where an exothermic peak can be clearly observed at 1010 °C, which confirms the transformation of kaolinite into a new crystalline phase at high temperatures. Such a peak, but of much lower intensity, is also observed on the DTA curve of clay A at 996 °C. The mass losses determined by this method are in good agreement with the annealing losses during chemical analysis.

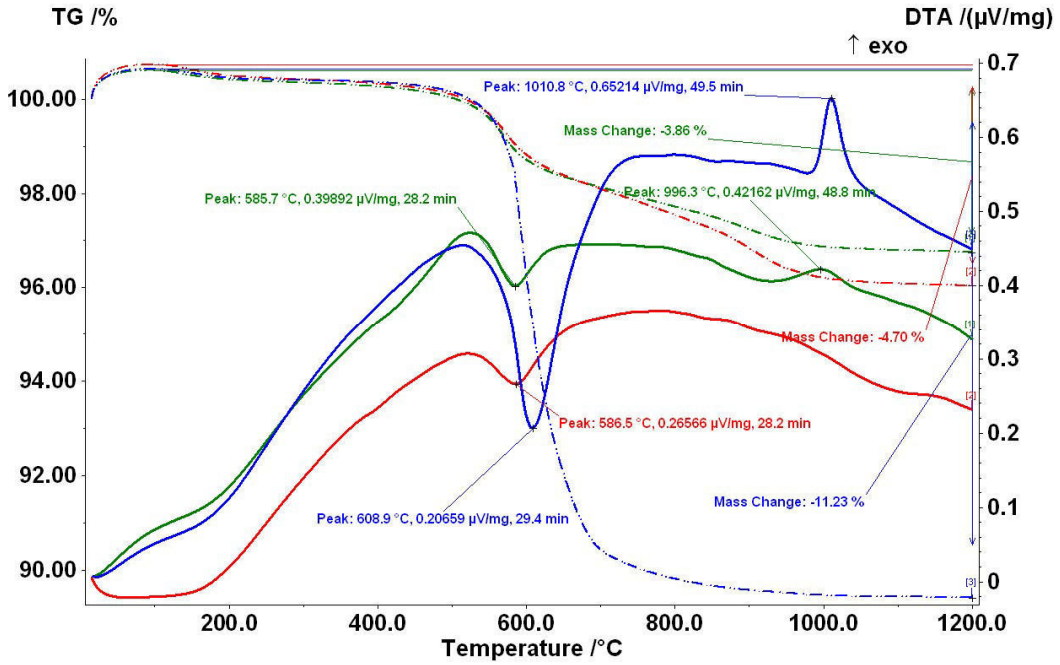

Figure 2. DTA/TG analysis of raw materials
(green – clay A, red – clay B, blue – kaolin K)

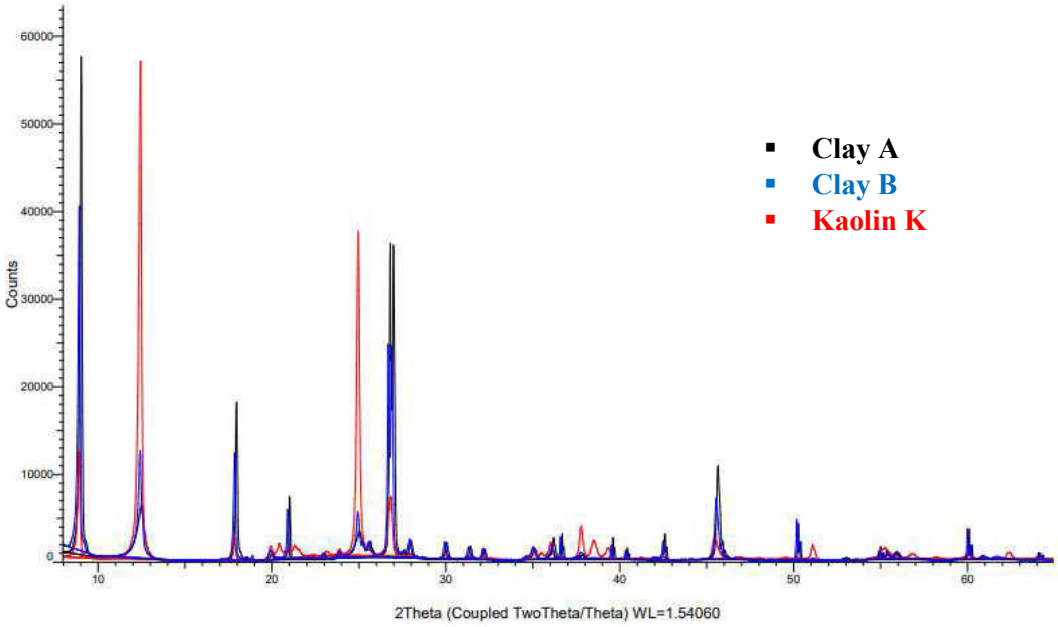

Figure 3. X-ray spectrum of raw materials

Figure 3 shows the diffractograms of the starting materials which show that they contain mainly muscovite and/or illite, kaolinite, and quartz. The diagrams also show that clay A has the most quartz, which agrees with the chemical analysis that shows that clay A has the largest amount of SiO_2. A higher amount of kaolinite is observed in clay B compared to clay A, which again coincides with the chemical analysis that shows a higher amount of Al_2O_3 in clay B compared to clay A. The amount of muscovite and/or illite is the highest in clay A, which does not match with the amount of K_2O in the chemical analysis where clay

B has the highest amount of K_2O, so it was to be expected that it also has the most illite and/or muscovite. However, there is a possibility that K_2O also comes from some other minerals, for example, felspar whose peaks are difficult to see on an X-ray, because they often overlap with the peaks of muscovite and quartz. Kaolinite is most abundant in kaolin K, in which smaller amounts of quartz and muscovite, and/or illite are also observed.
X-rays of clays and kaolin calcined at 800 °C show peaks of muscovite and/or illite and peaks of quartz, while the peaks of kaolinite have disappeared, which means that up to this temperature the kaolinite mineral has completely decomposed in all tested raw materials. The peaks of muscovite and/or illite are of lower intensity compared to uncalcined raw materials, which indicates that their decomposition also started at a temperature lower than 800 °C.
On the X-ray images of clays and kaolin calcined at 900 °C (Figure 4), the same peaks as for clay and kaolin calcined at 800 °C are observed, but the intensity of the peaks of muscovite and/or illite is lower, which means that their decomposition has continued. In the X-ray image of kaolin calcined at 800 °C, the appearance of new peaks of low intensity is observed, which probably belong to the spinel-type phase or mullite recrystallizing from the liquid phase. Such a phase appears with clay B calcined at 900 °C, and with clay A only after calcination at 1000 °C.

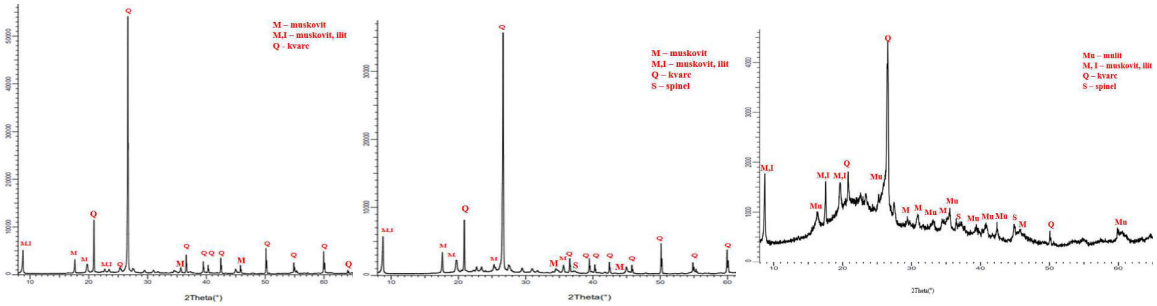

Clay A *b) Clay B* *c) kaolin K*

Figure 4. X-ray spectrum of raw materials calcined at 900 °C

In the case of raw materials calcined at 1000 °C, there are no more peaks of muscovite and/or illite, which means that their decomposition is complete, the peaks created by calcination at 900 °C intensify and new peaks corresponding to the spinel or mullite phase appear, especially pronounced in kaolin. Kaolin K calcined at all three temperatures shows a significantly more amorphous phase compared to calcined clays A and B.

3.2 Pozzolanic reactivity

Using the P test, the effect of different temperatures on the pozzolanic reactivity of calcined clays and kaolin was defined. Mass loss in the temperature range of 450-560 °C was determined on TG curves. The smaller this mass loss, the more portlandite was consumed in the reaction with the calcined raw materials, i.e. these calcined raw materials have a better pozzolanic reactivity.
The results (Figure 5) showed that calcined clay A and calcined clay B behave similarly. Slightly better reactivity in all test conditions is shown by calcined clay B. As the calcination temperature increases, so does the reactivity of these clays, which is probably the result of a decrease in the amount of the crystalline phase, i.e. the amount of muscovite and/or illite, and an increase in the amount of the more reactive amorphous phase.
Kaolin K calcined at 800 °C shows significantly higher reactivity compared to clays calcined at this temperature. Kaolin K calcined at 900 °C still has higher reactivity than clays calcined at this temperature, but it is less pronounced. Calcination of kaolin K at 1000

°C significantly reduces its reactivity, so that it is now less than the reactivity of clays. This is probably the result of a more pronounced crystallization of the spinel or mullite phase, and a decrease in the amount of the amorphous phase.
In all tested samples, reactivity increases with increasing reaction time. Kaolin K shows the best reactivity when calcined at 800 °C and after 28 days of holding at 40 °C, and clays A and B when calcined at 1000 °C and also after 28 days of holding at 40 °C.

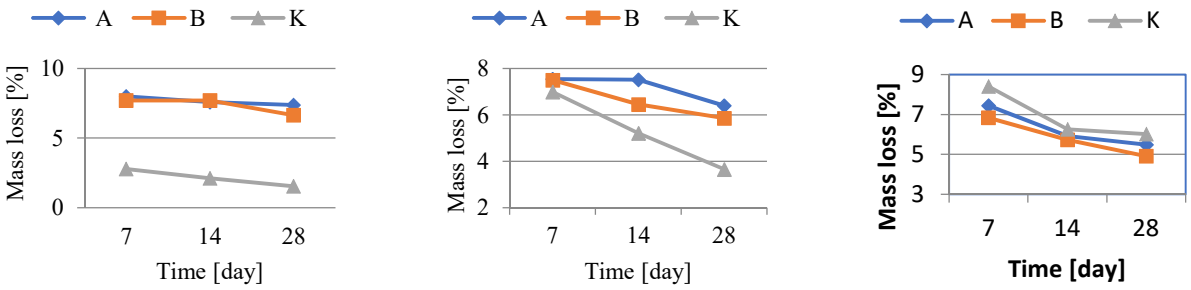

a) 800 °C *b) 900 °C* *c) 1000 °C*

Figure 5. Results of P test

The impact of replacing cement with calcined raw materials in the amount of 20 % was tested on the flexural and compressive strength of the cement mortar. The properties of tasted mortars were also compared with those of the control Portland cement CEM I mortar. The results of this test (Figure 6 and Figure 7) show the same behaviour trend as in the P test, i.e. the materials that showed better pozzolanic reactivity in the P test show higher compressive and flexural strength. Mortars with calcined clay A behave similarly to mortars with calcined clay B. Mortars with calcined clay B have slightly higher strength. As the calcination temperature increases, the strength of mortars with these clays increases.
The compressive strengths of mortars with kaolin calcined at 800 °C are close to the strengths of mortars with CEM I 52,5 N cement, while the strengths of mortars with clays calcined at the same temperature are significantly lower. All mortars with raw materials calcined at 900 °C and 1000 °C have lower compressive strength compared to the mortar with only CEM I 52,5N cement.
According to the EN 197-1 standard, which prescribes the criteria for the physical and mechanical properties of cement, all the tested samples show appropriate values. The compressive strength of cement with the addition of kaolin calcined at 800 °C after 28 days is 56.1 MPa, which corresponds to cement class 52.5. Cement with the addition of calcined kaolin at 900 °C has a compressive strength of 44.61 MPa, which corresponds to cement class 42,5 N. Samples with the addition of calcined kaolin, clay A and clay B at 1000 °C have a compressive strength of 35.1 MPa, which corresponds to class 32.5 cements [20].
Mortars with kaolin calcined at 800 °C have higher strength compared to mortars with clays calcined at this temperature. The strengths of mortars with kaolin calcined at 900 °C are slightly higher or even almost the same in relation to the strengths of mortars with clays calcined at this temperature. Mortars with kaolin calcined at 1000 °C have less strength than mortars with clays calcined at this temperature.
The strengths of all tested samples increase with the increase in the curing time of the mortar. Of the mortars with calcined kaolin, the mortar with kaolin calcined at 800 °C and after 90 days of care has the highest strength, and of the mortar with calcined clays, clays A and B when calcined at 1000 °C and also after 90 days of care.

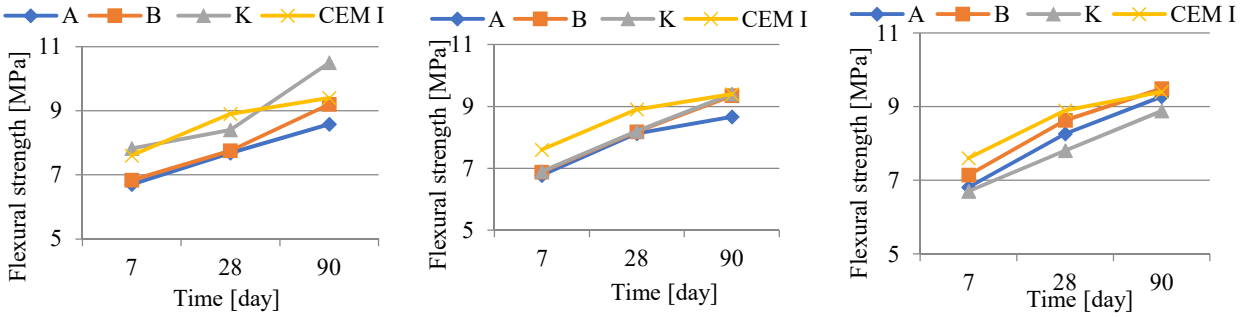

a) 800 °C *b) 900 °C* *c) 1000 °C*

Figure 6. Flexural strength

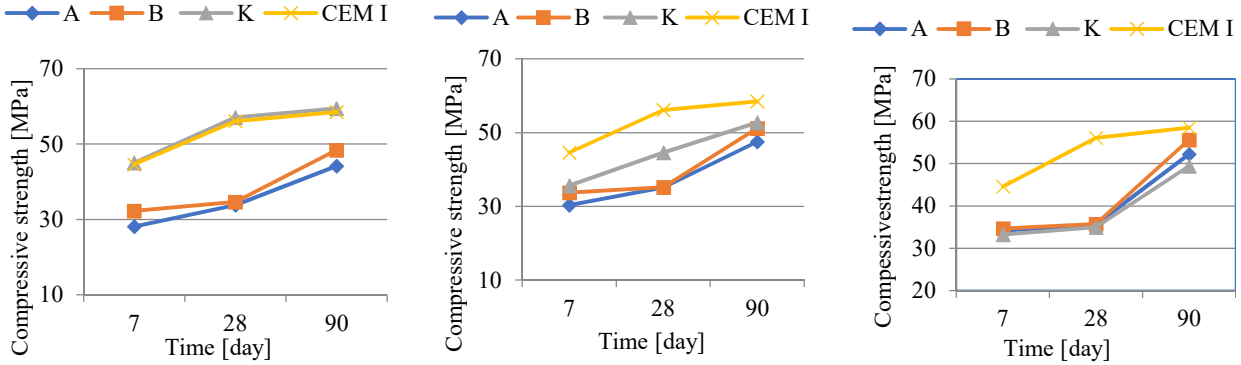

a) 800 °C *b) 900 °C* *c) 1000 °C*

Figure 7. Compressive strength

4. CONCLUSION

Based on the presented results, the following can be concluded:

- Kaolin K consists of smaller particles compared to clays, while clay B has the largest particles and the differences in granulation between clays A and B are smaller compared to the differences between kaolin and clays. It is known that cement has higher reactivity and better mechanical properties with higher grinding fineness.
- Diffractograms of the starting materials show that they contain mainly muscovite and/or illite, kaolinite, and quartz. The diagrams also show that clay A consists mostly of quartz. That agrees with the chemical analysis that shows that clay A has the largest amount of SiO_2. A higher amount of kaolinite is observed in clay B compared to clay A, which again coincides with the chemical analysis that shows a higher amount of Al_2O_3 in clay B compared to clay A.
- Kaolin K calcined at all three temperatures shows a significantly more amorphous phase compared to calcined clays A and B.
- Using the P test, the effect of different temperatures on the pozzolanic reactivity of calcined clays and kaolin was defined. The results showed that calcined clay A and calcined clay B behave similarly. Slightly better reactivity in all test conditions is shown by calcined clay B. As the calcination temperature increases, so does the reactivity of these clays, which is probably the result of a decrease in the amount of the crystalline phase, i.e. the amount of muscovite and/or illite, and an increase in the amount of the more reactive amorphous phase.
- The impact of replacing cement with calcined raw materials in the amount of 20 % was tested on the flexural and compressive strength of the cement mortar. The properties of tasted mortars were also compared with those of the control Portland cement CEM I

mortar. The results of this test show the same behavior trend as in the P test, i.e. the materials that showed better pozzolanic reactivity in the P test show higher compressive and flexural strength. Mortars with calcined clay A behave similarly to mortars with calcined clay B. Mortars with calcined clay B have slightly higher strength. As the calcination temperature increases, the strength of mortars with these clays increases.

- The compressive strengths of mortars with kaolin calcined at 800 °C are close to the strengths of mortars with CEM I cement, while the strengths of mortars with clays calcined at the same temperature are significantly lower.
- All the compressive strength values of the tested samples correspond to the criteria for the physical and mechanical properties of cement according to EN 197-1. The compressive strength of samples with kaolin decreases with increasing calcination temperature, which also decreases the cement class. The samples with clays A and B have approximate compressive strength values, regardless of the calcination temperature, and correspond to the cement of class 32.5.
- The strengths of all tested samples increase with the increase in the curing time of the mortar. Of the mortars with calcined kaolin, the mortar with kaolin calcined at 800 °C and after 90 days of care has the highest strength, and of the mortar with calcined clays, clays A and B when calcined at 1000 °C and also after 90 days of care.
- This research has shown that it is possible to partially replace cement with calcined clays from the area of Busovača and Kiseljak, although they lead to a slight decrease in the strength of the cement mortar. The most favorable temperature for calcination of tested clays is 1000 °C.

5. REFERENCES

[1] Worrell, E., Price, L., Martin, N., Hendriks, C., Meida, L. O.: Carbon dioxide emissions from the global cement industry, Annual Review of Energy and the Environment, 26(1), 303–329, 2001

[2] Tyrer, M., Cheeseman, C. R., Greaves, R.: Potential for carbon dioxide reduction from cement industry through increased use of industrial pozzolans, Advances in applied ceramics, 109, 275-279, 2010

[3] Siddique, R.: Utilization (recycling) of iron and steel industry by-product (GGBS) in concrete: strength and durability properties, Journal of Material Cycles and Waste Management, 16, 460-467, 2014

[4] Zhou, F. P., Barr, B. I. G., Lydon, F. D.: Fracture Properties of High-Strength Concrete with Varying Silica Fume Content and Aggregates, Cement and Concrete Research, 25, 543-552, 1995

[5] Vejmelková, E., Keppert, M., Rovnaníková, P., Ondráček, M., Keršner, Z., Černý, R.: Properties of high performance concrete containing fine-ground ceramics as supplementary cementitious material, Cement and Concrete Composites, 34, 55-61, 2012

[6] Zhang, Z., Zhang, B., Yan, P.: Hydration and microstructures of concrete containing raw or densified silica fume at different curing temperatures, Construction and Building Materials, 121, 483-490, 2016

[7] Wong, H. S., Razak, H. A.: Efficiency of calcined kaolin and silica fume as cement replacement material for strength performance, Cement and Concrete Research, 35, 696-702, 2005

[8] Schwarz N., Cam H., Neithalath N.: Influence of a fine glass powder on the durability characteristics of concrete and its comparison to fly ash, Cem. Concr. Compos., 2008, 30, (6), 486– 496

[9] Zhang, M. H., MALHOTRA, V. M.: Characteristics of a thermally activated alumino-silicate pozzolanic material and its use in concrete, Cement and Concrete Research, 25, 1713-1725, 1995

[10] Zhou D.: Developing supplementary cementitious materials from waste London clay, doctoral thesis, Imperial College London, Faculty of Engineering, 2016

[11] Mitrović A., Jevtić D., Miličić Lj., Ilić B.: Karakteristike portland cementa sa dodatkom metakaolina dobijenog kalcinacijom domaće kaolinske gline, Materijali i konstrukcije 53 (2010) 3 (32-43)
[12] Alujas, A., Fernández, R., Quintana, R., Scrivener, K. L., Martirena, F.: Pozzolanic reactivity of low grade kaolinitic clays: Influence of calcination temperature and impact of calcination products on OPC hydration, Applied Clay Science, 108, 94–101, 2015
[13] Wild, S., Khatib, J. M., OFARRELL, M.; Sulphate resistance of mortar, containing ground brick clay calcined at different temperatures. Cement and Concrete Research, 27, 697-709, 1997
[14] Tironi, A., Trezza, M. A., Scian, A. N., Irassar, E. F.: Assessment of pozzolanic activity of different calcined clays, Cement & Concrete Composites, 37, 319-327, 2013
[15] Badogiannis, E., Kakali, G., Dimopoulou, G., Chaniotakis, E., Tsivilis, S.: Metakaolin as a main cement constituent. Exploitation of poor Greek kaolins, Cement and Concrete Composites, 27, 197-203, 2005
[16] Chakchouk, A., Samet, B., Mnif, T.: Study on the potential use of Tunisian clays as pozzolanic material, Applied Clay Science, 33, 79-88, 2006
[17] Wang X., Eberhardt A. B., Scrivener K., Gallucci E.: Assessing early age properties of cementitious systems by water – isopropanol replacement, Cement and Concrete Research, 84: 76-84, 2016
[18] Mujkanović A., Bitić A., Jovanović M., Merdić N., Zahirović A., Karić A.: Effect of nano-silica addition on phisico-mechanical properties and durability of concrete, Journal of Sustainable Technologies and Materials, Vol. 2 (2022) 2, 9 – 19
[19] Kramar S., Ducman V.: Evaluation of Ash Pozzolanic Activity by Means of the Strength Activity Index Test, Frattini Test and DTA/TG Analysis, Tehnički Vjesnik - Technical Gazette, 25(6), 2018
[20] Bušatlić I., Bušatlić N., Merdić N., Haračić N.: Osnove hemije i tehnologije Portland cementa, Štamparija Fojnica dd, Zenica 2018.

POSSIBILITY OF PRODUCTION OF METALLURGICAL CEMENT TYPE CEM III/A 42.5N IN CEMENT PLANT KAKANJ

Nevzet Merdić, Nedžad Haračić
Cement Plant Kakanj
Kakanj, B&H

Ilhan Bušatlić, Nadira Bušatlić, Adnan Mujkanović
University of Zenica, Faculty of Metallurgy and Technology
Zenica, B&H

Keywords: Portland cement, clinker, granulated blast furnace slag, compressive strength, volume constancy, setting time

ABSTRACT
This paper examines the possibility of producing metallurgical cement type CEM III/A 42.5N at the Kakanj Cement Factory. The tested samples contain respectively 46%, 41%, and 38% of granulated blast furnace slag and the rest is clinker. According to the test results, all cement samples meet the EN 197-1 standard in terms of physical-mechanical properties both after the initial period (2 days) and after the final period (28 days). As a result of the conducted tests, it can be concluded that the production of metallurgical cement type CEM III/A 42.5N at the Kakanj cement factory is possible and that its production would provide a number of ecological and economic benefits.

1. INTRODUCTION

By reducing the clinker content and using granulated blast furnace slag in the production of cement, it is possible to reduce CO_2 emissions during production. If the content of clinker in cement is reduced, the number of natural resources needed for the production of clinker will also be reduced, thus having a positive effect on the preservation of ecology. Also, using a larger amount of granulated blast furnace slag for cement production opens up the possibility of producing cheaper cement because granulated blast furnace slag is a much cheaper material than clinker itself.

Metallurgical cement is obtained by grinding Portland cement clinker, gypsum, and granulated blast furnace slag, the content of which ranges from 36 to 95%. According to EN 197-1, metallurgical cement belong to the third group of cement (CEM III) and there are three classes of metallurgical cement, namely [1]:

- CEM III/A with granulated blast furnace slag content of 36 – 65 %,
- CEM III/B with granulated blast furnace slag content of 66 – 80 %.
- CEM III/C with granulated blast furnace slag content of 81 – 95 %.

The constituents discussed in this paper are:

- clinker produced in the Kakanj cement plant,
- granulated blast furnace slag of the company ArcelorMittal Zenica

2. EXPERIMENTAL

2.1 Materials and method

If one part of clinker, as the main ingredient of cement, is replaced with a certain amount of granulated blast furnace slag, the already existing depositing of granulated blast furnace slag is reduced, natural raw materials are saved, environmental pollution is reduced, and in

the end, cheaper cement can be produced. Also, using a larger amount of granulated blast furnace slag would reduce CO_2 emissions into the atmosphere. Of course, in order to produce this kind of metallurgical cement, the requirements of the EN 197-1 standard must be met.
Clinker is produced by a sintering process from a precisely specified mixture of raw meals. Clinker is a hydraulic material that mostly consists of four main minerals that give it a certain reactivity, namely alite (C_3S), belite (C_2S), tricalcium aluminate (C_3A), and tetracalcium ferrite (C_4AF). Granulated blast furnace slag (GBFS) is a byproduct of the iron production process in blast furnaces. It is a latent hydraulic material, because during the hydration of cement after the release of $Ca(OH)_2$, the hydration of the blast furnace slag continues unhindered. This means that for practical use an activator is needed to react with water and form hydrated phases similar to clinker hydration products. It is obtained when coke ash and limestone are added to iron ore to remove impurities. In the process of extracting iron from iron ore, a liquid slag is formed, consisting primarily of calcium silicates and aluminosilicates, and other phases, and it floats on top of the liquid iron. The liquid slag is separated from the liquid metal and cooled. If the liquid slag is rapidly cooled with water, granulated blast furnace slag is obtained. By grinding granulated blast furnace slag improves its reactivity during cement hydration [2,3].
The chemical analysis of clinker and granulated slag from blast furnaces is determined by XRF spectrometry and mineralogical composition was determined by diffractometer. The aim of this work is to examine the possibility of producing metallurgical cement type CEM III/A 42.5N in the Kakanj cement factory with the composition U1 (50% clinker, 46% granulated blast furnace slag, and 4% gypsum), U2 (55% clinker, 41% granulated slag blast furnace, and 4% gypsum) and U3 (58% clinker, 38% granulated blast furnace slag, and 4% gypsum). For the preparation of each sample, about 2 kg of the mixture (clinker, granulated blast furnace slag, and gypsum) was weighed. After grinding, the sample was shaken out of the ball mill, then sieved on a 1 mm sieve, and taken to the laboratory for further testing. The samples were kept in a room with a temperature of 20 ± 2 °C and relative humidity > 50 %.In this work, it will be investigated whether the new class of cement U1, U2, and U3 retains the properties of cement given by the already existing CEM II/B – W 42.5N composition of 68% clinker, 28% fly ash, and 4% gypsum.
Standard consistency, setting time, and volume constancy are determined according to EN 196 – 3 [4].

2.2 Test results

Table 1 shows the chemical analyses of clinker and GBFS. Table 2 shows the mineralogical composition of clinker and GBFS. In order for clinker and GBFS to be used for cement production, certain requirements must be met according to the European standard EN 197 – 1 (Table 3) [1].

Table 1. Chemical composition of clinker and GBFS

Component (%)	SiO_2	Al_2O_3	Fe_2O_3	CaO	MgO	SO_3	Na_2O	K_2O	Chloride
Clinker	20,84	5,64	3,02	66,62	1,10	0,57	0,14	0,52	0,009
GBFS	41,44	7,60	0,88	38,88	4,89	0,09	0,24	1,28	0,008

Table 2. Mineralogical composition of clinker and GBFS

Minerals	Clinker (%)	GBFS (%)
Alit (C_3S)	59,93	
C_2S	16,38	
C_3A	10,36	
C_4AF	8,39	
Free CaO	1,11	
Periclase (MgO)	0,19	
Quartz (SiO_2)	0,08	
Arcanite (K_2SO_4)	1,22	
Portlandite ($Ca(OH)_2$)	0,01	
Amorphous phase		99,70
Calcit		0,20
Mervinit		0,01
Quartz		0,04

Table 3. Requirements of EN 197-1 for clinker and GBFS [1]

	Requirements EN 197-1	Clinker	GBFS
$C_3S + C_2S$	≥66,6 %	76,31 %	
CaO/SiO_2	>2,0	3,20	
MgO	<5,0 %	1,10 %	
$CaO+MgO+SiO_2$	≥66,6 %		85,21 %
$(CaO+MgO)/SiO_2$	>1,0		1,057

Table 4. Chemical composition of metallurgical cement

Sample	SiO_2	Al_2O_3	Fe_2O_3	CaO	MgO	SO_3	Na_2O	K_2O
U1	28,98	6,43	2,28	51,53	3,84	2,75	0,18	0,84
U2	28,03	6,33	2,35	53,03	3,55	2,33	0,17	0,81
U3	27,46	6,27	2,39	53,92	3,37	2,32	0,16	0,79

Table 5 shows the physical and mechanical properties of the metallurgical cement examined in this paper, while Table 6 shows the requirements of the EN 197-1 standard for the physical-mechanical properties of cement.

Table 5. Physical and mechanical properties of cement

	R 009 (%)	Specific surface (cm^2/g)	Stand. conc. (%)	Setting time		Compressive strength (MPa, days)			
				Initial (min.)	Final (min.)	Flexural		Compressive	
						2	28	2	28
U1	0,1	4340	25,2	125	145	2,7	7,2	12,8	45,8
U2	0,1	4260	25,6	120	150	2,7	7,5	13,0	47,6
U3	0,1	4300	25,6	110	145	2,8	7,3	14,0	47,9
CEM II/B-W 42,5N	0,5	3450	27,0	185	245	2,9	7,9	15,0	50,4

Table 6. Requirements of EN 197-1 for physical-mechanical properties of cement [1]

Strength class	Compressive strength (MPa, days)				Initial setting time (min)	Soundness (mm)
	Early strength		Standard strength			
	2 days	7 days	28 days			
32,5 N	-	≥ 16,0	≥ 32,5	≤ 52,5	≥ 75	≤ 10
32,5 R	≥ 10,0	-				
42,5 N	≥ 10,0	-	≥ 42,5	≤ 62,5	≥ 60	
42,5 R	≥ 20,0	-				
52,5 N	≥ 20,0	-	≥ 52,5	-	≥ 45	
52,5 R	≥ 30,0	-				

3. DISCUSSION

The clinker also meets all the requirements of the European standard EN 197-1. The total content of CaO, SiO_2, and MgO in granulated blast furnace slag according to the EN 197-1 standard must be greater than 66.6%, and the granulated blast furnace slag used for these tests has a content of these components of 85.21 %. The standard consistency of all cement samples is very similar and ranges from 25.20 to 25.60 %. The difference at the beginning of the setting time between the samples is insignificant and the shortest setting time at sample U3 (110 minutes), which can be attributed to the highest content of clinker compared to the other samples, while the difference at the end of setting between the cement samples is about 5 minutes.

Regarding the compressive strength results, all three samples (U1, U2, and U3) have compressive strength values after 2 days greater than 10 MPa (12.8 MPa, 13.0 MPa, and 14.0 MPa) and they meet the requirements of the EN standard 197-1. After 28 days, all samples meet the requirements of the EN 197-1 standard in terms of compressive strength and have values greater than 42.5 MPa.

4. CONCLUSIONS

According to the test results, all cement samples meet the EN 197-1 standard in terms of physical-mechanical properties both after the initial period (2 days) and after the final period (28 days). In general, increasing the content of mineral additives (granulated blast furnace slag) and decreasing the clinker content opens up the possibility of many benefits. The production of the new class of cement U1, U2, and U3 would reduce the production of clinker by the corresponding percentage of clinker while maintaining the properties of the cement provided by the existing CEM II/B – W 42.5N. The Kakanj cement factory currently produces CEM II/B – W 42.5N with a clinker content of about 68 %, and if U1, U2, and U3 cement containing 50 %, 55 %, and 58 % of clinker were produced, the utilization of natural resources, i.e. raw materials for the production of clinker, and as a consequence CO_2 emissions into the atmosphere would also decrease. As a final goal, financial benefits would be achieved because clinker is the most expensive component in the production of cement. On the other hand, the consumption of granulated blast furnace slag would increase, which would mean less accumulation of this material in existing landfills. All three types of cement (U1, U2, and U3) would have the mark CEM III/A 42.5N.

5. REFERENCE

[1] EN 197-1, Cement – Dio 1: Sastav, specifikacija i kriteriji usklađenosti za obične cemente, 2013.

[2] N. Merdić, Razvoj nove klase portland-kompozitnih cemenata u tvornici Cementa Kakanj, doktorska disertacija, Univerzitet u Zenici, Fakultet za metalurgiju i materijale u Zenici, Zenica, 2015.

[3] N. Bušatlić, I. Bušatlić, N. Merdić, N. Haračić, Osnove hemije i tehnologije Portland cementa, Štamparija Fojnica d.d., Zenica, 2020.
[4] EN 197 – 3, Metode ispitivanja cementa – Dio 3: Određivanje vremena vezivanja i stalnosti zapremine, 2013.

DEVELOPMENT OF NEW CEMENT TYPE CEM II/C-M ACCORDING TO EN 197-5

Nedžad Haračić, Nevzet Merdić
Kakanj cement plant
Kakanj, B&H

Ilhan Bušatlić, Nadira Bušatlić
University of Zenica, Faculty of Metallurgy and Technology
Zenica, B&H

Keywords: cement CEM II/C-M (S+W), European standard EN 197-5, cement composition, cement properties

ABSTRACT
According to new EN 197-5 is possible to combine clinker with blast furnace slag, silica fume, pozzolana, fly ash, burnt shale, and limestone from 36 – 50% while clinker content should be from 50 – 64%. In this paper are presented results of laboratory testing concerning CEM II/C-M (S+W) production where a sample is prepared by mixing 50% of clinker, 23% of calcareous fly ash, 23% of granulated blast furnace slag, and 4 % of gypsum. The focus was on the physical and mechanical properties of laboratory-produced samples in terms of the specific surface, specific weight, setting time, and tensile/compressive strength. Besides the physical-mechanical properties, the main chemical parameters are also determined (SiO_2, Al_2O_3, Fe_2O_3, CaO, MgO, SO_3, Na_2O, and K_2O). The obtained results of CEM II/C-M (S+W) are compared with the results of cement CEM II/B-W 42,5N.

1. INTRODUCTION

For a long time, one of the main targets in the cement industry is to find a way how to use different types of secondary/alternative materials in this industry. On the global market, there are a lot of materials that can be used in the cement industry in different portions [1]. The new EN 197-5 European standard was created due to the growing need to replace the clinker content with some other alternative materials. Although EN 197-1 European standard cover a wide range of the various main constituents still there is a need for combining these constituents. EN 197-1 is published by the National Standardization Bodies as a national standard in all European countries (e.g. BS EN 197-1)[2].

Even though standard EN 197-1 allows to use of different types of main constituents in cement still there is a need to increase the content of materials that can replace the clinker content in cement [3]. In the past years, a lot of research has been done in order to combine different main constituents in different portions of the final product. All this research is united in the new standard EN 197-5 which is adopted last year. Certainly, the utilization of these materials in cement must be correlated with cement quality [4]. One of the main changes in EN 197-5 is related to limestone properties (L, LL). The calcium carbonate ($CaCO_3$) content calculated from the calcium oxide content shall be at least 40 % by mass and the sum of calcium carbonate and magnesium carbonate ($CaCO_3$ and $MgCO_3$) content calculated from the calcium oxide and magnesium oxide content respectively shall be at least 75 % by mass.The composition of Portland-composite

cement CEM II/C-M and Composite cement CEM VI covered by this document is specified in Table 1 [5].

Table 1. Portland-composite cement CEM II/C-M and Composite cement CEM VI [5]

Main types	Notation of the products (types of cement)		Composition (percentage by mass a)										
			Main constituents										Minor additional constituents
			Clinker	Blast-furnace slag	Silica fume	Pozzolana		Fly ash		Burnt shale	Limestone		
						natural	natural calcined	siliceous	calcareous				
	Type name	Type notation	K	S	D [b]	P	Q	V	W	T	L [c]	LL [c]	
CEM II	Portland-composite cement [d]	CEM II/C-M	50-64	←---------- 36-50 ----------→									0-5
CEM VI	Composite cement	CEM VI (S-P)	35-49	31-59	-	6-20	-	-	-	-	-	-	0-5
		CEM VI (S-V)	35-49	31-59	-	-	-	6-20	-	-	-	-	0-5
		CEM VI (S-L)	35-49	31-59	-	-	-	-	-	-	6-20	-	0-5
		CEM VI (S-LL)	35-49	31-59	-	-	-	-	-	-	-	6-20	0-5

[a] The values in the table refer to the sum of the main and minor additional constituents.

[b] In case of the use of silica fume, the proportion of silica fume is limited to 6-10 % by mass.

[c] In case of the use of limestone, the proportion of limestone (sum of L, LL) is limited to 6-20 % by mass.

[d] The number of main constituents other than clinker is limited to two and these main constituents shall be declared by designation of the cement (for examples, see Clause 6).

In additon, cements covered by this standard shall conform to the requirements listed in the Table 2.

Table 2. Additional requirements and limit values for single results for Portland composite cements CEM II/C-M and composite cements CEM VI [5]

1	2	3	4	5
Property	Test reference	Strength class	Requirements given as characteristic values [a]	Limit values for single results [a]
Sulfate content (as SO_3)	EN 196-2	all	≤ 4,0 [b]	≤ 4,5
Chloride content	EN 196-2	all	≤ 0,10 [c]	≤ 0,10 [c]

[a] Requirements are given as percentage by mass of the final cement.

[b] Portland composite cement with a T content > 20 % may contain up to 4,5 % sulfate (as SO_3) for all strength classes.

[c] Composite cement CEM VI may contain more than 0,10 % chloride by mass. If so, the value of 0,10 % chloride by mass shall be replaced by the upper limit for the chloride content expressed as a percentage by mass with two decimal places and this upper limit shall be stated on the packaging and/or the delivery note.

2. EXPERIMENTAL TECHNIQUES

For this research,a cement sample with a different portion of clinker as a main component, fly ash, granulated blast furnace slag and gypsum as a necessary component in cement is prepared. The recipe for cement sample preparation was:

- Clinker–50 wt. %
- Fly ash – 23 wt. %
- Granulated blast furnace slag –wt. 23 %
- Gypsum – wt. 4 %

Mixing of materials was carried out in the ball laboratory mill, where one of the targets was to reach ~ 4000 cm^2/g Blain-specific surface. After getting the suitable laboratory sampleof cement, the main chemical parameters as SiO_2, Al_2O_3, Fe_2O_3, CaO, MgO, SO_3, Na_2O, and K_2O were determined by the XRF technique.

Concerning physical and mechanical parameters the main parameters as specific surface, specific weight, setting time, and tensile/compressive strength was determined according to EN 197-1 as well.As a reference sample, was taken the cement type CEM II/B-W 42,5N in order to compare results with CEM II/C-M (S+W).

3. RESULTS AND DISCUSSION

The experimental results are presented in Tables 3 and 4.

Table 3. Chemical composition of prepared cement samples

	SiO_2	Al_2O_3	Fe_2O_3	CaO	MgO	SO_3	Na_2O	K_2O
	%	%	%	%	%	%	%	%
CEM II/C-M (S+W)	29,93	8,99	3,88	47,31	2,61	3,26	0,21	0,97
CEM II/B-W 42,5N	27,74	9,77	4,79	50,46	1,56	2,74	0,18	0,84

From Table 3it can be seen that the content of SiO_2 in CEM II/C-M (S+W) is higher than in the case of CEM II/B-W 42,5N. The reason for this is a high portion of granulated blast furnace slag in cement which presents high content of SiO_2.Also, we can notice that CaO content in CEM II/B-W 42,5N is higher than in CEM II/C-M (S+W) and MgO is higher in CEM II/C-M (S+W). The possible problem with CEM II/C-M (S+W) production could be SO_3 content since according to EN 197-1 requirement for $SO_3$is $\leq$ 3,5 % or 4,0 % depending onthe strength class.

Table 4. Physical and mechanical properties of prepared cement samples

	Specific weight (g/cm^3)	Specific surface (cm^2/g)	Stand.conc. (%)	Setting time		Strength (MPa, days)			
						Tensile		Compressive	
				Initial (min)	Final (min)	2	28	2	28
CEM II/C-M (S+W)	2,91	3960	25,4	195	255	2,7	7,4	13,1	42,8
CEM II/B-W 42,5N	2,99	3496	26,7	200	257	3,1	7,8	17,4	51,9

Concerning physical and mechanical properties from Table 4 it is evident that compressive strength after 2 and 28 days is much lower in the case of CEM II/C-M (S+W) than in the case of CEM II/B-W 42,5N. Even though CEM II/B-W 42,5N has a smaller specific surface (Blain) still the compressive strength is significantly higher than in CEM II/C-M (S+W). The reason for this behavior is the lower content of clinker in CEM II/C-M (S+W) since the clinker is still the most important component of strength

development. Other parameters like specific weights, and initial and final times of setting for both types of cementhave similar values.

4. CONCLUSION

- According to the results,it can be concluded that it is possible to produce a new type of cement CEM II/C-M (S+W) which could meet EN 197-5 requirements. In order to get acceptable results, especially in terms of strength, this cement has to be ground for a longerperiod of time than CEM II/B-W 42,5N, to get a higher specific surface. A higher specific surface requires longer grinding time and higher production costs.
- From the experimental results, it is obvious that the specific surface has to be higher than 4000 cm^2/g in order to produce cement CEM II/C-M (S+W) whose 28 days compressive strength will fulfill EN standard requirements.
- Laboratory results show that 28 days compressive strength is on the lower limit and definitely must be higher than 42,8 MPa, as the min. strength is 42,5 MPaaccording to relevant EN standards.

5. REFERENCE

[1] N. Haračić, Razvoj i proizvodnja metalurških cemenata, doktorska disertacija, Univerzitet u Tuzli, Tehnološki fakultet, Tuzla, 2014.

[2] BAS EN 197-1, Cement – Dio 1: Sastav, specifikacija i kriteriji usklađenosti za običnecemente.

[3] N. Bušatlić, I. Bušatlić, N. Merdić, N. Haračić, Osnove hemije i tehnologije Portlandcementa, Štamparija Fojnica d.d., Zenica, 2020.

[4] Osmanović, Z., Zelić, J., Proizvodnja Portland cementa, ISBN 978-9958-897-04-7, Tuzla,2010.

[5] BAS EN 197-5, Cement – Dio 5: Portland kompozitni cement CEM II/C-M i kompozitni cement CEM VI

STRENGTH DEVELOPMENT OF CONCRETE CONTAINING GROUND GRANULATED BLAST FURNACE SLAG FROM ARCELORMITTAL ZENICA AS A PARTIAL CEMENT REPLACEMENT

Adnan Mujkanović, Marina Jovanović, Nadira Bušatlić, Amel Zahirović
University of Zenica, Faculty of Metallurgy and Technology
Zenica, B&H

Anesa Bitić
Eurofins BioPharma Product Testing (DACH), Planegg,
Bayern, Germany

Nevzet Merdić
Kakanj Cement Plant
Kakanj, B&H

Keywords: concrete, cement replacement, GGBS, strength, dynamic modulus of elasticity

ABSTRACT
The strength development of concrete containing ground granulated blast-furnace slag (GGBS), a by-product of iron in blast-furnace, as a partial substitute for cement,was experimentally studied. Levels of replacement of cement by slag were 12.5 %, 25 %, 37.5 %, and 50 % by weight of cement. Slag taken immediately after it was discharged from the blast furnace was used.Tests performed on concrete samples include consistency, air content, compressive strength, flexural strength, and dynamic modulus of elasticity. It was found that the addition of GGBSleads to a significant increase in the consistency of fresh concrete, a decrease in early compressive strengths and flexural strengths, as well as dynamic modulus of elasticity. At a later age, the replacement of cement with slag resulted in increasing both the modulus and strength of concrete.

1. INTRODUCTION

An increasing trend in utilizing low-carbon footprint concrete for construction has been evident over the last decades. Ground Granulated Blast-furnace Slag (GGBS) is a by-product of iron manufacturing, which is widely used as a cementitious material used in concrete. Therefore, it is of great importance to maximize the ground granulated blast furnace slag (GGBS) percentage of the total binder in structural concrete [1,2]. EN 206-1 classifies GGBS into the group of reactive mineral additions for concrete (Type II). According to this standard, additions are defined as finely divided materials used in concrete to improve certain properties or to achieve special properties [3]. General suitability as type II addition is established for GGBS conforming to EN 15167-1 [4], and, in that case, GGBS can be directly mixed with other components of a concrete mixture in concrete plants. The other way in which GGBS is used is as a component of Portland composite types of cement CEM II, CEM III, and CEM V. In that case, the standard EN 197-1 must be followed [5].

The technique of the addition incorporation into the concrete mixtures, directly or as a factory blended cement, doesn't significantly influence concrete properties. Nevertheless, the utilization of additions in concrete plants results in some benefits such as:

- transport costs reduction, because the addition can be delivered directly to the concrete plant without having to go via a cement factory,
- the possibility of more accurate proportions, because the materials are weighed in a concrete plant,
- the flexibility of proportioning and thus optimization of the technical performance of the concrete.

GGBS is typically used in the proportion of 50% of the total binder. However, it is often beneficial to be able to vary the proportion to meet specific requirements. For example, 66 to 80% GGBS is recommended for high sulfate resistance or high resistance to chloride ingress. Or, 50 to 70% GGBS may be best to reduce the heat of hydration and control the early-age cracking. Similarly, to ensure high early strength, 20 to 40% GGBS is suggested [6].

Every year, ArcelorMittal produces large amounts of a granulated blast furnace which is a by-product of the iron production process. Even though this slag has been started to sell to cement producers recently, there are still large quantities of unused slag. The conformity of this GGBS according to the standard EN 15167-1 has been proven by the authors and published elsewhere [7]. In this paper, the GGBS from ArcelorMittal Zenica was used as a partial cement replacement and added directly to the concrete mixtures. The most important properties of fresh concrete mixtures, as well as the strength and durability of hardened concrete, were investigated. As far as the authors' knowledge, such a study on this slag has not been done before.

2. EXPERIMENTAL

2.1. Materials

Ordinary Portland cement type CEM I 52.5 N was used in this study. Crushed limestone with a maximum particle size of 16 mm that complies with the requirements of EN 12620 [8] was used as aggregate in the concrete mixes. A polycarboxylate-based high-range water-reducing admixture (HRWRA) and air-entraining agent formulated from modified naturally occurring and synthetic surfactants, both conforming to EN 934-2 [9] were used as additives. GGBS produced in ArcelorMittal Zenica, conforms with EN 15167-1 [4], with a specific surface area of 4.700 cm^2/g was used as a partial cement replacement. GGBS was taken immediately after it was discharged from the blast furnace. The chemical composition of GGBS determined according to BAS EN 196-2:2013 is listed in Table 1. The most important physical properties of cement and GGBS used are listed in Table 2.

Table 1. Chemical composition of GGBS [10]

Comp	SO_3	S^{2-}	MnO	SiO_2	Fe_2O_3	Al_2O_3	CaO	MgO	Cl^-	Na_2O	K_2O	H_2O
%	0.41	0.64	2.64	41.05	0.83	7.79	40.62	4.88	0.003	0.22	0.82	0.04

Table 2. Physical properties of GGBS and cement CEM I [10]

Sample	Density (g/cm^3)	Specific surface area (cm^2/g)	Stand. consistency (%)	Initial setting time (min)	Soundness (mm)	Strength (MPa)			
						Flexural		Compressive	
						7 days	28 days	7 days	28 days
CEM I	3.14	3600	26.0	180	-	-	-	41.4	49.3
GGBS	2.90	4700	24.4	235	0.0	5.1	9.2	28.9	51.9

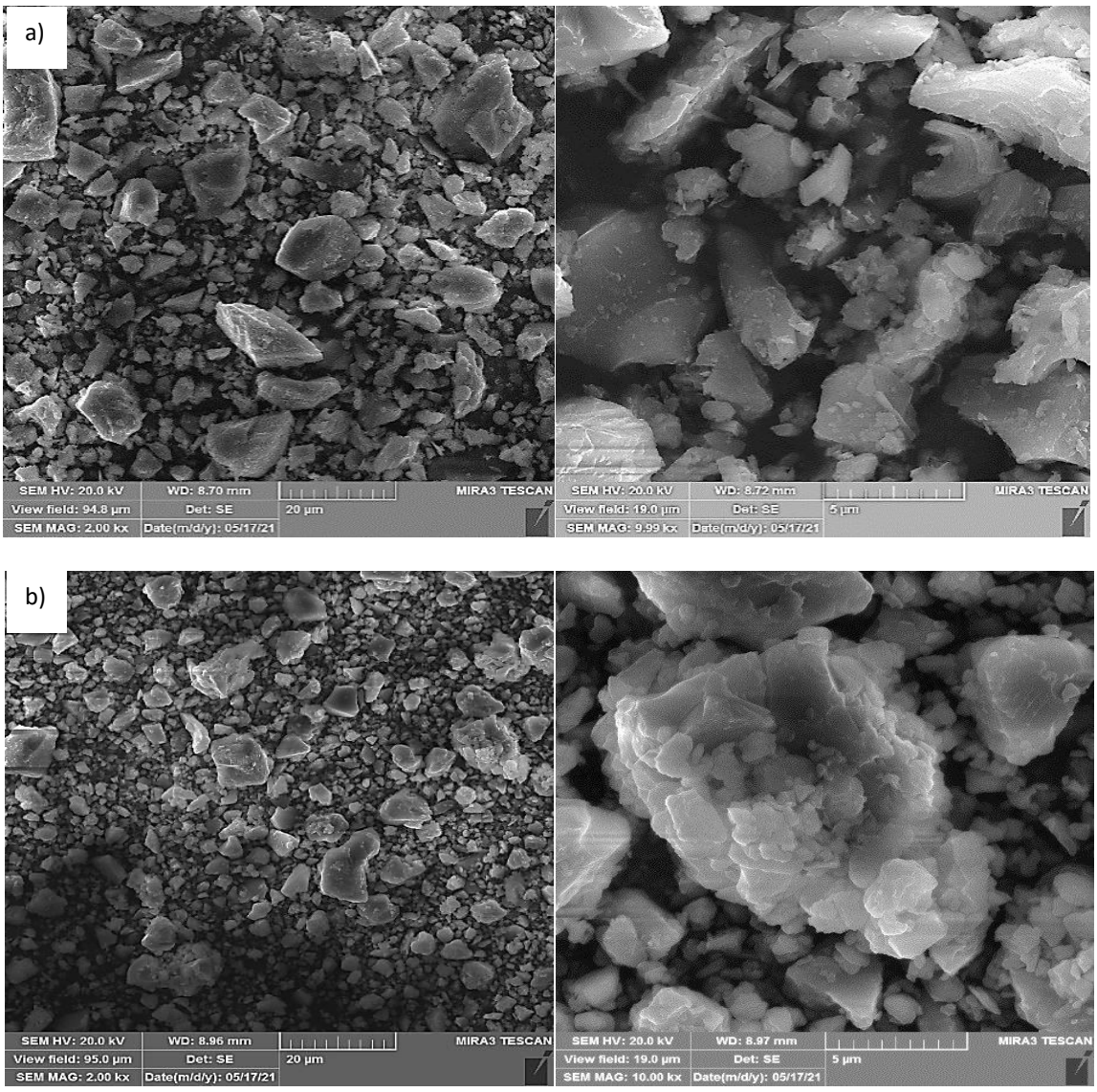

Figure 1. SEM analysis of cement (a) and GGBS (b) [10]

SEM analysis of GGBS and cement samples was carried out by scanning electron microscope Tescan Mira 3 (20keV). The micrographs presented on the left side of the image were taken at the magnification of 2000×, and the micrographs on the right side at the magnification of 10000×.

2.2. Mix proportions

Proportions of the reference mix and the mixes containing 12.5, 25.0, 37.5, and 50.0% GGBS by weight of cement are listed in Table 3.

Table 3. Mix proportion of concrete

Material		R	T-12.5	T-25	T-37.5	T-50
Cement (kg/m^3)		400	350	300	250	200
GGBS (%)		0	12.5	25.0	37.5	50.0
GGBS (kg/m^3)		-	50	100	150	200
Agreggate (kg/m^3)	0-4 mm	885	885	885	885	885
	4-8 mm	355	355	355	355	355
	8-16 mm	530	530	530	530	530
Water (kg/m^3)		176	176	176	176	176
HRWRA (kg/m^3)		3.2	3.2	3.2	3.2	3.2
Air entraining agent (kg/m^3)		0.4	0.4	0.4	0.4	0.4

2.3. Mixing procedure

First, cement and GGBS were mixed for 60 s, and after that the fine and coarse aggregates were added to the mixer, followed by dry-mixing for another 120 s. Then, around 75% of the total amount of water was added and mixed for another 120 s. Finally, the remaining mixing water and additives (HRWRA and Air entraining agent) were added to the mixer, during consecutive mixing for 180 s. The whole mixing time was 8 minutes.

2.4. Test methods

After mixing, the slump test was carried out on each mix following EN 12350-2 [11]. For testing hardened concrete properties cubes 100×100×100 mm and beams 100×100×400 mm were prepared. All specimens had been demolded after 24 hours and then stored in water at a temperature of 20 °C until tests were conducted. The compressive strength of the cubes was measured following the procedure described in the norms EN 12390-3 [12] at 2, 7, 28, 90, and 180 days. Before the compressive strength test, on cubic samples, a non-destructive test was carried out to determine the velocity of the ultrasonic pulse by direct method via a pulse velocity test device following the procedure described in the norm EN 12504-4 [13]. Dynamic modulus of elasticity is calculated according to the equation:

$$E_{bd} = \frac{V^2 \cdot \rho \cdot (1+\nu)(1-2\nu)}{(1-\nu)} \quad [Pa] \tag{1}$$

where is:
V – ultrasonic pulse velocity in m/s
ρ – apparent density in kg/m^3
ν – Poisson ratio (0.2 for concrete).

The flexural strength test was carried out on the beams according to the norm EN 12390-5 [14] at 2, 28, and 90 days.

3. RESULTS ANDDISCUSSION

The results of the slump test of fresh concrete mixes are presented in Table 4. The results show the slump of fresh concrete increases with an increasing portion of GGBS in the binder.

Table 4. Slump of concrete

Sample	R	T-12.5	T-25	T-37.5	T-50
Slump, mm)	160	160	180	210	220

The GGBS used has a greater specific surface area (SSA) than cement, and for that reason, one could expect that GGBS addition would decrease slump and have a negative effect on the concrete consistency. However, based on the slump test results, it can be concluded that the partial replacement of cement by GGBS lead to the improvement of the consistency of the concrete. This can be explained by the fact that the surface of GGBS is rather smooth, contrary to the cement particles' surface which tends to be rough. Additionally, GGBS particles are less angular and irregularly shaped than cement particles (Fig. 1). For these reasons, the water demand for binder mixes containing GGBS is generally lower than the water demand for mixes containing only cement.

Table 5. Air voids content of concrete

Sample	R	T-12.5	T-25	T-37.5	T-50
Air voids, (%)	2.9	3.2	3.1	2.8	3.4

The results listed in Table 5 show that GGBS introduction to the concrete mixes has not significantly influenced the air voids content of these mixes. The results of the compressive strength test of concrete at ages 2, 7, 28, 90, and 180 days tests are summarized in Table 6 and Figure 2.

Table 6. Compressive strength of concrete

Sample	Compressive strength [MPa]				
	2 days	7 days	28 days	90 days	180 days
R	38.9	58.3	71.6	75.7	77.4
T-12.5	35.9	56.5	70.5	80.2	83.6
T-25	29.7	52.8	69.8	84.9	88.9
T-37.5	22.9	45.7	67.2	81.0	85.1
T-50	13.7	38.2	64.0	80.6	83.8

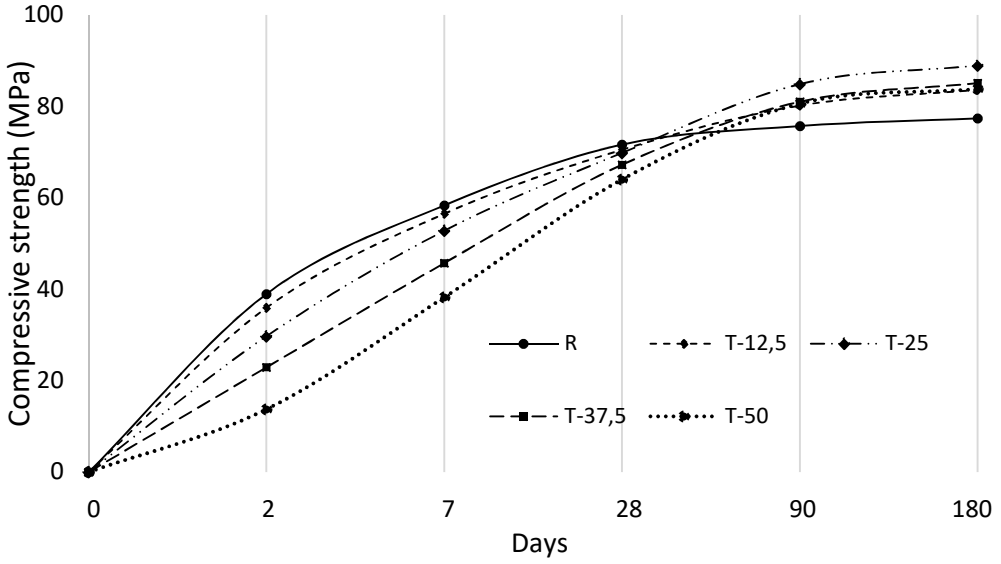

Figure 2. The development of compressive strength of concrete

Figure 2 shows that the partial replacement of cement by GGBS has the greatest effect on concrete's compressive strength at early ages (2 and 7 days). The loss in compressive strength increases with the increased content of GGBS. At the age of 28 days, concrete containing only cement as a binder (R) still has a greater compressive strength. However, at a later age (90 and 180 days) compressive strength of all concretes containing GGBS surpasses the compressive strength of the reference sample R. The greatest increase (around 15% compared to the reference sample) in compressive strength was observed in the sample containing 25 % GGBS. The results obtained are in coherence with the results published by Monteagudo [15] and Gruyaert [16].The flexural strength test results are listed in Table 7 and presented in Figure 3.

Table 7. Flexural strength of concrete

Sample	Flexural strength [MPa]		
	2 days	28 days	90 days
R	6.8	8.9	8.9
T-12.5	6.4	9.3	9.7
T-25	6.0	9.6	9.7
T-37.5	5.7	9.7	11.0
T-50	6.7	9.9	10.8

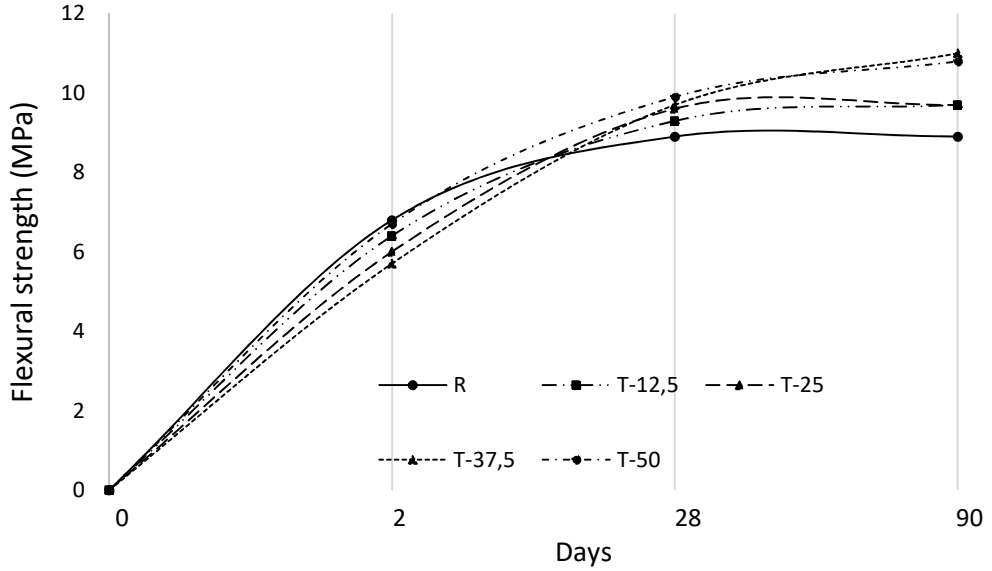

Figure 3. The development of flexural strength of concrete

The results show that, at the age of 2 days, flexural strength decreases with the increasing content of GGBS. At the ages of 28 and 90 days, all samples containing GGBS developed higher flexural strength than the reference sample. The highest flexural strength was observed in the sample with 37.5 % of GGBS, surpassing the flexural strength of the reference sample for 23.5 %. A similar trend of flexural strength development of concretes containing GGBS was observed by other authors [17].Values of dynamic modulus of elasticity calculated according to (1) are shown in Table 8 and Figure 4.

Table 8. Dynamic modulus of elasticity of concrete

Sample	Dynamic modulus of elasticity [GPa]				
	2 days	7 days	28 days	90 days	180 days
R	49.5	53.9	55.5	59.5	59.5
T-12.5	47.6	52.2	54.7	59.2	59.8
T-25	45.7	49.1	54.0	60.8	60.8
T-37.5	42.8	47.5	52.7	59.8	61.1
T-50	39.8	46.5	51.5	59.0	59.6

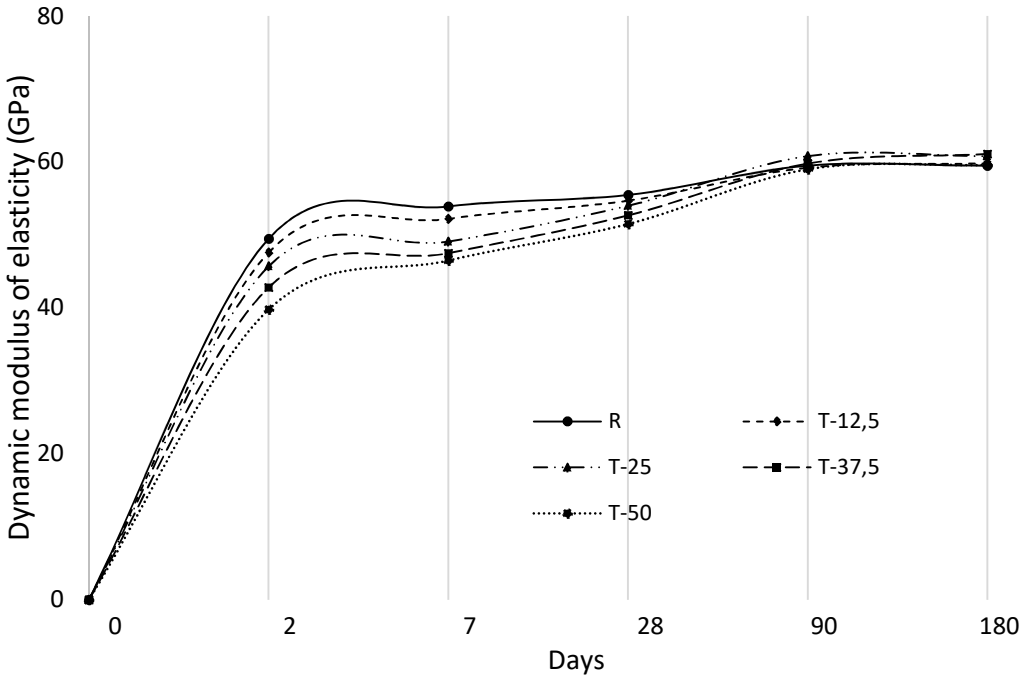

Figure 4. The development of dynamic modulus of elasticity of concrete

From the data obtained, it is evident that, at early ages, the modulus is strongly affected by the level of cement replacement. In that period, the concrete with the highest content of GGBS has the lowest value of modulus, and the modulus steadily decreases with increasing the content of GGBS in concrete. However, after 28 days these differences in values of modulus become smaller. At a later age, the modulus of concretes containing GGBS is higher than the modulus of reference concrete. These findings are in coherence with the results shown in [17].

4. CONCLUSIONS

Based on the test results, the following conclusion can be drawn:

- The replacement of cement with GGBS leads to an increase in a fresh concrete slump. The higher the level of replacement, the higher the slump.
- The air voids content has not been significantly affected by cement replacement.
- The early compressive strength showed a significant decrease at higher replacement levels, while at a later age, samples containing GGBS had greater compressive strength than samples containing only cement as a binder. The sample containing 25% GGBS developed the highest compressive strength at the age of 180 days, with an increase of 15% compared to the reference sample.

- The loss in flexural strength of samples containing GGBS was observed only at the age of 2 days. The reference sample has the lowest values of 28- and 90-day flexural strength. The samples with replacement levels of 37.5 and 50 % had the highest 28- and 90-day flexural strength.
- At an early age, the dynamic modulus of elasticity decreases with increasing the content of GGBS in concrete. At a later age, the modulus of concretes containing GGBS is higher than the modulus of reference concrete.

5. REFERENCES

[1] Kanavaris F., Soutsos M., Chen J-F.: Enabling sustainable rapid construction with high volume GGBS concrete through elevated temperature curing and maturity testing, Journal of Building Engineering, Volume 63, Part A, 2023, 105434, https://doi.org/10.1016/j.jobe. 2022.105434

[2] Bušatlić N., Bušatlić I., Merdić N., Haračić N.:Osnove hemije i tehnologije Portland cementa, Štamparija Fojnica d.d., Zenica, 2020.

[3] EN 206:2014, Concrete - specification, performance, production and conformity

[4] EN 15167-1:2006, Ground granulated blast furnace slag for use in concrete, mortar and grout

[5] EN 197-1:2019, Cement - Composition, specifications and conformity criteria for common cements

[6] https://ukcsma.co.uk/ggbs-concrete/addition-to-concrete (Accessed in March 2023)

[7] Mujkanović A., Ključanin A., Merdić N., Jovanović M., Zahirović A., Karić A., Halilović A.:Ocjena usklađenosti svojstava granulirane visokopećne troske iz tvornice ArcelorMittal Zenica sa zahtjevima standarda BAS EN 15167-1, Quality 2021 Neum, B&H, 17-19 June 2021, 89-94

[8] EN 12620:2013, Aggregates for concrete

[9] EN 934-2:2009+A1:2012, Admixtures for concrete, mortar and grout - Part 2: Concrete admixtures - Definitions, requirements, conformity, marking and labelling

[10] Ključanin A.:Granulirana visokopećna troska iz tvornice ArcelorMittal Zenica kao mineralni dodatak za beton visokih performansi, magistarski rad, Metalurško-tehnološki fakultet, Univerzitet u Zenici, 2021.

[11] EN 12350-2:2019, Testing fresh concrete. Slump test

[12] EN 12390-3:2019, Testing hardened concrete - Part 3: Compressive strength of test specimens

[13] EN 12504-4, Testing concrete - Determination of ultrasonic pulse velocity

[14] EN 12390-5: 2019, Testing hardened concrete - Flexural strength of test specimens

[15] Monteagudo S., Moragues A., Galvez J., CasatiM., Reyes E.: The degree ofhydration assessment of blended cement pastes by differential thermal and thermogravimetric analysis. Morphological evolution of the solid phases, ThermochimicaActa, t. 592, pp. 37-51, 2014

[16] Gruyaert E.: Effect of Blast-Furnace Slag as Cement Replacement on Hydration, Microstructure, Strength and Durability of Concrete, disertacija, Gent, 2011

[17] Belie N. D., Soutsos M., Gruyaert E.: Properties of Fresh and Hardened Concrete Containing Supplementary Cementitious Materials, State-of-the-Art Report of the RILEM Technical Committee 238-SCM, Working Group 4, Springer, 2018

CALCULATION OF THERMAL CONDUCTIVITY FOR CRYSTALLINE NANOSTRUCTURES

Siniša M. Vučenović
University of Banja Luka, Faculty of Sciences and Mathematics
Banja Luka, B&H

Jovan P. Šetrajčić
Academy of Sciences and Arts of the Republic of Srpska
Banja Luka, B&H

Keywords: ultrathin films, superlattices, phonons, thermodynamics, thermal conductivity

ABSTRACT
We have introduced a theory for the calculation of thermodynamic characteristics for some characteristic nanostructures (ultrathin films and superlattices), using the adapted method of two-time temperature Green's functions. In this paper, we have determined the coefficient of thermal conductivity using the definition of free energy and then compared their temperature dependence to the thermal conductivity behavior of the bulk structures. For the observed nanostructures, the thermal conductivity coefficient values are almost equal at low temperatures, but at the same time, significantly lower than the bulk sample values. That result could be useful for the possible achievement of better superconducting conditions in the observed compound nanostructures.

1. INTRODUCTION

Elementary particles – mechanical oscillations – phonons are a subsystem that is always present when analyzing the conducting, semiconducting or dielectric properties of the system. Accordingly, we will first analyze the kinetics of mechanical oscillations in nanoscopic–ultrathin films, which can be considered as a basis for investigating other properties of more complex nanostructures. In a way, this work represents a generalization of the previous research [1–6].

We will start with the definition expression for the coefficient of thermal conductivity [7,8]:

$$\kappa = D\,C\,\rho_M\,, \tag{1.1}$$

where is D - diffusion coefficient, C – specific heat, and ρ_M is the mechanical density of the observed structure. The diffusion coefficient D (strictly, it is the diagonal matrix element of diffusion tensor D_{ij}) will be found by the Kubo formula [7]. The temperature dependence of nanostructures density will be determined by the two-time, temperature-dependent Green's function method [9]. Using this method one can find the internal energy and the average value of the square of molecular displacements.

All analyzes will be calculated regarding the presence of specific boundary conditions on its surfaces, which are responsible for the appearance of unusual effects and changes in the basic properties of these structures [6].

2. CALCULATION OF THE DIFFUSION COEFFICIENT

In order to determine the diffusion coefficient, we will start with the Kubo formula [7,8]:

$$D_{ij} = \frac{1}{\beta}\int_0^{\infty} \mathrm{e}^{-\varepsilon t}\int_0^{\beta} d\lambda \left\langle \hat{v}_i(-i\eta\lambda)\hat{v}_j(t)\right\rangle \approx \lim_{t_0\to\infty}\int_0^{\infty}\mathrm{e}^{-\varepsilon t}\langle \hat{v}_i(0)\hat{v}_j(t)\rangle dt\,, \qquad (2.1)$$

where $\hat{v}_i$ and $\hat{v}_j$ ($i,j = x,y,z$) are the velocity operators in Heisenberg representation, ε is the perturbation parameter and the averages will be taken over a great canonical ensemble. We will find the correlation function $\langle \hat{v}_i(0)\hat{v}_j(t)\rangle$ through Green's function $\langle\langle p_i(t)\big| p_j(0)\rangle\rangle$ where $p_i(t), p_j(0)$ represent the components of the molecular momentum.

The Hamiltonian of the phonon subsystem of a superlattice with two motifs a and b (two ultrathin films) taken in harmonic and nearest neighbor's approximation [9], can be written as follows:

$$H = T + V_P + V_B; \quad T = \sum_{n,\alpha}\sum_{n_l=0}^{n_a-1}\frac{\left[p^{(a)}_{n,n_l,\alpha}\right]^2}{2M_a} + \sum_{n,\alpha}\sum_{n_l=n_a}^{n_a+n_b-1}\frac{\left[p^{(b)}_{n,n_l,\alpha}\right]^2}{2M_b}; \qquad (2.2)$$

where $M_{a/b}$ are the masses of molecules in first/second ultrathin films, $V_{P/B}$ are the potential energies of surface and bulk terms, $p \equiv M\,\dot{u}$ (u are molecular displacements) and $n_{a/b}$ are numbers of molecules in corresponding motive. Boundary conditions will be taken into account during the formation of a system of equations defining Green's function of the system.

We have determined the following Green's function, which will be written in the next form: $G_{n_x n_y n_z f, m_x m_y m_z g} = \langle\langle\, p_{n_x n_y f}(t)\big|\; p_{n_x n_y f}(0)\,\rangle\rangle$. Because of the valid relation: $p_i = M\,v_i$; $vi = \mathrm{d}u_i/\mathrm{d}t$, in the expression determining this function, appears the second Green's function of a type $\langle\langle\, u_{n_x n_y f}(t)\big|\; u_{n_x n_y f}(0)\,\rangle\rangle$ [10]. In this way, the correlation function of Green's function is given by a general formula [11,12]:

$$< p_f(t)p_f(0) >= \lim_{\varepsilon\to+0}\int_{-\infty}^{+\infty} d\omega\; \mathrm{e}^{-i\omega t}\,\frac{G_f(\omega+i\varepsilon) - G_f(\omega-i\varepsilon)}{\mathrm{e}^{\eta\omega/\theta}-1}\,. \qquad (2.3)$$

Green's function can be expressed as a sum of elementary fractions [10]. In this way, we obtain the correlation function (2.3), i.e. corresponding velocity correlation function:

$$< v_f(t)v_f(0) >= \frac{\eta C_H}{M^2\omega_k}\left(\frac{\mathrm{e}^{-i\omega_k t}}{\mathrm{e}^{\eta\omega_k/\theta}-1} - \frac{\mathrm{e}^{i\omega_k t}}{\mathrm{e}^{-\eta\omega_k/\theta}-1}\right). \qquad (2.4)$$

In accordance with the general formula (2.2) the diffusion coefficient is given by:

$$D_{ii}(k) = \left|\frac{\eta C_H}{M^2\omega_k}\int_0^{\infty}\left(\frac{\mathrm{e}^{-i\omega_k t}}{\mathrm{e}^{\eta\omega_k/\theta}-1} - \frac{\mathrm{e}^{i\omega_k t}}{\mathrm{e}^{-\eta\omega_k/\theta}-1}\right)dt\;\right| = \frac{\eta C_H}{M^2\omega_k^2}\,. \qquad (2.5)$$

It is seen that the phonon diffusion coefficient of the superlattice, as well as that of the bulk, does not depend on temperature [13].

3. THERMODYNAMIC BEHAVIOUR OF SUPERLATTICE

The internal energy of the system is given by the standard formula [11-13]:

$$U_s = \frac{3}{(2\pi)^3}\,Na^3\int_0^{2\pi} d\varphi\int_0^{\pi}\sin\theta d\theta\int_0^{k_M} dk\,k^2\eta\Omega ka\left(\mathrm{e}^{\frac{\eta\Omega ak}{\theta}}-1\right)^{-1}, \qquad (3.1)$$

where the phonon dispersion law is given by the basic formula: *Phonon-reduced* frequencies and intermolecular distance are expressed through the geometric mean of

phonon frequencies, i.e. of intermolecular distances in separate motifs: $\Omega = \sqrt{\frac{C_a}{M_a}\frac{C_b}{M_b}}$; $a = \sqrt{a_a a_b}$. Quantity θ is thermodynamic temperature: $\theta = k_B T$.

After partial integration in (3.1) and introducing notations: $\Delta_m \equiv E_k\big|_{k=k_M} = \eta\Omega\, ak_M$, we obtain the following expression:

$$U_s = \frac{3N}{2\pi^2}\theta\left\{6\varsigma(4)\frac{\theta^3}{(\eta\Omega)^3} - \left[a^3k_M^3 Z_1(\frac{\Delta_m}{\theta}) + 3\frac{\theta}{\eta\Omega}a^2k_M^2 Z_2(\frac{\Delta_m}{\theta}) + \right.\right.$$
$$\left.\left. + 6\left(\frac{\theta}{\eta\Omega}\right)^2 ak_M Z_3(\frac{\Delta_m}{\theta}) + 6\left(\frac{\theta}{\eta\Omega}\right)^3 Z_4(\frac{\Delta_m}{\theta})\right]\right\}. \qquad (3.2)$$

Since the specific heat is given by $C_{vs} \equiv C_s = \frac{k_B}{N}\frac{\partial U}{\partial\theta}$ using (3.2), we find that:

$$C_s = \frac{3k_B}{2\pi^2}\left\{a^3k_M^3\frac{\Delta_m}{\theta}\frac{1}{1-\mathrm{e}^{\Delta_m/\theta}} - 4a^3k_M^3 Z_1(\frac{\Delta_m}{\theta}) - 12\frac{\theta}{\eta\Omega}a^2k_M^2 Z_2(\frac{\Delta_m}{\theta}) - \right.$$
$$\left. - 24(\frac{\theta}{\eta\Omega})^2 ak_M Z_3(\frac{\Delta_m}{\theta}) + 24(\frac{\theta}{\eta\Omega})^3\left[\varsigma(4) - Z_4(\frac{\Delta_m}{\theta})\right]\right\}. \qquad (3.3)$$

Temperature dependence of the thermal capacity is determined by two specific terms. The first term is: $\approx (1-\mathrm{e}^{\Delta_m/\theta})^{-1}/\theta$ which is "responsible" for the behavior of the system at low and high temperatures. The second term containing Z-functions characterizes temperature behavior in the middle-temperature range.

Based on the results of the previous research on the phonon contribution to the thermodynamic behavior of the ultra-thin film structures [1–3], and the well-known behavior of the bulk [7,11–13], Fig.1 is showing a comparative display of the specific heat for the superlattice, ultra-thin film and the bulk structures in dependence of the reduced temperature: $\mathrm{x} = \theta/\Delta_\mathrm{m}$

From Fig.1, one can conclude that the behavior of the thermal capacity of a superlattice in a low-temperature range is similar to bulk ones. The temperature behavior of the thermal capacity of a superlattice in middle-temperature region is similar to film ones. The difference in these capacities is most pronounced in the high-temperature area.

Now we will approach the determination of the temperature behavior of the superlattice thermal conductivity. The expression for the dynamical density of superlattice:

The primary text heading should be numbered by 1., 2., ... and should be in 12-pt., bold, capital letters, flush left with margin. The spacing from text to the next heading is one line.

$$\rho_M = \frac{M}{<(a_0+u)^3>} = \frac{M}{<a_0^3>}\quad\frac{1}{1+3<u^2><a_0^2>^{-1}} \approx \rho_0\left(1-\frac{3<u^2>}{<a_0^2>}\right) \qquad (3.4)$$

The averages of squares of displacements for molecular superlattices we can find as in Debye's representation. After integration, the expression for the density becomes:

$$\rho_M = \rho_0\left(-1+\frac{9}{2\pi^2}\frac{\eta(n_a+n_b)}{a^2\omega_D M}\frac{\theta}{\eta\Omega}\left\{(ak_M)^2 Z_1\left(\frac{\Delta_M}{\theta}\right) + 2ak_M\frac{\theta}{\eta\Omega}Z_2\left(\frac{\Delta_M}{\theta}\right) + \right.\right.$$
$$\left.\left. + 2\left(\frac{\theta}{\eta\Omega}\right)^2\left[Z_3\left(\frac{\Delta_M}{\theta}\right) - \varsigma(3)\right]\right\}\right). \qquad (3.5)$$

Diffusion coefficient is given by the relation (2.5), where:

$$< \omega_k >= \frac{1}{I_0} \int_0^{2\pi} d\varphi \int_0^{\pi} \sin\theta \, d\theta \int_0^{k_M} dk \; \omega(k); \quad I_0 = \int_0^{2\pi} d\varphi \int_0^{\pi} \sin\theta \, d\theta \int_0^{k_M} dk \; k^2 \tag{3.6}$$

are the average value phonon frequencies. After elementary calculations we obtain for the diffusion coefficient:

$$D = \frac{16}{9} \frac{\eta}{M} \frac{1}{a^2 k_M^2} = \frac{16}{9} \frac{\eta}{M} \left[\frac{2}{3} k_D^2 + (k_z^{\max})^2 \right]^{-1}. \tag{3.7}$$

Introducing notations: $\theta/\Delta_m = x$, we reduce the expression (1.1) for thermal conductivity coefficient to the form:

$$\kappa = \frac{8}{3} \frac{\eta k_B a k_M}{\pi^2 a^3} J_1(x) \, J_2(x), \tag{3.8}$$

where

$$J_1(x) = \frac{\delta}{x} \frac{1}{1 - e^{\delta/x}} - 4Z_1(\delta/x) - 12\frac{x}{\delta} Z_2(\delta/x) - 24\left(\frac{x}{\delta}\right)^2 Z_3(\delta/x) + 24\left(\frac{x}{\delta}\right)^3 [\varsigma(4) - Z_4(\delta/x)],$$
$$J_2(x) = 1 + \frac{9}{2\pi^2} \frac{\eta(n_a + n_b)}{a^2 \omega_D M} (a k_M)^3 \frac{x}{\delta} \left\{ Z_1(\delta/x) + 2\frac{x}{\delta} Z_2(\delta/x) + 2\left(\frac{x}{\delta}\right)^2 [Z_3(\delta/x) - \varsigma(3)] \right\} \tag{3.9}$$

Temperature dependence of the thermal conductivity coefficient is determined by two specific terms. Similar to the expression for thermal capacity, here is the first term: $\approx (1 - e^{\Delta_m/\theta})^{-1}/\theta$, which is "responsible" for behavior of the system at low and high temperatures. Also, the second term containing Z-functions, characterizes temperature behavior in middle-temperature range. Graphical presentation of dependence of relative thermal conductivity coefficient $\kappa/\kappa_0 \equiv \lambda = 2.13 \, J_1(x) \, J_2(x)$ on scaled temperature $x = \theta/\theta_D$ is given the Fig. 2.

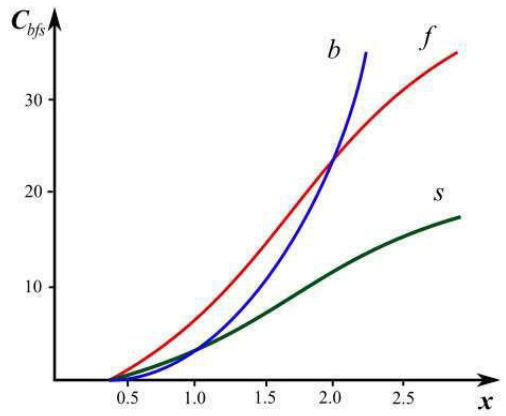

Figure 1. Specific heats of bulk (b), films (f), and superlattice (s) structures

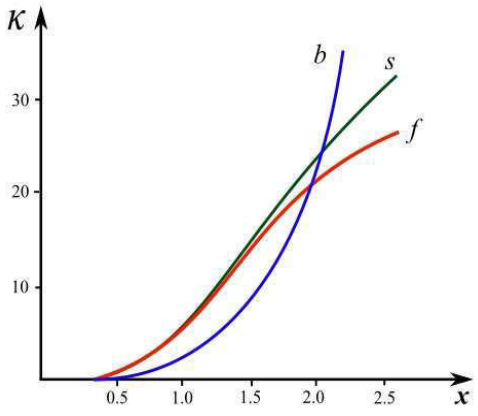

Figure 2. Conductivity coefficient of bulk (b), films (f), and superlattice (s) structures

From Fig. 2 it can be concluded that the behavior of the thermal conductivity coefficient of the superlattice is similar to the ultrathin film one (it is higher than in bulk structure). The difference is more expressive in the middle and high-temperature ranges. So, it can be concluded that the superlattices in the low-temperature range are somewhat better heat conductors than the bulk structures. At the same time, the heat conduction of the film is higher than in superlattices. On the other hand, in the high-temperature range superlattices

are much better heat isolators than film structures and the corresponding infinite crystal structures.

As our results were obtained theoretically, we looked for experimental confirmation in the scientifically available literature. An extensive analysis of the available experimental results was carried out [14–21], of which we will in this paper present, for the sake of brevity, only a few of them. In the paper [14], the thermodynamic characteristics of micrometer SiN film structures were measured. Although these are not real nanostructures (because the thickness of these films is about 1.5 μm), film microstructures still show similar behavior of specific heat and thermal conductivity as our theoretically obtained and predicted dependences for film structures (Fig. 3).

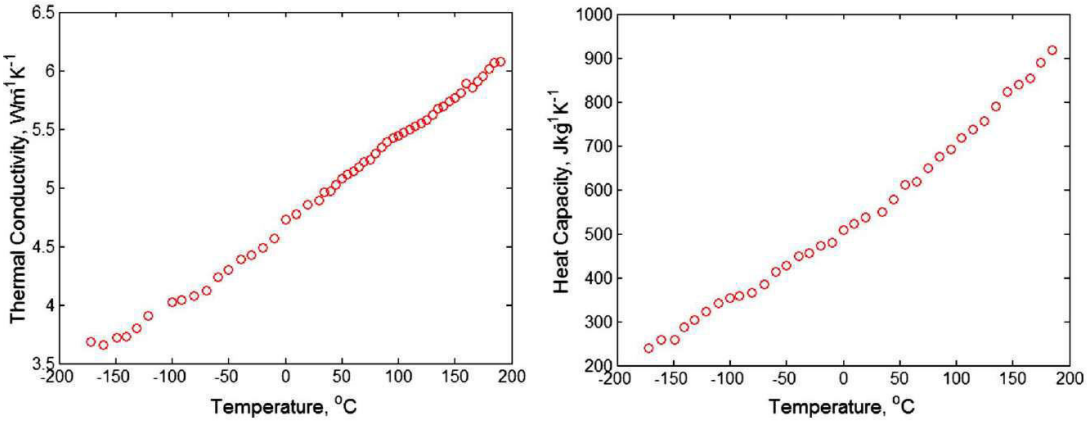

Figure 3. Thermal conductivity and heat capacity for 1.5 μm silicon nitride films [14]

Since graphene is one of the most studied materials today, and it is a true member of nano-thin (film) structures, it was justified to compare our results with the thermodynamic behavior of graphene. In the paper [15], the specific heat was measured for graphene (nano-film structure of carbon atoms), AB-stacked bilayer graphene (AB-BLG), and graphite (which represent an essential bulk structure).

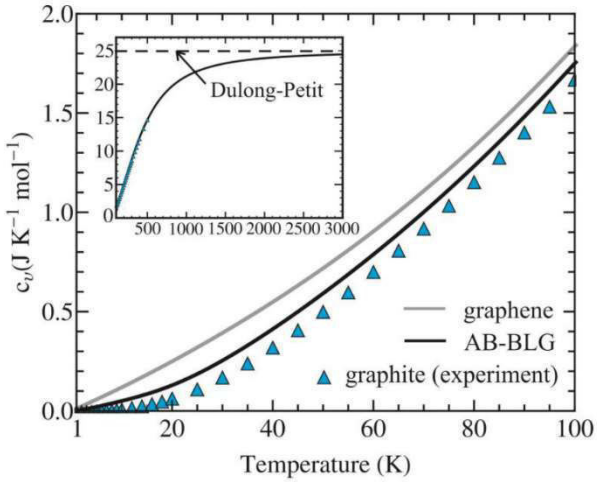

Figure 4. Phonon-specific heat capacity in graphene, AB-BLG, and graphite [15,16]

It is clearly visible that our calculations show a similar behavior of the dependence of the specific heat on the temperature for the film structure, compared to the bulk structures, in the domain of low temperatures (i.e. on the temperatures interesting for many phenomena - such as superconductivity). Fig. 4, in the frame, shows the dependence of specific heat at high temperatures, which obeys the Dulong-Petit law.

4. CONCLUSION

The results obtained here show that the thermal conductivity coefficients of the film and the superlattice at low and high temperatures are significantly lower than the thermal conductivity coefficient of the corresponding bulk structures, where thermal coefficient dependence from temperature is: T^3. This result is also practically applicable: a sandwich of several films would be a better thermal insulator than a bulk structure of the same thickness.

Here presented theoretical results are compared with experimental data [14–21]. Our theoretically predicted results are in satisfactory agreement with experimental data.

According to the Viedeman-Frantz rule, electrical conductivity is proportional to thermal conductivity. This leads to the conclusion that films and superlattices are weaker electrical conductors than bulk structures of the same material at low and high temperatures.

For future research would be interesting to evaluate the superconducting properties of observed structures. The general behavior for today's materials is that the worse conductors at the room temperature region, become the better superconductors at the low (cryogenic) temperature region. In such a way, the ultrathin films and superlattices could be structures with high superconductivity potential, not only for the low-temperature but also for the high-temperature region.

5. ACKNOWLEDGEMENT

The research presented in this paper was financially supported by the Ministry of Scientific and Technological Development, Higher Education and Information Society of the Republic of Srpska (Projects No. 19.032/961-36/19 and 19.032/961-42/19).

6. REFERENCES

[1] J. P. Šetrajčić, D. Lj. Mirjanić, S. M. Vučenović, D. I. Ilić, B. Markoski, S. K. Jaćimovski, V. D. Sajfert and V. M. Zorić, Phonon Contribution in Thermodynamics of Nano-Crystalline Films and Wires, Acta Phys. Pol. A 115, 778-782, 2009

[2] J. P.Šetrajčić, V. M. Zorić, N. V. Delić, D. Lj. Mirjanić and S. K. Jaćimovski, Phonon Participation in Thermodynamics and Superconductive Properties of Thin Ceramic Films, Ch. 15, pp. 317-348, In „Thermodynamics", Ed. M. Tadashi, ISBN: 978-953-307-544-0, InTech, Vienna (Austria), 2011

[3] J. P. Šetrajčić, S. K. Jaćimovski and V. D. Sajfert, Phonon Contribution to Heat Capacitance of Nanolayered Crystalline Structures, Mod. Phys. Lett.B 29(4), 1550008 [13 pages], doi: https://doi.org/10.1142/S0217984915500086, 2015

[4] J. P. Šetrajčić, V. D. Sajfert, and S. K. Jaćimovski, Fundamental Preferences of the Phonon Engineering for Nanostructural Samples, Rev. Theor. Sci. 4/4, 353-401, doi: https://doi.org/10.1166/rits.2016.1067, 2016

[5] J. P. Šetrajčić, S. K. Jaćimovski and S. M. Vučenović, Diffusion of Phonons Through (Along And Across) the Ultrathin Crystalline Films, Physica A 486(5), 839-848, doi: https://doi.org/10.1016/j.physa.2017.06.003, 2017

[6] J. P. Šetrajčić, D. I. Ilić and S. K. Jaćimovski, The Influence of the Surface Parameter Changes onto the Phonon States In Ultrathin Crystalline Films, Physica A 496, 434-445, doi: https://doi.org/10.1016/j.physa.2017.12.138, 2018

[7] R. J. Kubo, Statistical-Mechanical Theory of Irreversible Processes. II. Response to Thermal Disturbance, J. Phys. Soc. Jpn 12, 570, 1957

[8] V. M. Agranovich, M. D. Galanin, Migration of Electron Energy Excitations in Condensed Matter, Nauka, Moskwa, 1978
[9] J. P. Šetrajčić, S. K. Jaćimovski, V. D. Sajfert, Phonon Engineering Theory of Crystalline Layered Nanostructures, pp. 57, ISBN: 978-3659-80775-6, LAP Lambert Academ. Publ., Saarbrücken (Germany), 2015
[10] J. P. Šetrajčić, S. K. Jaćimovski, S. M. Vučenović, Green's Functions in Quantum Statistical Physics – Condensed Matter Physics, International Conference on Applied Sciences, Banja Luka. 2022
[11] A. Isihara, Statistical Physics, ISBN: 9781483274102, Academic Press, New York, 1971
[12] S. V. Tyablikov, Methods of Quantum Theory in Magnetism, Nauka, Moscow, 1975
[13] C. Kittel, Introduction to Solid State Physics, Wiley, New York, 1986
[14] A. Jain, K. E. Goodson, Measurement of the Thermal Conductivity and Heat Capacity of Freestanding Shape Memory Thin Films Using the 3ω Method, J. Heat Transfer 130/10, doi: 10.1115/1.2945904, 2008.
[15] D. L. Nika, A. A. Balandin, Phonons and Thermal Transport in Graphene and Graphene-Based Materials, arXiv: 1606.00488 [cond-mat.mtrl-sci], 56 pages, doi: https://doi.org/10.48550/arXiv.1606.00488; Rep Prog. Phys. 80, 036502, 2017
[16] D .L.Nika, A. I. Cocemasov and A. A. Balandin, Specific heat of twisted bilayer graphene: Engineering phonons by atomic plane rotations Appl. Phys. Lett. **105**, 031904, 2014
[17] D. H. Santamore, M. C. Cross, The Effect of Surface Roughness on Universal Thermal Conductance, 1) Phys.Rev.B 63, (2001); doi: 10.1103/PhysRevB.63.184306. 2) Physica B 316(1), 389-392 (2002); doi: 10.1016/S0921-4526(02)00522-7
[18] Schwab et al, Measurement of the Quantum of Thermal Conductance, Nature 404, 974 (2000); doi: 10.1038/35010065
[19] V. N. Popov, Low-Temperature Specific Heat of Nanotube Systems, Phys.Rev.B 66 153408 (2002); doi: 10.1103/PhysRevB.66.153408
[20] A. Alofi, G. P. Srivastava, Phonon Conductivity in Graphene, J.Appl.Phys. 112, 013517 (2012); doi: 10.1063/1.4733690
[21] A. I. Cocemasov, D. L. Nika, A. A. Balandin, Engineering of Thermodynamic Properties of Bilayer Graphene by Atomic Plane Rotations: the Role of out-of-plane Phonons, Nanoscale 7, 12851 (2015); doi: 10.1039/C5NR03579A

CHARGE CARRIERS STATES IN A MODEL OF CuO SUPERCONDUCTIVE CERAMICS

Jovan P. Šetrajčić
Academy of Sciences and Arts of the Republic of Srpska
Banja Luka, B&H

Siniša M. Vučenović
University of Banja Luka, Faculty of Sciences and Mathematics
Banja Luka, B&H

Keywords: ceramic oxides, charge carriers, dispersion law, energy states

ABSTRACT
The translational symmetry of the distribution of atoms (ions) of the charge carriers (electrons or holes) system is broken by sputtering (doping),and due to the existence of two boundary surfaces. This is a model of high-temperature superconductors in which the observed symmetry breaking orthogonal to the CuO plane is treated as a perturbation. Single-particle fermion wave functions and possible charge carrier energies were determined. The competing existence of superconducting and normal regions in such a sample is shown in agreement with experimental data. The conditions for the formation of superconducting states and the limits of the current density values in the planes parallel to the boundary surfaces (in the CuO planes) were obtained and discussed.

1. INTRODUCTION

High-temperature superconducting ceramics have "broken" the myth of an exclusively low-temperature effect of superconductivity [1–4]. Although they were discovered and improved at the end of the last century, the mechanism of superconductivity has not been figured out to date. The biggest difficulty is their highly anisotropic structure (Figure 1).

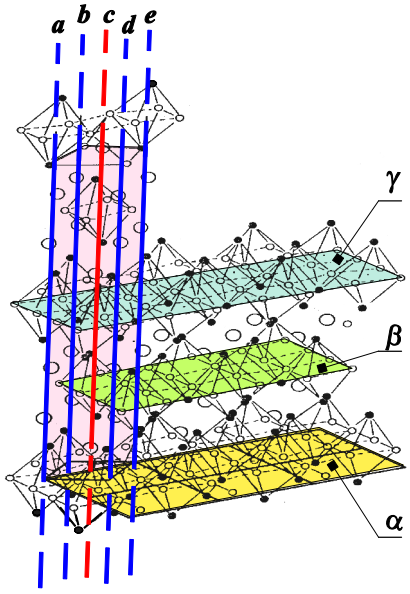

Figure 1: Model of high-temperature superconductors – CuO *ceramics*

The answer to the question of the oxide ceramics superconductivity mechanism must be undoubtedly sought in the phonon subsystem, in the elementary charges subsystem as well as in the interaction of these subsystems. With regard to the very anisotropic structure of the superconductive ceramics [1,2], we have attempted to construct a theoretical model conveying the broken translational symmetry of atoms (molecules) arrangement along one direction in the crystal lattice, the difference of masses of these molecules and the presence of two boundary planes along this direction [5,6].

The phonon system is drawn out in this model [6]. We have determined the phonon states and their energy spectra and we have shown that, due to the broken crystal symmetry

(actually because of deformed and tiny granular structure), the phonons of optical type owning the energy gap are present here [7]. The next task that we have attempted to solve is to determine and analyse the spectra of free charge carriers (electrons or holes), Landau criterion, the probabilities of states, and entropy within the same model. The preliminary results are already presented [8,9].

2. MODEL HAMILTONIAN

In order to obtain Hamiltonian of the charge carriers in the structure with broken translational symmetry, it is most suitable to start with the standard Hamiltonian of the electron system in an ideal infinite structure [10–12]:

$$H_{id} = \sum_{\vec{k}} \frac{\hbar^2 \vec{k}^2}{2m^*} C_{\vec{k}}^+ C_{\vec{k}} \tag{1}$$

where m^* is electron effective mass, while $C_{\vec{k}}^+$ and $C_{\vec{k}}$ are Fermi creation and annihilation operators of electrons with momentum $\hbar\vec{k}$ and energy $\hbar^2\vec{k}^2(2m^*)^{-1}$. If we go over to the configuration space using the transformations:

$$C_{\vec{k}} = \frac{1}{\sqrt{N}} \sum_{\vec{n}} C_{\vec{n}} \mathrm{e}^{-i\vec{k}\vec{n}}; C_{\vec{k}}^+ = \frac{1}{\sqrt{N}} \sum_{\vec{n}} C_{\vec{n}}^+ \mathrm{e}^{i\vec{k}\vec{n}} \tag{2}$$

where N is the number of molecules in the considered structure, we get:

$$H_{id} = \sum_{\vec{n}} \Lambda C_{\vec{n}}^+ C_{\vec{n}} - \sum_{\vec{n},\vec{m}} W_{\vec{n}\vec{m}} C_{\vec{n}}^+ C_{\vec{m}} \tag{3}$$

Here $\Lambda = N^{-1} \sum_{\vec{k}} \frac{\hbar^2 \vec{k}^2}{2m^*}$ and $W_{\vec{n}\vec{m}} = -N^{-1} \sum_{\vec{k}} \frac{\hbar^2 \vec{k}^2}{2m^*} \mathrm{e}^{i\vec{k}(\vec{n}-\vec{m})}$. Due to the canonicity of the transformation (2), the operators $C_{\vec{n}}^+$ and $C_{\vec{n}}$ are also Fermi operators.

Let us recall the most important assumptions of our model: we consider the tetragonal i.e. generalized cubic structure with very high anisotropy along the z-axis. It means that the lattice constant in this direction (a_z) is a few times larger than the lattice constant a_x, a_y in the directions x and y. The translational symmetry is fully conserved in the XY planes, while the symmetry of the masses arrangement along the z direction is broken (during the doping of the ceramic structure by the introduction of foreign atoms, the sputtered atoms locate along this direction because it is energetically most convenient). We also assume here that the structure under consideration is a film (not necessarily thin!). It means that the components of lattice vector $\vec{n} \equiv (n_x, n_y, n_z)$ vary in the following way:

$$n_r \in \left(-\frac{N_r}{2}, +\frac{N_r}{2}\right), r = (x, y); n_z \in [0, N_z]. \tag{4}$$

The numbers of atoms N_x and N_y along the directions x and y, respectively, may be indefinitely high since we have the translational symmetry along these directions. The number of atoms along z direction (N_z) is limited. The above-described model, i.e. the highly anisotropic matrix along the z direction, necessarily doped with foreign atoms, can be used for getting some qualitative conclusions about the behaviour of the superconductive ceramic. It is known [1–3] that the ceramic oxides are anisotropic along one privileged direction and that the superconductive state is realised by doping. But the real structure of the ceramic oxides–perovskites is approximated by the tetragonal structure. It is also assumed in the model that the sputtering is symmetric on both boundary planes: $n_z = 0$ and $n_z = N_z$ and between the layers $n_z = 0$ and $n_z = 1$ (as well as between the layers $n_z = N_z - 1$ and $n_z = N_z$) n_0 foreign particles are placed, in such a way that the structure of the doped matrix is unchanged near the middle of the film.

If the behaviour of the quantities from (3) may be expressed by the law:

$$W_{\vec{n}\vec{m}} = \frac{W_0}{|\vec{n}-\vec{m}|^h}; W_0 > 0; \qquad h > 0 \tag{5}$$

in the nearest neighbors approximation we get:

$$W_{n_s; n_s \pm 1} \equiv W_s = W_0 a_s^{-h}; s = (x, y, z). \tag{6}$$

According to the described view of the doping, it is obvious that lattice constant a_z in the doped structure becomes dependent on the position n_z, i.e. $a_z \longrightarrow a_z(n_z)$. Because of the symmetry on the boundaries: $a_z(0) = a_z(N_z) = a_z(n_0 + 1)^{-1}$; $a_z(N_z/2) = a_z$, we may take:

$$a_z(n_z) = a_z\left(1 - \frac{n_0}{n_0+1}N_z^2\right); N_z^2 = 2n_z N_z^{-1} - 1. \quad (7)$$

The dependence of the lattice constant on the index n_z causes the dependence of the interaction along z direction on the index n_z, i.e.:

$$W_z \longrightarrow W_z(n_z) = W_0 a_z^{-h}(n_z) = W_0 a_z^{-h}\left(1 - N_z^2\frac{n_0}{n_0+1}\right)^{-h} \approx W_z(1 + \Phi N_z^2), \quad (8)$$

where $\Phi = hn_0(n_0 + 1)^{-1}$. The interactions W_x and W_y, according to the described picture, are unchanged. We must notice that the last two expressions are valid for even N_z. But, for large enough N_z ($N_z \approx N_z + 1$), or during the transition from n_z to continual variable z, the deviations from the formulas (7) and (8) for odd N_z are not essential. The values of Λ are not dependent on the index of the site, because they are unchanged during the doping. Hence we can write the Hamiltonian of the doped structure in the form:

$$H = H_{\mathrm{B}} + H_{\mathrm{V}}, \quad (9)$$

where:

$$\begin{aligned} H_{\mathrm{B}} = \sum_{n_x,n_y}\Big\{ & C^+_{n_x n_y 0}\Big[\Lambda C_{n_x n_y 0} - W_x\left(C_{n_x+1,n_y 0} + C_{n_x-1,n_y 0}\right) - \\ & - W_y\left(C_{n_x n_y+1,0} + C_{n_x n_y-1,0}\right) - W_z(1-\Phi)C_{n_x n_y 1}\Big] + \\ & + C^+_{n_x n_y N_z}\Big[\Lambda C_{n_x n_y N_z} - W_x\left(C_{n_x+1,n_y N_z} + C_{n_x-1,n_y N_z}\right) - \\ & - W_y\left(C_{n_x n_y+1,N_z} + C_{n_x n_y-1,N_z}\right) - W_z(1-\Phi)C_{n_x n_y N_z-1}\Big]\Big\}, \end{aligned} \quad (10)$$

and, as we can see, it is related to the boundary layers ($n_z = 0$ and $n_z = N_z$), where obviously $W_{n_x,n_y,0;n_x,n_y,-1} = W_{n_x,n_y,N_z;n_x,n_y,N_z+1} = 0$, and for H_{V} we find:

$$\begin{aligned} H_{\mathrm{V}} = \sum_{n_x,n_y}\sum_{n_z=0}^{N_z-1}\Big\{ & C^+_{n_x n_y 0}\Big[\Lambda C_{n_x n_y 0} - W_x\left(C_{n_x+1,n_y 0} + C_{n_x-1,n_y 0}\right) - \\ & - W_y\left(C_{n_x n_y+1,0} + C_{n_x n_y-1,0}\right) - W_z(1-\Phi)C_{n_x n_y 1}\Big] + \\ & + C^+_{n_x n_y N_z}\Big[\Lambda C_{n_x n_y N_z} - W_x\left(C_{n_x+1,n_y N_z} + C_{n_x-1,n_y N_z}\right) - \\ & - W_y\left(C_{n_x n_y+1,N_z} + C_{n_x n_y-1,N_z}\right) - W_z(1-\Phi)C_{n_x n_y N_z-1}\Big]\Big\}. \end{aligned} \quad (11)$$

3. SINGLE-PARTICLE STATES OF THE SYSTEM

We shall analyse the system described by Hamiltonian (9) using the orthonormalized single-electron state functions [12]:

$$|\Psi\rangle = \sum_{n_x,n_y,n_z} A_{n_x,n_y,n_z} C^+_{n_x,n_y,n_z}|0\rangle; \sum_{n_x,n_y,n_z} |A_{n_x,n_y,n_z}|^2 = 1. \quad (12)$$

We obtain the equations for finding the coefficient A_{n_x,n_y,n_z} using the equations of motion for operators C_{n_x,n_y,n_z}. From $C_{n_x,n_y,n_z}(t) = C_{n_x,n_y,n_z}(0)e^{i\omega t}$, $\omega = E/\hbar$, it follows:

$$EC_{n_x,n_y,n_z} - \left[C_{n_x,n_y,n_z}, H\right] \equiv O_{n_x,n_y,n_z}; O_{n_x,n_y,n_z} = O. \quad (13)$$

On the basis of equations (9 –11) and (13), we form operators $O_{n_x,n_y,0}$, $O_{n_x,n_y,N_z,}$ and O_{n_x,n_y,n_z}. After applying them to the functions (12) and using the substitution:

$$A_{n_x,n_y,n_z} = A_{n_z} e^{i(n_x a_x k_x + n_y a_y k_y)} \quad (14)$$

where $k_j = \frac{2\pi}{N_j a_j}\nu_j$; $j = (x, y)$; $\nu_j \in \left(-\frac{N_j}{2}, +\frac{N_j}{2}\right)$ and on the basis of the fact that $\Lambda = 2\sum_{xyz} W_j$, we find the following system of difference equations:

$$(E - 4Q - 2W_z)A_0 + W_z(1-\Phi)A_1 = 0, n_z = 0;$$

$$(E-4Q-2W_z)A_{N_z}+W_z(1-\Phi)A_{N_z-1}=0, n_z=N_z; \quad (15)$$

$$(E-4Q-2W_z)A_{n_z}+W_z(1+\Phi N_z^2)\left(A_{n_z+1}+A_{n_z-1}\right)=0, \quad 1\le n_z\le N_z-1, \quad (16)$$

where $Q\equiv Q_{k_xk_y}=W_x\sin^2\left(\frac{a_xk_x}{2}\right)+W_y\sin^2\left(\frac{a_yk_y}{2}\right)$. We shall perform further analysis in the continual approximation in order to avoid the complications arising during the determination of the coefficient A_n from the system of difference equations (15). Introduction the continual variable z through $n_z\to z/a_z(N_z\to L/a_z)$ causes the following transformations of the expressions (7) and (8):

$$a_{z;n_z}\to a_z(z)=a_z\left[1-\frac{n_o}{n_o+1}\left(2\frac{z}{L}-1\right)^2\right], W_{z;n_z}\to W_z(z)=W_z\left[1+\Phi\left(2\frac{z}{L}-1\right)^2\right]. \quad (17)$$

The coefficients A_{n_z} will be transformed in the following way:

$$A_n\to A(z); A_{n+1}+A_{n-1}\to A(z+\bar{a}_z)+A(z-\bar{a}_z), *\ 1.0mm$$

$$A(z\pm\bar{a}_z)\approx A(z)\pm\bar{a}_z\frac{dA}{dz}+\frac{\bar{a}_z^2}{2}\frac{d^2A}{dz^2}; \bar{a}_z\equiv\bar{a}_z(z)=\frac{1}{L}\int_0^L dza_z(z)=a_z\frac{2n_o+3}{3(n_o+1)}.$$

The important consequence of the transition to the continuum is the fact that the first two equations from (15) vanish from the calculation at $n_z\to z$, i.e. they are merged into the last of equations from (15), which is the continual approximation has the form:

$$\frac{d^2A}{dz^2}+\frac{E-4Q-\Phi(E-4Q-2W_z)\left(2\frac{z}{L}-1\right)^2}{\bar{a}_z^2(z)W_z}A=0. \quad (18)$$

By the assumption:

$$E>4Q+2W_z\equiv E_z^{(0)} \quad (19)$$

and by the substitution: $2z/L-1=\tau\zeta$, with $\tau^4=W_z(\bar{a}_zL)^2[4\Phi(E-4Q-2W_z)]^{-1}$, the equation (17) becomes known Hermite-Weber equation:

$$\frac{d^2A}{d\zeta^2}+(\kappa-\zeta^2)A=0 \quad (20)$$

where $\kappa=\frac{L}{2\bar{a}_z}(E-4Q)\left[\Phi(E-E_z^{(0)})W_z\right]^{-1/2}$. Here we introduce the requirement that the amplitudes A are finite for arbitrary structure thickness (it means even for $L\to\infty$ too). For satisfying this requirement we must take the known condition of the finiteness for the solutions for Hermite-Weber equation: $\kappa=2\mu+1;\mu=0,1,2,\ldots$ On the basis of this, we find:

$$E_{1,2}=4Q+2b^2(2\mu+1)^2\Phi W_z\left\{1\pm\left[1-\frac{2}{(2\mu+1)^2b^2\Phi}\right]^{1/2}\right\} \quad (21)$$

were $b=\bar{a}_z/L$. The expression for energies (20) indicates that index μ must be limited from below (the energies must be real):

$$2\mu\ge b^{-1}\sqrt{2/\Phi}-1. \quad (22)$$

It means that the minimum allowed value of the index μ is the minimal integer which is bigger than the final term in (20). As we can see, the lower boundary of quantum number μ depends on the number of structural layers (through N_z), on the way of sputtering (through n_0), and on the type of ion-ion interaction (through h). If the thickness of the structure increases, the lower value of μ increases too.

For simplification, instead of the expression (20), we will use the approximate expressions for energies, which we obtain by the expansion of the square root up to the quadratic terms:

$$E_1=E_z^{(0)}+4b^2(2\mu+1)^2\Phi W_z-\frac{W_z}{2(2\mu+1)^2b^2\Phi} \quad (23)$$

and

$$E_2=E_z^{(0)}+\frac{W_z}{2(2\mu+1)^2b^2\Phi}. \quad (24)$$

It is very easy to notice that both obtained expressions for energies satisfy the necessary condition (18). However, by the analysis of (22) and (23), we can conclude the following.

– Since $E_2 < E_1$, the states with energy E_2 are more stable and more populated and so they essentially define the normal behavior of the system.
– From expressions (21) and (23) it follows that the increase of film thickness (the increase of N_z) causes the increase of the lower boundary of the index μ, and the correction of E_2, which depends on sputtering, decreases. This is in complete agreement with the conclusions that we can accomplish without going over to continuum, i.e. directly analysing discrete eq.s (15).

We can see in expressions defining ζ – text under (18), that the boundaries of the interval for ζ are proportional to $L/\bar{a}_z = b^{-1}$ and so we can approximately take: $\zeta \in [-\infty, +\infty]$, where the approximation is better if the film is thicker. We can then express the solutions of equation (19) using Hermite polynomials:

$$A_\mu(\zeta) = \frac{e^{-\zeta^2/2}}{(2^\mu \mu! \sqrt{\pi})^{1/2}} H_\mu(\zeta); H_\mu(\zeta) = (-1)^\mu e^{\zeta^2} \frac{d^\mu}{d\zeta^\mu}(e^{-\zeta^2}) \mu = 0,1,2, \ldots (25)$$

In this way we have defined single-particle degenerate states of the system: for the wave functions – by the equations (12), (14), and (24) and for energies – by (20).

4. CHARGE CARRIERS DISPERSION LAW

We shall perform the diagonalization of the electron Hamiltonian in the following stages.

1) In the framework of the continual approximation, Hamiltonian H_B "melted" in Hamiltonian H_V using the formulas for transition to continuum:

$$C_{n_x n_y n_z} \to C_{n_x n_y}(\zeta); W_z \left[1 + \frac{4\Phi}{L^2}\left(z - \frac{L}{2}\right)^2\right] \to W_z \left(1 + \frac{4\Phi\tau_\mu}{L^2}\zeta^2\right).$$

(Because of the transformation $n_z \to z \to \tau\zeta$, it is obvious that the sum over n_z must be changed by integral over ζ: $\sum_{n_x n_y n_z} \longrightarrow \tau \bar{a}_z^{-1} \sum_{n_x n_y} \int_{-\infty}^{\infty} d\zeta$).

2) From the operators $C_{n_x n_y}(\zeta)$ we go over to new operators $C_{k_x k_y \mu}$ using the canonical transformations:

$$C_{n_x n_y}(\zeta) = \sum_{k_x k_y \mu} A_{n_x n_y}^{k_x k_y}(\mu, \zeta) C_{k_x k_y \mu}. \quad (26)$$

Therefore we can write Hamiltonian H_V in the continual approximation in the form:

$$H_V \longrightarrow H = \frac{\tau}{a_z} \sum_{n_x n_y} \int_{-\infty}^{\infty} d\zeta C_{n_x n_y}^+(\zeta) \Big\{\Lambda C_{n_x n_y}(\zeta) -$$
$$- W_x \left[C_{n_x+1, n_y}(\zeta) + C_{n_x-1, n_y}(\zeta)\right] - W_y \left[C_{n_x n_y+1}(\zeta) + C_{n_x n_y-1}(\zeta)\right] -$$
$$- W_z \left(1 + \frac{4\Phi\tau^2}{L^2}\zeta^2\right)\left[2C_{n_x n_y}(\zeta) + \frac{\bar{a}_z^2}{\tau^2}\frac{d^2 C_{n_x n_y}(\zeta)}{d\zeta^2}\right]\Big\}. \quad (27)$$

We can now perform the diagonalization of Hamiltonian. After the substitutions (26) into (27) we have:

$$H = \frac{\tau}{\bar{a}_z} \sum_{k_x k_y \mu} \sum_{q_x q_y \nu} C_{q_x q_y \nu}^+ C_{k_x k_y \mu} \sum_{n_x n_y} \int_{-\infty}^{\infty} d\zeta \left[A_{n_x n_y}^{q_x q_y}(\nu; \zeta)\right]^* \Big\{\Lambda A_{n_x n_y}^{k_x k_y}(\mu; \zeta) -$$
$$-2W_x \left[A_{n_x+1, n_y}^{k_x k_y}(\mu; \zeta) + A_{n_x-1, n_y}^{k_x k_y}(\mu; \zeta)\right] - 2W_y \left[A_{n_x n_y+1}^{k_x k_y}(\mu; \zeta) + A_{n_x n_y-1}^{k_x k_y}(\mu; \zeta)\right] -$$
$$- 2W_z \left(1 + \frac{4\Phi\tau^2}{L^2}\zeta^2\right)\left[2A_{n_x n_y}^{k_x k_y}(\mu; \zeta) + \frac{\bar{a}_z^2}{\tau^2}\frac{d^2 A_{n_x n_y}^{k_x k_y}(\mu; \zeta)}{d\zeta^2}\right]\Big\}. \quad (28)$$

On the basis of (14) one can write: $A_{n_j+1}^{k_x k_y}(\mu; \zeta) + A_{n_j-1}^{k_x k_y}(\mu; \zeta) = 2A_{n_x n_y}^{k_x k_y}(\mu; \zeta)\cos(a_j k_j)$, $j = (x, y)$. If we substitute E with $E_{k_x k_y \mu}$ and z with ζ in the last of (15), we find $W_z(1 + \frac{4\Phi\tau^2}{L^2}\zeta^2)\left[2A_\mu(\zeta) + \frac{\bar{a}_z^2}{\tau^2}\frac{d^2 A_\mu(\zeta)}{d\zeta^2}\right] = \left(E_z^{(0)} - E_{k_x k_y \mu}\right) A_\mu(\zeta)$, which yields

$$W_z\left(1+\frac{4\Phi\tau^2}{L^2}\zeta^2\right)\left[2A_{n_xn_y}^{k_xk_y}(\mu;\zeta)+\frac{\bar{a}_z^2}{\tau^2}\frac{d^2A_{n_xn_y}^{k_xk_y}(\mu;\zeta)}{d\zeta^2}\right]=\left(E_z^{(0)}-E_{k_xk_y\mu}\right)A_{n_xn_y}^{k_xk_y}(\mu;\zeta).$$

Using this and the orthonormalization condition from (12), we diagonalize the expression (28) for Hamiltonian of the system:

$$H=\sum_{k_xk_y\mu}E_{k_xk_y\mu}C_{k_xk_y\mu}^{+}C_{k_xk_y\mu}. \tag{29}$$

This expression represents the Hamiltonian of the electron subsystem which was the subject of this study. Together with Hamiltonian of the phonon subsystem derived earlier [5–7], it enables the continuation of the investigation of superconductivity mechanism in high-temperature oxide ceramics. Analyses performed until now enable us to conclude that the theoretical model of symmetrically deformed structures satisfies the basic experimental indicators of superconductive perovskites behavior. It is primarily related to the proved presence of a gap in the spectrum of elementary excitations in this system (phonons or electrons) and its behavior in the structures with different stoichiometry. The question of the interaction between the subsystem of elementary charges and the subsystem of phonons (optical type) is still open; this question is crucial for the understanding of the nature of the new superconductive state.

5. ESTIMATE OF SYSTEM ORDERING

In this section of the paper, we shall analyse Landau superfluidity criterion and determine the probabilities of states and entropy of the system. Landau criterion for superfluid motion is $\min v>0$, where $v=E(p)/p$. The expression for energies (20) (using the approximations: $a_x\cong a_y\equiv a$, $a_z\cong 3a$, $W_x\cong W_y\equiv W$, $W_z=W/3^h$, $\sin\alpha\simeq\alpha$, $k_x=k\sin\theta\cos\varphi$, $k_y=k\sin\theta\sin\varphi$,$k_z=k\cos\theta$) yields the following expression:

$$E_{1;2}(p)=\frac{Wa^2}{\hbar^2}\left[p^2\sin^2\theta+g_{\pm}^2(\mu)\right] \tag{30}$$

where $g_{\pm}^2(\mu)=23^{-h}\hbar^2a^{-2}f^2(\mu)\left[1\pm\sqrt{1-2f^{-2}(\mu)}\right]$; $f^2(\mu)=b^2(2\mu+1)^2\Phi$. For the phase velocity we get:

$$v_{1;2}(p)=\frac{E_{1;2}(p)}{p}=\frac{Wa^2}{\hbar^2}\left[p\sin^2\theta+\frac{1}{p}g_{\pm}^2(\mu)\right] \tag{31}$$

The condition $dv/dp=0$ yields $p_e=g_{\pm}(\mu)\sin^{-1}\theta$. Because of $\theta\in[0,\pi]\Rightarrow v_{1,2}^2\geq 0$, and because $g_+\geq g_-\Rightarrow v_1^2\geq v_2^2$. It follows that the state with the energy E_1 has more expressive minimum than the state with the energy E_2. For the second derivative we get:

$$\frac{d^2v_{1;2}}{dp^2}|_{p=p_e}=2Wa^2\hbar^{-2}g_{\pm}^{-1}(\mu)\sin^3\theta\geq 0 \tag{32}$$

We can see that the known – Landau criterion is satisfied for both energies, but it is "stronger" for the states with the energies $E_1(\geq E_2)$ because E_1 has a bigger gap than E_2.
We shall now determine the probability of the state of the system under consideration. If we introduce the notation

$$\epsilon_{1;2}\equiv E_{1;2}-E_z^{(0)}=2W_z\left[3^ha^2\hbar^{-2}g_{pm}^2(\mu)-1\right] \tag{33}$$

we can find – see text under the (18):

$$\tau_{1;2}=\left(\frac{\bar{a}_z}{2}L\right)^{1/2}\left(\Phi\epsilon_{1;2}W_z^{-1}\right)^{-1/4} \tag{34}$$

Then the wave function (12) has the form:

$$\Psi_{1;2}(k_x,k_y,k_z)=\frac{\tau_{1;2}}{\bar{a}_z}\sum_{n_xn_y}\int_{-\infty}^{+\infty}d\zeta|A_{n_xn_y}^{k_xk_y}(\mu;\zeta)|_{1;2}C_{n_xn_y}^{+}|0\rangle \tag{35}$$

where $|A_{n_xn_y}^{k_xk_y}(\mu;\zeta)|_{1;2}=N_{1;2}e^{i(n_xa_xk_x+n_ya_yk_y)}A_\mu(\zeta)$ and norm-factor is defined on the following way $N_{1;2}=\bar{a}_z\left(N_xN_y\tau_{1;2}\right)^{-1}$. The probability of finding the elementary charges with the energy E_1 (and E_2), in agreement with (35), is:

$$P_{1;2}(\mu;\zeta) = \left(\frac{\tau_{1;2}}{\bar{a}_z}\right)^2 |A^{k_x k_y}_{n_x n_y}(\mu;\zeta)|^2_{1;2} = N_x^{-2} N_y^{-2} A^2_\mu(\zeta) \tag{36}$$

wherefrom:

$$P_1(\mu;\zeta) = P_2(\mu;\zeta) \equiv P_\mu(\zeta) \tag{37}$$

On the basis of the last expression, we can see that both states appear with equal probabilities!

The entropy of the system under consideration is:

$$S_{1;2}(\mu) = -\frac{\tau_{1;2}}{\bar{a}_z} I(\mu) \tag{38}$$

where the integral $I(\mu) \equiv \int_{-\infty}^{+\infty} d\zeta P_\mu(\zeta) \ln P_\mu(\zeta)$ is need not be calculated, since, from (4.9) and (34), it follows:

$$\frac{S_1(\mu)}{S_2(\mu)} = \frac{\tau_1}{\tau_2} \equiv \left(\frac{\epsilon_2}{\epsilon_1}\right)^{1/4} \leq 1 \Longrightarrow S_1(\mu) \leq S_2(\mu) \tag{39}$$

(Since $E_1 \geq E_2$, we get $\epsilon_{1;2} \geq 0$ and $\epsilon_1 \geq \epsilon_2$). This expression yields that the states Ψ_2 (with E_2) are less ordered than the states Ψ_1 (with E_1). It means that the states with E_1 (with higher energy and lower population) are probably responsible for superconductive effects in the observed system. The states with E_2 (with lower energy and higher population) are responsible for the normal behaviour of this system. This is in agreement with the above comments about these two possible energies.

6. CONCLUSION REMARKS

The particular features of high-temperature superconductors on the basis of oxide ceramics are their granular structure and the anisotropy of properties. The existence of the weak isotopic effect and Cooper pairs of charge carriers is experimentally verified, similar in the conventional superconductors, but BCS model was not able to explain high critical temperature. For that reason and on the basis of established experimental results [1–3,13–15], we have proposed the model of ceramic structure as tetragonal i.e. generalised cubic structure in which interatomic distances along one direction are a few times bigger than along the other two directions. It is, energetically, most convenient if the sputtered atoms locate themselves just along this direction.

The analysis of the phonon spectrum in our model yields that we have phonon branches of optical type only in the spectrum (there exists an energy gap). It means that for phonon excitation it is necessary that the energy (heat) is bigger than the energy gap.

The analysis of the electron spectrum in these symmetrically deformed structures (with respect to the planes $n_z = 0$ and $n_z = N_z$) yields that, as a consequence of the existence of the boundaries along z axes, we have two energy branches in the spectrum of charge carriers. The lower value of energy is related to more populated states and contains the term depending on the sputtering. This term decreases with increasing the film thickness. The higher value of energy in the spectrum of charge carriers is not particularly analysed because these levels are low populated.

In addition to this, in the framework of the model under consideration, we have determined the orthonormalized single-particle state functions of this system, entropy, and the probabilities of possible states. The theoretical investigation in the framework of the presented model is not finished. It is necessary to form Hamiltonian of the interaction between charge carriers and phonons and separate from it the essential part only, which describes the formation of Cooper pairs. Only after this, the thermodynamical analysis of the complete system follows.

7. ACKNOWLEDGMENTS

The research presented in this paper was financially supported by the Ministry of Scientific and Technological Development, Higher Education and Information Society of the Republic of Srpska (Projects No. 19.032/961-36/19 and 19.032/961-42/19).

8. REFERENCES

[1] J. G. Bednorz and K. A. Müller: *Perovskite-Type Oxides* – the New Approach to High-T_c Superconductivity; *Nobel Lecture,* Stockholm, December 8, (1987)
[2] P. H. Hor, et.al, Superconductivity above 90 K in the square-planar compound system ABa$_2$Cu$_3$O$_{6+x}$ with A=*Y*,La,Nd,Sm,Eu,Gd,Ho,Er and Lu, *Phys.Rev.Lett.* 58, 1891 (1987)
[3] A. A. Abrikosov: Theory of High−Tc Superconducting Cuprates Based on Experimental Evidence, *http://www.lanl.gov./find/cond.mat.* No: 9912394 (1999)
[4] N. M. Plakida: High-Temperature Superconductors, *Springer-Verlag*, Berlin 1995
[5] B. S.Tošić, J. P. Šetrajčić, R. P. Djajić and D. Lj. Mirjanić; Phonons in Broken-Symmetry Structures, *Phys.Rev.* B 36, 9094 (1987)
[6] J. P. Šetrajčić, R. P. Djajić, D. Lj. Mirjanić and B. S. Tošić; Phonon Spectra in Superconducting Ceramics, *Phys. Scr.* 42, 732 (1990)
[7] J. P. Šetrajčić, V. M. Zorić, N. V. Delić, D. Lj. Mirjanić and S. K. Jaćimovski, Phonon Participation in Thermodynamics and Superconductive Properties of Thin Ceramic Films, Chapter 15, pp. 317-348, In „Thermodynamics", Ed. M. Tadashi, ISBN: 978-953-307-544-0, *InTech*, Vienna (Austria) 2011; Available from:
[8] http://www.intechopen.com/articles/show/title/phonon-participation-in-thermodynamics-and-superconductive-properties-of-thin-ceramic-films
[9] J. P. Šetrajčić, S. M. Vučenović and S. K. Jaćimovski, Possible States of Charge Carriers in Thin Multilayered Superconductive Ceramics, *Zaštita Materijala* **57**/2, 239-243 (2016)
[10] S. M. Vučenović, J. P. Šetrajčić and D. I. Ilić, Superconductivity of Lanthanum Hydride To 250 K, *Proceedings 12th ContMat* (ISBN 978-99976-42-30-1), 91-103 (2020).
[11] Ch. Kittel, Introduction to Solid State Physics, *Wiley*, New York 2004
[12] P. Hoffmann, Solid State Physics, *Wiley*, New York 2015
[13] S. M. Girvin and K. Yang, Modern Condensed Matter Physics, *Cambridge Univ. Press*, Cambridge 2019
[14] R. Simon; High-*T*c Thin Film and Electronic Devices, *Physics Today* 44, 64 (1991)
[15] D. R. Harshman and A. P. Mills, *Phys.Rev. B* 45, 10684 (1992)
[16] W. E. Pickett *Rev. Mod. Phys.* 61, 433 (1989)

CATECHOLASE ACTIVITY AND SUBSTITUENT EFFECTOF NEW HOMOLEPTIC COPPER(II) CHALCONE COMPLEXES

Selma Hadžalić, Irnesa Osmanković, Adnan Zahirović
University of Sarajevo, Laboratory for Inorganic and Bioinorganic Chemistry,
Department of Chemistry, Faculty of Science
Sarajevo, B&H

Keywords: copper, chalcone, catecholase activity

ABSTRACT
*Three new neutral complexes of copper(II) containing chalcone ligands derived from 2'-hydoxyacetophenone and 4-substituted benzaldehydes were synthesized. Complexes were prepared by solution synthesis and characterized by spectroscopy. The catalytic activity of complexes was examined in the reaction of 3,5-di-test-butyl catechol (DTBC) oxidation. The kinetics of DTBC catalytic oxidation by copper(II) complexes **(1–3)** was investigated spectrophotometrically under pseudo-first-order conditions. Catalytic parameters, the maximum reaction rate (v_{max}), Michaelis-Menten constant (K_M), catalytic efficiency, catalytic reaction rate constant (k_{cat}), turnover number (TON), and turnover frequencies (TOF) for complexes **1–3** in DTBC oxidation were collected. The studied complexes **1** and **2** were found to have moderate catalytic activity, while complex **3** does not show catalytic properties.*

1. INTRODUCTION

The ability of copper proteins to process dioxygen at ambient conditions has inspired numerous research groups to study their structural, spectroscopic, and catalytic properties. Catechol oxidase (CO), also known as *o*-diphenol oxidase, is a member of the type-3 copper proteins[1]. COs are found in plant tissues and some insects and crustaceans. CO catalyzes exclusively the oxidation of catechols (i.e., *o*-diphenols) to the corresponding *o*-quinones which can rapidly polymerize to form melanin, a dark pigment thought to protect a damaged tissue from pathogens and grants damaged fruits their dark brown coloration [2].
A great number of mononuclear and dinuclear copper(II) complexes have been investigated as biomimetic catalysts for catechol oxidation, regarding the binding of catechol substrate in the first step of the catalytic cycle [3-7]. While no clear relation between the catalytic activity and the redox potential of the copper species has emerged, dinuclear copper complexes are generally found to be more reactive than mononuclear compounds, and a steric match between the dicopper site and the substrate is assumed to be advantageous [8]. The presence of carbonyl oxygen, phenolic oxygen, and/or heteroatom(s) in a heterocyclic ring system makes chalcones excellent chelating ligands for metal coordination. The metal complexes of bidentate chalcone have shown great potential in antiviral, antimalarial, antimicrobial, antioxidant, therapeutic, and catalytic applications [9-13]. Recent studies present that copper(II) chalcone complexesshow evidence of catalysis in the oxidation reaction of catechol to o-quinone under atmospheric dioxygen [2,14,15]. The catalyzing potential of two novel copper complexes of chalcone derivatives in the oxidation reaction of catechol to o-quinone was investigated by Kahrović et al [16].

We report the synthesis of three novel neutral copper(II) complexes (1–3) containing chalcone ligands including the study of their catalytic activity towards the 3,5-di-*tert*-butylcatechol oxidation.

2. EXPERIMENTAL SECTION

2.1 Materials

All used chemicals were commercially available and used as received. Copper(II) acetate hydrate, 2'-hydroxyacetophenone, 4-chlorobenzaldehyde, 4-methylbenzaldehyde, and 4-methoxybenzaldehyde were obtained as reagent-grade chemicals from Sigma. The 3,5-di-test-butyl catechol (DTBC) (98 % *w/w*) was obtained from Sigma. Anhydrous DMSO (water content < 0.005%) and anhydrous methanol (water content < 0.002%) were supplied commercially.

2.2 Physical Measurements

Infrared spectra were recorded as KBr pallets in the 4000 – 400 cm^{-1} region on Perkin Elmer BX FTIR. Electronic spectra were collected in DMSO (5×10^{-5} M) in the 260 – 900 nm range on a Perkin Elmer Lambda 35.

2.3 Ligands Syntheses

All ligands were synthesized by following the standard method of preparation. Chalcones (HL^1, HL^2, HL^3) were obtained by the aldol condensation reaction between 2'-hydroxyacetophenone and 4-chlorobenzaldehyde or 4-methylbenzaldehyde or 4-methoxybenzaldehyde with a base catalyst [17].

Synthesis of Chalcone Ligands HL^1, HL^2, and HL^3. In ethanol solution of 4-chlorobenzaldehyde or 4-methylbenzaldehyde or 4-methoxybenzaldehyde (20 mmol) and 2'-hydroxyacetophenone (20 mmol, 2.41 mL) sodium hydroxide (17.2 mL, 5 mol dm^{-3}) was added portion-wise. The reaction mixture was stirred over 24 hours at room temperature. A thick mixture was obtained and acidified by the addition of acetic acid (30% *w/w*) until pH = 6 was reached. The resulting chalcone was isolated by vacuum filtration, washed with water, purified by recrystallization from ethanol solvent, and vacuum dried over silica.
Yield: 4.087 g (79%) for HL^1; 2.596 g (54%) for HL^2; 3.675 g (72%) for HL^3.

2.4 Syntheses of Copper(II) Complexes, 1–3

Appropriate chalcone ligand (1.0 mmol, 258 mg HL^1; 238 mg HL^2; 254 mg HL^3) dissolved in methanol (20 mL) was added in a methanolic solution (25 mL) of the dinuclearcopper(II) acetate dihydrate (0.25 mmol, 100 mg). The reaction mixture was refluxed for one hour. After cooling, red substances precipitated. Products were filtered out, washed with ice-cold methanol, and dried under a vacuum.

Complex 1. 176 mg (59%); UV-Vis(DMSO) λ_{max}/ nm(log ε): 314 (4.26) and 443 (3.53); IR (KBr), ν_{max}/cm^{-1}: 1631 (C=O), 1609 (C=C), 1360 (C–O), 574 (Cu–O).
Complex 2. 163 mg (57%); UV-Vis(DMSO) λ_{max}/nm (log ε): 338 (4.55) and 436 (0.55); IR (KBr), ν_{max}/cm^{-1}: 1633 (C=O), 1607 (C=C), 1354 (C–O), 577 (Cu–O).
Complex 3. 102 mg (34%); UV-Vis(DMSO) λ_{max}/ nm (log ε): 361 (4.68) and 434 (4.36); IR (KBr), ν_{max}/cm^{-1}: 1628 (C=O), 1606 (C=C), 1354 (C–O), 577(Cu–O).

2.5 Catalytic Activity

The catecholase activity of complexes **1–3** was examined by taking DTBC as a model substrate. Catalysis of the DTBC oxidation reaction by copper(II) complexes was estimated spectrophotometrically, in DMSO solution at room temperature under aerobic conditions. Six experiments were performed for each of the complexes, during which the concentration

of the observed complexes (1.25×10^{-5}mol dm^{-3}, 1000 μL) and the hydrogen peroxide co-oxidant (30% *w*/*w*, 25 μL) was kept constant, while the concentration of the DTBC substrate was varied (1×10^{-2} mol dm^{-3}, 500 – 25 μL, and DMSO was added up to a volume of 2000 μL). Over 10 minutes, every 30 seconds, an increase in absorption intensity at 400 nm was monitored, originating as a consequence of the formation of 3,5-di-*tert*-butylquinone (DTBQ). Michaelis–Menten method of enzymatic kinetics was applied to obtain Lineweaver–Burk plot and values of K_M, $v_{max,}$ and k_{cat}. The conversion of the reaction rate units from A/s to M/s was done using $\varepsilon = 2818\ M^{-1}\ cm^{-1}$ for 3,5-DTBQ in DMSO with an absorption maximum at 400 nm [18].

3. RESULTS AND DISCUSSION

3.1 Syntheses

Complexes **1–3** contain copper(II) metal centers to which various chalcones (HL^1, HL^2 or HL^3) are bound as ligands. The synthesis were carried out under reflux in a methanolic solutions, in which both ligand and starting compound, binuclear copper(II) acetatedihydrate, were soluble, while obtained products had poor solubility and therefore can be isolated by filtration. The molar ratio of binuclear copper(II) acetate and appropriate chalconewas1:4. This stoichiometry was aimed to ensure the coordination of twobidentate anionic chalcone ligands through the carbonyl oxygen atom and the oxygen atom of the deprotonated hydroxyl group (O, O donor atoms) to the copper metal center.

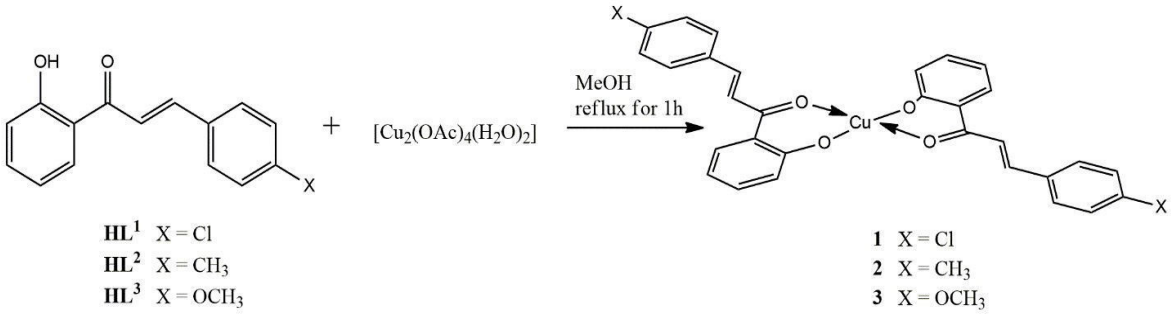

*Figure 1. The synthetic route for complexes **1-3***

Complexes of copper(II) with chalcone ligands were characterized based on infrared and electronic spectroscopy.

3.2 Spectroscopic Characterization

Infrared spectra

The infrared spectra of complexes **(1 – 3)** have bands at similar positions, which indicates their structural similarities.

Chalcones are bounded to the copper(II) metal center as bidentate anionic ligands *via* the deprotonated hydroxyl oxygen atom and the carbonyl oxygen atom. After ligand coordination, strong intensity bands assigned to the stretching vibrations of the carbonyl groups (C=O) and C=C stretching vibrations, shifted to lower wave numbers: 1631 and 1609 cm^{-1} for **1**; 1633 and 1607 cm^{-1} for **2**; 1628 and 1606 cm^{-1} for **3,** compared to the free ligands (Figure 2). The coordination of chalcone ligands is further indicated by the shift of the C–O stretching vibrations to higher wave numbers in the spectra of complexes (1360 cm^{-1} for **1**and 1354 $cm^{-1}$for **2** and **3**) compared to the spectra of free ligands (1339 cm^{-1} for HL^1, 1341 cm^{-1} for HL^2 and 1344 cm^{-1} for HL^3)[19].

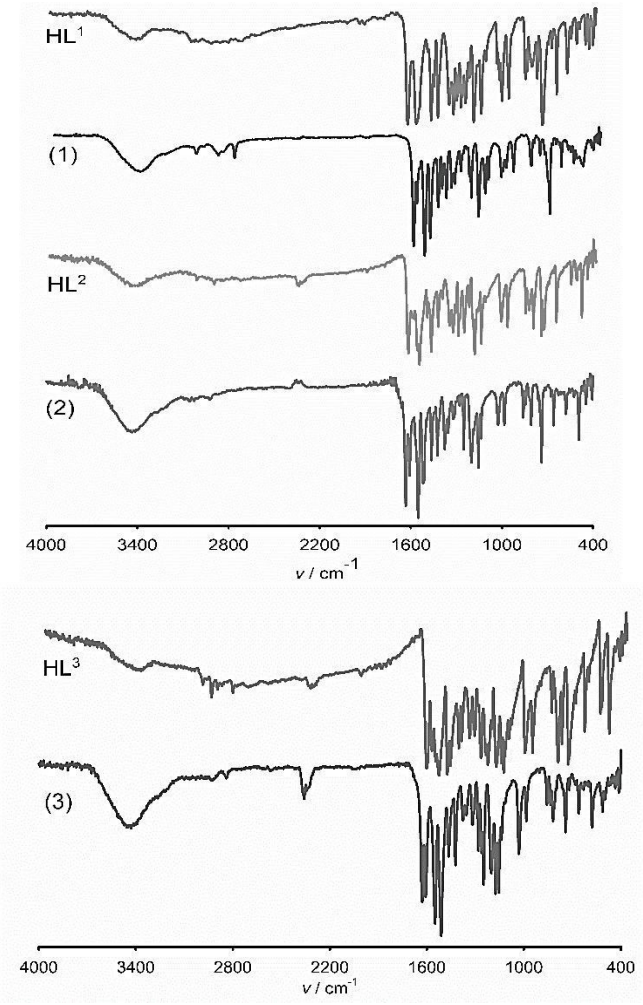

*Figure 2. Infrared spectra of copper(II) complexes (**1–3**) and free chalcone ligands (HL^1 – HL^3)*

In the low-frequency region in spectra of all complexes, a new band, attributed to stretching vibrations of the newly formed Cu–O bond, appeared. Cu–O stretching vibration appeared at 574 cm^{-1} for **1**; 577 cm^{-1} for **2**; 577 cm^{-1} for **3**.

*Table 1. The most important vibrational bands in FTIR spectra of chalcone ligands and complexes of copper(II) **1–3***

Compound	ν(O–H)	ν(C–H)$_{aromatic}$	ν(C–H)$_{aliphatic}$	ν(C=O)	ν(C=C)	ν(C–O$_{enol}$)	ν(Cu–O)
			cm^{-1}				
HL^1	3547	3066, 3021		1641	n.o.	1339	
(1)		3061, 3010	2916, 2884	1631	1609	1360	574
HL^2	3521	3061, 3025		1639	1615	1341	
(2)		3057, 3022	2921, 2869	1633	1607	1354	577
HL^3	3527	3074, 3023		1642	1610	1342	
(3)		3066, 3029	2929, 2842	1628	1606	1354	577

Electronic spectra

Electronic spectra of complexes and corresponding ligands were recorded in DMSO solutions. After coordination of the chalcone ligands HL^1 and HL^2, the bands a scribed to the carbonyl group (314 nm for HL^1 and 338 nm for HL^2, Figure 3(a), appeared on similar positions in the spectra of corresponding complexes **1** and **2**, which indicated coordination *via* a carbonyl oxygen atom. The band in the HL^3 spectrum at 370 nm, after coordination on the copper(II), shifted to a lower wavelength, 361 nm (complex **3**), also indicating the participation of the carbonyl group in coordination with the metal center. In the spectra of all three complexes, after coordination of the chalcone ligands, new bands appeared with maxima in the 430–450 nm region, Figure 3(b). Based on their positions and extinction coefficients they could be identified as charge transfer bands.

*Table 2. Data on electronic spectra of chalcone ligands and corresponding copper(II) complexes **1–3***

Compound	n→π*	CT
	nm (ε)	
HL^1	314 (4.26)	
(1)	314 (4.17)	443 (3.53)
HL^2	338 (4.35)	
(2)	338 (4.55)	436 (4.04)
HL^3	370 (1.23)	
(3)	361 (4.68)	434 (4.36)

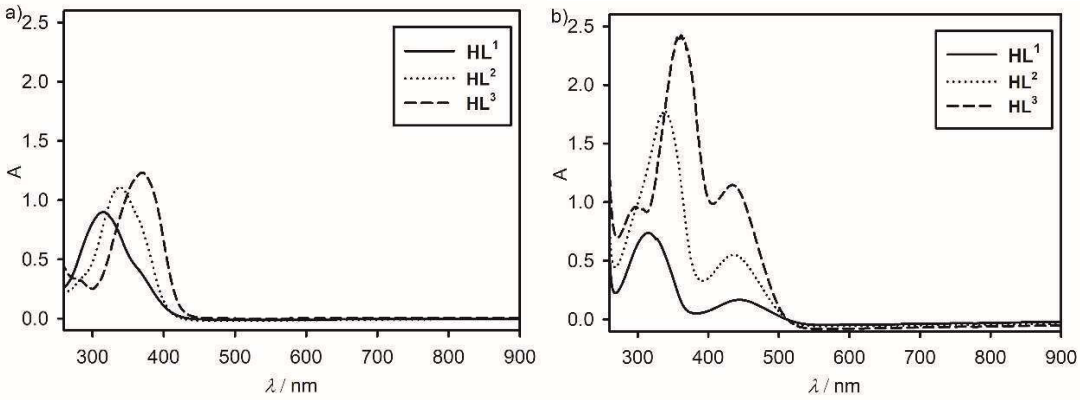

*Figure 3. Electronic spectra of free ligands HL^1– HL^3(a) and complexes **1**–**3**(b)*

3.3. Spectroscopic Evidence of the Catalysis

Catalytic activities of complexes **1**–**3** were investigated by spectroscopic measurements. DTBC was used as a substrate in all experiments due to its low oxidation potential and absence of any concomitant or successive reaction upon its oxidation to DTBQ.

In all three cases, the reaction mixture containing DTBC, hydrogen peroxide, and the observed complex showed an absorbance increase of the quinone band near 400 nm (λ_{max}= 400 nm; ε = 2818 mol^{-1} dm^3 cm^{-1}). In the absence of copper(II) complexes, no significant change in the spectrum of the DTBC was observed, which confirms the catalytic nature of this oxidation process. Complexes **1**–**3** are stable in DMSO solutions and their activity can be ascribed to the originally formulated complex species.

3.4 Kinetic Measurements

Kinetic measurements of the catalytic activity of complexes **1**–**3** were carried out in a DMSO solution using DTBC as a substrate. The chemical reaction kinetics of the oxidation of DTBC to DTBQ is pseudo-first-order and was investigated using the method of initial rates (Figure 4). The concentrations of the complexes and co-oxidant were kept constant, while the concentration of the substrate was varied.

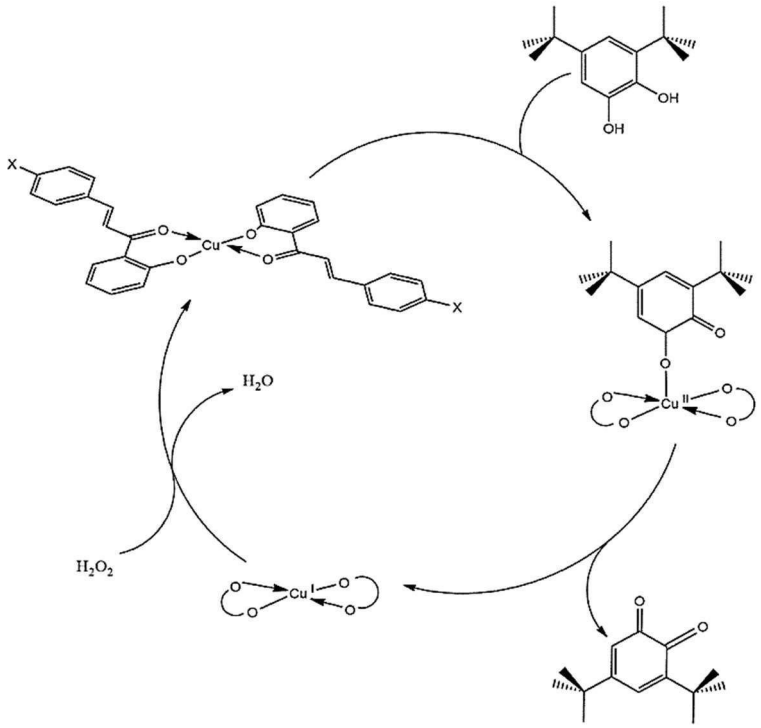

*Figure 4.Possible reaction pathway for DTBC oxidation in the presence of complexes **1**–**3***

Michaelis–Menten method of enzymatic kinetics was applied to obtain Lineweaver–Burk plot and values of catalytic parameters, the maximum reaction rate (v_{max}), Michaelis-Menten constant (K_M), catalytic efficiency, catalytic reaction rate constant (k_{cat}), turn over number (TON), and turn over frequencies (TOF) for synthesized complexes.

*Table 3. Catalytic parameters of complexes **1** and **2** for DTBC oxidation*

Complex	v_{max} / 10^{-7} mol dm^{-3} s^{-1}	K_M / 10^{-4} mol dm^{-3}	*Efficiency* / mol^{-1} dm^{-3} s^{-1}	k_{cat} / h^{-1}	TON	TOF/10^{-2} s^{-1}
1	5.06	4.23	191	291.72	54.3	9.04
2	4.20	2.08	324	241.89	42.1	7.02

Based on the conducted research, it was concluded that complexes **1** and **2** catalyze the oxidation reaction of DTBC to DTBQ and obey Michaelis-Menten kinetics in the range of observed concentrations, while complex **3** did not act as a catalyst for the mentioned reaction. This can be explained as a consequence of the significant substituent effect. Complex **3** containing chalcone ligand with electron-donating methoxy substituent in *para* position HL^3did not show catalytic properties. Complex **2**, including a methyl group as a substituent on the chalcone ligand, showed higher catalytic efficiency and greater affinity for binding to the DTBC substrate compared to complex **1** containing chloro substituent.
Reaction rate constants k_{cat} are most often used to compare the catalytic properties of observed catalysts. Complexes **1** and **2** could be compared with other examples of copper complexes possessing catalytic properties (Table 4).

*Table 4. Comparison of complexes **1** and **2** with some reported catecholase-like biomimetic complexes*

Complex	Solvent	k_{cat} / h^{-1}	Ref.
$[Cu_2(L)(\mu\text{-}OH)(H_2O)(ClO_4)_2]$	DMSO	76	[20]
$[Cu_2(L_2)(\mu OAc)](ClO_4)\times H_2O\times(CH_3)_2CHOH$	MeOH	183	[15]
$[Cu_2(HL_1)_2(\mu HL)_2]$	MeOH	752	[16]
$[Cu_2(H_2L\text{-}(CH_3)_{11})(OH)(H_2O)(NO_3)]^{3+}$	MeOH	3.24×10^4	[21]
$[Cu(phen)(OH_2)_2(NO_3)](NO_3)$	MeOH	3.91×10^3	[22]
[CuL(NCO)]	MeOH	23.5	[23]
1	DMSO	291	This work
2	DMSO	241	This work

The TON value represents the number of moles of substrate that a mole of catalyst can convert before it becomes inactivated and it is given as the ratio of the DTBQ and complex concentration at the defined time (10 min). Although the k_{cat} value for **2** is higher than for **1**, a higher TON value suggests that **1** is the more promising catalyst due to the higher conversion rate of DTBC to DTBQ for 3% as compared to complex **2**.

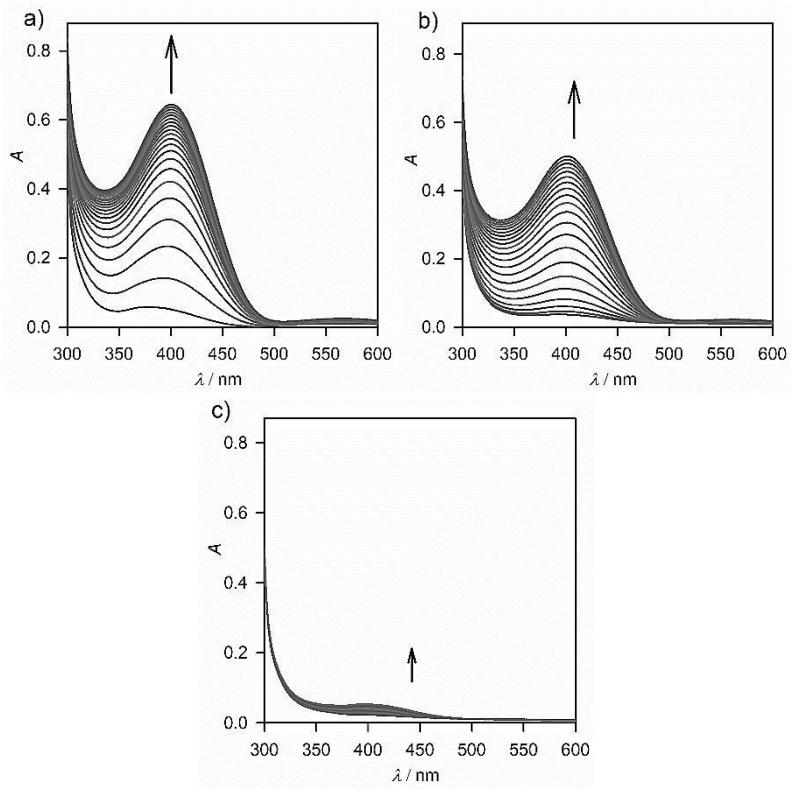

*Figure 5. Changes in the absorption spectra in the course of catalytic oxidation of DTBC (2.5×10^{-3} mol dm^{-3}) by complexes **1** (a), **2** (b) and **3** (c) (6.28×10^{-6} mol dm^{-3}) in the presence of hydrogen peroxide (0.12 mol dm^{-3}) in DMSO at room temperature during 10 minutes*

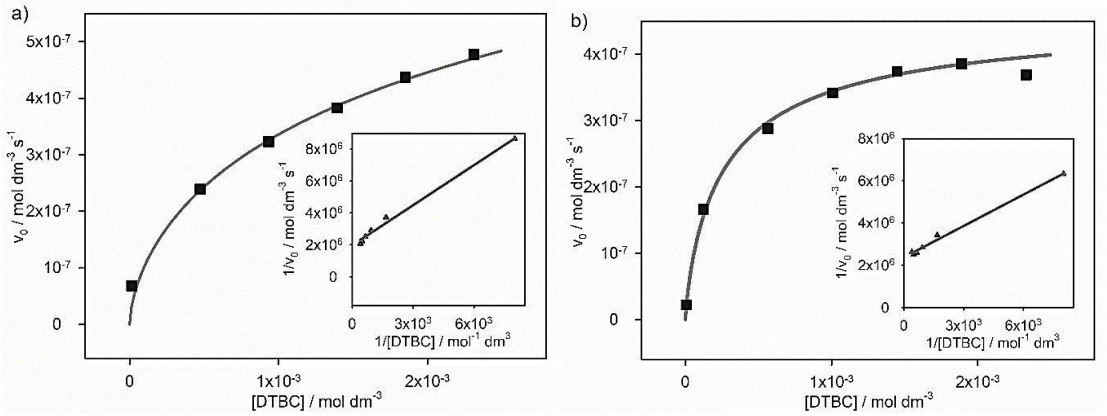

*Figure 6. Michaelis-Menten saturation curve: Dependence of the initial rate of oxidation vs DTBC concentration in the presence of the complexes **1** (a) and **2** (b). Inset: Lineweaver-Burk plot*

4. CONCLUSION

Three new copper(II) complexes were prepared by solution synthesis from copper(II) acetate and appropriate chalcone ligands (HL^1, HL^2 and HL^3). Infrared spectroscopy suggested coordination of the chalcones as bidentate anionic ligands to the metal center *via* the deprotonated hydroxyl oxygen atom and the carbonyl oxygen atom. Electron spectroscopy showed the formation of new bands in the spectra of products that were assigned to charge transfer bands of the new copper(II) chalcone complex species. Catalytic measurements revealed moderate catalytic properties of complexes **1** and **2**, while complex **3** did not catalyze the DTBC oxidation reaction. TON and TOF values suggested that **1** is the more promising catalyst due to the higher conversion rate of DTBC to DTBQ as compared to complex **2**.

5. REFERENCES

[1] Gerdemann, C., Eicken, C., Krebs, B.: The crystal structure of catechol oxidase: new insight into the function of type-3 copper proteins. Accounts of chemical research. 2002, 35, 183-91

[2] Koval, I. A., Gamez, P., Belle, C., Selmeczi, K., Reedijk: J. Synthetic models of the active site of catechol oxidase: mechanistic studies. Chemical Society Reviews. 2006, 35, 814-40

[3] Ording-Wenker, E.C., Siegler, M. A., Lutz, M., Bouwman, E.: Catalytic catechol oxidation by copper complexes: development of a structure–activity relationship. Dalton Transactions. 2015, 44, 12196-209

[4] Garai, M., Dey, D., Yadav, H. R., Choudhury, A.R., Maji, M., Biswas, B.: Catalytic fate of two copper complexes towards phenoxazinone synthase and catechol dioxygenase activity. ChemistrySelect. 2017, 2, 11040-7

[5] Balla, J., Kiss, T., Jameson, R. F.: Copper (II)-catalyzed oxidation of catechol by molecular oxygen in aqueous solution. Inorganic Chemistry. 1992, 31, 58-62

[6] Selmeczi, K., Réglier, M., Giorgi, M., Speier, G.: Catechol oxidase activity of dicopper complexes with N-donor ligands. Coordination chemistry reviews. 2003, 245, 191-201

[7] Panda, M. K., Shaikh, M. M., Butcher, R. J., Ghosh, P.: Functional mimics of catechol oxidase by mononuclear copper complexes of sterically demanding [NNO] ligands. Inorganica Chimica Acta. 2011, 372, 145-51

[8] Ackermann, J., Meyer, F., Kaifer, E., Pritzkow, H.: Tuning the activity of catechol oxidase model complexes by geometric changes of the dicopper core. Chemistry–A European Journal. 2002, 8, 247-58

[9] Sulpizio, C., Breibeck, J., Rompel, A.: Recent progress in synthesis and characterization of metal chalcone complexes and their potential as bioactive agents. Coordination Chemistry Reviews. 2018, 374, 497-524

[10] Aly, M. R. E. S., Fodah, H. H. A. E. R., Saleh, S. Y.:Antiobesity, antioxidant and cytotoxicity activities of newly synthesized chalcone derivatives and their metal complexes. European Journal of medicinal chemistry. 2014, 76, 517-30.
[11] Da Silva, J. G., Despaigne, A. A. R., Louro, S. R., Bandeira, C. C., Souza-Fagundes, E. M., Beraldo, H.: Cytotoxic activity, albumin and DNA binding of new copper (II) complexes with chalcone-derived thiosemicarbazones. European Journal of Medicinal Chemistry. 2013, 65, 415-26.
[12] Sulpizio, C., Müller, S. T., Zhang, Q., Brecker, L., Rompel, A.: Synthesis, characterization, and antioxidant activity of Zn 2+ and Cu 2+ coordinated polyhydroxychalcone complexes. Monatshefte für Chemie-Chemical Monthly. 2016, 147, 1871-81
[13] Mallikarjun, K.: Antiviral activity of substituted chalcones and their respective Cu (ii), Ni (ii) and Zn (ii) complexes. E-Journal of Chemistry. 2005, 2, 58-61
[14] Thabti, S., Djedouani, A., Rahmouni, S., Touzani, R., Bendaas, A., Mousser, H., et al.: Synthesis, X-ray crystal structures and catecholase activity investigation of new chalcone ligands. Journal Of Molecular Structure. 2015, 1102, 295-301
[15] Osório, R. E., Peralta, R. A., Bortoluzzi, A. J., de Almeida, V R., Szpoganicz, B., Fischer, F. L., et al.: Synthesis, magnetostructural correlation, and catalytic promiscuity of unsymmetric dinuclear copper (II) complexes: Models for catechol oxidases and hydrolases. Inorganic chemistry. 2012, 51, 1569-89
[16] Kahrović, E., Zahirović, A., Višnjevac, A., Osmanković, I., Turkušić, E., Kurtagić, H.: Chalcone and Flavonol Copper (II) Complexes Containing Schiff Base Co-Ligand: Synthesis, Crystal Structures and Catecholase-like Activity. Croatica Chemica Acta. 2018, 91, 195-208
[17] Rammohan, A., Reddy, J. S., Sravya, G., Rao, C. N., Zyryanov, G. V.: Chalcone synthesis, properties and medicinal applications: a review. Environmental Chemistry Letters. 2020, 18, 433-58
[18] Zengin, A., Karaoğlu, K., Emirik, M., Menteşe, E., Serbest, K.: Mononuclear Cu (II) complex of an oxime ligand derived from N-Heterocyclic hydrazide: Synthesis, spectroscopy, electrochemistry, DFT calculations and catecholase activity. Journal of Molecular Structure. 2019, 1193, 444-9
[19] Johnson, J., Yardily, A. Chalconoid metal chelates: spectral, biological and catalytic applications. Journal of Coordination Chemistry. 2019, 72, 2437-88
[20] Majumder, I., Chakraborty, P., Das, S., Kara, H., Chattopadhyay, S. K., Zangrando, E., et al.: Solvent dependent ligand transformation in a dinuclear copper (II) complex of a compartmental Mannich-base ligand: synthesis, characterization, bio-relevant catalytic promiscuity and magnetic study. RSC Advances. 2015, 5, 51290-301
[21] Banu, K. S., Chattopadhyay, T., Banerjee, A., Bhattacharya, S., Zangrando, E., Das, D.: Catechol oxidase activity of dinuclear copper (II) complexes of Robson type macrocyclic ligands: Syntheses, X-ray crystal structure, spectroscopic characterization of the adducts and kinetic studies. Journal of Molecular Catalysis A: Chemical. 2009, 310, 34-41
[22] Dey, D., Das, S., Yadav, H. R., Ranjani, A., Gyathri, L., Roy, S., et al.: Design of a mononuclear copper (II)-phenanthroline complex: Catechol oxidation, DNA cleavage and antitumor properties. Polyhedron. 2016, 106, 106-14
[23] Shyamal, M., Mandal, T. K., Panja, A., Saha, A.: Influence of anionic co-ligands on the structural diversity and catecholase activity of copper (II) complexes with 2-methoxy-6-(8-iminoquinolinylmethyl) phenol. RSC advances. 2014, 4, 53520-30

PROTECTION ENVIRONMENT AND SUSTAINABLE DEVELOPMENT

PYROPHYLLITE AS AN ECOLOGICAL MINERAL OF THE FUTURE

**Jasmina Kustura, Belma Halilhodžić, Enita Kurtanović,
Kenan Kozlo, Amra Čizmić, Adnan Teletović, Atif Hodžić, Muhamed Harbinja**
Innovative Scientific Development Center (INRC), AD Harbi LLC
Sarajevo, B&H

Keywords: pyrophyllite shale Parsovići, properties, industrial application, agriculture, environmental protection

ABSTRACT
Pyrophyllite ($Al_2Si_4O_{10}(OH)_2$) is a layered phyllosilicate mineral with a basic 2:1 crystal structure, consisting of an aluminum octahedral layer placed between two silicon tetrahedral layers (T-O-T), connected by weak Van der Waals forces, which results in easy structural disruption. Natural pyrophyllite has an electroneutral surface, which causes a hydrophobic character. Due to its unique properties, such as low thermal and electrical conductivity, high refractive behavior, low coefficient of expansion, rheological properties, low bulk density, low deformation under high temperature, and chemical inertness, pyrophyllite is widely used in various industrial branches: refractory, ceramic, construction, pharmaceutical and cosmetic industry, production of pesticides, fertilizers, paper, paints, plastics, tires. Thanks to its unique properties, pyrophyllite shale from the Parasovići deposit, Konjic, Bosnia and Herzegovina, has shown the possibility of being used in many areas of life. This paper presents the results of research so far, which confirmed the wide application of natural, modified, and enriched pyrophyllite in various industrial branches, agriculture, and environmental protection.

1. INTRODUCTION

Pyrophyllite belongs to the group of aluminosilicate minerals with the chemical formula $Al_2Si_4O_{10}(OH)_2$, and it is found in nature in the form of shale. It got its name from the Greek words *pir*-fire and *phylon*-leaf because it spreads like a fan when heated. It is a part of the isomorphic order of aluminosilicates that contain bound water. It is characterized by a three-layer crystal lattice, which has a tetrahedral structure in the outer layer, and an octahedral structure in the inner layer (Figure 1). The crystals are plate-like, soft, and greasy to the touch. It is electroneutral and not reactive in its natural form. Pyrophyllite is not soluble in water and does not swell. It is thermally stable. Depending on the admixture, the color of pyrophyllite varies from white, and gray to purple.

In previous research, the presence of 34 minerals and over 60 chemical elements have been confirmed in the pyrophyllite schist (hereinafter referred to as pyrophyllite) from the Parsovići deposit, Konjic, Bosnia and Herzegovina (Figure 2) [2-6].

Thanks to its unique properties, pyrophyllite has shown the possibility of use in many areas of life. By crushing pyrophyllite and mechanochemical activation, the structure changes, the bonds of aluminosilicate and OH groups are broken, the specific surface area and porosity of the particles increase, the size of the particles decreases, the solubility and cation exchange capacity increase, all of which contribute to its greater reactivity and surface charging. Due to its electroneutrality in its natural form, pyrophyllite has a lower CEC (cation exchange capacity) compared to other layered minerals, and its reactivity is

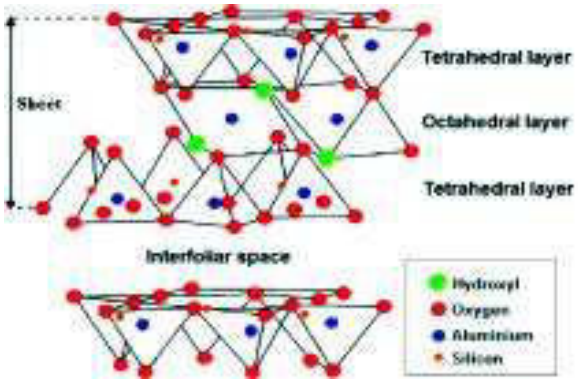

Figure 1. Pyrophyllite structure [1]

Figure 2. Pyrophyllite shale mine, Parsovići

increased by physicochemical, chemical, mechanochemical, and thermochemical treatment. By modifying pyrophyllite with organic, inorganic, polar, and non-polar surfactants, the reactivity and efficiency of pyrophyllite are improved. By modifying pyrophyllite, products with target characteristics of wide industrial-agro-ecological application are obtained. The chemical and mineralogical composition and physical properties of pyrophyllite are tabulated in Table 1, Table 2, and Table 3 [7].

Table 1. Average chemical composition of pyrophyllite

Component	SiO_2	Al_2O_3	Fe_2O_3	FeO	TiO_2	CaO	MgO	CO_2	Na_2O	K_2O	H_20^-	H_20^+	Other elements
Composition [wt. %]	61	23.1	1.1	0.25	0.12	1.85	1.94	4.30	0.61	1.44	0.61	4.66	<0.1

Table 2. Average physical characteristics of pyrophyllite

Characteristic	Value
pH	8.0 - 9.0
Hardness (by Mohs)	1.0 - 1.5
Specific gravity [g/cm^3]	2.6 - 2.8
Volumetric weight without shaking (33 μm) [g/cm^3]	0.38 - 0.42
Volumetric weight with shaking (33 μm) [g/cm^3]	0.525 - 0.55
Volumetric weight without shaking (63 μm) [g/cm^3]	0.508 - 0.53
Volumetric weight with shaking (63 μm) [g/cm^3]	0.75 – 0.82

Table 3. Average mineralogical composition of pyrophyllite

Mineral	Mineralogical composition, [wt.%]
Pyrophyllite	44 - 52 %
Quartz	12 - 18 %
Carbonates	10 - 12 %
Kaolinite	18 - 22 %
Serecite	6 - 12 %
Other minerals in smaller percentages	

2. APPLICATION OF PYROPHYLLITE IN INDUSTRY AND AGRICULTURE

AD Harbi LLC Sarajevo through its own research and research with a team of expert associates and scientific advisors from eminent scientific institutions from the country and the region, has implemented a large number of projects, studies, and scientific works, the results of which result in a wide range of possibilities for using pyrophyllite in various industrial branches, agriculture, and environmental protection. AD Harbi LLC Sarajevo continues to research the possibilities of using pyrophyllite in new, more sophisticated, and

profitable industrial branches, and to develop its own products for applied applications, as well as solutions that are environmentally efficient as possible, and innovative and fully functional in the application. Pyrophyllite is used in the following industries: refractory, ceramic, construction, chemical industry, environmental protection, agriculture, and in the cosmetic, pharmaceutical, and medical industries. The subject and goal of this paper are to present the results of previous research, knowledge, and experience in the development of new products based on the mineral pyrophyllite from the Parsovići, Konjic, Bosnia and Herzegovina, deposits in various industrial areas.

2.1 Refractory industry

Due to the property that heat treatment transforms pyrophyllite into mullite, resistant to high temperatures up to 1810 °C, with high electrical resistance, high compressive strength, tensile strength, and impact strength, pyrophyllite is widely used in the refractory industry. By researching the procedures for preparing ceramic fillers based on pyrophyllite for obtaining refractory materials and primarily refractory coatings, it was shown that pyrophyllite occupies an important place either as a final product or as a raw material for various refractory products. As a result of this research, the optimal compositions of Lost foam refractory coatings with micronized (mechanically activated) filler based on pyrophyllite (average particle size between 14 and 16 μm) were determined. Procedures for the preparation of coating suspensions were defined, which achieved predetermined properties of the coating in terms of fire resistance, desired gas permeability, easy application and adhesion to the model surfaces, easy adjustment of the thickness of the coating layers on the surface of the sand molds and cores, without the appearance of bubbles, cracking and rubbing of the dried coating layers. Coating suspensions, the density of 2000 kg/m^3, showed high sedimentation stability (below 4.5 % of precipitated substances in the first 300 min). The application of coatings based on water-based pyrophyllite filler, thinner layers (0.5x10^{-3}m), and polystyrene models of lower density (19 kg/m^3) had a positive effect on the surface quality, structural and mechanical properties of aluminum alloy castings obtained by the new casting method with polymer models [8].

2.2 Ceramic industry

Clay minerals are the most important components in traditional ceramic products. Ceramic products can be prepared using different types of clay with different proportions in the mixture, as well as different temperatures. Since pyrophyllite becomes mullite at high firing temperatures, this gives it the possibility of being used as a component in ceramic products [9]. By examining the microstructural and morphological changes of pyrophyllite during thermal treatment at 1050 °C and a pressure of 50 MPa, results were obtained that indicate that pyrophyllite can be used to obtain semipermeable membranes with a homogeneous pore arrangement, for the purpose of purifying pollutants in aqueous solutions [10,11].
In one of the works, the resistance under the effect of cavitation of samples of sintered pyrophyllite was examined. To assess the cavitation resistance, the change in the mass of the sample as a function of the cavitation time was monitored. The ultrasonic vibration method with a stationary sample was applied. Based on the value of the cavitation speed and the analysis of the morphology of the surface damage, the cavitation resistance of the tested samples based on pyrophyllite was determined. The obtained results indicate that samples of sintered pyrophyllite have satisfactory resistance to the effect of cavitation and can be used under conditions of lower cavitation loads [12].

2.3 Construction industry

Instrumental analyzes proved that activated pyrophyllite, which was applied as a mineral additive/cement replacement in cement binders, acts as a pozzolan. Cement-pyrophyllite binders showed a very similar hydration path to Portland cement with a slight acceleration in the early stages of hydration, reduced the hydration energy of cement, and increased the amount of cement mineral alite in the later stages of hydration. The micronized crystalline foil characteristic of pyrophyllite formed a micro-reinforcement inside the voids in the cement microstructure, which could improve the mechanical properties of the cementitious material [13].

The use of pyrophyllite as an ecological material in construction, more precisely as a material for making facades in areas where coal is used as an energy source, has proven to be effective. The research results confirm the possibility of using pyrophyllite with "bare" titanium dioxide as a suitable material for making facades with an air purification effect. Pyrophyllite affects the photocatalytic decomposition of coal combustion products (CO_X, NO_X, SO_X), which contributes to the improvement of air quality in polluted areas, and in this sense is an ecologically very interesting and valuable material [14].

2.4 Electrical industry

Pyrophyllite, as a material with good surface properties, can be used as an electrochemically active component, using this material as a carbon paste electrode. The obtained results open a new field for further research concerning pyrophyllite as a sensor for the detection of pollutants in water. An electroanalytical method was developed for the detection and determination of carbendazim pesticides [15,16].

2.5 Chemical industry

$LiAlH_4$ is a material suitable for hydrogen storage primarily due to the high gravimetric capacity of hydrogen. However, the relatively poor kinetics of the desorption or hydrogen release process limits its commercial use. An improvement in the reaction kinetics and a change in the reaction mechanism of hydrogen desorption from $LiAlH_4$ can occur during the synthesis of composites of this hydride with different catalytically active materials. Within the concept of green chemistry, it is desirable to use as many natural raw materials as possible, including pyrophyllite, and for this reason, the effect of the addition of pyrophyllite, which is known as a good adsorption material, on the desorption and structural characteristics of $LiAlH_4$ as a hydrogen storage material was examined [17].

2.6 Environmental protection

Pyrophyllite has shown great efficiency in the adsorption of heavy metals from contaminated wastewater as well as wastewater from electroplating plants. According to current regulations, the allowed pH value in wastewater from industrial plants before its discharge should be 7, which dictates the need for its neutralization before discharge into waterways. Optimizing the process of adsorption of heavy metals from the wastewater of the electroplating plant, it was concluded that the adsorption of metals is most favorable at a mass of pyrophyllite of 10 g, a fraction size of 0.10 mm, at pH 7 and a contact time of 2 hours [18,19].

The results of the research into the efficiency of the raw and modified pyrophyllite (modified with boric acid) in the adsorption of heavy metals speak of the justification of further research, but also of the practical application of pyrophyllite in the purification of industrial wastewater. Analysis of waste and treated water also found that pyrophyllite treatment reduces: organic carbon; ammonia; total inorganic nitrogen; total phosphorus; total alkalinity. The results showed the additional effectiveness of pyrophyllite on the

reduction of organic compounds, indicating that pyrophyllite can be an effective agent for the treatment of wastewater in mines, the metal industry, and landfill leachate [20].
Chemical stabilization of soil contaminated with heavy metals using natural aluminosilicate materials (pyrophyllite and zeolite) has generally been observed as a very effective measure from the point of view of reducing the accessibility of heavy metals in the soil, and therefore also from the point of view of reducing the possibility of their entering the plant, i.e. into the food chain. The results of this research support the thesis that zeolite, and especially pyrophyllite, have the ability to firmly bind heavy metals to their structure, which, on the one hand, reduces the possibility of their uptake by plants, and on the other hand, contributes to environmental protection, because by immobilizing heavy metals it reduces the possibility of their leaching from the surface layers of the soil into underground water courses. The use of aluminosilicate materials is not demanding from the aspect of performance and cost, so it should be taken very seriously into consideration when making a decision on the method of remediation of land contaminated with heavy metals [21,22].

2.7 Agriculture

The production of health-safe food has become a priority task for food manufacturers, thanks to the increase in consumer standards. Because of this, they operate in a split between two conflicting requirements, to produce as much food as possible while its quality is as good as possible. At the same time, the application of artificial fertilizers in agricultural production resulted in the gradual degradation of the soil as well as numerous other processes such as depletion, leaching, and soil pollution with dangerous substances from the industry. For this reason, in recent years there has been an increasing interest in the use of natural aluminosilicates in order to maintain and improve soil productivity. One such solution is pyrophyllite. Pyrophyllite is one of the best detoxifying clays, partly because it has a balanced mineral composition, and partly because it can be reduced to extremely small particle size. The smaller the particle size, the greater the specific active surface area for removing toxins. It is rich in electrolytes and exchanges a lot of free ions in the cation exchange, which makes it an excellent soil conditioner [19]. Pyrophyllite has the ability to quickly neutralize acidic solutions in dynamic conditions, as well as the ability to buffer them [23].
The two-year research carried out on cabbage of the Bravo variety confirmed the effectiveness of pyrophyllite as a bio-stabilizer and soil conditioner, its effect on increasing the pH value of the soil, on the absorption and firm cross-linking of heavy metals, and its stimulating effect on the growth and development of plants, increasing the yield and components of the nutritional value of the head Cabbage of the Bravo variety [24]. Based on a two-year study on the effect of pyrophyllite on the vitamin C content found in the Bravo F1 cabbage hybrid (*Brassica oleraceae var. Capitata*), it can be concluded that pyrophyllite has a positive effect on the vitamin C content [25].
It was established that the natural mineral pyrophyllite can be used in the production of pepper and cabbage seedlings in a protected area as an addition to the commercial substrate (pyrophyllite was used in a concentration of 20%). To continue further research, it would be best to use the following substrate mixtures: soil + earthworm + pyrophyllite, soil + earthworm + manure + peat + pyrophyllite, peat + manure + pyrophyllite, peat + manure [26].
The positive effect of pyrophyllite in the open space on the following cultivated crops was determined: vegetable crops - pepper (*Capsicum annuum*), tomato (*Solanum lycopersicum*), fruit crops - pomegranate (*Punica granatum)*, aronia (*Aronia melanocarpa)*, fig (*Ficus carica)* and medicinal cultures - lavender (*Lavandula angustifolija*), immortelle (*Helichrysum italicum*) and lemon balm plant (*Mellisa officinalis*). The changes recorded in the cultures are

vegetative - increase in plant growth and green mass (because of the silicon content in it, it affects the better habitus of the plant), strengthening of the plant stem, and generative - increase in yield, earlier ripening of fruits, better quality fruits. The results of the analyzes for the fruits, which were carried out in the laboratory of the Federal Institute of Agriculture, showed that pyrophyllite influenced the increase of dry matter and ash in the fruit, and the content of micro and macro elements. The end result was a fruit without heavy metals and pesticide residues and with an increase in nutritional value [27].

After conducting a research experiment, multiple effects of pyrophyllite on soil, yield, and quality of cabbage (fruit size, organoleptic properties, and appearance) were observed [28]. Pyrophyllite showed a positive effect on selected physiological and biochemical parameters, such as a reduction of oxidative stress in selected field crops (two varieties of wheat, Brkulja, and Spelt) and vegetable crops (salads and endives), an increase in protein concentration and, to a certain extent, an increase in chlorophyll concentration [29,30].

The use of pyrophyllite reduces the use of mineral fertilizers without negative effects on yield and quality, which ultimately enables significant material savings because it is a cheaper product than mineral fertilizers. At the same time, its application also makes an immeasurable contribution to environmental protection, because the same agrotechnical measure reduces the possibility of leaching of nutrients from the zone of the root system of cultivated culture (lettuce) into the lower layers of soil and groundwater. The fertilizer variant, in which the ratio of fertilizer and pyrophyllite was 75%:25%, proved to be the most effective combination in order to achieve the highest yield. All fertilization variants in which pyrophyllite was used showed a positive effect on increasing the plant's antioxidant capacity, especially the variant in which pyrophyllite with finer granulation was used in relation to the 25%:75% with fertilizer. The above data point to the conclusion that the use of pyrophyllite as a substitute for part of the fertilizer can significantly contribute to the increase of the antioxidant capacity of the plant, and therefore to its greater health value. Since pyrophyllite also affects the reduction of uptake and accumulation of heavy metals, the conclusion follows that its application can influence the creation of an agricultural product of greater health value. Namely, the high content of heavy metals in the edible parts of the plant is undesirable for the reason that it can negatively affect the physiological processes in the human body, on his health, and even have a carcinogenic effect [31].

Natural pyrophyllite enriched with the nitrogen of non-protein origin (NPN) from urea has shown effective application in agriculture, primarily in crop production (farming and vegetable growing, fruit growing, and viticulture) and feeding ruminants. Namely, it is concluded that the pyrophyllite-urea composite (with minor corrections by the addition of sulfur as a building block in the synthesis of essential amino acids, methionine, and cystine) can be used in the diet of ruminants as a source of nitrogen that bacteria in the rumen use for the synthesis of their own high-quality protein of microbial origin, which it is then digested in the digestive tract and used as a source of nitrogen and amino acids for the maintenance of the body and the production of meat and milk. Also, this composite in which pyrophyllite is a carrier of urea, i.e. NPN, can, with certain supplements and corrections with other minerals (P, K, etc.), be used in a process of feeding plants [32].

The use of a multifunctional fertilizer (as a complex solid inorganic fertilizer/liming material/soil improver), based on pyrophyllite and dolomite in the conditions of growing beetroot (*Beta vulgaris var. Conditiva*) had a positive effect on the formation of plant biomass (leaf length, root length, and root diameter) and an increase in root yield, which was higher by 48.97 % compared to the control treatment (CT). Fertilizing the soil with multifunctional fertilizer also had a positive effect on the chemical properties and nutritional value of beets expressed on 100 % dry matter. The pH value of the soil where

beets were grown (ET) increased from 5.06 (H_2O) and 4.04 (KCl) before sowing, to 6.40 (H_2O) and 5.73 (KCl), respectively, after harvesting the beets [33].
As part of research in agriculture, the possibility of obtaining pellets based on pyrophyllite and organic fertilizer obtained during poultry farming was investigated. Among the chemical characteristics, the pH factor was examined as an interesting indicator for the use of the product thus obtained in agriculture, especially in acidic soils. This indicator, although it is a small sample, points to the attitude that increasing the fertilizer content increases the basicity of the obtained pellets [34].
Experimental testing confirmed that pyrophyllite can be used as an effective adsorbent for the adsorption of nitrates and phosphates from artificial fertilizers, and thus can be used for the process of fertilizing plants [35,36].
Examining the effect of pyrophyllite on the quality of silage of corn plants, seven weeks after ensiling, the results showed that the presence of *Salmonella spp*. has not been proven, while the presence of *Staphylococcus aureus, Clostridium perfringens, and Clostridium spp.* was <10 cfu/g, below detection limits [37].
Pyrophyllite also showed efficiency in the adsorption of aflatoxin B1, zearalenone, and ochratoxin. In in vitro test conditions on a liquid chromatography (HPLC) instrument, it was determined that the adsorption index was better on the finer granulation sample. The researchers assume that the better adsorption index on finer-grained pyrophyllite could be the result of a larger contact surface, i.e. a higher content of pyrophyllite in the sample, which was 75 to 80 % for the finer-grained sample and 50 % for the larger-grained pyrophyllite sample. These results indicate that the finer granulation of pyrophyllite had aflatoxin B1 adsorption efficiency similar to or at the level of adsorption of this mycotoxin by other aluminosilicate minerals such as zeolite, bentonite, and similar adsorbents [38].
It was found that pyrophyllite can inhibit the development of gram-negative bacteria *Escherichia coli* (67.20 - 84.80 %) and gram-positive bacteria *Enterococcus faecalis* (74.42 - 81.33 %). Better results were achieved by using finer granulation of pyrophyllite. In contrast, no inhibition of the development of *Staphylococcus aureus* was found, probably due to the pronounced defense mechanism of this bacteria [39,40].
In vitro, testing of the effect of fractions of micro gelled and mechanically micronized pyrophyllite of different granulations added in different concentrations to the PDA nutrient medium on the growth of the fungal phytopathogens *Fusarium oxysporum, Phoma glomerata,* and *Rhizoctonia solani* showed the best result in limiting the growth of *P. glomerate* (micro gelled granulation < 100 μm and mechanically modified granulation < 45 μm) [40,41].
It was observed that pyrophyllite, and especially the mechanically modified fraction 0 - 2 mm, significantly reduces the wilting symptoms of plants and thus reduces the loss of potato yield in soil contaminated with *F. oxysporum.* The obtained results indicated the possibility of using pyrophyllite in the biological control of soil contaminated with *F. oxysporum*, which would greatly contribute to the production [40,42,43].
Since plants produce electrical signals (weak negative electric fields), electropositive dusting agent during treatment not only adhere better to plant parts but also their distribution is much more uniform than is the case with electronegative dusting agents Electropositive dusting agents can cover 2 - 3 times larger plant area than the same amount of electronegative dusting agent. In addition, these dusting agent cover well both the face and the back of the leaf and are also distributed around the bud, flowers, and lower parts of the plants. Talc, kaolin, bentonite, and diatomite have a negative electrostatic potential, and pyrophyllite, carbonates, and gypsum have a positive electrostatic potential [44].

Based on the physical properties of pyrophyllite, especially its granulometric content, particle shape, and its ability to disperse, and then electrostatic nature, as well as the results of chemical compatibility, pyrophyllite can be used without unreservedly for dusting agent formulation, for dusting tested fungicides and insecticides [45].
Pyrophyllite proved to be a good adsorbent for glyphosate (organophosphorus herbicide), so in the future, it could be used as a filter in many experiments where it is necessary to examine the possibility and efficiency of adsorption, with fact that when examining the effect of pH on the efficiency of glyphosate adsorption, the basic medium proved to be more effective. The pH value of 13.47 proved to be the most effective in terms of glyphosate adsorption [46,47].

2.8 Pharmaceutical industry

The unique physical and chemical properties of pyrophyllite make this mineral special and suitable for use in many industries and as a substitute for talc [48]. Recent research into nanocomposites as potential carriers in pharmacy is focused on the use of inorganic substances with a layered structure that are part of bioactive molecules/medicines. One such promising inorganic material with a layered structure is clay, which is also a common component in pharmaceutical products, and as a secondary or active substance. Clay is not only an "inert ingredient", it can also be used to reduce or increase dissolution rate, delay and/or target drug release, stop side effects, camouflage taste or increase stability. On the basis of testing the stability of pyrophyllite and bioactive molecule/drug using methods of thermal analysis (differential thermal analysis/thermogravimetric analysis-TGA/DTA) and Fourier transform infrared spectroscopy (FTIR), it was concluded that pyrophyllite retained good thermal stability in the powder mixture. The thermal stability and inertness of pyrophyllite are a very good basis for its potential use as a pharmaceutical carrier. Based on the value of the pre-exponential factor, it was assumed that both pyrophyllite and talc do not interact with other ingredients in the mixture [49].
Pyrophyllite clay proved to be very thermally stable. The process of thermal transformation includes the reaction of evaporation, dehydroxylation, and the formation of a new phase, mullite. Antimicrobial tests have shown that both PYRO and PYRO/Ag have antibacterial activity. Pyrophyllite has great potential for development in pharmaceutical and medical applications as a filler and can serve as an alternative to talc, as it does not contain associated toxic minerals such as asbestos [9,50].

3. CONCLUSION

Aluminosilicate natural mineral raw material pyrophyllite from the Parsovići deposit, Konjic, Bosnia and Herzegovina, thanks to its physical and chemical characteristics, in natural or modified form, is widely used in industry, through a diverse range of the above-mentioned branches. From this comes the conclusion that it is worth continuing the research in new, more sophisticated, and profitable industrial branches, in order to eventually reach the product of applied application. The results of the research should serve as a critical review of the path traveled and as a basis for defining a new direction of research and development of new products based on the mineral pyrophyllite. From the wide range of possibilities of using pyrophyllite in different industrial branches, a whole series of products will result, which will contribute to meeting the needs of the market with products of this type based on domestic raw materials, which will reduce the need for imports and increase exports.

GRATITUDE
We also express our gratitude to our professional associates and scientific advisors for their unselfish professional support: Ph.D. Mirjana Stojanović, Ph.D. Milan Adamović, Ph.D. Jasmina Grbović-Novaković, Ph.D. Tanja Trtić-Petrović, Ph.D. Ljubiša Andrić, Ph.D. Dragan Radulović, Ph.D. Nedžad Alić, Ph.D. Suzana Atlagić-Gotovac, Ph.D. Dijana Jelić, Ph.D. Ahmed Džubur, Ph.D. Senad Murtić, Ph.D. Duška Delić, Ph.D. Ivana Koleška, Ph.D. Aleksandra Bočarov-Staničić.

4. REFERENCES

[1] *https://images.search.yahoo.com/search/images?p=pyrpphillite+structure&fr=mcafee&type=E210US91213G0&imgurl=https%3A%2F%2Fwww.researchgate.net*
[2] Alić N.: Istraživanje mogućnosti koncentracije pirofilita iz ljubičastog varijiteta škriljca, ležišta Parsovići, Univerzitet u Tuzli, Rudarsko geološko građevinski fakultet, Tuzla, 2020.
[3] Izvještaj o rezultatima ispitivanja ruda i stena pirofilita iz Konjica, Rudarsko geološki fakultet, Beograd, 1964.
[4] Alumina d.o.o. Zvornik: Rezultati analize uzoraka firme AD HARBI d.o.o., Sarajevo, 2021.,
[5] Bureau Veritas Commodities Canada Ltd., University of Zagreb, Department of Geology: Certificate of Analysis, 2021.
[6] PD AD Harbi d.o.o. Sarajevo, 2018.
[7] OOUR "RUDAR" KONJIC JUGOSLAVIJA, Feroelektro Sarajevo, Pirofilit
[8] Andrić Lj., Radulović D., Pavlović M., Petrov M., Stojanović J.: Mogućnost primene pirofilita kao punioca u vatrostalnim premazima, Zaštita materijala 61 (3) 210 - 219 (2020)
[9] Jelić D., Todorović J., Saletović M., Šmitran A., Mentus S.: Thermal stability and antimicrobial properties of pure and modified pyrophyllite (PYRO/Ag) clay, Journal of Thermal Analysis and Calorimetry, 148(4) 2022.
[10] Tošić K.: Karakterizacija termički tretiranog pirofilita, Univerzitet u Beogradu, Fakultet za fizičku hemiju, Master rad, 2021.,Beograd
[11] Tošić K., Paskaš-Mamula B., Novaković N., Medić Ilić M., Milanović I., Dimitrijević D., Grbović Novaković J.: Thermally activated pyrophyllite as ceramic membrane, Nineteenth Young Researchers Conference-Materials Science and Engineering December 1-3, 2021, Belgrade, Serbia
[12] Andrić LJ., Pavlović M., Dojčinović M., Radulović D.: Određivanje otpornosti na dejstvo kavitacije uzoraka pirofilita, Zaštita materijala 62 (2), 126 - 134 (2021)
[13] Terzić A., Radulović D., Pezo M., Stojanović J., Pezo L., Radojević Z., Andrić LJ.: Prediction model based on artificial neural network for pyrophyllite mechano-chemical activation as an integral step in production of cement binders, Construction and Building Materials, Volume 258, 20 October 2020.
[14] Gotovac-Atlagić S., Kostadinović A., Mirošljević D., Sukur S., Stević D.: TiO_2/Pyrophyllite Natural Alumosilicate Filler for Air-purifying Facades, Regional butterfly innovation award 2022.
[15] Mitrović-Rajić A., Milićević J., Gotovac-Novaković J.: Development of modified pyrophyllite carbon paste electrode for carbendazim detection, Materials and Manufacturing Processes, 2022.
[16] Milićević J., Kurko S., Paskaš-Mamula B., Trtić-Petrović T., Pantić T., Milošević-Govadarović S., Hodžić A., Grbović-Novaković J.: Elektrochemical behaviouof pyrophylitte carbon paste composite electrode, ESC-IS 2028., 3rd Int. Symposium on Materials for Energy Storage and Conversion, Belgrade, Serbia, 2018.
[17] Grbović-Novaković J., Kurko S., Pantić T., Govedarović-Milošević S.: $LiAlH_4$-pyrophyllite nanocomposite as a potential material for solid-state hydrogen storage, Međunarodni simpozij o materijalima za pohranu i pretvorbu energije – mESC-IS 2018, Beograd, Srbija, 10.-12. 9. 2018.
[18] Kulović E.: Utvrđivanje kapaciteta adsorpcije teških metala iz vode na pirofilitu, Univerzitet u Sarajevu, Priridno-matematički fakultet, Magistarski rad, 2017., Sarajevo
[19] Halilović N.: Optimizacija procesa adsorpcije teških metala iz otpadne vode na pirofilitu, Univerzitet u Sarajevu, Prirodno-matematički fakultet, Magistarski rad, 2018., Sarajevo

[20] Trtić-Petrović T., Pušica I., Purenović M., Vaštoh Đ.: Mechanically and chemically modified pyrophyllite for removal of heavy metals frome aqueous solutions, Engineering, Environment and Materials in Processing Industry 2021, Jahorina
[21] Čivić H., Murtić S., Sijahović E.: Elaborat o modelima zaštite i remedijacije zemljišta onečišćenim teškim metalima u industrijskim područjima Federacije Bosne i Hercegovine, Univerzitet u Sarajevu, Poljoprivredno-prehrambeni fakultet, 2020., Sarajevo
[22] Murtić S., Čivić H., Sijahović E., Koleška I., Jurković J., Tvica M.: Use of pyrophyllite to reduce heavy metals mobility in a soil environment, Agron. Res., 2020, 18, 194–205
[23] Sukur S.: Kinetika neutralizacije kiselih rastvora suspenzijom prirodnog pirofilita, Univerzitet u Banjoj Luci, Prirodno-matematički fakultet, Diplomski rad, 2020., Banja Luka
[24] Pašić S.: Ispitivanje uticaja pirofilita kao hranjiva na prinos i hranidbenu vrijednost kupusa sorte Bravo, Univerzitet „Džemal Bijedić“ Mostar, Agromediteranski fakultet, Diplomski rad, 2019., Mostar
[25] Pašić S., Govedarica-Lučić A., Knežević D., Stjepanović S.: Examination of influence of different pyrophyllite fertilization treatments on vitamin C content in cabbage Hybrid Bravo (*Brassica oleracea var. Capitata*), 3rd International Symposium Modern Trends Agricultural Production Rural Development and Environmental Protection, 2021., Vrnjačka Banja, Serbia
[26] Džubur A., Hadžiabulić A., Rahimić A., Aliman J., Duraković Ć., Hasanbegović J., Kaljanac A., Kukić M., Golubić M., Đikić A., Kozić A.: Uticaj pirofilita na proizvodnju rasada paprike i kupusa u zaštićenom prostoru, AD Harbi u saradnji sa Univerzitetom u Mostaru, Agromediteranski fakultet, 2017, Mostar
[27] Džubur A., Kaljanac A., Kukić M., Golubić M., Đikić A., Kozić A.: Izvještaj za eksperimentalni poligon u Blagaju, AD Harbi u saradnji sa Univerzitetom u Mostaru, Agromediteranski fakultet, 2017, Mostar
[28] Kurtović O., Harbinja M., Kadić H., Kaljanac A., Kozić S.: Upotreba pirofilita u poljoprivrednoj proizvodnji sa posebnim aspektom na ekologiju, prinos i kvalitet kupusa, AD Harbi u saradnji sa Federalnim zavodom za poljoprivredu, Sarajevo, 2017.
[29] Koleška I.: Rezultati istraživanja uticaja pirofilita “Parsovići” Konjic na biohemijske parametre kod dvije vrste žitarica, Univerzitet u Banjoj Luci, Poljoprivredni fakultet, 2019., Banja Luka
[30] Koleška I.: Rezultati istraživanja uticaja pirofilita “Parsovići” Konjic na odabrane fiziološke i biohemijske parametre kod zelene salate i endivije u različitim uslovima fertilizacije, Univerzitet u Banjoj Luci, Poljoprivredni fakultet, 2019., Banja Luka
[31] Murtić S.: Primjena pirofilita kao oplemenjivača zemljišta u uzgoju povrtnih kultura, Univerzitet u Sarajevu, Poljoprivredno-prehrambeni fakultet, 2019., Sarajevo
[32] Adamović M., Stojanović M., Bočarov-Stančić A., Harbinja M., Kustura J.: Uticaj prirodnog i oplemenjenog pirofilita na prinos crnog luka (*Allium cepa*), XI International Symposium on Agricultural Sciences Agrores, 2022., Trebinje, Bosnia and Herzegovina
[33] Stojanović M., Adamović M., Kustura J., Kurtanović E., Harbinja M.: Multifunctional fertilizer based on pyrophyllite in accordance with the regulation EU 2019/1009, 53rd International October Conference on Mining and Metallurgy, 2022, Bor, Serbia,
[34] Alić N.: Preliminarna laboratorijska istraživanja u proizvodnji peleta od pirofilita iz Parsovića, Univerzitet u Tuzli, Rudarsko-geološko-građevinski fakultet, 2017., Tuzla
[35] Hasanbegović E.: Utvrđivanje kapaciteta adsorpcije nitrata iz umjetnih gnojiva i tla na pirofilitu, Univerzitet u Sarajevu, Prirodno-matematički fakultet, Magistarski rad, 2018., Sarajevo
[36] Bradić A.: Utvrđivanje kapaciteta adsorpcije fosfata iz vještačkih gnojiva i tla na pirofilitu, Univerzitet u Sarajevu, Prirodno-matematički fakultet, Magistarski rad, 2017., Sarajevo
[37] Adamović M., Stojanović M., Harbinja M., Maslovarić M., Bočarov-Stančić A., Pezo L.: Efficiency investigation of the use of pyrophyllite in ensiling maize plant, Food and Feat Research, Journal of the Institute of Food Technology – FINS Univesity of Novi Sad, 2020.
[38] Radulović D., Andrić Lj.: Studija fizičko-hemijskih, mineraloških i tehnoloških ispitivanja pirofilitskog škriljca ležišta „Parsovići“ Konjic (Bosna i Hercegovina), Institut za nuklearne i druge mineralne sirovine, Beograd, 2019.

[39] Dimitrijević-Branković S.: Izveštaj o ispitivanju potencijala antimikrobne aktivnosti uzoraka pirofilita, Tehnološko-metalurški fakultet u Beogradu, 2018.
[40] Bočarov-Staničić A., Maslovarić M., Krulj J., Bodroža-Solarov M., Jovanović R., Beskorovajni R., Adamović M.: Contribution of pyrophyllite to the production of safe food-antimicrobial activities, VII International Congress, Engineering, Environment and Materials in Process Industry, Jahorina, Republic of Srpska, BIH, 2021.
[41] Delić D.: Izveštaj o istraživanju uticaja mehanički i mikrogelovanog modifikovanog pirofilita na suzbijanje rasta micelija fitopatogenih gljiva i njegove moguće primjene kao aktivne materije u sredstvima za zaštitu bilja, Univerzitet u Banjoj Luci, Poljoprivredni fakultet, 2019., Banja Luka
[42] Delić D.: In vivo istraživanja antifungalnog dejstva mehanički modifikovanog pirofilita u krompiru na gljive iz roda Fusarium, Univerzitet u Banjoj Luci, Poljoprivredni fakultet, 2020., Banja Luka
[43] Voruna M.: Ispitivanje efikasnosti pirofilita u suzbijanju Fusarium oxysporum (Snyd. et Hans) u krompiru, Univerzitet u Banjoj Luci, Poljoprivredni fakultet, Završni rad, 2020., Banja Luka
[44] Fizičko-hemijska svojstva pesticida i metode njihovog određivanja, Poljoprivredni fakultet Novi Sad, Laboratorija za fitofarmaciju, 1965.
[45] Ostojić N.: Istraživanje domaćih sirovina kao razređivača za proizvodnju praškovitih hemijskih sredstava za zaštitu bilja, Institut za zaštitu bilja NR Srbije, 1967., Beograd
[46] Boloban N.: Spektrofotometrijsko određivanje glifosata i njegova adsorpcija na pirofilitu, Univerzitet u Sarajevu, Prirodno-matematički fakultet, Završni rad, 2020., Sarajevo
[47] Tolić T.: Ispitivanje uticaja pH na adsorpciju glifosata na pirofilit, Univerzitet u Sarajevu, Prirodno-matematički fakultet, Završni rad, 2021., Sarajevo
[48] Kostadinović A., Balaban M., Senatore A., Sarno M., Cirillo C., Massiani P., Baghdad K., Launay F., Gotovac-Atlagić S.: Natural Pyrophyllite as a Substitute for Talc in Medical and Pharmaceutical Applications, International Conference on Medical and Biological Engineering, Switzerland, 2019.
[49] Šmitran A., Božić Lj., Đermanović M., Bojanić Lj., Jelić D.: Nanocomposite (clay based) as suitable carriers for bioactive molecules: stability and antimicrobial aspect, Journal of Hygienic Engineering and Design, 2021.
[50] Todorović J., Saletović M., Mihajlović D., Gajić D., Blagojević D., Jelić D.: Development of long-lasting antimicrobial and potential hemostatic nanocomposites (pyrophyllite based) with PVP-coated colloidal silver nanoparticles, Contemporary Materials, XIII-1 (2022)

REMOVAL OF HEAVY METALS FROM LANDFILL LEACH WATER USING PYROPHYLLITE AS ADSORBENT

**Jasmina Kustura, Belma Halilhodžić, Enita Kurtanović,
Amra Čizmić, Kenan Kozlo, Adnan Teletović, Atif Hodžić, Muhamed Harbinja**
Innovative Scientific Development Center (INRC), AD Harbi LLC
Sarajevo, B&H

Keywords: pyrophyllite Parsovići, adsorption, heavy metals, landfill water

ABSTRACT
Leachate water from sanitary landfills represents one of the most complex global environmental problems. This paper examines the possibility of using aluminosilicate material, pyrophyllite, from the Parsovići deposit, as an adsorbent. It was researched the influence of two granulations of pyrophyllite (0-53 μm and 0-100 μm) on the degree of adsorption of heavy metals (Fe, Ni, Mn) from leachate water from the municipal landfill "Desetine", Tuzla. The adsorption experiment was performed using the Batch method, depending on the contact time between the adsorbent and the adsorbate, the mixing speed, and the mass of the adsorbent, pyrophyllite, through two treatments. The results indicate a higher efficiency of the finer fraction of pyrophyllite, and in the competition of the three examined metals, iron is completely removed in the first treatment with both granulations and then nickel with finer granulation and manganese with coarser. After the first treatment, the unpleasant smell was removed, which is certainly a consequence of the removal of ammonia compounds as the most abundant compounds in leachate water. In these pioneering researches, pyrophyllite proved to be effective, and at the same time, it is a cheap, easily available, and environmentally friendly material for leachate water purification.

1. INTRODUCTION

Leachate water from sanitary landfills represents highly polluted wastewater and can be defined as all water that has "been in contact" with waste disposed of at the landfill. Leachate landfill water is created by the percolation of precipitation through the layers of disposal of waste, then partly originates from water that is included in the composition of disposed waste, and partly arises during the process of decomposition of waste [1,2].

The amount and quality of leachate formed in the body of the landfill depends on the size of the landfill, age, working conditions, biological, chemical, and physical processes at the landfill, climatic conditions at the location, composition, and amount of waste that is disposed of, etc.

Landfill leachate water is mainly loaded with the following pollutants [3]:

- nitrogen compounds in organically bound form or in the form of ammonia,
- compounds with phosphorus,
- heavy metals
- cations - the most common cations that occur are Na^+, K^+, Mg^{2+}, Ca^{2+}
- anions - Cl^-, SO_4^{2-}, S^{2-} i HCO^{3-}
- organic pollution
- chlorinated hydrocarbons and pesticides
- specific organic compounds: aromatic hydrocarbons, phenols, chlorinated aliphatic compounds.

Conditions for the treatment of leachate water are prescribed by legal acts, and the application of treatment technology depends on the amount and composition of leachate water and the conditions of discharge into an open watercourse or public drainage system [4].
Mechanical, biological, and chemical purification procedures are used for wastewater treatment. Chemical purification processes are processes in which purification is carried out using certain chemical reactions or certain physical-chemical phenomena. The basic procedures of chemical wastewater treatment are the removal of certain dissolved substances: chemical precipitation, ion exchange, oxidation, aeration, and adsorption [5].
Adsorption is a diffusion operation by which one or more components are removed from the gas or liquid phase using solid porous materials, called adsorbents. A solid substance on the surface on which the adsorption process takes place is called an adsorbent, while the substance that binds is called an adsorbate [6].
Adsorption is performed under the influence of physical or chemical forces when the adsorbed ions or molecules come close enough to the adsorbent. Physical phenomena occur in the form of Van der Waals electrostatic forces. Chemical adsorption occurs when molecules on the surface of the adsorbent and adsorbate molecules react. The effect of adsorption depends on the total surface area of the grain by mass, i.e. of the specific surface area [7].
The most commonly used adsorbents in wastewater treatment are activated carbon, silica gel, zeolites, and more recently the so-called "low-cost" adsorbents (waste biomass such as sawdust of various types of wood, straws of various kinds of wheat, rice husks, walnut husks, hazelnut husks, stems and leaves of various types of plants, etc.) [8].
Clay minerals, including pyrophyllite, are highly valued for their adsorptive properties. The widespread use of clays in the industry for wastewater treatment applications is often recommended today due to their local availability, technical feasibility, engineering application, ions, and cost-effectiveness [9].
Clay minerals appear as colloidal aggregates of small particles. Their large surface area is responsible for a number of unique physical and chemical properties such as cation exchange and pH-dependent sorption [10].
Pyrophyllite has shown great efficiency in the adsorption of heavy metals from contaminated wastewater as well as wastewater from electroplating plants. According to current regulations, the allowed pH value in wastewater from industrial plants before its discharge should be 7, which dictates the need for its neutralization before discharge into waterways. Optimizing the process of adsorption of heavy metals from the wastewater of the electroplating plant, it was concluded that the adsorption of metals is most favorable at a mass of pyrophyllite of 10 g, a fraction size of 0.10 mm, at pH 7, and a contact time of 2 hours [11,12].
The results of the research into the effectiveness of raw and modified pyrophyllite (modified with boric acid) in the adsorption of heavy metals speak of the justification of further research, but also of the practical application of pyrophyllite in the purification of industrial wastewater. Analysis of waste and treated water also found that pyrophyllite treatment reduces: organic carbon, ammonia, total inorganic nitrogen, total phosphorus, and total alkalinity. The results showed the additional effectiveness of pyrophyllite on the reduction of organic compounds, indicating that pyrophyllite can be an effective agent for the treatment of wastewater in mines, the metal industry, and landfill leachate water [13].
Preliminary experimental results of heavy metal removal (Pb, Cu, Cd, Zn and Ni) with PIR (pyrophyllite), PIR-B (pyrophyllite modified with boric acid) and PIR-B-V (pyrophyllite modified with boric acid and washed with water) singled out pyrophyllite PIR as the most effective adsorbent, which has a particular affinity for lead: 47.25 mg/g, for the described

operating conditions. This capacity stands out in relation to pyrophyllites from other sites. During the conduct of the experiment, the pH value was not adjusted, and during the sorption of lead ions, there was the smallest deviation between the initial and final pH values. Due to the fact that unmodified pyrophyllite was used without adjusting the pH value, the application itself is more economically profitable and simpler. Based on these experimental results, pyrophyllite can be used to remove lead from wastewater [14].
Chemical stabilization of soil contaminated with heavy metals using natural aluminosilicate materials (pyrophyllite and zeolite) has generally been shown to be a very effective measure from the point of view of reducing the accessibility of heavy metals in the soil, and therefore also from the point of view of reducing the possibility of their entering the plant, i.e. into the food chain. The results of this research support the thesis that zeolite, and especially pyrophyllite, have the ability to firmly bind heavy metals to their structure, which, on the one hand, reduces the possibility of their uptake by plants, and on the other hand, contributes to environmental protection, because by immobilizing heavy metals of metals reduces the possibility of their leaching from the surface layers of the soil into underground water courses [15, 16].
During the research, pyrophyllite proved to be a good adsorbent for glyphosate (organophosphorus herbicide), so in the future, it could be used as a filter in many experiments where it is necessary to examine the possibility and efficiency of adsorption [17].
Taking into account all previous research that was carried out on a laboratory-prepared sample contaminated with heavy metals, the goal of this work was to examine the effectiveness of pyrophyllite, as a heavy metal adsorbent, in the process of purifying waste landfill water.

2. MATERIALS AND METHODS

The removal of toxic metals from wastewater through the process of adsorption on natural materials such as clays is an efficient, inexpensive, and environmentally friendly procedure for preserving the environment. The material used in this work is pyrophyllite shale (hereafter pyrophyllite) from the Parsovići deposit, Konjic, Bosnia and Herzegovina. Pyrophyllite belongs to the group of aluminosilicate minerals of the chemical formula $Al_2Si_4O_{10}(OH)_2$, and in nature, it is found in the form of shale. It got its name from the Greek words *pir*-fire and *philon*-leaf because it spreads like a fan when heated. It is part of the isomorphic order of aluminosilicates that contain bound water. It is characterized by a three-layer crystal lattice, which has a tetrahedral structure in the outer layer, and an octahedral structure in the inner layer. The crystals are plate-like, soft, and greasy to the touch. It is electroneutral and not reactive in its natural form. Pyrophyllite is not soluble in water and does not swell. It is thermally stable. Depending on the admixture, the color of pyrophyllite varies from white, and gray to purple. The chemical and mineralogical composition and physical properties of pyrophyllite are shown in Tables, 1, 2, and 3:

Table 1. Average chemical composition of pyrophyllite

Composition	SiO_2	Al_2O_3	Fe_2O_3	FeO	TiO_2	CaO	MgO	CO_2	Na_2O	K_2O	H_20^-	H_20^+	Other elements
%	61±	23.1±	1.1	0.25	0.12	1.85	1.94	4.30	0.61	1.44	0.61	4.66	<0.1

Table 2. Average physical properties of pyrophyllite

pH	8.0-9.0
Hardness (by Mohs)	1.0-1.5
Specific gravity g/cm^3	2.6-2.8
Volumetric weight without shaking (33 μm) u g/cm^3	0.380-0.420
Volumetric weight with shaking (33 μm) u g/cm^3	0.525-0.550
Volumetric weight without shaking (63 μm) u g/cm^3	0.508-0.530
Volumetric weight with shaking (63 μm) u g/cm^3	0.750-0.820

Table 3. Average mineralogical composition of pyrophyllite

Pyrophyllite	44-52 %
Quartz	12-18 %
Carbonates	10-12 %
Kaolinite	18-22 %
Serecit	6-12 %
Other minerals in smaller percentages	

Pyrophyllite has naturally hydrophobic properties on the surface in aqueous solutions, which acts as a neutral adsorption site, accessible for non-polar organic species. Edges are hydrophilic in aqueous solutions. Cation exchanges (e.g. Al^{3+} instead of Si^{4+} in the tetrahedral layer or Mg^{2+}, Fe^{2+}, Ti^{2+} instead of Al^{3+} in the octahedral layer) contribute to the negative charge which contributes to the adsorption of cations or organic polar pollutants.
A sampling of pyrophyllite was carried out at the site of the Parsovići mine, Konjic, Bosnia and Herzegovina. The pyrophyllite samples used were mechanically activated by crushing, grinding, and sieving. The effect of mechanochemical activation of pyrophyllite leads to significant changes in the mineral structure, i.e. to partial amorphization, due to an increase in the number of lattice defects and deformations in the crystal structure, which results in an increase in specific surface area and reactivity. During grinding, easy splitting of layers occurs, while ionic and covalent bonds in the structure are broken at the edges. This is why flat, layered surfaces are hydrophobic while edges are hydrophilic in aqueous solutions, forming negatively charged sites. Two granulation samples: 0-53 μm and 0-100 μm were used to test the adsorption of heavy metals in this work.
Leachate landfill water was sampled at the sanitary municipal landfill "Desetine", Tuzla. The basic characteristics of landfill soil are the structure of sediments: clay, marl, sandstone, conglomerate, and sand. Clays and marls, i.e. the zones they build act as a hydrogeological insulator, while the zone with conglomerates, sand, and sandstones represent a collector of integral porosity. The greater the thickness of the clay and the greater its density, the greater the effect of purifying the filtrate. All leachate water from the waste material and from the surface, porous soil located on the impermeable layer is collected by a drainage system and controlled under an earthen dam [18]. Collected wastewater does not undergo any purification treatment before discharge into the recipient, surface water.
Parameters that exceed the permitted limit value in relation to the current legal regulation are heavy metals: Fe, Ni, Mn, and biological oxygen consumption (BPK_5). In this paper, the focus of purification is on the removal of heavy metals to the satisfactory values prescribed by Regulation [4].
Heavy metal adsorption experiments were performed using the "Batch" method, direct contact of a certain amount of pyrophyllite, and a real sample of landfill leachate in the Laboratory of AD Harbi LLC, Sarajevo.

3. EXPERIMENTAL PART

Visual characteristics of the initial sample of landfill leachate water: dark yellow, slightly turbidity water with a very sharp and unpleasant smell.

The leachate water is divided into three parts for further treatment:

- **Sample 1** - landfill water without treatment,
- **Sample 2** - landfill water for treatment with pyrophyllite granulation 0-53 μm in a concentration of 5%,
- **Sample 3** - landfill water for treatment with pyrophyllite granulation 0-100 μm in a concentration of 5%.

The laboratory equipment used was a laboratory balance, a magnetic stirrer type Velp Scientifica, an electric vacuum pump type KNF Neuberger and other standard laboratory accessories and dishes. Pyrophyllite granulation 0-53 μm and 0-100 μm in a concentration of 5% were added to water samples 2 and 3, after which they were mixed on a laboratory stirrer at a speed of 200 rpm, for 2 hours (*Figure 1*).

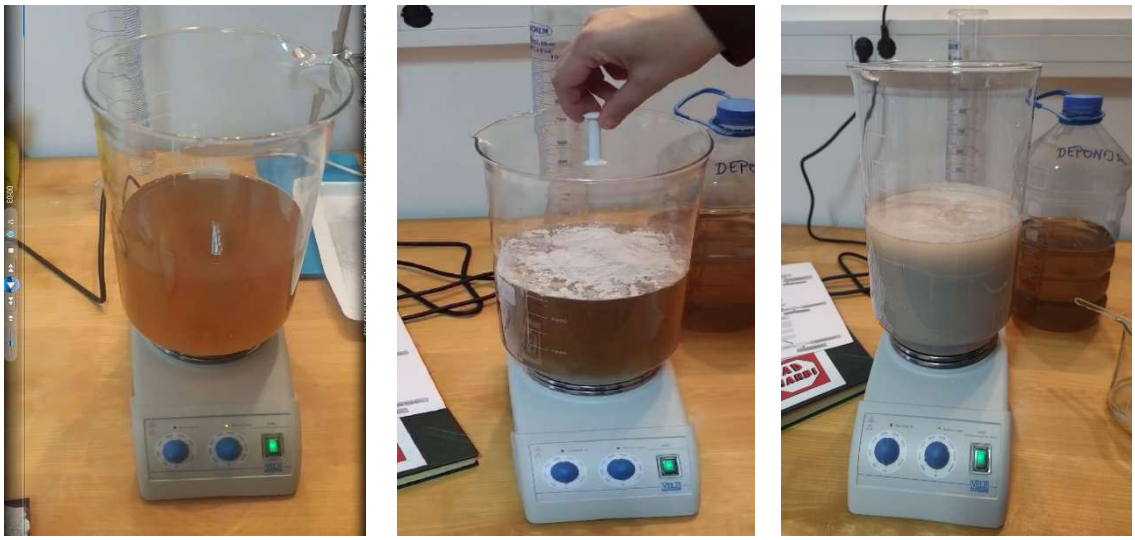

a) *b)* *c)*

Figures1. Sample of landfill leachate water before a), during b), and after c) the addition of pyrophyllite

At the end of 2 hours, the mixture of wastewater and pyrophyllite was filtered on a Büchner funnel, through a filter paper blue strip with the use of an electric vacuum pump, for assisted filtration. The treatment was repeated twice with both granulations of pyrophyllite, by adding the same amount of pyrophyllite (concentration 5%) to the filtrates after the first treatment.

Laboratory determination of the content of iron, nickel, and manganese in leachate landfill water was done in cooperation with the Laboratory of the Institute of Chemical Engineering Tuzla, using standard methods EPA Method 7000 B and BAS ISO 11047:2000. Both mentioned methods are based on flame atomic absorption spectrophotometry, and instruments manufactured by Perkin Elmer, type Optima 2100 DV (optical emission spectrometer-plasma) and manufactured by VARIAN, type AA 200 (Atomic Absorption Spectrometer) were used for testing.

4. RESULTS AND DISCUSSION

Below is a tables and figures overview of experimentally obtained results.

Table 4. Initial and limiting pH values and metal values

Metal	Concentration in the initial water sample (mg/l)	* Limit value for surface water bodies (mg/l)
Fe	2.766	2.0
Ni	0.656	0.5
Mn	3.307	1.0
pH	7.12	6.5-9.0

* *in accordance with the applicable legislation, Annex 1. [4]*

Table 5. pH value, metal concentrations in the initial sample of landfill leachate water, and after I and II treatment with pyrophyllite granulation 0-53 µm

Metal	Concentration in initial sample (mg/l)	I treatment (mg/l)	II treatment (mg/l)
Fe	2.766	<0.006	<0.006
Ni	0.656	0.117	0.108
Mn	3.307	1.096	0.201
pH	7.12	7.42	7.63

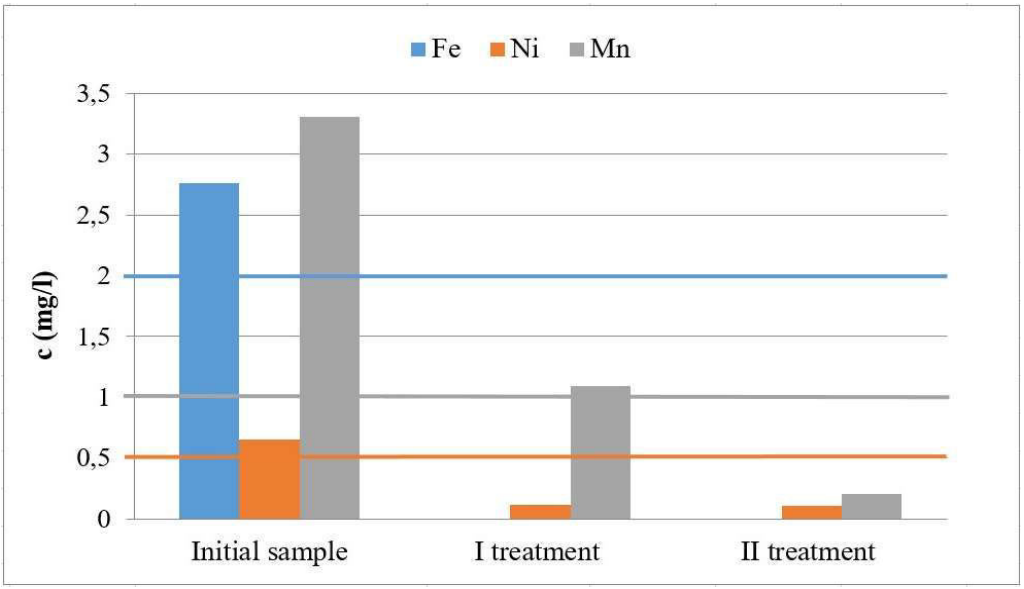

Figure 2. Presentation of limiting metal concentrations, metal concentrations in the initial sample of leachate landfill water and after I and II treatment with pyrophyllite granulation 0-53 µm

Table 6. pH value, metal concentrations in the initial sample of leachate landfill water after I and II treatment with pyrophyllite granulation 0-100 µm

Metal	Concentration in initial sample (mg/l)	I treatment (mg/l)	II treatment (mg/l)
Fe	2.766	0.231	<0.006
Ni	0.656	0.200	0.107
Mn	3.307	0.665	0.198
pH	7.12	7.37	7.44

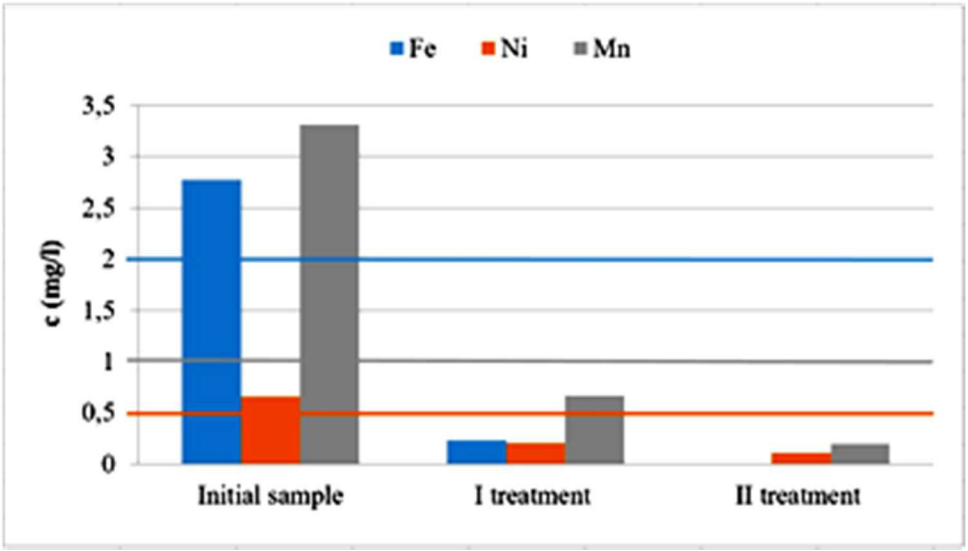

Figure 3. Presentation of limit concentrations of metals, the concentration of metals in the initial sample of landfill leachate water after Ist and IInd treatment with pyrophyllite granulation 0-100 µm

Table 7. Overview of adsorption efficiency depending on pyrophyllite granulation

Metal	% adsorption			
	I treatment 0-53 µm	I treatment 0-100 µm	II treatment 0-53 µm	II treatment 0-100 µm
Fe	100.0	91.6	0	100
Ni	82.2	69.5	7.7	46.5
Mn	66.9	79.9	81.7	70.2

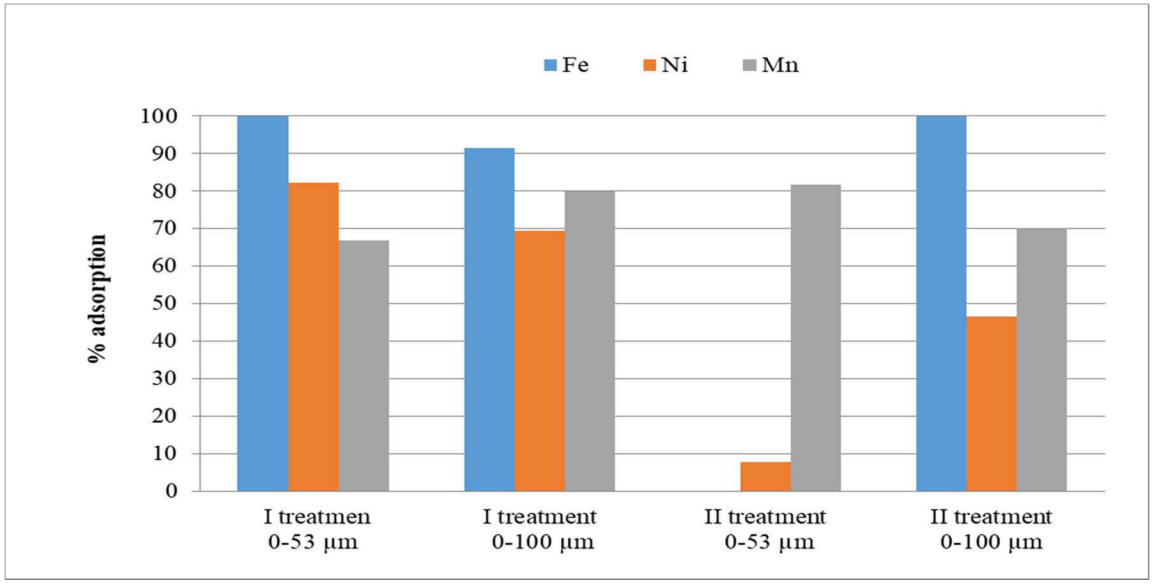

Figure 4. Presentation of adsorption efficiency depending on granulation

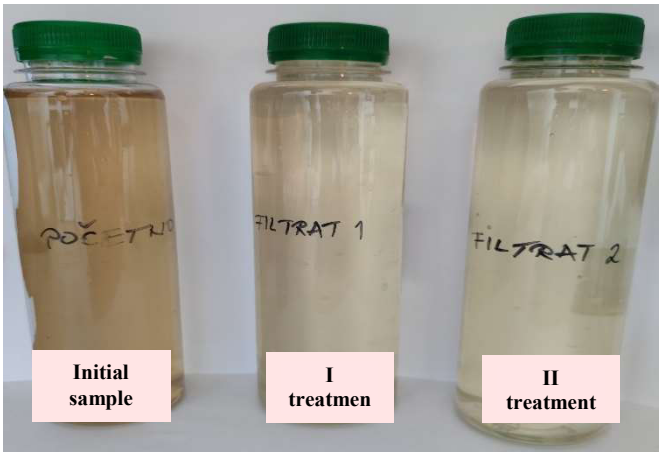

Figure 5. Visual representation of samples of landfill leachate before and after treatments

After the first treatment, the unpleasant smell was significantly reduced in both treated samples, and after the second it was almost gone. As leachate water is rich in ammonia compounds, with an intense smell, it is clear that pyrophyllite plays a role in binding them and neutralizing the smell. After both treatments of landfill leachate with pyrophyllite, a lighter color of the sample is observed, as seen in Figure 5.

When it comes to the change in pH value, the initial sample had a value of 7.12, and after the IInd treatment, the pH value was 7.63 (for granulation 0-53 μm) and 7.44 (for granulation 0-100 μm). An increase in pH, i.e. alkalinity of the environment, indicates an increase in hydroxyl ions and cations as a consequence of adsorption chemistry.

The results of the experiment conducted on Sample 1 (pyrophyllite granulation 0-53 μm) are shown in Table 5 indicate a decrease in the concentration of iron from the initial value of 2.766 mg/l to a value less than 0.006 mg/l immediately after the Ist treatment, the concentration of nickel from the initial value of 0.656 mg/l to a value of 0.117 mg/l after Ist treatment or 0.108 mg/l after the IInd treatment, and manganese concentration from the initial value of 3.307 mg/l to a value of 1.096 mg/l after the Ist treatment or 0.201 mg/l after the IInd treatment.

The results of the experiment conducted on Sample 2 (pyrophyllite granulation 0-100 μm) shown in Table 6 indicate a decrease in iron concentration from the initial value of 2.766 mg/l to a value of less than 0.231 mg/l after the first treatment, i.e. to a value of less than 0.006 mg/l after the II treatment, nickel concentrations from the initial value of 0.656 mg/l to a value of 0.200 mg/l after the Ist treatment, i.e. 0.107 mg/l after the IInd treatment, and manganese concentrations from the initial value of 3.307 mg/l to a value of 0.665 mg/l after the first treatment or 0.198 mg/l after the second treatment.

5. CONCLUSION

The results of the research prove that pyrophyllite from the "Parsovići" deposit, Konjic, Bosnia and Herzegovina, can be used as an effective agent (adsorbent) for removing iron, nickel, and manganese from the landfill leachate taken from the sanitary landfill "Desetine" in Tuzla. (Figures 2, 3, and 4).

The paper examined the effectiveness of two granulations of pyrophyllite (0-53 μm and 0-100 μm) on the degree of adsorption of heavy metals, Fe, Ni, and Mn present in landfill leachate water.

The research results indicate that the iron in the sample can be completely removed immediately after the first treatment with pyrophyllite of both pyrophyllite granulations (granulation 0-53 μm) and (granulation 0-100 μm).

The removal of nickel from landfill leachate water was achieved immediately after the first treatment with pyrophyllite in the amount of 82.2% (for granulation 0-53 μm) and 69.5% (for granulation 0-100 μm) in relation to the initial concentration. The stated efficiency in both cases indicates that the remaining concentrations of nickel in leachate landfill water are below the permitted limit value and that this leachate can be discharged into the final recipient without further treatment. The IInd treatment with pyrophyllite for the purpose of reducing nickel in this water was not even necessary.
Manganese in the landfill leachate sample exceeded the permitted limit value the most (up to 3 times) and its removal from the landfill leachate water required both treatments. Better adsorption efficiency in the amount of 79.9% was shown by the coarser granulation of the used pyrophyllite (0-100 μm) after the first treatment, while in the second treatment, the efficiency was better with the granulation 0-53 μm and was 81.7% compared to initial sample.
When using both granulations, manganese was removed from the landfill leachate water, and the remaining concentrations were below the legally prescribed values.
Bearing in mind the number of sanitary landfills in Bosnia and Herzegovina and the region, which represent an increasing environmental problem and challenge, and the fact that they do not have any leachate treatment, pyrophyllite as a valuable natural mineral with proven adsorption properties is emerging as an effective ecological and innovative solution to the problem of pollution heavy metals.

6. ACKNOWLEDGMENT

We hereby express our gratitude to our professional associates and scientific advisors for their unselfish professional support and research that contributed to proving the adsorption capacity of pyrophyllite shale: Dr. Mirjana Stojanović, Dr. Milan Adamović, Ph.D. Jasmina Grbović-Novaković, Ph.D. Tanja Trtić-Petrović, Dr. Ljubiša Andrić, Ph.D. Dragan Radulović, Ph.D. Nedžad Alić, Ph.D. Suzana Atlagić-Gotovac, Ph.D. Dijana Jelić, Ph.D. Ahmed Džubur, Ph.D. Senad Murtić, Ph.D. Emina Sijahović, Ph.D. Lejla Klepo, Ph.D. Jasna Huremović and dr. Tidža Muhić-Šarac.

7. REFERENCES

[1] Serdarević A.: Izbor procesa prečišćavanja procjednih voda sanitarnih deponija, Univerzitet u Sarajevu, Građevinski fakultet, UDK: 628.35, Vodoprivreda, 0350-0519, Vol. 49 (2017) No. 288-290 p. 297-304
[2] Serdarević A.: Upravljanje procjednim vodama: produkcija, sastav, prikupljanje i obrada, Univerzitet u Sarajevu, Građevinski fakultet
[3] Buzdovačić A.: Obrada procjedne vode odlagališta otpada primjenom šaržnog hibridnog procesa korištenjem prirodnog zeolite, Sveučilište u Splitu, Kemijsko-tehnološki fakultet, 2018.
[4] Uredba o uslovima ispuštanja otpadnih voda u okoliš i sisteme javne kanalizacije "Službene novine Federacije BiH br. 26/20" i Uredba o izmjenama i dopunama Uredbe o uslovima ispuštanja otpadnih voda u okoliš i sisteme javne kanalizacije „Službene novine Federacije BiH br. 96/20"
[5] Kitanović R., Šušteršič V.: Tretman otpadnih voda, Fakultet inženjerskih nauka, Kragujevac, Vojnotehnički glasnik/Military technical courier, 2013., vol. lxi, No. 3.
[6] Šetka, I.: Obrada otpadnih voda nakon postupka galvanizacije metala, Diplomski rad, University of Zagreb, Faculty of Mining, Geology and Petroleum Engineering, Department of Chemistry, 2014
[7] Goletić, Š., Imamović, N., Avdić, N: Obrada otpadnih voda, Univerzitet u Zenici, 2014.
[8] Kulović E.: Utvrđivanje kapaciteta adsorpcije teških metala iz otopadne vode na pirofilitu, Univerzitet u Sarajevu, Prirodno-matematički fakultet, Magistarski rad, Sarajevo, 2017.

[9] Erdemoğlu, M., Erdemoğlu, S., Sayılkan, F., Akarsu, M., Şener, Ş., & Sayılkan, Organo-functional modified pyrophyllite: preparation, characterisation and Pb(II) ion adsorption property, *Applied Clay Science*, *27*(1-2), 41-52, 2004
[10] Churakov, S. V.: Ab initio study of sorption on pyrophyllite: Structure and acidity of the edge sites. The Journal of Physical Chemistry B, 110(9), 4135-4146, 2006
[11] Halilović N.: Optimizacija procesa adsorpcije teških metala iz otpadne vode na pirofilitu, Univerzitet u Sarajevu, Prirodno-matematički fakultet, Magistarski rad, 2018., Sarajevo
[12] Kulović E.: Utvrđivanje kapaciteta adsorpcije teških metala iz vode na pirofilitu, Univerzitet u Sarajevu, Prirodno-matematički fakultet, Magistarski rad, 2017., Sarajevo
[13] Trtić-Petrović T., Pušica I., Purenović M.,Vaštoh Đ.: Mechanically and chemically modified pyrophyllite for removal of heavy metals from aqueous solutions, Engineering, Environment and Materials in Processing Industry 2021, Jahorina
[14] Lopičić Z., Milojković J., Radulović D.: Studija ispitivanja rovnog i modifikovanog pirofilita „Parsovići" i njihove moguće primene u uklanjanju teških metala, Institut za nuklearne i druge mineralne sirovine, Beograd, 2019.,
[15] Čivić H., Murtić S., Sijahović E.: Elaborat o modelima zaštite i remedijacije zemljišta onečišćenim teškim metalima u industrijskim područjima Federacije Bosne i Hercegovine, Univerzitet u Sarajevu, Poljoprivredno-prehrambeni fakultet, 2020., Sarajevo
[16] Murtić S., Čivić H., Sijahović E., Koleška I., Jurković J., Tvica M., Use of pyrophyllite to reduce heavy metals mobility in a soil environment, Agron. Res., 2020, 18, 194–205
[17] Boloban N.: Spektrofotometrijsko određivanje glifosata i njegova adsorpcija na pirofilitu, Univerzitet u Sarajevu, Prirodno-matematički fakultet, Odsjek za hemiju, Završni rad 2020.
[18] Služba za komunalne poslove, izgradnju i poslove mjesnih zajednica, Centar za ekologiju i energiju, Plan upravljanja otpadom za grad Tuzla, 2017–2022, Juni, 2017.

HEAVY METAL CONCENTRATIONS IN SURFACE WATER AND SEDIMENT FROM DRINA RIVER, BIH

Aida Bilajac, Sabina Žero, Amar Karadža
University of Sarajevo, Faculty of Science
Sarajevo, B&H

Keywords: heavy metals, FAAS, Drina River, BiH

ABSTRACT
In this paper, an analysis of the surface water and sediment of the Drina River was carried out. Samples were taken from different six locations along the course of the Drina River in Bosnia and Herzegovina. Selected heavy metals were determined in the sediment after acid digestion using atomic absorption spectrometry - flame technique. The same method was used to determine Cd, Cr, Cu, Fe, Mn, Ni, Pb, and Zn in surface water samples. The obtained results indicate that the Drina River in the investigated part of the course meets most of the prescribed metal limit values. The results obtained for the river Drina were compared with the results obtained in the studies of the rivers Bosna, Trstionica, and Spreča in Bosnia and Herzegovina.

1. INTRODUCTION

The rapid process of urbanization and industrial activities has led to the pollution of rivers around the world [1,2,3]. Pollution of river water with heavy metals as a result of natural and anthropogenic processes represents a danger for ecosystems and humans due to their possibility of accumulation and toxicity [4]. The accumulation of heavy metals in water and sediment often has harmful effects on biota and inhabitants when the pollutant concentration exceeds the limit values [5].

Heavy metals are ecologically very important. They circulate through the ecosystem, i.e. they move through the ecosystem and have their own biochemical cycle. The circulation of heavy metals through the ecosystem depends on a number of factors, such as climatic conditions, proximity to pollution sources, as well as the activities of biological systems. Some of heavy metals such as Fe, Mn, Zn, and Cu belong to the group of essential elements for plants. In small amounts, they are necessary for numerous functions of a living organism. However, heavy metals in higher concentrations can cause toxic effects on living organisms, and when they reach the food chain; they can endanger the health of people, animals, and plants [6]. Metals such as Pb and Ni exhibit toxicological properties on the environment, which can lead to severe consequences in the ecosystem. Today, heavy metals are increasingly released into the environment through anthropogenic activities [7,8,9,10].

As Bosnia and Herzegovina (BiH) is rich in natural resources, especially rivers, and in the last few years there is not a large number of studies on the water and sediment of the Drina River in the literature, so the main aim of this study was to analyze the surface water and sediment of Drina River, so that the results can serve as a starting point for further research in the field of environment protection, especially rivers in Bosnia and Herzegovina. In this study, Cd, Cr, Cu, Fe, Mn, Ni, Pb, and Zn are determined in different river water and sediment samples of the Drina River by atomic absorption spectrometry, and flame technique (FAAS).

2. MATERIAL AND METHODS

2.1. Sampling area

Drina River belongs to the Sava River Basin. The considered part of the Drina River includes the area from the settlement of Hubjeri downstream from Goražde to the settlement of Vitkovići in a length of 14.5 km in Bosnia and Herzegovina. It is a relatively narrow valley in which the town of Goražde and its industrial zone Vitkovići are located.

2.2. Sample collection, preparation, and analysis

In this study, river water samples (n=6) and river sediment samples (n=6) were taken during May 2021. River water and sediment samples were taken side by side except for location 6. A sampling of river water was carried out in acid-clean polypropylene bottles. Prior to sampling, each sampling bottle was washed several times with river water. During the sampling the opening of the bottle facing the direction of the river flow; water sampling was done 20 cm below the river level during stable weather conditions. Sediment samples were also sampled in a similar manner to river water samples. Containers for sediment sampling were pre-washed, and at the sampling site rinsed with river water several times, then the surface part (from 0 cm to 5 cm depth) of the sediment was taken for the heavy metal analysis. General sampling data are given in Table 1.

Table 1. General sampling data for the river water and sediment of Drina River

River water and sediment samples							
Location	1	2	3	4	5	6 river water	6 sediment
Air temperature	24 °C	24 °C	24 °C	24 °C	23 °C	23 °C	23 °C
River water temperature	12 °C	12 °C	12 °C	12 °C	12 °C	12 °C	12 °C
GPS coordinates	N43.676765 E19.015765	N43.666504 E18.973296	N43.597469 E18.851106	N43.629139 E18.968890	N43.666070 E18.976347	N43.664808 E18.972116	N43.656008 E18.968466

To ensure the reliability of the results, appropriate quality procedures were taken. Recovery values for metals in spiked samples ranged from 89 % for Cr to 110 % for Zn. Double distilled water was used throughout the complete experimental work and the reagents were of analytical grade purchased by Merck (Darmstadt, Germany).

Before the sieving and homogenization process, the sediment samples were air-dried for two weeks. Each homogenized sample was transferred to a sieve, and sieved for 5 min, at about 150±3 vibrations/min. The sediment fraction with a diameter of 0.063 mm was used for the analysis of heavy metals in the sediment.

In order to determine the metal content in the sediment of the Drina River, the following procedure was applied: 1.5 g ± 0.10 mg of the sediment sample was weighed. All samples were prepared in triplicate to ensure analytical quality control of the results. A blank sample was also prepared, and the blank sample was treated in the same way as the samples were treated. The samples were transferred to glass beakers and 15 mL aqua regia (HNO_3+3HCl) and 5 mL of hydrogen peroxide (30 % H_2O_2) were added. After digestion at temperatures below 100 °C, the samples were filtered on a blue strip filter paper, then the samples were quantitatively transferred into a measuring vessel of 50 mL. Measuring vessels were filled with double distilled water up to the mark and transferred to polypropylene bottles until further analysis.

The content of Cd, Cr, Cu, Fe, Mn, Ni, Pb, and Zn in different river water and sediment samples of the Drina River was determined by atomic absorption spectrometry, flame technique (FAAS), using an AA240FS atomic absorption spectrometer (Varian, Australia).

3. RESULTS AND DISCUSSION

The concentration of eight heavy metals (Cd, Cr, Cu, Fe, Mn, Ni, Pb, Zn) in river water and sediment samples of Drina River was determined, and the results are presented in Figures 1 and 2. The results were compared with the values given in Rulebooks (1, 2, and 3) given in Table 2. Moreover, the obtained results have been compared to the results obtained in the studies of the rivers Bosna [11], Trstionica [12]and Spreča [13]in Bosnia and Herzegovina. The studies are carried out by Kevilj-Olovčić et al. (2018), Delibašić et al. (2020) and the Center for Ecology and Energy in Tuzla (2016), respectively.

Table 2. Limit values for metals in surface water and sediment

Legal framework	Cr	Cu	Mn	Fe	Ni	Cd	Pb	Zn
	(mg/L)							
Rulebook 1*	0.5	0.3	1.0	1.0	0.5	/	0.2	1.0
Rulebook 2**	0.5	0.3	1.0	2.0	0.5	0.01	0.2	1.0
	Cr	Cu	Mn	Fe	Ni	Cd	Pb	Zn
	(µg/g)							
Rulebook 3***	50	50	/	/	30	0.5	50	100

**Rulebook on limit values of dangerous harmful substances of water that after purification from the public sewage system is discharged into a natural receiver [14];*
***Rulebook on limit values of hazardous harmful substances for technological wastewater before its discharge into the public sewage system or into another receiver [15];*
****Rulebook on the determination of permitted amounts of harmful and hazardous substances in the soil and methods of their testing [16].*

Manganese in the water samples (52.6 µg/L) of Drina River was determined only in the sample from location 2, while the concentration in the other samples was not detected by using FAAS. Moreover, Mn content in sediment samples of Drina River was the highest (773 µg/g) also in the sample from location 2, and the lowest (242 µg/g) in the sample from location 3. If we compare the obtained results with the results for the river water of Trstionica and Bosna, we observe the following: the concentration of Mn determined in the river water of Trstionica (0.024 mg/L) is higher compared to results for River Drina (except for sample from location 2). Mn concentration in Bosna River (0.007 mg/L to 0.128 mg/L) is slightly higher compared to the Mn concentration values in Drina River. Manganese concentration in Spreča River sediment samples ranged from 724.6 µg/g to 941.7 µg/g. By comparing the results of this study with the results for the River Spreča it can be seen that the Mn concentration values in Spreča River sediment samples are higher compared to the Mn concentrations in the Drina River samples.

The highest **copper** content in the river water (148 µg/L) and sediment (493 µg/g) samples of the Drina River was determined at location 2, and the lowest Cu concentration was found in the river water sample (3.1 µg/L) from the location 5. The lowest Cu content (14.10 µg/g) in sediment samples was determined in the sample from location 3. Compared to the river water of River Trstionica, where the concentration of Cu ranged from 0.06 mg/L to 0.61 mg/L, lower results were obtained for River Drina, except for the sample from location 2. The results for River Bosna are higher compared to the results of this study, Cu concentration in the Bosna River ranged from 0.074 mg/L to 0.112 mg/L. Copper concentration in Spreča River sediment samples ranged from 58.4 µg/g to 69.3 µg/g. In comparison with the results of this study, the results for Spreča River are higher, except for the sample from location 2. The concentration of Cu in Drina River sediment samples does not exceed the limit values, except for the sample from location 2.

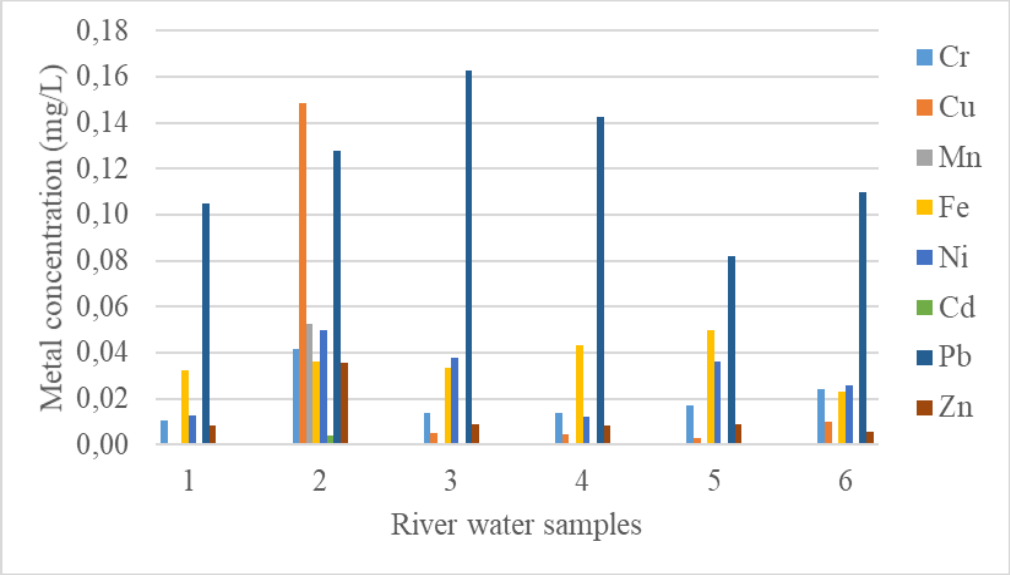

Figure 1. Heavy metal concentrations in surface water samples from Drina River, BiH

The highest **chromium** content in river water (41.5 µg/L) and sediment (290 µg/g) samples of Drina River was found at location 2, and the lowest in river water (13.8 µg/L) from location 3, while in the sediment, the lowest content (17.3 µg/g) was determined in the sample from location 1. By comparing the results of this study with the results for the River Trstionica (in all samples it was below the detection limit except for the sample taken from the location Brežani-0.006 mg/L) and Bosna (0.05 mg/L) it can be noted that the concentration of Cr is higher in Drina River in relation to the Trstionica and Bosna rivers. The obtained values were compared with the Cr results for the Spreča River sediment samples (400.5 µg/g to 890.2 µg/g). The Cr content values in the Spreča River sediment samples are significantly higher than the results obtained in this study. The limit value according to Regulation 3 for Cr is 50.00 µg/g, and the value obtained at location 2 is almost 6 times higher.

The highest **iron** content in river water (43.4 µg/L) and sediment (1649 µg/g) samples of Drina River was found in the sample from location 4. The lowest Fe concentration in river water (23.3 µg/L) was found at location 6, while the lowest Fe content in the Drina River sediment sample (1584 µg/g) was from location 1. The concentration of Fe in the water samples of the River Trstionica ranged from 0.04 mg/L to 0.21 mg/L, which are higher values for Fe compared to the results of this study. The results for Bosna River (0.13 mg/L-0.92 mg/L) are higher in comparison to the results obtained in this study.

The highest concentration of **nickel** and **cadmium** in water samples (Ni: 49.7 µg/L; Cd: 3.8 µg/L) of the Drina River was in the sample from location 2, and the lowest Ni concentration in the sample from location 4 (11.9 µg/L), while Cd was not detected by FAAS in water samples from the locations of 1, 3, 5 and 6. The contents of Ni (49.6 µg/g) and Cd (1.60 µg/g) in the sediment samples of the Drina River were the highest in the sample from location 6. The lowest content of Ni and Cd (Ni: 28.10 µg/g; Cd: 0.60 µg/g) in the sediment samples is found at location 3. Ni concentrations found in Drina River were higher compared to the values (below the limit of detection) obtained for the Trstionica River. The concentration of Cd in the water samples of Drina River does not exceed the limit values given in Rulebook 2. The concentration of Ni in the sediment samples of Spreča River ranged from 94.6 µg/g to 322,5 µg/g. The Ni concentration values in Spreča river sediment samples are significantly higher compared to the Ni content in the Drina River sediment samples. The Ni content in the sediment samples of

Drina River exceeds the limit value given by Rulebook 3, except for the sample from location 3. The limit value for Cd was exceeded in all sediment samples of Drina River.

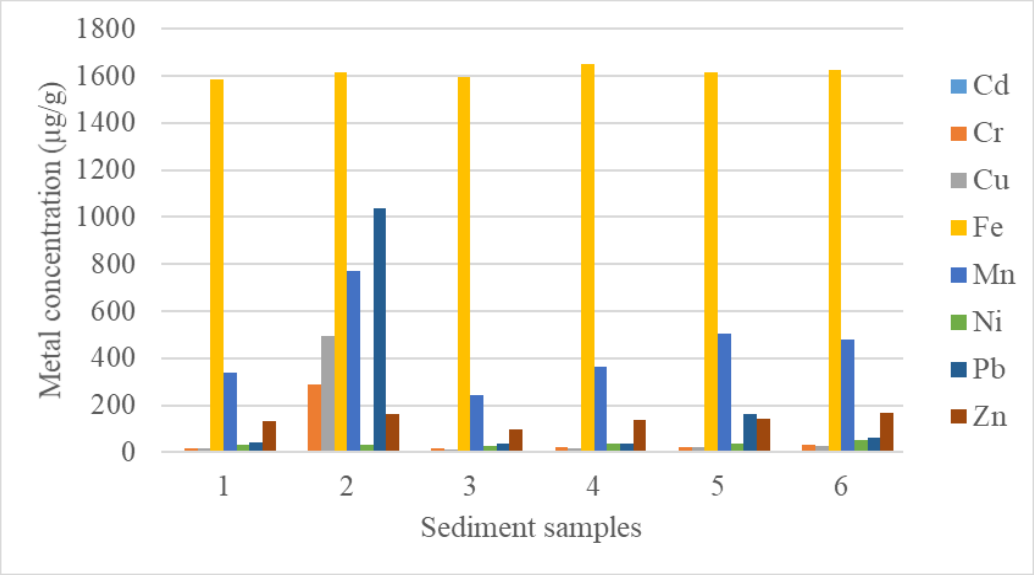

Figure 2. Heavy metal concentrations in sediment samples from Drina River, BiH

The highest concentration of **lead** in water samples (162.9 µg/L) of Drina River was in the sample from location 3, and the lowest concentration (82.2 µg/L) was in the sample from location 5. While the Pb content in the sediment samples (1037 µg/g) of Drina River was the highest in the sample from location 2, and the lowest (36.90 µg/g) in the sample from location 4. Pb concentrations in water samples of Drina River are significantly higher than Pb concentrations in water samples of the Trstionica River (0.04 mg/L-0.21 mg/L) and Bosna River (0.004 mg/L-0.009 mg/L). The Pb concentration in sediment samples of Spreča River (20.5-25.1 µg/g) is much lower compared to the values of Pb content in Drina River sediment. The Pb content exceeded the limit value in samples from locations 2, 5, and 6.

The highest **zinc** concentration in Drina River water samples (35.4 µg/L) was in the sample from location 2, and the lowest concentration (5.8 µg/L) was in the sample from location 6. Zn content in the Drina River sediment was the highest (166 µg/g) in the sample from location 6, and the lowest (98.20 µg/g) in the sample from location 3. Compared to the water samples of River Trstionica (0.004 mg/L-0.07 mg/L) and Bosna (0.0003 mg/L-0.035 mg/L), the obtained Zn values in River Drina are lower. The Zn concentration in Spreča River sediment samples ranged from 87.1 µg/g to 100.2 µg/g. By comparing the results for the Drina and Spreča rivers, it can be seen that Zn concentrations determined in the Spreča River samples are lower compared to the Zn content values for Drina River. The Zn content in all samples was higher than the limit value, except for the sample from location 3.

4. CONCLUSION

The concentrations of the examined heavy metals (Cd, Cr, Cu, Fe, Mn, Ni, Pb, and Zn) did not exceed the limit values in river water samples, while for Cd, Ni, Pb, and Zn they exceeded the limit value in almost all sediment samples (for Ni and Zn the sample from location 3 did not exceed the limit value, for Pb the sample from location 4 did not exceed the limit value). In the river sediment, Fe is the most abundant, along with Mn, which could be expected considering that they occur in nature in the form of various ores and minerals. The content of heavy metals in water samples compared to the content of heavy

metals (Cd, Cr, Cu, Fe, Mn, Ni, Pb, and Zn) in the sediment of Drina River is quite low. It is necessary to carry out additional research with the aim of determining the heavy metal contamination of the river water and sediment of River Drina in Bosnia and Herzegovina.

5. REFERENCES

[1] Briffa, J., Sinagra, E., & Blundell, R. (2020). Heavy metal pollution in the environment and their toxicological effects on humans. Heliyon, 6(9), e04691

[2] Pržulj, S., Radojičić, A., Kašanin-Grubin, M., Pešević, D., Stojadinović, S., Jovančićević, B., & Veselinović, G. (2022). Distribution and provenance of heavy metals in sediments of the Vrbas River, Bosnia and Herzegovina. Journal of Serbian Chemical Society,*87*(4), 519-530

[3] Tamim, U., Khan, R., Jolly, Y. N., Fatema, K., Das, S., Naher, K., ... & Hossain, S. M. (2016). Elemental distribution of metals in urban river sediments near an industrial effluent source. Chemosphere, 155, 509-518

[4] Pavlović, P., Marković, M., Kostić, O., Sakan, S., Đorđević, D., Perović, V., ... & Mitrović, M. (2019). Evaluation of potentially toxic element contamination in the riparian zone of the River Sava. Catena, 174, 399-412

[5] Islam, M. A., Das, B., Quraishi, S. B., Khan, R., Naher, K., Hossain, S. M., ... & Hossen, M. B. (2020). Heavy metal contamination and ecological risk assessment in water and sediments of the Halda river, Bangladesh: A natural fish breeding ground. Marine Pollution Bulletin, 160, 111649

[6] Zhang, Z., Lu, Y., Li, H., Tu, Y., Liu, B., & Yang, Z. (2018). Assessment of heavy metal contamination, distribution and source identification in the sediments from the Zijiang River, China. Science of the Total Environment, 645, 235-243

[7] Xie, Q., & Ren, B. (2022). Pollution and risk assessment of heavy metals in rivers in the antimony capital of Xikuangshan. Scientific reports, 12(1), 14393

[8] Zhou, Q., Yang, N., Li, Y., Ren, B., Ding, X., Bian, H., & Yao, X. (2020). Total concentrations and sources of heavy metal pollution in global river and lake water bodies from 1972 to 2017. Global Ecology and Conservation, *22*, e00925

[9] Islam, M. S., Ahmed, M. K., Raknuzzaman, M., Habibullah-Al-Mamun, M., & Islam, M. K. (2015). Heavy metal pollution in surface water and sediment: a preliminary assessment of an urban river in a developing country. Ecological indicators, 48, 282-291

[10] Bikić, F. (2013). Preliminary Analysis of Heavy Metals Content in the River Bosna Upstream and Downstream from the Industrial Plants in Zenica and Pollution Assessment. Bulletin of the Chemists and Technologists of Bosnia and Herzegovina, 41, 48-51

[11] Kevilj-Olovčić, A., Olovčić, A., Huremović, J., & Žero, S. (2018). Water quality of the Bosna River. Kemija u industriji: Časopis kemičara i kemijskih inženjera Hrvatske, 67(13 (special issue)), P119-P126

[12] Delibašić, Š., Huremović, J., Žero, S., & Gojak-Salimović, S. (2020). Water Quality of the Trstionica River (Bosnia and Herzegovina). Kemija u industriji: Časopis kemičara i kemijskih inženjera Hrvatske, 69(7-8), 371-376

[13] Centar za ekologiju i energiju (2016) Prisustvo teških metala u površinskim i industrijskim otpadnim vodama na području općine Lukavac, dostupno na http://ekologija.ba/wp-content/uploads/2018/03/Teski-metali-u-otpadnim-vodama.pdf

[14] Pravilnik o graničnim vrijednostima opasnih i štetnih materija za vode koje se nakon prečišćavanja iz sistema javne kanalizacije ispuštaju u prirodni prijemnik, dostupno na https://www.voda.ba/uploads/docs/25_57_b.pdf

[15] Pravilnik o graničnim vrijednostima opasnih i štetnih materija za tehnološke otpadne vode prije njihovog ispuštanja u sistem javne kanalizacije odnosno u drugi prijemnik, dostupno na https://www.voda.ba/uploads/docs/25_56_b.pdf

[16] Pravilnik o utvrđivanju dozvoljenih količina štetnih i opasnih materija u zemljištu i metode njihovog ispitivanja, dostupno na https://fmpvs.gov.ba/wp-content/uploads/2022/12/03-Pravilnik-opasne-tvari-zemlj-96-22.pdf

THE LONG-TERM IMPACT OF HEAVY METALS FROM THE BOSNA RIVER ON HUMAN HEALTH

Aida Šapčanin
University of Sarajevo, Faculty of Pharmacy
Sarajevo, B&H

Farzet Bikić
University of Zenica, Faculty of Metallurgy and Technology
Zenica, B&H

Keywords: heavy metals, river Bosna, health risk assessment

ABSTRACT
Heavy metals can enter into rivers through industrial and consumer waste, activities of acidic rain to soils, etc. Long-term exposure can result in damaging: mental and nervous function, blood composition, lungs, kidneys, liver, and other vital organs. Estimating a health risk based on the contents of heavy metals found in river Bosna was the aim of this study. The hazard coefficient (HQ), non-carcinogenic hazard index (HI), and carcinogenic risk (RI) have been calculated. Overall, HQ and HI did not show direct risk to human health from heavy metals in the investigated area; however, these levels should be monitored in a long-term perspective.

1. INTRODUCTION

1.1. Health risk assessment

The scientific aspects of risk assessment refer to the preparation of the protocols on which an assessment will be based. The application of risk assessment is carried out through risk management, i.e. by adopting specific measures to reduce risk, by adopting regulations, and by making decisions on risk acceptability. The risk assessment itself ensures the transition between scientific knowledge and social needs. It is based on the probability of an undesirable event and the intensity of the consequences of such an event [1]. Because of the above, HQ and HI are usually calculated, as well as non-carcinogenic and cancerogenic risk [2]. As with the water quality standard approach, a quantitative health risk assessment is a parameter-based approach that involves studying each component in the water separately. It is based on: the presence of harmful substances and microorganisms in the water; acceptable and infective doses; estimations of the exposure of the water users. Using these data, the health risk can be calculated and compared with the risk that is could be acceptable. Modeling techniques based on quantitative risk assessment allow quite accurate estimations of exposure and risk, provided the necessary input data are available. In the case of a chemical risk assessment, hazard identification consists of finding the components in the water that are hazardous and are present in sufficiently high concentrations to adversely affect health [2,3,4]. Furthermore, an investigation is being carried out into the harmful effects of chemicals on humans and on the environment. In the past, numerous new chemicals were released into the environment without estimating their consequences to humans and nature. Today, it is necessary to examine the toxicity of newly synthetized chemicals before commercial production. Additionally, international organizations have

been created to identify and investigate potentially toxic chemicals, in order to minimize their harmful effects.

1.2. Heavy metals impact human health

Heavy metals in water, cause a certain effect, which may be beneficial or toxic depending on their concentration variation in the aquatic system. Heavy metals such as lead (Pb), arsenic (As), copper (Cu), antimony (Sn), mercury (Hg), and cadmium (Cd) reach the environment from anthropogenic and natural sources. Therefore, they can be found in soil, water, air, food chain, vegetable, and animal foods [4,5]. The biggest polluters of the environment are lead, zinc (Zn), iron (Fe), cadmium (Cd), molybdenum (Mo), As, cobalt (Co), manganese (Mn), and Hg, and their main sources are industrial production, metal processing, roads, vehicles, pigments and batteries [5,6,7]. Burning of fossil fuels leads to pollution of the atmosphere with particles of heavy metals and by their deposition, they pollute water, soil, plants, and fish [2,3,4,5]. Once absorbed by the body, heavy metals continue to accumulate in vital organs like the brain, liver, bones, and kidneys, for years or decades causing serious health consequences [4,6]. Some metals like Cu, Co, and Zn are essential for normal body growth and functions of living organisms and are referred to as essential elements. Other elements are referred to as non-essential, high concentrations of these metals like Cd, Cr, and Pb are considered highly toxic to human and aquatic life [6,7]. Cr(III) is much less toxic than Cr(VI). The respiratory tract is also the major target organ for Cr(III) toxicity, similar to Cr(VI). Cr(III) is an essential element in humans. The body can detoxify some amount of Cr(VI) to Cr(III). The respiratory tract is the major target organ for Cr(VI) toxicity, for acute (short-term) and chronic (long-term) inhalation exposures [4,5,8,9]. Like Cr, Co is also one of the required metals needed for normal body functions as a metal component of vitamin B12. However, high intake of Co via consumption of contaminated food and water can cause abnormal thyroid artery, polycythaemia, over-production of red blood cells, and right coronary artery problems [10,11]. All of these are reasons for the necessity of assessing the impact of heavy metals on human health.

2. MATERIAL AND METHODS

a) The research area

The Bosna River is 273 km long, 1-3 m deep (up to 10 m deep in the springs), and 35-170 m wide. It narrows the most between Maglaj and Doboj. Its banks are 1.5 to 6 m high and are partially overgrown with forest and bushes. It creates waterfalls and rapids in several places. Its average drop is 1.48 m/km, and the average water flow is about 100 m^3/s. The highest water level is in the period March-May and November, and the lowest is in August and September. Surprisingly, it is also one of the few large Balkan rivers without hydroelectric power plants or large dams. The Bosna River Valley is the most populated area of Bosnia and Herzegovina and is home to almost a million inhabitants as well as the industrial center of the country. The settlements along river Bosnia are of the road type, in some places quite sparse. In the Bosna valley are the cities of Sarajevo, Visoko, Kakanj, Zenica, Zavidovići, Žepče, Maglaj, Doboj, Modriča, and Bosanski Šamac.

b) Sample collection

To evaluate the health risk posed by heavy metals (Cd, Pb, Cr, Ni, Cu, Zn, Co, and As) five representative water samples were collected from selected locations of river Bosna (Fig.1.) four times during 2022 in the different season (winter, spring, summer, and autumn) and analysed by using a graphite furnace atomic absorption spectrometry [10,11,12]. Samples were taken from selected locations of Sarajevo (43°49'04.8"N 18°16'08.4"E), Visoko

(43°59'27.2"N 18°10'58.5"E), Kakanj (44°08'10.2"N 18°04'50.5"E), Zenica (44°12'45.6"N 17°54'58.8"E), Maglaj (44°32'36.7"N 18°05'59.6"E) and Doboj (44°43'15.0"N 18°05'36.0"E). Samples were collected at a depth of 0-1 m, and stored in 500 mL PTE bottles with the addition of 2 mL 1% HNO_3 (for stabilization of heavy metals) prior to analysis.

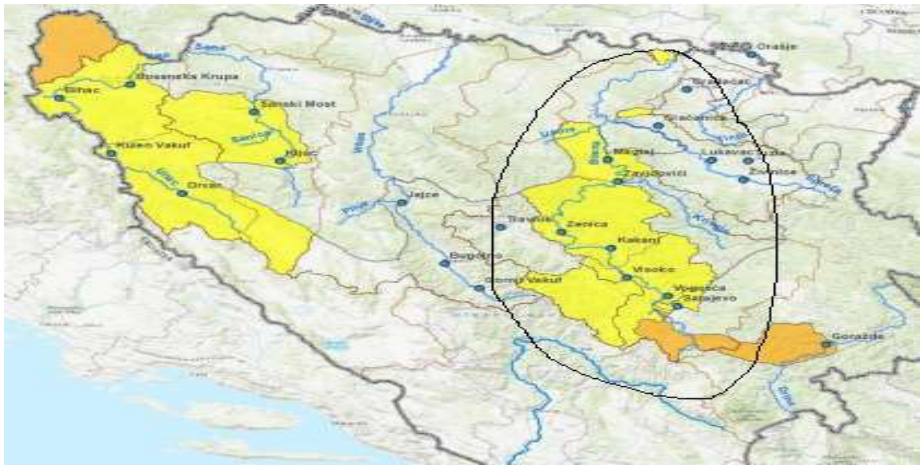

Figure 1. The Bosna river valley

c) Potential health risk assessment and correlation analysis

Furthermore, the potential health risk assessment was calculated for a lifetime of exposure (ingestion, inhalation, and dermal) based on USEPA model [2,3,4,5,13,14], also cumulative carcinogenic and non-carcinogenic risks were determined. The value of the total hazard index (HI) is calculated for minimal content of heavy metals for children and adults [10,15,16]. Correlation between determined heavy metals was calculated [15].

2.1. Non-carcinogenic Risk Assessment

Non-carcinogenic and carcinogenic effects of heavy metals were estimated by using equations, as follows:

$$ADDing = Cw\ X\ \frac{IngR\ X\ EF\ X\ ED}{BW\ X\ AT}\ X\ 10^{-6} \quad (1)$$

$$ADDinh = Cw\ X\ \frac{InhR\ X\ EF\ X\ ED}{PEF\ X\ BW\ X\ AT} \quad (2)$$

$$ADDder = Cw\ X\ \frac{SA\ X\ AF\ X\ ABS\ X\ EF\ X\ ED}{BW\ X\ AT}\ X\ 10^{-6} \quad (3)$$

Where: ADDing - Average daily doses (mg/kg per day) via ingestion; ADDinh - Average daily doses (mg/kg per day) via inhalation; ADDder - Average daily doses (mg/kg per day) via dermal contact; *C*w is the concentration of selected heavy metals in the water sample; *IngR* is the ingestion rate; *InhR* is the inhalation rate*; ED* is the exposure duration; *EF* is the exposure frequency and *BW* is the body weight of children and adults given; *AT* is the average time for both adults and children; *SA* is the surface area of the skin exposed to heavy metals.

$$HQ = \frac{ADD}{RfD} \quad (4)$$

$$HI = \sum_{k=1}^{n} HQ_k = \sum_{k=1}^{n} \frac{ADD_k}{RfD_k} \quad (5)$$

Where: HQ – Hazard quotient; HI-hazard index; RfD – Chronic reference dose (mg/kg per day) of specific heavy metal. According to the USEPA [13] classification, at HI < 1, the non-carcinogenic risk of the exposed individuals occurs within the acceptable range. At HI > 1, the non-carcinogenic heavy metals are potentially harmful to human health. Values of RfD among the health risk assessment model parameters for each heavy metal are listed in [3,5, 13].

2.2. Carcinogenic Risk (RI) Assessment

Due to the lack of available values for the slope factors (SF), we only estimated the carcinogenic risk for exposure to metals whose concentrations were the highest measured in the tested samples.

$$Risk_{pathway} = \sum_{k=1}^{n} ADD_k \, CSF_k \quad (6)$$

Risk –unitless probability of an individual developing cancer over a lifetime;
ADD_k- Average daily intake (mg/ kg per day) for kth heavy metal
CSF_k – Cancer slope factor (mg/ kg day)$^{-1}$ for heavy metal

$$Risk_{total} = Risk_{ing} + Risk_{inh} + Risk_{der} \quad (7)$$

$Risk_{ing}$, $Risk_{inh}$, and $Risk_{der}$ are risks contributions through ingestion, inhalation, and dermal pathways. The assessment is based on the following: If RI < 10^{-6}, the carcinogenic risk to health can be considered as negligible; If the RI is in the range of 1×10^{-6} to 1×10^{-4}, then these values are within the acceptable risk for human health, and If RI > 10^{-4}, then there is a high risk for the development of cancer in humans.

3. RESULTS AND DISCUSSION

The obtained results of noncarcinogenic children's health risk, based on metal concentrations in river water and exposure by three different pathways (ingestion, inhalation, and dermal) are shown in Figure 2.

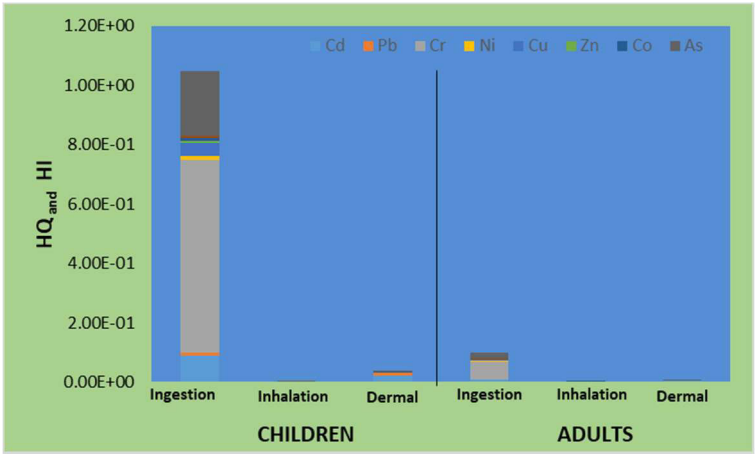

Figure 2. The hazard coefficient (HQ) and hazard index (HI)

The obtained results of carcinogenic children's health risk, based on metal concentrations in river water and exposure by three different pathways (ingestion, inhalation, and dermal) are shown in Figure 3.

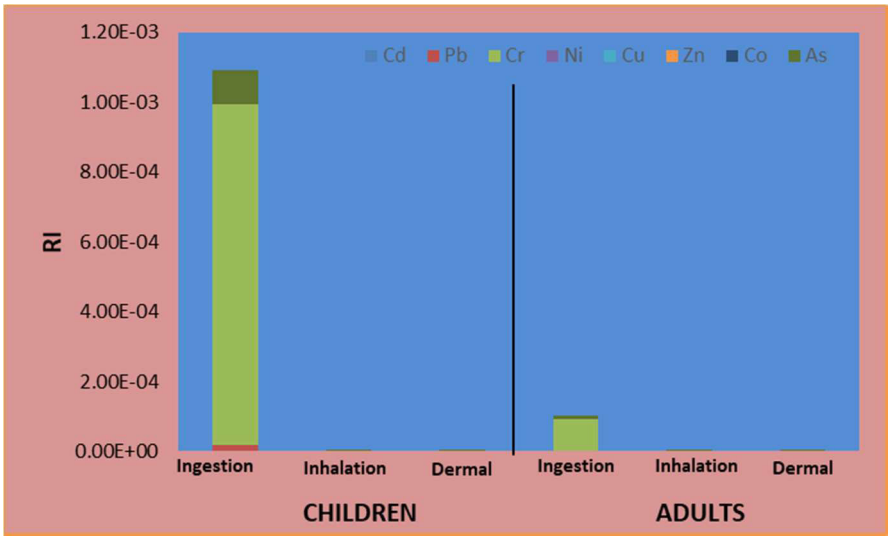

Figure 3. The carcinogenic risk estimation

Generally, results showed that ingestion and dermal are the main pathway of contamination by heavy metals from river water. Some foreign authors did not calculate HI, HQ, and RI for inhalation exposure hypothetically [15,16]. As same as to the HI values, the RI values for children were also higher compared to the values for adults. The RI value for adults was less than 10^{-6}, which indicates that the carcinogenic risk of Pb, Cr, and As in water could be neglected. However, the RI value for children indicates an acceptable risk to human health. These results suggest that children have a higher health risk than adults posed by heavy metals exposure. Similar conclusions were stated by other authors [5,6].
The correlation between investigated heavy metals was calculated and shown in Table 1.

Table 1. Pearson correlation coefficients of heavy metal concentrations in the river water

	Cd	Pb	Cr	Ni	Cu	Zn	Co	As
Cd	1							
Pb	0.13039	1						
Cr	0.07519	0.163246	1					
Ni	0.678469	-0.29651	0.594147	1				
Cu	-0.36986	-0.44097	-0.4469	-0.39615	1			
Zn	-0.33704	-0.84015	0.259798	0.318862	0.313788	1		
Co	0.643337	0.776055	0.307002	0.249959	-0.41714	-0.75662	1	
As	-0.03827	0.802859	0.59441	-0.08652	-0.24538	-0.41015	0.663672	1

Based on a statistical analysis of the contents of the eight heavy metals in the river water, in the study area, the correlation between the various heavy metals was analyzed, and the Pearson correlation coefficient was calculated. The results shown in Table 1 reveal that the correlations between the heavy metals were different, and higher correlation coefficients ($r > 0,7$) between certain elements suggest similar sources. These results could indicate that their concentration changes are very similar and that the sources and migration paths of these elements could be the same [15].

4. CONCLUSION

This study gives a short view of the inorganic pollution levels and health risks posed by heavy metals in river water, and the health risks assessment should be a priority considering the continuous increase in heavy metals and general environmental pollution globally in water, air, and soil. The risk assessment, especially in industrial and populated regions, such

as the watercourse of the river Bosna, needs to be carried out periodically. This will enhance proper monitoring and ensure the safety of adults especially children who are more vulnerable to the toxicity of heavy metals. RI calculations suggest that children have a greater health risk than adults for exposure to potentially contaminated water.

5. REFERENCES

[1] Ružić, I.: Procjena rizika po zdravlje čovjeka i kvalitetu okoliša, Hrvatske vode: časopis za vodno gospodarstvo, 1998; 6 (22): 43-57

[2] USEPA:Risk Assessment Guidance for Superfund: Human Health Evaluation Manual. EPA/540/1-89/002, vol.1. Office of Solid Waste and Emergency Response, 1989

[3] USEPA: Risk Assessment Guidance for Superfund Volume I: Human Health Evaluation Manual (Part A); Office of Emergency and Remedial Response: Washington, DC, USA, 2004

[4] World Health Organization, Environmental Health Criteria Series, EHC 228. Principles and Methods for the Assessment of Risk from Essential Trace Elements. WHO Geneva, 2002 https://apps.who.int/iris

[5] US EPA: A review of the reference dose and reference concentration processes. EPA/630/P-02, 2002. https://www.epa.gov/risk/risk-assessment-guidance

[6] Sreedhara, Nayaka, B. M., Ramakrishna, S., Jayaprakash, M.: Impact of heavy metals on water, fish (Cyprinus carpio) and sediments from a water tank at Timkur, India. International Journal of Oceanography and Hydrobiology. 2009; 38(2): 17-28

[7] Qing, X., Yutong, Z., Shenggao, L. Assessment of heavy metal pollution and human health risk in urban soils of steel industrial city (Anshan), Liaoning, Northeast China, Ecotoxicology and Environmental Safety, 2015; 120:377-385

[8] Szyczewski, P., Siepak, J., Niedzielski, P., Sobczynski, T.: Research on Heavy Metals in Poland. Polish Journal of Environmental Studies.2009; 18(5): 755-768

[9] Bishop, P. O.: Neurophysiology of binocular vision, in J., Houseman (Ed,), Handbook of physiology, 4 New York: Springer-Verlag, 1970, pp 342-366

[10] Šapčanin, A., Pehlić, E., Salihović, M., Smajović, A.: Human risk assessment based on the content of inorganic and organic pollutants in Sarajevo's playgrounds. In Karabegovic (Eds.) New Technologies, Development and Application LNNS Springer Cham. 2020; 128:779-785

[11] Šapčanin, A., Cakal, M., Jaćimović, Z., Pehlić,E., Jancan, G.: Soil Pollution fingerprints of children playgrounds in Sarajevo city, Bosnia and Herzegovina, Environmental Science and Pollution Research, 2017; 24(12): 10949-10954

[12] Vandecasteel, C., Block, C.B.: Atomic Absorption Spectrometry, In: Modern Methods for Trace Element Determination. John Wiley and Sons Ltd, Chichester, England, 1997; pp 93-137

[13] US EPA: United States Environmental Protection Agency, in Quantitative Risk Assessment Calculations, 2015; pp 7–9. https://www.epa.gov/risk/risk-assessment-guidance

[14] World Health Organization, International Programme on Chemical Safety, Publications. IPCS/EHC Series. 2002; https://apps.who.int/iris/

[15] Jiang, C., Zhao, Q., Zheng, L., Chen, X., Li, C., Ren, M. Distribution, source and health risk assessment based on the Monte Carlo method of heavy metals in shallow groundwater in the area affected by mining activities, China, Ecotoxicology and Environmental Safety, 2021; 224, 112679

[16] Xie, Q., Ren, B. Pollution and risk assessment of heavy metals in rivers in the antimony capital of Xikuangshan, Scientific Reports, 2022; 12: 14393

INFLUENCE OF CURRENT DENSITY ON LEACHATE TREATMENT EFFICIENCY BY ELECTROCOAGULATION WITH ZEOLITE ADDITION

Nediljka Vukojević Medvidović, Ladislav Vrsalović, Sandra Svilović, Mirjana Cestarić
University in Split, Faculty of Chemistry and Technology in Split
Split, Croatia

Keywords: current density, electrode surface, aluminium

ABSTRACT
The electrocoagulation with zeolite addition was used to treat compost leachate. The effects of different current densities and zeolite particle sizes on electrode dissolution, electrode surface condition, and removal efficiency were investigated. The surface of the electrodes was analysed by optical microscope, while the consumption of the aluminium electrodes was investigated by weighing. The results confirmed that the removal efficiency could be improved by conducting the experiment at higher current densities, but the electrodes used were significantly more damaged. Significant damage was also observed on the electrode used in the experiment with larger zeolite particles, which can be related to the stronger abrasion effect.

1. INTRODUCTION

Electrocoagulation (EC) is a process that combines coagulation, flocculation, flotation, and electrochemical anodic and cathodic reactions to remove pollutants from wastewater. It is based on the formation of flocs of metal hydroxides by dissolving the electrodes, which serve as flocculants on which pollutants can be removed by the *sweep flock* mechanism [1-7]. In general, the electrochemical reactions taking place in an EC reactor with immersed metal electrodes (M), and with aluminium electrodes can be represented by the following equations [2,8]:
anode

$$Al_{(s)} \rightarrow Al_{(aq)}{}^{3+} + 3e^- \quad (1)$$

$$2H_2O_{(l)} \rightarrow 4H^+{}_{(aq)} + O_2(g) + 4e^- \quad (2)$$

cathode

$$2H_2O_{(l)} + 2e^- \rightarrow 2H_{2(g)} + OH^- \quad (3)$$

$$2O_{2(g)} + 4H^+ + 4e^- \rightarrow 2H_2O \quad (4)$$

Oxidation of the aluminum occurs at the anode, causing the aluminium anode to dissolve (or corrode) and produce aluminium metal cations that instantly undergo further reactions to form different metal (oxy) hydroxides. At the same time, an anodic oxygen evolution reaction (OER) takes place (reaction 2), so there is competition between aluminium dissolution and OER. According to Tegladza et al. [2], at low current density, aluminium dissolution mainly occurs, while at high current density, both processes compete. At the cathode, a hydrogen evolution reaction (HER) occurs (reaction 3), while under the condition of high dissolved oxygen content, an oxygen reduction reaction (ORR) also takes place (reaction 4) [2,8].

Corrosion product formation reaction of $Al(OH)_3$ which serves as flocculants are given by equation (5). Namely, the Al^{3+} ions generated at the anode and OH^- produced at the cathode undergo several speciation reactions and generate intermediate species (such as $Al(OH)^{2+}, Al_2(OH)_2^{4+}, Al_7(OH)_{17}^{4+}, Al_{13}O_4(OH)_{24}^{7+}$, which are the precursors to the formation of the stable insoluble $Al(OH)_3$ flocs [8].

$$Al_{(aq)}^{3+} + 3OH^- \rightarrow Al(OH)_{3(s)} \quad (5)$$

During EC processes, the appearance of passivation on the metal surface of the electrode causes an increase in potential [2]. Thus, passivation can reduce the dissolution process of metal cations from the electrodes and leads to increased electricity consumption. To prevent the occurrence of passivation, the addition of specific anions in the solution (so-called activators, like chloride ions), regular mechanical cleaning, and rinsing of the electrode surface or electrode polarity change are usually used [2,9-12]. Therefore, further research is needed to provide a new solution that can contribute to better electrode dissolution. Our previous researches confirm that the zeolite addition in the EC process may enhance the EC treatment efficiency [13-16]. Moreover, the abrasive effect of zeolite particles on the electrode surface was also recorded, which can reduce the passivation effect.
The purpose of this paper is to investigate how changing the parameters of the EC experiments, such as different sizes of zeolite particles and different current densities, will affect the change in the surface of aluminium electrodes during the EC experiment, electrode consumption, and removal efficiency. The surfaces of the electrodes were analysed by optical microscope, while the consumption of the aluminium electrodes was investigated by weighing method. Treatment efficiency was evaluated by measuring pH, temperature, total solids, COD, and turbidity decrease.

2. EXPERIMENT

2.1. Materials

Compost leachate was collected during the composting of biowaste in the "C-EcoForHome" composter with the use of "Compost Help" anaerobic microorganisms. Compost leachate is characterized by acidic pH (pH=4.03), very high organic load (initial COD equals 10427.6 mg O_2/L), very high electrical conductivity of 3.54 mS/cm, turbidity of 397 NTU, and total solids (TS) of 10.33 g/L. All measured parameters are determined according to the Standard Water and Wastewater Testing Methods [17].

Electrode material: The aluminum alloy AA 2007 series 2000 was used as electrodes (anode and cathode), in which the main alloying element is copper (Al=92.58%, Cu=3.84%).

Synthetic zeolite: The synthetic zeolite NaX was purchased from Sigma-Aldrich (zeolite type with $r_{Si/Al}$ = 1.23). Before use, the zeolite was crushed and sieved into two different granulations of NaX particles of 160-600 μm and < 90 μm.

2.2. Performance of the electrocoagulation process

Electrocoagulation (EC) was carried out in a 350 mL of electrochemical cell, with immersed aluminum electrodes and with the addition of 20 g/L NaX zeolite (particle zeolite size of <90 μm or 160-600 μm), without the addition of electrolyte. The initial pH of the solution was 4.03. Distance between electrodes was maintained at 3 cm and a

mixing speed of 100 rpm and the working EC time was 30 min. The applied current density values were i = 0.018 A/cm^2 and 0.009 A/cm^2. Experiments labeling and working conditions are summarized in Table 1.

Table 1. Experiments labeling and working conditions

Experiments labeling	Working conditions Al electrode, t = 30 min, electrode distance = 3 cm, mixing speed =100 rpm
A1	EC, NaX (< 90 μm), i=0.009 A/cm^2
A2	EC, NaX (< 90 μm), i=0.018 A/cm^2
A3	EC, NaX (160-600 μm), i=0.009 A/cm^2
A4	EC, NaX (160-600 μm), i=0.018 A/cm^2

For each EC process, pH, temperature, total solids, turbidity, and COD were measured according to Standard Methods of Water and Wastewater Analysis [17].

2.3. Electrode surface preparation and consumption loss analysis

Before each measurement, the surfaces of the Al electrodes were ground with P240, P400, P600, and P800 grit water-based abrasive papers using Metkon Forcipol 1V metallographic grinding and polishing machine manufactured by Metkon, Turkey. After mechanical processing, the electrodes were ultrasonically degreased in ethanol, washed in deionized water, dried, and weighed on an analytical balance before use. The electrode consumption was determined by weighing both electrodes (anode and cathode) on analytical balance before and after each experiment.

2.4. Examination of the electrode surface with a light microscope

The electrode surface of the aluminum electrodes (anode and cathode) after EC process was examined with a light microscope MXFMS-BD, Ningbo Sunny Instruments Co. with a magnification of 100 times. The is a trinocular microscope on which a Canon EOS 1300D digital camera is mounted and used to photograph the surface of the samples. The microscope is connected to the computer via a camera, and the image of the surface is projected on the computer monitor.

3. RESULTS AND DISCUSSION

3.1. Analysis of the electrode surface before and after the implementation of the electrocoagulation process using a light microscope

Electrochemical processes at the anode and cathode, as well as exposure of the electrodes to leachate produced by anaerobic composting, lead to significant changes on the surface of the electrodes. For this reason, it is important to examine the condition of the surface of the electrodes after carrying out the process in order to determine the degree of wear and the form of corrosion attack on the electrodes. Therefore, the surfaces of the anodes and cathodes, before and after the implementation of the electrocoagulation process, were recorded using a light microscope with a magnification of 100 times and comparisons are given in Figure 1.

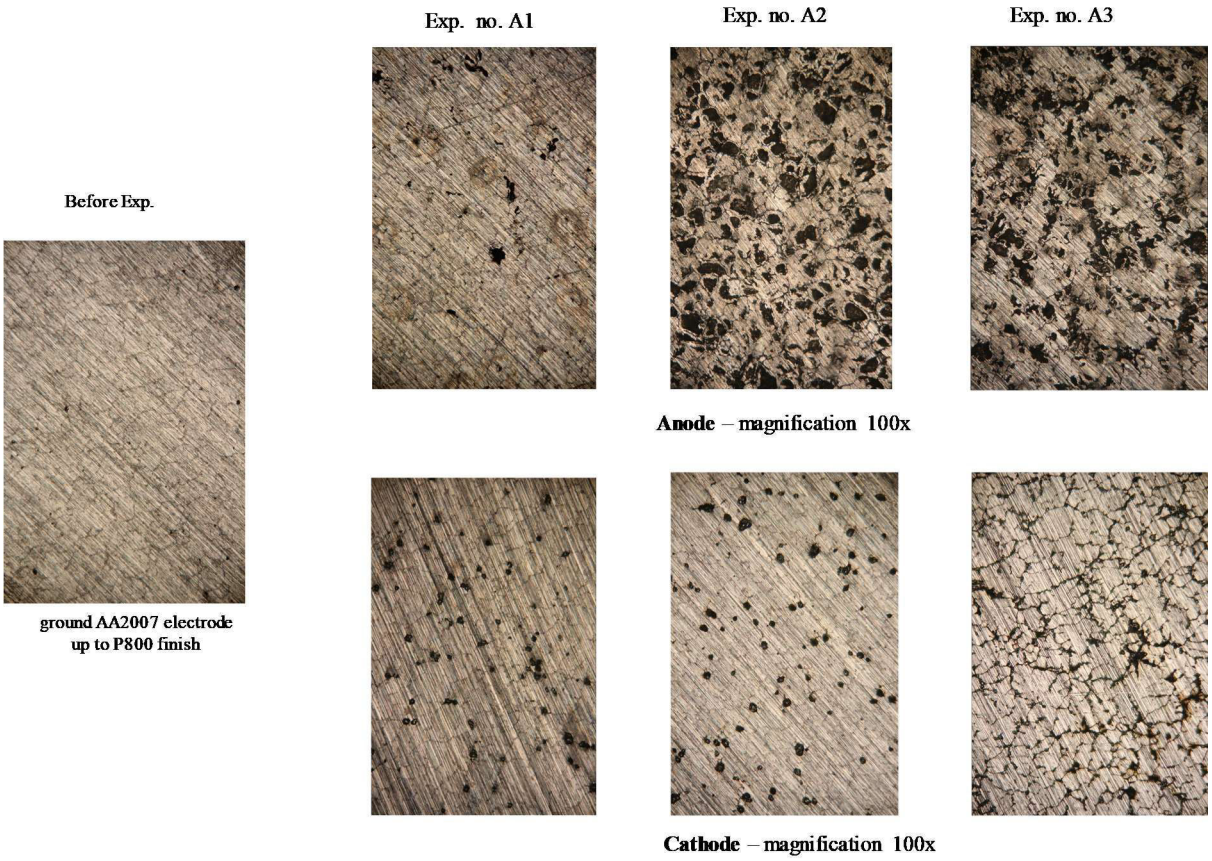

Figure 1. Comparison of Al electrode surface before and after EC process at experimental conditions of A1, A2, and A3

Despite the fact that polished Al alloy electrodes are shiny and smooth (image on the left side of Figure 1), microscopic pictures reveal surface inhomogeneities. Microscopic images of the electrodes after mechanical processing by grinding and before the EC process (image on the left side of Figure 1) show sandpaper "lines" which are clearly visible. The surface's small residual roughness aids in the dissolution of the electrodes, which is helpful in this situation, and no additional polishing is needed. Namely, the main alloying element of the 2000 series alloys is Cu, which improves the mechanical properties of the alloys of this series, but at the same time worsens their corrosion properties. Consequently, such alloys have significantly lower corrosion resistance compared to pure Al.

The image for anodes and cathodes on the right side of Figure 1 shows the appearance of the electrodes after the EC process. After each experiment, the anode and cathode lost their shine and smoothness, and damage and "roughness" of the surface caused by corrosion processes are visible. The surfaces of the anodes are significantly corroded due to the intensive dissolution process, whereby two dominant forms of corrosion are visible: general and pitting corrosion. Dots on the cathodes indicate the occurrence of pitting corrosion. The amount and size of the dots depending on the experimental conditions. In addition to dots, cracked surfaces are also present, indicating the existence of a layer of corrosion products.

Comparing the surface of the electrodes after process A1 (with a current density of 0.009 A/cm^2) and A2 (with a current density of 0.018 A/cm^2), significantly greater damage is visible on the electrodes with higher values of current density. The difference in the

surface appearance of the electrodes in experiment A1, in which zeolite with smaller particle sizes was used, and in experiment A3, in which zeolite with larger particle sizes was used, is also visible. The electrodes, used for experiment A3, were significantly damaged, which can be connected to the stronger abrasive effect of larger zeolite particles.

3.2. Electrode consumption analysis

Electrode consumption was determined during each experiment by weighing the anode and cathode before and after the EC process and the results are presented in Figure 2.

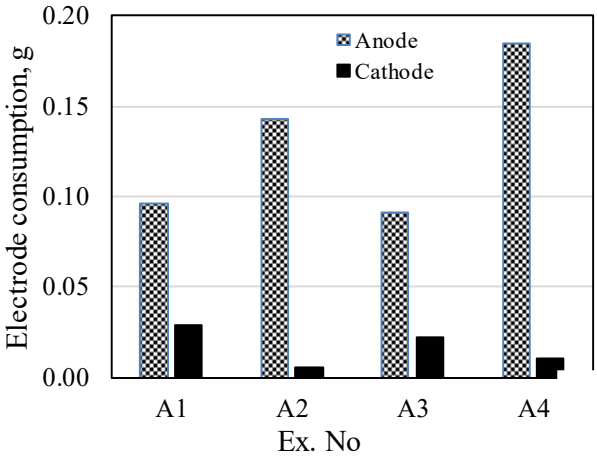

Figure 2. Comparison of anode and cathode electrode consumption

High anode consumption is observed in all EC experiments, but cathode consumption was also evident. Regarding the influence of current densities, higher anode consumption was observed in experiments with higher current densities of 0.018 A/cm^2, while at lower values of the current density of 0.009 A/cm^2, the cathode consumption was higher. The impact of zeolite particle size was almost insignificant for lower current density (experiment A1/A3). However, at higher current density, particle size affects cathode and anode consumption (experiment A2/A4).

The corrosion of the anode was expected, however, the corrosion of the cathode confirms the occurrence of a different mechanism of electrode dissolution in the EC process, which is characteristic of Al electrodes [13-16].

3.3. Efficiency analysis

During each EC experiment, the pH, temperature, total solids, and COD were determined and the results are summarised in Table 2.

Table 2. Results of pH in final solutions, initial and final temperature values, the total solids, and COD for each EC experiment

Exp. no.	Experiment mark	pH_{fin}, -	T_{in}, ^oC	T_{fin}, ^oC	TS, g/L	Turbidity decrease, %	COD decrease, %
A1	EC-NaX (< 90 µm), *i*=0.009 A/cm^2	6.76	23.2	28.9	11.45	87.88	17.56
A2	EC-NaX (< 90 µm), *i*=0.018 A/cm^2	7.14	22.8	34.1	11.99	70.28	32.82
A3	EC- NaX (160-600 µm), *i*=0.009 A/cm^2	5.76	22.8	29.6	11.03	88.94	31.30
A4	EC-NaX (160-600 µm), *i*=0.018 A/cm^2	5.83	23.5	41.6	10.19	97.00	51.91

An increase of initial pH values from 4.03 to pH in the range of 5.76-7.14 is evident in all experiments, which is mainly associated with the formation of OH^- ions at the cathode (reaction 3) [2]. A slightly higher increase is observed with a smaller zeolite particle site of < 90 μm (pH is in the range of 6.76-7.14), compared to the larger zeolite particle size (pH is in the range of 5.76-5.83). Also, higher current density values result in a slightly higher increase in pH values. Even though a rise in pH is observed in all experiments, this rise is lower than it is expected according to literature (pH ≈8) [13-16], which can be attributed to the complex composition of the initial compost leachate solution, which practically acts like a buffer.

During each experiment, a significant increase in temperature is observed (final temperature is in the range of 28.9-41.6 ºC), which is connected with higher electrode consumption (see Figure 2). A similar was observed previously [13-16]. Values of TS oscillate around initial TS values of 10.33 g/L, in dependence on experimental conditions. Namely, the initial TS values are significantly high, and thus no significant reduction was observed in the final solution.

Turbidity and COD decrease was observed. The turbidity decrease was significant (in the range of 70.28-97.00 %) compare to the COD decrease (in the range of 17.56-51.91%). The best turbidity and COD removal was observed at experiment A4 (at higher zeolite particle and higher current density). This indicates that larger zeolite particle size and higher current density enhance Al electrode dissolution and formation of Al flock, thus removal of a higher amount of soluble and colloidal species from compost leachate is observed.

Even significant turbidity reduction was achieved with the application of the EC process, final values of COD in all experiments significantly exceed the limit values prescribed by Croatian regulation for discharge into natural surface water and public sewage system (125 mg O_2/L) [18], thus addition treatment process needs to be performed before final discharge.

4. CONCLUSION

Microscopic images of the electrodes after the electrocoagulation process indicate significant damage to the electrode surface. The surfaces of the anodes were severely corroded due to the intense dissolution process, with general and pitting corrosion observed. The appearance of pitting corrosion is visible on the cathodes, along with the presence of a cracked surface indicates the existence of a layer of corrosion products. Increased values of current density induced higher electrode damage. Also, significant damage was observed on the electrode that was used in the experiment with larger zeolite particles, which can be associated with its stronger abrasive effect. Anode consumption was more pronounced at higher values of current density and higher zeolite particle size, with the highest turbidity and COD decrease observed.

5. REFERENCES

[1] Sen S., Prajapati A. K., Bannatwala A., Pal D., Electrocoagulation treatment of industrial wastewater including textile dyeing effluent – a review, *Desalination and Water Treatment* 161 (2019) 21–34, doi: 10.5004/dwt.2019.24302

[2] Tegladza, I. D.; Xu, Q.; Xu, K.; Lv, G.; Lu, J. Electrocoagulation processes: a general review about role of electro-generated floc in pollutant removal, *Process Saf. Environ. Prot.* 146 (2021) 169-189. https://doi.org/10.1016/j.psep.2020.08.048

[3] Kabdaşlı I., Arslan-Alaton I., Ölmez-Hancı T., Tünay O., Electrocoagulation applications for industrial wastewaters: a critical review, *Environ. Technol. Rev.* (2012) 1-44. https://doi.org/10.1080/21622515.2012.715390

[4] Moussa D. T., El-Naas M. H., Nasser M., Al-Marri M. J., A comprehensive review of electrocoagulation for water treatment: Potentials and challenges. *J Environ Manage* 186 (2017) 24–41. doi:10.1016/j.jenvman.2016.10.032
[5] Bharath, M.; Krishna, B. M.; Kumar, B. M. A review of electrocoagulation process for wastewater treatment, *Int. J. Chem. Tech. Res.* 11 (2018) 289-302., doi: http:77dx.doi.org/10.20902/IJCTR.2018.110333
[6] Tahreen A., Jami M. S., Ali F., Role of electrocoagulation in wastewater treatment: A developmental review, *J. Water Process Eng.* 37 (2020) 101440 https://doi.org/10.1016/j.jwpe.2020.101440
[7] Mousazadeh M., Niaragh E. K., Usman M., Khan S. U., Sandoval M. A., Al-Qodah Z., Khalid Z. B., Gilhotra V., Emamjomeh M. M., A critical review of state-of-the-art electrocoagulation technique applied to COD-rich industrial wastewaters, *Environ. Sci. Pollut. Res.* 28 (2021) 43143–43172. https://doi.org/10.1007/s11356-021-14631-w.
[8] Hashim K. S., Shaw,A., Al Khaddar R., Pedrola M. O., Phipps D. Iron removal, energy consumption and operating cost of electrocoagulation of drinking water using a new flow column reactor. *Journal of Environmental Management* 189 (2017) 98–108. doi:10.1016/j.jenvman.2016.12.035
[9] Vargel C., Jacques M., Corrosion of Aluminium, Elsevier 2004. p. 96-101
[10] Tao J., Surface composition and corrosion behavior of an Al-Cu alloy. Université Pierre et Marie Curie - Paris VI, 2016. https://tel.archives-ouvertes.fr/tel-01412882
[11] Mouedhen G., Feki M., De Petris Wery M., Ayedi H. F., Behavior of aluminum electrodes in electrocoagulation process, *J. Hazard. Mater.* 150 (2008) 124–135 doi:10.1016/j.jhazmat.2007.04.090
[12] Ingelson M., Yasri N., Roberts E. P. L., Electrode passivation, faradaic efficiency, and performance enhancement strategies in electrocoagulation – a review, *Water Res.* 180 (2020) 116433., https://doi.org/10.1016/j.watres.2020.116433
[13] Vukojević Medvidović, N.; Vrsalović, L.; Brozinčević, T.; Svilović, S., Treatment of municipal wastewater by electrocoagulation and natural zeolite – influence of initial pH values. In: Szramowiat-Sala, K.; Karczewski, M.; Sornek, K.; Figaj, R. (eds.), Book of Abstracts of the 4th International Conference on the Sustainable Energy and Environmental Development, Krakov, Institute of Sustainable Energy, 2021. pp. 11-11
[14] Vukojević Medvidović, N.; Vrsalović, L.; Ugrina, T.; Jukić, I. Electrocoagulation augmented with natural zeolite—the new hybrid process for treatment of leachate from composting of biowaste. in: Dolić, N.; Zovko Brodarac, Z.; Brajčinović, S.; (Eds.), Proceedings of the 19th International Foundrymen Conference: Humans—Valuable Resource for Foundry Industry Development, Split, Croatia, 16–18 June 2021; Faculty of Metallurgy, University of Zagreb, Zagreb, Croatia, 2021; pp. 489–498. https://ifc.simet.hr/?page_id=2518
[15] Vukojević Medvidović N., Vrsalović L., Svilović S., Bobanović A., Electrocoagulation vs. Integrate Electrocoagulation-Natural Zeolite for Treatment of Biowaste Compost Leachate—Whether the Optimum Is Truly Optimal, *Minerals* 12 (2022) 442 https://doi.org/10.3390/min12040442
[16] Svilović S., Vukojević Medvidović N., Vrsalović L., Kulić A., Combining Natural Zeolite and Electrocoagulation with Different Electrode Materials – Electrode Surface Analysis and Taguchi Optimization, *App. Surf. Sci. Adv.* 12 (2022) 100330 https://doi.org/10.1016/j.apsadv.2022.100330
[17] Eaton A. D., Clesceri L. S., Rice E. W., Greenberg A. E., Franson M. A. H., (Eds.). Standard Methods for the Examination of Water and Wastewater, 21st ed.; American Public Health Association (APHA); American Water Works Association (AWWA); Water Environment Federation (WEF): Washington, DC, USA, 2005
[18] Regulation on emission limit values in wastewater, NN 26/2020 (in Croatian)

STUDY OF INTERACTIONS BETWEEN METAL IONS AND CROWN ETHERS IN LIQUID ORGANIC MEMBRANE SYSTEMS

Edita Bjelić, Jasmin Suljagić
University of Tuzla, Faculty of Technology
Tuzla, B&H

Mersiha Suljkanović
University of Tuzla, Faculty of Natural Sciences and Mathematics
Tuzla, B&H

Keywords: organic ligands, crown ethers, Pb(II), Cd(II) ions

ABSTRACT
Considering the toxic properties of heavy metals and their effects on the environment, there is an increasing interest in studying their interactions with different ligands and searching for possibilities to remove those ions from the environment. Compared to other ligands, crown ethers possess the highest selectivity as ligands for metal cations, due to their "macrocyclic effect". In this paper, interactions between Pb(II), Cd(II) ions and various crown ethers (18 crown-6, benzo-18-crown-6, dibenzo-18-crown-6, dicyclohexane-18-crown-6 ether), were analyzed. The UV/VIS spectrometric method was used to record absorption diagrams of "model systems" of varying complexity. Cd(II) and Pb(II) ions were monitored using flame atomic absorption spectrometry. In different organic solvents used (chloroform, dichloromethane), UV/VIS and FAAS measurements showed that higher absorption intensity caused more stable complexes in the membrane, complicating the release of ions. With the benzo-18-crown-6 ether as ligand, Pb(II) ions released into the aqueous phase at a rate higher than 60%, compared with Cd(II) ions released at a rate of 49%. In a model system containing a nonionic surfactant (TX-100), metal ions interact more intensely with the membrane, and cation release is reduced in the aqueous phase, indicating that the reverse micellar aggregates incorporate metal ions that result in higher absorption intensities. According to the macrocycle selected, the presence of benzo- and cyclohexyl groups (B18C6, DB18C6, DCH18C6) probably reduces interactions between substituted macrocyclic ligands and metal cations, resulting in lower values of Pb(II) and Cd(II) ions measured in the aqueous phase compared with a model system with 18 crown-6 ether.

1. INTRODUCTION

A major problem in the world is the pollution of water caused by the discharge and accumulation of heavy metals. Natural waters usually contain trace amounts of heavy metals, but many are toxic even at very low concentrations [1]. Controlling Pb(II) and Cd(II) ions in environmental samples is of crucial importance due to their industrial importance and its environmental pollution [2]. In analytical chemistry, and especially in industrial processes, it is critical to separate metal cations from complex matrices. As well as finding the most efficient and reliable methods for determining undesirable components, attention is focused on removing them from the environment. Crown ethers are generally heterocyclic compounds with high binding affinity. The unique structure of crown ethers has made them widely used in drug delivery, solvent extraction, cosmetics manufacturing, material studies, catalysis, separation, and organic synthesis. This class of organic compounds has an interesting structure with a hydrophobic ring surrounding a

hydrophilic cavity [3]. Hydrophobic rings surround hydrophilic cavities in these molecules, enabling them to form stable complexes with metal ions and contribute to host-guest chemistry [4,5]. The interaction between ligands and metal cations is determined by the nature of the metal cation as well as the number, distance, and orientation of the ligand donor atoms structurally accessible to the complex metal cation [6]. Pedersen studied the properties and manufacturing of crown ether for the first time in 1967 [7,8]. According to Pedersen's proposal, metal ions are electrostatically attracted to oxygen atoms in crown ether rings (host-guest complexes), and a ligand that exhibits less affinity for transition metal cations than alkali and alkaline earth metal cations [9].

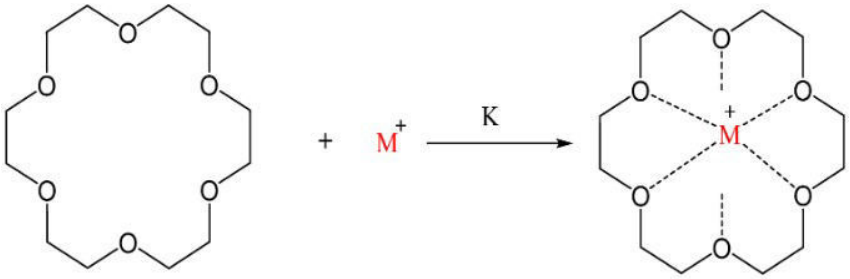

Figure 1. Binding of M+ by 18-crown-6 ether; K is complex stability constant [10]

In this paper, interactions between Pb(II), Cd(II) ions and various crown ethers (18 crown-6, benzo-18-crown-6, dibenzo-18-crown-6, dicyclohexane-18-crown-6 ether), were analyzed. After complexation of the carrier with Pb(II) and Cd(II) ions on the left side of the membrane $(CE\text{-}Pb^{2+})(CE\text{-}Cd^{2+})$, $(Pic^{-})^2$ ion-pair is formed at the SP-MP interface and diffuses down its concentration gradient within the organic phase. Liquid membrane is known as a green technology because of its green characteristics such as being eco-friendly and its low consumption of organic solvent [11]. A liquid membrane system used involves an organic liquid membrane that serves as a semi-permeable barrier between two aqueous phases, the source phase (SP) and receiving phase (RP). On the right side of the membrane, at the MP-RP interface, the metal ion would be released into the receiving phase via the formation of ternary adducts (carrier-metal ion-stripping agents/carrier-metal ion-surfactants).

.

2. MATERIALS AND METHODS

Materials

Feed solutions were prepared from:

- Standard Pb(II), and Cd(II) solution (1000 mg/L), Merck
- Picric acid ($C_6H_3N_3O_7$), c = $1 \cdot 10^{-3}$ mol/L, 99%, Kemika
- Formic acid buffer solution (pH=3), prepared from HCOOH and NaOH (g.r., Merck)

Organic solutions were prepared from:

- Organic solvents: chloroform (CHCl3), dichloromethane (CH2Cl2) and 1,2-dichloroethane (C2H4Cl2)
- Macrocyclic ligands: 18-crown-6 (18C6), benzo-18-crown-6 (B18C6), dibenzo-18-crown-6 (DB18C6), dicyclohexano-18-crown-6 (DCH18C6)

Stripping solutions were prepared from:

- Triton X-100 surfactant (1,4·10-3 mol/L)
- Disodium-EDTA (1·10-3 mol/L)

– Acetic acid buffer solution (pH=5), prepared from CH3COOH (purris. p.a., Fluka) and NaOH (g.r., Merck).

Extraction procedure
Liquid-liquid extraction – LLE is based on the distribution of the analyzed substance from one liquid phase to another liquid phase. Liquid phases do not mix with each other: e.g. water and hydrophobic organic solvents, then alcohol and ether, etc.
LLE is the most commonly used separation method, where the metal ion from the aqueous phase passes into the organic phase by complexing with some hydrophobic ligand.
In order for the extraction to take place at the molecular level, the metal ion and the ligand must react and diffuse together, which can be shown schematically (Figure 2.).

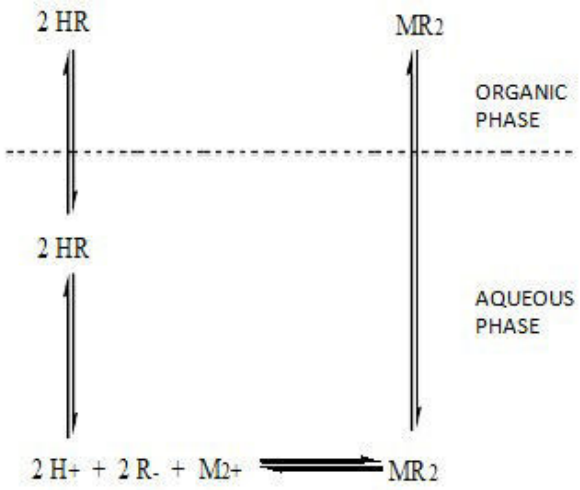

Figure 2. Balances in the system during the extraction of M^{2+} cations by the chelating agent

The source phase (SP) contained 10 mL of a mixture of tested Pb(II) ions ($1 \cdot 10^{-3}$mol/L) and Cd(II) ($1 \cdot 10^{-3}$mol/L). The receiving phase (RP), which is outside the central tube, contained a stripping agent. The membrane phase (MP) contained a suitable ligand ($1 \cdot 10^{-3}$mol/L) dissolved in an organic solvent; the membrane layer lies beneath the aqueous phases and connects them. The membrane phase is mixed with a magnetic stirrer so that under these conditions the contact surfaces between the aqueous phases are straight and precisely defined [12]. Spectrophotometric measurements of the membrane phase were performed with UV/VIS spectrophotometer (CECIL CE 2021).
Quantification of metal ions removed during the transport experiments was obtained by Flame Atomic Absorption Spectrometry technique, using the instrument Perkin Elmer AAnalyst 200.

3. RESULTS AND DISCUSSIONS

The macrocyclic structure of organic ligands ensures high stability of the formed complexes with metal ions due to the "macrocyclic effect" [13]. The affinity of the ligand to the metal ion depends on the structural characteristics of the ligand, primarily on the number and type of donor atoms, polarity, the hydrophilic-lipophilic balance of the ligand, chirality and other stereochemical indicators with heteroatoms (oxygen atoms). In particular, the highest selectivity is expected in cases where the ratios of cation radius and ligand cavity radius are closest to 1. One of the main factors determining transport

efficiency is the nature of the membrane. In complexation, solvation is an important factor in determining the interactions between metal cations and ligands, which includes ligand, metal cation, and complex together. This can be explained by Cram's reorganization principle, which states that both host and guest are involved in solvent interactions [14].
Effective interactions, according to the acid-base concept (classification into so-called hard and soft bases and acids), Pb(II) ions have a less "soft character", so they can form a more stable complex with oxygen atoms that donates B18C6 as a “hard” base.
Experiments involved different ligands dissolved in organic solvents as carriers for Pb(II) and Cd(II) ions. Results showed that benzo-18-crown-6 ether achieved the highest efficiency in removing Pb(II) ions in chloroform (60%) compared with dibenzo-18-crown-6 ether, and dycyclohexano-18-crown-6 ether. In addition, Pb(II) ions carry a high charge density, and consequently in greater transport of Pb(II) ions with B18C6 compared to other ligands. Compared to the system with 18-crown-6 ether, where the ring size and cavity diameter remain the same (1.34 A^0), the presence of benzo- and cyclohexyl groups (B18C6, DB18C6, DCH18C6) probably reduces the interactions between substituted macrocyclic ligands and cations, which leads to lower values of measured Pb (II) ions in the final phase compared to the model system with 18C6 (70.4%). Actually, DB18C6 has the most rigid structure among the crown ethers studied [15,16].
The UV/VIS absorption spectra of 3-component systems (picrate + Pb(II) + ligand) showed a higher intensity of absorption band for 1,2-DCE as a membrane solvent (Figure 3). The higher absorption intensity probably refers to stronger interactions for model system PA+Pb+18C6 which result in a more stable complex formed in the membrane compared to model system PA+Pb+DB18C6 for both solvents used.

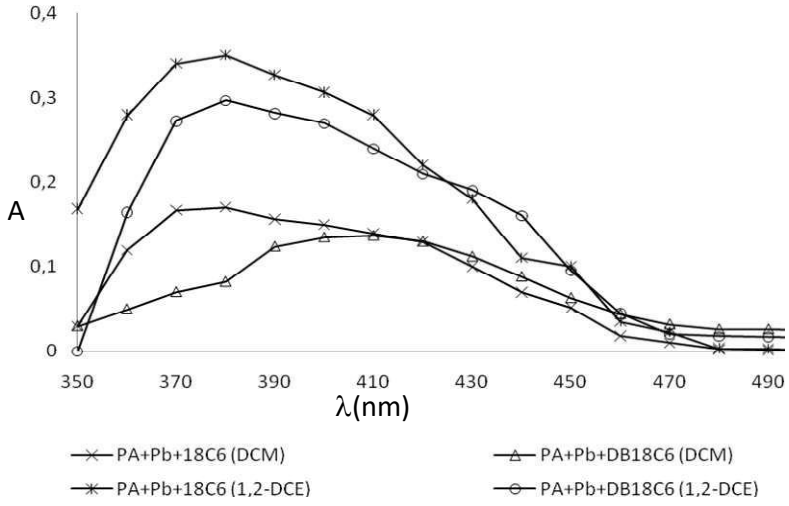

Figure 3. Comparison of absorption diagrams model - system: PA+ Pb(II)+18C6, PA+ Pb(II)+DB18C6 in the presence of different solvents in the liquid membrane

If we observe the absorption diagram of the 3-component system inside the membrane (PA+Cd(II)+ligand), we notice a lower intensity of absorption in chloroform (Figure 4.) compared to dichloromethane (DCM) and 1,2-dichloroethane (DCE) as membranes. Namely, a higher intensity of absorption means stronger interactions within the membrane, the complex formed in the membrane is more stable, and this further complicates the release of cations at the boundary between the membrane and the aqueous phase.

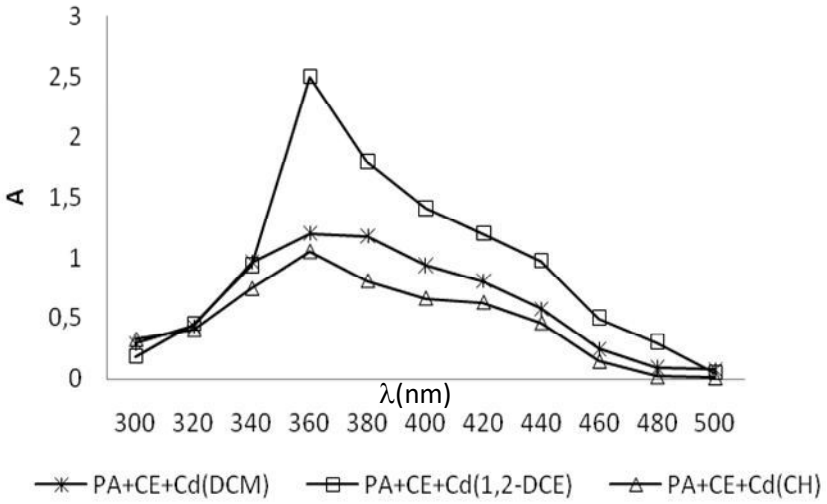

Figure 4. Comparison of absorption diagrams model - system: PA+ Cd(II)+18C6, PA+ Cd(II)+DB18C6 in the presence of different solvents in the liquid membrane

After 3 h of transport, the highest percentage of removed ions in the aqueous phase was measured for the system with a CH membrane, where the efficiency of removed Cd(II) ions was slightly lower (43.2%). For the system with a 1,2-DCE membrane, the efficiency of removed Cd(II) ions was 35.30%.

Interactions between cations and surfactants inside the membrane successfully provide cation removal from the source phase, but not their transfer to the receiving phase. The results show a lower transport efficiency for systems with added surfactants (TX-100 and TX-45), compared to systems containing only macrocyclic ligands. The influence of the surfactant structure is obvious: the comparison of Pb(II) transport results confirms the fact that the length of the polyether chain affects the metal-surfactant interactions. Despite the assumption that the spatial separation of cations from the binding sites of longer-chain surfactants reduces the level of interaction, the greater number of binding sites (oxygen atoms) in the structure of longer-chain surfactants speaks in favor of a greater possibility of interactions. The higher absorption intensity probably refers to stronger interactions within the membrane, the formed complex in the membrane is more stable, and consequently the release of metal ions to the receiving phase is reduced.

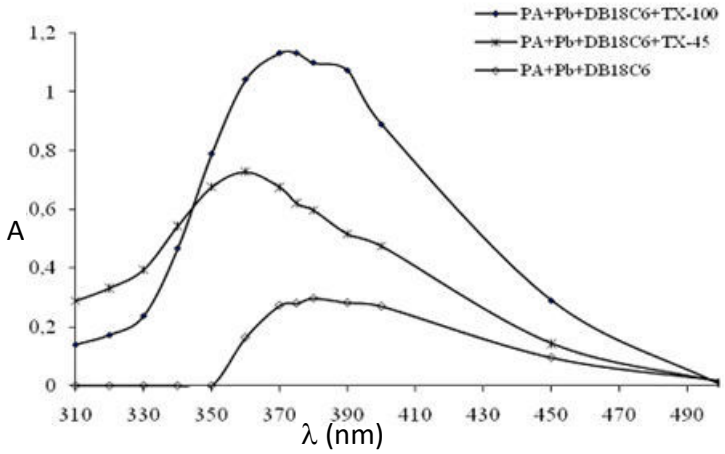

Figure 5. Comparison of absorption diagrams model - system: PA+ Pb(II)+DB18C6, PA+ Pb(II)+DB18C6+TX100, PA+ Pb(II)+DB18C6+TX45, in the presenceof 1,2-DCE in liquid membrane

4. CONCLUSIONS

The UV/VIS and FAAS measurements in different organic solvents found that higher absorption intensity caused more stable complexes in the membrane, resulting in a more difficult ion release. In the presence of benzo-18-crown-6 ether, Pb(II) ions release into the aqueous phase at a rate greater than 60%, compared with Cd(II) ions which are released at a rate of 49%. 18-crown-6 ether is the most suitable for the complexation of Cd(II) ions compared to dibenzo-18-crown-6, benzo-18-crown-6, and dicyclohexano-18-crown-6 due to its greater flexibility. The metal ions interact more strongly with the membrane in a model system with a nonionic surfactant (TX-100), reducing cation release in the aqueous phase, indicating that reverse micellar aggregates contain metal ions resulting in higher absorption rates.

5. REFERENCE

[1] Akif, M., Khan, A, R., Sok, K.,2002**.:** Textile effluents and their contribution towards aquatic pollution in the Kabul River (Pakistan). Journal of the Chemical Society of Pakistan, 24(2), pp.106–111

[2] Eslami, S., Moghaddam, A, H., Jafari, N., Nabavi, S. F., Nabavi, S. M., and Ebrahimzadeh, M. A.,2011.: Trace element level in different tissues of Rutilus frisii kutum collected from Tajan river, Iran. Biological Trace Element Research. 14(2), pp. 965–973

[3] Ethers, A.; Basok, S. S.; Schepetkin, I. A.; Khlebnikov, A. I.; Lutsyuk, A. F.; Kirichenko, T. I.; Kirpotina, L. N.; Pavlovsky, V. I.; Leonov, K. A.; Vishenkova, D. A.; et al.: Synthesis, Biological Evaluation, and Molecular Modeling of Aza-Crown Ethers. Molecules 2021, 26, 2225

[4] Bukhzam, A.; Bader, N. Crown Ethers: Their Complexes and Analytical Applications. J. Appl. Chem. 2014, 3, 237–244

[5] Alabdaly, B. I. Synthesis: Characterization and Antibacterial Activity of New Complexes of Some Lanthanide Ions with Benzo 18-Crown-6 and 221-Cryptand. IOSR J. Appl. Chem. 2013, 6, 32–39

[6] Salman, S. R., Derwish, G. A. W., Al-Marsoumi: S. M. H. 1996. Journal of Inclusion Phenomena and Molecular Recognition in Chemistry, 25 295-302. Gokel, G. W.; Leevy, W. M.; Weber, M.E. Crown ethers: Sensors for ions and molecular scaffolds for materials and biological models. Chem. Rev. 2004, 104, 2723–2750 [CrossRef]

[7] Pedersen, C. J. Cyclic polyethers and their complexes with metal salts: J. Am. Chem. Soc. 1967, 2, 7017–7036

[8] Ijeri, V.; Vocanson, F.; Martelet, C.; Jaffrezic-Renault, N.; Lyon, E.C. De Capacitive Sensing of Amino Acids Using Caliraxene-Coated Silicon Transducers: Electroanalysis. 2007, 19, 510–514

[9] Ushakov, E. N.; Alfimov, M. V.; Gromov, S. P. Crown Ether Based Optical Molecular Sensors and Photocontrolled Crown Ether-Based Optical Molecular Sensors and Phoocontrolled Ionophores: J. Macroheterocyc. 2010, 3, 189–200

[10] Chang, S. H., Teng, T. T., Ismail, N.,2010: Extraction of Cu(II) from aqueous solutions by vegetable oil-based organic solvents, J. Hazard. Mater. 181, pp. 868–872

[11] Nipamanjari D., Sanjib B., Mukherjee, A. K. 2010: Charge transfer complex formation between TX-100/CCl4. Molecular Physics 108 (11), 1505– 1511

[12] Geary C. D., Zudans I, Goponenko A. V., Asher, S. A. Weber, S. G: Anal. Chem., 2005, 7, 185

[13] D. J. Cram. From Design to Discovery: American Chemistry Society, Washington, DC (1991) p. 91

[14] Kashanian S., Shamsipur, M.: Anal, Chim. Acta, 1989, 155 203

[15] Amini M. K., Shamsipur M.: J. Solution Chem., 1992, 21, 275

RUTIN ANALYSIS BY HIGH-RESOLUTION LIQUID CHROMATOGRAPHY ON REVERSE PHASES IN RASPBERRY FLOWER EXTRACT (*Rubus idaeus* L.)

Dejana Kasapović, Farzet Bikić
University of Zenica, Faculty of Metallurgy and Technology
Zenica, B&H

Keywords: rutin, raspberry flowers, analysis, soxhlet extraction, ultrasonic extraction, liquid chromatography

ABSTRACT
Rutin belongs to the group of polyphenolic compounds, which consists of hormones, vitamins, and antioxidants in food. It is found mostly in plants and is one of the most biologically active flavonoids. It can act as an antioxidant, antibacterial, and anti-inflammatory and can prevent the formation of a tumor. The concentrationof rutin was determined in (Rubus idaeus L.) Polka raspberry by applying reverse-phase high-resolution liquid chromatography on reverse phases on Shimadzu Prominence Modular HPLC with UV/Vis detector. The analysis was performed in ethanolic extracts of Polka raspberry flower obtained by the Soxhlet extraction and the ultrasonic methods. Raspberry flowers (Rubus idaeus L.) Polka varieties were collected from two different localities in Bosnia and Herzegovina, namely: Starposle near Kakanj and Moševac near Maglaj. Rutin was determined in all analyzed samples of Polka raspberry. The highest rutin concentration was determined in the extract of the Polka raspberry flower from the Kakanj-Starposle site, using the ultrasonic method (31,46±13,90μg/cm^3), and the smallest in the Polka raspberry flower from the Kakanj-Starposle site, using Soxhlet extraction (3,16±0,08 μg/cm^3). The concentration of rutin was higher in the extract of Polka raspberry flower from the Kakanj-Starposle site, which suggests that these flowers of the Polka variety are recommended as better natural sources of rutin and that ultrasonic extraction has proven to be a more efficient method for extraction of rutin in ethanolic extracts, which is the goal of research.

1. INTRODUCTION

Rutin is one of the most active biological flavonoids, also known as vitamin P. Rutin is considered an activating factor for vitamin C. The name rutin comes from the plant Ruta graveolens, in which, according to the content of polyphenols, it predominates [1]. Raspberry is a perennial, shrubby, deciduous plant from the family Rosaceae of the genus *Rubus*. It consists of aboveground (leaf, flower, seed and fruit) and underground (root) organs. Polka Raspberry is one of the best varieties of raspberries. It is a permanent raspberry, a newer raspberry variety originating from Poland, created by the crossing of varieties: *Autumn Bliss*, *Lloyd George* and *Rubus crataegifolius*, introduced in 2001 and entered in the official registers in 2003. Raspberry belongs to the group of berries and is a natural source of bioactive compounds that benefit human health. It is rich in compounds such as vitamins, minerals and is one of the richest sources of natural antioxidant compounds such as polyphenols [2]. Rutin is a flavonoid found in citrus fruits, buckwheat, apples, green tea, carrots, grapes, linden and eucalyptus leaves, and various berries. The role of rutin in plants is the transport of cations and the supply of nutrients from the soil. Rutin is a flavonoid that shows numerous positive effects on human health, precisely because of its antioxidant effect [1].

2. EXPERIMENTAL PART

Raspberry flowers (*Rubus idaeus* L.) were collected from two different sites in Bosnia and Herzegovina, namely Starposle near Kakanj and Moševac near Maglaj. The difference between these two sites is the altitude. Moševac near Maglaj is located at an altitude of 169 meters, and Starposle near Kakanj at 470 meters. These two sites are far from industrial plants.

2.1. Obtaining extracts and samples of raspberry flower for HPLC analysis

Dried raspberry leaves were ground in a blender, and as such, used in the Soxhlet apparatus. Ethanol was used as the solvent. The extraction lasted for six hours, after which the obtained extract was evaporated to dryness. The extracts obtained in this way were stored in dark bottles in a refrigerator at a temperature of +4 ºC. The obtained extract samples were of resinous consistency, and well soluble in ethanol. Extractions were also performed in the ultrasonic bath under defined conditions: frequency (20-40 kHz), power (250-500 W), temperature (40ºC), and extraction time (30 min) [3]. Ethanol was used as the solvent. After treatment, the extracts were filtered and evaporated to dryness. The extracts obtained in this way were stored in dark bottles in a refrigerator at a temperature of +4 ºC. The fact that plants contain several thousand secondary metabolites creates a need to develop fast and precise extraction methods.Dry flower extracts (about 0.5 g), obtained by Soxhlet extraction and ultrasonic method, were dissolved in 50% methanol in an ultrasonic bath. Then filtered to remove impurities and transferred to vials.
The content of total phenols was determined spectrophotometrically, on the PerkinElmer, Lambda 650, UV – VIS spectrophotometer device, by the Folin-Ciocalteu method.

2.2. Rutin analysis using RP-HPLC-UV/Vis technique

Rutin analysis of Polka raspberry flower extracts from two different sites was performed by high-performance liquid chromatography on reversed phases on Shimadzu Prominence Modular HPLC with UV/Vis detector, mobile phase degasser, pump, autosampler, and column oven. Analysis of rutin was performed on a Nucleosil C18 column (250 mm × 4.6 mm, particle size 5 μm; Macherey-Nagel). As the mobile phase, a solvent system was used: A (1% formic acid) and B (acetonitrile) at a flow rate of 1 ml/min and using the following linear gradient: 0–10 min from 10 to 25% A; 10–20 min linear rise to 60% A, 20–30 min linear rise to 70% A. The column was balanced to initial conditions, 10% A, 10 min with an additional 5 min for stabilization [4,5]. The rutin standard was dissolved in 50% methanol. Chromatograms were recorded at 360 nm for flavonoids (rutin). Based on the obtained chromatograms and the calibration diagram of the standard rutin solution, the rutin concentration in the extracts was calculated ($\mu g/cm^3$) [4,5].
The rutin standard of different concentrations is shown in Table 1 and was used for HPLC analysis[3,4].

Table 1 Standard solution of rutin of different concentrations for HPLC analysis

Standard solution	Concentration ($\mu g/cm^3$)			
Rutin	4	5	6	100

The calibration curve of the analyzed rutin standard solution is shown in Figure 1.

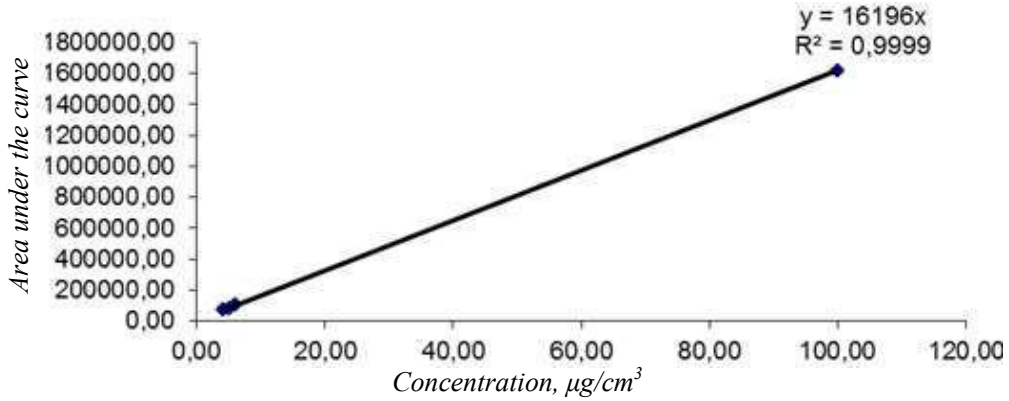

Figure 1. Calibration curve for rutin

3. RESULTS AND DISCUSSION

Extracts of Polka raspberry flower obtained by ultrasonic extraction showed a significantly higher total phenol content than extracts obtained using Soxhlet extraction, as shown in Table 2. Based on these results, it is safe to say that ultrasonic extraction leads to a higher yield of phenolic compounds in a shorter time, reducing energy consumption and phenol degradation. Ultrasonic extraction has been shown a better and more cost-effective technique than Soxhlet extraction for the extraction of Polka raspberry flower.

Table 2. Content of total phenols in Polka raspberry flowers extracts obtained by methods of Soxhlet and ultrasonic extractions

Plant extracts	Content of total phenols *(mg GA/g extract)*
SCPM	95,08±8,57
SCPK	62,65±2,33
UCPM	**148,99±9,02**
UCPK	**146,66±2,85**

SCPM - flower Polka Maglaj – Soxhlet; SCPK - flower, Polka Kakanj - Soxhlet UCPM - flower Polka Maglaj – ultrasonic;UCPK- flower Polka Kakanj – ultrasonic

All experiments were repeated three times.Results are expressed as mean ± SD (n = 3). The HPLC method was used to determine the concentration of rutin in the tested extracts of the Polka raspberry flower. The results of HPLC analyzes of these extracts are shown in Table 3. Figures 2 - 5 show HPLC chromatograms for rutin detected in Polka raspberry flower extracts.

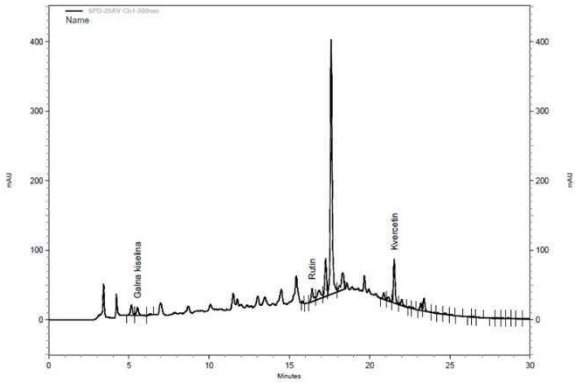

Figure 2. HPLC chromatograms of Maglaj Polka flower - Soxhlet extraction (SCPM)

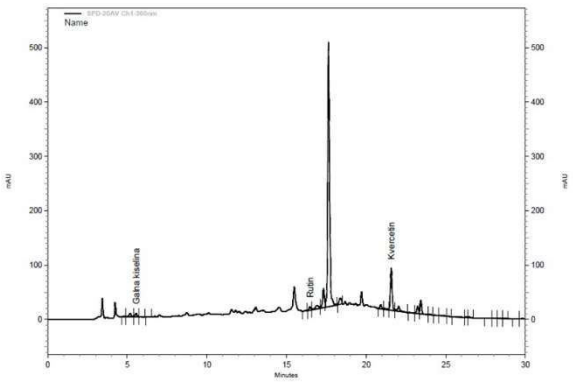

Figure 3. HPLC chromatograms of Kakanj Polka flower - Soxhlet extraction (SCPK)

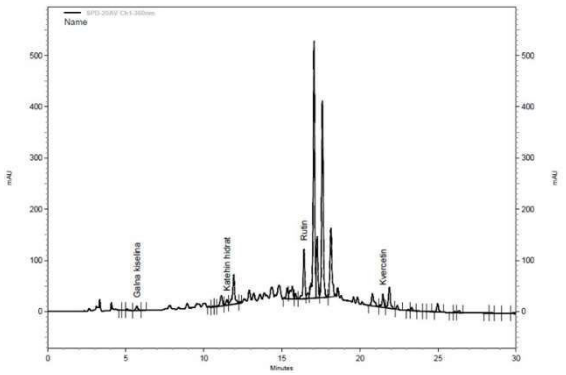

Figure 4. HPLC chromatograms of Maglaj Polka flower - ultrasonic extraction (UCPM)

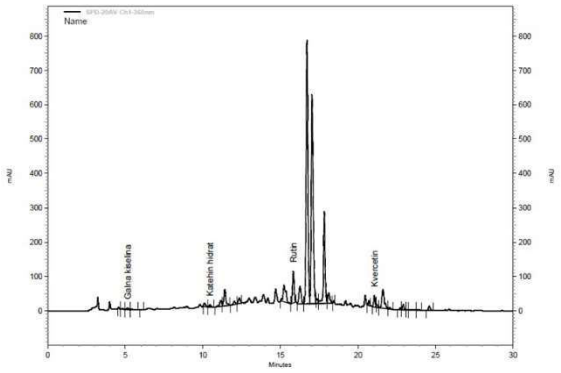

Figure 5. HPLC chromatograms of Kakanj Polka flower - ultrasonic extraction (UCPK)

HPLC chromatograms showed the presence of rutin in extracts of the Polka raspberry flower.

Table 3. Results of HPLC analysis of rutin in Polka raspberry flower extracts obtained by Soxhlet and ultrasonic extractions

Plant extract	RUTIN
	Concentration, $\mu g/cm^3$
SCPM	10,38±0,79
SCPK	3,16±0,08
UCPM	**29,88±21,22**
UCPK	**31,46±13,90**

Based on the results of spectrometric and HPLC analyzes, it can be concluded that the content of total phenols and rutin is much higher in all samples of:

- Maglaj Polka raspberry in relation to the Kakanj Polka raspberry obtained by Soxhlet Extraction;
- By ultrasound extraction in relation to Soxhlet extraction.

4. CONCLUSIONS

Rutin is a flavonoid that shows numerous positive effects on human health, precisely because of its antioxidant effect. Rutin was determined in all analyzed samples of Polka raspberry. The highest rutin concentration was determined in the extract of the Polka raspberry flower from the Kakanj-Starposle site, using the ultrasonic method (31,46±13,90 $\mu g/cm^3$), and the smallest in the Polka raspberry flower from the Kakanj-Starposle site, using Soxhlet extraction (3,16±0,08 $\mu g/cm^3$). The concentration of rutin was higher in the extract of Polka raspberry flower from the Kakanj-Starposle site, which suggests that these flowers of the Polka variety are recommended as better natural sources of rutin and that ultrasonic extraction has proven to be a more efficient method for extraction of rutin in ethanolic extracts.

5. REFERENCES

[1] K. Patel, DK. Patel: The Beneficial Role of Rutin, A Naturally Occurring Flavonoidin Health Promotion and Disease Prevention: A Systematic Review and Update, *Bioactive Food as Dietary Interventions for Arthritis and Related Inflammatory Diseases, 457-479,* 2019

[2] L. Maslov Bandić, M. Jenić, B. Duralija: Bioactive compounds in the fruit, leaves and seeds of raspberry (*Rubus idaeus* L.), *Glasnik zaštite bilja, 50-55,*5/2020
[3] A. S. Milenković Anđelković: *Ekstrakcija, karakterizacija, biološka aktivnost i potencijalna primena fenolnih jedinjenja iz plodova i lišća biljnih vrsta familija Rosaceae, Cornaceae i Grossulariaceae,* Doktorska disertacija, Univerzitet u Nišu, Prirodnomatematički fakultet, Niš, 2016.
[4] M. Vinčić: *Antioksidativna, antiproliferativna i antimikrobna aktivnost odabranih ekstrakata tropova bobičastog voća,* Doktorska disertacija, Univerzitet u Novom Sadu, Tehnološki fakultet, Novi Sad, 2017.
[5] D. Kasapović, F. Korać, F. Bikić: Gallic acid analysis by high-resolution liquid chromatography on reverse phases in raspberry flower extract (Rubus idaeus L.), Journal of Sustainable Technologies and Materials, 30 – 35, 1/2021

CHARACTERISTICS OF VACUUM DISTILLATION FRACTIONS DEPENDING ON THE CHARACTERISTICS OF THE INPUT HYDROCRACKED BASE OIL RAW MATERIAL OF THE MODRIČA OIL REFINERY

Azra Halilović, Ilhan Bušatlić, Šefkija Botonjić, Nadira Bušatlić, Edin Zolotić
University of Zenica, Faculty of metallurgy and Technology
Zenica, B&H

Keywords: BORM (base oil raw material), HC (hydrocracked) base oils, fractions, physical and chemical characteristics

ABSTRACT
Hydrocracked base oil raw material (BORM) is the basis for the production of hydrocracked base oils (HC-base oils) in the company „Modriča Oil Refinery“, which is engaged in the production of HC-base oils, various motor and industrial lubricating oils, and lubricating greases. The production of the mentioned HC-base oils consists of four production units, the first of which (hydrocracking) is located in Bosanski Brod, and the other three (vacuum distillation, deparaffinization,and final processing - bleaching) are located within the Modrič Oil Refinery. The aim of this work was to analyze the influence of different physicochemical characteristics of BORM, which undergoes certain production processes, on the quality of its distillates. Distillation curves are also presented in the paper, based on which the temperature regime of the vacuum column is monitored and set, and different yields of fractions can be obtained. The obtained results for all tested parameters of the obtained fractions using two different base oil raw materials are within the limits prescribed by the internal standard.

1. INTRODUCTION

In the past, pure mineral oils, or oil distillates without any additives, were sufficient for the lubrication of all types of mechanical systems. However, modern mechanical systems require lubricants with improved properties, which pure mineral oils cannot have, and in addition, from an ecological point of view, conditions in terms of toxicity and environmental protectionare set. Hydrocracked base oils are increasingly used for the production of different groups of lubricants because they are characterized by a high viscosity index, excellent oxidation stability, low content of sulfur and aromatic hydrocarbons, and low volatility. The most important group of liquid lubricants, motor oils, in today's formulations, require hydrocracked base oils of medium and higher viscosity, lower volatility, and higher viscosity index. In the case of hydraulic oils for special purposes, the demand for hydrocracked base oils of medium gradations has increased. On the other hand, base oils of lower viscosity are most often used to formulate water-soluble agents for metal processing [1]. The use of hydrocracked base oils in the formulations of motor and industrial oils ensures outstanding technical characteristics of finished products and compliance with valid European standards in the field of environmental protection [2]. Base oils form the basis of all lubricants - lubricating oils and lubricating greases and significantly influence their basic properties. They are divided into: mineral and synthetic. Mineral oils are produced by refining petroleum, and synthetic oils are by chemical synthesis from different components. The advantages of synthetic base oils are

biodegradability and non-toxicity and they have a longer service life, i.e. lower maintenance costs, but the main obstacle to more intensive development is the high cost of synthetic lubricants production. Internationally accepted motor oil specifications have been developed that serve engine and vehicle manufacturers, lubricant manufacturers, additive manufacturers, and motor oil users. The specifications are based on appropriate test procedures (tests), which were developed on representative engines, reference fuels, and oils [3]. They differ in API (American Petroleum Institute) classification of base oils, ACEA classification of base oils (Association des Constructeurs Européens d'Automobiles), and SAE (Society of Automotive Engineers) classification of motor oils according to viscosity grades. For the latest models of engines and vehicles, and according to the latest specifications of the quality of motor oils, base oils with significantly improved characteristics, with as little volatility as possible, ever cleaner combustion and low sulfur content, as well as having a low price, are required. All these requirements can be met with hydrocracked and synthetic base oils. Hydrocracked base oils are becoming more and more important, in terms of required characteristics and are very close to synthetic ones, but their prices are significantly lower than synthetic ones.

1.1. Production of hydrocracked base oils

The modern way of producing base oils is the application of only catalytic processes (eg hydrocracking - catalytic conversion of n-paraffin –hydro finishing). The product created in this way is clean and stable because molecules with poor lubricating properties have been converted into high-quality molecules. Also, this kind of technology is flexible and less sensitive to the quality of crude oil [1]. The advantage of the technology of hydrocracked (HC) base oils is that that all compounds, which from a technical and ecological point of view are undesirable in oils, are transformed into technically very desirable compounds, have a low content of sulfur and aromatic hydrocarbons and very low volatility [4]. Base oils obtained by hydrogen treatment processes are characterized by a low content of unsaturated compounds and hetero-elements, which provides them with not only a technical but also an ecological advantage [5]. Hydrocracking is a two-stage process that combines catalytic cracking and hydrogenation, where heavier fractions are split in the presence of hydrogen, to obtain more desirable products.

The production of HC base oils consists of the following production units:

atmospheric distillation of crude oil,

- vacuum distillation of the atmospheric residue,
- hydrocracking plant,
- vacuum distillation plant,
- deparaffinization plant,
- finishing-whitening unit.

Figure 1 shows the scheme of the domestic production process of hydrocracked base oilsBrod-Modriča oil complex.

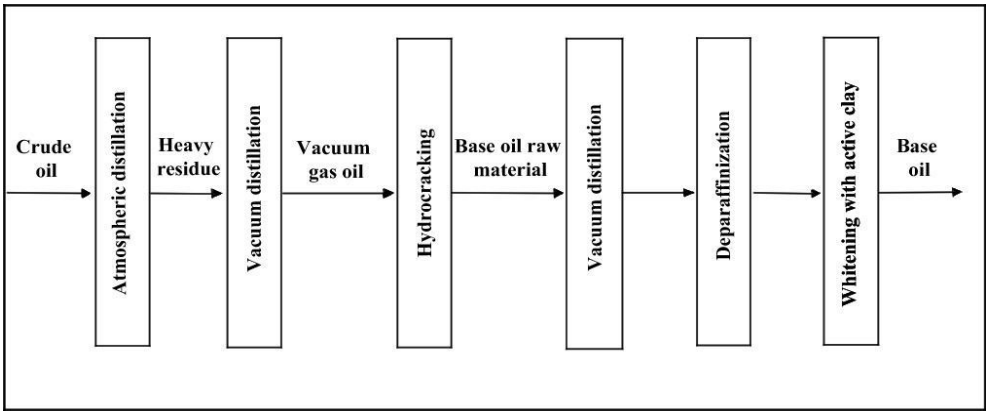

Figure 1. Block diagram of the process of obtaining hydrocracked base oils

It is important to emphasize that two products from vacuum distillation, heavy and light vacuum gas oil, are mixed and sent to the hydrocracking plant (ISOMAX), and the hydrocracking product contains light gaseous hydrocarbons, gasoline fraction, diesel fuel fraction, and the rest of the distillation represents the base oil raw material (BORM) that „Modriča Oil Refinery“ uses as a basic raw material for the production of HC base oils [6].
A vacuum distillation column is basically a rectification column. Distillation of the base oil stock is carried out in a vacuum column at reduced pressure. Figure 2 shows the vacuum distillation of BORM and the resulting products.

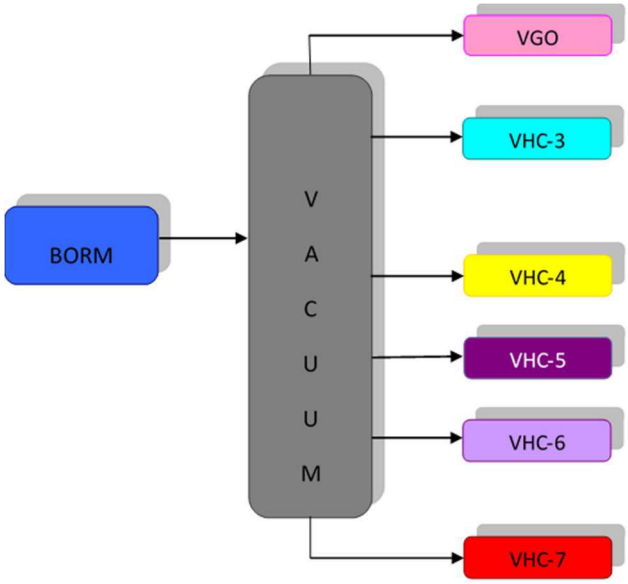

Figure 2. Block diagram of vacuum column flows
Legend: VGO - Vacuum gas oil; VHC-3 – leaves the column at 185 °C; VHC-4 - leaves the column at 220-230 °C; VHC-5 - leaves the column at 250°C; VHC-6 - leaves the column at 280 °C; VHC-7 - leaves the column at 320-350 °C

2. EXPERIMENTAL PART

The experimental part of the work was done in the company „Modriča Oil Refinery“ a.d. and includes the analysis of two base oil raw materials, as well as the analysis of their fractions.

2.1 Material and methods

Two basic oil raw materials and their fractions were used for the analysis, and the following parameters were determined:

- Determination of kinematic viscosity,
- Calculation of viscosity index from kinematic viscosity,
- Determining the pour point,
- Determining the flash point in an open container,
- Fractional distillation at reduced pressure.

The kinematic viscosity was determined according to the ISO 3104:2002 standard. Viscosity index (VI) is a number used to characterize changes in kinematic viscosity with temperature changes and was determined according to the BAS ISO 2909:2003 standard. Determination of the pour point was done according to the standard BAS ISO 3016. Determination of the flash point in an open container was done according to the standard BAS ISO 2592:2002.

Base oils are fractionated according to strict viscosity specifications with a controlled volatility, especially follow-viscosity oils. Vacuum distillation apparatus was used for the analysis, applying the method of fractional distillation at reduced pressure - ASTM D1160.Figure 3 shows the apparatus for vacuum distillation.

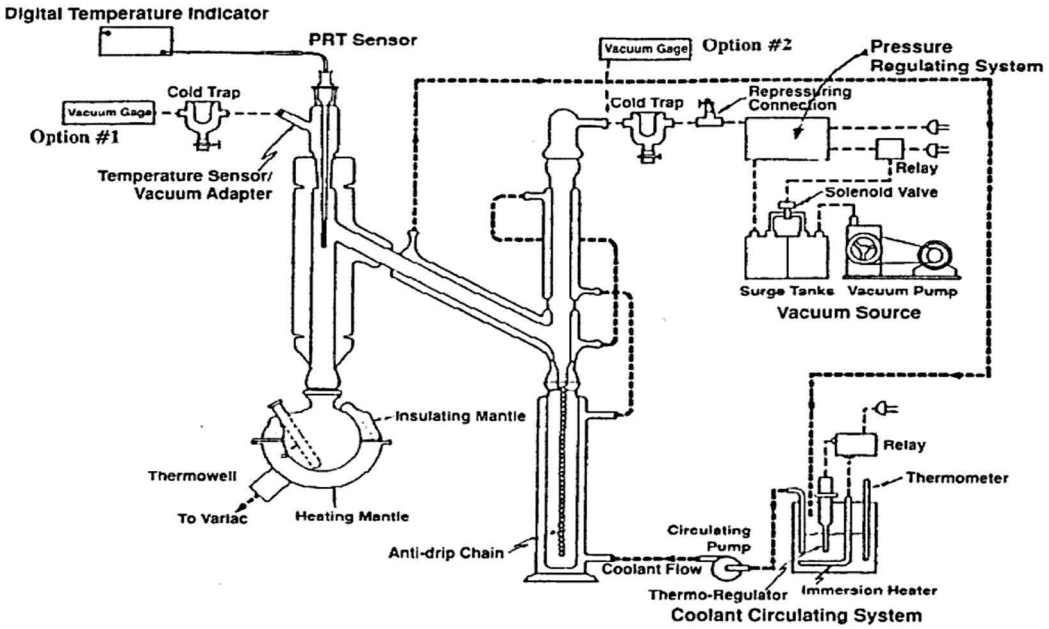

Figure 3. Vacuum distillation apparatus

3. RESULTS AND DISCUSSION

Tables 1 and 2 show the results of the determination of kinematic viscosity.

Table 1. Viscosity values for BORM1 and its fractions

Characteristic	BORM1	VGO	HC-3	HC-4	HC-5	HC-6	HC-7
υ 40°C [mm^2/s]	21,60	10,01	12,81	19,59	28,57	30,23	49,78
υ 100°C [mm^2/s]	4,47	3,10	3,12	4,22	5,61	5,81	8,31

Table 2. Viscosity values for BORM1 and its fractions

Characteristic	BORM2	VGO	HC-3	HC-4	HC-5	HC-6	HC-7
υ 40°C [mm^2/s]	21,23	10,05	12,63	18,62	24,42	33,40	43,10
υ 100°C [mm^2/s]	4,49	2,64	3,16	4,13	5,14	6,23	7,47

It can be concluded that HC-7 has the highest viscosity values, which means that it has a higher resistance to flow, that is, it flows harder compared to the other vacuums analyzed. Viscosity values play an important role when choosing a lubricating oil, considering that it affects many production specifications, the correct operation of equipment, the quality of lubrication, and thus the wear of parts.Tables 3 and 4 show the results of the viscosity index for BORM1 and BORM 2 and their fractions.

Table 3. Viscosity index for BORM1 and its fractions

Characteristic	BORM1	VGO	HC-3	HC-4	HC-5	HC-6	HC-7
VI	118	101	103	121	139	138	141

Table 4. Viscosity index for BORM2 and its fractions

Characteristic	BORM2	VGO	HC-3	HC-4	HC-5	HC-6	HC-7
VI	123	103	110	126	143	139	141

Based on the results, it can be seen that the heaviest fraction of the vacuum column HC-7 is also the fraction with the highest viscosity index, which means that it shows a smaller change in viscosity with temperature change compared to oils with a lower viscosity index. Tables 5 and 6 show the results of the pour point for BORM1 and BORM2 and their fractions.

Table 5. Pour point for BORM1 and its fractions

Characteristic	BORM1	VGO	HC-3	HC-4	HC-5	HC-6	HC-7
PP (°C)	30	13	14	29	35	38	49

Table 6. Pour point for BORM2 and its fractions

Characteristic	BORM2	VGO	HC-3	HC-4	HC-5	HC-6	HC-7
PP (°C)	33	15	17	30	35	40	41

It can be concluded that fractions from the lower floors of the vacuum column have the highest pour points, that is, the two heaviest fractions HC-6 and HC-7 have the highest values. Determining the pour point is an important characteristic, especially in areas with low temperatures. It is necessary to ensure that the oil maintains the required working properties, in order to prevent possible damage to the engine. Tables 7 and 8 show the flash point results for the analyzed samples.

Table 7. Flashpoint results for BORM1 and its fractions

Characteristic	BORM1	VGO	HC-3	HC-4	HC-5	HC-6	HC-7
FP(°C)	222	190	200	230	250	254	274

Table 8. Flashpoint results for BORM2 and its fractions

Characteristic	BORM2	VGO	HC-3	HC-4	HC-5	HC-6	HC-7
FP(°C)	201	192	207	228	246	251	260

It can be concluded that the fractions from the lower floors of the vacuum column, HC-6, and HC-7, have the highest flash point values. Determining the flash point is important for reliable information on the properties of the petroleum product, for assessing its quality, as well as for transportation and storage due to the risk of fire.

Table 9 shows the measured fractional distillation values at reduced pressure for BORM1, as wellas for its fractions.

Table 9. Distillation of BORM1 and its fractions

DISTILLATION	BORM1	HC-3	HC-4	HC-5	HC-6	HC-7
Start	342	359	406	409	417	423
5%v/v	375	380	420	441	454	468
10%v/v	387	391	430	456	457	482
20%v/v	400	394	438	470	465	503
30%v/v	411	396	441	475	476	516
40%v/v	420	401	443	477	485	528
50%v/v	429	405	447	484	491	540
60%v/v	437	408	450	492	498	552
70%v/v	450	413	455	500	503	562
80%v/v	466	418	458	506	511	576
90%v/v	487	427	462	516	522	593
95%v/v	507	430	463	530	538	603
98%v/v	507	439	466	530	541	606
End	537	444	478	544	550	606

Figure 4 shows a comparison of the distillation curves of BORM1 and its fractions.

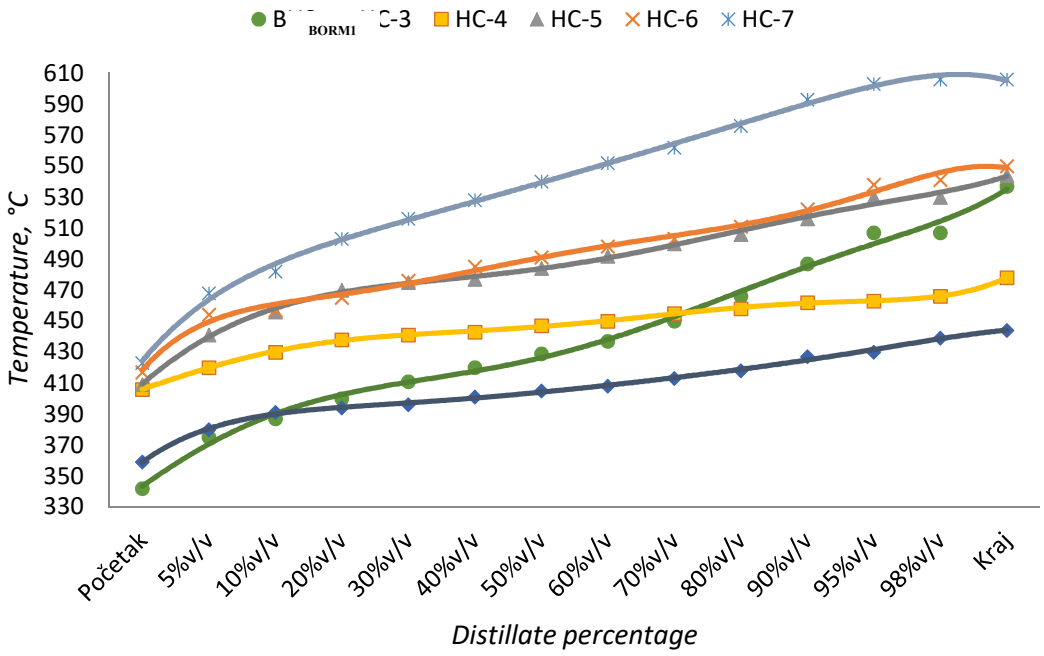

Figure 4. Comparison of the distillation curves of BORM1 and its fractions

Based on the results and the distillation curves shown in Figure 4, it can be seen that fractions VHC-3, VHC-4, and VHC-7 can be almost completely separated by the distillation process, while fractions VHC-5 and VHC-6 contain impurities of each other, i.e. do not have the so-called clean cut.

Based on the initial boiling temperatures and final boiling temperatures of the fractions, it can be concluded that the lightest fraction (a fraction with lower viscosity) is VHC-3, and the heaviest (fraction with higher viscosity) is VHC-7. Fraction VHC-4 has the narrowest

temperature range of extraction from BORM1, which can be seen on its distillation curve. This means that this fraction contains components that have similar physical properties.

Table 10 shows the measured values of fractional distillation at reduced pressure for BORM2, as well as for its fractions.

Table 10. Distillation of BORM2 and its fractions

DISTILLATION	BORM2	HC-3	HC-4	HC-5	HC-6	HC-7
Start	340	339	387	431	429	432
5% v/v	373	358	413	440	456	454
10% v/v	387	374	421	462	477	475
20% v/v	400	385	428	472	499	494
30% v/v	411	391	434	483	513	501
40% v/v	420	393	435	499	522	516
50% v/v	429	398	440	504	533	523
60% v/v	437	401	444	511	540	532
70% v/v	450	409	448	517	551	539
80% v/v	466	417	454	523	556	553
90% v/v	490	429	464	530	561	562
95% v/v	516	435	474	535	567	576
98% v/v	519	438	476	539	570	579
End	546	454	480	553	570	584

Figure 5 shows a comparison of distillation curves for BORM2 and its fractions.

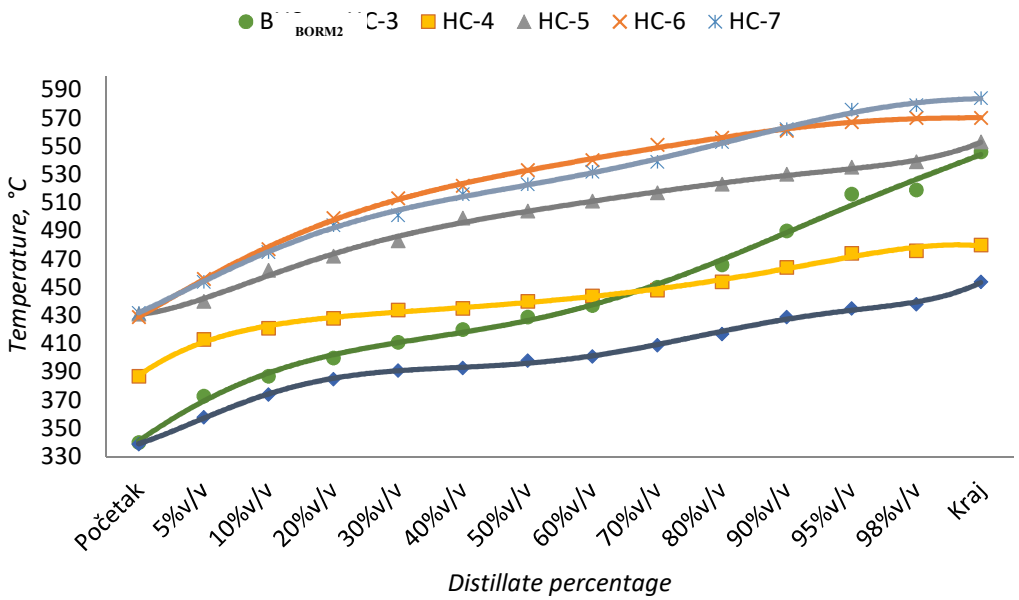

Figure 5. Comparison of the distillation curves of BORM2 and its fractions

Based on the results and the comparative presentation of the distillation curves in Figure 5, it can be concluded that fractions VHC-3, VHC-4, and VHC-5 can be almost completely separated by the distillation process, while fractions VHC-6 and VHC-7 contain impurities of each other. Based on the initial boiling temperatures and final boiling temperatures of the fractions, it can be concluded that the lightest fraction (a fraction with lower viscosity) is VHC-3, and the heaviest (fraction with higher viscosity) is VHC-7. Fraction VHC-4 has

the narrowest temperature range of extraction from BORM2, which can be seen on its distillation curve. This means that this fraction contains components that have similar physical properties.

4. CONCLUSION

The results of research of physicochemical characteristics in laboratory conditions: kinematic viscosity, viscosity index, pour point, flash point, as well as the distillation range for both base oil raw materials and their fractions contribute to the reduction of technological process costs and the optimization of technological parameters. The values for BORM1 and BORM2 differ very little and the characteristics of the obtained fractions are within the limits prescribed by the internal standard.

Hydrocracked base oils can meet the strict requirements of modern mechanical systems with a high viscosity index, the ability to lubricate in a wide temperature range, a low pour point, and very high thermal and oxidation stability. With a longer interval of use, they are more environmentally friendly.

5. REFERENCES

[1] Dugić G., Munjić N., Dugić P., Botić T.: Struktura proizvoda vakuum destilacije u zavisnosti od kvaliteta bazne uljne sirovine, III međunarodni kongres „Inženjerstvo, ekologija i materijali u procesnoj industriji“, Banja Luka, 2013.

[2] http://www.modricaoil.com

[3] Podobnik M., Bambić J., Oršić M.: Goriva i maziva, 41, 1 : 23-43, 2002.

[4] Petković V., Kovač O., Petković M.: Prednosti HC baznih ulja u formulaciji turbinskihulja; Goriva i maziva, 51, 4 : 329-340, 2012.

[5] Polcymann Gy., Baladincz J., Hancsok J.: Investigation of producing modern base oils, Hungarian Journal of industrial chemistry, 2008

[6] Interna dokumentacija Rafinerije ulja Modriča: Procesna knjiga postrojenja, uputstva za puštanje u pogon, Modriča 2011.

THE INFLUENCE OF THE HEATING VALUE OF COALS FROM COAL MINE „GRAČANICA“ d.o.o. GORNJI VAKUF ON QUALITY OF COAL AS ENERGYSOURCE IN ENERGY PRODUCTION

Azra Halilović, Šefkija Botonjić, Amila Krnjić, Lamija Sušić
University of Zenica, Faculty of metallurgy and Technology
Zenica, B&H

Keywords: coal, energy, heating value, chemical composition of coal, ash, moisture

ABSTRACT
Coal is the most important and widespread fuel sedimentary rock of organic origin. It is one of the main energy sources today and an industrial raw material for various products. Together with the oil and other natural bitumens, it belongs to the group of fossil fuels or caustobiolite.
Combustion represents one of the fundamental energy transformations by which the primary forms of energy, which are carriers of chemical energy, are transformed into thermal energy. In order to carry out the energy calculation of any process in which the conversion of fuel that is the carrier of chemical energy occurs, it is necessary to know the heating value of that fuel. The heating value of a fuel is directly related to or proportional to its efficiency. The basis for economic (price), environmental (emissions), and technical (energy) comparison of two or more energy sources is the heating value, which differs from energy source to energy source. The heating value of coal varies significantly depending on the ash content, moisture content, and the type of coal, that is, the chemical composition of the coal.
The aim of this work was to examine the influence of the heating value of coal on the quality of coal as an energy source in energy production in the Gračanica Coal Mine, Gornji Vakuf.

1. INTRODUCTION

In addition to being a fuel in industry and households, coal is widely used mainly in iron and steel metallurgy, the chemical industry, and the cement industry [1]. Coal is a black or black-brown sedimentary rock of organic origin that has the ability to burn, and is used as a fossil fuel that is extracted from the ground by mining methods. Natural or fossil coal mined from its natural deposit consists of an organic-combustible part and a mineral-non-combustible part. Coal is a heterogeneous substance composed of organic (85-95 %) and inorganic materials (5-15%) [2]. The basic elements of solid fuel are carbon (C), hydrogen (H), oxygen (O), nitrogen (N), and sulfur (S), whereby they form organic or coal mass, of which carbon and hydrogen are of greatest importance during combustion because they release the greatest amount of heat. The non-combustible part is designated as ballast or ballast substance. Ballast refers to mineral substances that appear as a residue during combustion - ash and part of the total moisture, which is called total moisture that leaves the coal during ordinary drying of coal in the air [3,4]. The quality of coal depends on the ratio of fuel, water, and ash. The ash content depends onthe coal type. The coal usability limit value is 35% of ash in regard to coal substance [3,5]. Each of these ingredients has its own special influence on the type of coal and can have different meanings, depending on the further application of the coal.The heating value of coal is the amount of potential energy in coal that can be converted into actual heat energy, i.e. the amount of heat that is developed during the complete combustion of a fuel unit (with complete combustion, the final products of combustion are formed: CO_2, H_2O, $SO_2$and

the maximum amount of heatis produced) is called heating value or combustion fuel heat or calorific value [3]. The calorific value depends on the geographical age, formation, ranking, and location of the coal mine. The higher heating valueleads to higher coal costs, but this is offset by lower logistics, storage, and ash disposal costs. The heating value is a complex function of the elemental composition of coal and can be determined experimentally using a calorimeter. From the beginning of calorimetry to the present day many calorimetric methods with specialized purposes and high sensitivity have been developed [6]. This is the most important parameter that determines the economy of thermal power plant operation [7].

2. EXPERIMENTAL PART

The research was carried out in the „Gračanica“ d.o.o. coal mine, Gornji Vakuf. The total number of examined samples is 115.

2.1. Material and methods

The experimental part of this work consisted of the following steps:

1. For all analyzes performed on coal, it is necessary to first determine and remove coarse moisture from the delivered coal. One kg of delivered coal is weighed, placed in a tin tray, and air-dried at a room temperature of 25 °C (it takes 24-48 hours). After drying, weighing is done again and the coarse moisture content is calculated from the difference in weight.

$$C_M = \frac{(m_1 - m_2) \cdot 100}{1000} = \frac{(m_1 - m_2)}{10} \quad (1)$$

C_M – coarse moisture content %,
m_1 – a mass of the container with coal before drying [g],
m_2 – a mass of the container with coal after drying [g].

2. An IKA C5001 type calorimeter operating in adiabatic mode was used to determine the heating value of coal using a calorimeter. The calorimeter consists of a combustion chamber, a container, a mixer, water, a temperature sensor, and wires with connectors necessary for igniting the fuel or wires for the thermometer. It is necessary to weigh up to 1 g of the sample, from which the coarse moisture has been removed, into a pot that is attached to the bomb cover of the calorimeter. A nickel-chromium wire, 4 to 5 cm long, is placed on the electrodes in the designated place. Then the pot with the sample is placed, and the sample is connected to the wire using a cotton thread. This thread ensures that the sample comes into contact with the ignition current, and it is necessary to tie it around a nickel-chromium wire and immerse it in the coal in a pot. Add 3-5 cm3 of distilled water to the bomb. The bomb is then closed and ready for measurement. The bomb thus closed is placed in a calorimeter vessel into which water is added. The bomb is filled with oxygen from a bottle under a pressure of 30 bar. When the temperature in the calorimetric system is stabilized, the sample is burned. In 10-15 minutes, the temperature stabilizes, which ends the test. This test determines the temperatures before and after the combustion of the sample. With these data and knowing the heat capacity of the calorimeter, the higher heating value of coal is determined. The higher heating value of coal is determined on the basis of practically obtained data according to the expression:

$$K_H = [(\Delta t \cdot H_o) - 383 - 515] \cdot f \quad (2)$$

K_H – higher heating value[kJ/kg],
H_0 – water value of the calorimeter = 10846 kJ/kg,
Δt – temperature difference of the calorimeter system [°C],
383, 515 – corrections for wire and thread,
f – factor which is calculated as follows:

$$f = \frac{100 - C_M}{100} \tag{3}$$

C_M – coarse moisture content.
The lower heating value is calculated according to the expression:

$$K_L = K_H - (23 \cdot T_M) \tag{4}$$

K_L – lower heating value[kJ/kg],
T_M – total moisture content, which is determined by calculation and represents the sum of coarse and hygroscopic moisture, i.e.:

$$T_M = C_M + H_M \tag{5}$$

T_M –total moisture content %.

3. Determining the share of hygroscopic moisture in coal is done by weighing one gram of air-dried coal in a measured glass vessel with a lid and drying it in a dryer at 105°C. Drying is done to a constant mass (on average 90 min). After drying, the measured container is removed from the dryer and placed in the desiccator to cool. The vessel is weighed again on an analytical scale and the hydroscopic moisture content is calculated from the difference:

$$H_M = f \cdot [(m_1 - m_2) \cdot 100] \tag{6}$$

H_M – hygroscopic moisture content %,
m_1 –a mass of vessel, lid, and sample before drying [g],
m_2 – a mass of vessel, lid, and sample after drying [g].

4. Determination of the ash content in coal is done by weighing one gram of air-dried coal on an analytical balance and placing it in a ceramic pot. It is heated in an electric furnace at a temperature of 815°C to a constant mass (3 h). After annealing, the pot is placed in a desiccator to cool, then weighed again and the ash content in the laboratory sample is calculated from the difference:

$$A = f \cdot [100 - (m_1 - m_2) \cdot 100] \tag{7}$$

A – ash content %,
m_1 – a mass of the pot and the sample before annealing [g],
m_2 – a mass of the pot and the sample after annealing [g],
f – factor that is calculated as described while calculating higher heating value.

5. The content of combustible substances in coal is determined by calculation based on the content of total moisture and the previously determined proportion of ash. The share of combustible materials expressed in % (CM) is determined according to the expression:

$$C_M = 100 - A - T_M \tag{8}$$

3. RESULTS AND DISCUSSION

The results ofthe examination of the lower heating value of coal in the period from April to September are shown in Table 1 and Figure 1. The overall average result is 10591 MJ/t, which confirms the fact that lignite is mined in the mine.

Table 1. Results of the lower heating value in the examined coal samples

Lower heating value [MJ/t]	Minimum	Maximum	Average
Examination I	9775	10860	10318
Examination II	9649	10933	10291
Examination III	10192	10964	10578
Examination IV	9532	10488	10010
Examination V	9567	11440	10504
Examination VI	10513	11346	10930
Examination VII	10047	11301	10674
Examination VIII	9733	11602	10668
Examination IX	9337	11202	10270
Examination X	9312	11749	10531
Examination XI	10175	11943	11059
Examination XII	10506	12023	11265

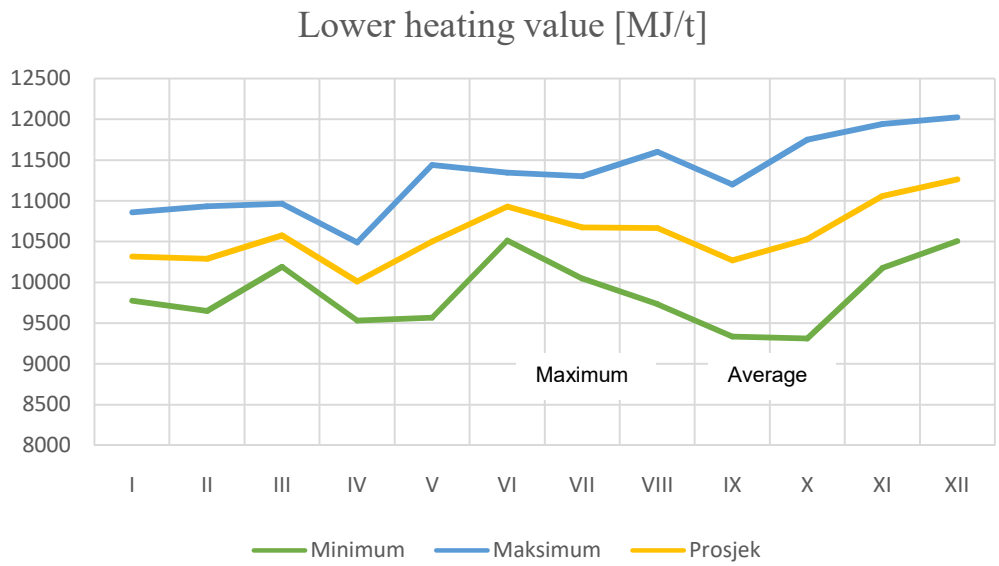

Figure 1. Results of the minimum, maximum, and average lower heating value in examining coal samples

In Figure 1, which shows the results of an examination of the lower heating values in the given period, it can be concluded that the lower heatingvalue of coal is uneven. In the period from April (examinations I and II), the value of the lower heating value is fairly uniform, while from May (examinations III and IV) to June (examinations V and VI), the lower heating value of coal fluctuated significantly, so that the first notice is the increase in its value, then a decrease and finally an increase in value again. In the period from the month of July (examinations VII and VIII) to the month of August (examinations IX and X), the lower heating value drops significantly and has the lowest values. In the month of September (examination XI and XII), the value of the lower heating is constantly increasing and in this period the highest values of the lower heating value were measured.

In Table 2 and Figure 2 is shown the influence of the value of the content of combustible materials on the value of the lower heating value of coal.

Table 2. The average values of the lower heating value and the content of combustible substances in the examined coal samples

Examination	Lower heating value [MJ/t]	Content of combustible substances [%]
Examination I	10318	44.43
Examination II	10291	43.95
Examination III	10578	44.98
Examination IV	10010	43.81
Examination V	10504	46.41
Examination VI	10930	46.87
Examination VII	10674	46.69
Examination VIII	10668	46.01
Examination IX	10270	43.21
Examination X	10531	44.45
Examination XI	11059	47.29
Examination XII	11265	48.00

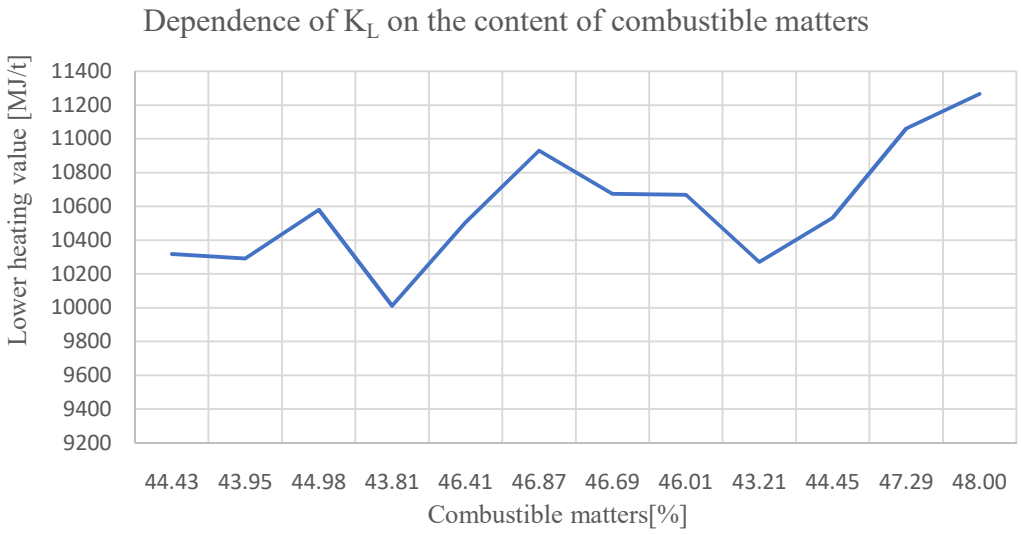

Figure 2. Dependence of the lower heating value of coal on the content of combustible substances

On the basis of the presented Figure 2, it can be concluded that the increase in the lower heating value of coal is proportional to the increase in the content of combustible substances (almost exclusively composed of carbon and free hydrogen) in it. The highest values of the content of combustible materials were measured in the month of September (examination XI and XII), and the highest values of the lower heating value of coal were also observed in that period of the examination.
The results of the examinationof the content of coarse, hydro, and total moisture in coals in the period from April to September are shown in Table 3 and Figure 3.

Table 3. The content of coarse, hygro and total moisture in the examined coal samples

	Coarse moisture content [%]			Hygro moisture content [%]			Total moisture content [%]		
	Min.	Max.	Avg.	Min.	Max.	Avg.	Min.	Max.	Avg.
Examination I	32.15	33.72	32.94	2.86	3.73	3.30	35.41	37.05	36.23
Examination II	32.09	32.99	32.54	3.18	3.86	3.52	35.30	36.21	35.76
Examination III	31.68	33.48	32.58	3.27	3.60	3.44	35.26	36.86	36.06
Examination IV	29.41	32.69	31.05	2.98	3.40	3.19	32.81	35.97	34.39
Examination V	31.44	32.78	32.11	2.85	3.89	3.37	34.93	36.54	35.74
Examination VI	30.83	32.17	31.50	3.46	4.64	4.05	34.97	35.79	35.38
Examination VII	29.33	31.95	30.64	3.05	4.81	3.93	33.41	35.67	34.54
Examination VIII	29.40	32.80	31.10	3.64	4.70	4.17	33.45	36.51	34.98
Examination IX	28.19	31.82	30.01	3.16	4.70	3.93	31.35	35.47	33.41
Examination X	29.55	32.42	30.99	3.25	5.02	4.14	33.50	37.04	35.27
Examination XI	29.02	32.41	30.72	3.52	5.19	4.36	32.76	36.42	34.59
Examination XII	29.41	32.95	31.18	2.80	5.55	4.18	34.39	37.18	35.79

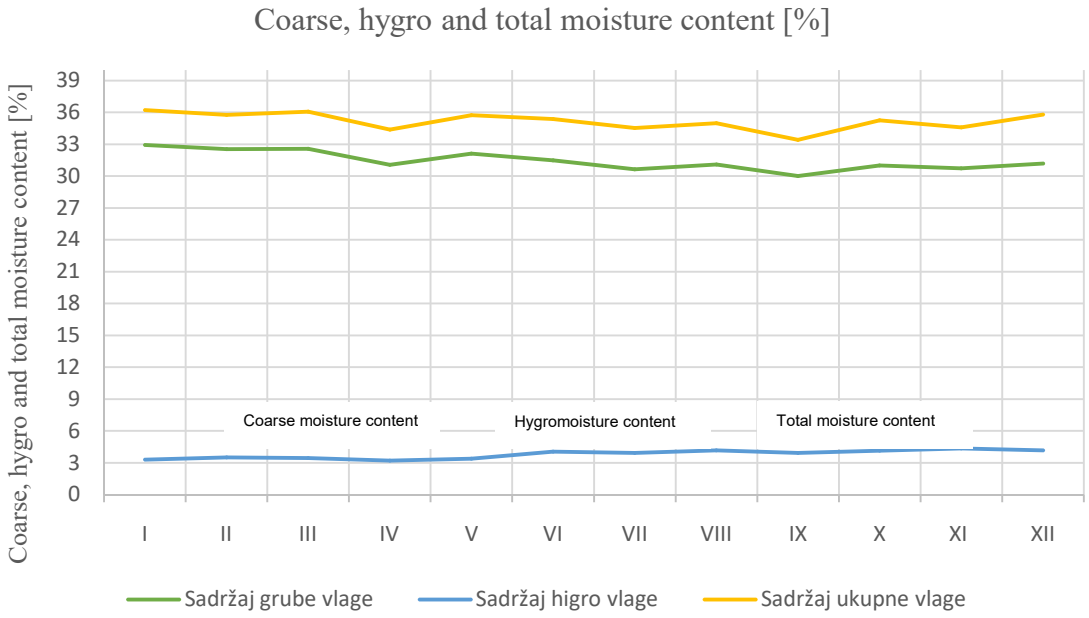

Figure 3. Average values of coarse, hydro, and total moisture content in the examined coal samples

In Figure 3, which shows the content of coarse, hydro, and total moisture in coal, it can be concluded that their content in coal is variable in the period from April to September. The largest drop in course moisture content was recorded in the month of August (examination IX), while the highest values were recorded in the month of April (examinations I and II), which may be caused by more abundant precipitation in that period. The largest drop in hydromoisture content was recorded in the month of May (examination IV), while the highest values were recorded in the month of September (examination XI and XII). The largest drop in total moisture content was recorded in the month of August (examination IX), while the highest values were recorded in the month of April (examination I) and the month of May (examination III).

Table 4 and Figure 4 show the influence of the ash content on the value of the lower heating value of coal.

Table 4. The average values of lower heating value and ash content in the examined coal samples

Examination	Lower heating value [MJ/t]	Ash content [%]
Examinations I and II	10304	19.70
Examinations III and IV	10294	20.27
Examinations V and VI	10717	17.93
Examinations VII and VIII	10671	19.57
Examinations IX and X	10400	22.81
Examinations XI and XII	11162	17.07

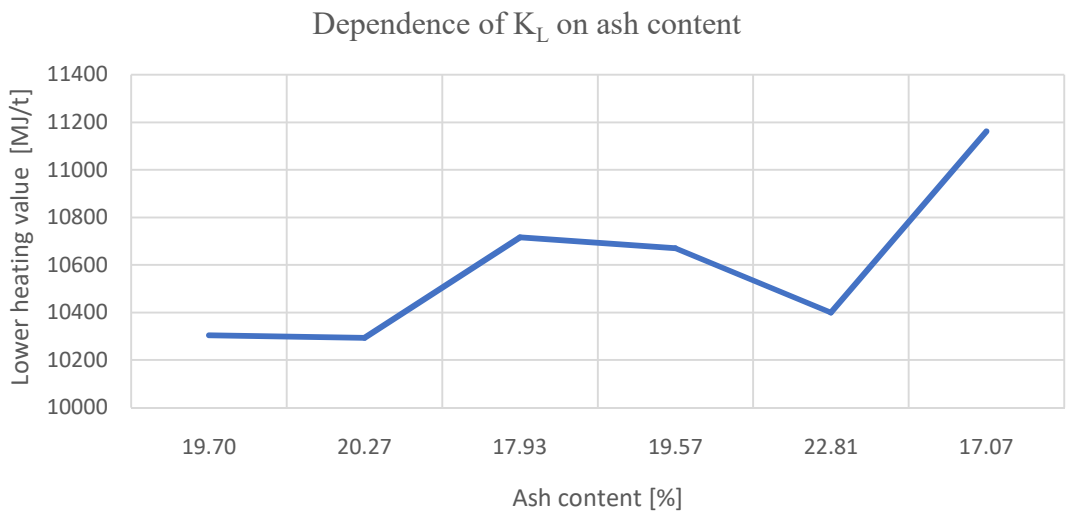

Figure 4. Dependence of K_L on ash content

On the basis of Figure 4, it can be concluded that increasing the ash content in coal decreases the value of the lower heating value of coal and vice versa. The lowest values of the ash content were measured in the month of September (examinations XI and XII), and in addition, the highest values of the lower heating value of coal were observed in that period of the examination.

4. CONCLUSION

In the experimental part of this work, the basic parameters of coal were examined, with a focus on thermal heating value, which affects the quality of coal as an energy source. The basic parameters of coal quality are lower heating value, combustible material content, ash content, and coarse, hygroscopic, and total moisture content. The lower heating values of coal are within the reference values for lignite, which confirms the fact that lignite is mined in the mine and can be used on certain occasions as an energy source in thermal power plants when there is a need for that. An increase in the content of combustible materials leads to an increase in the lower heat capacity of coal and vice versa. An increase in the ash content leads to a decrease in the lower heating value of coal and vice versa, i.e. an increase in the content of combustible substances leads to a decrease in the ash content in the coal. The higher the heating value of coal means the smaller the required amount of coal per unit of electricity. If one wants to achieve greater efficiency of coal as an energy source, it is necessary to use coals with higher heating value. A higher calorific value of coal can be achieved by some of the coal beneficiation processes by removing ballast such as mineral components and moisture, yielding a residue that is richer in combustible components.

5. REFERENCES

[1] Višković A., Softić B., Živković S. A.: Ugljen: sigurna energija, Graphis, Zagreb, 2011.
[2] Muhamedagić S., Mahmutović A.: Metalurški koks – proizvodnja i primjena, Zenica 2012.,
[3] Duraković J.: Goriva i sagorijevanje, Univerzitet u Zenici, Fakultet za metalurgiju i materijale, Zenica, 2017.
[4] Sadadinović J.: Organska tehnologija, knjiga 1 – Hemijska industrija, Univerzitet u Tuzli, Tehnološki fakultet, Tuzla, 1999.
[5] Tehnička enciklopedija; Jugoslavenski leksikografski zavod, Zagreb, 1963-.
[6] Horvat G.: Reakcijska kalorimetrija, Stručni rad, Sveučilište u Zagrebu, Prirodoslovno-matematički fakultet, Zagreb, 2014.
[7] Šilić Đ., Stojković V., Mikulić D.: Goriva i maziva, Veleučilište Velika Gorica, Velika Gorica, 2012.

THE MEASURES OF ENERGY EFFICIENCY IN NATRON-HAYAT MAGLAJ

Nusret Imamović
The University of Zenica, Faculty of Mechanical Engineering
Zenica, B&H

Armina Čamić, Haris Lepić
Natron-Hayat d.o.o.
Maglaj, B&H

Keywords: Energy efficiency**,** pulp and paper industry, environment

ABSTRACT
In industries such as the chemical industry, the oil industry, the steel industry, and the pulp and paper industry, energy systems are the basis of the production process and represent key indicators of the profitability of the process. Energy efficiency in industry is long-term related to technological development and the dynamics of renewal of production capacities. Increasing energy efficiency in the industry leads to a reduction in energy consumption but also reduces the negative impact on the environment. The rise in energy prices, both electricity and other energy sources, and the development of fees for emissions into the environment will mean important economic incentives in efforts to reduce energy consumption and emissions, thus increasing efficiency and the use of renewable sources in the industry. The paper presents several measures that achieve fuel, energy, and air savings in Natron-Hayat Maglaj.

1. ENERGY EFFICIENCY

Energy efficiency measures are actions taken to reduce energy consumption, getting the same or even better energy service level, but at the same time using the same or less energy. So, improving energy efficiency means avoiding/reducing energy losses without impairing comfort, the standard of living, or economic activity and can be realized both in the field of production and in the field of energy consumption [1,2]. The industrial sector in BiH has great potential for improving energy efficiency (EE) since, in most industrial plants, production is based on several decades-old technologies [1].

2. EXAMPLES OF MEASURES TO IMPROVE ENERGY EFFICIENCY IN NATRON-HAYAT MAGLAJ

Natron-Hayat is working continuously on improving energy efficiency (EE) in the production processes according to Energy Standard documentation ISO 50001 and literature [3,4]. This is provided through the set of company measures and activities with an ultimate goal of minimizing energy consumption, but remaining the same or improving productivity.
Further are shown some examples of energy savings in Natron-Hayat according to the suggestion of literature [2].

2.1. Utilization of waste heat oil cooling of screw compressors in Natron-Hayat - Recuperation

Only about 5% of the total energy supplied to the compressor is used to raise the air pressure. The remaining energy is present in the compressor in the form of heat. A large part of this heat (85-95%) is removed via compressor cooling water and lubricating oil. It is possible to achieve considerable savings by constructing an optimized heat recovery system. With air-cooled compressors, the available heat is hot air at 50-60°C, and with water-cooled compressors, the water that can be used for recuperation is at the temperature of 90-95°C. The waste heat of the compressor can be used satisfactorily for heating, drying, and preheating of combustion air, as well as for the preparation of hot process water [2].

There are five Kaeser rotary screw compressors installed in the compressed air area used to supply compressed air in Natron-Hayat Maglaj [5]. The system for compressors' waste heat energy recovery is designed in such a manner that heat is transferred from the cooling medium of compressors to demineralized water used for the feedwater tank in Energana II replenishing. Demineralized water is pumped from two tanks each of them 500 m^3 in volume.

Also, the heat recovery system of rotary screw compressors is automated to the required level, so the recovery system easily adapts to expected changes in system operation and achieves full efficiency in each operating mode without manual manipulation. The use of waste heat from rotary screw compressors is realized in two separate circuit exchangers, namely:

- The primary circuit where the heat from the compressors' oil is transferred to the working fluid (condensate) via the heat exchanger;
- The secondary circuit where the working fluid transfers the heat to the demineralized water used to replenish the supply tank;

Annual heat production expressed in MJ of installed Kaiser Compressors in Natron-Hayat is:

$$Q_{MJ/year} = 17{,}853{,}376.16 \text{ MJ/ann}$$

The recovery heat energy will be manifested through a reduction in 3.5 bar(g) steam consumption used for the boiler feed water heating, as a direct effect of the compressors' area recovery heat energy system operation, so we will show it through the saved amount of 3.5 bar(g) steam. So, the saved amount of steam for heating the feed water is

$$Q_{3.5\ bar} = 6{,}245.80 \text{ t/ann}$$

2.2. Analysis of system performance improvements and energy efficiency of the new method for control of pump operation in Natron-Hayat Maglaj

The pulp after the cooking process goes into the Blow tank (1,000 m^3). Pump "P002" is used to transport pulp with 4% consistency from the Blow tank to the primary knot separator. The control system of this pump runs with an electric motor as a drive is regulated through the pressure. This pressure is measured at the inlet to the centrifugal separator and represents feedback in the control loop. Control is performed in such a way that the desired pressure is achieved by damping the valve installed in the discharge pipeline. The default value is set to 2.2 bar and corresponds to a valve opening of approx. 40%. In this case, the motor always rotates at a constant rated speed, and the desired pressure at the separator inlet is adjusted by opening/closing the valve. In short, the new way of controlling this electric motor drive involves regulating the pressure at the entrance to the separator by changing the rotation speed of the electric motor drive,

instead of damping the valve. Based on the analysis and comparison, exact indicators of electricity savings were obtained. In addition to energy savings, a couple of additional issues were achieved; a reduction of CO_2 emissions, an improvement in the system operation stability, and easier management and maintenance of the desired parameters. As already mentioned, the consumption of electricity varies with the change of system parameters so the saving of electricity also varies from 206-309 MWh/ann.

2.3. Waste heat recovery of boilers' blowdowns in Natron-Hayat

In the process of operation of boilers, it is necessary to carry out continuous blowdown - desalination from boiler drums. In practice, this is called "constant boiler blowdown", and its amount is variable depending on the conductivity of the boiler water measured on the blowdown sample. Constant blowdown of the boiler drum drains a certain amount of water from the level where the water and steam meet each other, i.e. from the position where soluble salts float and their concentration is gradually increased by continuous water evaporation. Before the EE measure was implemented, the blowdown water from the boiler drums was discharged into an expansion vessel (atmospheric type), where it expanded and separated into two phases: the water phase and the steam phase - evaporation. The vapor from the expansion vessel was discharged directly into the atmosphere, and the liquid phase in the expander was cooled by direct mixing with mill water, and as such is discharged into the wastewater channel. Therefore, all the blowdown water from the boiler, i.e. the thermal energy contained in it, was irretrievably lost, along with the additional consumption of cooling mill water used for blowdown cooling. Since the blowdown water carries a certain content of impurities, it must be thrown into the wastewater channel as such, but the energy it carries with it can be used and returned to the process. The evaporated part of the blowdown that is separated in the expander does not contain impurities and as such can be directly returned to the process. The idea is to use this evaporated part of the blowdown to heat the boiler feed water in the feed tank, where normally the steam taken from the turbine at a pressure of 3.5 bar(g) is used. Using steam from the expander in this way directly reduces the consumption of 3.5 bar(g) of steam, that is, part of the energy that is currently lost is used. It is necessary to ensure with a technical solution that the pressure in the expander is at least 3.5 bar(g), so the vapor from the expander can be used altogether with extraction steam in heating the boiler feed water in the feed tank. The liquid phase of blowdown in the expander is "dirty water", and the only way to use it is to extract thermal energy through a heat exchanger before it is discharged into the wastewater channel. The process of using this thermal energy will be carried out in two steps - degrees, namely: The first-stage heat exchanger will take the heat from the blowdown water and transfer it to the turbine condensate, which returns from the turbine condenser to the feed tank [6]. The turbine condensate temperature ranges from 33 °C (winter) to 55 °C (summer), which is the actual process data; Heat exchanger 2^{nd} stage will take the remaining heat from the blowdown water (after passing through the 1^{st} stage) and deliver it to the demi-water used to replenish the boiler feed tank. The temperature of demi-water ranges from 5 °C (winter) to 30 °C (summer), determined on the basis of real data (local environmental dates). In this way, the liquid phase of the blowdown water will be cooled to the desired 35 °C, with a minimum consumption of demi water, the amount of which is limited. The technical solution enables fully automatic operation of the system for the utilization of waste heat of blowdown, and automatic adaptation to changes that occur in the process (change in the amount of boiler blowdown, change in the amount of turbine condensate, etc.). Recovery of thermal heat energy with boilers blowdown system, for an average descaling of 3.5 t/h for each of the two boilers.

This thermal energy amounts:

$$Q = 2{,}164.1\ kW$$

Energy absorbed from the system of heat recovery of blowdown on an annual basis:

$$Q_{ann} = 17.399.364\ kWh/ann$$

Expressed in MJ:

$$Q_{MJann} = 62.637.710{,}40\ MJ/ann$$

The used energy will be manifested through a reduction in steam consumption of 3.5 bar(g) for heating the boiler feed water, as a direct effect of the operation of the system for recovery of waste heat from boiler blowdown, so it will show that through the saved amount of steam 3.5 bar(g) per year.
So, the amount of saved steam for heating the feed water is:

$$Q_{3,5bar} = 21{,}913.09\ t/ann$$

2.4. Energy production from biomass in Natron-Hayat

The power plan named "Energana 1" as a part of the energy department in Natron-Hayat consists of a biomass boiler "BB-2" and condensing steam turbine with one controlled steam extraction is presented in Table 1.

Table 1. Design features of biomass boiler BB-2 Natron-Hayat

Boiler type	Two-drums with natural circulation
Maximum permanent boiler capacity	35 ton/h
Minimum permanent boiler capacity	12 ton/h
Pressure: Working/ Projected/ Tested	62 bar/ 68bar/ 93 bar
Outlet steam temperature	460°C
Boiler efficiency	82,5% (with 75-100% load)
Fuel	Biomass

The boiler is a two-drum type with natural circulation, designed for burning wood biomass, mainly conifer bark, which is a by-product of the pulp production process. The fuel is mechanically separated and chopped to the designed granulation d_e100 (equivalent diameter; in Austrian biomass standard "Onorm 20"- in the biomass preparation plant). The biomass is then transported to a daily biomass storage facility with a capacity of 1,000 m^3. From this storage, biomass is delivered to the boiler bunkers and from the bunkers is dosed into the combustion chamber, i.e. on the moving fire grid, which consists of five zones (first grid - drying and heating of fuel; second grid - first fuel combustion zone (ignition); third grid - fuel combustion zone (outgassing); fourth grid - fuel combustion zone (afterburning) and fifth grate - ash and slag removal zone). The combustion chamber is designed to burn wood biomass with a moisture content of up to 50%. The expected working combustion temperature is 750 to 1,100°C. The combustion chamber is closed by membrane walls composed of screen tubes. A steam superheater is installed at the exit of flue gases from the combustion chamber. Next comes the multi-cyclone, economizer, air heater, and electrostatic precipitator for good environmental standards (in the Federation of Bosnia and Herzegovina).
Fresh steam enters the turbine through a fresh steam valve connected to the inlet casing. The HP steam is distributed through throttling valves located on the inlet casing, which control the steam inlet to the first-stage nozzle groups depending on the turbine load. They are driven by a Voith actuator. Steam is continuing its path through the system of

nozzles, vanes, and blades releasing most of its energy to the turbine shaft rotating also the generator rotor. The steam turbine has the possibility of controlled steam extraction at the pressure of 4.5 bar(s) for the technological needs of production facilities. The amount of steam to be removed is regulated by the position of the LP valve, which is driven by a servo motor. The remaining steam flows towards the low-pressure side and enters the condenser where it condenses. In the condenser, there is a negative pressure provided by a steam ejector. Condensate is directed by condensate pumps to the supply tank or the mill condensate collector. The condenser is cooled by cooling water, provided by the cooling tower's closed circulation. All the necessary parameters of the turbo generator unit are given in Table 2.

Table 2. Design features of steam turbo generator "TG-4"

Turbine type	Condensing with controlled steam extraction
Maximum generator power	8.1 MW
Maximum fresh steam entering	35 ton/h
Design steam extraction flow	0 – 25 t/h
Fresh steam pressure	61 bar(a)
Fresh steam temperature	460°C
Steam extraction pressure	4.5 bar(a)
Exhaust steam pressure	0.08 bar(a)
Maximum steam condensing capacity	30 t/h

3. CONCLUSION

The pulp and paper industry is an intensive consumer of energy. The main factors affecting specific energy consumption per unit of output are:

- The part of the production of high-quality products requiring higher energy consumption;
- The part of waste recycling in the technological production process, which reduces the consumption of input raw materials and energy consumption;
- Degree of processing of waste materials from the technological process, which affects increased energy consumption;
- Structure, supervision, and way of managing own energy plant;

Measures to improve energy efficiency, the use of renewable energy sources, and environmental protection are constant and continuous processes at Natron - Hayat. There is a long list of successfully implemented projects, and it should certainly be highlighted that 7 years ago the largest biomass cogeneration plant in Bosnia and Herzegovina was put into operation in Natron - Hayat - a steam boiler of 35 MWth and a steam turbine with regulated steam extraction of 8.1 MWe. The company also showed its responsibility towards the environment in 2015 when, as the only industrial power plant in Bosnia and Herzegovina, it was accepted to be part of the National Emission Reduction Plan (NERP). This company has implemented several important international standards in its operations. The most important among them are ISO 9001, ISO 14001, FSC, ISO 50001 [7], ISO 45001, and ISO 31000. By implementing a minimum number of measures in the function of increasing energy efficiency, as shown in the examples in Natron-Hayat in Maglaj city, significant savings were achieved, which represents a very significant item that, with the implementation and energy efficiency measures in buildings, represents a significant impulse in increasing the profitability and competitiveness of the company itself. The waste heat of the compressor can be used satisfactorily for heating, drying, and preheating of combustion air, as well as for the preparation of hot process water. The recovery heat energy will be manifested through a reduction in 3.5 bar(g) steam consumption used for

the boiler feed water heating. Better energy management and investment in cost-effective energy efficiency measures can save up to 20% of the energy bill. Therefore, the Natron-Hayat company has recognized the importance of introducing ISO 50001, which enables a set of energy-related goals to be systematically set, thus achieving significant energy savings. The main measure of system performance success is obtained by analyzing energy efficiency indicators. According to data from 2020, about 17 certificates were issued in Bosnia and Herzegovina, and that number is growing. Based on the report of the ISO organization, the number of introduced ISO 50001 in the industry of pulp, paper and paper products is 172, which is another proof that the company Natron-Hayat Maglaj works as professionally as possible and according to all standards.

4. REFERENCES

[1] Harbaš N.: Projekti povećanja energijske efikasnosti u industriji BiH kao odgovor na COVID19 M-kvadrat, 2020 dostupno na: https://m-kvadrat.ba/projekti-povecanja-energijske-efikasnosti-kao-odgovor-na-covid19/, [12.03.2022.]

[2] Fawkes S., Oung K., Thrope D.: Best Practices and Case Studies for Industrial Energy Efficiency Improvement – An Introduction for Policy Makers, Copenhagen Centre on Energy Efficiency UNEP DTU PartnershipISBN: 978-87-93130-81-4, 2016

[3] Gvozdenac D., Gvozdenac-Urošević B., Morvaj Z.: Energetska efikasnost (put ka dekarboniziranom društvu), Fakultet tehničkih nauka, Novi Sad, 2021.

[4] Reference Document on Best Available Techniques for Energy Efficiency, European Commission, February 2009

[5] Projekat za iskorištenje otpadne toplote vijčanih kompresora, IBE d.d, Magaj, 2019.

[6] Neimarlija N.: Energetski sistemi, IPI d.o.o. Zenica, 2017.

[7] Šemić I.: Sistemi energetskog upravljanja: Tumačenje zahtjeva standarda ISO 50001:2018, Edukativni materijal za učesnike edukacije u kompaniji Natron-Hayat, Maglaj, 20

SCREENING OF PARTICULATE MATTER IN THE URBAN AREA OF SARAJEVO

Aida Šapčanin
University of Sarajevo, Faculty of Pharmacy
Sarajevo, B&H

Aida Hasanović
University of Sarajevo, Faculty of Medicine
Sarajevo, B&H

Farzet Bikić
University of Zenica, Faculty of Metallurgy and Technology
Zenica, B&H

Keywords: particulate matter, Laser particle sensor, the urban area of Sarajevo

ABSTRACT
Particulate matter enters the atmosphere as a result of human activity, as well as natural processes. Since we still cannot influence natural processes, reducing the concentration of floating particles is possible only by adjusting human activity. The emission of solid particles occurs during a large number of everyday activities. Depending on the activity, particles of different chemical compositions and sizes will be emitted. In this work, PM1, PM2.5, and PM10 particles were measured and their daily ratio was calculated over a period of three months in 2022. In Sarajevo's urban area. The measurement was carried out with a laser sensor installed in the urban part of Sarajevo. The results showed the presence of all three types of particles. Continuous monitoring should suggest serious measures to the authorities in order to significantly reduce PM's impact on the health of Sarajevo residents.

1. INTRODUCTION

1.1. Particulate matter (PM)

PM is an important indicator of air pollution and the type and the ratio of coarse and fine PM particles differentiate the possibility to affect urban population health [1,2,3]. Some of the main meteorological conditions that affect the concentration of suspended particles in the air are wind, temperature, precipitation, and relative humidity. Investigations of suspended particles in the open air are important both for climatological research and for assessing the impact on human health. However, people spend most of their time in closed spaces [2,3,4], so PM particles in such spaces can have a much greater impact on their health. Many studies investigated the composition, size, and transport of PM particles in residential areas, schools, and catering facilities, as well as the dependence of indoor concentrations on outdoor concentrations [4-7]. Research shows that the quality of the air in a closed space largely depends on the quality of the outdoor air. From the different foreign studies that indicate the negative consequences of air pollution, not only on human health but also on the ecosystem, it is evident how important it is to improve air quality in the whole world. In order to improve air quality, it is necessary to measure the concentrations of suspended solid particles in the air. Measurements of the concentration

of floating particles in the air are made using the reference method that is, by the gravimetric method or one of the methods for which equivalence has been proven, for example, the oscillating microbalance method, the β-radiation absorption method or the scattering method laser light [8-12]. The number of PM particles at a fine time resolution can be measured with an optical PM particle detector. Optical particle counters work on the principle of laser light scattering on particles. The laser light passes through a chamber containing air with suspended particles, due to which the light is scattered. The scattered light is directed by an optical system toward a photodetector that creates a signal for the processor. Concentrations and particle sizes are further calculated from the intensity of the scattered light [8-14]. A wider availability of small and low-cost PM sensor devices will enhance our ability to estimate the PM particles with high spatial and temporal resolution. A large number of such devices can be deployed simultaneously. They are designed to be used also as mobile wearable devices for personal exposure assessment in a larger population. They will help empower the citizen through, for example, citizen science which includes projects and programs designed to engage the public in scientific investigations, such as asking questions, collecting data, or interpreting results [15].

1.2. Chemical composition and impact on human health of different PM

According to WHO statistics, Bosnia and Herzegovina (BiH) has the highest European mortality rate attributed to air pollution. However, there are no official national data to support or deny this finding [16]. Public health institutes in the country currently do not collect data on the health impacts of air pollution and communicate environmental health risks to the public only sporadically. Although the legal framework for air quality is largely in place, implementation and enforcement remain weak. National recognition of the problem through strategic documents, local action plans with implementable solutions, and public awareness of the air pollution impacts and mitigation measures are all key to tackling the issue but are all missing in the country. According to new research conducted by the WHO, the main source of air pollution is traffic, and there is evidence that it has a direct impact on the increase in mortality, as well as on the increase in respiratory and cardiovascular diseases [16-21]. In the European Union, according to WHO research, around 100,000 premature deaths of adults occur each year that can be attributed to air pollution, and emissions from road traffic represent a significant part of this burden [11]. PM metals can be used as indicators of their emission sources, that is their origin. Fossil fuel combustion is one of the main anthropogenic aerosol sources [22,23]. Heavy metals in the composition of PM particles (As, Cd, Pb, Co, Cu, and Mo) are emitted due to the combustion of coal, while particles with a predominant V, Ni, and Pb are emitted due to the combustion of oil fuels. Cu, Zn, and Pb are usually related to traffic emissions [22,23].

All PM particles can be inhaled and deposited in the respiratory system. Floating particles from the air entering the respiratory system usually stop immediately in the nose due to a change in direction. When changing the direction of movement, particles from the air are retained in the mucous membranes of the respiratory system, and this is called impaction. Since the particles are of different mass and size, their impact will differ in size. Larger aerosol or dust particles do not penetrate the lower respiratory tract because they stop on the hairs and mucous membranes of the upper respiratory tract, unlike them, smaller particles of a size of several micrometers pass through the upper part of the respiratory tract and reach the bronchi on whose walls they settle [17-19]. For the smallest particles, PM1, their size enables the furthest penetration through the respiratory tract, i.e. penetration all the way to the lung alveoli. When talking about the penetration of gaseous pollutants, the key factor is their solubility, i.e. the more soluble the pollutants are, the easier they will pass through the mucous membrane and the faster they will be absorbed and broken down

in the respiratory system. It is assumed that PM1 particles represent the greatest danger because they can penetrate deep into the respiratory system [17-20]. Thus, PM1 is the smallest and therefore potentially dangerous particles whose aerodynamic diameter is less than 1 μm. Legal regulations do not yet have a limit value for this type of particle.

2. MATERIAL AND METHODS

2.1. Measuring point

Dolac Malta (43°51′13.91″N 18°22′40.79″E) is a Sarajevo settlement within the municipality of Novo Sarajevo, with about 12,500 inhabitants. It consists of the local communities of Dolac with headquarters in Marko Marulića Street and Malta with headquarters in Envera Šehovića Street (Fig.1). The settlement is located in the west of the municipality, and consists of the local communities of Dolac and Malta, which are separated by Paromlinska street. The south of the settlement consists of plains with residential buildings and large commercial buildings, while the north of the settlement (around the Obad cemetery) is hilly, and houses have been built. In the north and northeast, it borders Pofalići, in the southeast with Željeznička, in the south with Hero's Square and Čengić Villa, while in the west it borders Buća Potok in the neighboring municipality of Novi Grad. Drinska Street and an active railway line run through the north of the settlement.

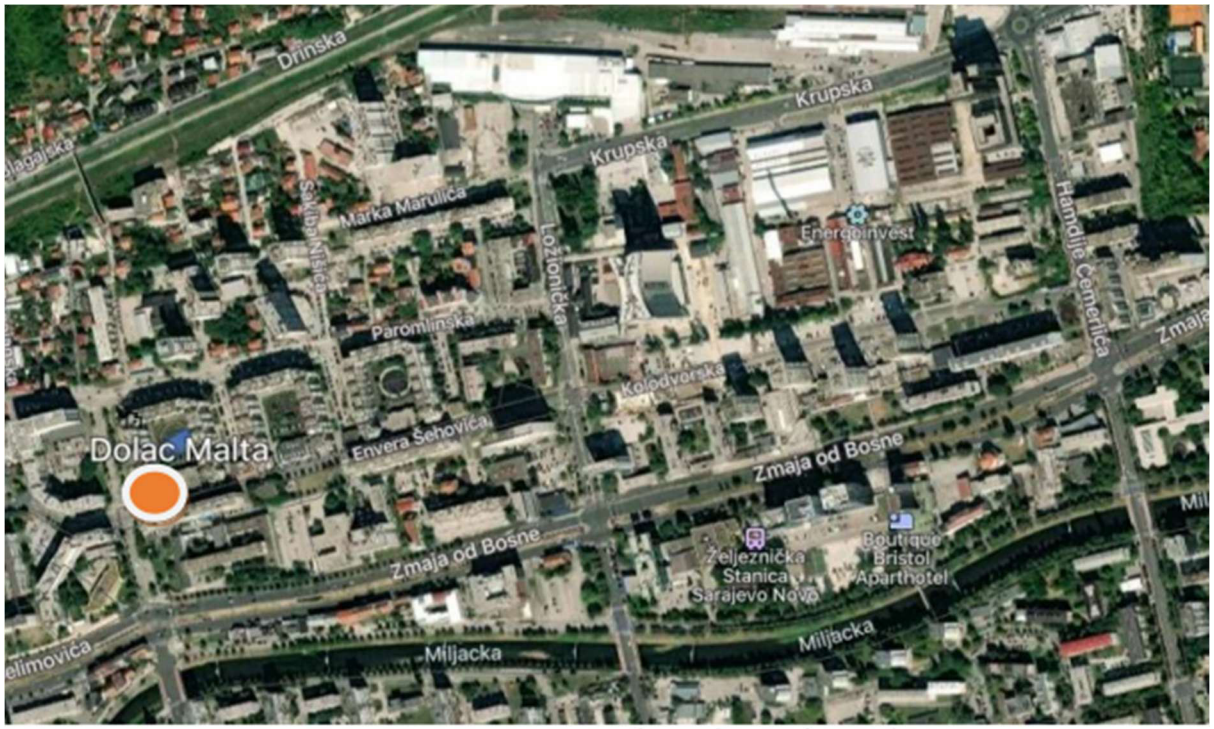

Figure 1. Measuring point in the Dolac Malta settlement

2.2. Measuring device

A laser particle sensor (Air quality monitor indoor/outdoor BR-V, Shenzen, China) is placed inside the balcony on the 3rd floor of the building (Envera Sehovica Street) in the area of the Dolac Malta settlement. In the immediate vicinity is a road with intensive traffic and a city heating plant. The device was not moved from the fixed measuring point during the three months period (Fig. 2).

Figure 2. Measuring device

2.3. Methods

The sensor measured the mass concentration (μg/m^3) of PM1, PM2.5, and PM10 particles from the outdoor air. The measurement was carried out every day at the same time (5 p.m. during rush hour) in the months of April, May, and June 2022. A permissible limit of 25 μg/m^3 for PM2.5 and 50 μg/m^3 for PM10 was used for the estimation of pollution epizodes [24]. Legal regulations do not yet have a limit value for PM1 particles. From time to time, our measured concentration of PM10 was compared with public data (obtained by reference method) in the nearest measuring points in Sarajevo's urban area. Public data for PM2.5 particles were not always available from public measurement points, and PM1 particles are not measured at all. Correlations between PM1 and PM2.5, a correlation between PM1 and PM10, and a correlation between PM2.5 and PM10, (respectively*)* were calculated [25]. To identify the dominant contribution of PM particles and to make aerosol-type classification, during the investigation period of the year, the ratio of PM1 and PM 2.5 to PM10 was calculated [26].

3. RESULTS AND DISCUSSION

Because of Sarajevo's geographical location and terrain configuration, during spring its tropospheric mixing is frequently low with regularly occurring temperature inversions. Extensive use of solid fuels during the cold, heating season and an old vehicle fleet coupled with Sarajevo's orography and meteorology causes the accumulation of pollutants within the city's plane, leading to episodes of high air pollution [13,14]. Other researchers investigated PM10 filter samples (for the concentration of heavy metals) collected at the site in the Sarajevo Canton: Bjelave (urban background site) in the city of Sarajevo operated by the Federal Hydrometeorological Institute of BiH (FHMIBiH) [13,14,22,23].

This study for the first time investigated the content of PM1 particles as the most dangerous for human health. Other researchers investigated the PM particles by using different sensors [8-14]. The obtained results, in our study area, of the content of PM1, PM2.5, and PM10 particles during April 2022 are shown in Figure 3.

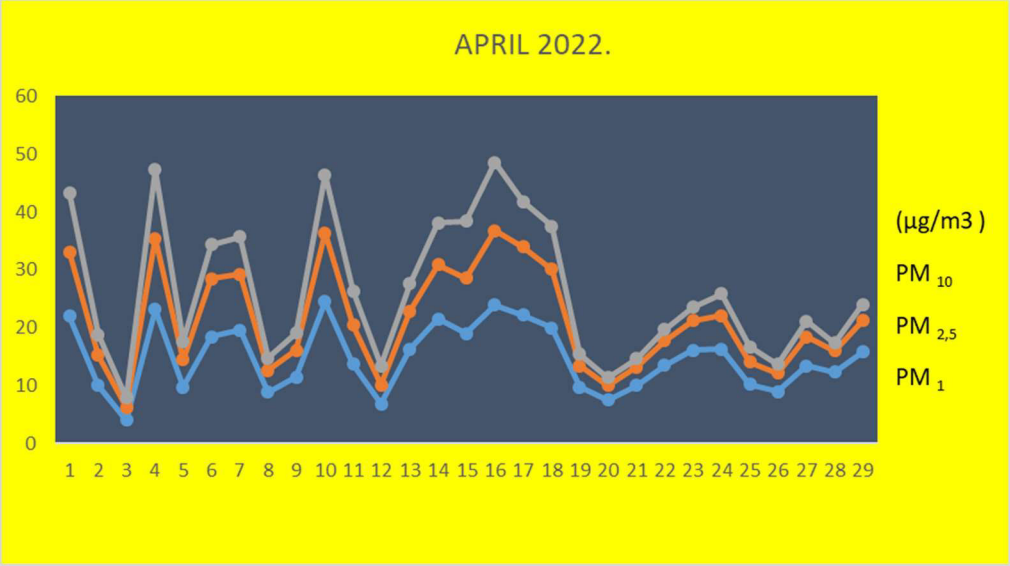

Figure 3. The daily variations of PM1, PM2.5, and PM10 particles during April 2022

Figure 3 shows the movement of the average daily concentrations of PM1, PM2.5, and PM10 particles in the air measured at the aforementioned measuring site during the month of April 2022. The concentration (µg/m^3) of measured PM1, PM2.5, and PM10 particles in April of 2022, were in the ranges of 4,06-24,48; 6,26-36,76 and 7,9-48,54, respectively. The obtained results of the content of PM particles during May 2022 are shown in Figure 4.

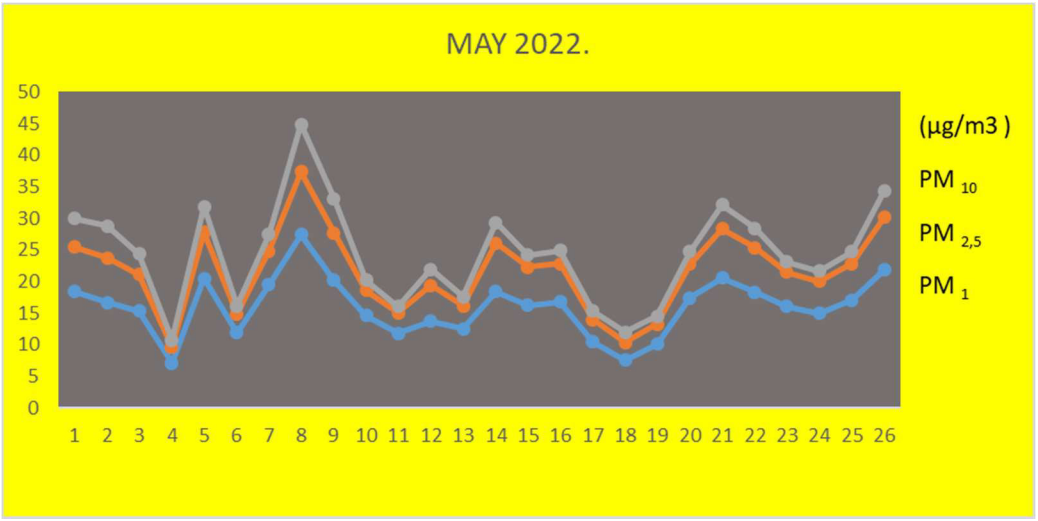

Figure 4. The daily variations of PM1, PM2.5, and PM10 particles during May 2022

Figure 4 shows the movement of the average daily concentrations of PM1, PM2.5, and PM10 particles in the air measured at the aforementioned measuring site during the month of May 2022. The concentration (µg/m^3) of measured PM1, PM2.5, and PM10 particles in May of 2022, were in the ranges of 7,12-27,39; 9, 67-37,4 and 10,73-44,84, respectively. The obtained results of the content of PM particles during June 2022 are shown in Figure 5.

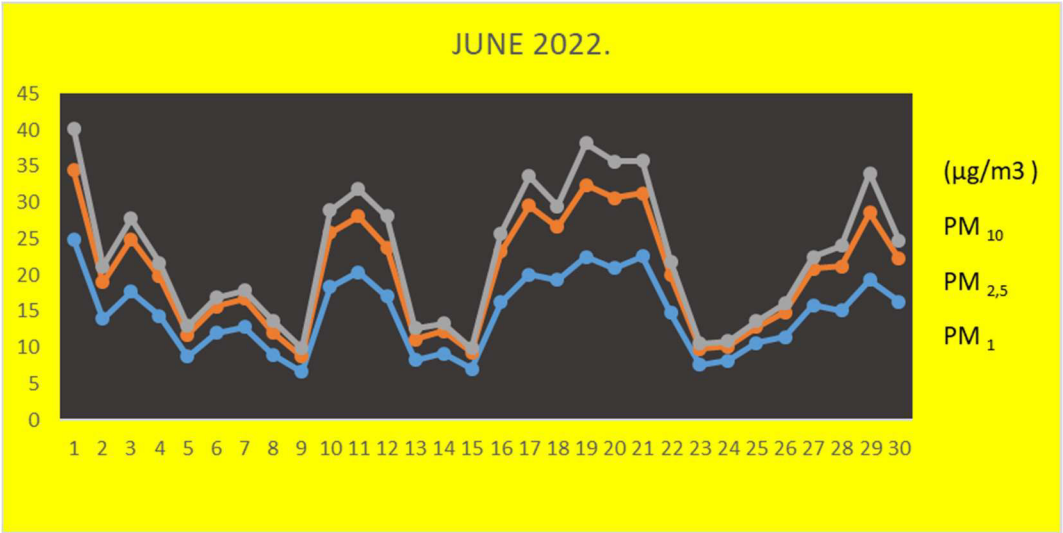

Figure 5. The daily variations of PM1, PM2.5, and PM10 particles during June 2022

Figure 5 shows the movement of the average daily concentrations of PM1, PM2.5, and PM10 particles in the air measured at the aforementioned measuring site during the month of June 2022. The concentration (µg/m^3) of measured PM1, PM2.5, and PM10 particles in June of 2022, were in the ranges of 6,63-24,95; 8,79-34,43 and 9,87-40,22, respectively. In the investigated three months period the PM1 particles were at high levels and PM2.5 levels were beyond the permissible limit of 25 µg/m^3 [24] these particles have a significant impact on mortality and morbidity caused by respiratory and cardiovascular diseases. More severe impacts affect people who are already ill. The elderly, children, and poor people are more susceptible. The concentration of PM10 particles was under the permissible limit of 50 µg/m^3 [24] and that was in accordance with weather conditions during the investigated period. The correlation between PM1 and PM2.5, the correlation between PM1 and PM10, and the correlation between PM2.5 and PM10 (respectively) are shown in Figures 6, 7, and 8.

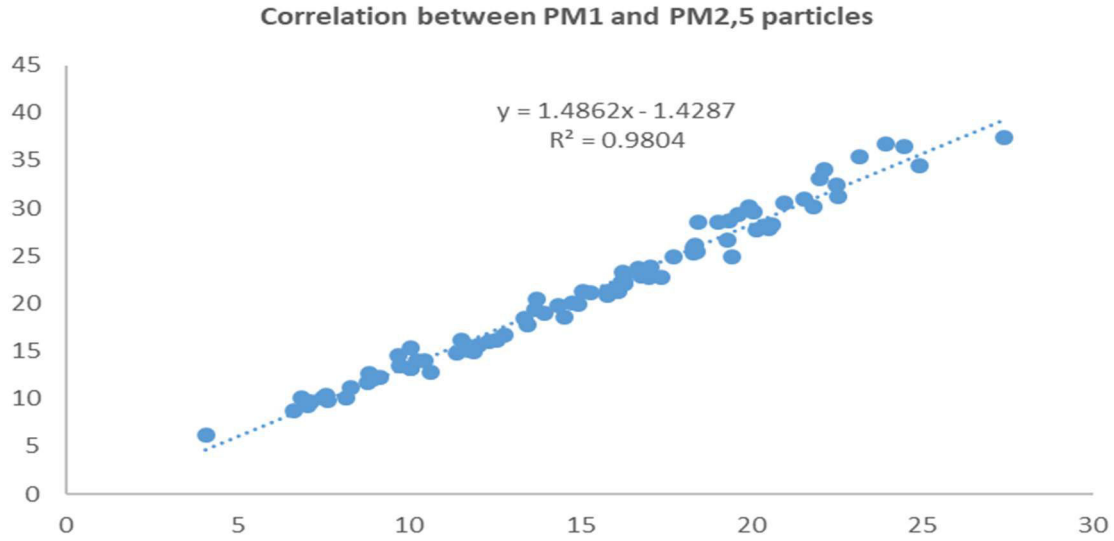

Figure 6. The correlation between PM1 and PM2.5 in investigated three-month period

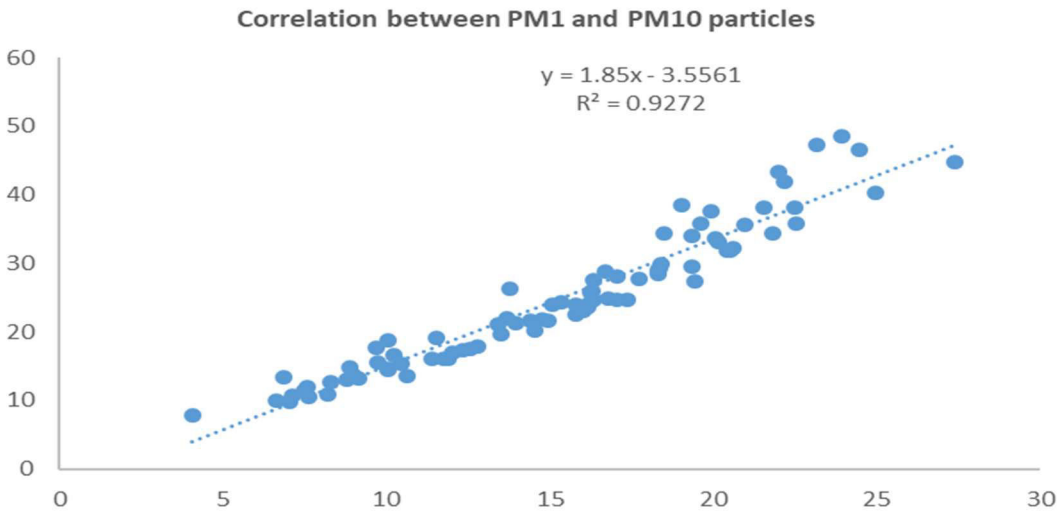

Figure 7. The correlation between PM1 and PM10 in investigated three-month period

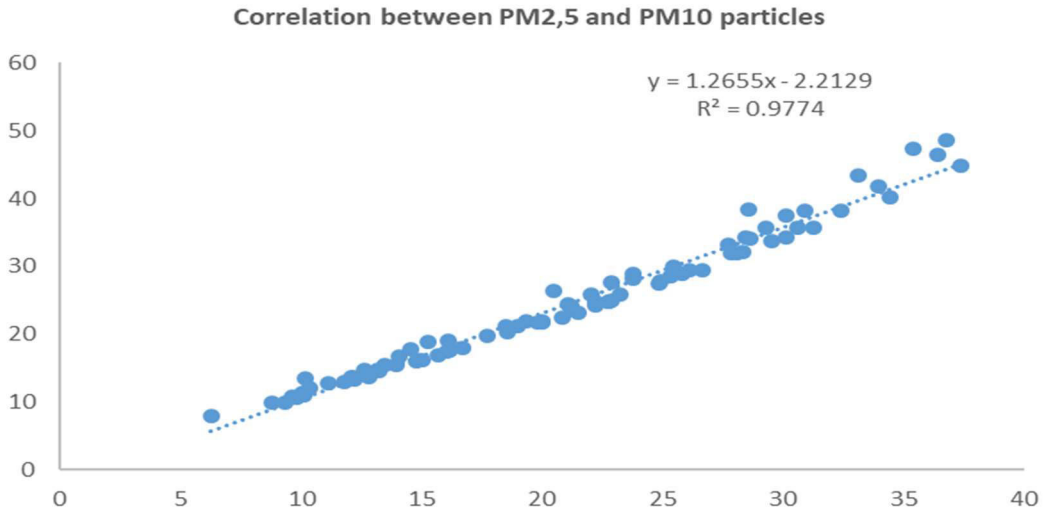

Figure 8. The correlation between PM2.5 and PM10 in investigated three-month period.

Results showed a very strong positive correlation. A similar investigation was conducted by foreign researchers [25]. The monthly variation in the ratio of PM particles is shown in Figure 9.

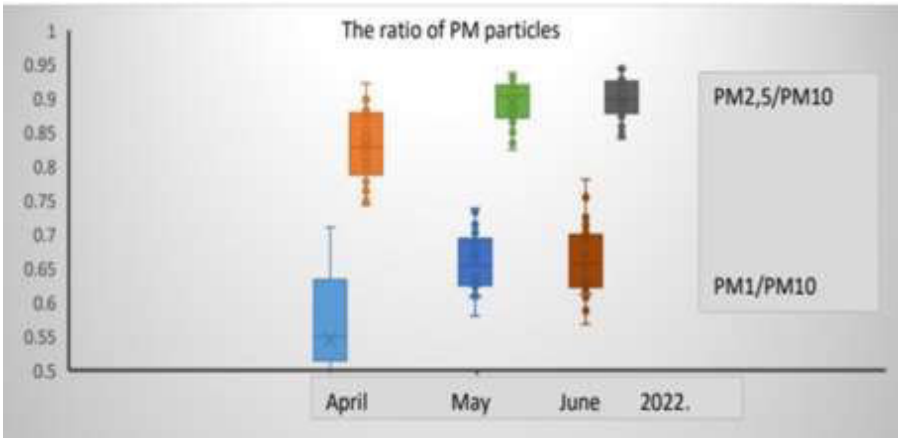

Figure 9. The monthly variations in the ratio of PM1 and PM2.5 to PM10

Results from Figure 9 generally showed that the ratio of PM1/PM10 and the ratio of PM2.5/PM10 was found to be > 0,5, in the three months period. Obtained results suggest an increase in fine-mode aerosol particles and coarse-mode aerosol particles and indicated a precaution to human respiratory health. A similar investigation was made in other countries [8-12,26]. Furthermore, modern laser sensor technology is available today to implement low-cost and reliable devices which are used by citizens as well as researchers. When such devices are deployed in multiple locations in urban areas of the city, they can provide highly temporal and spatial results and significantly contribute to the set of information important for exposure assessment and subsequent hazard mitigation. Experiences from foreign studies showed that for the wider use of such devices and the data that can be collected, it is necessary to develop the appropriate infrastructure and systems for quality assurance and control [8-13].

4. CONCLUSION

This study gives a short view of the content of different particulate matter determined by the commercially available laser sensor for indoor/outdoor monitoring in the urban environment of Sarajevo.

Measuring by laser sensor the content of PM1, PM2.5, and PM10 particles were registered at the three months period. The results showed lower contents of PM particles in the month of June compared to April and May, which is in accordance with meteorological conditions that significantly affect the movement of PM particles in the urban air.

Air Quality Management Plans shall address and recognize all sources of pollution prioritizing innovative and comprehensive measures that can provide multiple benefits.

Moving means of PM1, PM2.5, and PM10 and their concentrations in different seasons are useful in policy-making decisions aiming to improve the air quality in Sarajevo.

5. REFERENCES

[1] Fan, H., Zhao, C., Yang, Y., Yang, X. Spatio-Temporal Variations of the PM2.5/PM10 Ratios and Its Application to Air Pollution Type Classification in China. Frontiers in Environmental Science 2021; 9:1-13

[2] Donaldson, K. The biological effects of coarse and fine particulate matter. Occup Environ Med 2003.; 60(5): 313–314

[3] Braniš, M., P. Řezáčová, et al. Fine Particles (PM1) in Four Different Indoor Environments. Indoor and Built Environment 2002; 11: 184-190

[4] C. A. Pope III, D. W. Dockery, "Health effects of fine particulate air pollution: Lines that connect," Journal of the Air and Waste Management Association, 2006; 56 (6): 707–708

[5] Jacob, D. J. Introduction to Atmospheric Chemistry. Princeton University Press, 1999

[6] Feng S, Gao D, Liao F, Zhou F, Wang X. The health effects of ambient PM2.5 and potential mechanisms. Ecotoxicol Environ Saf 2016; 128: 67–74

[7] Guo Y, Jia Y, Pan X, Liu L, Wichmann H. E. The association between fine particulate air pollution and hospital emergency room visits for cardiovascular diseases in Beijing, China. Sci Total Environ 2009; 407: 4826–30

[8] Nguyen, N. H., Nguyen, H. X., Le, T. T. B. and Vu, C. D. Evaluating Low-Cost Commercially Available Sensors for Air Quality Monitoring and Application of Sensor Calibration Methods for Improving Accuracy. Open Journal of Air Pollution 2021; 10: 1-17

[9] Sayahi, T., Butterfield, A., Kelly, K. E. Long-term field evaluation of the Plantower PMS low-cost particulate matter sensors. Environmental Pollution, 2019; 245: 932-940.

[10] An evaluation of the U.S. EPA's correction equation for PupleAir sensor data in smoke, dust, and wintertime urban pollution events. Atmospheric Measurement Techniques,2023; 16: 1311-1322

[11] Bernasconi, S.; Angelucci, A.; Aliverti, A. A Scoping Review on Wearable Devices for Environmental Monitoring and Their Application for Health and Wellness. Sensors, 2022; 22: 5994
[12] Park, Y.M .; Sousan, S.; Streuber, D.; Zhao, K. GeoAir—A Novel Portable, GPS-Enabled, Low-Cost Air-Pollution Sensor: Design Strategies to Facilitate Citizen Science Research and Geospatial Assessments of Personal Exposure. Sensors, 202; 21, 3761
[13] Mašić. A., Bibić, D., Pikula, B., Blažević, A. Huremović, J., Zero, S. Evaluation of optical particulate matter sensors under realistic conditions of strong and mild urban pollution. Atmospheric Measurement Techniques, 2020, 13: 6427–6443
[14] Mašić, A., Pikula, B., Bibić, D. Mobile Measurements of Particulate Matter Concentrations in Urban Area, Proceedings of the 28th DAAAM International Symposium, pp.0452-0456, B. Katalinic (Ed.), Published by DAAAM International, ISBN 978-3-902734-11-2, ISSN 1726-9679, Vienna, Austria 2017
[15] Castell, N., Kobernus, M., Liu, H.Y., Schneider, P., Lahoz, W., Berre, A. J., Noll, A. J., Mobile technologies and services for environmental monitoring: the Citi-Sense MOB approach. Urban Clim, 2014; doi: 10.1016/j.uclim.2014.08.002
[16] WHO: More than 90% of the world's children breathe toxic air every day: https://www.who.int/news-room/detail/29-10-2018-more-than-90-of-theworld%E2%80%99schildren -breathe-toxic-air-every-day
[17] Ramachandran, G., J., Adgate, L., N., Hill, K., Sexton, G. Pratt, C., Bock, D., Comparison of Short-Term Variations (15-Minute Averages) in Outdoor and Indoor PM 2.5 Concentrations, Journal of the Air & Waste Management Association, 2000; 50; 7: 1157–1166
[18] Dominici, F., McDermott, A., Daniels, M., Zeger, S. and Samet, J. M. Revised analyses of the national morbidity, mortality, and air pollution study: Mortality among residents of 90 cities, J. Toxicol. Env. Heal. A, 2005; 68, 1071–1092
[19] Dockery, D. W. and Stone, P. H. Cardiovascular risks from fine particulate air pollution, NEJM, 2007; 356, 511–513
[20] Braniš, M., P. Řezáčová, et al. The effect of outdoor air and indoor human activity on mass concentrations of PM10, PM2.5, and PM1 in a classroom. Environmental Research 2005; 99(2): 143-149
[21] Chen, L. H., Knutsen, S. F. Beeson, L. Ghamsary, M. Shavlik, D. Petersen, F. and Abbey, D. The association between ambient particulate air pollution and fatal coronary heart disease among persons with respiratory symptoms/disease, Ann. Epidemiol. 2005; 15, 642–642
[22] Žero, S., et al. New Insight into the Measurements of Particle-Bound Metals in the Urban and Remote Atmospheres of the Sarajevo Canton and Modeled Impacts of Particulate Air Pollution in Bosnia and Herzegovina. Environmental Science & Technology 2022; 56 (11): 7052-7062
[23] Žero, S.; Huremović, J.; Memić, M.; Muhić-Šarac, T. Determination of Total and Bioaccessible Metals in Airborne Particulate Matter from an Urban and a Rural Area at Sarajevo. Toxicol. Environ. Chem.2017,99 (4), 641– 651
[24] Pravilnik o načinu vršenja monitoringa kvaliteta zraka i definiranju vrsta zagađujućih materija, graničnih vrijednosti i drugih standarda kvaliteta zraka (Sl. Novine FBiH 1/12), 2012.
[25] Zhou, X., Cao, Z., Ma, Y., Wang, L., Wu, R., Wang, W. Concentrations, correlations and chemical species of PM2,5/PM10 based on published data in China: Potential implications for the revised particulate standard. Chemosphere, 2016; 144:518-526
[26] Chauhan, P. K., Kumar, A., Pratap, V., Singh, A. K. Seasonal characteristics of PM1, PM2.5 and PM10 over Varanasi during 2019-2020. Frontiers in Sustainable Cities, 2022; doi: 10.3389/frsc.2022.909351

ANALYSIS OF THE ORIGIN OF AIR POLLUTION IN THE AREA ZENICA-DOBOJ CANTON

Vehid Birdahić, Muvedet Šišić, Nusret Imamović
University of Zenica, Faculty of Mechanical Engineering
Zenica, B&H

Halim Prcanović, Mirnes Duraković
University of Zenica, Institute “Kemal Kapetanović“
Zenica, B&H

Keywords: pollutants, emission sources, air quality.

ABSTRACT
The paper presents data on emissions of analyzed pollutants into the air (SO_2, NOx, CO, VOC, NH_3, PM_{10}, $PM_{2.5}$, PAH, Pb, Cd, and Hg) by sector (industry and energy, small combustion plants, road traffic and services-agriculture and animal husbandry), and by cities and municipalities in the area of the Zenica-Doboj Canton. Based on the analyzed data, it was determined that the air quality in the area of the Zenica-Doboj Canton is very endangered and does not satisfy the prescribed legal regulations, which can potentially affect people's health, ecosystems, economic prosperity, and development. According to the results of the research, it was determined that the main causes of excessive air pollution are the production of emissions from industrial and energy plants, local boiler houses and home fireplaces, road traffic, and the service sector (agriculture, processing industry, construction, trade), as well as unfavorable climatic conditions, with the presence of inadequate topographical conditions and other influencing factors.

1. INTRODUCTION

Air quality is a very important problem for human health, the economy, development, and the environment. Excessively polluted air has a significant impact on people's health and leads to numerous diseases, thereby causing financial costs for treating the sick and eliminating the consequences. The economy is affected by costs for treatment and loss of productivity and the impact on the environment is reflected in large and often unpredictable pressures that affect the quality of water, soil, and ecosystems. Pollutants that worsen air quality and cause negative effects on receptors, as well as the effects of acidification, eutrophication, and photochemical pollution, are sulfur dioxide (SO_2), hydrogen sulfur (H_2S), nitrogen oxides (NO_X), suspended particles (PM_{10} and $PM_{2.5}$), carbon monoxide (CO), ammonia (NH_3), ozone (O_3), volatile organic compounds (VOC), polycyclic aromatic hydrocarbons (PAH), sediment, heavy metals (Pb, Cd, Hg, and Fe). Air quality management includes a series of systemic measures aimed at ensuring air quality that will not cause ecological disturbances and consequences, and is based on measurements and assessments of emissions and air quality. The Zenica-Doboj Canton (Ze-do Canton) is located in the central part of Bosnia and Herzegovina, in the sub-basin of the Bosna river, it covers an area of 3,345 km^2 and ranks fourth in size in the Federation of BiH, and has favorable geotraffic and hydrographic characteristics, because it is located in the central part of Bosnia and Herzegovina, through which the river Bosna flows for the most part, and the route of the highway on corridor Vc, the main road M-17 and the railway line pass through [1]. By putting into operation integral production at the company

ArcelorMittal in Zenica, but also by the operation of other industrial and energy plants and facilities, such as the production of electricity in the Thermal Power Plant Kakanj (TE Kakanj), the production of thermal energy in numerous boiler houses, the production of packaging paper in "Natron Hayat" in Maglaj, leather processing in the company "Prevent-Leather" in Visoko, cement production in Kakanj, exploitation, and processing mineral raw materials, etc., as well as the development of road traffic, the use of a large number of small boiler houses and home fireplaces, the air quality in the area of the Zenica-Doboj Canton, above all in the cities located in the valley of the Bosna river, is highly threatened and does not meet the prescribed standards, which can potentially affect people's health, economy and development. The present high and often excessive emissions of harmful substances, as well as unfavorable climatic and topographical conditions result in exceeding the limit values of certain harmful substances in the air, especially SO_2, suspended particles, and other pollutants in certain parts of the Zenica-Doboj canton (Zenica, Kakanj, and Maglaj). Taking into account the above indicators, it is very important to approach the systematic planning of air quality management in a studious and comprehensive manner in regions where air quality is threatened and excessively polluted in order to achieve and maintain the prescribed air quality, protect human health, and develop this area.

2. MAIN SOURCES OF EMISSIONS RESPONSIBLE FOR AIR POLLUTION

The main emission sources and production potentials of the Zenica-Doboj Canton are concentrated in the energy, mining, and processing industry. In the structure of production, the processing industry participates with 45.41%, electricity, gas, and water supply with 34.77%, and mining with 19.82%. Likewise, a large number of small and medium-sized enterprises with the finalization of products in the metal and wood processing industry, exploitation and processing of mineral raw materials, and food technologies characterize the economy of the Zenica-Doboj Canton as a base-energy-raw material (coal-energy-metallurgy). According to the data from the Register of Plants and Pollution of the Zenica-Doboj Canton, the dominant sources of air pollutant emissions are [2]:

- Industrial plants (point sources): metallurgical industry, cement industry, leather processing industry, textile industry, paper, and cardboard industry, wood processing industry, metal processing industry;
- Energy plants (point sources): Thermal power plant Kakanj, Heating plant "Natron Hayat" Maglaj, Heating plant in ArcelorMittal Zenica, Heating plant Tešanj, Heating plant Žepče, Heating plant Zavidovići, heating plants in the production complex "Prevent" Visoko;
- Small fireplaces where solid fuel is dominantly used;
- Traffic (road and rail);
- Service sector (agriculture, processing industry, construction, wholesale and retail trade, information and communications).

The database on pollutant emissions into the air was formed on the basis of the field collection of data on emissions from all identified sources by the project team for the purpose of establishing the Registry on plants and pollution in the Zenica-Doboj Canton. The database on emissions was formed by sector in order to analyze sectorial impacts on air quality. Figure 1 shows the dominant sources of air pollutant emissions in the Zenica Doboj Canton, which have the greatest impact on air pollution.

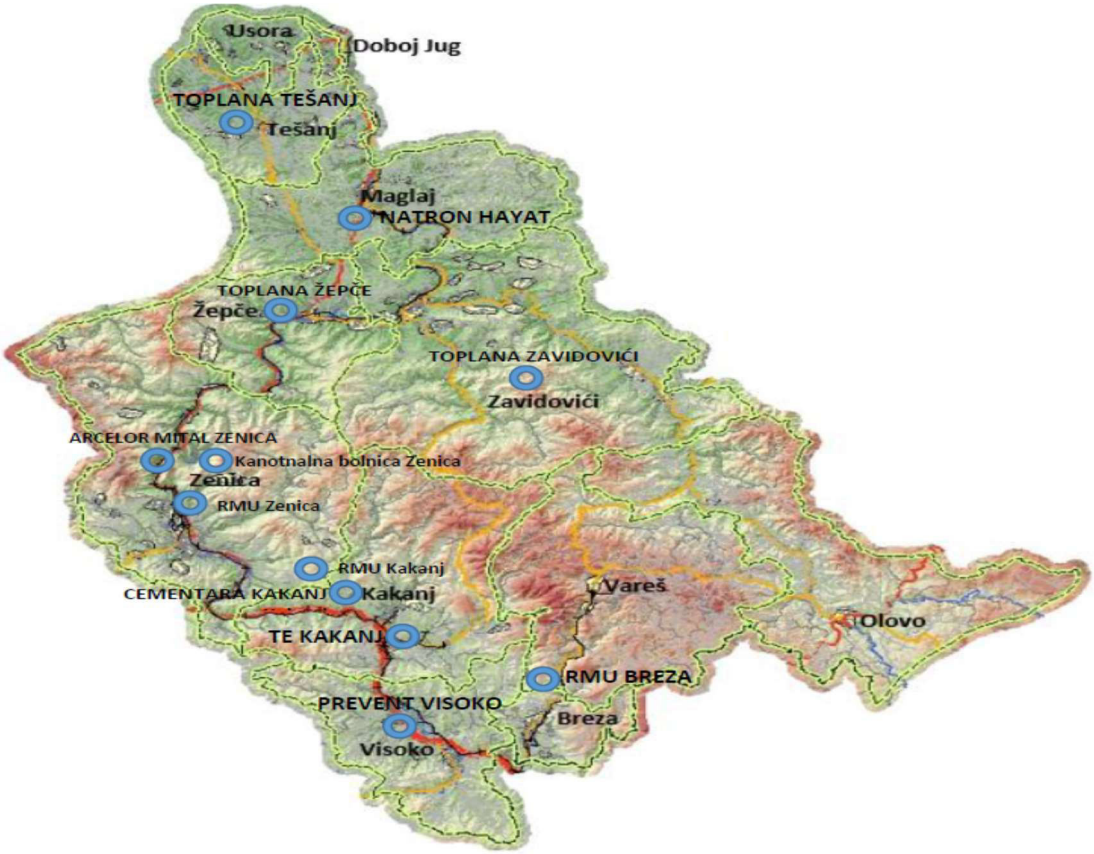

Figure 1. Dominant sources of air pollutant emissions in the area of Ze-do Canton [2]

3. TOTAL QUANTITY OF EMISSIONS FROM REGISTERED SOURCES

Data on the emission of pollutants into the air (SO_2, NOx, CO, VOC, NH_3, PM_{10}, $PM_{2.5}$, BC, PAH, Pb, Cd, and Hg) in the area of the Zenica-Doboj Canton were taken from the database of the Register of Plants and Pollution in the Zenica-Doboj Canton. of the Doboj canton, which is run by the Center for the Environment at the "Kemal Kapetanović" Institute in Zenica. Air pollutant emissions from industrial and energy plants as dominant sources of pollution in the area of Ze-do Canton are shown in Table 1.

Table 1. Emissions of industrial and energy plants in the area of Ze-do Canton [2]

City/Manicipality	SO_2 (kt)	NO_2 (kt)	VOC (kt)	CO (kt)	NH_3 (kt)	PM_{10} (kt)	$PM_{2,5}$ (kt)	BC (kt)	Pb (t)	Cd (t)	Hg (t)	PCDD/ PCDF (gI-TEQ)	PAH (t)	PCB (kg)
Zenica	4,84	1,25	0,22	1,39	0	1,68	1,17	0,06	6,36	0,0	0,16	12,09	2,69	11,06
Kakanj	69,87	7,33	0,10	0,54	0	0,17	0,21	0,07	0,31	0,03	0,05	0,44	2,36	7,67
Maglaj	1,38	0,38	3,02	9,49	0,04	0,12	0,11	5,2	0,39	0,02	0,03	0,79	2,27	11,46
Zavidovići	0,002	0	0,01	0,00	0	0,05	0,00	0	0,00	0,00	0,00	0,00	0,00	6,92
Total	**76,10**	**8,97**	**3,36**	**11,43**	**0,04**	**2,041**	**1,515**	**5,34**	**7,07**	**0,06**	**0,25**	**13,33**	**7,34**	**37,10**

A significant source of air pollution is also small fireplaces and local boiler houses, for which Table 2 shows the share of emissions from small fireplaces by local communities in the area of the Zenica-Doboj Canton, which shows that the largest share of pollutant

emissions is in the area of the City of Zenica as the seat of the canton, which is understandable because Zenica is the largest urban industrial center.

Table 2. Overview of the share of pollutant emissions from small furnaces into the air by local communities in the area of the Zenica-Doboj Canton [2]

City/Manicipality	Participation SO_2 %	Participation CO %	Participation PAH %
Zenica	38%	35%	37%
Maglaj	9%	9%	9%
Visoko	8%	9%	8%
Tešanj	9%	10%	9%
Kakanj	3%	3%	3%
Other municipalities	33%	34%	34%

Analyzing data on the balance of pollutant emissions from various sources of pollution, the following was determined: Emissions from energy and industrial plants are by far the largest compared to other sectors, with a total of 76,103 t/y SO_2, 8,976 t/y NOx, 3,365 t/y VOC, 2,041 t/y of PM_{10} and 1,515 t/y of $PM_{2.5}$ (Figure 2). Emissions from small boiler houses and domestic fireplaces follow in terms of quantity, second in relation to energy and industrial plants, and amount to a total of 8,070 t/y SO_2, 724 t/y NOx, 3,399 t/y VOC, 3,860 t/y PM_{10} and 3,713 t/y g $PM_{2.5}$, as shown in Figure 3 [3].

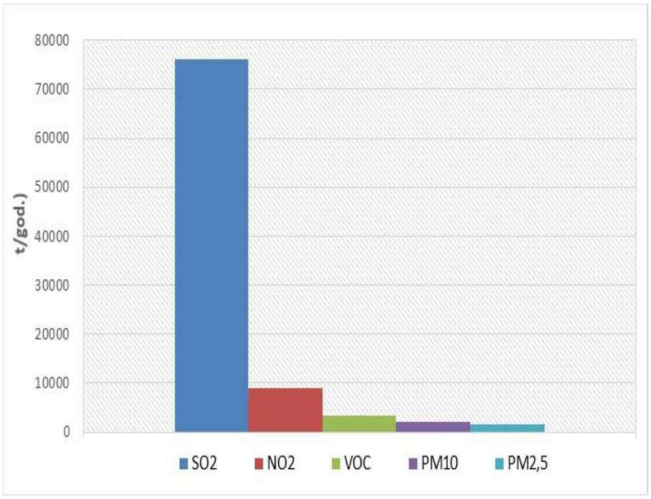

Figure 2. Energy and industrial emissions facilities in the area of Ze-do canton[1,2]

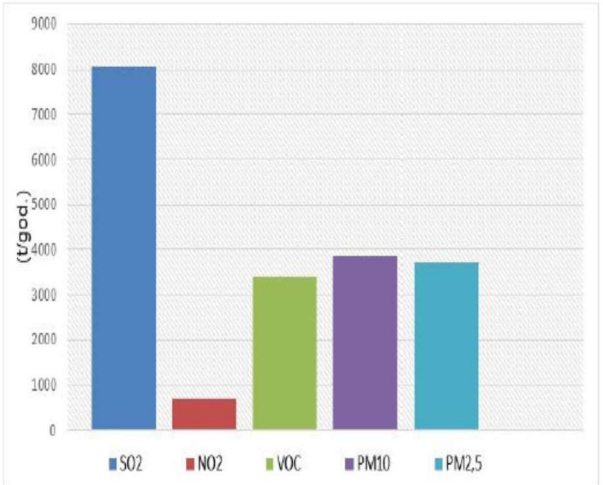

Figure 3. Emissions from small boilers and home fireplaces in the area of Ze-do canton [1,2]

According to the produced emissions from road traffic by quantity, it was determined that they are in third place in relation to the energy and industry sector and amount to 62 t/y SO_2, 1260 t/y NOx, 312 t/y VOC, 146 t/y PM_{10} and 120 t/y of $PM_{2.5}$, which are given in Figure 4.

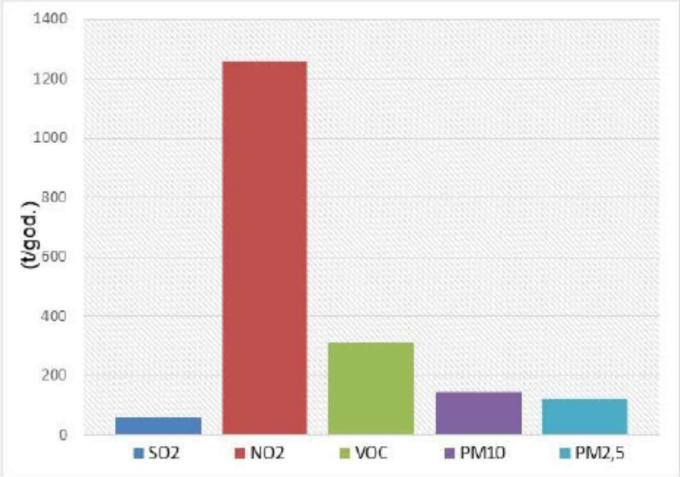

Figure 4. Emission of road traffic in the area of Ze-do canton [1,3]

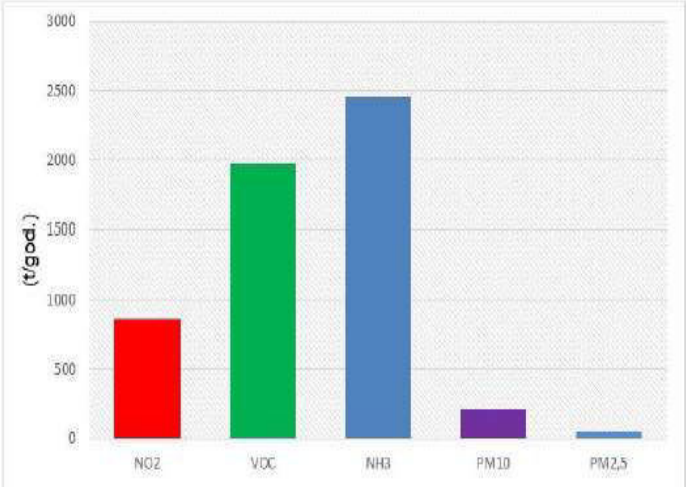

Figure 5. Emission of the service sector (agriculture-livestock) [1,3]

Emissions from the service sector (agriculture-livestock) total: 863 t/y NOx, 1959 t/y VOC, 2467 t/y NH_3, 214.5 t/y PM_{10}, and 45 t/y $PM_{2.5}$, which are shown in Figure 5.
By combining all relevant data on total emissions, Table 3 shows the total emissions for the entire area of the Ze-do Canton, where the largest SO_2 emission is evident in the amount of 84,195 kt.

Table 3. Overview of total emissions in the area of the Zenica-Doboj Canton [2]

SO_2 (kt)	NO_2 (kt)	VOC (kt)	NH_3 (kt)	PM_{10} (kt)	$PM_{2.5}$ (kt)	BC (kt)	CO (kt)	Pb (t)	Cd (t)	Hg (t)	PAH_s (t)
84,195	12,373	12,818	3,222	7,199	5,513	5,776	37,358	9,881	0,123	0,274	11,628

3.1. Data on pollution that came from other regions/areas

Due to its geographical location and atmospheric circulation, the canton is exposed to the influence of pollution coming from the Tuzla region due to the presence of high emission sources (TE Tuzla and Gikil d.o.o. Lukavac), whose dominant sources are more than 40 km away from the area of the Zenica-Doboj canton as the crow flies. Likewise, due to the general circulation of the atmosphere, this area is exposed to the influence of cross-border transport of particles and particle precursors from distant industrially developed countries, which are significant sources of particle precursor emissions. Modeling estimated that approx. 20-40% of emitted polluting substances from TE Kakanj dissipate outside the area of the Zenica-Doboj Canton, which depends on the general circulation of the atmosphere and meteorological conditions [1,2].

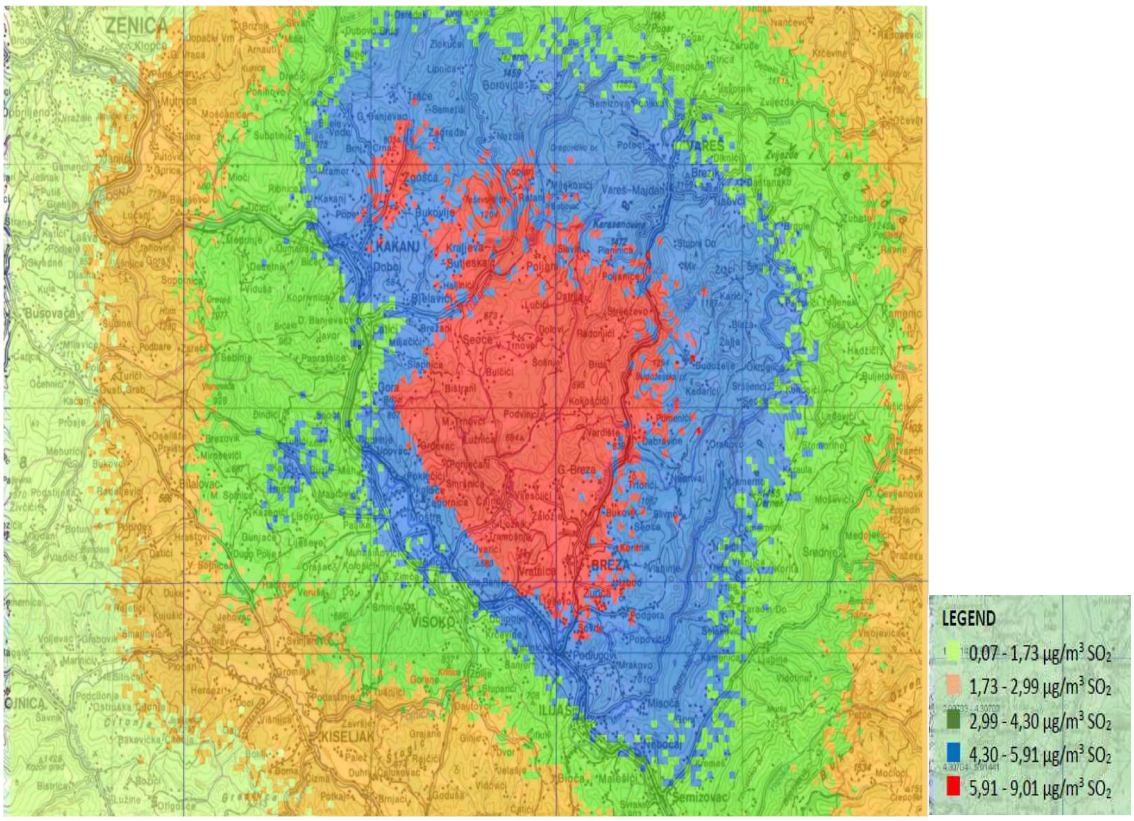

Figure 6. Dispersion of SO_2 emitted from the tall chimney of the TE Kakanj [1]

4. CONCLUSION

According to the results presented in this paper, it can be concluded that the origin of pollutant emissions by sector in the area of the Zenica-Doboj Canton is as follows:

- SO_2 emissions show that energy and industrial plants are by far the largest sources of emissions of this pollutant with a share of 90.35 %, followed by small boiler houses and home fireplaces with 9.58%, while SO_2 emissions from road traffic are negligible (0.07%).
- PM_{10} emissions show that small combustion plants are the largest sources of emissions of this pollutant with 61.65 %, followed by energy and industrial plants with 3.60%, while the agriculture sector has significantly fewer emissions with 3.42%, and traffic emissions are the smallest at 2.33% of PM_{10}.
- The emission of $PM_{2.5}$ shows that small boilers and home fireplaces are the biggest sources of emissions of this pollutant with a share of 68,8 %, followed by energy and

industrial plants with a share of 28.09%, while traffic emissions have a much smaller share with 2.23% of $PM_{2.5}$, and emissions from the agriculture sector are very small with a share of 0.83%.

- The contribution of different emission sources to air pollution does not depend only on the number of substances emitted into the air, but also on the location of the emission source, and emission conditions, such as chimney height, flue gas velocity, flue gas temperature, and atmospheric circulation and relief conditions as well as dispersion conditions.
- The air quality in Ze-do Canton, in addition to the present pollutant emissions, is significantly affected by unfavorable meteorological and topographical conditions, because the atmosphere, given its volume and dynamics, tolerates a certain amount of polluting substances and gradually dilutes them through the processes of dispersion and chemical transformation.
- Improving the quality of air can only be achieved with an integrated approach to all subjects by consistently harmonizing all sectoral policies. For this reason, the mobilization and synergy of all entities are necessary, starting from business entities whose facilities excessively pollute the air, local self-government units, and the Zenica-Doboj Canton to the Government and competent ministries of the Federation of Bosnia and Herzegovina, to create the necessary conditions for the implementation of measures and projects to achieve the planned improvement air quality in order to protect the health of the population, ensuring the conditions for a healthy life and coordinated development with social and ecological conditions.

5. REFERENCES

[1] Kantonalni akcioni plan za poboljšanje i zaštitu kvaliteta zraka na području Zeničko-dobojskog kantona, JU Univerzitet u Zenici, Metalurški institut "Kemal Kapetanović" Zenica, 2020.

[2] Registar o postrojenjima i zagađivanjima na području Zeničko-dobojskog kantona, Metalurški institut "Kemal Kapetanović" Zenica, 2019.

[3] Izvještaj o rezultatima mjerenja zagađenosti zraka u Zenici za period juli-novembar 2019. godine (Izvještaj sa automatskih stacionarnih mjernih stanica), JU Univerzitet u Zenici, OJ Institut "Kemal Kapetanović" u Zenici, 2019.

RESEARCH OF THE POSSIBILITY OF USING THE HEAT GENERATED IN THE AEROBIC BIODEGRADATION PROCEDURE

Muvedet Šišić, Vehid Birdahić, Sanela Beganović, Mirnes Duraković
University of Zenica, Faculty of Mechanical Engineering
Zenica, B&H

Farzet Bikić
University of Zenica, Faculty of Metallurgy and Technology
Zenica, B&H

ABSTRACT
The paper describes the research methodology of the heat generated by the biological decomposition of a mixture of sludge from WTP (wastewater treatment plant) and biowaste and its use outside the system for a controlled biodegradation process. Earlier research in this area defined the optimal mixtures of sludge and biowaste that ensure quality management of the biological decomposition process. The research described in this paper aims to prove that the heat generated in the process of a biological enclosure can be taken outside the biodegradation system and used without violating the assumptions of optimal management of the process.

Keywords: sludge, biowaste, heat, bioreactor, heat exchanger

1. INTRODUCTION

In the process of biological decomposition of waste materials, in addition to the benefits related to the conversion of waste materials into a useful product - compost, certain heat is also produced, the potential of which needs to be investigated. In doing so, it is necessary to analyze the impact of individual solutions and designs of heat separators on the stability of the composting process, that is, to define the optimal process conditions that will provide heat separation in a way that does not endanger the process of aerobic biodegradation. The character of certain influential factors can be observed and evaluated through the parameters of the previously defined regression model with the addition of factors related to the design of the heated separator.

Earlier research in this area defined significant potentials of sludge and biowaste, as well as their optimal mixtures that ensure quality management of the composting process [1]. The research in this project, while respecting previous research and the need to establish a more stable process, included monitoring the input and output parameters of the composting process of organically saturated sludge from municipal wastewater treatment plants and biowaste created by the maintenance of urban green areas.

2. MATERIALS AND METHODS

Sludge for the purposes of the research was taken from the location of the municipal wastewater treatment plant in Srebrenik and Gradačac, since in earlier research these locations proved to be a source of sludge of optimal consistency and other characteristics important for the biodegradation process.

Before the final processing, the waste materials that are the subject of research need to be processed. The processing depends on the content of the mixture or the characteristics of

individual waste materials. The method of primary processing also depends on the method of final use [2].
It is necessary to foresee the following processing procedures: thickening, stabilization, and drying in the case of sludge and shredding in the case of biowaste. Sludge stabilization reduces the number of pathogenic microorganisms and unpleasant odors [1]. Stabilization and drying were carried out by leaving it for 15 days in natural conditions outside.
In order for sludge to be used for composting after stabilization, it must meet certain physical-chemical-biological criteria.
Samples of individual sludges were separated and the necessary analysis was performed. The results of the analysis of individual sludges are presented in Table 1. Where sample 1 represents sludge from the wastewater treatment plant in Gradačac and sample 2 represents sludge from the wastewater treatment plant in Srebrenik.

Table 1. Results of chemical analysis of individual sludges

Parameter	Sample 1	Sample 2
pH	8,5	7,3
Dry matter/moisture content [%]	63,02/36,98	67,88/12,12
Content ∑N [mg/kg]	48200	25900
Content ∑C [mg/kg]	305000	373800
Ratio C/N	6:1	14:1
Cd [mg/kg]	<0,1	<0,1
Cu [mg/kg]	100	50
Ni [mg/kg]	100	50
Co [mg/kg]	<1	<1
Pb [mg/kg]	<1	<1
Zn [mg/kg]	500	150
Cr [mg/kg]	<1	<1
As [mg/kg]	<1	<1
Hg [mg/kg]	<1	<1

By analyzing the values in Table 1, we can see that the concentrations of certain heavy metals are lower in sample 2. Also, the pH value and the C/N ratio are closer to the optimal values for the process of aerobic biodegradation in sample 2 [1]. For these reasons, it was decided to use the sludge designated as sample 2 in the research, sludge from the municipal wastewater treatment plant in Srebrenik.
After stabilization, the sludge was mixed with shredded biowaste, and compost mixtures were prepared as shown in Figure 1.

Figure 1. Biowaste preparation process and composting mixture

All components in the compost mixture also need to be analyzed in order to check the condition and content of the components determining the loss and successful management of the composting process. Earlier research in this area at the University of Zenica defined the optimal content of the mixture, i.e., the ratio of sludge to biowaste (in volume ratio sludge 30%, biowaste 70%) [1]. After defining the content, a chemical analysis of the compost mixture will be performed, which includes the parameters that determine the success of starting the composting process:

- mass fraction of dry matter,
- mass fraction of total organic carbon in dry matter,
- pH value of the mixture,
- mass fraction of total nitrogen in dry matter,
- mass fraction of total phosphorus in dry matter in.

The prepared compost mixtures were placed in three plastic containers-bioreactors (Figure 2a). The biodegradation process and research were carried out at the "Kemal Kapetanović" Institute of the University of Zenica..

a) *b)*

Figure 2. Controlled biodegradation system: a) Sterns in series, b) Water circulation system

The tanks with compost mixtures are connected in a system that provides water circulation through heat exchangers including a common cold water tank as shown in Figure 2b). Three different types of heat exchangers are installed in three different tanks as shown in Figure 3.

a) *b)* *c)*

Figure 3. Different forms of heat exchangers, a) bioreactor 1, b) bioreactor 2, c) bioreactor 3

The temperature of the compost mixture and the temperature of the water before and after the exchanger was monitored with the help of sensors placed in all three systems with the possibility of electronic recording. The composting process is accelerated by blowing air with the help of a compressor. The general concept of the established bioreactor is represented by the scheme in the following figure.

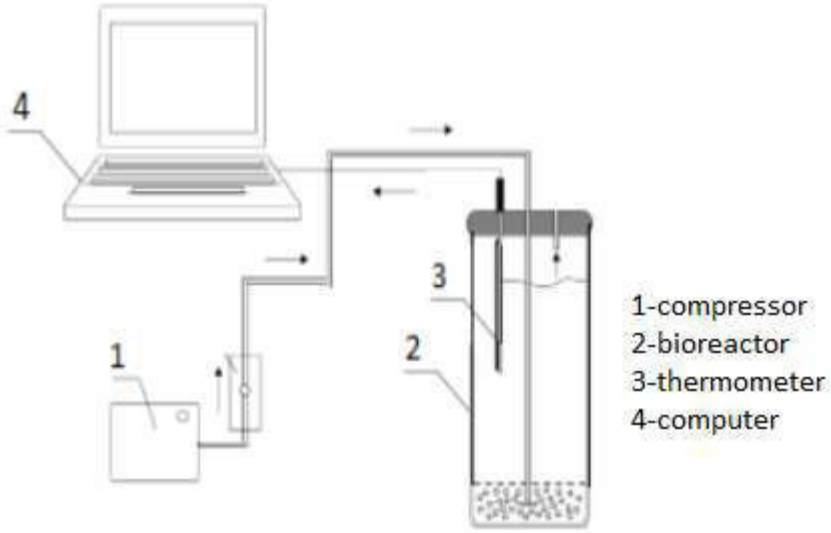

Figure 4. The general concept of the bioreactor

compost mixtures and the achieved process conditions, the temperature of the compost mixture in certain phases exceeds 70 °C [1]. In these situations, it is necessary to physically mix the mixture in order to reduce the temperature, which represents an unfavorable environment for the survival and development of bacteria that carry out the decomposition process.

In certain stages of the biodegradation process, i.e., after the end of the process, it is necessary to analyze the quality of the compost mixture, i.e., the finished compost, in order to determine the quality and justification of its use as a soil improver. Chemical analysis of compost includes the following parameters:

- pH reaction,
- total carbon,
- total nitrogen and C/N ratio,
- the concentration of easily accessible P_2O_5,
- the concentration of easily accessible K_2O,
- the concentration of total Ca and Mg [3].

The analysis of the content of heavy metals in the sludge was carried out using the Shimadzu Analytical Methods for Atomic Absorption Spectrometry method, and the preparation of samples for the chemical analysis required the application of standard methods of shredding the air-dried sample [4]. The pH value was measured using the method with a solution of 0.1M $CaCl_2$, 1M KCl, and H_2O in a ratio of 1:2.5 (m/v) for soil/compost and 1:5 (m/v) for waste sludge [5]. Determination of dry matter content and moisture content was performed using a standard gravimetric method [6]. The 4500-Norg B method was used to determine the total nitrogen content [7]. The total phosphorus content was determined using spectrometric methods with ammonium molybdate [8]. Determination of the concentration of readily available P_2O_5, K_2O, Ca, and Mg was performed using liquid ion chromatography methods [9].

The biodegradation process started properly immediately after placing the compost mixtures in the bioreactors. With the help of a compressor and an additional probe, the air

was blown into the interior of the bioreactor every day. The liquid that was generated in the biodegradation process was returned back to the bioreactor.

3. RESULTS OF DISCUSSIONS

After 15 days from the start of the process, samples were taken from all three bioreactors, and an analysis of the necessary parameters was performed in order to evaluate the degree of biodegradation. The results of the analysis are presented in Table 2.

Table 2. Results of compost analysis after 15 days from the start of the process

Parameter	Sample 1*	Sample 2*	Sample 3*
pH	8,0	8,1	8,3
Dry matter/moisture content [%]	86,71/13,29	87,52/12,48	87,33/12,67
Content ∑N [mg/kg]	21700	21800	18600
Content ∑C [mg/kg]	370000	342500	367500
Ratio C/N	17:1	15:1	19:1
Ca [mg/kg]	139000	133000	118000
Mg [mg/kg]	4800	4800	4700
P_2O_5 [%]	0,595	0,595	0,527
K_2O [%]	0,73	0,87	0,82

**The sample number corresponds to the number of bioreactors*

The analysis of the same parameters was also carried out after 28 days after the start of the process. The results of the analysis are presented in Table 3.

Table 3. Results of compost analysis after 28 days from the start of the process

Parameter	Sample 1*	Sample 2	Sample 3
pH	6,4	6,2	6,3
Dry matter/moisture content [%]	88,04/11,96	87,84/12,16	86,98/13,02
Content ∑N [mg/kg]	33600	29800	29300
Content ∑C [mg/kg]	330300	371200	387700
Ratio C/N	10:1	12:1	13:1
Ca [mg/kg]	260430	251150	243050
Mg [mg/kg]	6437	6210	5718
P_2O_5 [%]	0,939	0,87	0,962
K_2O [%]	6,92	2,96	0,15

**The sample number corresponds to the number of bioreactors*

Process parameters were monitored for one month. The analysis of samples of individual compost mixtures presented in Tables 2 and 3 show the changes that characterize the course of the aerobic biodegradation process:

- reduction of the C/N ratio,
- increasing the concentration of nutrients.

The characteristics of the "product" obtained by the process that was the subject of research indicate the possibility of its application as a soil improver [1].

The temperature of the biodegradation process in all bioreactors was constantly monitored in the manner presented in Figures 5, 6, and 7.

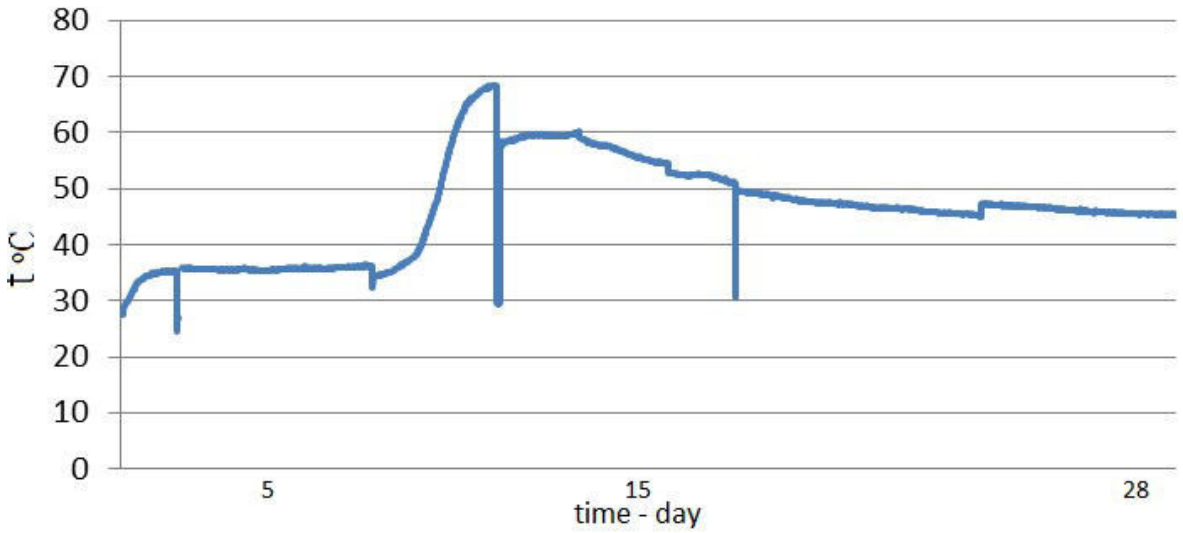

Figure 5. The temperature produced in the composting process – bioreactor 1

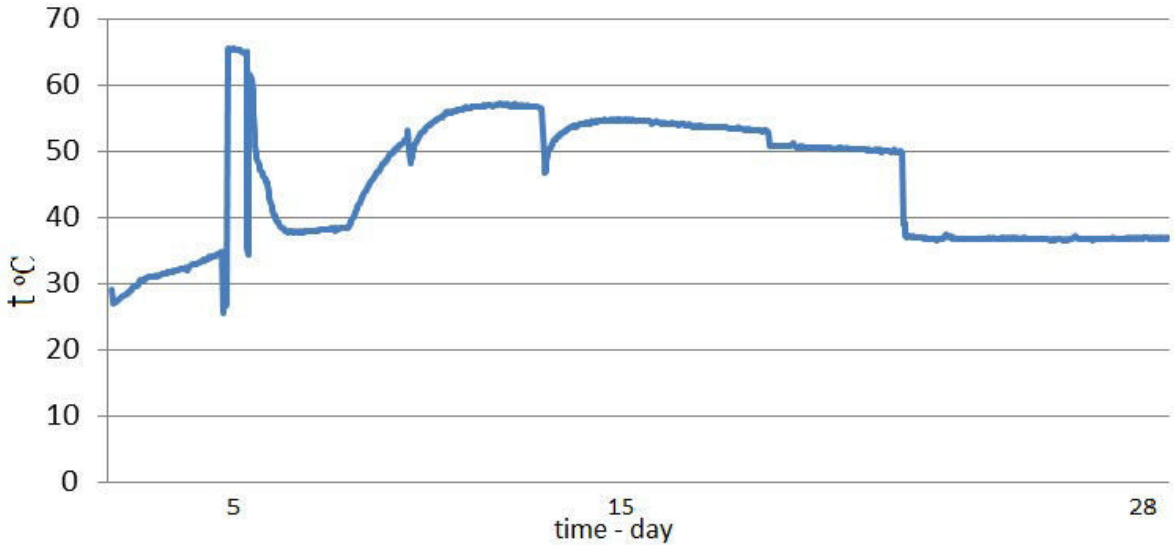

Figure 6. The temperature produced in the composting process – bioreactor 2

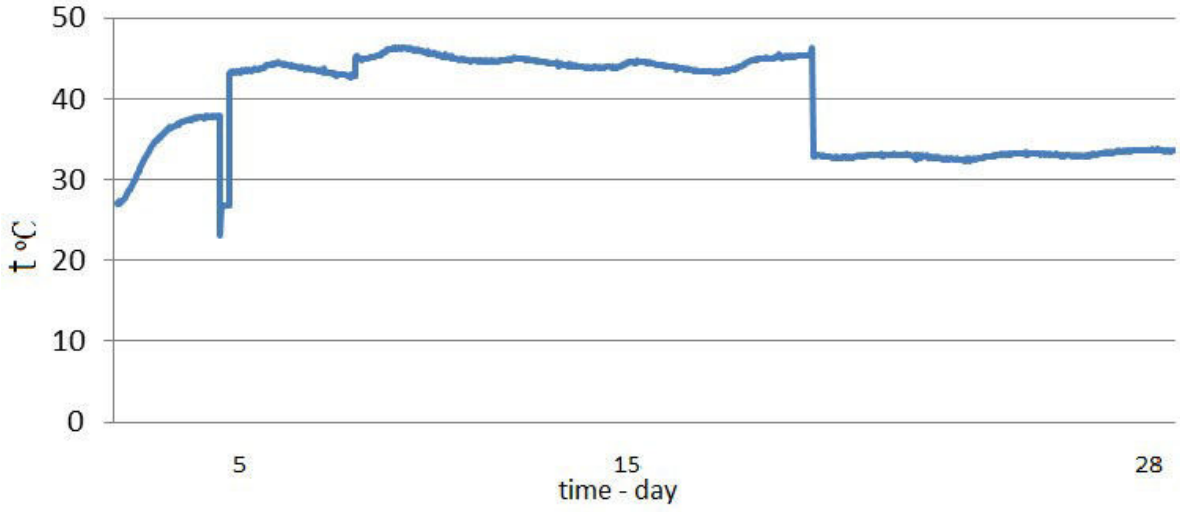

Figure 7. The temperature produced in the composting process – bioreactor 3

The bioreactor was alternately connected to the water circulation system, which extracted the produced heat from the bioreactor. By measuring the water temperature in the circulation system, it was determined that every 60 minutes the temperature increases by an average of 5 ºC. Extraction of the generated heat from the biodegradation system did not cause any disruption to the process

4. CONCLUSION

Taking into account the analysis of process parameters, it can be stated that compost as a product of aerobic biodegradation meets most of the criteria that determine the possibility of its use as a soil improver.

The current version of the Rulebook on determining the permitted amounts of harmful and dangerous substances in the soil and the methods of their testing ("Official Gazette of the Federation of Bosnia and Herzegovina", number: 96/22) [10] limits the possibility of using this compost in agriculture, but the possibility of using this compost as a soil improver certainly remains in the production of ornamental plants, maintenance of parks, etc.

In addition to the benefits of recycling sludge and biowaste as waste materials, this research proves the justification of using that is, transferring the generated bioheat with different technological solutions to other systems that can use it usefully. The research also proves that the release of this heat will not interfere with the process of aerobic biodegradation. In the phases where the excess generated heat has negative effects on the process of aerobic biodegradation, its extraction from the system is desirable [1,3].

5. REFERENCES

[1] Šišić, M.: Istraživanje mogućnosti kompostiranja mulja s komunalnih uređaja za prečišćavanje otpadnih voda, Doktorski rad, Univerzitet u Zenici, Mašinski fakultet, Zenica, 2018.

[2] Stuhli, V.: Karakterizacija otpadnog mulja iz postrojenja za prečišćavanje gradskih otpadnih voda u funkciji određivanja mogućnosti njegove anaerobne digestije, Magistarski rad, Univerzitet u Tuzli, Tehnološki fakultet, Tuzla, 2011.

[3] Vouk, D., Malus, D., Tadeschi, S.: Konačna obrada mulja otpadnih voda grada Zagreba, Sveučilište u Zagrebu, Građevinski fakultet, Zagreb, 2012.

[4] ISO 11464:1994 (1994). Preparation of samples for physical and chemical analysis Drying: air-dried (soil and sludge)

[5] ISO 10390:2004 (2004). Determination of pH

[6] ISO 11465:2004 (2004), Determination of dry matter (DM) and moisture contents

[7] Standard Methods for the Examination of Water and Wastewater 20th edition APHA, Washington was used

[8] ISO 6878:2006 (2006). Determination of phosphorus

[9] ISO 14911:2001 (2001). Determining readily available P, K, and Mg i Ca

[10] Pravilnik o utvrđivanju dozvoljenih količina štetnih i opasnih materija u zemljištu i metode njihovog ispitivanja („Službene novine Federacije BiH“, broj: 96/22)

THE ROLE OF WOOD-BASED PRODUCTS IN SUSTAINABLE DEVELOPMENT

Petar Ćurić, Jelena Obranković, Andreja Pirc Barčić
University of Zagreb, Faculty of Forestry and Wood Technology
Zagreb, Croatia

Keywords: wood-based sector; wooden products, cascade use of wood, sustainable development

ABSTRACT
Wood is renewable, recyclable, climate-friendly material, and presents an important segment in achieving circular economy and sustainability concepts. To be able to link these two concepts, production and consumption systems need to transform towards sustainability. Wood-based products play a role in mitigating climate change by reducing carbon from the atmosphere. Their special properties, such as carbon storage capacity, high recyclability, renewal of raw materials, and a direct impact on the reduction of greenhouse gases in the atmosphere, make them the best product to combat climate change. This paper aims to present the role of the wood-based industry and its products in achieving sustainable development goals.

1. INTRODUCTION

Sustainable development, bio-economy, and circular economy are concepts that complement each other. Furthermore, the wood-based sector together with forest and forest-based sectors plays a central role in achieving sustainability, because it provides material, bioenergy, and wealth. It is especially important regarding the fact that, besides seas and oceans, wood represents the most important atmosphere carbon storage. Opposite to expectations of individuals that cutting the forests creates an imbalance in the ecosystem, it is important to observe the problem in total to present the carbon balance correctly for certain products, regarding its specific qualities, use of additional material, local energy resources, and technology, possibilities of recycling and, of course, principles of sustainable forestry. Furthermore, the cascade use of wood is a concept with a long history of debate and analysis in EU bio-based industries. The cascade use of wood is the smart way to use a natural resource – putting it to good use before it is reused, recycled, and finally burnt for energy. It strongly overlaps with circular economy and sustainability concepts. To be able to link these two concepts, production and consumption systems need to transform towards sustainability. This paper aims to present the role of the wood-based industry and its products in achieving sustainable development goals.

2. WOOD – BASED INDUSTRY IN NUMBERS

According to Forest Products Annual Market Review (2021) [1] the COVID-19 pandemic resulted in a large contraction in economic activity across the UNECE region in 2020, albeit with differences between countries due to the diversity of economic structures and policy responses. Total housing starts in the United States were estimated at 1.38 million in 2020, an increase of 6.9% over 2019 and higher than the historical average of 1.01 million units. Total Canadian housing starts increased by 3.8% in 2020, year-on-year. About 57% of the total in Canada were apartments. The new European Union (EU) Reconstruction Plan is anchored in the European Green Deal. Through its links to the EU's Biodiversity Strategy and Climate Policy, the strategy is expected to have a medium- and long-term influence on

forest product markets. Although the forest products industry in Eastern Europe, Caucasus, and Central Asia was not one of the most affected sectors in the early stages of the pandemic, it did encounter significant reductions in the production, trade, and consumption of wood products. The furniture and wood-based panels segments experienced the biggest declines. Port closures reduced exports of wood-based products from the United States by 32% in 2020 compared with 2019, and the country's imports dropped by 26%. Exports of wood-based products in March 2021 were, however, nearly identical to those in March 2020, and imports were about 36% higher. Value-added wood products are primary wood products that have been further processed into secondary products such as furniture, builders' joinery, carpentry (BJC), profiled wood, and engineered wood products (EWPs). Demand is linked to drivers such as economic growth; housing and construction; home renovation; fashion and design; and demographics. BJC comprises a wide array of wood products, including wooden windows and doors; pre-assembled wooden flooring; posts and beams; and shakes and shingles. EWPs include I-beams (also called I-joists); finger-jointed sawnwood; glulam (sawnwood glued into beams); laminated veneer lumber (LVL); and mass timber panels, including cross-laminated timber (CLT). The COVID-19 pandemic has had a surprising impact on value-added wood product demand, with people suddenly having more time for do-it-yourself projects. Improvements and repairs of owner-occupied homes will remain solid in the United States through 2021 and into 2022. The office-furniture segment has been a clear loser in the pandemic, with stay-at-home orders reducing demand. On the other hand, such orders have meant that workers have focused on their homes and comfort, and many have adapted their spaces to the needs of working from home. This will likely have longer-term effects on office workspace design and use and could lead to a reduction in total required space as more people work remotely at least part of the time. Building with wood has been boosted by the introduction of CLT, particularly in markets with a lower share of wood construction. Global CLT production capacity was estimated at 2.8 million m^3 in 2020, and actual production likely exceeded 2 million m^3. According to the Eurostat document Agriculture, forestry and fishery statistical book [2] the EU's wood-based industries cover a range of downstream activities, including woodworking industries, large parts of the furniture industry, pulp and paper manufacturing and converting industries, and the printing industry. Together, some 393 000 enterprises were active in wood-based industries across the EU in 2020; they represented one in five (19 %) manufacturing enterprises across the EU, highlighting that - except for pulp and paper manufacturing that is characterized by economies of scale - many wood-based industries had a relatively high number of small or medium-sized enterprises. The wood-based industries employed 3.1 million persons across the EU in 2020 or 10.5% of the manufacturing total. There were more than 900 000 persons employed within both the manufacture of wood and wood products and the manufacture of furniture, whereas the employment of 555 000 persons was recorded for printing and service activities related to printing, representing the lowest employment of the four activities. The economic importance of an industry can be measured by the share of its gross value added (GVA) in the economy. In 2020, the GVA of wood-based industries in the EU was €136 billion or 7.2% of the total manufacturing industry. Within the EU's wood-based industries, the largest GVA was recorded for pulp, paper, and paper products manufacturing (34% or €46 billion), while the manufacture of furniture and manufacturing of wood and wood products each made up between 23% and 27%. After the temporary decrease in 2020, roundwood production in the EU increased by 3.9% in 2021. In 2021 it reached an estimated 507 million m^3. This is 25.6% more than at the beginning of the millennium. Except for four EU Member States where the roundwood production decreased or remained stable and a further five Member States where lack of latest data does not allow the trend to be evaluated

all EU countries recorded an increase in roundwood production in the period of 2000–2021. The largest relative increase during the two decades in the amount of harvested wood took place in the Netherlands (190%), Czechia (126%), Poland (66%), and Slovenia (65%). In 2021, Germany was the largest producer of roundwood in EU (82 million m^3), followed by Sweden, Finland, and France (each producing between 50 and 75 million m^3). Wood has been increasingly used as a source of renewable energy. Almost a quarter (2%) of the EU's roundwood production in 2021 was used as fuelwood, while the remainder was industrial roundwood mostly used for sawnwood and veneers or pulp and paper production. This represents an increase of 6 percentage points (pp) compared with 2000 when fuelwood accounted for 17% of the total roundwood production. In some EU Member States, specifically the Netherlands, Cyprus, and France, fuelwood represented the majority of roundwood production (more than 50%) in 2021. On the other hand, Slovakia and Sweden reported that over 90 % of their total roundwood production was industrial roundwood. The total output of sawnwood across the EU increased by approximately 15% from 2000 to 2021, reaching 112 million m^3 in 2021. Germany and Sweden were the EU's leading sawnwood producers in 2021, accounting for approximately 23% and 17% of the EU's total sawnwood output, respectively.

3. WOOD PRODUCTS AND SUSTAINABILITY

Wood is renewable, recyclable, climate-friendly, and versatile and is increasingly being used to replace non-renewable materials. It is a critical material to the efforts to address the global threats to climate, biodiversity, and the environment caused by the excessive use of non-renewable materials [3]. More precisely, it's renewable, sustainable, recyclable, grown locally, versatile, biodegradable, and has a smaller energy, water, and carbon life cycle footprint than other products. Increasingly, wood is being recognized in the architecture, engineering, and construction communities as a green building product with important environmental advantages over other building materials. Mass timber and engineered wood products in construction, man-made cellulose fiber for textile production, and more modern forms of wood for energy are the most prominent wood products for large-scale substitution of non-renewable materials. According to Salzman et al. [4] forests are natural systems that provide multiple goods and ecosystem services, including raw materials, various non-wood forest products, climate regulation, carbon storage, and biodiversity, while wood and wood-based products can contribute to climate change mitigation through carbon storage in materials and by avoiding GHG emissions through material and energy substitution [5]. In recent years the wood-based sector has been developing new and innovative products that have the potential in achieving sustainability, such as textile fibers, composites, chemicals, and packaging materials [6,7] Sustainable development concept is an effort to achieve the balance between economic, social, and ecological demands, with the final goal to satisfy the needs of nowadays without endangering the abilities of future generations to satisfy their future needs [8]. The socially responsible business regards to responsibilities of a company to contribute to sustainable development with its manufacturing and business activities. The lack of knowledge of the sustainable development concept makes many actors in the chain of creating value for a product misunderstand the principles of sustainability of the environment with activities of decreasing the impact of the production process on the environment. However, according to principles of environmental sustainability, the goal of the so-called green process is to try to decrease the impact of all activities in all life cycle phases of product and/or service (material-production-use-re-use/recycling) on the environment through emission decreasing, giving priorities to renewable material and decreasing the total costs of product/service life cycle [9]. Total tracking of product or service, life cycle in perspective of sustainable development can give

decision makers a clear view and better understanding of three pillars of sustainable development (3P): People, Planet, and Profit/Prosperity during the full supply/demand chain. All activities based on principles of the sustainable environment using suitable methodology, techniques, and tools, and which can contribute to this goal, are recommended. The sustainable use of natural resources, including forests, is a key tenet of the 2030 Agenda for Sustainable Development. The 2015 Paris Agreement also highlights the contribution of forests to climate change mitigation and adaptation. Technical and methodological progress has facilitated better monitoring of the life cycle of harvested wood products. This gives them a key role in strategies for transitioning to low-carbon economies. Concurrently, the impact of sustainable forest management on enhancing livelihoods, contributing to landscapes and cities, and reducing the world's carbon and material footprints, is growing. That kind of approach puts in focus the importance of observing the relationship between sustainable production and sustainable consumption. According to Znkhan and Carlson [10], the primary goal for producers is to choose production, process, and management activities that will have the lowest impact on human health and the environment, and for final consumers the primary goal is to choose product or service which will have the lowest impact on the environment, taking into consideration the costs.

4. SUSTAINABLE ARCHITECTURE, DESIGN, AND USAGE OF WOOD-BASED PRODUCTS

When it comes to a sustainable built environment, material choices matter. Wood is a natural, renewable, and sustainable material for building. Maximizing wood usage in both residential and commercial construction could remove an estimated 21 million tons of CO_2 from the atmosphere annually—equal to taking 4.4 million cars off the road [11]. Because 80% of a building's embodied carbon comes from the structural materials used to build it, building material specification is impactful. Wood performs better than concrete and steel when it comes to both its carbon footprint and air and water pollution. Its low-carbon benefits, and other sustainability advantages, including certified wood, recycled/reused materials, local sourcing of materials, waste minimization, and indoor air quality, make wood one of the best tools in the toolkit to reach net-zero carbon for buildings.

One example that highlights sustainability principles in the field of wood furniture is IKEA. IKEA has been piloting various initiatives across its European stores to see how they can build circularity into their offer to customers with an aim to support customers to care and repair, rent, share, bring back, and resell their IKEA products to prolong product life.

Concerning eco-friendly furniture, the socio-demographic elements of consumers (income, residence, age, and educational level) and family size have a significant influence on their willingness to buy this type of furniture [12]. Vlosky et al. [13], who investigated furniture consumers in the United States, and Xiaolei et al. [14], who investigated customer preference for kitchen cabinets in China, ascertained that consumers preferred eco-friendly furniture. According to Anderson and Hansen [15], consumers in the United States are willing to pay a premium for eco-friendly wood products. Pirc et al. [16] determined that Croatian consumers most often view domestic furniture as high-quality and well designed, but also expensive.

Regarding the environmental consciousness of the respondents of both countries, the authors theorize that appealing to "green" consumers and consumers that express an indifferent attitude towards the environmental attributes of furniture could create an interesting potential for a market with eco-labeled furniture products. This presumption could be supported by similar findings from other Central-European consumer studies [17,18,19]. Moreover, there are challenges for furniture manufacturers because of Green

Growth and Circular Economy measures and legislative proposals recently adopted in EU countries. The main areas are connected to the waste management policy (e.g. waste prevention program, changes in the waste hierarchy), designing of products, setting up of production processes, and utilization of resources.
The results show that the group of architects that participated in the study in general have had a good experience with EWPs, have a positive attitude towards using EWPs, and think that their use will increase in the future. They have, however, limited possibilities to influence material selection, and the main hindrance to using new EWPs is that other actors with a greater influence over material selection prefer other materials. The level of knowledge of EWPs among the architects is in general moderate and lack of knowledge and information about EWPs is also seen as a hindrance of importance when it comes to introducing new EWPs. Factors that seem to influence the likelihood of increased use of EWPs in buildings are environmental concerns, perceptions of the aesthetic appearance, amount of experience, influence over the material selection, level of knowledge of EWPs, and the architects' attitude towards using EWPs in buildings [20].
Only recently, from a historical perspective of use, has wood been developed to form a range of increasingly functional products, based on a combination of performance and sustainability requirements, i.e. engineered wood products (EWPs) [21]. This has been possible because new industrial processes have been developed for the modification of wood, and because residues and lower-grade trees are being increasingly used for more versatile and consistent products with dimensions considerably larger than that of the tree. The result is a vast array of EWPs used in contemporary architectural design. There are EWPs suitable e.g. floors, walls and roof elements, beams, columns, insulation, cladding, decking, and also a number of engineered panel products that can be used to add bracing and shear strength to timber constructions [22]. Mamić and Domljan [23] analyzed the production processes and observed what is left as residue, how it is produced, and how to turn residue back into valuable raw material from which a new eco-friendly product could be created. The research findings noted that waste raw material can be turned into a more usable raw material, as well as into a final product with a higher added value, and thus contributes to improving the market competitiveness of the company. When it comes to wood residue revision, they pointed out the vast majority of oak-cut veneer waste is selected on an aesthetic basis, due to which the raw material is eliminated. Wood does not have the same characteristic as plastic, for example, so visual defects in wood are a natural occurrence. Today’s trends encourage the use of wood that emphasizes the natural appearance and irregularities, in contrast to the recent desirable perfectly flat, uniform grain and wooden strips. The results from Burnard and Kutnar [24] indicated that, under certain conditions, using wood in the built indoor environment may lead to improved stress responses. For example, stress responses indicated by salivary cortisol levels were lower in the test environment with oak furniture than in the corresponding control environment. They discussed that the reduced reaction to stress has a small effect on any single stressful situation, but, over time, even small reductions to stress responses can contribute to improved mental and physical health outcomes.

5. CONCLUSION

Sustainability is increasingly becoming a key consideration of all stakeholders within the wood-based sector and its products since the world is moving towards zero-energy construction. More rational use of raw materials is also very important, particularly when this material has a significant impact on reducing CO_2 emissions compared to other materials. The higher promotion of wood in construction and interior design and encouragement of the use of wood raw materials in production is needed because they

contribute to environmental protection. By increasing the quality of individual and overall life of the population, the increase in well-being is measured. To achieve sustainable development on a global scale level, it is necessary to implement systemic changes from the market and politics to institutions and behaviors that support innovations and feel the need to introduce them. Wood and wood products can be used in any form and they can be a good substitute for other products and that they can compete with materials that people think are stronger, stronger, and better quality. The wood industry with its product, process, and business innovations contributes to the achievement of goals of sustainable development and keeping forests and ecosystems healthy. Therefore, the market is important to inform, educate and direct in sustainable development about the importance of using wood, innovations wood products, as well as recycling and reusing them. Rational by using wood and innovations, we can greatly contribute to the reduction of harmful emissions into the atmosphere and in achieving greater energy efficiency and reduced climate change.

6. REFERENCES

[1] United Nations Economic Commission for Europe (UNECE) and the Food and Agriculture Organization of the United Nations (FAO)UNECE/FAO (2021): Forest Products Annual Market Review, 2020-2021. Geneva, pp 1-100

[2] The Agriculture, forestry and fishery statistical book is an online Eurostat publication presenting a summary overview of recent European Union (EU) statistics on agriculture, forestry and fisheries. It is also available in print format and as a downloadable PDF file (latest edition), ISBN 978-92-76-21522-6, doi: 10.2785/143455, Cat. No: KS-FK-20-001-EN-N)

[3] Sustainable Wood for Sustainable World - https://www.fao.org/forestry/sustainable-wood/en/

[4] Salzman, J.; Bennett, G.; Carroll, N.; Goldstein, A.; Jenkins, M. The Global Status and Trends of Payments for Ecosystem Services. Nat. Sustain. 2018, 1, 136–144

[5] Hassegawa, M., Karlberg, A., Hertzberg, M., & Verkerk, P. J. (2022). Innovative forest products in the circular bioeconomy. Open Research Europe, 2, 19

[6] Hurmekoski, E.; Jonsson, R.; Korhonen, J.; Jänis, J.; Mäkinen, M.; Leskinen, P.; Hetemäki, L. (2018): Diversification of the Forest Industries: Role of New Wood-Based Products. Can. J. For. Res. 48, 1417–1432

[7] Maximo, Y. I., Hassegawa, M., Verkerk, P. J., & Missio, A. L. (2022). Forest bioeconomy in Brazil: potential innovative products from the forest sector. Land, 11(8), 1297

[8] Brundtland, G. H. (1987). Our common future—Call for action. Environmental conservation, 14(4), 291-294

[9] Shrivastava, P.; & Hart, S. (1995): Creating sustainable corporations. Business strategy and the environment, 4(3), 154-165

[10] Zinkhan, G. M.; & Carlson, L. (1995): Green advertising and the reluctant consumer. Journal of advertising, 24(2), 1-6

[11] Think Wood - https://www.thinkwood.com/sustainable-architecture-design

[12] Chitra, K. (2007). "In search of the green consumers: A perceptual study," Journal of Services Research (1), 173-191

[13] Vlosky, R. P., Ozanne, L. K., and Fontenot, R. J. (1999). "A conceptual model of US consumer willingness-to-pay for environmentally certified wood products," J. Consum. Mark. 16(2), 122-140. DOI: 10.1108/07363769910260498

[14] Xiaolei, C., Jun, S., and Bing, L. (2014). "Customer preferences for kitchen cabinets in China Using conjoint analysis," Journal of Chemical and Pharmaceutical Research 6(2), 14-22

[15] Anderson, R. C., and Hansen, E. N. (2004). "The impact of environmental certification on preferences for wood furniture: A conjoint analysis approach," Forest Prod. J. 54(3), 42-50

[16] Pirc, A., Moro, M., Ojurović, R., and Bublić, A. (2008). "Consumer decision – Croatian furniture: YES or NO?," in: Proceedings of the International Scientific Conference Ambienta, Zagreb, Croatia, pp. 39-44

[17] Maťová, H., and Kaputa, V. (2017). “Green preferences of generation Y,” in: Proceedings of the 17th International Scientific Conference – Globalization and its socio-economic consequences, Rajecke Teplice, Slovakia, pp. 1510-1517
[18] Kaputa, V., and Šupín, M. (2010). “Consumer preferences for furniture,” in: Proceedings of the 3rd International Scientific Conference – Wood Processing and Furniture Manufacturing, Vyhne, Slovakia, pp. 81-90
[19] Koszewska, M., Militki, J., Mizsey, P., and Benda-Prokeinova, R. (2017). “Comparative analysis of sustainable consumption and production in Visegrad region-conclusions for textile and clothing sector,” in: IOP Conference Series: Materials Science and Engineering, IOP Publishing, Vol. 254, No. 20, p. 202003
[20] Markström, E., Kuzman, M. K., Bystedt, A., Sandberg, D., & Fredriksson, M. (2018). Swedish architect’s view of engineered wood products in buildings. Journal of Cleaner Production, 181, 33–41.
[21] Sandberg, D. (2016). Additives in wood products—today and future development. Environmental impacts of traditional and innovative forest-based Bioproducts, 105-172
[22] Ramage, M. H., Burridge, H., Busse-Wicher, M., Fereday, G., Reynolds, T., Shah, D. U., & Scherman, O. (2017). The wood from the trees: The use of timber in construction. Renewable and Sustainable Energy Reviews, 68, 333-359
[23] Mamić, D., & Domljan, D. (2023). Design of Decorative Wooden Wall Panels from Sliced Pedunculate Slavonian Oak (Quercus robur L.) from Veneer Production Residue. Forests, 14(2), 414
[24] Michael David Burnard & Andreja Kutnar (2020) Human stress responses in office-like environments with wood furniture, Building Research & Information, 48:3, 316-330, DOI: 10.1080/09613218.2019.1660609